

MATERIALS PHYSICS AND MECHANICS

Vol. 53, No. 3, 2025

MATERIALS PHYSICS AND MECHANICS

Principal Editors:

Alexander Belyaev

Institute for Problems in Mechanical Engineering of the Russian Academy of Science (RAS), Russia

Andrei Rudskoi

Peter the Great St. Petersburg Polytechnic University, Russia

Founder and Honorary Editor: Ilya Ovid'ko (1961-2017)

Institute for Problems in Mechanical Engineering of the Russian Academy of Sciences (RAS), Russia

Associate Editor:

Anna Kolesnikova

Institute for Problems in Mechanical Engineering of the Russian Academy of Sciences (RAS), Russia

Artem Semenov

Peter the Great St. Petersburg Polytechnic University, Russia

Editorial Board:

S.V. Bobylev

Institute for Problems in Mechanical Engineering (RAS), Russia
A.B. Freidin

Institute for Problems in Mechanical Engineering (RAS), Russia D.M. Klimov

Institute of Problems of Mechanics (RAS), Russia

S.A. Kukushkin

Institute for Problems in Mechanical Engineering (RAS), Russia

A.I. Melker

Peter the Great St. Petersburg Polytechnic University, Russia

R.R. Mulyukov

Institute for Metals Superplasticity Problems (RAS), Russia

A.E. Romanov

Ioffe Institute (RAS), Russia

A.G. Sheinerman

Institute for Problems in Mechanical Engineering (RAS), Russia

E.C. Aifantis

Aristotle University of Thessaloniki, Greece

U. Balachandran

Argonne National Laboratory, USA

G.-M. Chow

National University of Singapore, Singapore

G. Kiriakidis

IESL/FORTH, Greece

N.M. Pugno

Politecnico di Torino, Italy

A.M. Sastry

University of Michigan, Ann Arbor, USA

K. Zhou

Nanyang Technological University, Singapore

A.I. Borovkov

Peter the Great St.Petersburg Polytechnic University, Russia

I.G. Goryacheva

Institute of Problems of Mechanics (RAS), Russia

G.E. Kodzhaspirov

Peter the Great St. Petersburg Polytechnic University, Russia

V.P. Matveenko

Institute of Continuous Media Mechanics (RAS), Russia

Yu.I. Meshcheryakov

Institute for Problems in Mechanical Engineering (RAS), Russia

Yu.V. Petrov

St. Petersburg State University, Russia

N.V. Skiba

Institute for Problems in Mechanical Engineering (RAS), Russia

R.Z. Valiev

Ufa State Aviation Technical University, Russia

K.E. Aifantis

University of Florida, USA

A. Bellosi

Research Institute for Ceramics Technology, Italy

D. Hui

University of New Orleans, USA

T.G. Langdon

University of Southampton, U.K.

B.B. Rath

Naval Research Laboratory, USA

B.A. Schrefler

University of Padua, Italy

"Materials Physics and Mechanics" Editorial Office:

Phone: +7(812)552 77 78, ext. 224 E-mail: mpmjournal@spbstu.ru Web-site: http://www.mpm.spbstu.ru

International scientific journal "Materials Physics and Mechanics" is published by Peter the Great St. Petersburg Polytechnic University in collaboration with Institute for Problems for Mechanical Engineering in the Russian Academy of Sciences in both hard copy and electronic versions. The journal provides an international medium for the publication of reviews and original research papers written in English and focused on the following topics:

- Mechanics of composite and nanostructured materials.
- Physics of strength and plasticity of composite and nanostructured materials.
- Mechanics of deformation and fracture processes in conventional materials (solids).
- Physics of strength and plasticity of conventional materials (solids).
- Physics and mechanics of defects in composite, nanostructured, and conventional materials.
- Mechanics and physics of materials in coupled fields.

Owner organizations: Peter the Great St. Petersburg Polytechnic University; Institute of Problems of Mechanical Engineering RAS.

Materials Physics and Mechanics is indexed in Chemical Abstracts, Cambridge Scientific Abstracts, Web of Science Emerging Sources Citation Index (ESCI) and Elsevier Bibliographic Databases (in particular, SCOPUS).

© 2025, Peter the Great St. Petersburg Polytechnic University © 2025, Institute for Problems in Mechanical Engineering RAS



МЕХАНИКА И ФИЗИКА МАТЕРИАЛОВ

Materials Physics and Mechanics

Том 53, номер 3, 2025 год

Учредители:

Редакционная коллегия журнала

Главный редактор

д.т.н., академик РАН А.И. Рудской

Санкт-Петербургский политехнический университет Петра Великого

Главный научный редактор

д.ф.-м.н., чл.-корр. РАН А.К. Беляев

Институт проблем машиноведения Российской академии наук (РАН)

Основатель и почетный редактор

д.ф.-м.н. И.А. Овидько (1961-2017)

Институт проблем машиноведения Российской академии наук (РАН)

Ответственные редакторы

д.ф.-м.н. А.Л. Колесникова

Институт проблем машиноведения

Российской академии наук (РАН)

д.ф.-м.н. А.С. Семенов

Санкт-Петербургский политехнический университет Петра Великого

Международная редакционная коллегия:

д.ф.-м.н. С.В. Бобылев

Институт проблем машиноведения РАН, Россия д.ф.-м.н., проф. Р.З. Валиев

Уфимский государственный технический университет, Россия

д.ф.-м.н., академик РАН Д.М. Климов

Институт проблем механики РАН, Россия

д.ф.-м.н., проф. С.А. Кукушкин

Институт проблем машиноведения РАН, Россия

д.ф.-м.н., проф. А.И. Мелькер

Санкт-Петербургский политехнический ун-т Петра Великого, Россия д.ф.-м.н., чл.-корр. РАН Р.Р. Мулюков

Институт проблем сверхпластичности металлов РАН, Россия

д.ф.-м.н., проф. А.Е. Романов

Физико-технический институт им. А.Ф. Иоффе РАН, Россия

д.ф.-м.н., проф. А.Б. Фрейдин

Институт проблем машиноведения РАН, Россия

Prof., Dr. E.C. Aifantis

Aristotle University of Thessaloniki, Greece

Dr. U. Balachandran

Argonne National Laboratory, USA

Prof., Dr. G.-M. Chow

National University of Singapore, Singapore

Prof., Dr. G. Kiriakidis

IESL/FORTH, Greece Prof., Dr. N.M. Pugno

Politecnico di Torino, Italy

Prof., Dr. A.M. Sastry

University of Michigan, Ann Arbor, USA

Prof., Dr. K. Zhou

Nanyang Technological University, Singapore

к.т.н., проф. А.И. Боровков

Санкт-Петербургский политехнический ун-т Петра Великого, Россия

д.ф.-м.н., академик РАН И.Г. Горячева

Институт проблем механики РАН, Россия

л.т.н., проф. Г.Е. Коджаспиров

Санкт-Петербургский политехнический ун-т Петра Великого, Россия

д.ф.-м.н., академик РАН В.П. Матвеенко

Институт механики сплошных сред РАН, Россия

д.ф.-м.н., проф. Ю.И. Мещеряков

Институт проблем машиноведения РАН, Россия

д.ф.-м.н., академик РАН Ю.В. Петров

Санкт-Петербургский государственный университет, Россия

д.ф.-м.н. Н.В. Скиба

Институт проблем машиноведения РАН, Россия

д.ф.-м.н. **А.Г. Шейнерман**

Институт проблем машиноведения РАН, Россия

Dr. K.E. Aifantis

University of Florida, USA

Dr. A. Bellosi

Research Institute for Ceramics Technology, Italy

Prof., Dr. D. Hui

University of New Orleans, USA

Prof., Dr. T.G. Langdon

University of Southampton, UK

Dr. B.B. Rath

Naval Research Laboratory, USA

Prof., Dr. B.A. Schrefler

University of Padua, Italy

Тел.: +7(812)552 77 78, доб. 224 E-mail: mpmjournal@spbstu.ru Web-site: http://www.mpm.spbstu.ru

Тематика журнала

Международный научный журнал "Materials Physics and Mechanics" издается Санкт-Петербургским политехническим университетом Петра Великого в сотрудничестве с Институтом проблем машиноведения Российской академии наук в печатном виде и электронной форме. Журнал публикует обзорные и оригинальные научные статьи на английском языке по следующим тематикам:

- Механика композиционных и наноструктурированных материалов.
- Физика прочности и пластичности композиционных и наноструктурированных материалов.
- Механика процессов деформации и разрушения в традиционных материалах (твердых телах).
- Физика прочности и пластичности традиционных материалов (твердых тел).
- Физика и механика дефектов в композиционных, наноструктурированных и традиционных материалах.
- Механика и физика материалов в связанных полях.

Редколлегия принимает статьи, которые нигде ранее не опубликованы и не направлены для опубликования в другие научные издания. Все представляемые в редакцию журнала "Механика и физика материалов" статьи рецензируются. Статьи могут отправляться авторам на доработку. Не принятые к опубликованию статьи авторам не возвращаются.

Журнал "Механика и физика материалов" ("Materials Physics and Mechanics") включен в систему цитирования Web of Science Emerging Sources Citation Index (ESCI), SCOPUS u РИНЦ.

Contents

Contact problems with a stamp in the form of an acute-angled wedge acting on an anisotropic composite layer V.A. Babeshko, O.V. Evdokimova, O.M. Babeshko, V.S. Evdokimova	1-8
Static and dynamic analysis of trapezoidal cantilever plates E. Kumari, B. Choudhary	9-23
Enhancing EDM performance of Monel-400 super alloy through process parameter optimization: RSM-based experimental and microstructural analysis M.R. Panda, S.K. Mishra, P.K. Sahoo	24-36 5
Effect of traverse speed on three-point bending behavior and surface quality of AA5083-H111 friction stir welds M.A.A. Hanifi, M. Zemri, M. Merzoug	37-47
Polymer weld characterization and defect detection through advanced image processing techniques G.C. Ganesha, C. Mukti, S. Arungalai Vendan, R. Sharanabasavaraj	48-68
General model of the carbonate acidizing process with different injection rate R.M. Ganopolskij, K.M. Fedorov, A.E. Folomeev	69-78
Influence of alkali treatment and fiber percentage on the mechanical and thermophysical properties of gypsum composites filled with hemp fiber K. Sunil Ratna Kumar, S.B.R. Devireddy, T. Gopala Rao, B. Sudheer Kumar, K. Bala F.	79–93 Prasad
Temperature-dependent phase leg and non-local thermoelastic damping and frequency shift in thermoelastic plates R. Kumar, P. Singhal	94-115
Creep and long-term strength of high-entropy alloys R.R. Saitova, A.R. Arutyunyan	116-121
Evaluating the impact of functionalized graphene integration on thermal properties of CFRP composites D.N. Choudhury, S.K. Panda	122-139
Structural and thermal changes in the polyaniline lead sulphide nanocomposite J.B. Bhaiswar, S.P. Dongre, D. Meghe	140-148
Effect of electromagnetic waves on the thermoelastic Hookean unbounded domains based on fractional Fourier law N. Samir, M.A. Abdou, E. Awad	149-164

Elastic deformation and elastic wave velocity in metals (Au, Cu) and interstitial 165-176 alloy (CuSi) with FCC structure

Q.H. Nguyen, K.V. Tran, S.G.K. Quach, Q.T. Doan, N.P.A. Nguyen, T.S.M. Nguyen, D.H. Nguyen, A.T. Tran

Комплексное исследование вязкоупругопластических свойств нанокомпозитов 177–218 с повышенной износостойкостью на основе Фторопласта-4. Часть 1

А.В. Хохлов, А.А. Охлопкова, С.А. Слепцова, Н.Н. Лазарева, П.Н. Тарасова, А.В. Бабайцев, А.В. Шапорев, В.В. Гулин

Submitted: February 15, 2025 Revised: March 28, 2025 Accepted: June 6, 2025

Contact problems with a stamp in the form of an acute-angled wedge acting on an anisotropic composite layer

V.A. Babeshko ^{1 \subseteq (1)}, O.V. Evdokimova ², O.M. Babeshko ^{1 (1)}, V.S. Evdokimova ¹

ABSTRACT

In this paper, for the first time, the block element method provides an exact solution to the contact problem of the action of a rigid wedge-shaped stamp with an acute angle on a layer of composite material having arbitrary anisotropy. The research is based on the application of the block element method. In comparison with strip stamps, it contains an additively additional term describing the concentration of contact stresses at the angular point, that is, at the top of the stamp. The calculation of the indicator of the peculiarity of the concentration of contact stresses at this point is close to the values performed by numerical methods in a number of works. In the zone considered away from the top of the stamp, the exact solution turns into a solution for the case of a semi-infinite stamp. The developed method is applicable to composites of arbitrary anisotropies arising in linearly elastic materials and crystals of any cross sections that allow the construction of the Green function, and hence the two-dimensional Wiener-Hopf integral equations. The exact solution of two-dimensional Wiener-Hopf integral equations has made it possible, thanks to fractality, homeomorphism of stamp carriers and solution functions, to construct exact solutions to contact problems for wedge-shaped, sharply angled stamps.

KEYWORDS

contact problems • anisotropy • composite • Wiener-Hopf integral equation • block element • factorization wedge-shaped region with an acute angle

Funding. The work was carried out with the financial support of the Russian Science Foundation and the Kuban Science Foundation, regional project 24-11-20006.

Citation: Babeshko VA, Evdokimova OV, Babeshko OM, Evdokimova VS. Contact problems with a stamp in the form of an acute-angled wedge acting on an anisotropic composite layer. *Materials Physics and Mechanics*. 2025;53(3): 1–8.

http://dx.doi.org/10.18149/MPM.5332025_1

Introduction

Mixed tasks, including contact tasks, play an important role in a wide variety of practice areas. They arise in the problems of strength and fracture [1], wave propagation in elastic bodies [2], acoustics [3], non-destructive testing methods [4], the theory of scattering of electromagnetic waves and the creation of an electronic element base [5], the theory of waves in a liquid [6,7], geophysics [8], tribology [9,10]. Studies of anisotropic problems, including for composites and contact problems, were carried out using both analytical and numerical methods in [9–27]. It should be noted that the transition in spatial problems to anisotropic media, and especially to composites, is associated with significant difficulties due to the complexity of differential equations describing such media. For the cases of layered media, the construction of Green's functions is carried out using integral Fourier transforms. Difficulties arise when calculating the roots of a



¹ Kuban State University, Krasnodar, Russia

² Southern Scientific Center of the Russian Academy of Sciences, Rostov-on-Don, Russia

[™] babeshko41@mail.ru

characteristic equation and when studying the properties of Green's functions, in particular, determining all its features. In isotropic cases, this can be done, and in anisotropic cases, for composites, it is almost impossible. To illustrate this, the form of the integral equation of the contact problem is given below for an orthotropic layer of thickness. It is assumed that the friction-free layer lies on a rigid base and a rigid friction-free stamp acts on the layer [15]. The orthotropic layer is characterized by a state matrix of the form:

$$\boldsymbol{C} = \begin{bmatrix} \begin{bmatrix} C_{11} & C_{12} & C_{13} & 0 & 0 & 0 \\ C_{21} & C_{22} & C_{23} & 0 & 0 & 0 \\ C_{31} & C_{32} & C_{33} & 0 & 0 & 0 \\ 0 & 0 & 0 & C_{44} & 0 & 0 \\ 0 & 0 & 0 & 0 & C_{55} & 0 \\ 0 & 0 & 0 & 0 & 0 & C_{66} \end{bmatrix}.$$

The integral equation is represented in the form:

$$\begin{split} & \textit{K}q = \iint_{\Omega} \ k(x - \xi, y - \eta) q(\xi, \eta) d\xi d\eta = f(x, y), \ x, y \in \Omega, \\ & k(x, y) = \frac{1}{4\pi^2} \int_{-\infty}^{\infty} \int_{-\infty}^{\infty} K(\alpha, \beta) e^{-i(\alpha x + \beta y)} d\alpha d\beta, \\ & K(\alpha, \beta) = G_1(\alpha, \beta) G_2^{-1}(\alpha, \beta), \\ & G_k(\alpha, \beta) = det \|g_{mn}(k, \alpha, \beta)\|, \\ & g_{1n}(1, \alpha, \beta) = g_{1n}(2, \alpha, \beta) = i\alpha \gamma_5 \Big(v_n^2 B_n^{(1)} - B_n^{(3)} \Big) sh v_n, \\ & g_{2n}(1, \alpha, \beta) = g_{2n}(2, \alpha, \beta) = i\beta \gamma_4 (v_n^2 B_n^{(2)} - B_n^{(3)}) sh v_n, \\ & g_{3n}(1, \alpha, \beta) = B_n^{(3)} sh v_n, \\ & g_{3n}(2, \alpha, \beta) = v_n (B_n^{(3)} + \gamma_7 \alpha^2 B_n^{(1)} + \gamma_8 \beta^2 B_n^{(2)}) ch v_n, \\ & \gamma_4 = \frac{c_{44}}{c_{33}}, \quad \gamma_5 = \frac{c_{55}}{c_{33}}, \quad \gamma_7 = \frac{c_{13}}{c_{33}}, \quad \gamma_8 = \frac{c_{23}}{c_{33}}. \end{split}$$

The parameters, three of which are taken to describe the core, are the roots of a complex equation [15]: $b_0 v^6 + b_2 v^4 + b_4 v^2 + b_6 = 0$. Obviously, the relations turned out to be extremely complex and the use of previously developed methods for solving them, using detailed properties of the kernels of integral equations [12–17], becomes practically impossible. However, the creation of new structural materials, including anisotropic composites, leads to the need to apply solutions to contact problems in engineering practice, and demands the greatest possible proximity of the approximate solutions obtained to the exact ones, including in non-classical fields. For example, the approximation of solutions by splines, boundary elements, and eigenfunctions loses some important properties of contact stresses in approximate solutions. In some cases, they do not describe the concentration of contact stresses at the stamp boundaries, especially at the corner points. The tendency of the malleability of the medium is not always caught when the size of the stamps is reduced. A special place is occupied by contact problems in areas whose boundaries have angular sets. In [24], an exact solution of the contact problem in the quarter plane is constructed for the isotropic case. This approach has proved useful for constructing a solution to this contact problem for the anisotropic case. The research is based on the block element method, in an application for integral equations. He allowed the problems formulated above for anisotropic problems to be bypassed and transferred to the problems of calculating contour integrals, which is already quite simple to implement numerically, and something can be studied asymptotically.

Setting the task

The contact problems of the action of an absolutely rigid stamp on a multilayer medium in the area of a quarter plane (Fig. 1) [24], and in an acute-angled wedge (Fig. 2), are considered.

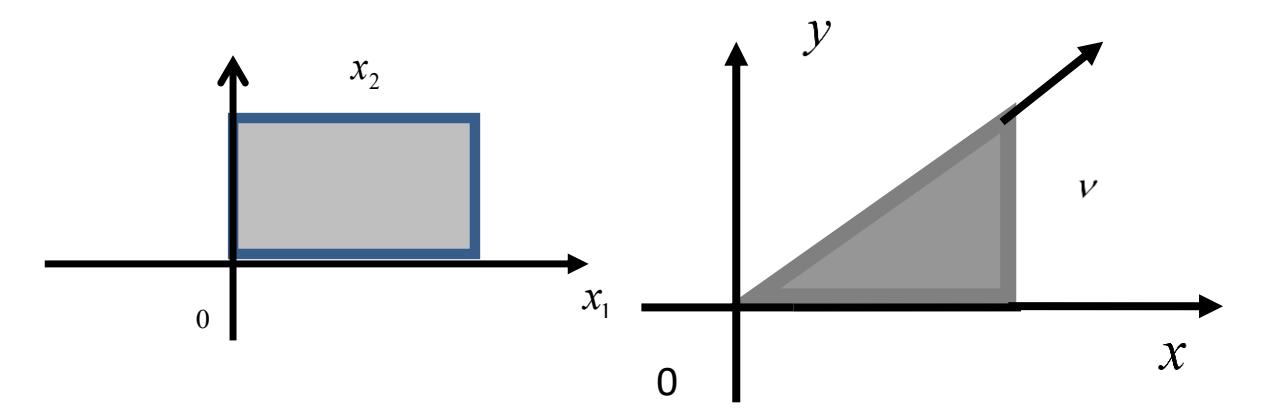


Fig. 1. The figure shows a part of the unlimited area of the first quadrant occupied by the stamp

Fig. 2. The contact area of the sharp-angled stamp, with the angle of the ν

It is assumed that the multilayer medium is an anisotropic composite for which the Green's function is constructed. With its help, the integral equation of the contact problem is obtained. Methods for constructing Green's functions for anisotropic media are described in sufficient detail in [12-17]. Their peculiarity is the complexity of the kernels of the integral equations of contact problems, which leads to significant complications of the methods of their solution. This is reflected in the complex nature of the stress-strain state of the medium at the boundary and in the inner region. In [9-17], the construction of Green's functions for a sufficiently large set of media of complex rheology, including anisotropic composites, is considered. In [12-14], the behavior of a number of surface characteristics for various layered media used in engineering practice was studied. In a number of works, approximate methods for solving mixed problems for such materials have been developed. At the same time, as practice shows, approximate methods do not always catch all the features of solving contact problems. In this regard, the construction of exact solutions allows us to develop approximate methods in such a way that they are consistent with correctly reflecting all aspects of the behavior of the stress-strain state of the contact problem. This is especially important in contact problems considered in non-classical fields, when the stamp boundaries contain angular points. With this in mind, an integral equation is considered, the properties of the core of which cover a wide range of types of anisotropic composites. Fourier transforms of the kernels of integral equations are just analytical functions that have a certain asymptotic behavior at infinity and do not have special points on each of the real axes. The Wiener-Hopf integral equation, given in the first quadrant [24], Fig. 1, is considered. It has the form:

$$Kq = \int_{0}^{\infty} \int_{0}^{\infty} k(x - \xi, y - \eta) q(\xi, \eta) d\xi d\eta = f(x, y), \quad 0 \le x \le \infty, \quad 0 \le y \le \infty,$$

$$k(x, y) = \frac{1}{4\pi^{2}} \int_{\Gamma_{1}} \int_{\Gamma_{2}} K(\alpha, \beta) e^{-i(\alpha x + \beta y)} d\alpha d\beta,$$

$$Q(\alpha, \beta) = \int_{0}^{\infty} \int_{0}^{\infty} q(\xi, \eta) e^{i(\alpha \xi + \beta \eta)} d\xi d\eta \int_{\Gamma_{1}},$$

$$F(\alpha, \beta) = \int_{0}^{\infty} \int_{0}^{\infty} f(\xi, \eta) e^{i(\alpha \xi + \beta \eta)} d\xi d\eta.$$

$$(1)$$

The function $K(\alpha, \beta)$, which is generally complex-valued, is generated by solving an anisotropic boundary value problem in a multilayer medium, is continuous and summable on the axes for both arguments, with behavior at infinity of the form:

$$K(\alpha, \beta) = O(\alpha^{-1}), \ \beta = \text{const}, \ K(\alpha, \beta) = O(\beta^{-1}), \ \alpha = \text{const}, \ |\alpha|, \ |\beta| \to \infty.$$
 (2)

The solution of the integral equation

The contours Γ_1 , Γ_2 are taken in accordance with the implementation of the Mandelstam principle [14]. The uniqueness theorems are valid for integral equation (1) [14]. The research carried out in [24,25] made it possible by the method of factorization and block element to construct an exact solution of the integral equation (1), which is given by the theorem: under the conditions of uniqueness, the solution of the integral equation (1) for a function summable on a semi-axis and having a continuous first derivative is given by the equation:

$$q(x,y) = \frac{1}{4\pi^2} \int_{-\infty}^{\infty} \int_{-\infty}^{\infty} Q(\alpha,\beta) e^{-i(\alpha x + \beta y)} d\alpha d\beta.$$
 (3)

The designation is accepted here:

$$Q(\alpha,\beta) = K^{-1}F - \frac{1}{2} \left[K_{+\alpha}^{-1} \left\{ K_{-\alpha}^{-1}F \right\}_{-\alpha} + K_{+\beta}^{-1} \left\{ K_{-\beta}^{-1}F \right\}_{-\beta} + K_{+\alpha+\beta}^{-1} \left\{ K_{-\alpha}^{-1}F \right\}_{+\alpha} \right\}_{-\beta} + K_{+\beta+\alpha}^{-1} \left\{ K_{+\beta-\alpha}^{-1} \left\{ K_{-\beta}^{-1}F \right\}_{+\beta} \right\}_{-\alpha} \right].$$

$$(4)$$

The operators in curly brackets are described in detail in [14] and have the form:

$$\{G(\alpha,\beta)\}_{+\alpha} = \frac{1}{2\pi i} \int_{\Gamma_{1}} \frac{G(\xi,\beta)}{\xi-\alpha} d\xi, \quad \alpha \in \Pi_{\alpha}^{+}, \quad \{G(\alpha,\beta)\}_{-\alpha} = -\frac{1}{2\pi i} \int_{\Gamma_{1}} \frac{G(\xi,\beta)}{\xi-\alpha} d\xi, \quad \alpha \in \Pi_{\alpha}^{-},$$

$$\{G(\alpha,\beta)\}_{+\beta} = \frac{1}{2\pi i} \int_{\Gamma_{2}} \frac{G(\alpha,\eta)}{\eta-\beta} d\eta, \quad \beta \in \Pi_{\beta}^{+}, \quad \{G(\alpha,\beta)\}_{-\beta} = -\frac{1}{2\pi i} \int_{\Gamma_{2}} \frac{G(\alpha,\eta)}{\eta-\beta} d\eta, \quad \beta \in \Pi_{\beta}^{-},$$

$$K_{+\alpha}(\alpha,\beta) = \exp \frac{1}{2\pi i} \int_{\Gamma_{1}} \frac{\ln K(\xi,\beta)}{\xi-\alpha} d\xi, \quad \alpha \in \Pi_{\alpha}^{+},$$

$$K_{-\alpha}(\alpha,\beta) = \exp \left(-\frac{1}{2\pi i} \int_{\Gamma_{1}} \frac{\ln K(\xi,\beta)}{\xi-\alpha} d\xi\right), \quad \alpha \in \Pi_{\alpha}^{-},$$

$$K_{+\beta}(\alpha,\beta) = \exp \frac{1}{2\pi i} \int_{\Gamma_{2}} \frac{\ln K(\alpha,\eta)}{\eta-\beta} d\eta, \quad \beta \in \Pi_{\beta}^{+},$$

$$K_{-\beta}(\alpha,\beta) = \exp \left(-\frac{1}{2\pi i} \int_{\Gamma_{2}} \frac{\ln K(\alpha,\eta)}{\eta-\beta} d\eta\right), \quad \beta \in \Pi_{\beta}^{-}.$$

$$(5)$$

Here Π_{α}^+ , Π_{α}^- are the complex areas above, plus, and below, minus, the contour Γ_1 , and are the areas Π_{β}^+ , Π_{β}^- above, plus, and below, minus, the contour Γ_2 , respectively.

Proof. We show that the integral equation (1) is exactly satisfied by the functions (3) and (4). We introduce the function (3) into the integral equation (1), represented as: $Kq = \frac{1}{4\pi^2} \int_0^\infty \int_0^\infty \int_{-\infty}^\infty \int_{-\infty}^\infty K(\alpha,\beta) e^{-i[\alpha(x-\xi)+\beta(y-\eta)]} q(\xi,\eta) d\xi d\eta d\alpha d\beta = f(x,y).$

After using the notation (1), we get the representation: $\mathbf{K}q = \frac{1}{4\pi^2} \int_{-\infty}^{\infty} \int_{-\infty}^{\infty} K(\alpha,\beta) Q(\alpha,\beta) e^{-i(\alpha x + \beta y)} d\alpha d\beta = f(x,y)$. Let's add from Eq. (4) to this formula $Q(\alpha,\beta)$ and examine the integral on the left. As a result of a simple analysis of the exclusion of terms that turn the integral to zero, we are convinced that the ratio is obtained: $\mathbf{K}q = \frac{1}{4\pi^2} \int_{-\infty}^{\infty} \int_{-\infty}^{\infty} e^{-i(\alpha x + \beta y)} F(\alpha,\beta) d\alpha d\beta = f(x,y)$. This proves the theorem.

Investigation of the properties of the solution

1. In the solution presented by Eq. (4), the first term on the right forms a forced component of the solution describing it in the zone farthest from the boundaries of the

quarter plane. Therefore, it does not contain stress concentrations. Note that the degenerate component is formed equally by each of the axes.

2. The second and third terms contain the boundary stress concentrations characteristic of the one-dimensional Wiener-Hopf integral equations [14]. Similar to the one-dimensional case [14], they give features of the form $x^{-\frac{1}{2}}$ and $y^{-\frac{1}{2}}$ on the rectilinear boundaries of the stamp. To study estimates of the behavior of the solution q(x,y) near the boundaries and at the corner point of the stamp, using an estimate of the behavior of the function $Q(\alpha,\beta)$, the following method of estimating the Fourier integral is used.

Estimation of Fourier integrals with a small parameter calculated from continuous functions with the property having the form:

$$\int_{-\infty}^{\infty} u^{\lambda} e^{-iux} S(u) du, \quad m >> 1, \quad S(u) = O(u^{-1}), \quad u >> 1, \quad x \to 0.$$
 (6)

It is obtained by replacing the integration parameter $u=tx^{-1}$. It gives the value: $\int_{-\infty}^{\infty} (tx^{-1})^{\lambda} e^{-it} S(xt^{-1}) x^{-1} dt \sim x^{-\lambda} \int_{-\infty}^{\infty} t^{\lambda} e^{-it} O(t^{-1}) dt \sim O(x^{-\lambda}), \quad Re \ \lambda < 1, \quad x \to 0.$

3. The fourth and fifth terms describe stress concentration at the angular point of the stamp. Below are several examples that reveal properties of solutions to the two-dimensional Wiener-Hopf integral equation that were not previously known.

Example 1. This is the simplest example that shows that the obtained solution (3) turns into an exact solution of the integral equation (1) for the case when Eq. (1) decomposes into one-dimensional equations solved by the traditional one-dimensional method of Wiener-Hopf equations [5]. This happens when there is a separation of variables in the core of integral equation (1), that is $k(x,y)=k_1(x)k_2(y)$. It happens when the Fourier transform has a kernel, called the symbol $K(\alpha,\beta)$ of the integral equation, with the property $K(\alpha,\beta)=K_1(\alpha)K_2(\beta)$. Performing the calculations required by Eq. (4) on the symbol, we find: $K_{+\alpha+\beta}(\alpha,\beta)=K_{1+\alpha+\beta}(\alpha)K_2(\beta)=K_1(\alpha)K_{2+\beta+\alpha}(\beta)=0$. Thus, in Eq. (4), the last two terms on the right disappear and solutions of one-dimensional integral equations remain.

Example 2. Thanks to operators (5) according to Eqs. (3) and (4), the solution of the two-dimensional Wiener-Hopf equation can be constructed for fairly general anisotropic contact problems in an integral form. The construction of the solution q(x, y) values must be obtained by performing numerical inversion of the integral (3) for specific tasks. To identify the properties of the solution of the two-dimensional Wiener-Hopf integral equation, one can use the approach first introduced by W. Koiter for one-dimensional Wiener-Hopf integral equations. In contact tasks, W. Koiter [14] introduced the approximation of the complex kernel of the one-dimensional Wiener-Hopf integral equation by a simpler function to simplify its solution. In the case under consideration, we choose the approximation of the kernel by the function:

$$K(\alpha,\beta) \approx (\alpha^2 + B^2\beta^2 + A^2)^{-\frac{1}{2}} \equiv M(\alpha,\beta), \quad A,B > 0.$$
 (7)

This approximation is anisotropic and satisfies condition (2). We investigate the integral equation (1) with the symbol $M(\alpha, \beta)$. We show the rule of forming the terms of the integrand function $Q(\alpha, \beta)$. When factorizing by some parameter, the rest are on the real axis, although, for accuracy, they should also tend to infinity. Factoring the function $M(\alpha, \beta)$ by parameter onto the upper half-plane, we obtain: $M_{+\alpha}(\alpha, \beta) = \left[\alpha + i(B^2\beta^2 + A^2)^{\frac{1}{2}}\right]^{-\frac{1}{2}} = O(\alpha^{-\frac{1}{2}})$ A > 0.

Factorization of a function $M_{+\alpha}(\alpha,\beta)$ by a parameter β onto an upper complex half-plane can be performed precisely, in integral form, by normalizing $M_{+\alpha}(\alpha,\beta)$ to 1 for $|\beta| \to \infty$. To do this, consider a function tending to unity at. We have: $G(\alpha,\beta) = \sqrt{i}(B^2\beta^2 + c^2)^{\frac{1}{4}}M_{+\alpha}(\alpha,\beta) \to 1$, $|\beta| \to \infty$, c = const, from here: $M_{+\alpha+\beta}(\alpha,\beta) = (B\beta + ic)^{-\frac{1}{4}}exp\frac{1}{2\pi i}\int_{\Gamma_2}\frac{\ln G(\alpha,\eta)}{\eta-\beta}d\,\eta$, $\beta\in\Pi_{\beta}^+$.

From here we get an estimate: $M_{+\alpha+\beta}(\alpha,\beta) \to C(B\beta+ic)^{-\frac{1}{4}} = O(\beta^{-\frac{1}{4}}), \quad |\beta| \to \infty.$ They are evaluated in exactly the same way: $M_{+\beta}(\alpha,\beta) = O(\beta^{-\frac{1}{2}}), \quad M_{+\beta+\alpha}(\alpha,\beta) = O(\alpha^{-\frac{1}{4}}).$ Introducing these estimates in the form $M_{+\beta}^{-1}(\alpha,\beta), \quad M_{+\beta+\alpha}^{-1}(\alpha,\beta)$ on Eq. (6), we obtain, as a result of a simple analysis: $q(x,y) = O(r^{-\frac{3}{4}}), \quad r = \sqrt{x^2 + y^2}.$

The result obtained makes it possible to make a comparison with the previously studied isotropic case using the considered example. Assuming B=1 in Eq. (7), we proceed to the isotropic case considered in [17,24]. Figure 2 shows a graph of the singularities at the top of the wedge for their various values 2θ , $0<\theta<\pi$, approximately calculated in [17]. In Fig. 2, it is necessary to consider the case $\frac{\theta}{\pi}=0.25$ corresponding to the case of a right angle. There is no friction between the stamp and the base for $\varepsilon=0$. Asymptotic approximations of Bessel functions were used for the estimation in [17]. It shows that the value of the contact stress concentration at the angular point obtained in this work $r^{-\frac{3}{4}}$ is close to the value calculated by the approximate method.

Example 3. The described approach is applicable to wedge-shaped stamp of angle ν having solutions in the range $0 \le \nu \le 90^\circ$. The possibility of solving this problem is provided by the application of topological transformations. Topology Recently, it has been increasingly penetrating into various areas of mechanics [28–35]. In this case, to solve the problem of contact problems for sharp-angled stamps, it is necessary to construct a homeomorphic mapping of the topological space generated by the carrier and the function of the sharp-angled stamp and the topological space for the stamp with a right angle. The result is a solution to the integral equation for an acute-angled wedge. In the constructed solution, then, a return is made to the initial parameters describing the coordinates of the acute-angled wedge. One of the tests of the correctness of the constructed solution for an acute-angled die is the exact satisfaction of the integral equation of the contact problem and the values of the contact stress concentration indicators at the angular points of the acute-angled stamps of different angles of the solution. The values of the contact stress concentration at the corner points of the die, calculated by the above method for different angles of the wedge solution, are given in the table. They are close to the values obtained earlier by the approximate method in [17]. The solutions for contact problems for sharp-angled stamps have the form (3), (4), in which it is necessary to introduce the parameters of the inverse mapping of the constructed homeomorphisms for stamps. Omitting the details, we present a table of the features calculated by the described method at the angular point of the wedge-shaped die for different solutions of the wedge angle ν .

Omitting the details, we present a table of calculated features at the angular point of the wedge-shaped die for different solutions of the wedge angle ν . Calculated

indicators of the contact stress characteristics at the angular point of a wedge-shaped die for different solutions of the wedge angle are presented in Table 1. All values are close to those calculated by the approximate method in [17]. The advantage of the obtained result is the representation of contact stresses in the form of decomposition into components that perform a certain role by specifying the values of the concentration of contact stresses under the stamp. This opens up the possibility of controlling the degree of impact of the stamp on the deformable base by selecting the appropriate properties of the stamp sole f(x, y).

Table 1. Calculated indicators of the contact stress characteristics at the angular point of a wedge-shaped die for different solutions of the wedge angle $q(x, y) = O(r^{-\lambda})$

ν	0°	10°	20°	30°	40°	50°	60°	70°	80°	90°
λ	1	0.9608	0.9222	0.8850	0.8498	0.8178	0.7902	0.7687	0.7548	0.7500

Conclusions

In this paper, for the first time, an exact solution of the two-dimensional Wiener-Hopf integral equation is constructed by the factorization method. It allows solving a wide range of contact problems for anisotropic composite materials and obtaining accurate solutions in an integral form. In addition, the method allows us to construct high-precision approximate solutions of contact problems in two-dimensional nonclassical domains, more accurate than those performed by one-dimensional ones [12–17]. This approach replaces, when applied [12–17], the need to detail the symbol of the integral equation in the anisotropic case by calculating contour integrals, which is easily implemented by standard computer programs. The paper presents the most general properties of the solution of this integral equation, which will undoubtedly be enriched in the study of specific problems. The solution can be used both in seismology to identify new precursors of seismic growth in mountainous areas with anisotropic properties of the environment [26], and in engineering practice when designing products using structural materials.

CRediT authorship contribution statement

Vladimir A. Babeshko Sc: writing – review & editing, writing – original draft; Olga V. Evdokimova Sc: writing – original draft; Olga M. Babeshko Sc: writing – original draft; Vladimir S. Evdokimov Sc: writing – original draft.

Conflict of interest

The authors declare that they have no conflict of interest.

References

- 1. Freund LB. Dynamic Fracture Mechanics. Cambridge: Cambridge University Press; 1998.
- 2. Achenbach JD. Wave propagation in Elastic Solids. Amsterdam: North-Holland Pub. Co.; 1973.
- 3. Abrahams ID, Wickham GR. General Wiener-Hopf factorization matrix kernels with exponential phase factors. *Journal of Applied Mathematics*. 1990;50(3): 819–838.
- 4. Norris AN, Achenbach JD. Elastic wave diffusion by a semi infinite crack in a transversely isotropic material. *Journal of Applied Mathematics and Mechanics*. 1984;37(4): 565–580.

- 5. Noble B. Wiener-Hopf method. Moscow: Publishing house of foreign literature; 1962. (In Russian)
- 6. Tkacheva LA. The planar problem of vibrations of a floating elastic plate under the action of periodic external load. *Applied mechanics and technical physics*. 2004;45(3): 420-427. (In Russian)
- 7. Chakrabarti A, George AJ. Solution of a singular integral equation involving two intervals arising in the theory of water waves. *Applied Mathematics Letters*. 1994;7(5): 43–47.
- 8. Davis AMJ. Continental shelf wave scattering by a semi-infinite coastline. *Geophysics, Astrophysics, Fluid Dynamics*. 1987;39(1-2): 25–55.
- 9. Goryacheva IG. Mechanics of frictional interaction. Moscow: Nauka; 2001. (In Russian)
- 10. Goryacheva IG, Meshcheryakova AR. Modeling of accumulation of contact fatigue damage and wear in contact of imperfectly smooth surfaces. *Physical Mesomechanics*. 2022. 25(4): 44–53. (In Russian)
- 11. Bazhenov VG, Igumnov LA. *Methods of boundary integral equations and boundary elements.* Moscow: Fizmatlit; 2008. (In Russian)
- 12. Kalinchuk VV, Belyankova TI. Dynamics of the surface of inhomogeneous media. Moscow: Fizmatlit; 2009. (In Russian)
- 13. Kalinchuk W, Belyankova Tl. Dynamic contact problems for prestressed bodies. Elektrostal: Physical education; 2002. (In Russian)
- 14. Vorovich II, Babeshko VA. Dynamic mixed problems of elasticity theory for nonclassical domains. Moscow: Nauka; 1979. (In Russian)
- 15. Vatulyan AO. Contact problems with adhesion for an anisotropic layer. *Journal of Applied Mathematics and Mechanics*. 1977;41(4): 727–734. (In Russian)
- 16 Kolesnikov VI, Belyak OA. *Mathematical models and experimental studies the basis for the design of heterogeneous antifriction materials*. Moscow: Fizmatlit; 2021. (In Russian)
- 17. Babeshko VA, Glushkov EV, Zinchenko JF. Dynamics of inhomogeneous linear elastic media. Moscow: Nauka; 1989.
- 18. Christensen R. Introduction to the mechanics of composites. Moscow: Mir; 1982. (In Russian)
- 19. Kushch VI. Micromechanics of Composites: Multipole Expansion Approach. Waltham: Elsevier; 2013.
- 20. McLaughlin RA. Study of the differential scheme for composite materials. *International Journal of Engineering Science*. 1977;15(4): 237–244.
- 21. Garces G, Bruno G, Wanner A. Load transfer in short fibre reinforced metal matrix composites. *Acta Materialia*. 2007;55(16): 5389–5400.
- 22. Babeshko VA, Evdokimova OV, Babeshko OM. On the problem of evaluating the behavior of multicomponent materials in mixed boundary conditions in contact problems. *Materials Physics and Mechanics*. 2022;48(3): 379–385.
- 23. Babeshko VA, Evdokimova OV, Babeshko OM. On the influence of multiple surface defects on the behavior of media of different rheology. *Materials Physics and Mechanics*. 2020;37(5): 558–563.
- 24. Babeshko VA, Evdokimova OV, Babeshko OM. The exact solution by a universal method of modeling a contact problem in a quarter plane of a multilayer medium. *Applied Mathematics and Mechanics*. 2022;86(5): 628–637.
- 25. Babeshko VA, Evdokimova OV, Babeshko OM. Exact Solution to the Contact Problem in a Quarter-Plane of a Multilayer Medium by the Universal Simulation Method. *Mechanics of Solids*. 2022;57: 2058–2065. (In Russian)
- 26. Babeshko VA, Evdokimova OV, Babeshko OM. On a mechanical approach to the prediction of earthquakes during horizontal motion of litospheric plates. *Acta Mechanica*. 2018;229: 4727–4739.
- 27. Zaalishvili VB, Melkov DA, Gabaraev AF, Merzlikin TI. Nonlinear vibrations of the soil column according to instrumental and numerical data. *Geology and Geophysics of the South of Russia*. 2021;11(4): 70–82. (In Russian)
- 28. Awrejcewiez J, Krysko VA, Mitskievich SA, Zhigalov MV, Krysko AV. Nonlinear dynamics of heterogeneous shells. Part 1: Statics and dynamics of heterogeneous variable stiffness shells. *International Journal of Non-Linear Mechanics*. 2021;130:103669.
- 29. Edore G. Arhore, Mehdi Yasaee, Iman Dayyani. Comparison of GA and topology optimization of adherend for adhesively bonded metal composite joints. *International Journal of Solids and Structures*. 2021;226–227: 11107.
- 30. Fernandez L, Novotny AA, Prakash R, Sokołowski J. Pollution Sources Reconstruction Based on the Topological Derivative Method. *Applied Mathematics & Optimization*. 2021;84(5): 1493–1525.
- 31. Gonsalves JF, Moreira JBD, Salas RA, Mohammad MG, Wilfredo MR, Emílio CNS. Identification problem of acoustic media in the frequency domain based on the topology optimization method. *Structural and Multidisciplinary Optimization*. 2020;62: 1041–1059.
- 32. Huang M, Lim X, Lei Y, Gu J. Structural damage identification based on modal frequency strain energy assurance criterion and flexibility using enhanced Moth-Flame optimization. *Structures*. 2020;28(1–2): 1119–1136.
- 33. Pena M, Rapun ML. Application of the topological derivation to post-processing infrared time-harmonic thermograms for defect detection. *Journal of Mathematics in Industry.* 2020;10: 4.
- 34. Xavier M, Van Goethem N, Novotny AA. Hydro-mechanical fracture modeling governed by the topological derivatives. *Computer Methods in Applied Mechanics and Engineering*. 2020;365: 112974.
- 35. Babeshko VA, Evdokimova OV, Babeshko OM. Topological Structures of Boundary Value Problems in Block Elements. *Doklady Physics*. 2016;61(10): 510–513.

Submitted: October 6, 2024 Revised: March 25, 2025 Accepted: June 12, 2025

Static and dynamic analysis of trapezoidal cantilever plates

E. Kumari Dp., B. Choudhary

MBM University, Rajasthan, India

[™] emarti.me@mbm.ac.in

ABSTRACT

Static and dynamic behaviour of trapezoidal cantilever plate are analysed in this work using ANSYS software. Static and dynamic analysis of trapezoidal cantilever plate has been carried out and studied the effect of change in taper ratio α_t , aspect ratio a/b and varying tip to root width ratio c/b. It has been observed that at $\alpha_t = 0.6$ and c/b = 0.2, non-dimensional frequency of the trapezoidal cantilever plate is higher side, when both parameters varied. In bending analysis under uniformly distributed load when $\alpha_t = 0.8$ and c/b = 0.8 then tip deflection and stresses will be maximum, whereas under edge load when $\alpha_t = 0.8$ and c/b = 0.2 (smallest tip width) will have maximum deflection and stresses. Hence, present numerical results will be helpful for further researchers and designers to design safe thin-wall structures.

KEYWORDS

trapezoidal cantilever plate • modal analysis • buckling • bending • beam

Acknowledgement. This work is supported by Research Program supported by the Department of Engineering and Technology (Higher Education), India.

Citation: Kumari E, Choudhary B. Static and dynamic analysis of trapezoidal cantilever plates. *Materials Physics and Mechanics*. 2025;53(3): 9–23.

http://dx.doi.org/10.18149/MPM.5332025_2

Introduction

Free vibration analysis of trapezoidal cantilever plates is a topic of interest in structural dynamics and engineering applications such as aircraft wings, turbine blades, balconies, etc. A trapezoidal cantilever plate is a plate with one end fixed and the other end free, and with a non-uniform cross-section that narrows from the fixed end to the free end. The free vibration of such a plate is the natural oscillation that occurs when the plate is subjected to an initial displacement or velocity and then left to vibrate on its own. The natural frequency and mode shape of the plate depend on its geometry, material properties, boundary conditions, and stiffness distribution. Several methods have been proposed in the literature to study the static and dynamic behaviour of trapezoidal cantilever plates, such as transformation of variables, finite element method, Rayleigh-Ritz method, and separation of variables.

Advantages of trapezoidal plate over other types of plates

A trapezoidal cantilever plate is a type of plate that has one end fixed and the other end free. The trapezoidal shape means that the width of the plate decreases from the fixed end to the free end, resulting in a tapered shape geometry. This shape has several advantages over a rectangular or uniform cantilever plate as discussed by [1,2]. Following are some advantages (i) reduced weight and material consumption (that will reduce the inertial forces, damping effects, stress concentration and fatigue failure on the plates;



save costs and resources, and also improve the performance and efficacy of structure); (ii) increased stiffness and strength (especially near the fixed end where the bending moment is maximum and prevent excessive deflection or deformation of the plate and also enhance its load-bearing capacity and durability moreover increased stiffness can also increase the natural frequency and resonance quality factor of the thin-walled structures, which can improve its sensitivity and selectivity for sensing or energy harvesting applications); (iii) improved energy harvesting (trapezoidal shape can improve the energy harvesting capability of the plates, especially when it is coupled with a piezoelectric material; these plates can increase the output voltage and efficiency of the energy harvester by creating a larger strain gradient along the length of the plates). Additionally, the trapezoidal shape can increase the bandwidth and adaptability of the energy harvester by tuning its natural frequency according to different vibration sources or environments.

Applications in different fields of engineering and industry

Trapezoidal cantilever plates have various applications in different fields of engineering such as automotive industry, construction industry, energy industry, biomedical industry, etc as discussed by [3–6]. A trapezoidal cantilever plate can improve the sensitivity and selectivity of this detection method by increasing its stiffness and natural frequency near its fixed end; applications of trapezoidal plate for aircraft wing is shown in Fig. 1. Also, it can also reduce the noise and interference from the environment or other sources by increasing its resonance quality factor and damping ratio.

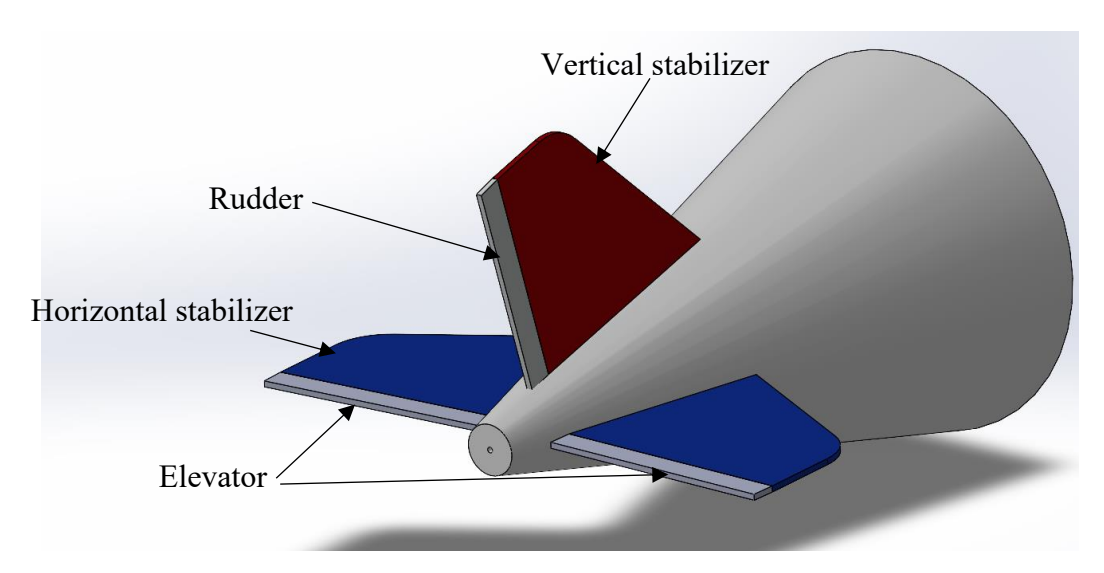


Fig. 1. Applications of trapezoidal plate i.e. plane fin / vertical stablizer

In this communication, authors reviewed the research papers on trapezoidal cantilever plates, focusing on their design, bending, buckling and vibration analysis thin-walled structures. Majidi et al. [3] analysed a cantilever CNT trapezoidal plate and modelled it using FSDT & Generalized differential quadrature method (GDQ). Authors derived the governing equations and boundary conditions using Hamilton's principle. They studied the effect of geometrical parameters, volume fraction and distribution of

CNTs on the natural frequencies of the plate. Numerical results of study showed that adding CNTs to cantilever trapezoidal plates leads to considerable rise in all natural frequencies and in order to increase natural frequencies it is better to increase volume fraction of CNTs and using FG-X pattern for distribution of CNTs. Also, Numerical examples showed that increase in thickness of the plate leads to increase in natural frequencies but increase in width of the plate decreases all natural frequencies and may change sequence of modes.

Jena et al. [4] studied the vibration behaviour of trapezoidal cantilever plate-like composite beams made of a combination of fibre-reinforced polymer (FRP) composite and aluminium alloy using finite element method (FEM). In this study they examined the impact of various geometric parameters, such as taper angle, thickness, and width, as well as material properties on the modal frequencies and mode shapes of the composite beam. Additionally, the results indicated that the modal frequencies and mode shapes were influenced by the thickness and width of the beam, as well as the material properties. Zamani et al. [7] used the first-order shear deformation theory (FSDT) to derive the governing equations of motion for the laminated composites trapezoidal plates. Generalized differential quadrature (GDQ) method was employed for solution of governing equation and determined the natural frequencies and mode shapes of the plates. The effects of different boundary conditions, such as clamped, simply supported, and free, on the vibration behavior of the plates were also investigated.

Wang et al. [8] examined the vibration characteristics of triangular plates with different boundary conditions using finite element method. The findings of the study showed that the boundary conditions had a significant impact on the vibration characteristics of the triangular plates. Specifically, the natural frequencies of the plates decreased as the number of support points increased, and the vibration modes became more complex for plates with more support points. Torabi and Afshari [9] investigated the vibration characteristics of cantilevered trapezoidal thick plate with variable thickness through ANSYS. FSDT was used for kinetic and strain energy; Hamilton's principle used for governing equation and boundary condition. Natural frequency and mode shape are derived numerically using differential quadrature method. As value of the aspect ratio rises, the width of the plate grows which increase both stiffness and mass of the plate but value of the increase in mass is more than the increase in stiffness of the plate.

The analysis of hybrid metal-composite plates has gained significant attention in structural engineering due to their wide-ranging applications and superior mechanical properties. Shokrollahi and Shafaghat [10] introduced an approach for the free vibration analysis of hybrid plates with a trapezoidal platform by incorporating the first-order shear deformation plate theory (FSDT) and the global Ritz method. The proposed algorithm accurately considers the non-classic effects of transverse shear deformation and rotational inertia. Jiang et al. [11] investigated the nonlinear vibration characteristics of trapezoidal plates by incorporating von Karman's geometric nonlinearity through a finite element method. The authors employed Hamilton's principle to establish the equation of motion for each element of the trapezoidal plate, and by assembling these elements, they derived the equation of motion for the composite laminated trapezoidal plate. The study explored the effects of ply angle and length-height ratio on the nonlinear vibration frequency ratios of the composite laminated trapezoidal plates. Through numerical simulations and analysis

of frequency-response curves for different ply angles and harmonic excitation forces, several conclusions are drawn. Overall, this study contributes to the understanding of nonlinear vibration characteristics in composite laminated trapezoidal plates; by utilizing FEM and Hamilton's principle, the authors establish the equation of motion and investigate the effects of ply angle and length-height ratio.

Huang et al. [12] studied the free vibration behaviour of cantilever trapezoidal plates using experimental and numerical methods. They utilize the amplitude-fluctuation electronic speckle pattern interferometry (AF-ESPI) technique with an out-of-plane setup for non-contact and full-field measurement of plate vibrations. Twenty different plate configurations, including triangular and trapezoidal plates, are analysed to measure their first seven vibration modes. The AF-ESPI method enables the determination of resonant frequencies and mode shapes without the need for contact sensors.

Majidi et al. [13] investigated the effect of carbon nanotube (CNT) reinforcements on the flutter boundaries of cantilever trapezoidal plates exposed to yawed supersonic fluid flow. The research utilized the first-order shear deformation theory (FSDT) to model the plate structure and calculates the effective mechanical properties using the extended rule of mixture. The aerodynamic pressure was estimated through the piston theory, and the governing equations and boundary conditions are derived using Hamilton's principle. To obtain numerical solutions for natural frequencies, mode shapes, critical speed, and flutter frequency, the generalized differential quadrature method (GDQM) was employed. The findings reveal that incorporating CNTs enhances the critical speed at which flutter occurs and increases the flutter frequency. It is observed that placing the CNTs away from the middle layer of the plate expands the range of speeds at which flutter is minimized. Additionally, decreasing the width of the plate near the outer edge and adjusting certain angles contribute to improved resistance against flutter. Emelyanov and Kislov [14] determined the state of stresses and lifespan of thin-walled structures under mechanical load in the presence of hydro-chemical medium. Chernyshov et al. [15] considered the three different boundary conditions for rectangular bar to study displacement response and stresses in it and optimized the boundary conditions for rectangular bar. Ropalekar et al. [16] investigated the fatigue strength of composite materials under different loads. Large amplitude flexural vibration behaviour of trapezoidal panels was studied by Kumari and Lal [17] using finite element method. Recently, static and dynamic behaviour of trapezoidal flat and curved panels under various loading and boundary conditions were studied [18-22]. From literature review it is noticed that further research work required to understand the static and dynamic behaviour of cantilever laminated composite trapezoidal plates. Hence, in this article authors investigated the bending, buckling and vibration characteristics of cantilever trapezoidal plates.

Problem formulation

Schematic representation of trapezoidal plate is shown in Fig. 2 with variable thickness. The finite element method based commercial software ANSYS 18.1 is used investigate the bending, buckling and vibration characteristics of trapezoidal panels under different loading and boundary conditions. Eight-node shell 281 is used here to discretize the trapezoidal panel having six degrees of freedom, in which three translational

displacement u_x , u_y , u_z and three rotational θ_x , θ_y and θ_z along and about x-axis, y-axis and z-axis, respectively.

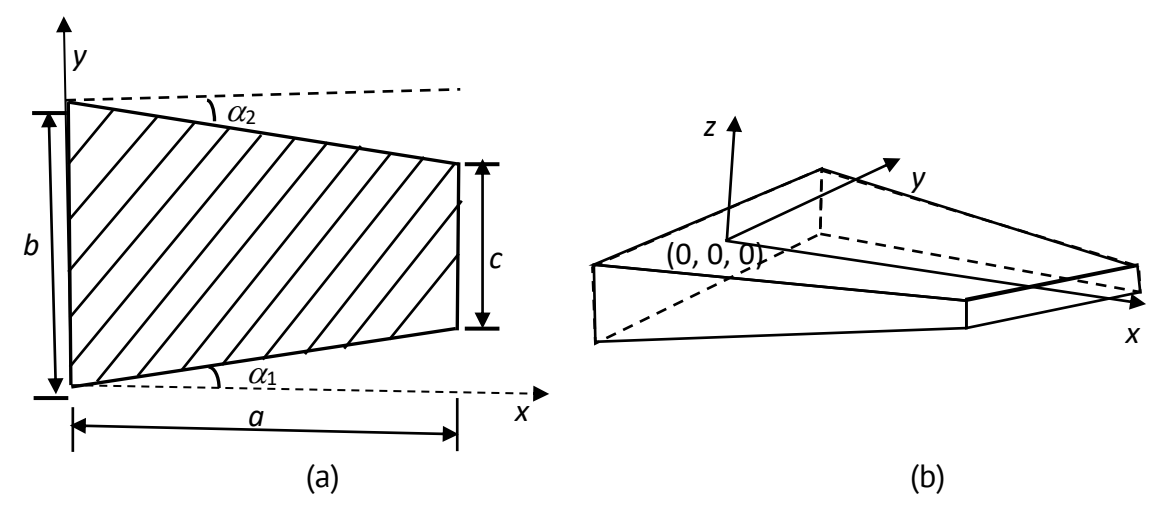


Fig. 2. Geometry of (a) symmetric trapezoidal plate and (b) trapezoidal plate with variable thickness

For a vibrating thin / moderately thick trapezoidal plate as shown in Fig. 2, the strain energy U and kinetic energy T are expressed as:

$$U = \int_0^a \int_0^b \frac{D}{2} \left[\left(\frac{\partial^2 \delta}{\partial x^2} \right)^2 + \left(\frac{\partial^2 \delta}{\partial y^2} \right)^2 + 2\nu \left(\frac{\partial^2 \delta}{\partial x^2} \right) \left(\frac{\partial^2 \delta}{\partial y^2} \right) + 2(1 - \nu) \left(\frac{\partial^2 \delta}{\partial x \partial y} \right)^2 \right] dx dy, \tag{1}$$

$$T = \int_0^a \int_0^b \frac{\rho h}{2} (\dot{\delta})^2 dx dy, \tag{2}$$

where, δ is the displacement vector, $\dot{\delta}$ is the velocity vector, ρ is the mass per unit area, h_0 is the plate thickness, D is the plate flexural rigidity, v is the Poisson's ratio.

For the dynamic analysis equations of motion is expressed by Hamilton's principle: $\int_{t_1}^{t_2} (\delta T - \delta U + \delta W_{NC}) \, dt = 0. \tag{3}$

Here, δT is a first variation in kinetic energy, δU is a first variation in strain energy of conservative force fields, δW is the virtual work of non-conservative force fields.

Bending analysis

Firstly, carried out the bending analysis of trapezoidal cantilever plate under pure compression, pure shear and pure moment and combination of shear and moment using following governing equation:

$$[K_L]\{\delta\} = \{F\},\tag{4}$$

where, $[K_L]$ is the linear stiffness matrix, $\{\delta\}$ is the displacement vector and $\{F\}$ is the force vector.

Static analysis of trapezoidal cantilever panels under various loading conditions has to be conducted to investigate the bending deformation, normal (σ_{xx} , σ_{yy} , σ_{zz}), shear (τ_{xy} , τ_{yz} , τ_{zx}) and principal stresses (σ_{11} , σ_{22} , σ_{33}) in it.

Dynamic analysis

Assumptions:

(a) Quasi-static analysis – inertia forces are negligible: if the smallest time period of forcing function is significantly greater than the largest natural time period of the structure, then dynamics analysis is carried out.

(b) Dynamic analysis – inertia forces are significant, hence included in the analysis: If the smallest time period of forcing function is comparable to the largest natural time period of the structure.

Kinetic energy is:

$$T = \frac{1}{2} \int_{V} (\dot{u}^2 + \dot{v}^2 + \dot{w}^2) \rho dV. \tag{5}$$

For the free vibration analysis of structures, the governing equation of motion might be written as:

$$[M]\{\ddot{\delta}\} + [K_L]\{\delta\} = \{0\},\tag{6}$$

where, [M] is the mass matrix and $\{\ddot{\delta}\}$ is the acceleration vector. Equation (6) is used to calculate the eigenvalues or vibration frequencies, and eigenvector to plot mode shapes as given by [23,24].

Results and Discussion

Bending analysis of trapezoidal cantilever plate

In bending analysis of the trapezoidal cantilever plate (schematic geometry of trapezoidal plate is shown in Fig. 3) carried out to find the tip deflection, normal stress, shear stress and von-mises stress under uniformly distributed load (UDL) and edge load. Here first validation of the bending results done with trapezoidal cantilever plate, then bending results with varying thickness and tip to root width ratio obtained. Loading of the structure is done under uniformly distributed load over the upper face and concentrated loading at the free edge of the cantilever plate.

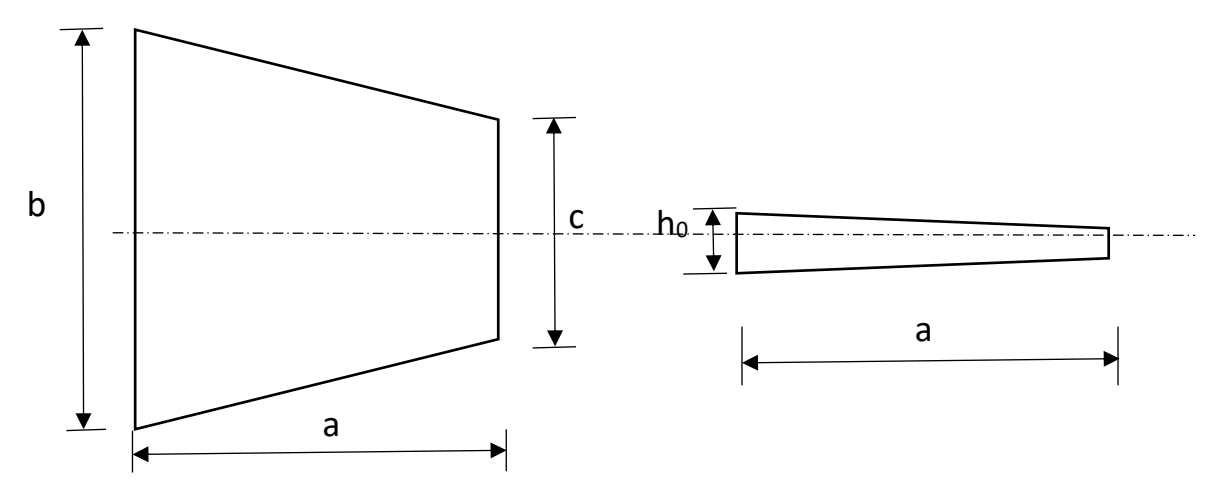


Fig. 3. Trapezoidal plate geometry with varying thickness

Validation of bending results

For validation of the results obtained for *CFCF* ($u = v = w = \theta_x = \theta_y = \theta_z = 0$, along x = 0, a) trapezoidal plate made of isotropic material (v = 0.3) subjected to uniformly distributed load ($q_0 = 30 \times 10^3 \text{ N/m}^2$) is compared with Zhao et al. [25] and Liew and Han [26] as given in Table 1. It is noticed that percentage of error is 13.95 and 11.29 % with Zhao et al. and Liew and Han, respectively. Here, percentage of error is higher because three-dimensional numerical results are compared with two-dimensional results.

Von-Mises stress

Max shear stress

Normal stress

Table 1. Comparison of central deflection of a homogeneous CFCF trapezoidal plate (E = 206 GPa, $\rho = 7800 \text{ kg/m}^3$ and v = 0.3. a/b = 1, c/b = 0.7, $h_0 = 0.2 \text{ m}$) UDL of 30000 N/m²

Reference	Boundary condition	Deflection, m
Present (24 × 28 × 6)	CFCF	8.9314 × 10 ⁻⁷
Zhao et al. [25]	CFCF	7.8379 × 10 ⁻⁷
Liew and Han [26]	CFCF	8.0252 × 10 ⁻⁷

Bending of trapezoidal cantilever plate having constant c/b ratio and variable thickness in x-direction

Next, analysed trapezoidal cantilever plate (*CFFF* such as $u = v = w = \theta_x = \theta_y = \theta_z = 0$, along x = 0) having variable thickness of the plate in x-direction ($h = h_0(1 - \alpha_t(x/a))$, α_t is taper ratio) under uniformly distributed load ($q_0 = 10 \times 10^3 \text{ N/m}^2$) and edge load ($q_0 = 100 \text{ kN}$). By considering following geometric and material properties: $a/h_0 = 15$, $h_0 = 0.5$, c/b = 0.6, v = 0.3, $E = 2 \times 10^5 \text{ MPa}$, $\rho = 7800 \text{ kg/m}^3$, (a) square cantilever plate: a/b = 1 and (b) rectangular cantilever plate: a/b = 3.

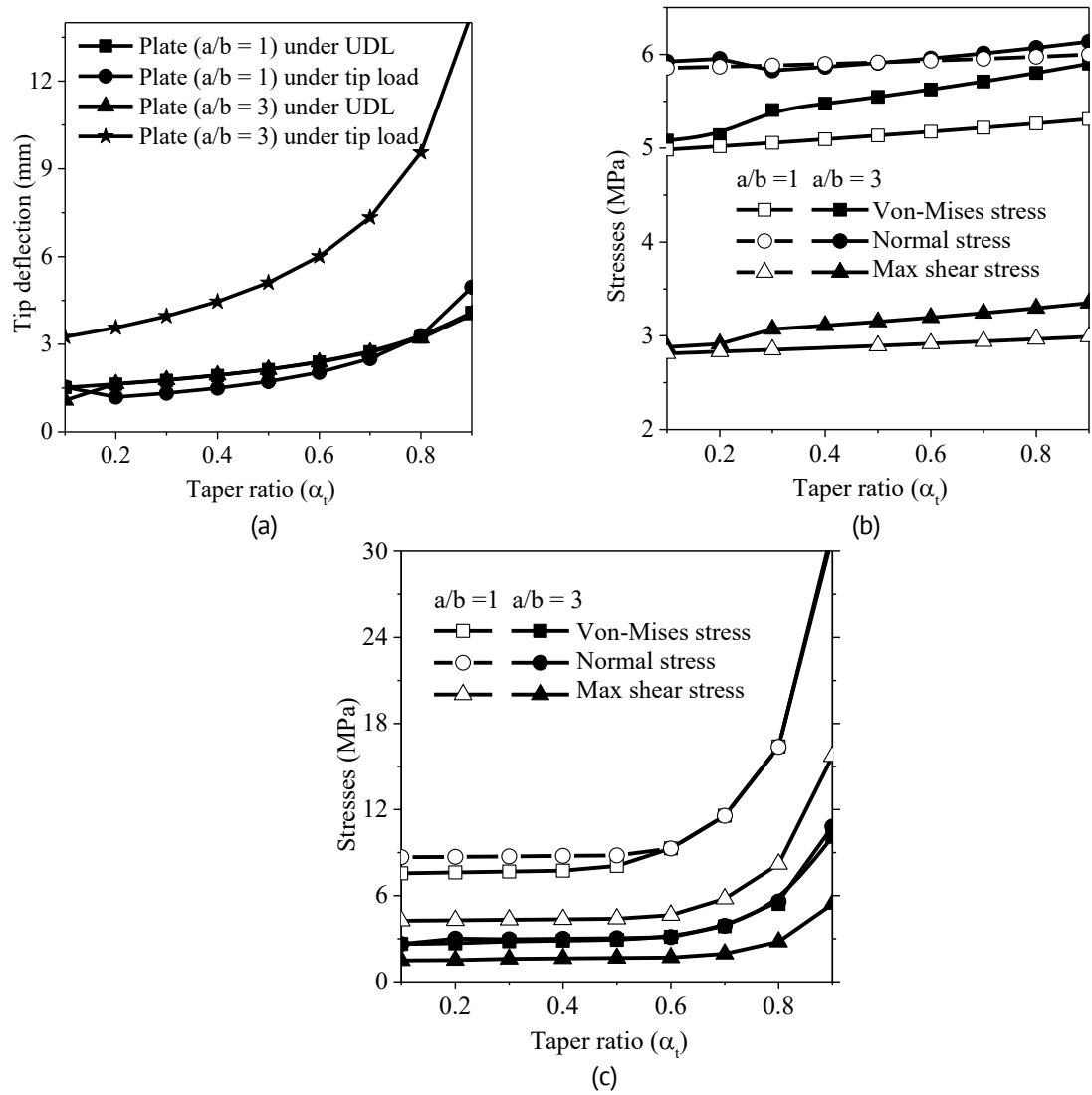


Fig. 4. Tip deflection and stresses of trapezoidal cantilever plate with variable thickness function linearly tapered along x-direction $h = h_0(1 - \alpha_t(x/a))$, under uniformly distributed load ($q_0 = 10000 \text{ N/m}^2$) and edge load ($q_0 = 100 \text{ kN}$): (a) tip deflection under UDL and tip load; (b) stresses under UDL; (c) stresses under tip load

The responses of tip deflection, and stresses (von-mises stress; normal stress and maximum shear stress) of square (a/b = 1) and rectangular (a/b = 3) cantilever trapezoidal plates under UDL and edge load are plotted in Fig. 4, as taper ratio increases max deflection of the plate increases exponentially whereas all other stresses increases in linear manner under UDL as shown in Fig. 4(b). Under Edge load deflection as well as stresses increase in similar manner. When aspect ratio of the plate increases from 1 to 3 then under UDL there is no major change in the deflection and stresses but under edge load when aspect ratio is 3 then deflection and all stresses (von-mises, normal, max shear) increases significantly as can be seen from the Fig. 4(a,c).

Bending results of trapezoidal cantilever plate having variable thickness in x-direction $(h = h_0(1 - \alpha_t(x/a)))$ and variable c/b ratio

After analysing plate under separately for keeping one parameter constant and other variable, now here both of the parameter taper ratio (α_t) and tip cord to root width ratio (c/b) varied together and analysed the bending response of trapezoidal cantilever plate.

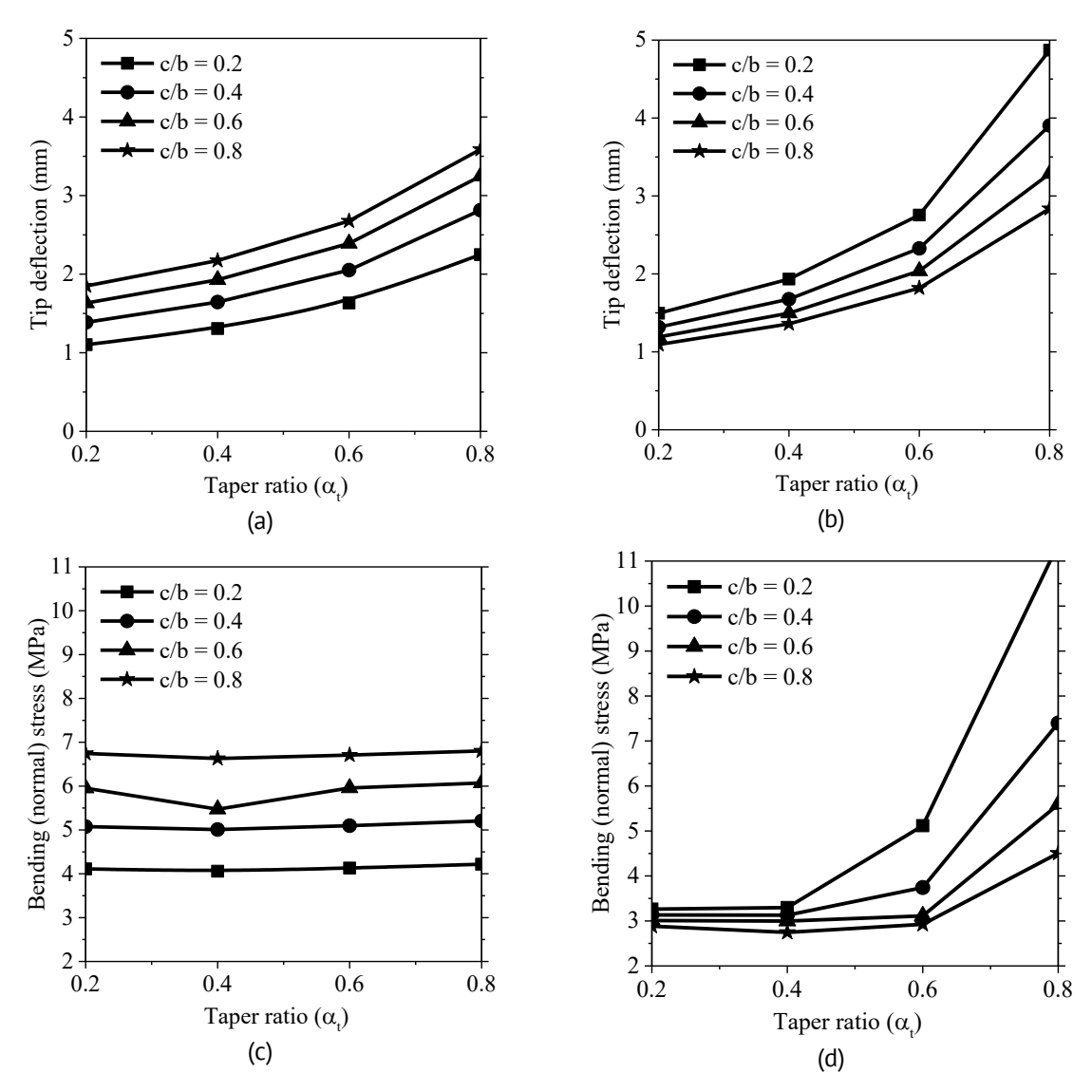


Fig. 5. Deflection and bending stress of trapezoidal cantilever plate with variable taper ratio and variable c/b ratio: (a) deflection under UDL; (b) deflection under edge load; (c) bending stress under UDL; (d) bending stress under edge load

The response of tip deflection and bending stress under UDL and edge load is presented in Fig. 5. In Fig. 5(a), as taper ratio increases then the smallest free end width of the trapezoidal plate at c/b= 0.2 have the lowest deflection under uniformly distributed load $(q_0 = 10 \times 10^3 \text{ N/m}^2)$. Whereas, when the load on the trapezoidal cantilever plate applied at the end edge $(q_0 = 100 \text{ kN})$, then as taper ratio (α_t) increases from 0.2 to 0.8 and root to cord ratio (c/b) decreases from 0.8 to 0.2, deflection of the plate is maximum at the lowest tip width c/b = 0.2 and taper ratio α_t = 0.8 as shown in Fig. 5(b). In Fig. 5(c,d) bending stresses under UDL and edge load plotted respectively, which shows that under UDL stresses will be highest when c/b = 0.8 but there is no major variation on the stress due to change in the taper ratio along the x-direction as presented in Fig. 5(c); whereas under edge load plate will be highly stressed when taper ratio is max (α_t = 0.8) and root to cord ratio is minimum (c/b = 0.2). So, we can conclude that when load is not uniform and only at the end then trapezoidal plate will experience more deflection and stresses, as illustrated in Fig. 5(d).

Dynamic analysis

Next, free vibration analysis of the trapezoidal cantilever plate, firstly validation of the results obtained from ANSYS for different modes shape done with the available results in the literature for free vibration. Then results of trapezoidal cantilever plate for various parameters like thickness, aspect ratio, tip to root width ratio (c/b) and combination of these obtained here.

Validation of 3D geometry using ANSYS with available 2D literature results

For validation of free vibration results, a rectangular plate (a = 1 m, b = 0.5 m, $h_0 = 0.01 \text{ m}$) is created using ANSYS 18.1 design modeller and meshing has been done for uniform quality mesh which resulted in 1272 nodes and 162 elements of uniform quads with four node each. DOF of the node was 6 (displacement u, v, w and rotation ϑ_x , ϑ_y , ϑ_z in x, y and z direction respectively).

Results have been validated from different authors [27–30] with non-dimensional frequency parameter where different taper ratio (α = 1- h_{min}/h_0) is varied for thickness variation from base to tip of the plate which is given by $h = h_0(1-\alpha_t (x/a))$. In Table 2, cantilever rectangular plate with a/b = 2 where a is length of the plate and b is width and h_0 is thickness of the plate at the fixed point or root. Elastic constant and poison's ratio is 100 kPa, 0.3, respectively. Non-dimensional frequency parameter (ϖ) is calculated for different taper ratio (α_t), where thickness of the plate varies in x-direction. Eight modes of the plate have been evaluated and shown in Fig. 6 and corresponding non-dimensional frequency written in Table 2. From Table 2, we can observe that result obtained from ANSYS is well converged and showing very minimal % of error. Result obtained in this work can be considered more accurate as 3D analysis has been done in this work. Error % at α = 1 is highest as we can see in Table 2 this is because of the triangular tip at the end and triangular elements in 3D work which resulted in more error. As taper ratio increases thickness at the tip decreases which resulted in decrement of ϖ as taper ratio decreases except for mode 1. For a particular α , ϖ increases with modes which can be seen in Table 2.

Table 2. Fundamental non-dimensional frequency parameter $(\varpi = \omega \times a^2 \sqrt{\rho h_0}/D_0)$ of isotropic rectangular cantilever (*CFFF*) plate $(a/b = 2, a/h_0 = 100, h_0 = 1.0, v = 0.3)$ considering variable thickness function is linearly tapered along x-direction $h = h_0 (1 - \alpha_t(x/a))$

Taper	Reference	atong x t	an ection i	$t = n_0(1$		odes			
ratio α _t	- North Control	1	2	3	4	5	6	7	8
	Present	3.458	14.769	21.544	48.080	60.414	92.373	92.929	118.712
	Kumari [27]	3.439	14.779	21.424	48.089	60.108	92.327	93.130	118.556
	Liew et al.								
0.0	[28]	3.4394	14.803	21.435	48.183	60.154	92.530	93.104	118.450
	Liu and Chang [29]	3.429	14.53	21.34	47.50	60.26	92.110	92.930	119.200
	Huang et al. [30]	3.436	14.703	21.414	47.856	59.940	92.907	-	-
	Present	3.543	14.192	20.159	43.176	54.994	80.175	82.747	107.373
	Kumari [27]	3.5250	14.206	20.054	43.079	54.743	80.382	82.702	107.297
0.2	Liew et al. [28]	3.5257	14.225	20.063	43.243	54.766	80.320	82.826	107.130
	Liu and Chang [29]	3.526	14.090	20.070	43.100	55.160	81.500	83.320	108.600
	Present	3.662	13.545	18.684	38.007	49.237	66.807	72.592	95.222
	Kumari [27]	3.646	13.560	18.595	38.006	49.036	67.013	72.552	95.233
0.4	Liew et al. [28]	3.6470	13.574	18.602	38.046	49.041	66.926	72.610	95.025
0.4	Liu and Chang [29]	3.649	13.600	18.690	38.490	49.660	69.660	74.000	96.900
	Huang et al. [30]	3.646	13.500	18.585	37.848	48.902	66.763	-	-
0.6	Present (9 × 18)	3.848	12.790	17.096	32.478	42.954	52.823	61.682	81.663
	Present (31 × 61)	3.837	12.772	17.039	32.409	42.808	52.806	61.516	81.476
	Kumari [27]	3.834	12.805	17.023	32.471	42.807	53.010	61.645	81.823
	Liew et al. [28]	3.834	12.813	17.027	32.490	42.800	52.909	61.654	81.600
	Liu and Chang [29]	3.813	13.020	17.110	33.570	43.440	57.010	63.940	84.120
	Present	4.191	11.872	15.397	26.451	35.481	38.464	49.546	64.487
	Kumari [27]	4.178	11.881	15.341	26.434	35.439	38.544	49.523	64.776
	Liew et al. [28]	4.179	11.886	15.345	26.442	35.417	38.461	49.490	64.583
0.8	Liu and Chang [29]	4.047	12.280	15.120	27.980	35.880	43.610	52.520	70.600
	Huang et al. [30]	4.179	11.846	15.331	26.352	35.495	38.209	-	-
	Present								
	(11772	5.182	12.22	14.979	25.771	30.449	34.440	48.755	53.063
	triangular)								
	Present								
1.0	(202744	5.176	11.497	14.867	21.644	24.706	29.625	37.404	41.286
1.0	triangular)								
	Kumari [27]	5.176	11.483	14.866	21.507	24.123	29.619	36.591	39.372
	Liew et al. [28]	5.177	11.484	14.870	21.500	24.021	29.600	36.159	37.978
	Liu and Chang [29]	4.388	10.840	11.570	20.550	26.730	27.880	40.580	52.930

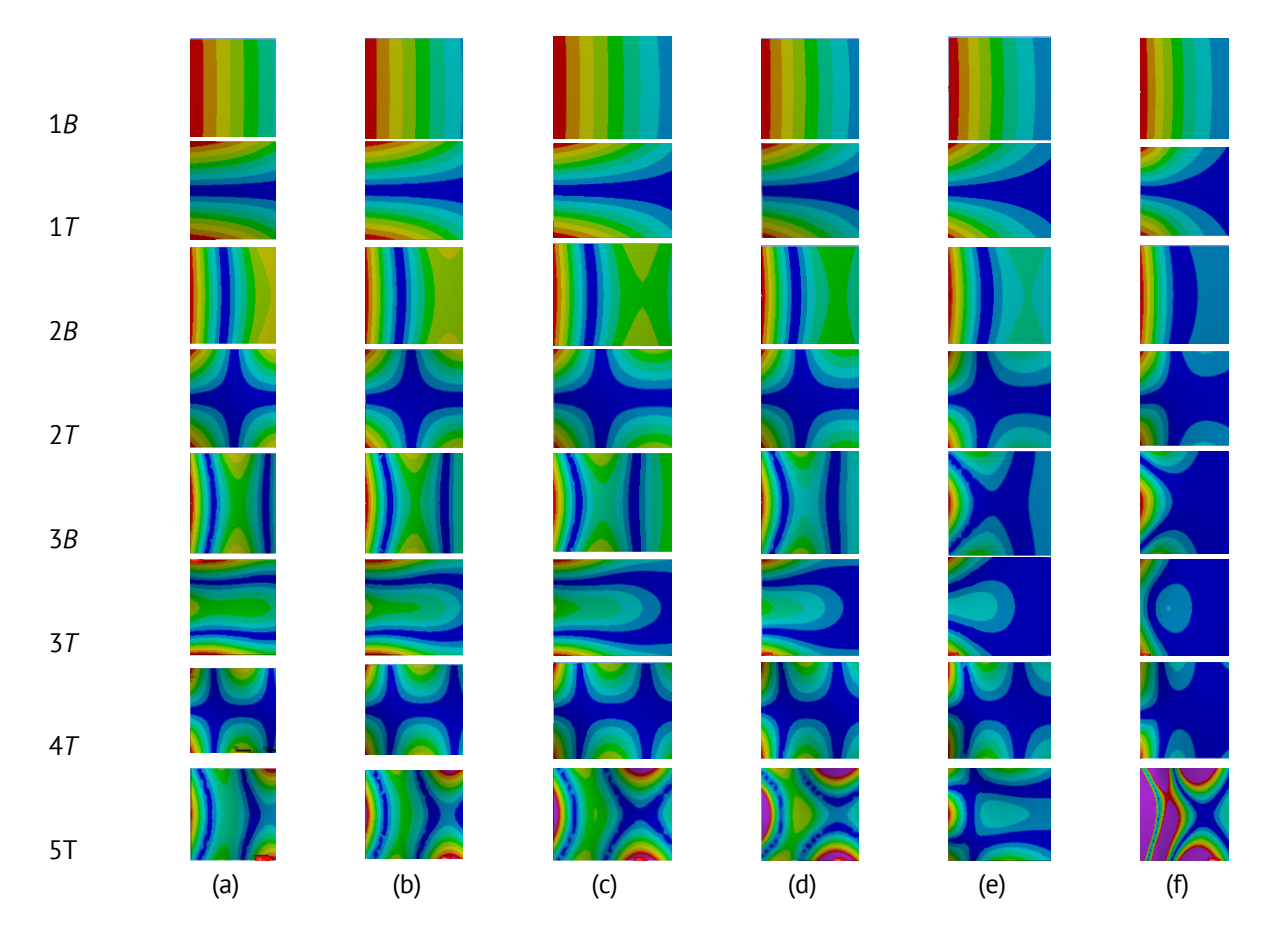


Fig. 6. Mode shapes of first eight modes of cantilever plate having variable thickness along span: (a) $\alpha = 0$; (b) $\alpha = 0.2$; (c) $\alpha = 0.4$; (d) $\alpha = 0.6$; (e) $\alpha = 0.8$; (f) $\alpha = 1$

Non dimensional frequency of cantilever trapezoidal plate with different taper ratios

Next, performed the modal analysis results of the isotropic (v = 0.3) trapezoidal plate having aspect ratio a/b = 3, $a/h_0 = 15$ and c/b = 0.6, and validated the present results with available published results. The aspect ratio and geometry considered here is shown in Fig. 7, that will be equivalent to an aeroplane wing size. Dimensions of the symmetric trapezoidal plate is as follows: a = 7.5 m, b = 2.5 m, c = 1.5 m, $h_0 = 0.5$ m. Non-dimensional frequency parameter: $\varpi = \omega \times a^2 \sqrt{\rho h_0/D_0}$, where ω is circular frequency in rad/s, density of the material $\rho = 1800$ kg/m³, flexural rigidity of plate $D_0 = \frac{E h_0^3}{12(1-v^2)}$, Young's modulus or elastic constant $E = 45 \times 10^3$ MPa.

Table 3. Non-dimensional frequency parameter ($\overline{\omega} = \omega \times a^2 \sqrt{\rho h_0/D_0}$)) of isotropic trapezoidal cantilever (*CFFF*) plate (a/b = 3, a/c = 5, $a/h_0 = 15$, $h_0 = 0.5$, v = 0.3) considering variable thickness function is linearly tapered along x-direction $h = h_0 (1 - \alpha_t(x/a))$

Taper ratio	Present	Modes							
α_{t}	Present	1	2	3	4	5	6	7	8
0.0	$10 \times 38 \times 3$	3.943	16.86	21.792	28.198	57.466	68.781	74.088	86.304
0.2	10 × 38 × 2	4.030	17.922	20.48	27.766	52.902	68.729	70.266	90.014
0.4	10 × 38 × 2	4.151	19.049	19.348	27.165	47.884	62.577	72.172	89.135
0.6	10 × 38 × 2	4.337	17.482	21.415	26.346	42.281	55.378	74.868	78.054
0.8	10 × 38 × 2	4.681	15.775	24.806	25.144	35.777	46.357	64.702	74.345
1.0	4636 elements	5.687	15.225	23.479	29.482	31.889	34.651	48.426	51.832

In Table 3, non-dimensional frequency (ϖ) is calculated for trapezoidal cantilever plate having variable taper ratio ranging from 0.2 to 1. Modes for all taper ratio up to 8 modes drawn. As previously seen in validation results here also first Mode increases with increase in taper ratio and all other modes decreases with increase in taper ratio. These signifies that as thickness at tip of the cantilever plate decreases vibration frequency also decreases as shown in Table 3 and modes of the results in different taper ratio shown in Fig. 7.

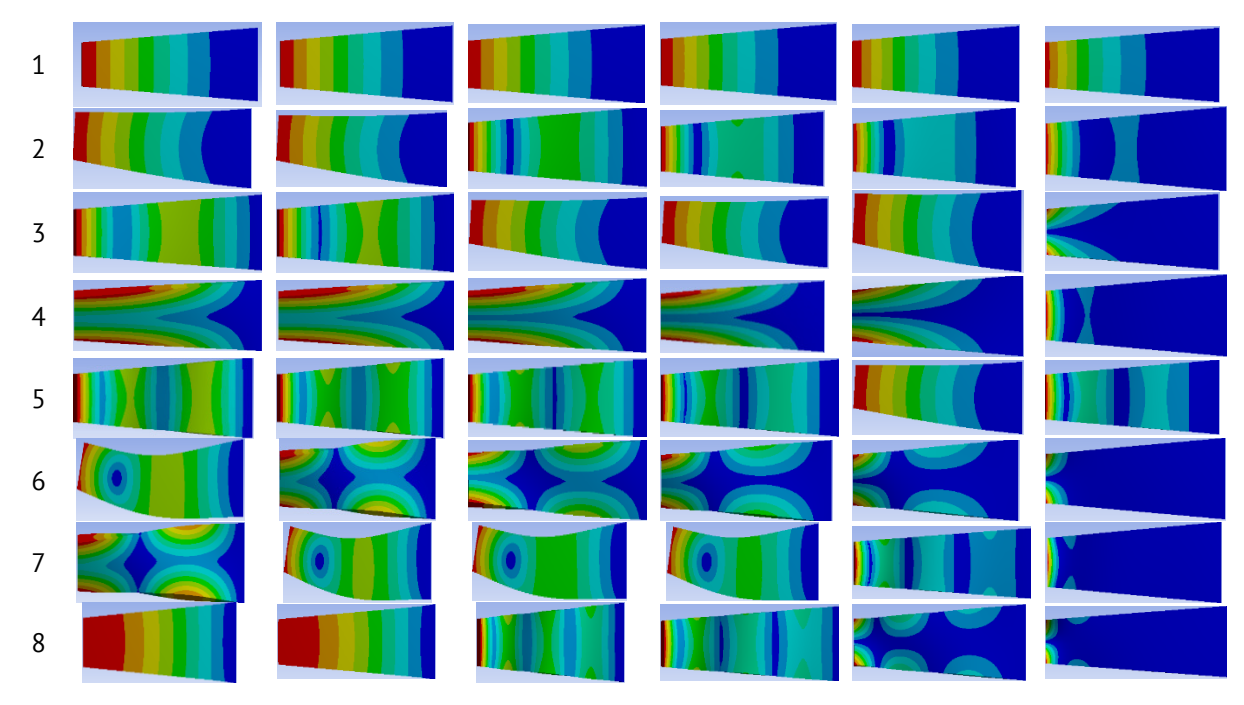


Fig. 7. Mode shapes of different taper ratio of isotropic trapezoidal cantilever (CFFF)

Non dimensional frequency of cantilever trapezoidal plate with uniform thickness and different tip to root width ratios (c/b)

Now keeping the thickness of the trapezoidal plate uniform and varying the tip to root ratio (c/b = 0.9 to 0.1) of the plate non-dimensional frequency (ϖ) calculated for eights modes. In Table 4, keeping the whole dimension and material properties same as previous

Table 4. Non-dimensional frequency parameter ($\overline{\omega} = \omega \times a^2 \sqrt{\rho h_0/D_0}$) of isotropic trapezoidal cantilever (*CFFF*) plate (a/b = 3, $a/h_0 = 15$, $h_0 = 0.5$, v = 0.3) considering uniform thickness along x-direction

Tip to reat width ratio (a/b)	Duscout		<u> </u>	Мо	odes		
Tip to root width ratio (c/b)	Present	1	2	3	4	5	6
0.9	$12\times38\times3$	3.505	15.857	20.908	21.024	56.831	62.367
0.8	$12\times38\times3$	3.629	16.15	21.246	22.957	57.013	65.763
0.7	$11\times38\times3$	3.773	16.479	21.498	25.362	57.218	69.626
0.6	$10\times38\times3$	3.943	16.86	21.792	28.198	57.466	68.781
0.5	$9 \times 38 \times 3$	4.147	17.31	22.146	31.548	57.774	67.711
0.4	$8 \times 38 \times 3$	4.401	17.864	22.589	35.49	58.19	66.426
0.3	$7 \times 38 \times 3$	4.727	18.582	23.18	40.075	58.788	64.917
0.2	$5 \times 38 \times 3$	5.165	19.578	24.043	45.288	59.764	63.226
0.2	$7 \times 65 \times 4$	5.164	19.575	24.035	45.27	59.741	63.217
0.1	$4 \times 66 \times 4$	5.798	21.131	25.509	51.01	61.694	61.703
0.1	$10\times152\times10$	5.796	21.129	25.501	50.986	61.684	61.684

analysis except the thickness parameter. Here first five modes of the plate corresponding to the different c/b ratio increases with decrease in c/b ratio whereas 6^{th} mode of the cantilever plate increase up to 0.7 c/b ratio then decreases. So, the more taper towards the tip then vibration frequency of the trapezoidal plate increases.

Non dimensional frequency of cantilever trapezoidal plate with variable thickness along x-direction and variable tip to root width ratios (c/b)

In Table 5, thickness of the plate along the x-direction (α_t = 0.2, 0.4, 0.6 and 0.8) and tip to root ratio (c/b = 0.8 to 0.2) both varied. The non- dimensional frequency parameter obtained for different cases up to 6 modes as presented in Table 5.

Table 5. Non-dimensional frequency parameter ($\overline{\omega} = \omega \times a^2 \sqrt{\rho h_0/D_0}$) of isotropic trapezoidal cantilever (*CFFF*) plate (a/b = 3, $a/h_0 = 15$, $h_0 = 0.5$, v = 0.3) considering variable thickness function is linearly tapered along *x*-direction $h = h_0(1 - \alpha_t(x/a))$ and different ratio of c/b

Taper	Tip to root	Present study			Мо	odes		
ratio α _t	width ratio (<i>c/b</i>)	(elements)	1	2	3	4	5	6
	0.8	$15 \times 50 \times 3$	3.715	17.194	19.960	22.514	52.430	60.460
0.2	0.6	$13\times50\times3$	4.028	17.919	20.470	27.750	52.869	68.683
0.2	0.4	$10\times50\times3$	4.487	18.941	21.218	35.116	53.565	67.818
	0.2	$6 \times 50 \times 3$	5.253	20.679	22.592	45.086	55.055	64.525
	0.8	$15\times50\times2$	3.837	18.574	18.600	21.952	47.454	54.546
0.4	0.6	$13 \times 50 \times 2$	4.15	19.045	19.346	27.163	47.875	62.572
0.4	0.4	$10\times50\times2$	4.609	19.741	20.391	34.589	48.529	69.631
	0.2	$6 \times 50 \times 2$	5.377	21.031	22.158	44.735	49.926	66.235
	0.8	$15 \times 50 \times 2$	4.023	17.050	20.635	21.191	41.882	47.707
0.6	0.6	$13 \times 50 \times 2$	4.337	17.480	21.413	26.345	42.274	55.368
0.6	0.4	$10\times50\times2$	4.796	18.119	22.490	33.814	42.887	66.823
	0.2	$6 \times 51 \times 2$	5.566	19.319	24.293	44.145	44.177	68.715
	0.8	$15 \times 50 \times 2$	4.366	15.393	20.088	23.966	35.421	39.361
0.8	0.6	$13\times50\times2$	4.681	15.773	24.803	25.143	35.772	46.352
0.8	0.4	$10\times50\times2$	5.141	16.351	25.938	32.675	36.326	57.307
	0.2	$6 \times 51 \times 2$	5.910	17.457	27.781	37.494	43.280	66.244

Conclusion

Static and dynamic analysis of trapezoidal cantilever plate has been carried out in this study using ANSYS 18.1. To analyse trapezoidal plate in vibration and bending, two parameters (taper ratio α_t and tip to root width ratio c/b) of the trapezoidal plate and combination of these parameters varied.

It can be concluded from this study that at lower aspect ratio, stresses and deflection of a trapezoidal cantilever plate is lower than higher aspect ratio. In modal analysis at $\alpha_t = 0.6$ and c/b = 0.2 maximum non-dimensional frequency for the plate observed when both parameters varied. In bending analysis under UDL when $\alpha_t = 0.8$ and c/b = 0.8 then deflection and stresses will be maximum, whereas under Edge load when $\alpha_t = 0.8$ and c/b = 0.2 (smallest tip width) will have maximum deflection and stresses.

Trapezoidal cantilever plate is used in various field of engineering and this geometry widely acceptable for its high strength to weight ratio. So, this analysis can be

helpful for selecting thickness, aspect ratio and free end width of the trapezoidal plate for various applications based on different industry uses. Also, future scope of the analysis available for different coating of the plate for surface strength for in-plane stresses and composite materials with different boundary conditions.

CRediT authorship contribution statement

Conflict of interest

The authors declare that they have no known competing financial interests or personal relationships that could have appeared to influence the work reported in this paper.

References

- 1. Hosseinpour E, Baharom S, Yadollahi Y. Evaluation of steel shear walls behavior with sinusoidal and trapezoidal corrugated plates. *Advances in Civil Engineering*. 2015;2015: 715163.
- 2. Labibzadeh M, Salehnia A, Hossain KMA, Jing DH. Comparison of Performance of the Flat, Trapezoidal, and Sinusoidal Steel Plate Shear Walls Under Cyclic Loads. *Iranian Journal of Science and Technology, Transactions of Civil Engineering*. 2022;46(14); 3571–3589.
- 3. Majidi MH, Azadi M, Fahham H. Vibration analysis of cantilever FG-CNTRC trapezoidal plates. *Journal of the Brazilian Society of Mechanical Sciences and Engineering*. 2020;42: 118.
- 4. Jena PC, Parida SP, Dash RR. Modal study of trapezoidal cantilever plate like composite beam. *Materials Today: Proceedings*. 2018;5(9): 19680–19692.
- 5. Na Y, Lee MS, Lee JW, Jeong YH. Horizontally assembled trapezoidal piezoelectric cantilevers driven by magnetic coupling for rotational energy harvester applications. *Energies*. 2021;14(2): 498.
- 6. Caron J. How Wing Design Affects Your Ride, and How to Preflight for Safety. *J. Fly America*. 2020;January/February: 20–23.
- 7. Zamani M, Fallah A, Aghdam MM. Free vibration analysis of moderately thick trapezoidal symmetrically laminated plates with various combinations of boundary conditions. *European Journal of Mechanics-A/Solids*. 2012;36: 204–212.
- 8. Wang Q, Xie F, Liu T, Qin B, Yu H. Free vibration analysis of moderately thick composite materials arbitrary triangular plates under multi-points support boundary conditions. *International Journal of Mechanical Sciences*. 2020;184: 105789.
- 9. Torabi K, Afshari H. Vibration analysis of a cantilevered trapezoidal moderately thick plate with variable thickness. *Engineering Solid Mechanics*. 2017;5(1): 71–92.
- 10. Shokrollahi S, Shafaghat S. A global Ritz formulation for the free vibration analysis of hybrid metal-composite thick trapezoidal plates. *Scientia Iranica*. 2016;23(1): 249–259.
- 11. Jiang G, Li F, Li X. Nonlinear vibration analysis of composite laminated trapezoidal plates. *Steel Compos Struct.* 2016;21(2): 395–409.
- 12. Huang CH, Hsu CH, Lin YK. Experimental and numerical investigations for the free vibration of cantilever trapezoidal plates. *Journal of the Chinese Institute of Engineers*. 2006;29(5): 863–872.
- 13. Majidi MH, Azadi M, Fahham H. Effect of CNT reinforcements on the flutter boundaries of cantilever trapezoidal plates under yawed supersonic fluid flow. *Mechanics Based Design of Structures and Machines*. 2022;50(2): 630–650.
- 14. Emelyanov IG, Kislov AN. Strength analysis of thin-wall structures operating in aggressive environments for prolonged periods. *Materials Physics and Mechanics*. 2022;50(3): 475–484.
- 15. Chernyshov AD, Goryainov VV, Kovaleva EN. Simulation of the stress-strain state of a rectangular bar using fast trigonometric interpolation in various statements of boundary value problems. *Materials Physics and Mechanics*. 2023;51(4): 160–171.

- 16. Ropalekar AR, Ghadge RR, Anekar NA. Experimental investigation on flexural fatigue strength of graphene oxide modified E-Glass epoxy composite beam. *Materials Physics and Mechanics*. 2024;52(1): 132–141.
- 17. Kumari E, Lal S. Studies of trapezoidal panels under thermo-mechanical load: a nonlinear dynamic analysis. *Materials Physics and Mechanics*. 2024;52(2): 90–105.
- 18. Kumari E, Lal S. Nonlinear bending analysis of trapezoidal panels under thermo-mechanical load. *Forces in Mechanics*. 2022;8: 100097.
- 19. Kumari E. Dynamic response of composite panels under thermo-mechanical loading. *Journal of Mechanical Science and Technology*. 2022;36(8): 3781–3790.
- 20. Kumari E. Perspective Chapter: Dynamic Analysis of High-Rise Buildings Using Simplified Numerical Method. In: Yousuf LS. (ed.) *Chaos Monitoring in Dynamic Systems Analysis and Applications*. IntechOpen; 2024.
- 21. Kumari E. Nonlinear bending analysis of cylindrical panel under thermal load. *International Research Journal on Advanced Science Hub.* 2021;3(7): 145–150.
- 22. Kumari E, Singha MK. Nonlinear response of laminated panels under blast load. *Procedia Engineering*. 2017;173: 539–546.
- 23. Kumari E, Saxena D. Buckling analysis of folded structures. *Materials Today: Proceedings.* 2021;43: 1421–1430.
- 24. Adhikari B, Dash P, Singh BN. Buckling analysis of porous FGM sandwich plates under various types non-uniform edge compression based on higher order shear deformation theory. *Composite Structures*. 2020;251: 112597.
- 25. Zhao Z, Feng C, Wang Y, Yang J. Bending and vibration analysis of functionally graded trapezoidal nanocomposite plates reinforced with graphene nanoplatelets (GPLs). *Composite Structures*. 2017;180: 799–808. 26. Liew KM, Han JB. Bending solution for thick plates with quadrangular boundary. *Journal of Engineering Mechanics*. 1998;124(1): 9–17.
- 27. Kumari E. Free vibration analysis of rotating laminated composite plate type blades with variable thickness. *Materials Today: Proceedings*. 2021;43: 1762–1773.
- 28. Liew KM, Lim CW, Lim MK. Transverse vibration of trapezoidal plates of variable thickness: unsymmetric trapezoids. *Journal of Sound and Vibration*. 1994;177(4): 479–501.
- 29. Liu WH, Chang IB. Some studies on the vibration of cantilever plates with uniform and non-uniform thickness. *J. Sound Vib.* 1989;130(2): 337 341.
- 30. Huang M, Ma XQ, Sakiyama T, Matuda H, Morita C. Free vibration analysis of orthotropic rectangular plates with variable thickness and general boundary conditions. *Journal of Sound and Vibration*. 2005;288(4–5): 931–955.

Submitted: July 11, 2024 Revised: March 20, 2025 Accepted: May 31, 2025

Enhancing EDM performance of Monel-400 super alloy through process parameter optimization: RSM-based experimental and microstructural analysis

M.R. Panda ¹, S.K. Mishra ², P.K. Sahoo ¹

¹ GIET University Gunupur, Rayagada, India

ABSTRACT

A nickel-copper alloy Monel-400 renowned for its corrosion resistance and thermal properties finds extensive application in chemical, fitting, fastener, and marine industries. However, machining intricate, delicate components from this alloy using conventional methods presents significant challenges. EDM is a non-traditional process capable of producing precise, high-quality surfaces, which emerges as a viable alternative. The die-sinking EDM of Monel-400 are investigated with a particular focus on the machined surface microstructure. A Box-Behnken design was employed to evaluate the influence of discharge current, pulse-on time, and voltage gap on material removal rate, tool wear rate, and surface roughness. Results indicate that impact of peak current and pulse-on time are primary determinants of Monel-400 machining characteristics. While impact of peak current exhibited the most significant impact on MRR, pulse-on time was identified as the critical factor affecting tool wear rate and surface roughness. A comprehensive metallographic examination of the machined surface was conducted to elucidate wear mechanisms.

KEYWORDS

EDM • Monel-400 alloy • microstructure • RSM • box-behnken design • SEM

Acknowledgements. The author M.R. Panda and P. K. Sahoo would like to express their sincere gratitude to all those who contributed to the successful completion of this research. Special thanks to the Department of Mechanical Engineering at GIET University Gunupur, Odisha, for providing the necessary resources and facilities.

Citation: Panda MR, Mishra SK, Sahoo PK. Enhancing EDM performance of Monel-400 super alloy through process parameter optimization: RSM-based experimental and microstructural analysis. *Materials Physics and Mechanics*. 2025;53(3): 24–36.

http://dx.doi.org/10.18149/MPM.5332025_3

Introduction

Electrical discharge machining (EDM) is a computer-controlled, non-traditional machining process that utilizes a series of controlled electrical discharges (sparks) to remove material from the workpiece. The electric spark produced as a result of potential difference is mainly used as the cutting tool to cut (erode) the material [1]. EDM is mainly applied to the family of materials that are difficult to machine by traditional manufacturing techniques, but the process is limited to conductive materials only [2]. Due to its beneficial properties like better strength-to-weight ratio and corrosion resistance, super alloys such as Monel-400 find widespread uses in aircraft, oil production and refining, musical instruments, valves, fasteners and maritime applications [3]. Monel-400 alloy's poor thermal diffusivity causes high tool tip temperatures during traditional machining, rendering traditional methods inefficient [4,5]. Non-traditional techniques, such as EDM, offer a more viable approach to



² VSSUT Burla, Odisha, India

[™] srimantnitrkl@qmail.com

machining this challenging material. Several process parameters, including electrode material, discharge current, pulse-on time, duty cycle, and gap voltage, significantly influence EDM performance when machining Monel-400 alloy [6]. Copper, brass and graphite are mainly used as electrode materials due to their high melting point and conductivity [7]. Owing to its better load bearing and non-corrosive properties, Monel-400 is hardened by the cold working process as a result it becomes very tough to machine by conventional machining [8,9]. Monel-400 has an electrical conductivity of roughly 34 % IACS, a specific gravity of 8.80, a melting point temperature of 1300–1350 °C, and a hardness of 65 Rockwell. Monel-400 offers exceptional toughness that is maintained across a wide temperature range [10–14].

Optimizing process parameters is critical to enhancing the efficiency of EDM when applied to the Monel-400 superalloy. Because of its inherent high strength and poor heat conductivity, Monel-400 presents significant challenges to traditional machining methods, necessitating the exploration of alternative processes like EDM [15,16]. Research suggests that advanced techniques like Wire EDM and Electrical Discharge Diamond face grinding (EDDFG) show promise in improving material removal rates and surface quality for Monel-400 components [15,17]. By meticulously controlling process parameters such as pulse duration and applied current, and by judiciously selecting electrode materials, substantial enhancements in machining efficiency and precision can be realized [16,18]. The use of modern optimization techniques like as Taguchi analysis and genetic algorithms has the potential to improve Monel-400's EDM process, leading in higher performance and lower costs [17-19]. Gupta and Gupta [20], Shanmugha Sundaram [21], and Amuthak Kannan et al. [22] investigated the EDM of hybrid Al-Al₂O₃/B₄C, Al-Si alloy-graphite, and basalt fiber composites, respectively. Their research focused on identifying optimal process parameter combinations for these materials. Gopala Kannan et al. [8] investigated the EDM of a novel aluminum 7075 matrix composite reinforced with 10 % Al₂O₃ particles using a copper electrode. The impact of process factors on MRR, TWR, and SR was investigated using a mathematical model based on response surface methodology (RSM). Furthermore, ANOVA was used to determine the impact of peak current (I_p) , pulse-on time (T_{on}) , voltage (V), and pulse-off time (T_{off}) on EDM performance. Jahan et al. [10] investigated the optimization of surface finish during the EDM of WC composites, renowned for their exceptional hardness, strength, and wear resistance. Their study explored the influence of electrode materials, including tungsten, copper tungsten, and silver tungsten. Sivasankar et al. [23] studied EDM performance on ZrB₂ using a wide range of electrode materials such as graphite, aluminum, tantalum, niobium, copper, brass, silver, tungsten, and titanium. Their research focused on hole quality metrics, including roundness, form, and diameter are among the usual EDM responses, along with SR, MRR, and TWR. A desirability function analysis was carried out to assess tool performance. Assarzadeh and Ghoreishi [24] proposed a dual response surface-desirability method for modeling and optimizing process parameters in Al₂O₃ powder-mixed electrical discharge machining (PMEDM).

After a far-reaching and comprehensive investigation of the published works of literature, numerous gaps were figured out in the EDM process. The majority of experimenters or analysts have probed the effect of the finite number of machining parameters in the computation of results or execution on the machined surface on EDM.

Also observed inadequate exploration of the microstructural changes and their influence on EDM performance. The purpose of this study was to investigate the effects of pulse-on time, peak current, and voltage gap on Monel-400 electrical discharge machining (EDM). Response surface methodology (RSM) was used to optimize these process parameters in order to maximize material removal rate (MRR) while decreasing surface roughness (Ra) and tool wear rate (TWR). To further understand the material's behavior to different process parameter combinations, a complete microstructural examination of the machined surfaces was performed, including the recast layer, heat-affected zone, and worn tool surfaces.

Materials and Methods

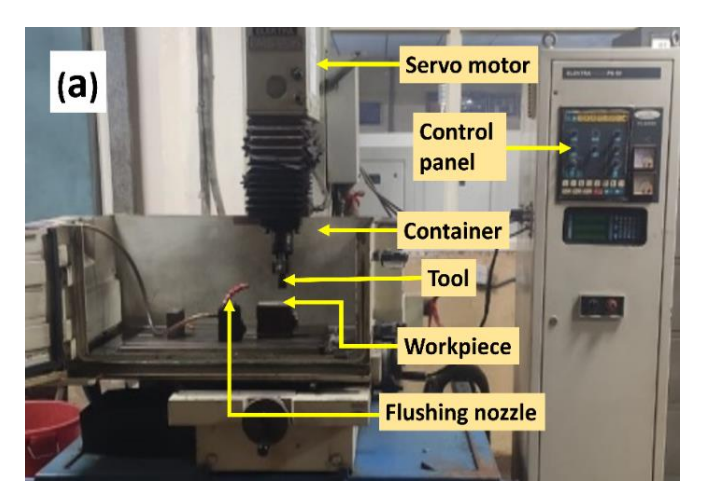
The Monel-400 alloy used as the workpiece material in this study is a commercially available nickel-copper alloy, procured from M/s Metal Mart Pvt. Ltd., Mumbai, India. The alloy is composed primarily of nickel (~ 63 %) and copper (~ 30 %), with minor quantities of iron, manganese, silicon, and carbon. The typical chemical composition of Monel-400 is reported in Table 1.

Table 1. Chemical composition of selected material

Element	Ni	Cu	Fe	Mn	Si	С
Wt. %	63.0	30.0	2.5	2.0	0.5	0.3

The alloy sheet was supplied in a cold-rolled condition with a thickness of 5 mm and was subsequently cut into rectangular samples of $50 \times 50 \text{ mm}^2$ using a precision abrasive cutter to maintain dimensional accuracy and edge integrity. The copper electrode, with a diameter of 9 mm, was sourced from M/s ElectroTech Supplies, Bhubaneswar, India. The electrode material was electrolytic copper with a purity of 99.9 %, chosen for its high electrical and thermal conductivity.

Investigations are performed in the die-sinking NC EDM machine shown in Fig. 1 by maintaining a constant servo head gap. The EDM 30 dielectric oil was supplied by Hindustan Petroleum Corporation Ltd., having a specific gravity of 0.8 at room temperature. It was used without any additives to ensure consistency across all trials.



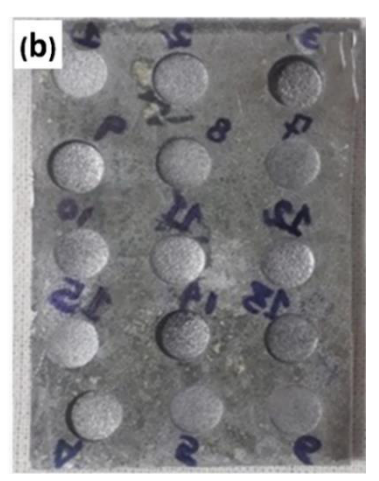


Fig. 1. Illustration of EDM machining: (a) EDM machine, (b) workpiece material after machining

Because electrical conductivity is a critical need for EDM electrodes, copper was chosen as the electrode material for this experiment. All materials were inspected for quality prior to experimentation. The Monel-400 workpieces were cleaned with acetone to remove surface contaminants, while the copper electrodes were polished to ensure proper electrical contact during the machining process. Each experimental run consists of 3 min of machining time. A precision electronic weight-measuring machine is used after each experimental run to determine the material loss from the tool and workpiece.

In EDM of Monel-400, careful selection of process parameters is essential due to the alloy's high strength and low thermal conductivity, which can complicate machining. Parameters such as pulse current, pulse on-time, and pulse off-time were chosen based on their known influence on key performance indicators like material removal rate (MRR), tool wear rate (TWR), and surface roughness. These parameters directly affect spark energy, discharge frequency, and cooling time between sparks, making them critical for efficient and stable machining. The range for each parameter was established through a combination of literature review and preliminary experiments to ensure a comprehensive yet practical design space. Table 2 shows the values of chosen process parameters. The order of parameters is selected in such a way that the experimentation on the workpiece can be conducted smoothly to achieve accomplishment. The rest parameters are polarity, flushing pressure, and duty cycle held constant throughout the experiment.

Table 2. Process parameters and their order

Duasass managementan	Cumbal	l lmis	Order			
Process parameter	Symbol	Unit	Order -1	Order 0	Order 1	
Pulse on time	(Ton)	μs	500	1000	2000	
Peak current	(I_p)	Α	18	33	50	
Voltage	(V)	V	3	7	10	

Table 3. Experimental layout

		Factor 1	Factor 2	Factor 3	Response 1	Response 2	Response 3
Std	Run	A: Peak	B: Pulse on	C: Voltage	MRR,	TWR,	Surface
Stu	Kuli	current	time	gap	mm³/min	mm³/min	roughness, µm
8	1	1	0	1	26.515	1.737	2.031
2	2	1	-1	0	20.83	1.86	2.382
4	3	1	1	0	66.28	3.78	3.955
11	4	0	-1	1	3.78	0.567	1.226
9	5	0	-1	-1	18.93	0.894	1.392
7	6	-1	0	1	5.68	0.782	1.3
3	7	-1	1	0	9.56	2.87	2.987
10	8	0	1	-1	5.68	3.24	3.453
6	9	1	0	-1	32.19	2.65	2.518
1	10	-1	-1	0	11.26	0.456	1.15
13	11	0	0	0	7.575	1.864	2.455
14	12	0	0	0	7.575	1.864	2.223
12	13	0	1	1	22.72	3.065	3.151
15	14	0	0	0	7.12	1.864	2.223
5	15	-1	0	-1	6.54	1.2	1.625

Design of experiment

The design of experiment is arranged in accordance with the RSM Box-Behnken design. Fifteen investigations are performed on the workpiece. Subsequently, as per the experimental design obtained from Design Experts software, the machining on Monel-400 is executed. During the machining, the dielectric fluid was continuously flushing on the machining surface to clean the surface from debris. Table 3 depicts the different experiment arrangements.

Measurement of responses

Material removal rate (MRR) may be defined as the rate of material removed from the surface of the workpiece per unit time. The equation used for the evaluation of MRR is mentioned below [25]: $\mathbf{MRR}\left(\frac{\mathbf{mm^3}}{\mathbf{min}}\right) = \frac{\mathbf{Mw1-Mw2}}{t \times \rho}$, where machining time t = 3 min (fixed), a density of MONEL-400 material is $\rho = 8800$ kg/m², $\mathbf{Mw1}$ is a mass of workpiece material prior to machining, $\mathbf{Mw2}$ is a mass of workpiece material after machining.

Tool wear rate (TWR) may be defined as the rate of material removed from the surface of the tool material per unit time. The TWR is calculated by using the following equation [26]: $\text{TWR}\left(\frac{\text{mm}^3}{\text{min}}\right) = \frac{Mt1-Mt2}{t\times\rho}$, where t is machining time, density of copper is $\rho = 8940 \text{ kg/m}^2$, Mt_1 is a mass of tool material prior to machining, Mt_2 is a mass of the tool material after machining.

A surface roughness (SR) analyser (model SJ-410, portable type) was used to quantify R. The instrument's parameters were set at 4 Pa measurement force, 25 mm evaluation length, and $0.000125 \, \mu m$ resolution.

Performance evaluation

To explore the influence of process variables on response parameters, a Box-Behnken design was used in conjunction with response surface methodology (RSM). This experimental design necessitated a minimum of fifteen experimental runs, including three center points. ANOVA was used to determine the contribution of each input parameter to the output responses. Table 3 shows how different machining factors affect the reaction.

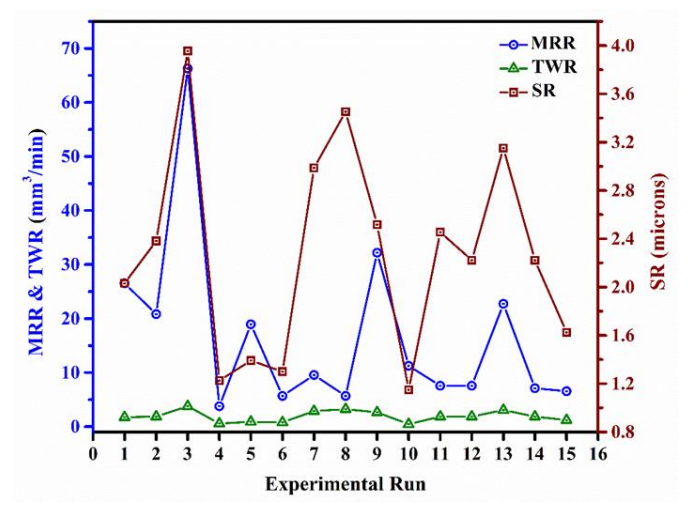


Fig. 2. MRR, TWR and SR plot for each experimental run

Figure 2 shows the plot for responses for each experimental run. As evident from the graphical representation, the optimum value for all three measured responses were obtained during the third experimental run, conducted with pulse on time of 2000 μ s, current of 50 A, and voltage of 7 V. Furthermore, the plot clearly indicates a positive correlation between increasing current and pulse on time and the resulting material removal rate from both the workpiece and the tool surface. This enhanced material removal consequently leads to an increase in surface roughness.

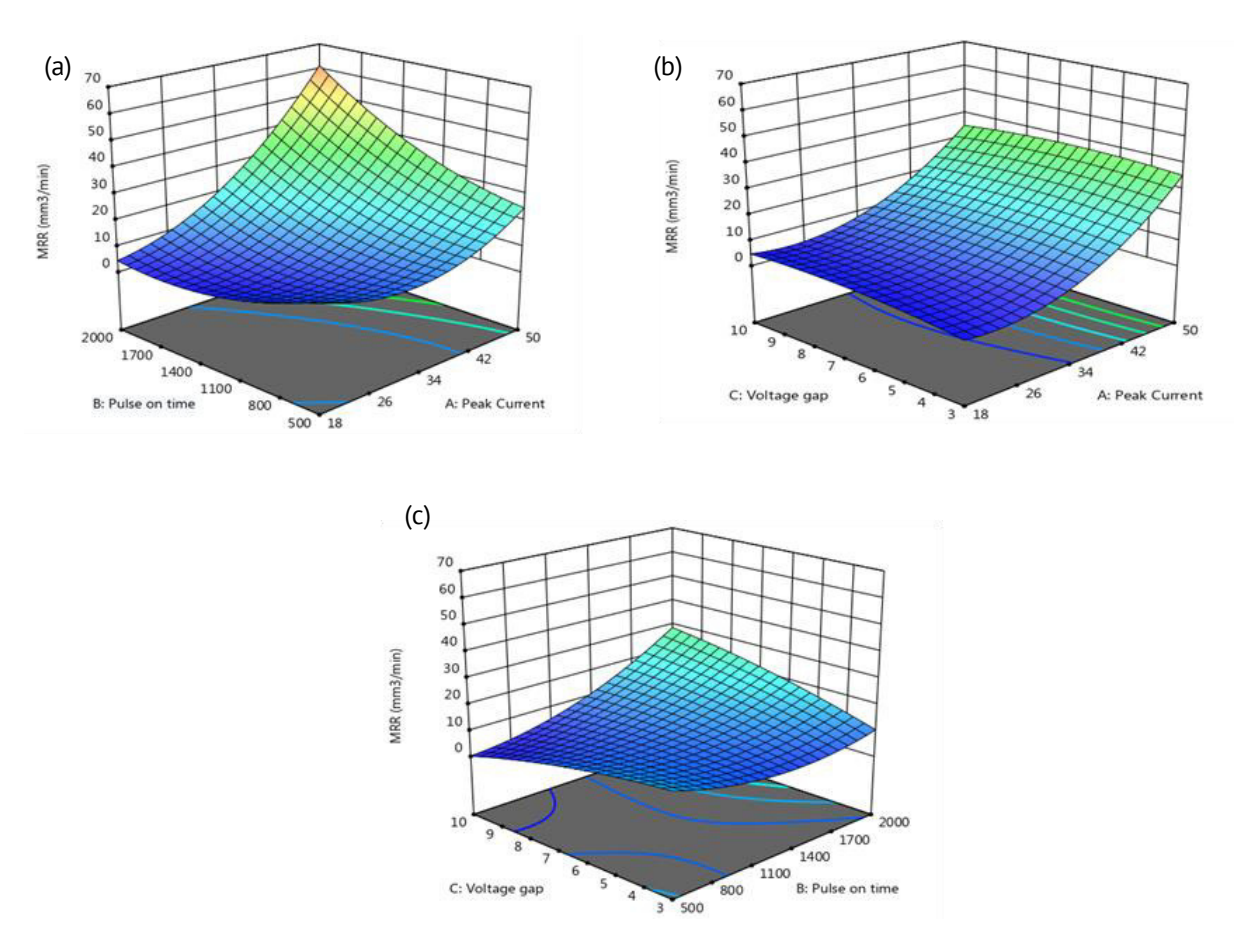


Fig. 3. Surface plot of MRR with (a) T_{on} and I_{o} , (b) voltage and I_{o} , (c) T_{on} and voltage gap

Table 4 presents the ANOVA table for rate of material removal, excluding non-significant variables. T_{on} (B), I_p (A), the quadratic term A^2 , and interaction terms AB and AC were determined to be highly significant. Ip demonstrated the most significant impact on MRR, accounting for 53.34 % of the response. The surface plots in Fig. 3 illustrate the relationship between MRR, pulse-on time (T_{on}), peak current (I_p), and voltage gap (V). Figure 3(a,b) demonstrates a positive correlation between MRR and both T_{on} and I_p . This is due to the direct relationship between current and spark density, which causes more material removal at higher current levels. Similarly, with an increase in T_{on} , the discharging of the spark occurs for a longer duration hence resulting in greater material removal. Extended pulse-on time (T_{on}) facilitates deeper heat flux penetration into the workpiece, promoting the formation of a larger plasma area and consequently enhancing material removal rate (MRR) significantly [27,28]. As depicted in Fig. 3(b,c), a marginal increase in MRR is observed with escalating voltage.

Table 4. ANOVA for response 1: for MRR

Saurea	Sum of	DE	Mean	F. volve			0/
Source	squares	DF	square	F-value	p-value		% contribution
Model	3585.68	9	398.41	16.77	0.0032	significant	
A-peak	1975.87	1	1975.87	83.19	0.0003		53.34
current	1973.07	1	197 3.07	03.19	0.0003		75.54
B-pulse on time	280.68	1	280.68	11.82	0.0185		7.57
C-voltage gap	4.79	1	4.79	0.2015	0.6723		0.13
AB	629	1	629	26.5	0.0036		17.0
AC	4.94	1	4.94	0.208	0.6675		0.133
BC	304.8	1	304.8	12.83	0.0158		8.22
A ²	460	1	460	19.4	0.0070		12.41
B ²	96.7	1	96.7	4.07	0.0996		2.61
C ²	13.27	1	13.27	0.5585	0.4885		0.36
Residual	118.76	5	23.75				3.20
Lack of fit	118.62	3	39.54	573.0	0.0017	not significant	3.20
Pure error	0.140	2	0.07				0.00372
Cor total	3704.43	14					

Table 5. ANOVA for response 2: for TWR

Table 5. ANOVA		C 2. IC					
Source	Sum of squares	DF	Mean quare	F-value	p-value		% contribution
Model	14.71	9	1.63	68.44	0.0001	significant	
A-peak	2.78	1	2.78	116.52	0.0001		18.74
current	2.70		2.76	110.52	0.0001		10.74
B-pulse on time	10.53	1	10.53	440.74	< 0.0001		71
C-voltage gap	0.4200	1	0.4200	17.58	0.0085		2.83
AB	0.0610	1	0.0610	2.55	0.1709		0.41
AC	0.0613	1	0.0613	2.56	0.1702		0.41
ВС	0.0058	1	0.0058	0.2418	0.6438		0.039
A ²	0.0007	1	0.0007	0.0308	0.8675		0.004
B ²	0.4875	1	0.4875	20.41	0.0063		3.28
C²	0.3018	1	0.3018	12.63	0.0163		2.035
Residual	0.1195	5	0.0239				0.805
Lack of fit	0.1195	3	0.0398			not significant	0.805
Pure error	0.0000	2	0.0000				0.0000
Cor total	14.83	14					

Table 5 shows the ANOVA table for TWR subsequent rejection of all unimportant variables. The Model F-value of 68.44 implies the model is significant. With a 71 % contribution, pulse on time proves to be the most influencing factor for TWR followed by peak current. In this case, A, B, C, B², and C² are significant model terms.

Figure 4 indicates the surface plots for TWR against pulse on time (T_{on}), peak current (I_p), and voltage gap (V). It clearly shows that, with an increase in current that to for a longer duration of time, a large amount of heat accumulates at the tool surface which subsequently results in higher tool wear. With an increase in current and time of

discharging the TWR increases while the increase in voltage gap results in a decrease of wear rate on the tool.

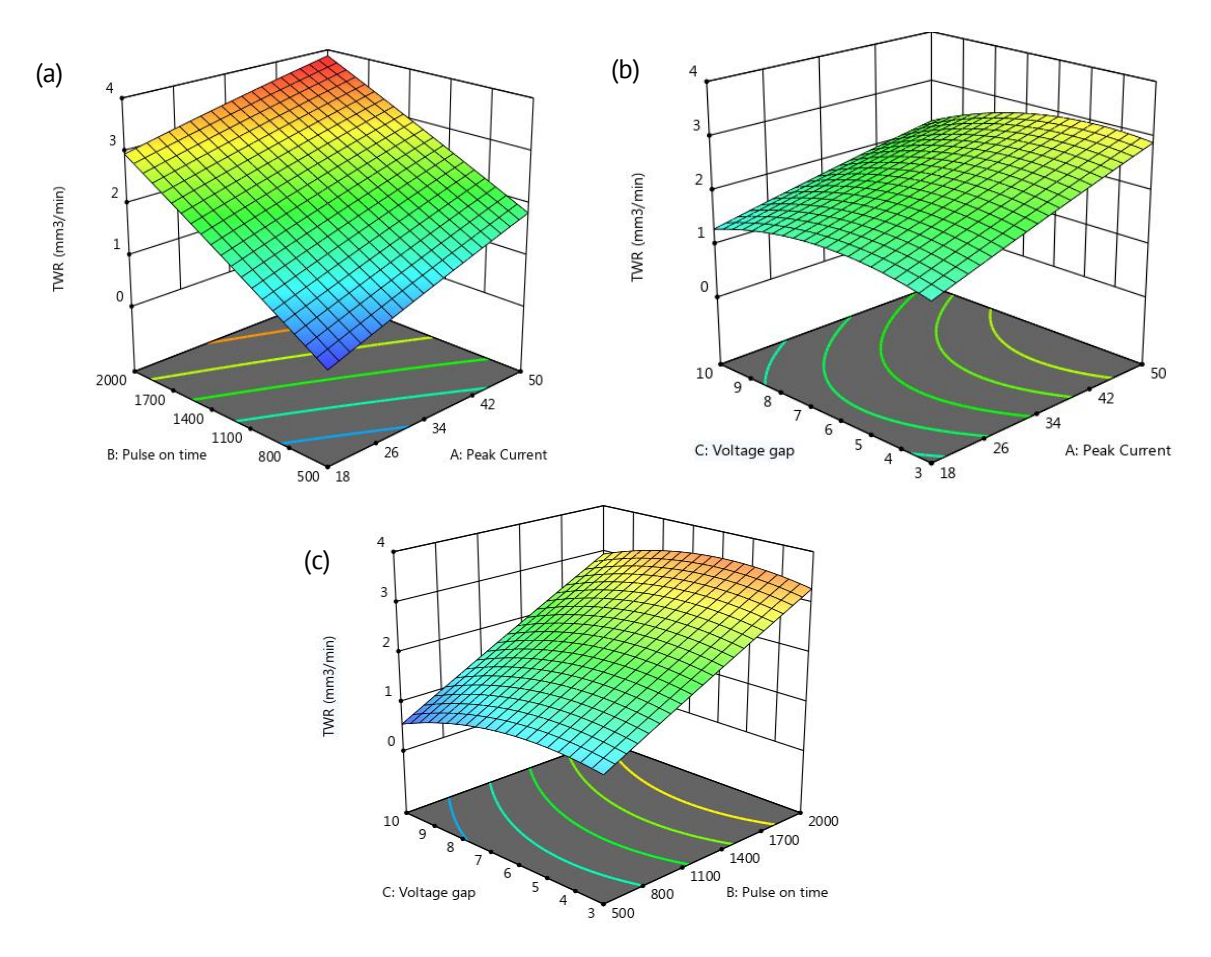


Fig. 4. Surface plot of TWR with (a) pulse on time and peak current, (b) voltage and peak current, (c) pulse on time and voltage gap

Table 6. ANOVA for response 3: for SR

Table 6. ANOVA for response 3: for 5k							
Source	Sum of squares	DF	Mean square	F-value	P-value		% contribution
Model	10.04	9	1.12	41.73	0.0004	significant	
A-peak	1.83	1	1.83	68.40	0.0004		17.994
current	1.03	1	1.03	00.40	0.0004		17.554
B-pulse on time	6.84	1	6.84	255.86	< 0.0001		67.25
C-voltage gap	0.2048	1	0.2048	7.66	0.0394		2.01
AB	0.0174	1	0.0174 0.6520		0.4561		0.17
AC	0.0066	1	0.0066	0.2455	0.6413		0.06
BC	0.0046	1	0.0046	0.1730	0.6947		0.04
A ²	0.0130	1	0.0130	0.0130			0.12
B ²	0.5264	1 0.526		19.70	0.0068		5.17
C ²	0.5121	1	0.5121	19.16	0.0072		0.0503
Residual	0.1336	5	0.0267				1.31
Lack of fit	0.0977	3	0.0326	1.82	0.3744	not significant	0.953
Pure error	0.0359	2	0.0179				0.3529
Cor total	10.17	14					

Table 6 shows the ANOVA table. The model shows that pulse on time has the highest contribution (67 %) in the formation of SR. In this case, A, B, C, B², and C² are significant model terms. In the EDM process, the surface mainly produced dues presence of different surface irregularities such as craters, cracks, globules and debris, etc. It is evident from the surface plot (Fig. 5) of surface roughness with I_p and T_{on} that, both the parameters are directly proportional to SR. With an increase in current (I_p) the intensity of the spark increases and when this highly intense spark strikes the work surface, it results in the formation of large craters. Similarly, with an increase in T_{on} , the spark strikes the surface for a longer duration and with improper flushing the debris may accumulate over the machined surface resulting in an increase the roughness.

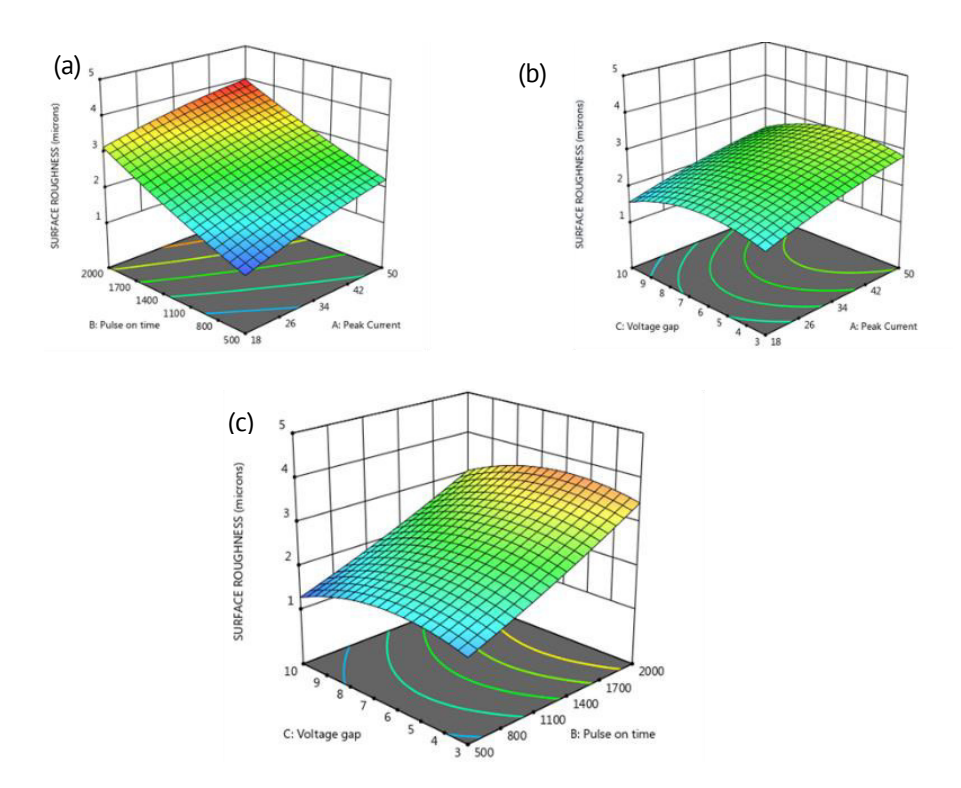


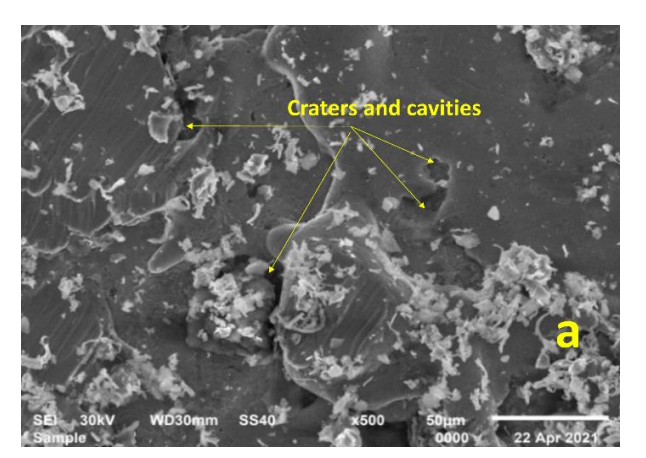
Fig. 5. Surface plot of *R*a with (a) pulse on time and peak current, (b) voltage and peak current, (c) voltage and pulse on time

The coefficient of determination (R^2) and adjusted R^2 of the developed model were found to be more than 95 % for all the responses, hence it is concluded that the lack of fit is not significant for all the responses.

Microstructural analysis

A microstructural analysis is carried out to the extent of evaluation of microstructure at the machined surface on the workpiece at different magnification levels. The microstructure of a material can strongly influences physical properties such as strength, toughness, ductility, hardness, corrosion resistance, etc. For this experiment, the Monel-400 superalloy has been taken for microstructural analysis after machining on EDM. The machined surfaces have been examined by SEM (scanning electron microscopy).

The spark in EDM is produced due to the movement of electrons and ions at very high kinetic energy between the two polarities in the dielectric medium. When these electrons and ions strike the surface of a workpiece or tool, it results in the conversion of kinetic energy into thermal energy or heat flux [29,30]. This intense localized heat flux at a high concentration of electrons and ions forms the plasma. Now upon withdrawal of the potential difference, the plasma channel bursts resulting in the formation of cracks and craters as shown in Fig. 6. Part of the molten material from the machined surface comes out as microchips may accumulate on the machined surface itself due to improper flushing is termed as debris or globules as depicted in Fig. 7(a).



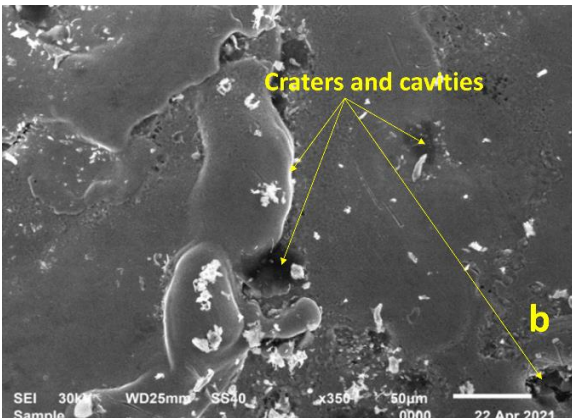
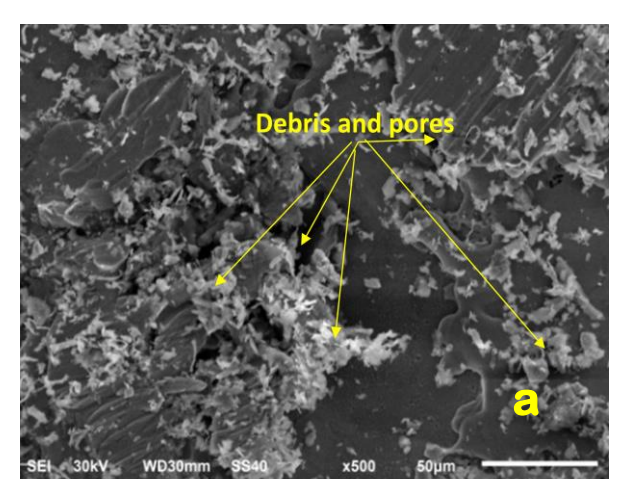


Fig. 6. Depiction of craters and cavities (a) 500x SEM image for Ip = 33, $T_{on} = 2000$ and V = 10, (b) 350x SEM image for $I_p = 50$, $T_{on} = 1000$, V = 7



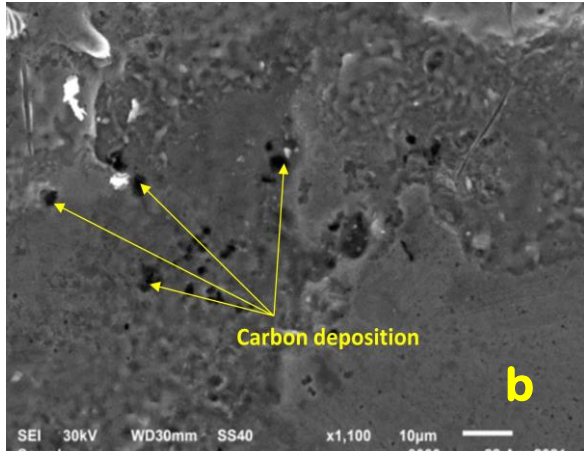
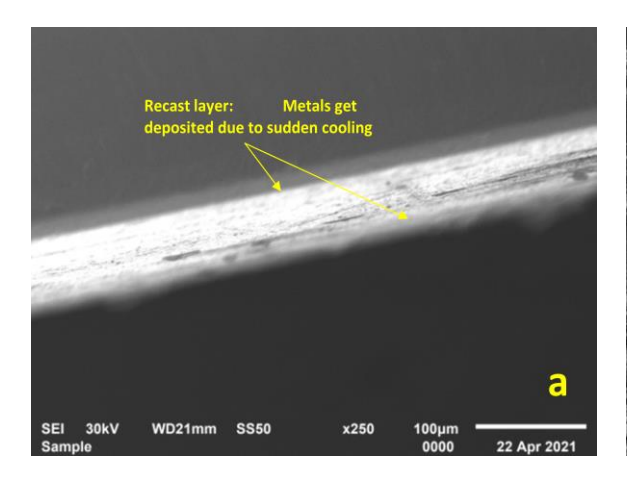


Fig. 7. (a) Formation of Debris, pores at the machined surface for $I_p = 50$, $T_{on} = 1000$, V = 3 and (b) carbon deposition at 1100x for $I_p = 50$, $T_{on} = 2000$, V = 7

Figure 7(b) shows the carbon particles getting deposited on the machined surface; this may be due to the burning of dielectric molecules in the plasma channel. At the time of the EDM machining process, a tremendous amount of heat is produced which melts the metal's surface. After machining, the metal experiences ultra-rapid cooling termed "quenching" due to flushing by dielectric fluid. A layer formation occurs on the workpiece surface explicated as a recast layer after solidification, as shown in Fig. 8. From micrographs, the thickness of the recast layer was calculated and found to be 81 μ m.



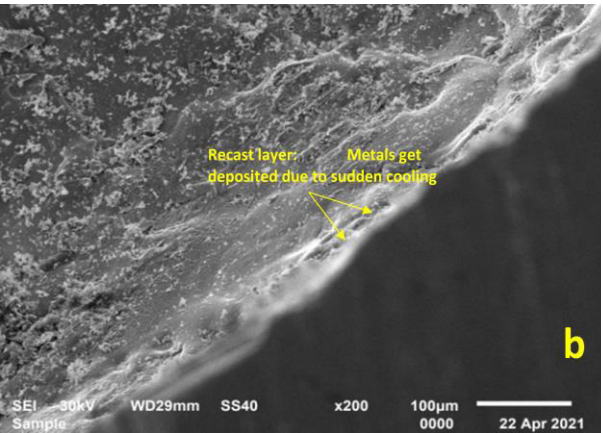


Fig. 8. Depiction of Recast layer at the edge of the machined surface (a) 250x SEM image for $I_p = 50$, $T_{on} = 2000$, V = 7, (b) 200x SEM image for $I_p = 18$, $T_{on} = 500$, V = 7

Conclusions

The empirical study on the impact of various EDM parameters on Monel-400 superalloy using cylindrical copper electrodes focused on key performance metrics such as material removal rate (MRR), tool wear rate (TWR), and surface roughness (SR). Subsequently, the correlation between process parameters and performance outputs was assessed utilizing response surface methodology (RSM), yielding the following conclusions:

- 1. From the findings of the result for MRR, peak current (I_p) played the most significant influencing factor with a 53.3 % contribution followed by pulse-on-time (T_{on}). Consequently, elevated I_p and T_{on} levels are correlated with enhanced MRR.
- 2. From the findings of the result for tool wear rate, the T_{on} played the most important influencing factor with a 71 % contribution followed by I_p . An increase in T_{on} and I_p correlates with an elevated tool wear rate, whereas an increment in inter-electrode-gap results in a marginal reduction of tool wear rate.
- 3. Analysis of surface roughness (SR) revealed that pulse-on-time (T_{on}) exerted the most significant influence, contributing 67 % to the response, followed by peak current (I_p). A better-machined surface can be obtained by limiting the values of Ton and Ip. It was also mentioned in some works of literature that, with effecting flushing the SR can be reduced.
- 4. Inter-electrode gap (IEG) was determined to have a negligible impact on all evaluated performance metrics.
- 5. Microstructure images revealed that most of the surface irregularities on the machined surface are obtained at higher levels of Ip and Ton. It can be reduced by proper flushing at the tool-workpiece interface.

CRediT authorship contribution statement

Manas R. Panda (DSC): writing – review & editing, writing – original draft, conceptualization, supervision; Srimant K. Mishra (DSC): writing – review & editing, supervision, data curation, Prabin K. Sahoo (DSC): writing – original draft, Investigation.

Conflict of interest

The authors declare that they have no conflict of interest.

References

- 1. Vikas, Shashikant, Roy AK, Kumar K. Effect and Optimization of Machine Process Parameters on MRR for EN19 & EN41 materials using Taguchi. *Procedia Technology*. 2014;14: 204–210.
- 2. Muthuramalingam T, Mohan B. A review on influence of electrical process parameters in EDM process. *Archives of Civil and Mechanical Engineering*. 2015;15(1): 87–94.
- 3. Kumar V, Kumar V, Jangra KK. An experimental analysis and optimization of machining rate and surface characteristics in WEDM of Monel-400 using RSM and desirability approach. *Journal of Industrial Engineering International*. 2015;11: 297 307.
- 4. Kuppan P, Rajadurai A, Narayanan S. Influence of EDM process parameters in deep hole drilling of Inconel 718. *The International Journal of Advanced Manufacturing Technology*. 2008;38(1–2): 74–84.
- 5. Kanagarajan D, Karthikeyan R, Palanikumar K, Paulo Davim J. Optimization of electrical discharge machining characteristics of WC/Co composites using non-dominated sorting genetic algorithm (NSGA-II). *The International Journal of Advanced Manufacturing Technology.* 2008;36(11–12): 1124–1132.
- 6. Kumar SS, Kumar N. Optimizing the EDM Parameters to Improve the Surface Roughness of Titanium Alloy (Ti-6AL-4V). *International Journal of Emerging Science and Engineering*. 2013;1: 2319–6378.
- 7. Mahalingam M, Varahamoorthi R. Investigation on tool wear rate of brass tool during machining of Monel-400 alloy using electric discharge machine. *Materials Today Proceedings*. 2020;26: 1213–1220.
- 8. Gopalakannan S, Thiyagarajan S, Kalaichelvan K. Modelling and Optimization of EDM of Al 7075/10wt% Al2O3 Metal Matrix Composites by Response Surface Method. Advanced Materials Research. *Advanced Materials Research*. 2012;488–489: 856–860.
- 9. Kung K, Chiang K. Modelling and analysis of machinability evaluation in the wire electrical discharge machining (wedm) process of aluminium oxide-based ceramic. *Materials and Manufacturing Processes*. 2008;23(3): 241–250.
- 10. Jahan MP, Wong YS, Rahman M. A study on the fine-finish die-sinking micro-EDM of tungsten carbide using different electrode materials. *Journal of Materials Processing Technology*. 2009;209(8): 3956–3967.
- 11. Lee SH, Li XP. Study of the effect of machining parameters on the machining characteristics in electrical discharge machining of tungsten carbide. *Journal of Materials Processing Technology*. 2001;115(3): 344–358.
- 12. Mahalingam M, Umesh BA, Varahamoorthi R. Effect of Wire Electric Discharge Machining Process Parameters on Surface Roughness of Monel 400 Alloy. In: *Green Materials and Advanced Manufacturing Technology*. Boca Raton: CRC Press; 2020. p.161–172.
- 13. Sameh SH. Study of the parameters in electrical discharge machining through response surface methodology approach. *Applied Mathematical Modelling*. 2009;33(12): 4397–4407.
- 14. Soveja A, Cicala E, Grevey D, Jouvard J-M. Optimisation of ta6v alloy surface laser texturing using an experimental design approach. *Optics and Lasers in Engineering*. 2008;46(9): 671–678.
- 15. Natarajan M, Pasupuleti T, Kiruthika J, Kumar V, Duraisamy P, Polanki V. Optimization of Spark Erosion Machining of Monel 400 Alloy for Automobile Applications. In: *International Conference on Advances in Design, Materials, Manufacturing and Surface Engineering for Mobility*. SAE International; 2023. p.2023–20–0140.
- 16. Pasupuleti T, Natarajan M, Kumar V, Katta LN, Kiruthika J, Silambarasan R. Predictive Modelling and Process Parameter Prediction for Monel 400 Wire Electrical Discharge Machining for Rocket Frames. In: *International Conference on Advances in Design, Materials, Manufacturing and Surface Engineering for Mobility*. SAE International; 2023. p.2023–28–0088.
- 17. Kulshrestha AS, Haldar B, Unune DR, Dargar AK. Evaluating the Performance of Electrical Discharge Face Grinding on Super Alloy Monel 400. *Materials Research Express.* 2023;10(9): 096516.
- 18. Narkhede AR. Mathematical Analysis for Optimizing Electro Discharge Machining Parameters and Enhancing Hastelloy Machining Efficiency. *Communications on Applied Nonlinear Analysis*. 2024;31(1s): 106–120.
- 19. Rajamani D, Kumar MS, Balasubramanian E. Multi-response optimization of plasma arc cutting on Monel 400 alloy through. whale optimization algorithm. In: *Handbook of Whale Optimization Algorithm. Variants, Hybrids, Improvements, and Applications.* 2024. p.373–386.

- 20. Gupta PK, Gupta MK. Hybrid optimization approach on electrical discharge machining process for hybrid Al-Al2O3/B4C composites. *Materials Physics and Mechanics*. 2022;50(2): 200–215.
- 21. Shanmughasundaram P. Influence of abrasive water jet machining parameters on the surface roughness of eutectic Al-Si alloy-Graphite composites. *Materials Physics and Mechanics*. 2014;19(1): 1–8.
- 22. Amuthakkannan P, ArunPrasath K, Manikandan V, Uthayakumar M, Sureshkumar S. Investigation of the machining performance of basalt fiber composites by abrasive water jet machining. *Materials Physics and Mechanics*. 2021;47(6): 830–842.
- 23. Sivasankar S, Jeyapaul R, Prasad VV. Performance study of various tool materials for electrical discharge machining of hot pressed zrb2. *Multidiscipline Modeling in Materials and Structures*. 2012;8(4): 505–523.
- 24. Assarzadeh S, Ghoreishi M. A dual response surface-desirability approach to process modeling and optimization of Al2O3 powder-mixed electrical discharge machining (PMEDM) parameters. International *Journal of Advanced Manufacturing Technology*. 2012;64(9–12):1459–1477.
- 25. Yadav HNS, Das M. Evaluation of plasma parameters' impact on MRR and surface roughness in plasma polishing of fused silica: An investigation of surface characterization. *Vacuum.* 2024;225: 113263.
- 26. Panda MR, Biswal SK, Sharma YK. Experimental analysis on the effect of process parameters during CNC turning on nylon-6/6 using tungsten carbide tool. *International Journal of Engineering Sciences & Research Technology*. 2016;5(4): 79–84.
- 27. Arun Kumar NE, Ganesh M, Vivekanandan N. Optimization of machining parameters in WEDM of Monel 400 using Taguchi technique. *Materials Today: Proceedings.* 2020;22: 2199–2206.
- 28. Mohanty A, Gangadharudu T, Gangopadhyay S. Experimental investigation and analysis of EDM characteristics of Inconel 825. *Materials and Manufacturing Processes*. 2014;29(5): 540–549.
- 29. Hourmand M, Farahany S, Sarhan AAD, Yusof NM. Investigating the electrical discharge machining (EDM) parameter effects on Al-Mg2Si metal matrix composite (MMC) for high material removal rate (MRR) and less EWR-RSM approach. *The International Journal of Advanced Manufacturing Technology*. 2015;77(5): 831–838.
- 30. Naik S, Das SR, Dhupal D. Analysis, predictive modelling and multi-response optimization in electrical discharge machining of Al-22 %SiC metal matrix composite for minimization of surface roughness and hole overcut. *Manufacturing Review.* 2020;7: 20.

Accepted: May 29, 2025

Submitted: February 02, 2025

Revised: March 6, 2025

Effect of traverse speed on three-point bending behavior and surface quality of AA5083-H111 friction stir welds

M.A.A. Hanifi, M. Zemri 📵, M. Merzoug 🖾 📵

University of Djillali Liabes, Sidi Bel Abbes, Algeria

[™] m_merzoug01@yahoo.fr

ABSTRACT

The FSW was developed to obtain a good joint in terms of surface quality, mechanical property and microhardness in aluminum and other alloy systems. This study investigates the effect of traverse speed on the three-point bending behavior and surface quality of friction stir welds in AA5083-H111 aluminum alloy by using with different parameters such as weld speeds (16, 20, 25, 30, 40, 50 and 63 mm/min) while maintaining constant rotational speed (1400 rpm) and tool geometry. The resulting welds were subjected to three-point bending tests to evaluate their mechanical performance, specifically focusing on yield strength, ultimate tensile strength, and ductility. Additionally, the investigation includes macrostructure, microhardness, and fracture toughness evaluations. The findings indicated that an augmentation in traverse speed led to elevated tensile strength and hardness levels due to enhanced material flow and bonding, while higher speeds led to increased surface roughness and reduced weld integrity. The study suggests that superior joints with favorable mechanical properties can be achieved by utilizing an intermediate rotational speed of 1400 rpm and a traverse speed of 20 mm/min.

KEYWORDS

friction stir welding • surface roughness • aluminum 5083H111 • parameters • bending test

Citation: Hanifi MAA, Zemri M, Merzoug M. Effect of traverse speed on three-point bending behavior and surface quality of AA5083-H111 friction stir welds. *Materials Physics and Mechanics*. 2025;53(3): 37–47. http://dx.doi.org/10.18149/MPM.5332025 4

Introduction

Friction stir welding (FSW) is a recently invented solid state welding process, especially for aerospace or aeronautics applications and for welding of large tank for launch vehicles involving aluminum alloys [1,2]. In many industrial programs steels are conveniently replaced by non-ferrous alloys, in most cases using aluminum alloys, the joining of those materials can occasionally cause serious problems [3]. Various joint configurations can also be assembled by FSW process like lap, but T joint which gave wide use for technology [4,5]. Tool geometry, rotating speed and welding speed among the factors influenced on quality joint welded by FSW [6]. In one study, increasing the rotational speed results in an increase in the peak temperature, leading to the expansion of the nugget zone (NZ) and the softened region within the joint [7]. Raj Kumar et al. [8] studied the influence of post-weld heat treatments (PWHT) on friction stir welded joints of AA2014 and AA7075 dissimilar alloys, such as PWHT conditions, namely artificial aging (AA), solution treatment and artificial aging, solution treatment (ST), and natural aging (NA). The study revealed that natural aging showed the best strength of 347.5 ± 7.78 MPa among all the PWHT conditions and that in other PWHT welds, fractures occurred outside the weld region. Saravanakumar et al. [9] recommends that the



This is an open access article under the CC BY-NC 4.0 license (https://creativecommons.org/li-censes/by-nc/4.0/)

nugget zone (NZ) exhibits recrystallized fine grains with an equiaxed structure as a result of dynamic recrystallization (DRX), resulting in improved mechanical properties of the joint.

AA5083-H111 is a high-strength magnesium alloy primarily composed of aluminum. This alloy is commonly used in various applications (marine, shipbuilding, aerospace and automotive industry due to its favorable combination of properties, including excellent corrosion resistance, good weldability, and high strength.

Bending in friction stir welding (FSW) refers to the effect of bending on the strength and microstructure of the welded materials. Several studies have investigated the impact of bending on FSW joints, and the result varied depending on the welding conditions [10–12]. Saravanakumar et al. [13] studied that the mechanical properties of the AA5083 UWFSW joint, such as its average ultimate tensile strength and hardness, have been greatly improved using a straight hexagonal tool profile, tool rotational speed of 1200 rpm and welding speed of 20 and 40 mm/min.

For better understand the phenomenon of FSW and the impact of process parameter on welded joint, depth research was investigated on microhardness and surface roughness of joint. Sumit et al. [14] used three passes on the FSW of AA5083 and 6082 dissimilar joints and the observed that FSWeld reinforced joint exhibited the highest tensile strength, strain (%), and microhardness due to higher grain refinement. Xu et al. [15] conducted a study on the microhardness of friction stir welded (FSW) joints in different plate thicknesses of AA2219-O aluminum alloy. Oluwaseun et al. [16] suggests that understanding the effect of microstructure and defects on FSW joint failure will facilitate optimization of process variables, weld quality assurance and decision making. They found that the maximum hardness was on the advanced side of the nugget, and the upper part of the weld joint was harder than the bottom in the nugget due to the high temperature and intense mechanical agitation [15,16]. Miloudi et al. [17] found that decrease in rotation speed leads to better hardness quality of AA3003 aluminum alloy welded joint. In [18], it was mentioned that the surface roughness (R_a) of the welded area is influenced by the rotational speed of the tool, with higher tool rotary speeds resulting in decreased surface roughness. Optimizing the welding parameters can lead to improved surface roughness of FSW joints, enhancing their functional properties and durability. In a study [19], the effect of welding parameters on mechanical properties and fracture behavior of FSW for aluminum alloy 5083 H111, a joint coefficient C_i is evaluated for the qualification of the good mechanical strength of welded joints.

This study contributes to the growing research focused on optimizing friction stir welding parameters for superior joint quality and mechanical properties (tensile, hardness). The impact of the shoulder's side surface on heat generation is also taken into account. The research investigates the effect of various processing parameters (rotating speed, welding speed, dwell time) on the quality and mechanical properties of joints made by FSW using AA5083 aluminum alloy. In addition to optimize the FSW parameters which will led to significant improvements in the mechanical properties of aluminum alloy welds, making it a promising technique for various industrial applications.

Materials and Methods

AA 5083H111 alloy of 5 mm thickness was used. Samples were cut according to the shape shown in Fig. 1. The samples of the three-point bending test were chosen (as GB/T 232-999 standard). The external sheets were welded parallel to the rolling direction while the central sheet was put in the long transverse direction for FSW process in order to limit potential effect of rolling texture. The chemical composition of the aluminum 5083H111 sheet is presented in Table 1 and the mechanical properties of the sheets are presented in Table 2. The chemical composition was obtained by SEM-EDX (scanning electron microscopy-energy dispersive X-ray analysis) method [19].

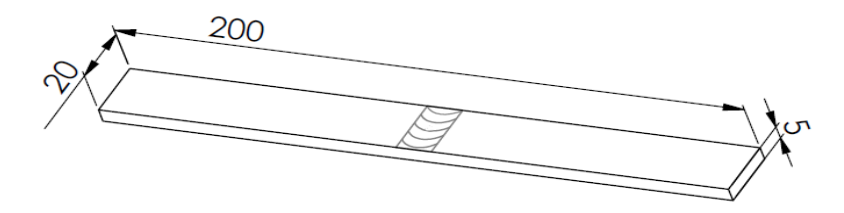


Fig. 1. Geometry of three-point bending specimen

Table 1. Chemical composition of 5083 H111 aluminum alloy (BM)

Al	Si	Fe	Cu	Mn	Mg	Cr	Zn	Ti
0.50	0.40	0.40	0.10	0.10	4.90	0.25	0.25	0.15

Table 2. Mechanical properties of 5083 H111 aluminum alloy

			,	T	
<i>E</i> , MPa	MPa <i>YS</i> , MPa <i>UTS</i> ,		UTS, MPa A, %		HV
71008	155	236	16.5	45	88



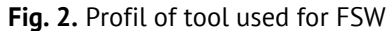




Fig. 3. Vertical milling machine

The welding tool used for the joint is made of steel type 42CrMo4 (Fig. 2), it has the mechanical properties (R = 750/1300 MPa, A = 10-14 %, $R_e = 500/900 \text{ MPa}$ and E = 210000 MPa), a threaded cylindrical pin (5 mm in diameter and 4.7 mm in length) and shoulder (20 mm diameter). This selection of material was also motivated by cost and

availability. The geometry of the tool, including the pin and shoulder design, significantly affects the material flow and heat distribution and, consequently, the distribution of hardness in the weld zones.

A vertical milling machine was used for the production of the joints. It is characterized by: a power of 5 KW,a rotation speed range of 45 to 2000 rpm and a range of feed speeds from 16 to 800 mm/min. The fixture was first fixed on the machine bed with help of clamps . The plates were held in the fixture properly for friction stir welding as shown in Fig. 3.

Welds by FSW was conducted at selected a constatnt rotation speeds of 1400 rpm and selected travel speeds of 16, 20, 25, 30, 40, 50 and 63 mm/min. An example photo of the joints produced with the different used welding speed is presented in Fig. 4. After the FSW welding process, the tensile test were carried out on an CONTROLAB bending machine, as shown in Fig. 5. The hardness on the weld cross-section was measured point wise for each specimen with a load 1000 g and a dwell time of 10 s.The surface quality of the FSW sample was obtained by the arithmetic average roughness value (R_a) using a Mututiyo surf test sv-400 roughness meter.



Fig. 4. Example of welded joints obtained with different welding speed



Fig. 5. Testing machine CONTROLAB and specimen for three-point bending test

Results and Discussions

Effect of welding speed on surface roughness

Figure 6 shows the effect of welding speed on the quality of the joint measuring by arithmetic average roughness value (R_a). An increase in welding speed effect directly the increase of surface roughness of the joint. Reducing surface roughness can lead to improved corrosion resistance, better mechanical properties, and enhanced aesthetics.

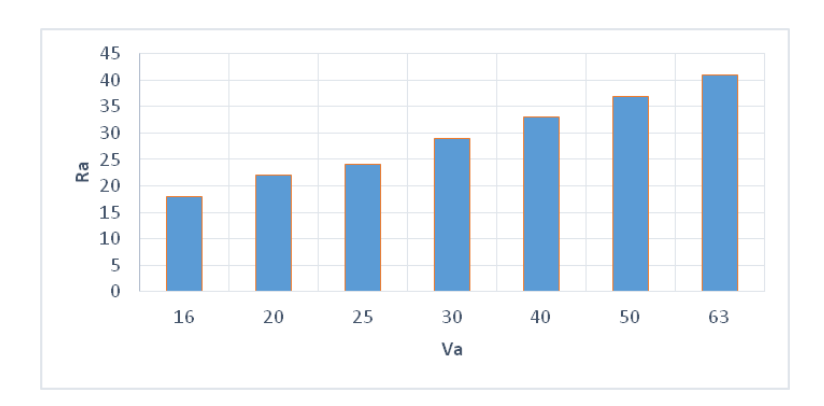


Fig. 6. Surface roughness of different welding parameter

The result of each specimen show that the highest value of surface roughness obtained at 1400 rpm of rotational speed and when we increase welding speed at 63 mm/min which is 41 μ m, however, lowest surface roughness of 18 μ m was obtained at 1400 rpm and feed rate of 16 mm/min. R. Kumar et al. [20] observed that value of surface roughness increase when they increase welding speed. However, in [21,22], another study surface roughness decreases when we decrease welding speed.

Microhardness measurements

In the majority of welds made, it was found that there was significant hardness variation in the weld zones in AA5083-H111 FSWeld joints, as shown in Fig. 7. The cylindrical pin achieved symmetrical hardness distribution with regard to the center line of the FSW keyhole for all the applied tool welding speeds and constant rotational speed. The hardness in the HAZ is generally the lowest compared to the SZ and TMAZ. The grain coarsening, combined with the loss of strengthening precipitates (due to over-aging effects), causes a significant reduction in hardness. The hardness in this zone is 20-30~% lower than in the base material and can be the weakest point in the weld, making the HAZ more susceptible to failure under stress.

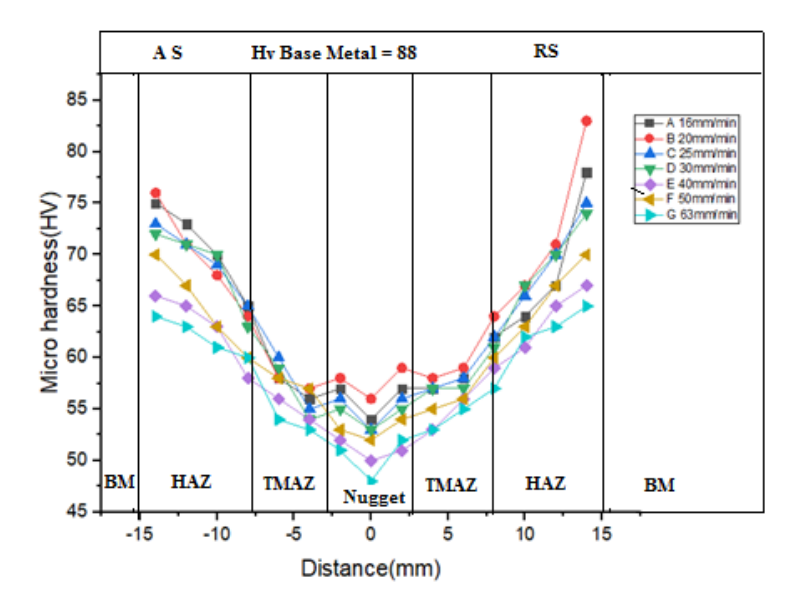


Fig. 7. Variation of the hardness for the rotational speed 1400 rpm

The outcome of hardness higher values 82 HV in TMAZ region on retreating side (RS) for welding speed 20 mm/min and decreases at 75 HV in the advancing side (AS). It is due to the much-refined grain size and higher dislocation densities in the stir zone [23]. It should be emphasized that the size of the ZS area is governed by the pin diameter while the TMAZ area is generated by the size of the tool shoulder of the tool. This degradation in hardness is mostly characterized in the TMAZ. This is attributed to a combination of high stresses and large strains resulting in the deformation of the grain structure, where re-crystallization did not take place, caused a coarse grain structure [24,25]. This dynamic recrystallization observed in the weld region results in a decrease in grain size and an increase in hardness in the joints [26–29].

Bending test

The bending test is a crucial evaluation method in assessing the mechanical properties and performance of friction stir welded (FSW) joints, particularly for AA 5083-H111 aluminum alloy. Three-point bending tests were conducted using a CONTROLAB machine for all specimen (A to G) the results are presented in Fig. 8 and 9. The bending tests were performed on the face and the root of the joint as an important tool to understand the ductility and toughness of friction stir welds (bond strength). Most of the welds presented good ductility, especially in case the joint made at 1400 rpm and 20 mm/min



Fig. 8. Three-point bending test

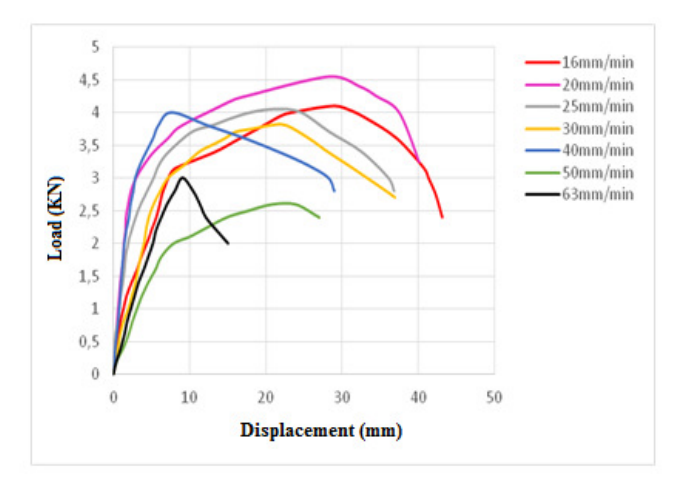


Fig. 9. Three-point bending test-displacement

Table 3. Fracture position on the specimens							
V, mm/min / Angle of Bend, °	Weld photos	Observations					
16/80		No fracture					
20 / 83		No fracture					
25 / 83		No fracture					
30 / 86		Crack on bend surface					
40 / 80		Crack on bend surface					
50 / 80		Crack on bend surface					
63 / 82		Crack on bend surface					

(configuration A) where the maximum deflection reached to 43 mm with efficiency of about 90 % compared to the base metal, this is due to higher temperatures involved during FSW, so the Base Metal adequately soften to go higher bending strength [30]. The immediate growth in force that appear in configuration G (63 mm/min) at about 15 mm deflection came from some slipping occurred between bending specimens and device jaw so that slipping didn't affected on the total results because that shifting occurred in all specimens and the comparison between base metal and welded specimens stilled in the same values [31]. Finally, these results of bending tests can be correlated with microstructural characteristics of the welds, such as grain size and distribution, heat-affected zone (HAZ) properties, and the presence of defects. This correlation helps in understanding how microstructural changes due to FSW affect the mechanical performance of the joints. The results of the bending tests conducted on all the FSW weld joints produced at rotation speed of 1400 rpm and welding speeds of 16, 20, 25, 30, 40, 50, 60 mm/min are hereby presented in Table 3.

The defects found are mainly lack of penetrations, wormholes or voids, as well as root flaws [32]. Other defects observed include inclusions which were rich in iron and from analysis these inclusions can be classified as iron oxide particles in the weld. For the first three samples for welding speeds 16, 20 and 25 mm/min, the post-bending results showed the tested specimens without failure. This means that the welded materials have bonded well during welding. For all the FSW experimental work and because rotational speed and welding speed significantly the bowing quality the bending strength by influencing the heat generated in the weld zones [32].

Weld microstructures and properties of FSW joint

Friction stir welding (FSW) of AA 5083-H111 commonly used aluminum alloy in marine and automotive applications, results in distinct microstructural changes in the weld metal. The microstructures of weld region of weldments were perceived using an optical microscope, and the relevant micrographs are presented in Fig. 10. While all the fracture surfaces display dimples, the size and shape of the dimples show differences. However, there are dimple-free flat regions, as can be seen in Fig. 10(a,c,e), and a ductile fractured surface can be identified. Figure 10(b,d,f) shows many defects such as voids, cracks and porosities. Conversely, the rise of the heat input decreases the hardness of the heat-affected zone, where recrystallization does not occur. The river marks diverging downwards on the surface of the tool marks (Fig. 10(b)) and upwards at the ending of the unconsolidated onion rings (Fig. 10(d)), indicated that they were the primary regions of crack initiation in the weld tunnel.

What's more, the HAZ had the highest grain size in contrast with the stir zone in which the finest grain size could be seen [33]. In the stir zone, the temperature is the highest, and the material experiences intense plastic deformation due to the rotating tool. This causes significant grain refinement, leading to a fine-grained microstructure. The grain size in this region is typically much smaller than in the base material. As the SZ presents the smaller and more significant quantity of second-phase particles, therefore a greater number of cracking sites is available, the SZ is a favorable crack initiation site [34,35]. Consequently, this synergistic effect promotes a more rapid and thorough process of dynamic recrystallization which refines the grains in the stir zone and forces the fracture

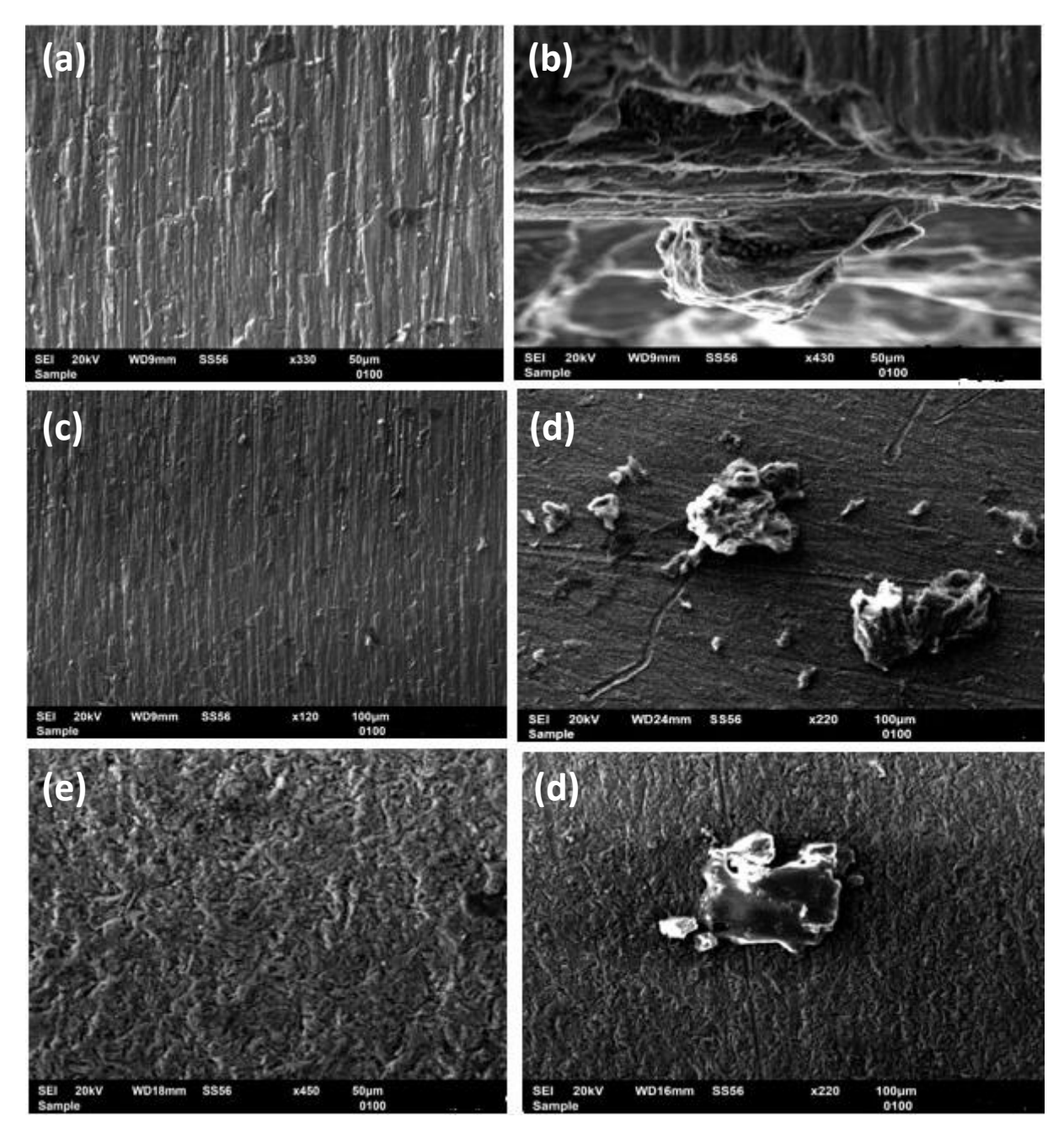


Fig. 10. SEM-images of the welded specimen

outside the stir zone [36]. The stir zone may also exhibit "onion-ring" patterns, which are a result of the material flow around the rotating tool. These patterns are typically visible in the microstructure and can influence local variations in the mechanical properties.

Conclusions

In friction stir welding (FSW) of AA5083-H111 aluminum alloy, traverse speed significantly influences both the three-point bending behavior and surface quality of the welds. An optimal traverse speed ensures adequate heat input and material flow, leading to improved mechanical properties and surface finish. Conversely, excessively high traverse speeds can result in inadequate bonding and surface defects, adversely affecting the weld's mechanical performance.

The main findings of this investigation are:

- 1. Highest bending strength by using rotation speed 1400 rpm and travel speed 20 mm/min because of no necking or cracking were noticed in the weld zone.
- 2. Most of the defects produced in the root surface because of the effect of unwelded zone. while the defects in the face of welded region because of the tunnel hole or internal crack defect.
- 3. The highest hardness at 1400 rpm and 20 mm/min due to the very fine grain size created by FSW.
- 4. The weld nugget/TMAZ interface was not a weak region in FSW AA5083-H111.
- 5. Increased welding speeds resulted in a reduction in vertical pressure that caused increased size, number, and severity of weld defects.

The fracture almost always took place in the heat affected zone in particular on the retreating side.

CRediT authorship contribution statement

Mohamed Amine Adda Hanifi: investigation; **Mokhtar Zemri DSC®**: investigation; **Mohammed Merzoug SC®**: writing – original draft, conceptualization, supervision.

Conflict of interest

The authors declare that they have no conflict of interest.

References

- 1. Alaeibehmand S, Mirsalehi SE, Ranjbarnodeh E. Pinless FSSW of DP600/Zn/AA6061 dissimilar joints. *Journal of Materials Research and Technology*. 2021;15: 996–1006.
- 2. Kavathia K, Badheka V. Application of Friction Stir Welding (FSW) in Automotive and Electric Vehicle. In: Parwani AK, Ramkumar P, Abhishek K, Yadav SK. (eds) *Recent Advances in Mechanical Infrastructure*. *Lecture Notes in Intelligent Transportation and Infrastructure*. Singapore: Springer; 2022. p. 289–304.
- 3. Dellal N, Merzoug M, Mimmi A, Benamara N. Relationship between mechanical behavior and process factors in friction stir welding aluminum alloys. *Incas Bulletin*. 2024;16(2): 47–60.
- 4. Beygi R, Talkhabi AA, Zarezadeh Mehrizi M, Marques EAS, Carbas RJC, da Silva LFM. A Novel Lap-Butt Joint Design for FSW of Aluminum to Steel in Tee-Configuration: Joining Mechanism, Intermetallic Formation, and Fracture Behavior. *Metals*. 2023;13(6): 1027.
- 5. Çam G, Javaheri V, Heidarzadeh A. Advances in FSW and FSSW of dissimilar Al-alloy plates. *Journal of Adhesion Science and Technology*. 2022;37(2): 162–194.
- 6. Mroczka K, Dymek S, Węglowska A, Hamilton C, Kopyściański M, Pietras A, Kurtyka P. Comprehensive Research of FSW Joints of AZ91 Magnesium Alloy. *Materials*. 2023;16(11): 3953.
- 7. Saravanakumar R, Rajasekaran T, Pandey SM, Sirohi S, Pandey C. Effects of welding parameter on the microstructure and mechanical properties of friction stir-welded non-heat treatable alloy AA5083. *Journal of Adhesion Science and Technology.* 2024: 1–19.
- 8. Kumar R, Upadhyay V, Pandey C. Effect of Post-Weld Heat Treatments on Microstructure and Mechanical Properties of Friction Stir Welding Joints of AA2014 and AA7075. *Journal of Materials Engineering and Performance*. 2023;32: 1098910999.
- 9. Saravanakumar R, Rajasekaran T, Pandey C. Underwater Friction Stir Welded Armour Grade AA5083 Aluminum Alloys: Experimental Ballistic Performance and Corrosion Investigation. *Journal of Materials Engineering and Performance*. 2023;32: 10175–10190.
- 10. Kareem NS, Ahmed ZMS, Sahar HA. Evaluation of FSW Process Parameters of Dissimilar Aluminium Alloys. *Innovative Systems Design and Engineering*. 2016;7(9): 55–69.

- 11. Nagano Y, Takeda J, Hashimoto T, Miyamichi T, Namba K. Bending properties of friction stir welded joints Studies on characteristics of friction stir welded joints in structural aluminum alloys (report 4). *Welding International*. 2008;22(1): 1–6.
- 12. Bušić M, Kožuh Z, Klobčar D, Samardžić I. Friction stir welding (FSW) of aluminium foam sandwich panels. *Metalurgija*. 2016;55(3); 473–476.
- 13. Saravanakumar R, Rajasekaran T, Pandey C. Optimisation of underwater friction stir welding parameters of aluminum alloy AA5083 using RSM and GRA. *Sage Journals*. 2022;237(6): 2334–2348.
- 14. Sumit J, Mishra RS, Husain M. Influence of SiC Microparticles and Multi-Pass FSW on Weld Quality of the AA6082 and AA5083 Dissimilar Joints. *Silicon*. 2023;15: 6185–6197.
- 15. Xu W, Liu J, Luan G, Dong C. Temperature evolution, microstructure and mechanical properties of friction stir welded thick 2219-O aluminum alloy joints. *Materials & Design*. 2009;30(6): 1886–1893.
- 16. Oluwaseun JD. Fracture mechanics and mechanical behaviour in AA5083-H111 friction stir welds. *Scientific African*. 2020;8: e00265.
- 17. Chekalil I, Miloudi A, Planche MP, Ghazi A. Prediction of mechanical behavior of friction stir welded Joints of AA3003 aluminum alloy. *Frattura ed Integrità Strutturale*. 2020;54: 153–168.
- 18. Abeer E, Os M. Influence of Process Parameters of Friction Stir Welding (FSW) on the Mechanical Properties and the Surface Quality of Welded Joint. *ERJ: Engineering Research Journal*. 2022;45(1): 51–64
- 19. Merzoug M, Ghazi A, Lousdad A, Benamara N, Miloudi A, Boulenouar A. Effect of the parameters affecting the properties during friction stir welding of AA 5083 H111 alloy. *Materials Physics and Mechanics*. 2023;51(5): 115–125. 20. Bhushan RK, Sharma D. Investigation of mechanical properties and surface roughness of friction stir welded AA6061-T651. *International Journal of Mechanical and Materials Engineering*. 2020;15(7): 1–14.
- 21. Chinchanikar S, Gharde S, Gadge M. Investigation of tool forces, weld bead micro-hardness and surface roughness during friction stir welding of aluminium 6063 alloy. *Advances in Materials and Processing Technologies*. 2020;8(1): 1–9.
- 22. Abdullah IS, Mohammed SA, Abdallah S. Artificial neural network modelling of the surface roughness of friction stir welded AA7020-T6 aluminum alloy. *Engineering Research Journal-Faculty of Engineering (Shoubra)*. 2020;1(46): 1–5.
- 23. Wang B, Chen F, Liu F, Wang W, Xue P, Ma Z. Enhanced mechanical properties of friction stir welded 5083Al-H19 joints with additional water cooling. *Journal of Materials Science & Technology*. 2017;33(9): 1009–1014.
- 24. Mumvenge I, Akinlabi SA, Mashinini PM, Fatoba SO, Okeniyi JO, Akinlabi E. Evaluation of Friction Stir Welds by X-ray Digital Radiographic Non- Destructive Approach. *Materials Science and Engineering*. 2018;413(1): 012035.
- 25. Ahmed MMZ, Ataya S, El-Sayed Seleman MM, Mahdy A. Heat input and mechanical properties investigation of friction stir welded AA5083/AA5754 and AA5083/AA7020. *Metals*. 2021;11(1): 68.
- 26. Umasankar D, Vijay T. Bending Strength Evaluation Of Friction Stir Welded AA6101-T6 And AA6351-T6 Aluminum Alloys Butt Joint. *Materials Today Proceeding*. 2018;5(5): 11556–11562.
- 27. Rana PK, Narayanan RG, Kailas SV. Friction Stir Spot Welding of AA5052-H32/HDPE/AA5052-H32 Sandwich Sheets at Varying Plunge Speeds. *Thin-Walled Structures*. 2019;138: 415–429.
- 28. Tiwan, Ilman MN, Kusmono K. Microstructure and Mechanical Properties of Friction Stir Spot WeldedAA5052-H112 Aluminum Alloy. *Heliyon*. 2021;7(2): e6009.
- 29. Merzoug M, Mazari M, Berrahal L, Imad A. Parametric Studies of the Process of Friction Spot Stir Welding of Aluminium 6060-T5 Alloys. *Material & Design*. 2010;31(6): 3023–3028.
- 30. Msomi V, Mbana N. Mechanical Properties of Friction Stir Welded AA1050-H14 and AA5083-H111 Joint: Sampling Aspect. *Metals*. 2020;10(2): 214.
- 31. Muhsin J, Ayad MT, Nawzad KK. Comparison between friction stir welding (FSW) and friction stir processing (FSP) of AA5086 aluminium alloy. *International Journal of Technical Research and Applications*. 2015;3(6): 205–210.
- 32. Naimuddin SK, Ahamad T, Kampurath V, Ali Y. Mechanical properties of friction stir welding joints of similar & disimilar aluminium alloys AA6061 & 6082. *International Journal of Mechanical Engineering and Technology*. 2016;7(4): 256–266.
- 33. Dellal N, Merzoug M, Mimmi A, Ghazi A, Lousdad A. Experimental Based Determination And Analysis Of Mechanical Properties Of AA 3003 Alloy Welded With Friction Stir Lap Welding Process. *Journal of Applied Engineering Science*. 2023;21(2):451–461.
- 34. Dorbane A, Harrou F, Sun Y. Exploring Deep Learning Methods to Forecast Mechanical Behavior of FSW Aluminum Sheets. *Journal of Materials Engineering and Performance*. 2022;32: 4047–4063.
- 35. Dorbane A, Ayoub G, Mansoor B, Hamade RF, Imad A. Effect of temperature on microstructure and fracture mechanisms in friction stir welded Al6061 joints. *Journal of Materials Engineering and Performance*. 2017;26(6): 2542–2554.
 36. Abdul Khaliq U, Muhamad MRB, Yusof F, Ibrahim SB, Mohd Isa MS, Chen Zh, Çam G. A review on friction stir butt welding of aluminum with magnesium: A new insight on joining mechanisms by interfacial enhancement. *Journal of Materials Research and Technology*. 2023;27: 4595–4624.

Submitted: April 22, 2025 Revised: May 13, 2025 Accepted: July 10, 2025

Polymer weld characterization and defect detection through advanced image processing techniques

G.C. Ganesha ^{1,2} , C. Mukti ¹, S. Arungalai Vendan ¹, R. Sharanabasavaraj ¹

ABSTRACT

Welding defect detection in a radiographic image is vital in industrial non-destructive testing. It is significant in evaluating weld anomalies and surface and subsurface imperfections in welded joints. Digital image processing techniques can make automation feasible in the weld microscopic image interpretation, thus reducing the instances of observational human errors in weld inspection. This technique will give more reliability, speed and reproducibility to the inspection system. This paper uses MATLAB image processing tools for weld defect detection using scanning electron microscope images of ultrasonically welded polymer samples. Image processing features of gray scaling, image resizing, histogram equalization, edge detection, thresholding, filtering, texture analysis, and image segmentation have been implemented for the detection and characterization of defects in weld scanning electron microscope images. Thorough insights into the structure of these defects are an essential step in appreciating the weld's quality. The approach is well-suited for defect detection of any welding technique.

KEYWORDS

image processing • weld defects • scanning electron microscope analysis

Acknowledgements. The authors thank Mr. Alwin Raj Lobo, Head, UltraTechSonic Solutions, Bangalore, for extending research facilities to undertake this project.

Citation: Ganesha GC, Mukti C, Arungalai Vendan S, Sharanabasavaraj R. Polymer weld characterization and defect detection through advanced image processing techniques. *Materials Physics and Mechanics*. 2025;53(3): 48–68.

http://dx.doi.org/10.18149/MPM.5332025_5

Introduction

Basic structure and mechanical or physical properties of weld gets affected due to the varying imperfections and irregularities that may appear in a weld. The weld defects can be categorized into superficial and internal defects, depending on the location of the defect. Control of welding quality and reliability is significant for industrial activities like component manufacturing and structure assembly. Significant functional abnormalities may result as a consequence of the welding anomalies. Defect detection is considered particularly challenging owing to the factors like insufficient contrast, the noised nature of the radiographic film, or the reduced geometric dimensionality of irregularities. Radiography provides detailed internal visualization of the welds and enables manufacturers to verify compliance with safety standards, specifications, and manufacturing codes.

Image processing refers to the manipulation and analysis of digital images using a variety of algorithms and methods. Digital image processing techniques are employed to



¹ Dayananda Sagar University, Bangalore, India

² Dayananda Sagar College of Engineering, Bangalore, India

[™] arungalaisv@yahoo.co.in

automate defect detection and identification, enhance visual representation of data, and standardize radiographic analysis methods, thereby increasing their reliability and consistency. Digital image processing covers improving and extracting intrinsic details from digital images and results in the generation of new images or specific assessments from the images. To consider the elaborations in micro-imaging and for accurate indication of the discrepancy, appropriate preprocessing and segmentation methods need to be selected. Reproducibility and reliability of results are the essential requirements in the automation of non-destructive testing, mainly in image characterization, to be at par with human judgment. This work aims to identify anomalies and defects like porosity, cracks, lack of penetration, etc., using image processing of welded joint microscopic images.

The proposed MATLAB-based image processing system is well-suited for real-time deployment in manufacturing environments. It can interface with industrial cameras and data acquisition systems using the Image Acquisition Toolbox for continuous monitoring. MATLAB code can be compiled into standalone applications or converted to C/C++ for integration with embedded systems and industrial control platforms like PLCs and SCADA. The system supports edge computing through lightweight, optimized pipelines deployable on devices like Raspberry Pi or NVIDIA Jetson. Real-time performance is achieved using techniques such as ROI detection, frame skipping, and GPU acceleration. Additionally, the system can be integrated into production lines to automate actions such as triggering alarms, rejecting defective parts, and logging inspection data.

MATLAB trains a supervised learning model using extracted features and labels, common classifiers are as follows: fitcsvm – support vector machine (good for small datasets); fitcknn – k-nearest neighbors; fitctree – decision tree; trainNetwork – for CNN-based classification (deep learning toolbox).

State of the art in image processing for welding defect detection

Intensive research contributions are made to resolve the discrepancies in the image processing techniques utilized for weld image characterization. Xu Y. et al. [1] proposed an enhanced Canny edge detection algorithm based on their analysis of the gray gradient in the weld image. Results showed that real-time seam tracking objectives can be met by precisely controlled image processing. Nacereddine N. et al. [2] proposed a few variations in the image processing sequence significant for effective defect detection in images. The process is initiated by concentrating on the region of interest (ROI) to ensure a targeted analysis. A median filter is applied to minimize noise and enhance image quality, vital for accurate assessments. Dynamic stretching and local contrast enhancement improve clarity across various backgrounds, facilitating effective feature extraction. Finally, the Otsu method is utilized to optimize segmentation, allowing for precise identification of defects. In 2009, Liao G. and Xi J. [3] proposed a pipeline welding machine image detection method using the largest variance threshold method to establish adaptive segmentation. The process converts images to black and white, removes small noise, and utilizes level projection for efficient real-time defect detection and quality inspections. In 2007, Yang S.M. et al. [4] employed automation in Metal Inert Gas welding using a CCD camera with a laser stripe for seam tracking and adaptive Hough transformation for weld point extraction. A generalized delta rule algorithm-based neural network optimizes welding parameters, with joint width and depth as inputs from the images and is observed to influence overall weld quality significantly. Roca Barceló F. et al. [5] introduced an automated system using TOFD, image processing, and neural networks for accurate weld defect detection and classification. The TOFD method has a drawback associated with the appearance of speckle noise.

In 2020, Li Y., Hu M. and Wang T. [6] presented a deep learning-based weld seam image recognition algorithm using the Adam adaptive moment estimation for efficient convolutional neural network training. The adaptive threshold method for weld seam extraction was tested on 4500 tube images, and the results show effective identification and classification of weld defects in terms of parameters like false detection rate, recall rate, and overall accuracy. Pan H. et al. [7] developed a novel approach using MobileNet feature extractor and leveraged a pre-trained deep learning architecture, originally optimized for diverse image recognition tasks, to extract key features for identifying welding defects. By integrating an additional classification layer, this hybrid model significantly outperformed other comparable methods, achieving an impressive accuracy rate of nearly 98 %. In 2019, Sun J. et al. [8] presented a machine vision algorithm for detecting and classifying weld defects in thin-walled canisters. Using a modified background subtraction method, the algorithm achieves over 99 % accuracy in real-world applications, proving effective for real-time and continuous weld defect detection. In 2002, Wang G. and Liao T.W. [9] developed an automatic computer-aided system for identifying welding defects using background subtraction and histogram thresholding techniques. In 2016, Ranjan R. et al. [10] used specific defect features like vertical intensity plot and defect spread region for weld defect identification, with respect to its location and severity, and classification into different kinds of imperfections or irregularities. In 2020, Kumar R.K. and Omkumar M. [11] explored the ultrasonic plastic welding of high-performance polyamides (HPPA) matrix composite. It is a glass-filled semi-crystalline and partially aromatic polyamide composite for automotive applications. A weld strength of 3.1 kN was achieved, with minimal voids and negligible weight loss. Key findings include decreased glass transition temperature and suitable degradation temperature for high-temperature applications. In 2019, Mohammad E.J. et al. [12] utilized the K-means method for optimal thresholding, showing sensitivity to small datasets but improved performance with larger datasets, especially when the number of clusters is minimal.

In 2023, Shaikh K. et al. [13] presented a hybrid architecture that uses a multilayer perceptron (MLP) for feature extraction and combines it with classical classifiers like random forest (RF) and support vector machines (SVM). Applied to wheel conicity defect detection, the MLP-RF combination yielded the best performance with up to 99 % accuracy. The hybridization allows for efficient learning from both structured sensor data and statistical features, making it suitable for mechanical fault diagnosis. In 2024, Tata R.K. et al. [14] proposed a hybrid convolutional neural network (CNN) and long short-term memory (LSTM) model. CNN extracts spatial features from surface images, while the LSTM captures temporal relationships (e.g., variations across sequences or production cycles). The hybrid model improves defect detection accuracy by ~ 20 % and reduces false positive rates by ~ 30 %, making it suitable for time-series-based industrial inspection tasks such as continuous casting or rolling. In 2024, Wang X. et al. [15] addressed the

challenge of detecting defects on dense IC surfaces, where information imbalance and micro-defects make detection difficult. A hybrid model combining ResNet50 and Vision Transformer (ViT) is developed. ResNet handles low-level feature extraction, while ViT captures long-range dependencies. The model achieves 98.6 % accuracy, outperforming standalone CNN or ViT architectures, and is particularly effective for microelectronic manufacturing.

The accuracy of defect detection using MATLAB-based image processing depends on several factors, including the type of defect, image quality, features used, classifier, and preprocessing methods. However, based on published studies and typical results from academic and industrial projects, Table 1 lists a few of the reference points [13–15].

Table 1. Accuracy in % for various techniques used for image defects detection

Application area	Defect type	Technique	Accuracy (approx.), %
Weld inspection	Cracks, voids, inclusions	LBP + SVM / Edge detection + Morphology	85-95
Composite materials	Delamination, air voids	GLCM + CNN / Ultrasound image processing	90-97
Metallic surfaces	Scratches, dents, porosity	Texture + Intensity histograms + Decision tree	80-90
PCB / Solder Missing pads, solder joints bridges		Template matching + Thresholding	88-93

Table 2. Comparison of MATLAB based image processing with baseline methods

Aspect	Baseline methods (e.g., manual inspection / traditional thresholding)	Proposed MATLAB-based approach		
Automation	Manual or semi-automatic, subjective, time-consuming	Fully automated using algorithms such as edge detection, morphological operations, or machine learning		
Accuracy	Typically lower due to human error and inconsistent criteria	Higher accuracy by using optimized filters and algorithm tuning		
Noise handling	Poor tolerance to lighting, contrast, or texture noise	Robust pre-processing steps (Gaussian filtering, histogram equalization, etc.) remove noise effectively		
Feature extraction	Manual or limited to basic statistics	Advanced techniques: texture analysis (e.g., LBP, GLCM), shape descriptors, color segmentation		
Defect classification	Usually not implemented or rule-based	Incorporates ML models (SVM, KNN, decision trees) trained on defect features		
Consistency & repeatability	Varies with operator and condition	Highly consistent, script-based processing ensures reproducibility		
Processing time	Slower and subjective	Faster with batch processing using MATLAB scripts/functions		

In MATLAB-specific workflows, using local binary pattern (LBP) or GLCM (gray-level cooccurrence matrix) for feature extraction and SVM or KNN for classification, the accuracy typically ranges from 85 to 95 %. When combined with image augmentation and proper labeling (using Image Labeler), detection rates can improve by 5–10 %. MATLAB's deep learning toolbox (e.g., using pre-trained CNNs like AlexNet or ResNet with transfer learning),

gives 95 %+ accuracy when sufficient labeled data is available. Performance comparison of MATLAB-based Image processing with other baseline methods is described in Table 2.

The proposed MATLAB-based image processing approach demonstrates superior performance compared to traditional thresholding and edge-based methods, as evident in higher classification accuracy (91.4 vs. 72.3 %), and improved robustness to noise and lighting variations. The integration of texture-based feature extraction (e.g., LBP) and machine learning classifiers significantly enhances the defect detection capability across multiple defect types.

Experimental work and image processing analysis

Preprocessing stage

The basic initiation in image processing is the initial set of operations performed on raw image data to prepare it for further analysis or processing. The goal of preprocessing is to enhance the quality of the image and to remove any distortions or irrelevant information that may hinder subsequent tasks.

This stage involves the following operations to be performed to prepare the image for further extraction of defect information:

- 1. Histogram equalization is a technique for improving an image's contrast by adjusting the histogram's intensity distribution. This method enhances the image's visibility and detail by spreading the most frequent intensity values. Histogram equalization is a powerful and widely used technique for enhancing image contrast, making it a fundamental tool in various image processing applications. The image's histogram is computed, a plot of the number of pixels for each intensity level (from 0 to 255 for an 8-bit image).
- 2. Resizing of Images: By resizing images appropriately, you can balance maintaining sufficient detail for analysis while optimizing computational and storage resources. This balance enhances the efficiency, effectiveness, and applicability of image-processing techniques across various domains.
- 3. Gray scaling transforms a color image into shades of gray. This involves reducing the image's depth from full color (usually 24-bit RGB) to 8-bit grayscale. In a grayscale image, each pixel represents a shade of gray, varying from black (0 intensity) to white (255 intensity). For each pixel, the intensity of the gray shade is calculated using the formula: $Gray=0.299\times R+0.587\times G+0.114\times B$ [2].

The following are the Inferences that can be drawn from the grey scaling mechanism:

- 1. Consistent gray levels across the weld bead indicate a consistent welding process.
- 2. Inconsistent gray levels may suggest issues such as varying penetration, inconsistent heat input, or changes in welding speed.
- 3. Dark spots can indicate porosity or voids within the weld. Darker areas usually represent areas of lower density.
- 4. Light spots or Brighter areas may indicate inclusions or areas of higher density. They could also point to overheating or burning through the material.
- 5. The gradient of gray Levels indicates the HAZ, which has a gradual transition from the base metal to the weld metal. Sharp changes in gray levels can indicate improper heat control.

- 6. Proper penetration is indicated by a consistent gray level throughout the weld depth.
- 7. Insufficient Penetration appears as a lighter gray area in the center of the weld cross-section, indicating the weld did not fully penetrate.
- 8. Cracks appear as distinct lines or streaks within the grayscale image, often darker than the surrounding material.

The study reviewed methods like image enhancement, segmentation, and machine learning techniques. The research highlighted the effectiveness of these approaches in identifying defects and imperfections. The research observation underscores the role of image processing in improving weld inspection quality. The work carried out in this research reflects on the advancement in the image processing technique for weld defect detection of polymer samples joined using ultrasonic welding. The stages of the image processing technique are illustrated in the flowchart, Fig. 1.

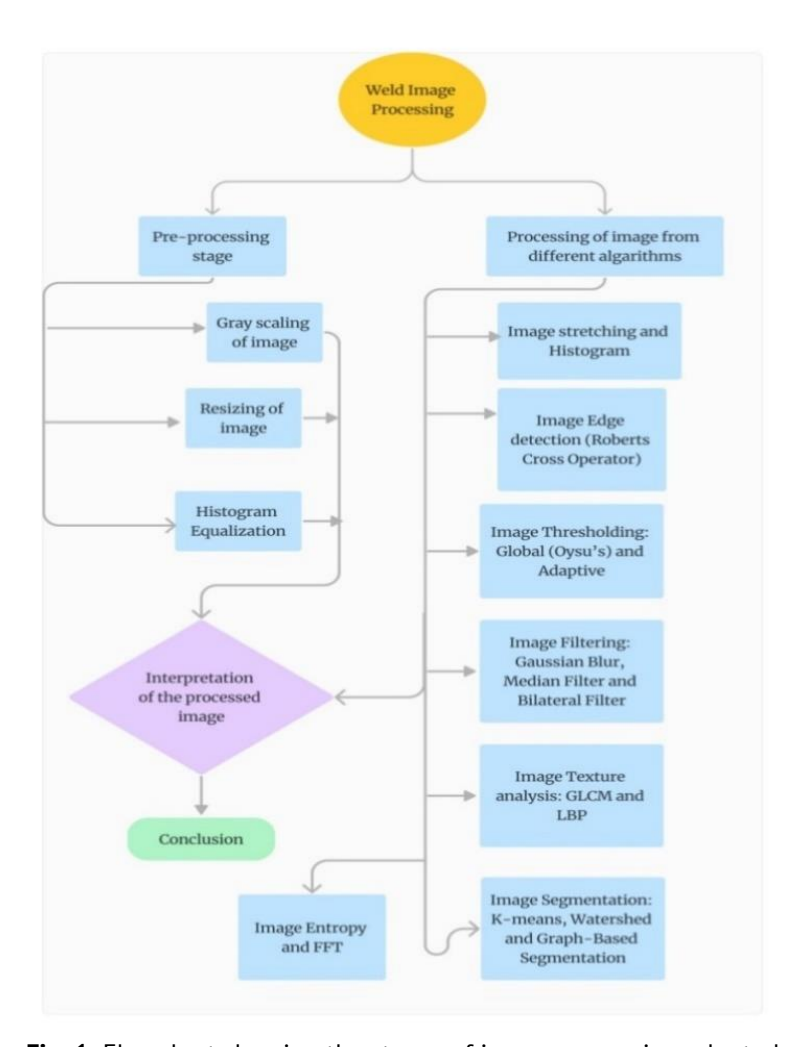


Fig. 1. Flowchart showing the stages of image processing adopted

Image processing was carried out with the scanning electron microscopy (SEM) images of the polymer weld samples. The polymer material is ABS, and the two parts of ABS are joined using ultrasonic welding. The ultrasonic welding involves providing ac supply at 240 V and 50 kHz to the piezoelectric crystal. This results in the generation of high-frequency mechanical vibrations, which are then transmitted to the weld material through the sonotrode and a horn, Fig. 2.

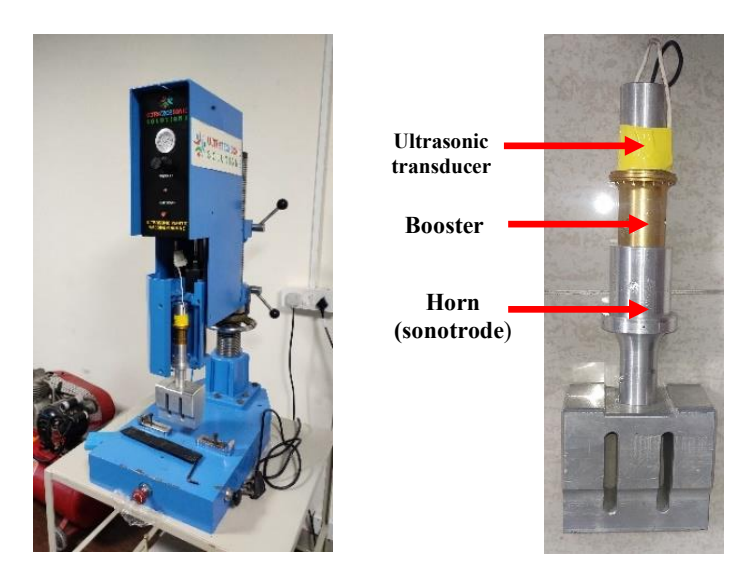


Fig. 2. Images of Ultrasonic weld machine, transducer, sonotrode (booster), horn assembly

The sonotrode horn also transmits and exerts static pressure on the weldment, apart from the vibrations generated in the piezoelectric converter. The horn is customized to suit the weld geometry, and the welding machine has parameter settings for the weld requirements. The parameters of importance are weld time, hold time, amperage corresponding to the energy requirement, and static pressure. The experimental work involved trials with different settings of the process parameters based on trial and error, and also based on the expertise of the technicians at UltraTech Sonic Solutions, Basavangudi.

 Table 3. Operating values of parameters and weld status for ABS Material (N.W - no weld, P.W - partial

weld, G.W - good weld with high strength, DT - destructive testing)

Sl. No	Test identification	DT, s	Weld time, s	Holding time, s	Current, mA	Pressure, Bar	Power, Watts	Weld status based on DT*		
1	1A				0.1	2	1	N.W		
2	1B	0.55	0.15	0		2	1	N.W		
3	1C					2	1	N.W		
4	2A					2	1	N.W		
5	2B	0.55	0.3	0	0.2	2	1	N.W		
6	2C					2	1	N.W		
7	2D						N.W			
8	2E	0.55	0.3	3 0	0.2	3	2	N.W		
9	2F							N. W		
10	3A	0.55						P.W		
11	3B		0.55	0.4	0.4 0	0.3	4	3	P.W	
12	3C							P.W		
13	3D	0.55						G.W		
14	3E		0.55	0.55	0.55 0.	0.5	0	0.3	4	3
15	3F							G.W		
16	3G			0	0.6	5	4	G.W.H		
17	3H	0.55	1	0	0.6	5	4	G.W.H		
18	31			1	0.8	5	5	Overburn		

The process parameter variation considered for this work has been listed in Table 3. The weld status has been provided based on the destructive testing on the weld samples.

Scanning electron microscopy (SEM) imaging of various samples provides insights into the effects of thermal gradients caused on the weld surface due to generated friction and viscous heating of the acrylonitrile butadiene styrene (ABS) material at various points of the joint formation. As the first step, a microscopic image of the base ABS material, without welding, was captured, serving as the basis of comparison with the SEM of the welded material sample.

Image processing was carried out in MATLAB ver.23a. The flowcharting (Fig. 3) highlights the methodology used in segmentation and feature extraction algorithms adopted to extract the morphological and image intensity features of the SEM images.

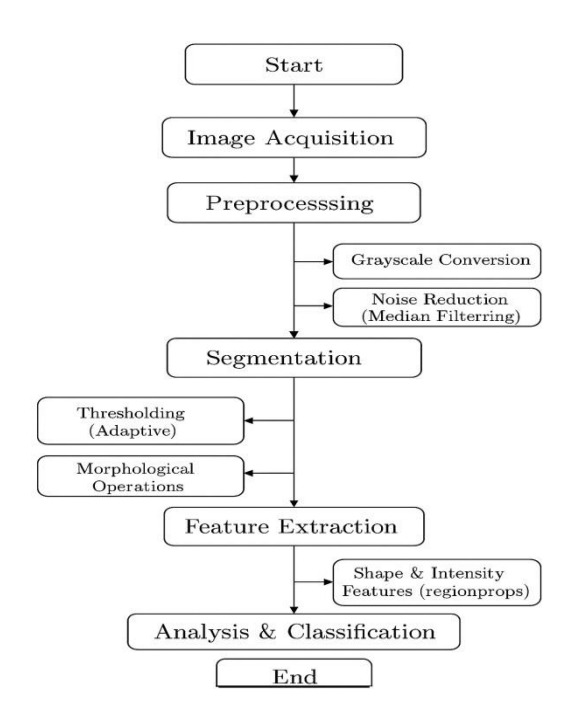


Fig. 3. Methodology of the segmentation and feature extraction

Similar processes have been adopted for algorithms such as texture analysis, entropy, FFT, and filters to extract the various properties of the images. For labeling, MATLAB's image labeler toolbox is used to manually annotate cracks and voids on the input images. Each defect was marked using bounding boxes or pixel-level masks, depending on its complexity and size. The annotated data was saved in ROI and label data formats compatible with supervised machine learning workflows in MATLAB. This labeled dataset served as the basis for training and evaluating defect classification models. The following analyses were performed on the SEM images of the polymer weld samples [16–23].

1. The histogram is utilized to reveal quality issues for the welded images. The overall position of the histogram along the x-axis indicates the image's brightness. If the histogram is skewed towards the left, the image is predominantly dark. If it is skewed towards the right, the image is predominantly bright. The contrasting features of the image are captured by the histogram span. A wide histogram that covers a broad range

of intensity values suggests high contrast, while a narrow histogram suggests low contrast. Uniform and expected distributions may indicate good-quality welds, while unexpected spikes or gaps could indicate defects or inconsistencies.

2. Edge detection: it enables the identification and location of critical discontinuities in the weld by variations in intensity or color introduced into the image. These discontinuities often represent the boundaries of objects within the image.

Weld seam identification. Continuous seam: A well-defined, continuous edge indicates a consistent and smooth weld seam, which indicates good quality. Gaps or discontinuities: breaks or gaps in the edge detection output may indicate defects such as cracks, incomplete fusion, or lack of penetration.

Weld geometry. Uniformity: consistent edge thickness and shape suggest uniform weld geometry, which is important for structural integrity. Irregularities: variations in edge thickness or shape may point to issues like excess weld material, undercutting, or burn-through.

Surface defect, porosity: small, irregular edges could indicate surface porosity or tiny holes in the weld. Spatter: additionally, unintended edges away from the main weld seam might be due to welding spatter.

Alignment and Fit-Up. Proper alignment: edges that follow a predictable, aligned path suggest that the welded components were properly aligned. Misalignment: deviations or offsets in the edge pattern can indicate misalignment or poor fit-up of the welded parts. Transition area: the edge detection can reveal the boundary between the weld region and the HAZ region, which is crucial for understanding the thermal impact on the material.

3. Thresholding is an effective process used to segment the image by converting it into a binary image. In this process, pixels are divided into two groups based on a chosen threshold value, and the pixels are then categorized into white and black. The method adopted is Global thresholding (Otsu's method), as it extracts more edges compared to direct edge detection algorithms

Global thresholding uses a common threshold value for the image under test. This value is applied uniformly to all pixels in the image. A threshold value is chosen, either manually or automatically. Adaptive thresholding involves estimation of the threshold value for segments of the image, thus resulting in variations of lighting and intensity where the image is divided into smaller regions or blocks. Global thresholding is best suited for simple images with uniform lighting, while adaptive thresholding is more versatile and effective for images with complex lighting conditions.

4. Image filtering: several methods are available for image filtering in the process of extracting the required image properties. The following methods are most commonly used in usual practice [24–33].

Gaussian blur: a linear filter that smoothens an image by averaging the pixels within a Gaussian window. It reduces noise and detail by weighting the pixels in the neighborhood based on a Gaussian function, which gives higher weights to the central pixels. It is suitable for blurring edges, reducing image sharpness. Not effective for non-Gaussian noise like salt-and-pepper noise. Best for overall noise reduction and obtaining

a smooth image, but at the cost of blurring details. The Gaussian function is defined as: $G(x,y) = \frac{1}{2\pi\sigma^2} * e\left(-\frac{x^2+y^2}{2\sigma^2}\right)$, where σ is standard deviation of the Gaussian distribution.

Median filter: causes replacement of each pixel value with its neighborhood median value. Salt-and-pepper noise is effectively reduced by this filtering method, with no impact on the identified edges. For each pixel, the filter considers the values of all pixels in a neighborhood around it, sorts these values, and selects the median value. This filter removes salt-and-pepper noise and preserves edges better than linear filters like Gaussian blur. It is ideal for removing specific types of noise (e.g., salt-and-pepper) while preserving edges, useful for inspecting fine details and small defects in welded images.

Bilateral filter: the bilateral filter is an edge-preserving and noise-reducing filter that combines Gaussian smoothing in the spatial domain with Gaussian smoothing in the intensity domain. This ensures that only similar pixel values are averaged, preserving edges. The bilateral filter considers both the spatial distance and the intensity difference between the central pixel and its neighbors. Balances noise reduction with edge preservation, making it suitable for images where retaining the edge details is crucial.

The filter function is: $I(x,y) = \frac{1}{W(x,y)} \sum_{x_i,y_i} I(x_i,y_i) \cdot e^{\frac{-(x_i-x)^2 + (y_i-y)^2}{2\sigma_d^2}} \cdot e^{\frac{-(l(x_i,y_i) - l(x,y))^2}{2\sigma_d^2}}$, where σ_d is the spatial standard deviation, σ_r is the intensity standard deviation, and W(x,y) is a normalization factor.

Compared to the Gaussian and median filtering methods, the bilateral filter gives better results by preserving edges while reducing noise, which represents the quality of the edges formed duringthe welding process and is effective for a wide range of noise types. This makes the weld image analysis more accurate.

5. Texture analysis: texture analysis involves examining the texture characteristics of an image to extract meaningful information, which can be used for classification, segmentation, and other image processing tasks. Two commonly used methods are used in this work.

GLCM (gray-level co-occurrence matrix): this method is used to analyze an image texture by examining the spatial relationships between pixel intensities. GLCM analyzes texture by quantifying how frequently specific intensity value combinations appear in predetermined directional arrangements throughout the digital image matrix. Using this technique, several statistical measures can be calculated to describe the texture.

Contrast: quantifies tonal variation by calculating brightness differentials between adjacent data points throughout the entire visual matrix, enabling measurement of textural roughness across the image: $contrast = \Sigma_{i,j}(i-j)^2 \cdot P(i,j)$.

Correlation: measures the correlation of adjacent pixels, $correlation = \sum_{i,j} \frac{[(i-\mu_i)(j-\mu_j)\cdot P(i,j)]}{\sigma_i*\sigma_j}$.

Energy (angular second moment): assesses uniformity of the texture by adding up the squared elements in the GLCM, $energy = \sum_{i,j} P(i,j)^2$.

Homogeneity (inverse difference moment): reflects the uniformity of pixel value relationships and distribution of elements in the GLCM cluster around the diagonal, $homogenity = \sum_{i,j} \frac{P(i,j)}{1+|i-j|}$.

Local binary patterns (LBP) is a texture operator that identifies patterns by evaluating adjacent pixel values against predetermined limits, enabling classification based on local spatial relationships within defined proximity boundaries. The LBP image is often represented as a histogram of the LBP codes, which serves as a texture descriptor.

6. Image segmentation: partitions the complete image into regions, making it easier to analyze and extract meaningful information. This process modifies the representation of an image into a form that is straight forward for analysis. Often by identifying objects or boundaries (lines, curves, etc.) within the image. The following methods are discussed in image segmentation.

K-means clustering: an unsupervised learning algorithm that is implemented to categorize data points into K clusters. In the context of image segmentation, it groups pixels based on their intensity or color similarity. The K-means clustering segments an image by grouping pixels into K clusters based on similarity in intensity or color. Simple and effective for basic segmentation tasks.

Watershed algorithm: a technique of segmentation in which the grayscale image is considered like a topographic surface. The algorithm finds the lines that separate different catchment basins, corresponding to the image regions. The Watershed Algorithm uses the topographic interpretation of the image to separate regions. Effective for segmenting touching or overlapping objects.

Graph-based segmentation: this technique treats the image as a graph, considering each pixel as a node, and the similarity between neighboring pixels is indicated by the edges. Segmentation is performed by finding minimum cuts in the graph based on pixel similarity. Offers flexible and powerful segmentation capabilities but may require more computational resources.

7. The entropy indicates the randomness to assess the degree of uncertainty in the image. Within the domain of image processing, entropy describes the texture and complexity of an image. An image with high entropy is characterized by intricate Higher entropy values indicate a more complex and detailed image, while lower entropy values suggest a more uniform or simple image. The entropy H of an image can be calculated using the following equation: $H = -\sum_{i=1}^{n} t_{i} \log_{2}(p_{i})$, where n is the count of variations in intensity in the image and 'pi' is the probability at which intensity of level I occurs.

Entropy is used to analyze and classify textures in an image. Entropy-based methods can be used to determine optimal thresholds for image segmentation. High entropy characterized by intricate details and complexity, while low entropy indicates a uniform or simple image. Entropy can be used as a feature for image recognition and classification tasks.

8. Fourier transform: in image processing, the Fourier Transform is a fundamental tool used to analyze the frequency components present in an image. Here's a concise explanation of what the Fourier transform entails. The Fourier transform converts a signal (in this case, an image) from its spatial domain into the frequency domain. It decomposes the image into its constituent frequencies. For a 2D image f(x,y), the Fourier transform F(u,v) is given by: $F(u,v) = \iint_{-\infty}^{\infty} f(x,y) \, e^{-i2\pi(ux+vy)} \, dx \cdot dy$, where u and v are wavenumber components.

The magnitude variation of an image refers to the representation of the magnitude (absolute value) of the Fourier transform coefficients of the image. The phase spectrum

of an image refers to the spatial distribution of phase information in the frequency domain of the image.

Results and Discussion

The analysis was carried out on four SEM images, and the interpretations for the various techniques of preprocessing are described in this section.

Histogram of weld images

Peaks indicate common intensity values. A narrow histogram suggests low contrast, while a wide histogram suggests high contrast. Expanding the range of intensity values makes images clearer, more detailed, and more suitable for visual inspection and automated analysis. The image in its stretched form and the corresponding histogram (Figs. 4 and 5) for samples 2H and 1C, indicate clear contrasting features of the image where the lack of fusion, slag formation, cracks, and unfilled gaps can be identified. These characteristics indicate the defects in the weld piece, which creates a non-uniform surface on the weld piece. While the histogram in Fig. 6 (for sample 3H) indicates no defect in the weld, corresponding to the sample performance, as listed in Table 1 [17].

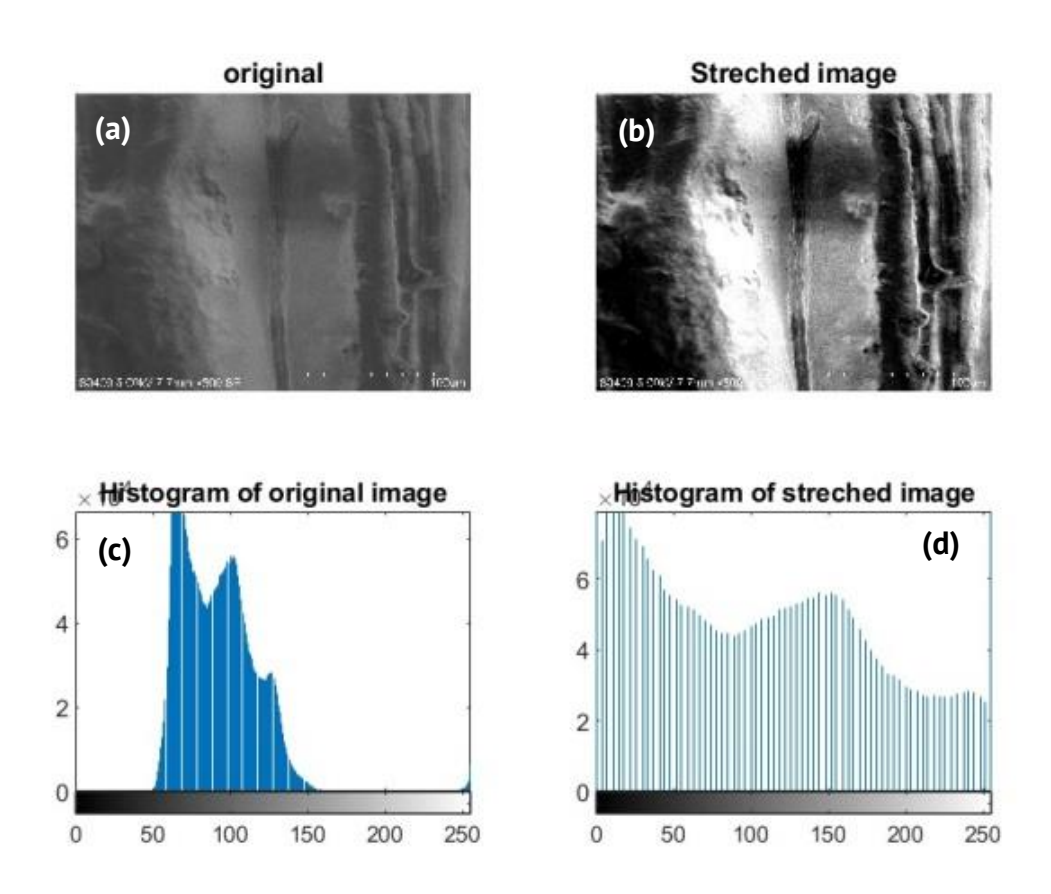


Fig. 4. SEM image of sample 2H (a,b) and its histogram stretched image (d) and its histogram (c)

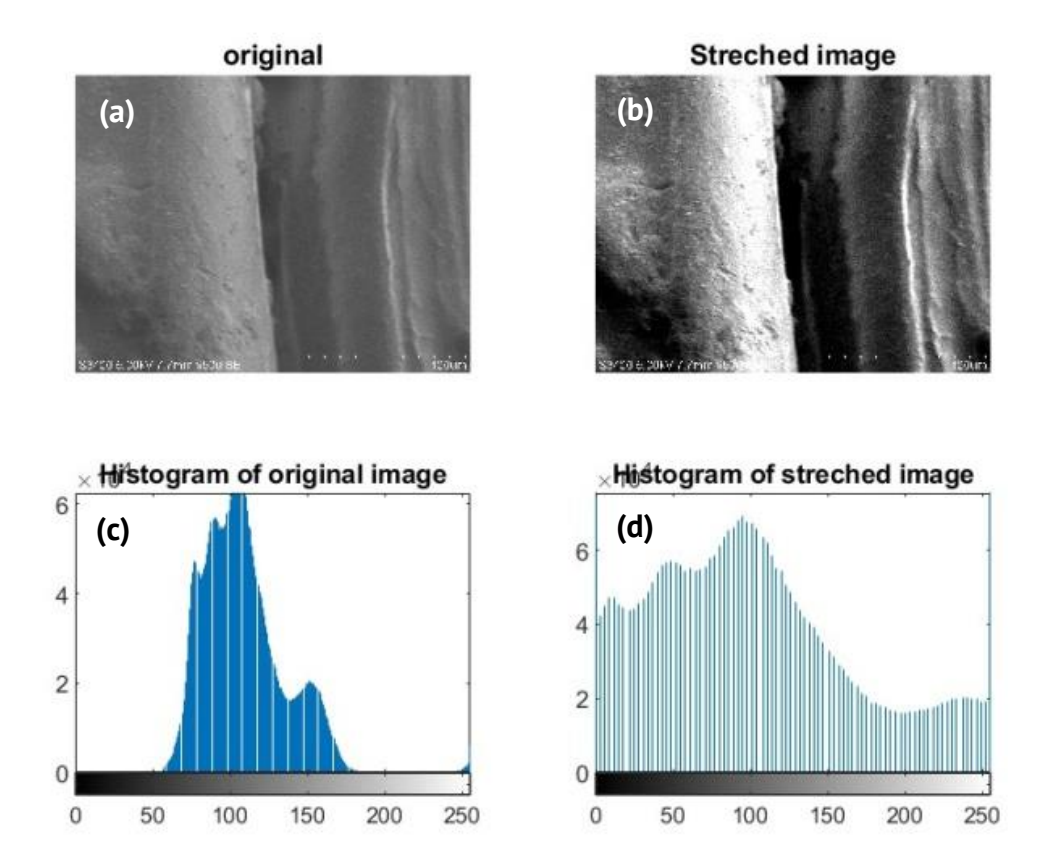


Fig. 5. SEM images of sample 1C (a,b) and its histogram stretched image (d) and its histogram (c)

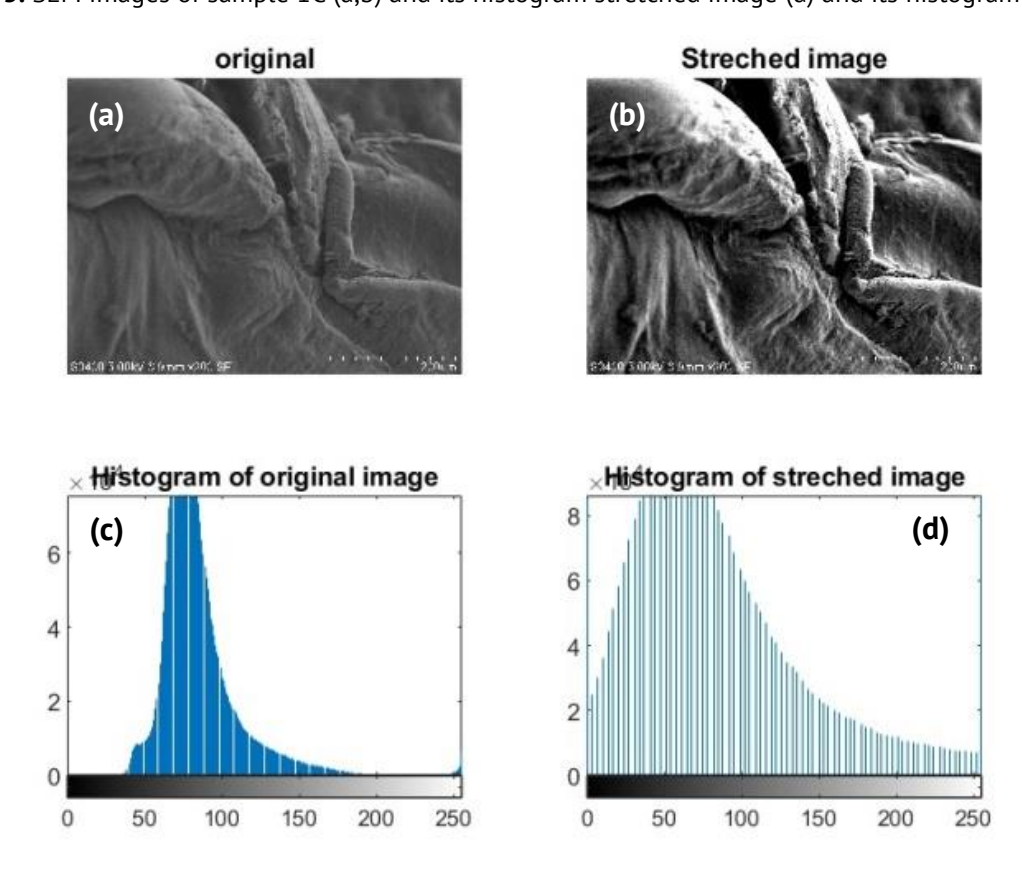
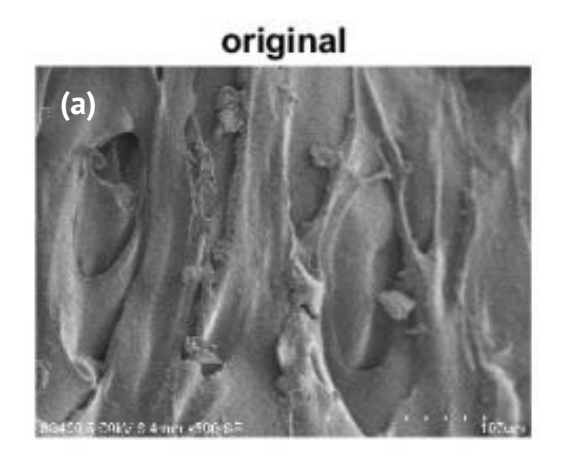


Fig. 6. SEM images of sample 3H (a,b) and its histogram stretched image (d) and its histogram (c)

Interpretation from edge detection

Figures 7 and 8 show the edge detection of samples 2F and 3H using their SEM images by the Roberts Cross Operator algorithm, which uses 2×2 convolution kernels to approximate the gradient. The edges seen in the images represent discontinuities in the weld formation that may be attributed to anomalies like slag, unfused, and uncut surfaces in the image, the whiter dots, the more the edge formation during welding. The clear image without white heads may indicate fewer discontinuities in the weld formation. These results indicate a contradiction to the actual weld performance and may indicate the need for further detailed analysis of the image processing results and inferences.



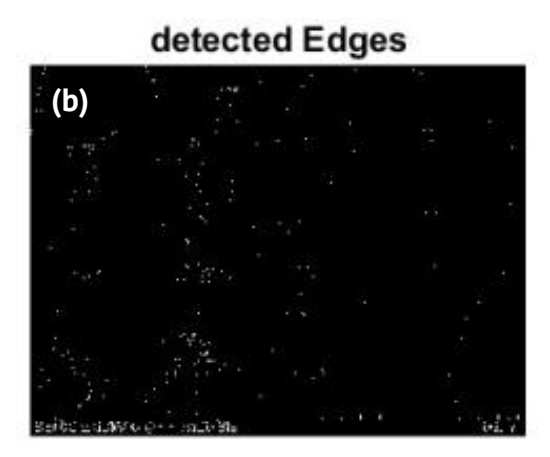
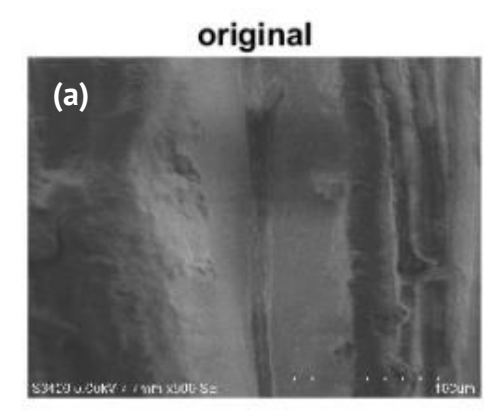


Fig. 7. SEM image surface of sample 3H (a) and edge detection image (b) for sample 3H



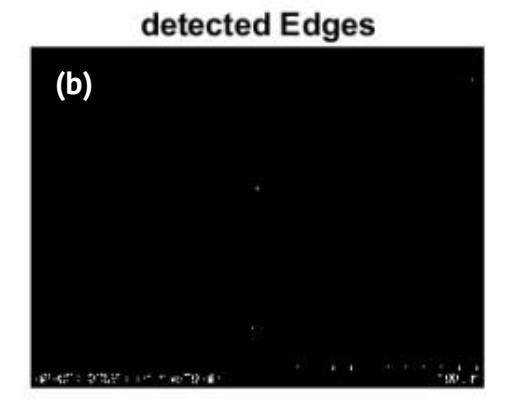


Fig. 8. SEM image surface of sample 2F (a) and edge detection image (b) for sample 2F

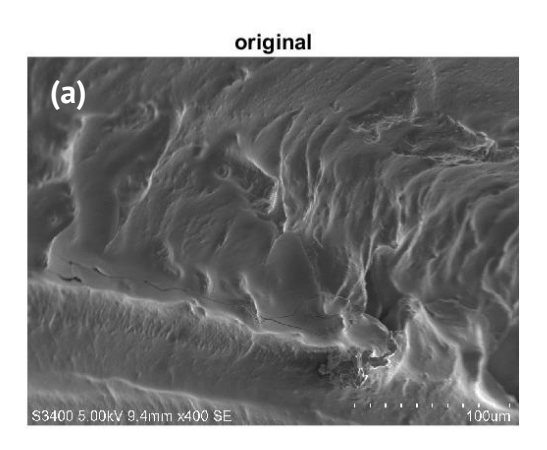
Interpretation from thresholding

Thresholding helps to isolate the weld bead from the rest of the image. This is vital for the assessment of the weld characteristics of quality, size, and shape.

Detection of anomalies like porosity, cracks, or incomplete fusion can be done with thresholding. Defects usually have different intensity values than the rest of the weld, making them stand out after thresholding.

Contrast enhancement makes it easier to inspect and analyze the weld visually. This is particularly useful in cases where the weld and the surrounding material have similar intensity values in the original image.

The thresholding image for Sample 3I, in Fig. 9, indicates the slag formed after welding, and the bulged surfaces can be seen more clearly, which represents the overwelding with improper finishing surfaces showing the white edges of excessive material spread. The welding status of sample 3I shows the weld to have caused overheating of the material, which is due to the higher parametric range than other samples.



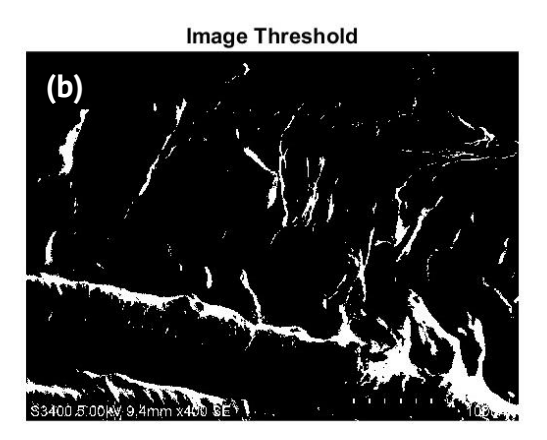
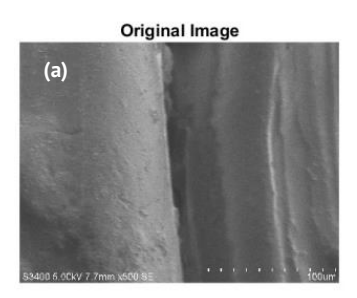
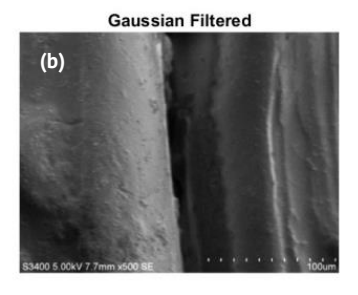


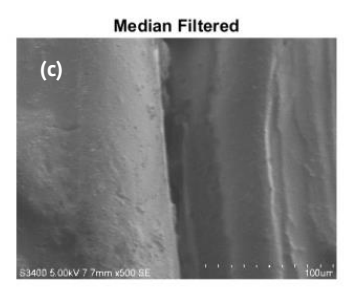
Fig. 9. Original SEM image (a) and its processed threshold (b)

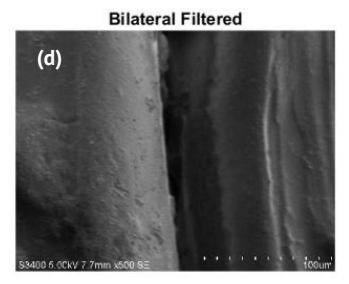
Filtering output

The filtering output for the SEM image of sample 2B, Fig. 10, has been analyzed in this section for the changes in texture properties with spatial factors. The common image filtering techniques were utilized, namely Gaussian blur, median filtering, and bilateral filtering, for noise removal and smoothing of the images. The smoothing effect differs in the form of uniform, non-linear, or adaptive smoothing [24]. The following features are obtained from the above image.









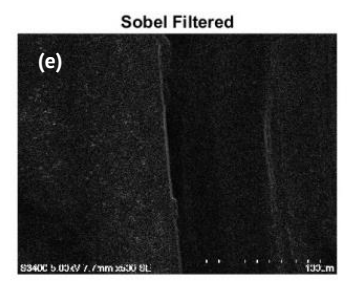


Fig. 10. SEM Images of Sample 2B filtered with different standard filtering methods (a-e)

GLCM features: GLCM is computed at specific spatial relationships defined by:

- 1. Directions: horizontal (0°), vertical (90°), diagonal (45°), anti-diagonal (135°), etc.
- 2. Distances: the number of pixels apart being analyzed. The matrix values thus represent how the texture property (e.g., contrast, correlation, etc.) changes with the analyzed direction/distance.
- 3. Contrast: [0.1255 0.1865 0.1336 0.1778].
- 4. Correlation: [0.8992 0.8502 0.8927 0.8571].
- 5. Energy: [0.4564 0.4319 0.4439 0.4358].
- 6. Homogeneity: [0.9613 0.9397 0.9510 0.9444]

Contrast in an image represents the difference in luminance or color that makes an object distinguishable. The correlation value shows the linear dependency of pixel intensities for a specific direction/distance. The high values indicate that pixel intensities are strongly related, regardless of direction or distance. Energy value reflects the uniformity of texture for a specific direction/distance. The moderate values suggest a somewhat uniform texture, but not perfectly repetitive. Homogeneity value measures how close pixel intensities are to one another for a given direction/distance. The high values indicate high similarity of neighboring pixel intensities in all directions, showing a smooth texture. Together, these values describe the variation of texture properties across different spatial relationships in the analyzed image.

Interpretation from the texture analysis

LBP (local binary patterns): the histogram shows the frequency of each LBP code in the SEM image of sample 3H (Fig. 11).

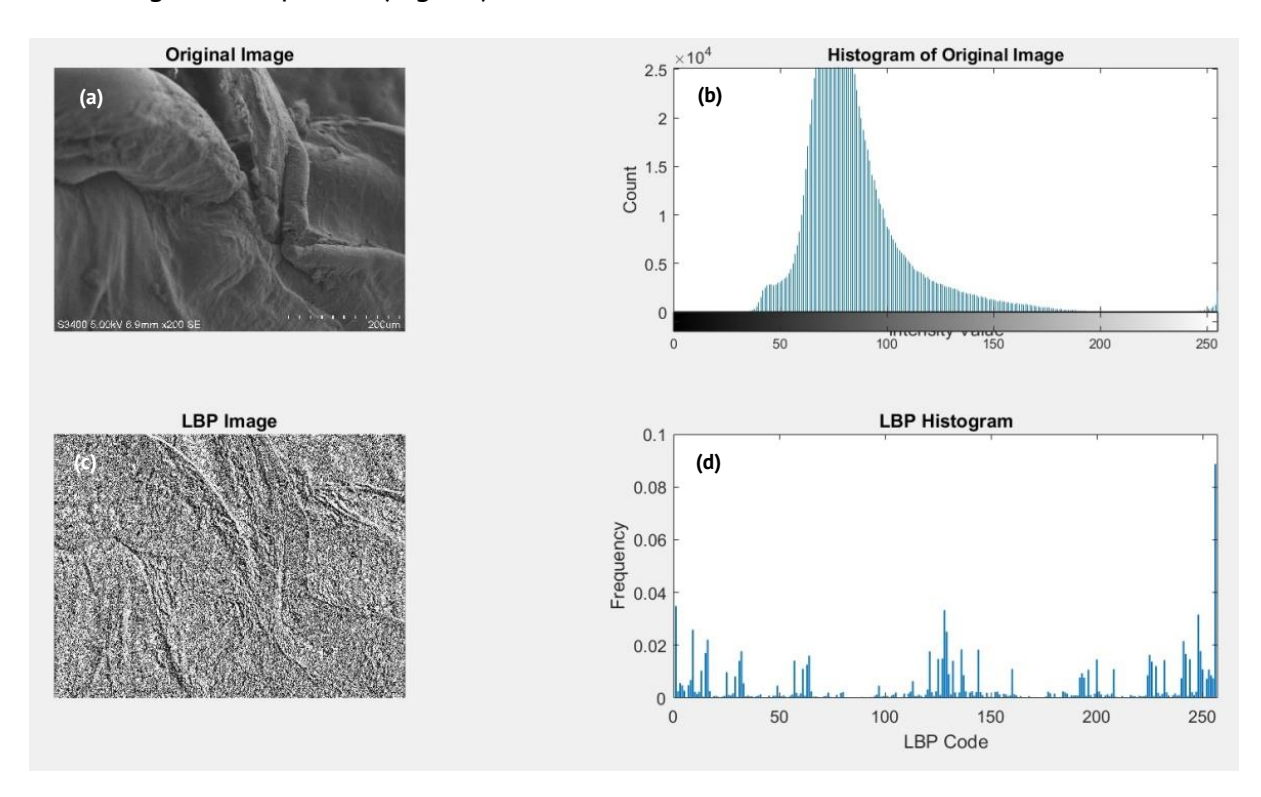


Fig. 11. Histogram of original (a,b) and LBP image (c,d)

From the above histograms of the original image and the LBP histogram, it's clear that the LBP histogram is more stretched than the original histogram, representing more edges on the image, implying non-uniform weld quality. By combining GLCM features from image filtering and LBP features from the texture analysis, a comprehensive understanding of the welded image texture can be obtained.

- 1. Consistency and quality: high homogeneity, high energy, high correlation (from GLCM), and a peaked LBP histogram with many uniform patterns suggest a high-quality weld with a smooth, consistent texture.
- 2. Defects and irregularities: high contrast, low homogeneity, low correlation (from GLCM), and a flat LBP histogram with many non-uniform patterns can indicate defects, roughness, or irregularities in the weld texture.
- 3. Surface properties: detailed examination of specific GLCM features like contrast and homogeneity, along with the LBP histogram, can help identify specific types of surface properties, such as the presence of cracks, porosity, or other surface defects.

Interpretations from image segmentation

The image segmentation technique was utilized for separating the features or regions of the SEM image of sample 2B. Figure 12 shows the result of image segmentation obtained with the above-mentioned techniques for sample 2B.

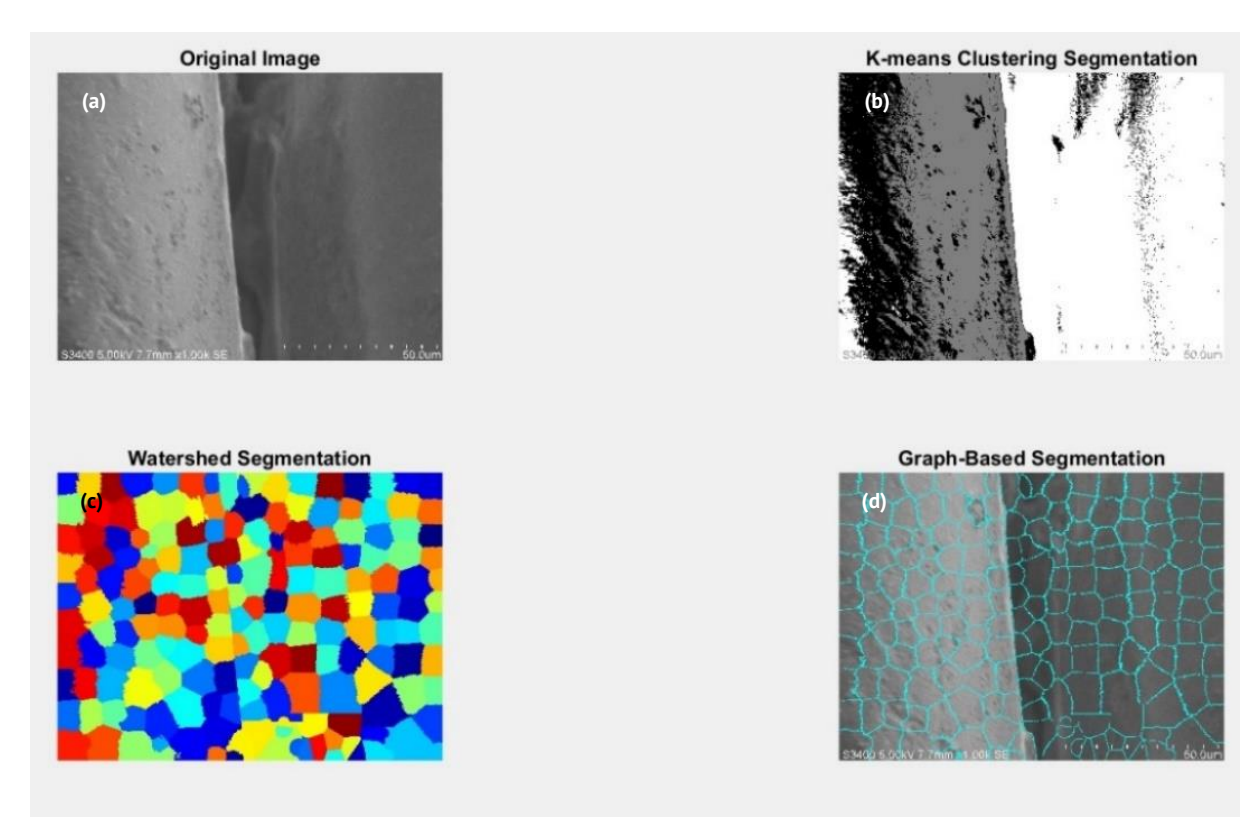


Fig. 12. Original SEM image of sample 2B (a) and results of K-means, watershed, and graph-based image segmentation (b-d)

The splitting of the SEM image into sections and the color gradations give an idea about the discontinuities in the weld formation, and also the difference in grain

distribution as a result of the thermal gradients created due to the friction and viscous heat created between the weld surfaces in the process of ultrasonic welding.

Entropy interpretation

An image with high entropy will show a complex scene with many details and textures, and its entropy value will be relatively high. Low-entropy image will show a uniform or simple scene. By comparing these entropy values, the complexity and information content of the images can be interpreted. Figure 13 represents the entropy values for samples 2B and 3H.

Image 1: Entropy = 6.5769

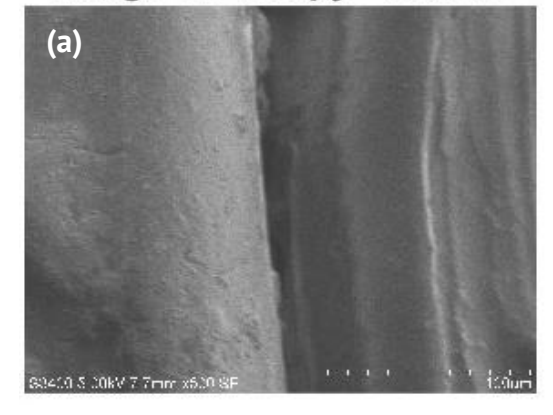


Image 2: Entropy = 6.8954

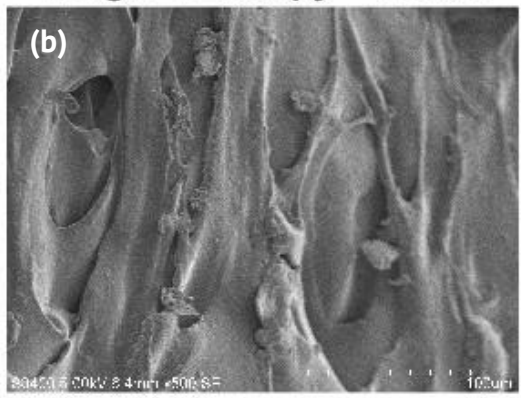


Fig. 13. Entropy values for the samples 2B (a) and 3H (b)

In Fig. 13(b), Image 2 has higher entropy (6.8954) compared to Image 1 (6.5769). This indicates that Image 2 has more complexity or randomness, which may be interpreted as a strong molecular bonding of the two weld pieces, as is observed in the weld performance of sample 3H.

Interpretation from the Fourier transform

Fourier transformation conveys information about the spatial frequency content of the image: Low frequencies represent areas of uniform intensity, representing smooth regions in the source image. High frequencies correspond to rapid changes in intensity, indicating edges or textures.

Fourier transform conducted on the SEM images of sample 3H, Fig. 14 indicates the components for all frequencies, with magnitude reducing for higher frequencies. The logarithmically transformed image also suggests the dominating directions, one vertical and one horizontal, in the Fourier image, both passing through the center. This infers a regular pattern of grain distribution in the baseline SEM image of sample 3H, confirming the status as obtained with the parameter settings of sample 3H.

The results obtained with the various image processing techniques applied to a small set of SEM images are observed to be either in sync or in variation with the destructive testing performance of the weld samples. This observation requires further analysis of these techniques applied to a larger set of SEM images to arrive at a definite

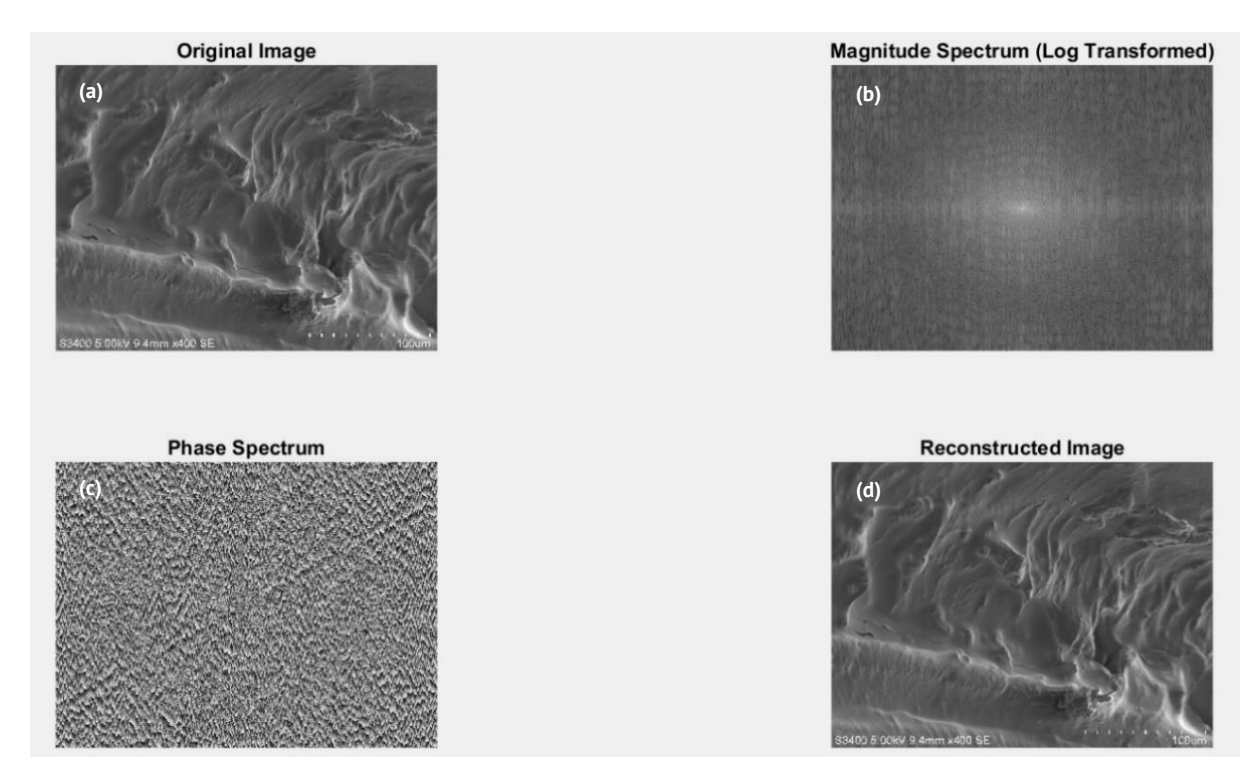


Fig. 14. Original SEM image of sample 3H (a) and Fourier transform output images (b-d)

pattern for the optimal selection of image processing techniques for weld defect detection. The variation in the results may be attributed to the broad range of non-uniformities in the weld formation due to thermal gradients, which usually result in varied characteristics. This makes it challenging to develop a generalized method of image-based defect detection. The characteristics of defects, like their appearance as regions of low contrast, non-uniform brightness, or irregular shapes, may result in anomalies in their detection.

Conclusions

Applying image processing techniques in the characterization and defect detection of weld samples using SEM images has significant potential toimplement automation in the weld defect detection domain. With further refinement of the analysis and detailed study, the image processing techniques can be effectively used for defect detection with the sample SEM images for welds formed with varying parametric levels. Techniques such as image segmentation, thresholding, and edge detection play a crucial role in isolating relevant features within complex microstructures, allowing for a more precise analysis of weld integrity. Furthermore, entropy detection aids in identifying anomalies by quantifying information variability, which is essential for assessing the quality of welds. The Fourier transform contributes to identifying periodic structures and defects, enhancing our understanding of the weld's mechanical properties. Additionally, texture analysis provides insights into the surface characteristics and microstructural variations, crucial for predicting performance under various conditions. Filtering techniques help in noise reduction, ensuring that the subsequent analysis reflects true structural characteristics rather than artifacts.

Collectively, these image-processing techniques enable a comprehensive assessment of weld quality, facilitating early detection of defects that could compromise structural integrity. This research underscores the importance of integrating advanced image processing methods into quality control processes in manufacturing, thereby enhancing reliability and safety in critical applications. The findings illustrate the potential for further advancements in the field, opening avenues for automation in defect detection methodologies. The following interpretations and guidelines can be deduced from the image processing algorithms discussed above:

- 1. The impact and significance of an algorithm can be assessed with a comparison of the original and processed Images.
- 2. Parameter sensitivity analysis can be effectively made with the variation of the algorithmic parameters and analysis of the change in results, e.g., threshold values in segmentation.
- 3. Algorithm performance can be quantitatively evaluated using metrics like precision, recall, or mean squared error, especially in machine learning and computer vision tasks.

Analysis and interpretation of errors introduced by the algorithm can guide improvements or alternative approaches. By systematically evaluating these aspects, we can effectively interpret image processing results from different algorithms, ensuring that they meet the desired goals and quality standards.

Credit authorship contribution statement

G.C. Ganesha Cocce : experimentation, simulation and writing; Chaturvedi Mukti Cocce : conceptualization, design of experiments, experimentation, paper writing, validations; Arungalai Vendan Subbiah Cocce : conceptualization, design of experiments, experimentation, paper writing, validations; Radder Sharanabasavaraj Cocce : testing and characterization, simulation, experimentation.

Conflict of interest

The authors declare that they have no conflict of interest.

References

- 1. Xu Y, Fang G, Chen S, Zou JJ, Ye Z. Real-time image processing for vision-based weld seam tracking in robotic GMAW. *Int J Adv Manuf Technol.* 2014;73: 1413–1425.
- 2. Nacereddine N, Zelmat M, Belaifa SS, Tridi M. Weld defect detection in industrial radiography based digital image processing. *Transactions on Engineering Computing and Technology*. 2005;2: 145–148.
- 3. Liao G, Xi J. Image processing technology for pipe weld visual inspection. In: *2009 WASE International Conference on Information Engineering*. IEEE; 2009. p.173–176.
- 4. Yang SM, Cho MH, Lee HY, Cho TD. Weld line detection and process control for welding automation. *Measurement Science and Technology.* 2007;18(3): 819.
- 5. Roca Barceló F, Jaén del Hierro P, Ribes Llario F, Real Herráiz J. Development of an ultrasonic weld inspection system based on image processing and neural networks. *Nondestructive Testing and Evaluation*. 2018;33(2): 229–236.
 6. Li Y, Hu M, Wang T. Weld image recognition algorithm based on deep learning. *International Journal of Pattern Recognition and Artificial Intelligence*. 2020;34(08): 2052004.
- 7. Pan H, Pang Z, Wang Y, Wang Y, Chen L. A new image recognition and classification method combining transfer learning algorithm and mobilenet model for welding defects. *IEEE Access*. 2020;8:119951–119960.

- 8. Sun J, Li C, Wu XJ, Palade V, Fang W. An effective method of weld defect detection and classification based on machine vision. *IEEE Transactions on Industrial Informatics*. 2019;15(12): 6322–6333.
- 9. Wang G, Liao TW. Automatic identification of different types of welding defects in radiographic images. *Ndt& E International.* 2002;35(8): 519–528.
- 10. Ranjan R, Khan AR, Parikh C, Jain R, Mahto RP, Pal S, Pal SK, Chakravarty D. Classification and identification of surface defects in friction stir welding: An image processing approach. *Journal of Manufacturing Processes*. 2016;22: 237–253.
- 11. Kumar RK, Omkumar M. Investigation and characterization of ultrasonically welded GF/PA6T composites. *Materials Today: Proceedings*. 2020;26: 282–286.
- 12. Mohammad EJ. Image processing of SEM image nano silver using K-means MATLAB technique. *Al-Mustansiriyah Journal of Science.* 2019;29(3): 150–157.
- 13. Shaikh K, Hussain I, Chowdhry BS. Wheel defect detection using a hybrid deep learning approach. Sensors. 2023;23(14): 6248.
- 14. Tata RK, Brahma Rao KBV. Hybrid CNN-LSTM Architecture for Automated Defect Detection in Industrial Surface Inspection. *Multidisciplinary Journal for Applied Research in Engineering and Technology.* 2025;5(1):11–16.
- 15. Wang X, Gao S, Guo J, Wang C, Xiong L, Zou Y. Deep learning-based integrated circuit surface defect detection: Addressing information density imbalance for industrial application. *International Journal of Computational Intelligence Systems*. 2024;17(1): 29.
- 16. Mu W, Gao J, Jiang H, Wang Z, Chen F, Dang C. Automatic classification approach to weld defects based on PCA and SVM. *Insight-Non-Destructive Testing and Condition Monitoring*. 2013;55(10): 535–539.
- 17. Khalifa W, Abouelatta O, Gadelmawla E, Elewa I. Classification of Welding Defects Using Gray Level Histogram Techniques via Neural Network. *MEJ-Mansoura Engineering Journal*. 2020;39(4): 11.
- 18. Rathod VR, Anand RS. A comparative study of different segmentation techniques for detection of flaws in NDE weld images. *Journal of Nondestructive Evaluation*. 2012;31: 1–16.
- 19. Rajab MI, El-Benawy TA, Al-Hazmi MW. Application of frequency domain processing to X-ray radiographic images of welding defects. *Journal of X-Ray Science and Technology*. 2007;15(3): 147–156.
- 20. Srinivasan K, Kumaran SS. Quality assessment of friction welding using image super-resolution via deep convolutional neural networks. *Materials Today: Proceedings*. 2020;22: 2266–2273.
- 21. Chu HH, Wang ZY. A vision-based system for post-welding quality measurement and defect detection. *The International Journal of Advanced Manufacturing Technology.* 2016;86: 3007–3014.
- 22. Xu H, Yan ZH, Ji BW, Huang PF, Cheng JP, Wu XD. Defect detection in welding radiographic images based on semantic segmentation methods. *Measurement*. 2022;188: 110569.
- 23. Hou W, Zhang D, Wei Y, Guo J, Zhang X. Review on computer aided weld defect detection from radiography images. *Applied Sciences*. 2020;10(5): 1878.
- 24. Cheng Y, Deng H, Feng Y, Xiang J. Weld defect detection and image defect recognition using deep learning technology. Researchsquare [Preprint]. Available from: doi.org/10.21203/rs.3.rs-149365/v1.
- 25. Civcik L, Aksin MA. Image Enhancement in Industrial Welding Environment With Image Processing Techniques. *Konya Journal of Engineering Sciences*. 2025;13(1): 238–259.
- 26. Chen Y, Li L, Chen F, Chen J. Application and prospect of image processing in welding. *Material Science and Technology*. 2003;11(1): 106–112.
- 27. Foorginejad A, Mohammad Emam S, Jamshidi H, Ranjbar S. Image processing technique for measuring the weld dilution and heat-affected zone to model the gas metal arc welding process by a neuro-fuzzy system. *Journal of Optical Technology*. 2023;90(12): 743–752.
- 28. Deng L, Guo Y, Chai B. Defect detection on a wind turbine blade based on digital image processing. *Processes.* 2021;9(8): 1452.
- 29. Ren Z, Fang F, Yan N, Wu Y. State of the art in defect detection based on machine vision. *International Journal of Precision Engineering and Manufacturing-Green Technology*. 2022;9(2): 661–691.
- 30. Argunova TS, Kohn VG, Roshchin BS, Nuzhdin AD, Lim JH, Lebedev SP, Ankudinov AV. Surface study by x-ray scattering technique and phase contrast imaging: the examples of graphene and sapphire. *Materials Physics and Mechanics*. 2024;52(5): 64–73.
- 31. Pozdnyakov AO, Sedakova EB. Thermal analysis of wear of polymer-polymer friction pairs in vacuum and atmosphere conditions. *Materials Physics and Mechanics*. 2024;52(4): 63–80.
- 32. Erofeev DA, Pirozhnikov PB, Keresten IA, Titov AG. Experimental determination of physical, chemical and surface properties of biocompatible thermoplastic. *Materials Physics and Mechanics*. 2024;52(3): 1–12.
- 33. Singh DP, Dwivedi VK, Agarwal M. Optimizing processing parameters for semi-solid casting: a comprehensive review. *Materials Physics and Mechanics*. 2024;52(2): 1–10.

Submitted: February 21, 2025 Revised: June 17, 2024 Accepted: July 7, 2025

General model of the carbonate acidizing process with different injection rate

R.M. Ganopolskij ^{1 🖂} 🗓 , K.M. Fedorov ¹ 🗓 , A.E. Folomeev ² 🗓

ABSTRACT

The process of dolomite rock acidizing is considered. Theoretical analysis considers three regimes of the chemical reaction: face and uniform dissolution and wormhole formation. The general model integrates two analytical solutions of the face and uniform dissolution and semi empirical model of wormhole formation. The analytical solutions consider in the paper, appropriate data on semi empirical approach was extracted from Fredd and Fogler investigations. These solutions had been transferred to the dependence of skin factor from the specific acid injection rate, slug volume and acid concentration. The approximation of the dependence involves two Gauss functions and matches to the appropriate asymptotes (low and high injection rates) and describes the wormhole local minimum in the vicinity of critical injection rate. The proposed approximation dependence may be used in different codes for a reservoir acid treatment process. It could be the basis of the process optimization procedure with maximum productivity increase criteria and determination of optimal impact parameters such as acid slug volume and concentration, injection rate and etc.

KEYWORDS

dolomite • hydrochloric acid • face and uniform dissolution • wormhole formation • reservoir acidizing analytical solution

Funding. This work has been supported by the grant of the Russian Science Foundation, RSF 25-21-00072.

Citation: Ganopolskij RM, Fedorov KM, Folomeev AE. General model of the carbonate acidizing process with different injection rate. *Materials Physics and Mechanics*. 2025;53(3): 69–78. http://dx.doi.org/10.18149/MPM.5332025_6

Introduction

The practice of acid stimulation of productivity in carbonate reservoirs began with the Schlumberger brothers and has a long history [1,2]. The permeability increase of the near wellbore zone and reduction of the skin factor are the main purpose of the stimulation.

At the end of the last century, Fredd and Fogler [3] established that the ratio of the reaction rate and the average mass velocity of acid flow determines the reaction type of an aqueous acid solution with a carbonate matrix. At low velocities, the type of reaction is "face dissolution" with cavern formation at the inlet surface of a well. At high velocities, the acid flows through almost all pore channels, dissolving their walls, increasing the size, and thus increasing the porosity and permeability. This type is often named "uniform dissolution". When the ratio of the reaction rate and acid injection is about one, a dominant channel is formed in the pore space, into which almost all the acid rushes. This leads to the formation of a channel with a diameter of about 1–5 mm, which is called a "wormhole" and the reaction type is named wormhole formation. The authors of the paper [4] considered new regime which they call channeling.



¹ University of Tyumen, Tyumen, Russia

² Irkutsk Oil Company LLC, Irkutsk, Russia

[™] r.m.ganopolskij@utmn.ru

Considering the ratio of permeability in the treated area and in the rest part of a reservoir, then for the first and third reaction types it is several orders of magnitude, for the uniform dissolution it does not exceed several units. The depth of acid penetration to a reservoir at the same volumes of injection is maximum for the uniform dissolution and minimum for the face dissolution type. A general model for predicting these effects or a general approach integrated all described reaction types is needed to predict, optimize the process of acid stimulation of carbonate reservoirs and analyze the technological and economic effect.

The paper proposes the integration of analytical solutions for face and uniform dissolution [5] and the application of semi-empirical models for the analysis of the wormhole formation [6–9]. These solutions are the framework of computational algorithm for the prediction of the volume and concentration of the injected acid slug influence on the well skin factor after stimulation. Of cause, there are some physical phenomenon that additionally affect skin factor. For example, permeability modification under pore pressure variation that considered in [10]. The algorithm bases on available experimental data [7,11,12] and the type of acid [3,13].

Solution of the face dissolution problem

The investigation begins with the consideration of the face dissolution problem on the simple example of vertical well stimulation with the open hole completion. Let's the reservoir is represented by dolomites and the chemical reaction with hydrochloric acid is described by the following equation: $4HCl + CaMg(CO_3)_2 = CaCl_2 + MgCl_2 + 2CO_2 + 2H_2O$.

Note that the problem of face dissolution refers to the case when the reaction rate significantly prevails acid flow velocity [14]. Let's proceed to formalization of the presented problem. The flow pattern during injection of acid solution into a carbonate formation depends on the well completion method, but is reduced to two types: radial and linear [15]. Here, the "exotic" spherical flow is not considered, and the flow near a horizontal well with strong formation anisotropy is reduced to the radial type by introducing new coordinates that take into account the reservoir anisotropy. Such simplification is valid for small volumes of acid injection, when its penetration into the bottomhole zone is limited by meter or less. The problem of an aqueous acid solution flow in the bottomhole zone of a well with residual (immobile) oil will be considered as single-phase two-component (1 – carrying water with reaction products, 2 – hydrochloric acid) flux. Note that radial or quasi-radial flows are observed near vertical, inclined and horizontal wells, and linear flow is observed near stimulation fractures.

Next, the radial flow pattern will be the focus of consideration; the solution for the linear flow pattern is sought similarly. The equations of the mass conservation of the acid and the aqueous solution with the reaction products in a polar coordinate system are as follows:

$$\begin{cases}
\frac{\partial \left(c\phi\rho_{w}h(1-S_{or})\right)}{\partial t} + 2\frac{\partial \left(vrc\phi\rho_{w}h(1-S_{or})\right)}{\partial r^{2}} = -Jh, \\
\frac{\partial \left((1-c)\phi\rho_{w}h(1-S_{or})\right)}{\partial t} + 2\frac{\partial \left(vr(1-c)\phi\rho_{w}h(1-S_{or})\right)}{\partial r^{2}} = \varkappa_{w}Jh, \\
\frac{\partial \left((1-\phi)\rho_{R}h\right)}{\partial t} = -\varkappa_{R}Jh.
\end{cases} \tag{1}$$

Here c, (1-c) are acid mass concentration and agues phase (water + reaction products); \emptyset , h are porosity and specific reservoir thickness; ρ_w , ρ_R are densities of aqua phase and matrix; v is mass averaged flow rate of aqua phase; S_{or} is residual oil saturation; J, $\varkappa_w = 1.26$, $\varkappa_R = 2.26$ are chemical reaction rate of acid with matrix, mass ratio of reaction products and acid consumption, mass ratio of reacting dolomite and acid.

For the face dissolution problem, the reaction rate *J* tends to infinity and the reaction itself occurs in a narrow region called reaction front. The movement speed of the reaction front (complete consumption of the injected acid) is determined by the conditions on the acid concentration shock from zero to the initial concentration in the injected solution. Let's transform the mass balance equations (1) to the conservative form:

$$\begin{cases}
\frac{\partial}{\partial t} \left(c \phi \rho_{w} h (1 - S_{or}) - (1 - \phi) \frac{\rho_{R} h}{\kappa_{R}} \right) + 2 \frac{\partial \left(vrc \phi \rho_{w} h (1 - S_{or}) \right)}{\partial r^{2}} = 0, \\
\frac{\partial}{\partial t} \left((1 - c) \phi \rho_{w} h (1 - S_{or}) + (1 - \phi) \frac{\kappa_{w} \rho_{R} h}{\kappa_{R}} \right) + 2 \frac{\partial \left(vr(1 - c) \phi \rho_{w} h (1 - S_{or}) \right)}{\partial r^{2}} = 0.
\end{cases} \tag{2}$$

The mass balance of the chemical reaction reduces to the equation:

$$-J + \varkappa_w J - \varkappa_R J = 0 \text{ or } \varkappa_w - \varkappa_R = 1. \tag{3}$$

The divergent or conservative form of the equations gives the possibility to define the algebraic conservation equations at the reaction front [16]:

$$\begin{cases}
D\left[c\phi\rho_{w}h(1-S_{or})-(1-\phi)\frac{\rho_{R}h}{\varkappa_{R}}\right]-2\left[v(1-S_{or})r_{f}c\phi\rho_{w}h\right]=0, \\
D\left[(1-c)\phi\rho_{w}h(1-S_{or})+(1-\phi)\frac{\varkappa_{w}\rho_{R}h}{\varkappa_{R}}\right]-2\left[v(1-S_{or})r_{f}(1-c)\phi\rho_{w}h\right]=0, \\
D=\frac{dr_{f}^{2}}{dt},
\end{cases}$$
(4)

where D is reaction front velocity, r_f is reaction front coordinate, square brackets denote the difference of function's values before and after the reaction front. The boundary conditions of the considered problem determine the solution of these algebraic differences. These conditions define the acid injection concentration co and entire matrix dissolution O = 1 on the inlet and the absence of the acid before the reaction front C = 0 and initial value of porosity $O = O_0$. Accordantly the balance of values before and after the reaction takes the form:

$$r \le r_f$$
: $c^+ = c_o$, $\emptyset = 1$, $Q^+ = Q_o = 2\pi h (1 - S_{or}) v^+ r_f$, $r > r_f$: $c^- = 0$, $\emptyset^- = \emptyset_o$, $Q^- = Q = 2\pi h (1 - S_{or}) v^- r_f \emptyset_o$. (5)

Here Q_0 is the flow rate of the injected acid solution into the reservoir, and Q is the flow rate of the aqueous phase with the reaction products before the reaction front to be determined. By substituting these values into the algebraic conservation equations at the reaction front (4), all unknown parameters can be determined:

$$D = \frac{Q_o}{\pi h} \frac{1}{(1 - S_{or}) + \frac{(1 - \emptyset_o)\rho_R}{c_o \varkappa_R \rho_w}},$$

$$Q = Q_o \left\{ 1 - (1 - \emptyset_o) \frac{(1 - S_{or}) - \frac{\rho_R}{\rho_w}}{(1 - S_{or}) + \frac{(1 - \emptyset_o)\rho_R}{c_o \varkappa_R \rho_w}} \right\},$$

$$r_f = \sqrt{Dt + r_w^2}.$$
(6)

For slug volume V with acid concentration c_o the skin factor after acidizing process could be determined by the formula connecting the skin factor S_f with the effective well radius r_f .

$$S_f = -\ln\left(\frac{r_f}{r_w}\right), \ r_f = \sqrt{\frac{1}{\pi h} \frac{V}{(1 - S_{or}) + \frac{(1 - \phi_o)\rho_R}{c_o \varkappa_R \rho_w}} + r_w^2}. \tag{7}$$

Unified dissolution problem

Another ultimate case is the unified dissolution when the acid flow rate is much higher than reaction rate. In this case filling of porous matrix is not practically accompanied by chemical reaction and dissolution of carbonate rock begins after saturation of pore space by acid. At this assumption, acid penetrates to the radius r of the near wellbore zone:

$$r_* = \sqrt{\frac{V}{\pi h \emptyset_O (1 - S_{OT})} + r_W^2}.$$
 (8)

Thus, the reaction proceeds without convection and is determined by the equations in the saturated area:

$$\begin{cases}
\frac{d(c\phi\rho_{w}(1-S_{or}))}{dt} = -J, \\
\frac{d((1-c)\phi\rho_{w}(1-S_{or}))}{dt} = \varkappa_{w}J, \\
\frac{d((1-\phi)\rho_{R})}{dt} = -\varkappa_{R}J.
\end{cases} \tag{9}$$

Note that J is the volumetric reaction rate with SI dimension kg / (m³s), i.e. takes place in a unit volume of the porous medium. In experimental studies, the reaction rate is determined by volumetric method (by measurement of carbon dioxide release) [17] or on a rotating disk installation [2,18,19]. In the first case, the dimension of reaction rate coincides with J, but the method works in the region of relatively low pressures (up to 70 atm). In the second method, the surface reaction rate j with the dimension kg/(m²s) is determined. To use it in the model, one should multiply j by the specific surface of the reservoir matrix A_s . The specific surface of the porous matrix is determined by the generalized Kozeni-Karman formula [20]:

$$A_S = \frac{B\sqrt{\phi_o}(1-\phi_o)}{\sqrt{k_o}}(1-S_{or}). \tag{10}$$

Here k_o is matrix permeability, B is the empirical parameter, which value according Kotyahov [21] investigations varies in the interval $1 - 3.5 \cdot 10^5$ for practical calculations ($[k_o] = \mu m^2$, $[\emptyset_o] = \text{shares of units.}$). For certainty the value $B = 2.5 \cdot 10^5$ was used in further calculations. Note that there are some new investigations connecting specific surface with porosity and permeability [22] during acidizing process.

The rate of surface or heterogeneous reaction is written as $j = Zc^n \rho_w$, where Z is the kinetic reaction constant depending on thermodynamic conditions; n is the reaction order. In the general case of heterogeneous reactions order may be a fractional value (these parameters are determined in an experimental installation with a rotating disk). Reactions of zero and first orders are usually considered [17,23].

$$J = ZA_{s}c^{n}\rho_{w}. \tag{11}$$

First, let's transform the system (6), considering the densities independent of time and neglecting the change in water saturation due to the chemical reaction:

$$\begin{cases}
c \frac{d\phi}{dt} + \frac{dc}{dt} \phi = -\frac{J}{\rho_w (1 - S_{or})}, \\
(1 - c) \frac{d\phi}{dt} - \frac{dc}{dt} \phi = \frac{\varkappa_w J}{\rho_w (1 - S_{or})}, \\
\frac{d\phi}{dt} = \frac{\varkappa_R J}{\rho_R}.
\end{cases}$$
(12)

For the zero reaction order the solution of the system under initial conditions t = 0, $c = c_o$, $\emptyset = \emptyset_o$ allows to obtain full time of the acid consumption, as well as the matrix porosity after consumption:

$$t_l = \tau \frac{c_0}{c_0 + c_*}, \ \emptyset_l = \emptyset_0 \left(1 + \frac{c_0}{c_*} \right), \ c_* = \frac{\rho_R}{\kappa_R \rho_W (1 - S_{or})}, \ \tau = \frac{\emptyset_l \rho_R}{c_* \kappa_R Z S_S}.$$
 (13)

For the first order of reaction rate, the solution procedure is more complex but it is obvious that the value of final reservoir porosity is the same as for zero reaction order. However, the formation of the final porosity occurs only asymptotically in time.

The dynamics of acid consumption for both orders of reaction rates are presented as follows equations:

for the zero order
$$\ln \frac{\left(1 - \left(\frac{c_0}{c_*} + 1\right)^{-1}\right)}{\left(1 - \left(\frac{c}{c_*} + 1\right)^{-1}\right)} + \left(\left(\frac{c_0}{c_*} + 1\right)^{-1} - \left(\frac{c}{c_*} + 1\right)^{-1}\right) = \frac{t}{\tau},$$
 for the first order $\ln \frac{(1 - x_0)}{(1 - x)} + (x_0 - x) = \frac{t}{\tau}, x = \frac{\emptyset}{\emptyset_l}, x_0 = \frac{\emptyset_o}{\emptyset_l}.$ (14)

The obtained dependencies of acid concentration from time are illustrated on Fig. 1.

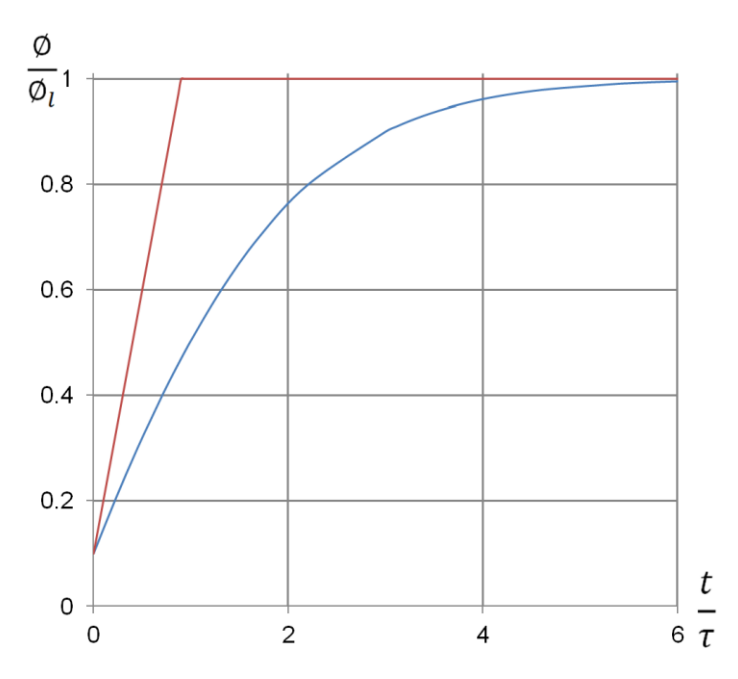


Fig. 1. Dependence of rock porosity from time during acidizing process for the zero and the first reaction order

The final time of acid consumption plays a significant role in the process technology because it defines the delay time for the reaction after acid injection. As for zero reaction order it is determined analytically, for the first order it can be only estimated, for example from Fig. 1 as $t_l \cong 2\tau$.

According to the Kozeni-Karman theory, for each rock of the same type, there is an unambiguous relationship between rock porosity and permeability [20]. Labrid's experiments [2] showed that a similar relationship could be used to relate rock porosity and permeability in the carbonate acidizing process:

$$\frac{k}{k_o} = K \left(\frac{\emptyset}{\emptyset_o} \right)^6. \tag{15}$$

The Hawkins formula [20] could be used for a skin factor determination. For this purpose, Eq. (15) should be applied for calculation of rock permeability determination at the value of final porosity after acidizing process. This procedure gives:

$$S_u = \left(\frac{k_o}{k} - 1\right) \ln\left(\frac{r_*}{r_w}\right). \tag{16}$$

Application of semi empirical model for calculation of wormhole formation

Semi empirical approach to wormhole formation bases of the results of the experiments of acid injection to a small cylindrical carbonate rock core [6,24,25]. It was found that under critical flow rate per unit surface q_{cr} the volume of acid until breakthrough takes the minimum value. This value is usually transferred to the dimensionless view by division on the core pore volume and is labeled as PV_{cr} . The dependence of PV_b on the specific value of flow rate q [12,26] with definitions of critical values is illustrated on the Fig. 2. The critical values are considered as the conditions of wormhole formation.

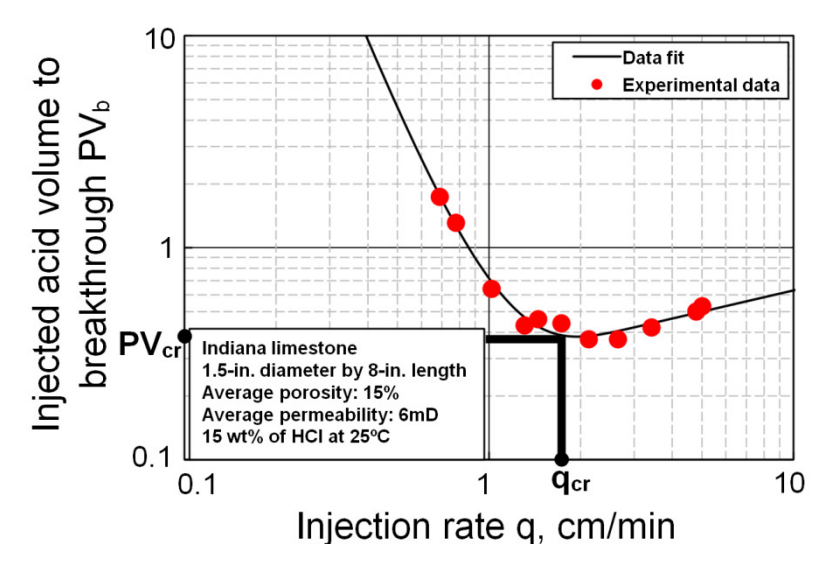


Fig. 2. The dependence of injected acid volume to breakthrough PV_b from the injection rate with determination of the critical values [12]

The determination of the wormhole's length in practice bases on the proposition of its formation similarity in experiments and in near wellbore area [2,23]:

$$l_{wh} = \frac{q_{cr}t}{PV_{cr}S\emptyset} = \frac{V}{PV_{cr}2\pi h r_w\emptyset},\tag{17}$$

where l_{wh} is the effective wormhole length. The real wormhole length differs from the effective value because of its fractal nature [8,23]. Daccord [23,26,27] connected the fractal structure of wormholes with the definition of effective length by the similar formula (17):

$$l_{wh} = \left(\frac{Vl^{d_f-1}}{PV_{cr}2\pi hr_w\emptyset}\right)^{\frac{1}{d_f}},\tag{18}$$

where d_f is the fractal dimension (1.5 < d_f < 1.7), f is the parameter of wormholes, defined from experiments. Application of Hawkins formula defines the expression of skin factor after acidizing of carbonate at critical injection rate:

$$S_{wh} = \left(\frac{k_o}{k} - 1\right) \ln\left(\frac{l_{wh} + r_w}{r_w}\right),\tag{19}$$

where the l_{wh} is extracted from Eq. (18).

The permeability of stimulated by wormholes zone is significantly higher than untreated reservoir. Daccord [28], Huzin [29] considered experimental data and proposed to neglect the ratio k_o / k thus simplified the skin determination:

$$S_{wh} = -\ln\left(\frac{l_{wh} + r_w}{r_w}\right). \tag{20}$$

General model formulation

The obtained solutions define the values of skin factors for all types of reactions. For example, consider the reservoir with typical characteristics: effective formation thickness h=20 m, porosity $\mathcal{O}_o=0.12$, reaction ratio $\mathcal{H}_w=1.26$, residual oil saturation $\mathcal{S}_{or}=0.3$, Labrid's coefficient K=1.7, well radius $r_w=0.1$ m, initial acid concentration $c_o=0.15$, densities of rock and solution $\rho_R=2804$ kg/m³, $\rho_W=1057$ kg/m³, injected slug volume V=60 m³, wormhole formation critical values $q_{cr}=1.4$ cm/min, $PV_{cr}=12.4$. Substituting these data to Eqs. (7), (16), (20) the following values of skin factors can be obtained:

$$S_f = -2.27, \ S_{wh} = -3.4, \ S_u = -1.98.$$
 (21)

If the wormhole formation regime is extracted from the analysis of the dependence of skin factor from flow rate the transformation between of face and unified dissolution should be connected by monotonous function. As an example, this function may be approximated by Gauss formula with the height of the curve's peak $|S_f - S_u|$ and half width corresponding by kinetic regime q_{ki} [30]:

$$S_{uf} = S_u + \left(S_f - S_u\right) \exp\left(-\frac{q^2}{q_{ki}^2}\right). \tag{22}$$

Here q_{ki} is the boundary rate of kinetic regime. This function has the appropriate asymptotes $q_{cr} \to 0, q_{cr} \to \infty$. At low flow rate, it gives the independent from rate skin factor. At high flow rates, the dependence tends to the value S_u with weak dependence

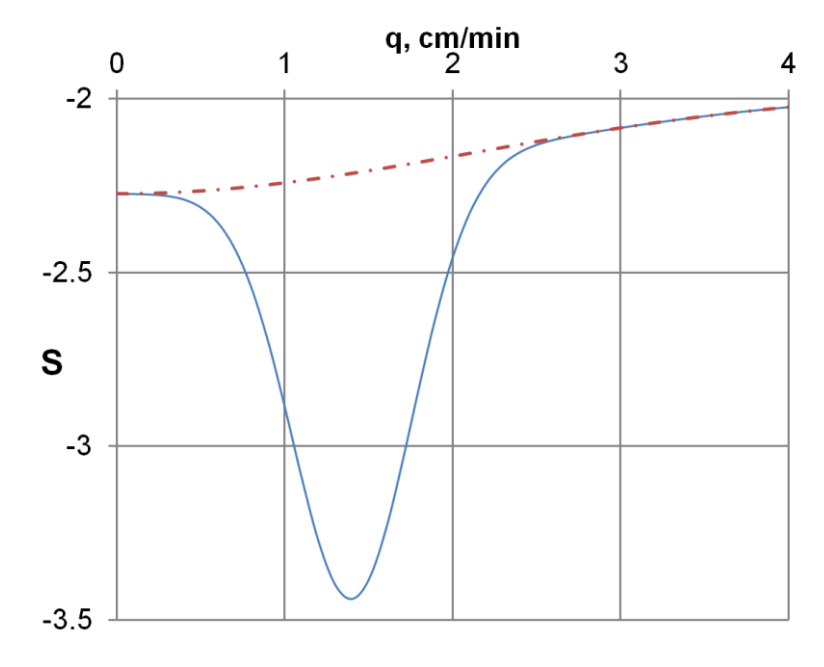


Fig. 3. The supportive (22) (dashed dotted line) and the general (23) (solid line) models of the dependence of skin factor and specific acid injection rate with correct asymptotes and local wormhole minimum close to the experimental data

from rate. The difference $(S_f - S_u)$ may be positive or negative and depends on reservoir parameters.

The wormhole formation regime is manifested in the relatively narrow interval of flow rate [7,31] and may be implanted by another Gauss function:

$$S_g = S_{uf} - \left(S_f - S_{wh}\right) \exp\left(-\frac{(q - q_{cr})^2}{\Delta q^2}\right),\tag{23}$$

where Δq is the half width of the specific flow rate of wormhole formation regime. Figure 3 also illustrates the general approximation (23) of the model of reservoir acid treatment. The function on Fig. 3 corresponds to the model reservoir data Eq. (21).

The proposed approximation formula may be used in different codes for a reservoir acid treatment process. It could be the basis of the process optimization procedure with maximum productivity increase criteria and determination of optimal impact parameters such as acid slug volume and concentration, injection rate and etc.

Note that the general model involves the main technological parameters: injection rate, slug volume and acid concentration through Eqs. (7), (8), (14), (18). For instance, the influence of the volume of injected acid slug on skin factor is shown in Fig. 4. From the obtained solutions, critical rate does not dependent from the slug volume and skin factor is proportional to $-\ln(V^{df}-1)$, which illustrates Fig. 4. On the other hand, the critical rate depends on concentration and acid concentration growth shifts the graph to the left this feature is shown in Fig. 5.

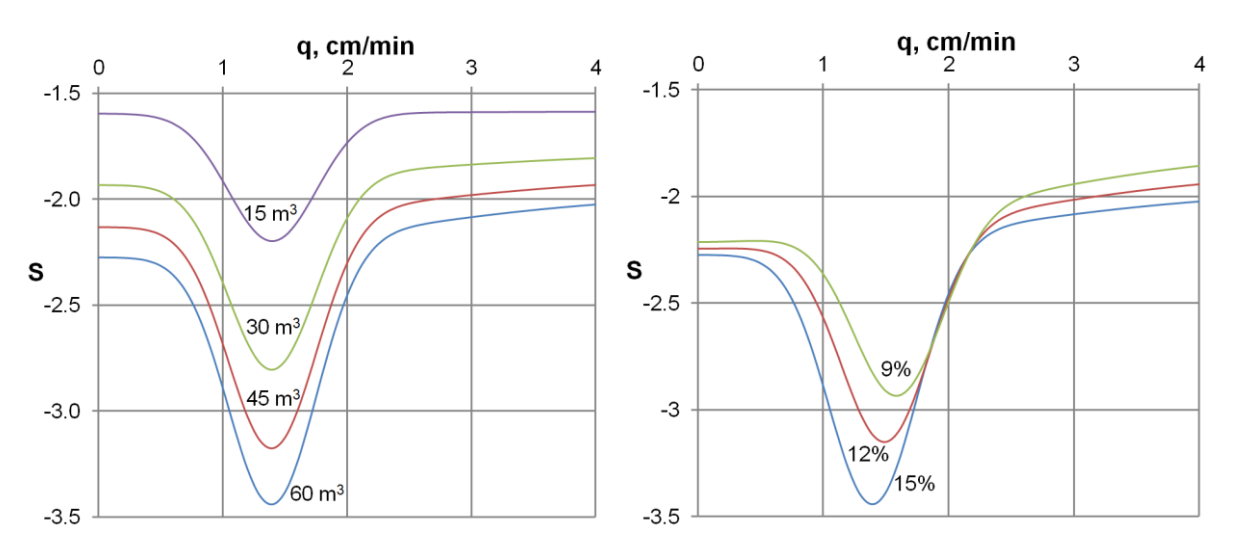


Fig. 4. Calculations of the influence of acid slug volume on the skin factor behavior. Volume values are indicated on graphs

Fig. 5. Skin factor dependence from acid concentration. Concentration values are indicated on graphs

Conclusions

The solutions of the problems of face and unified dissolution of carbonate reservoir due to the injection of acid were obtained. For the wormhole formation process the corrected Gong's model was used. All solutions were transferred to dependence of skin factor from process parameters.

The general model integrates the obtained solutions and Gong model for the prediction of skin factor dependence from injection rate, acid concentration and slug volume for the whole intervals of parameters variation. The model illustrated on the

example of stimulation of vertical well but can be easily transferred to the other types of well completion and acids.

The developed model matches to the appropriate asymptotes $(q_{cr} \rightarrow 0, q_{cr} \rightarrow \infty)$ and describes the wormhole local minimum in the vicinity of critical injection rate.

Note that since there is no analytical solution (1) for arbitrary speed, a dependency (22) should be obtained from numerical solution [32]. The development of wormhole formation theory will give the framework of approximation (23) improvement.

CRediT authorship contribution statement

Rodion M. Ganopolskij Sc: writing – section Unified dissolution problem, all calculations; **Konstantin M. Fedorov** Sc: writing – the general idea of the investigation, original draft; **Alexey E. Folomeev** Sc: writing – section Solution of the face dissolution problem, review & editing.

Conflict of interest

The authors declare that they have no conflict of interest.

References

- 1. Ibragimov GZ, Khisamutdinov NI. *Handbook on application of chemical reagents in oil recovery.* Moscow: Nedra Publisher; 1983. (In Russian)
- 2. Schechter RS. Oil Well Stimulation. Englewood Cliffs: Prentice Hall; 1993.
- 3. Fredd CN, Fogler HS. Optimum Conditions for Wormhole Formation in Carbonate Porous Media: Influence of Transport and Reaction. *SPE Journal*. 1999;4(3): 196–205.
- 4. Menke HP, Maes J, Geiger S. Channeling is a distinct class of dissolution in complex porous media. *Scientific Reports*. 2013;13: 11312.
- 5. Fedorov KM. Unsteady flow through a porous medium in the presence of chemical reactions. *Fluid Dynamics*. 1987;22:70–75.
- 6. Fredd CN, Fogler HS. The kinetics of calcite dissolution in acetic acid solutions. *Chemical Engineering Science*. 1998;53(22): 3863–3874.
- 7. Fredd CN, Fogler HS. Influence of Transport and Reaction on Wormhole Formation in Porous Media. *AIChE Journal*. 1998;44(9): 1933–1949.
- 8. Gong M, El-Rabaa AM. Quantitative Model of Wormholing Process in Carbonate Acidizing. In: *Proceedings of the SPE Mid-Continent Operations Symposium*, 28–31 March 1999, Oklahoma City, Oklahoma. 1999. p.SPE–52165–MS.
- 9. Ganopolskij RM, Fedorov KM, Gilmutdinov BR, Folomeev AE. Development of the semi empirical approach on wormhole formation in carbonates. *Materials Physics and Mechanics*. 2024;52(5): 119–126.
- 10. Zaitsev MV, Mikhailov NN. No-nadditive skin-factor in case of a formation complex damage. *Oilfield Engineering, scientific and technical journal*. 2019;1: 36–38.
- 11. Panga MK, Ziauddin M, Balakotaiah V. Two-scale continuum model for simulation of wormholes in carbonate acidization. *AIChE Journal*. 2005;51(12): 3231–3248.
- 12. Dong K, Zhu D, Hill AD. Theoretical and Experimental Study of Optimal Injection Rates in Carbonate Acidizing. *SPE Journal*. 2017;22(3): 892–901.
- 13. Alhamad L, Alrashed A, Al Munif E, Miskimins J. A review of organic acids roles in acidizing operations for carbonate and sandstone formations. In: *Proceedings of the SPE International Conference and Exhibition on Formation Damage Control 2020, 19–21 February 2020, Lafayette, USA.* Lafayette: Society of Petroleum Engineers (SPE); 2020. p.199291.
- 14. Kalia N, Balakotaiah V. Modeling and Analysis of Wormhole Formation in Reactive Dissolution of Carbonate Rocks. *Chemical Engineering Science*. 2007;62(4): 919–928.

- 15. Gringarten AC, Dawe RA, Wilson DC. Interpretation of well test transient data. In: Wilson DC, Dawe RA. (eds.) *Developments in Petroleum Engineering 1*. London: CRC Press; 1985.
- 16 Gelfand IM. Several Problems of the quazi linear equations. *Achievements in Mathematical Sciences*. 1959;14(2): 87–158.
- 17. Stromberg AG, Semchenko DL. *Physical chemistry. Manual for Chemistry Universities*. Moscow: High School Publisher; 1999. (In Russian)
- 18. Taylor KC, Nasr-El-Din HA. Measurement of Acid Reaction Rates with the Rotation Disk Apparatus. *Journal of Canadian Petroleum Technology*. 2009;48(6): 66–70.
- 19. Fan Y, Peng H, Chen G, Peng J, Han H, Qin Y, Liu D. Experimental study of the influences of different factors on the acid-rock reaction rate of carbonate rocks. *Journal of Energy Storage*. 2023;63: 107064.
- 20. Willhite PG. *Flooding of formations*. Moscow: Institute for Computer Studies, Regular and Chaotic Dynamics; 2009. (In Russian)
- 21. Kotyakhov Fl. *Physics of oil and gas reservoirs*. Moscow: Nedra; 1977. (In Russian)
- 22. Mohammadi M, Shadizadeh SR, Manshad AK, Mohammadi AH. Experimental study of the relationship between porosity and surface area of carbonate reservoir rocks. *Journal of Petroleum Exploration and Production Technology*. 2020;10: 1817–1834.
- 23. Buijse MA. Understanding wormholing mechanisms can improve acid treatments in carbonate formations. *SPE Production & Facilities*. 2000;15(3): 168–175.
- 24. Daccord G. Chemical dissolution of a porous medium by a reactive fluid. *Physical Review Letters*. 1987;58(5): 479.
- 25. Betelin VB, Galkin VA, Shpilman AV, Smirnov NN. Digital Core Simulator A Promising Method For Developing Hard-To-Recover Oil Reserves Technology. *Materials Physics and Mechanics*. 2020;44(2): 186–209. 26. dos Santos Lucas CR, Neyra JR, Araujo EA, da Silva DNN, Lima MA, Ribeiro DAM, Aum PTP. Carbonate acidizing A review on influencing parameters of wormholes formation. *Journal of Petroleum Science and Engineering*. 2023;220: 111168.
- 27. Daccord G, Touboul E, Lenormand R. Carbonate Acidizing: Toward a Quantitative Model of the Wormholing Phenomenon. *SPE Production Engineering*. 1989;4(1): 63–68.
- 28. Daccord G, Lietard O, Lenormand R. Chemical dissolution of a porous medium by a reactive fluid—II. Convection vs reaction, behavior diagram. *Chemical Engineering Science*. 1993;48(1): 179–186.
- 29. Huzin R, Shevko N, Melnikov S. Improving Well Stimulation Technology Based on Acid Stimulation Modeling, Lab and Field Data Integration. In: *Proceedings of the SPE Russian Petroleum Technology Conference, RPTC 2019, 22–24 October 2019, Moscow.* Moscow: Society of Petroleum Engineers (SPE); 2019. p. 196976.
- 30. Levich VG. Physico-chemical hydrodynamics. Moscow: PhysMatGiz Publisher, 1959. (In Russian)
- 31. Golfier F, Zarcone C, Bazin B, Lenormand R, Lasseux D. On the ability of a Darcy-scale model to capture wormhole formation during the dissolution of a porous medium. *Journal of Fluid Mechanics*. 2002;457: 213–254. 32. Jia C, Sepehrnoori K, Huang Z, Zhang H, Yao J. Numerical studies and analysis on reactive flow in carbonate matrix acidizing. *Journal of Petroleum Science and Engineering*. 2021;201(8): 108487.

Submitted: December 5, 2024 Revised: February 4, 2025 Accepted: July 8, 2025

Influence of alkali treatment and fiber percentage on the mechanical and thermophysical properties of gypsum composites filled with hemp fiber

K. Sunil Ratna Kumar ¹, S.B.R. Devireddy ², T. Gopala Rao ²,

B. Sudheer Kumar ³ , K. Bala Prasad ⁴

- ¹ SIR C R Reddy College of Engineering, Vatluru, Andhra Pradesh, India
- ² St. Ann's College of Engineering and Technology, Andhra Pradesh, India
- ³ Lakireddy Bali Reddy College of Engineering, Andhra Pradesh, India
- ⁴ RVR& JC College of Engineering, Andhra Pradesh, India

ABSTRACT

The influence of alkali treatment and fiber percentage on the physical, mechanical and thermal properties of hemp fiber reinforced gypsum composites are examined. Short hemp fibers (15 mm in length) were subjected to alkali treatment using 5, 10, and 15 wt. % NaOH concentrations for 5 h. Both untreated and NaOH treated hemp fiber reinforced gypsum composites were fabricated with fiber percentages of 3, 6, 9, 12, and 15 vol. % through the hand layup process. The fabricated composite samples were evaluated for density, water absorption, compressive strength, flexural strength, and thermal conductivity. The composite with 10 wt. % NaOH treated fibers, and 12 vol. % fiber content showed significant improvements, with a 337 % increase in flexural strength, a 136 % increase in flexural modulus, and a 109.8 % increase in compressive strength compared to pure gypsum. The results for thermal conductivity indicate that NaOH concentration has a minimal effect on enhancing thermal resistance compared to the influence of fiber percentage. SEM analysis of untreated and treated fibers revealed surface modifications and changes in fiber characteristics due to NaOH treatment. The results showed that stronger NaOH treatments and higher fiber content negatively impacted fiber suitability, stiffness, and overall composite properties.

KEYWORDS

alkali treatment • gypsum composite • hemp fiber • scanning electron microscopy • mechanical properties thermal conductivity • water absorption

Citation: Sunil Ratna Kumar K, Devireddy SBR, Gopala Rao T, Sudheer Kumar B, Bala Prasad K. Influence of alkali treatment and fiber percentage on the mechanical and thermophysical properties of gypsum composites filled with hemp fiber. *Materials Physics and Mechanics*. 2025;53(3): 79–93. http://dx.doi.org/10.18149/MPM.5342025_7

Introduction

Over the last decade, energy consumption in building sector has steadily increased due to rising comfort standards and population growth. The need for environmentally friendly and energy efficient materials to reduce energy consumption is critical as global energy reserves become increasingly strained. This has driven research into the development of thermal energy storage solutions, including electrochemical energy storage, latent heat storage, and sensible heat storage [1,2]. Gypsum based materials are widely used in commercial, residential, and industrial buildings for partitions, wall panels, and boards.



[™] sivabhaskararao@gmail.com

These materials have gained prominence as unique construction materials due to their affordability, lightweight properties, ease of application, and abundant availability [3]. The primary drawback of gypsum as a building material is its brittleness and heaviness. This limitation can be migrated by mixing gypsum with synthetic fibers, mineral particles and natural fibers [4]. Significant research has been conducted on the development of gypsum composites reinforced with natural fibers, including notable examples such as cellulose, hemp, palm, short sisal, and straw fibers [5-7]. Nindiyasari et al. [8] investigated the mechanical properties of cellulose fiber-reinforced gypsum composites and found that the addition of reinforcement increased the Young's modulus, compressive strength, and bending strength of the composites. This improvement was attributed to the fibers' ability to fill the voids within the composites. Selamat et al. [9] evaluated the thermal and mechanical performance of gypsum composites reinforced with rice husk and oil palm trunk fibers. The results indicated that the composite with 20 % fiber loading demonstrated improved thermal stability and flexural strength. Tesárek et al. [10] assessed the compressive strength of gypsum composites reinforced with recycled tire wires. Their study revealed that composites with large voids exhibited lower compressive strength due to damage localization in poorly compacted areas. Amuthakkannan et al. [11] examines the effect of fiber content on the mechanical properties of the short basalt fiber reinforced composites and revealed that composites with 10 mm fiber length exhibits better properties than other lengths of fiber.

In this way, natural reinforcements in gypsum matrices are increasingly important for the design and construction of buildings, particularly as insulation materials. Among various natural fibers, hemp fibers have demonstrated strong performance as a sustainable reinforcement, resulting in composites with enhanced physical and mechanical properties [12]. Several factors influence the properties of gypsum composite materials, including the properties of the individual constituents, fiber geometry, the orientation and distribution of the fibers, the fiber-matrix interface, as well as the fiber, size, shape, and the methods used for mixing and processing [13]. Previous investigations highlight that weak bonding at the interface between the reinforcement and matrix is a major drawback, primarily due to poor wetting between the matrix and natural fibers. As a result, numerous studies have focused on both physical and chemical treatments (such as mercerization, alkalization, acetylation and silane) of fibers to improve fiber-matrix adhesion, reduce moisture absorption, and enhance surface roughness [14–17]. Shejkara et al. [18] investigated the effect of NaOH treatment on the physical and mechanical properties of micro-sized walnut shell particulate (WSP) epoxy composites. Their findings indicated that an excessive NaOH concentration in the aqueous solution slightly degraded the material's properties. Yadav et al. [19] investigated the influence of NaOH treatment on the mechanical properties of sisal fiber-reinforced epoxy composites. Their analysis revealed that composites incorporating surface-modified sisal fibers with a 2M NaOH concentration demonstrated superior mechanical properties compared to other tested variants. In recent years, hemp fiber has garnered significant attention from researchers worldwide due to its relatively short cropping cycle and ability to thrive in diverse environments. It is an important natural fiber, extensively used in the production of composites for various industrial and construction applications [20]. With a tensile strength of up to 1110 MPa, hemp fiber is one of the strongest among all bast fibers [21].

Charai et al. [22] demonstrated that incorporating hemp fibers into gypsum-based composites enhanced both the thermal insulation and bending behavior of the composites.

Numerous studies on natural fiber composites employ short fibers (typically ~ 15 mm in length) to ensure compatibility with standard manufacturing techniques while optimizing mechanical performance after alkali treatment [19,23]. lucolano et al. [24] successfully produced gypsum composites reinforced with hemp and glass short fibers to enhance the mechanical properties of the gypsum material. Research on hemp fiber reinforced gypsum (HFRG) composites with alkali treated fibers is not reported in the literature. This study aims to investigate the effects of different alkali concentrations (5, 10, and 15 wt. %) and fiber volume percentages (3, 6, 9, 12, and 15 vol. %) on HFRG composites. The compressive strength, flexural strength, thermal conductivity, density, and water absorption of the composites with alkali treated fibers are compared to those of untreated HFRG composites.

Materials and Methods

Materials

In this study, hemp fibers and a gypsum matrix were used to fabricate HFRG composite materials. Hemp fibers were obtained from the local sources and chopped to an average length 15 mm. The physical, mechanical, and thermal properties of the hemp fibers are presented in Table 1. Gypsum, used as the matrix material, was in powder form. The β -gypsum powder (CaSO₄·0.5H₂O) utilized in this study was procured from Fiber Source India. The properties of the gypsum used are presented in Table 2.

Table 1. Properties of hemp fiber

Property	Value
Density, g/cm ³	1.47
Tensile strength, MPa	200-240
Tensile modulus, GPa	3.5-4.0
% elongation	2-4
Cellulous content, %	74.4
Hemicelluloses, %	17.9
Lignin content, %	3.7
Moisture content, %	12

Table 2. Properties of gypsum

Property	Value
Compressive strength, MPa	2.8
Flexural strength, MPa	1.5
Dry density, kg/m³	800-1200
Workability time, min	65-95
Final setting time, min	140
1000 μm, % passing	95
150 μm, % passing	60

Fiber treatment

The chopped hemp fibers were soaked separately in three different alkali concentrations (5, 10, and 15 wt. % NaOH). The fibers were immersed in the NaOH solutions for 5 h at room temperature to ensure better penetration of the solution into the fibers, as recommended [25,26]. The treated fibers were removed from the alkali solution and thoroughly rinsed multiple times with running tap water to remove any excess NaOH from the fiber surface. The cleaned hemp fibers were then dried in an oven at 70 °C for 4 h to eliminate any remaining moisture content.

Composites preparation

The composite specimens were fabricated by varying the volume percentage of hemp fiber (3, 6, 9, 12, and 15 vol. %) and using different NaOH concentrations (0, 5, 10, and 15 wt. %). The mix proportions of hemp and gypsum used to make the composite samples are provided in Table 3. The hemp fiber and gypsum matrix were initially mixed for 3 min to get a homogenized dry mixture and then water is added. The ratio of water and gypsum was maintained 0.6 to achieve gypsum slurry. The slurry was poured into three open molds of different shapes, with dimensions of $100 \times 100 \times 40$, $160 \times 40 \times 40$, and $120 \times 120 \times 20 \text{ mm}^3$. After 24 h, the composite samples were removed from the molds and stored at room temperature for 28 days prior to testing. The fabricated gypsum composite specimens were shown in Fig. 1.

Table 3. Mixed proportions of the NaOH concentration, hemp fiber, and gypsum

Composite	NaOH concentration, wt. %	Hemp fiber, vol. %	Gypsum, vol. %
C1	0	0	100
C2		3	97
C3		6	94
C4	0	9	91
C5		12	88
C6		15	85
C7		3	97
C8		6	94
C9	5	9	91
C10		12	88
C11		15	85
C12		3	97
C13		6	94
C14	10	9	91
C15		12	88
C16		15	85
C17		3	97
C18		6	94
C19	15	9	91
C20		12	88
C21		15	85



Fig. 1. Fabricated HFRG composite specimens

Physical properties of gypsum composites

The experimental density of the hemp fiber-reinforced gypsum composites was determined using the Archimedes method in accordance with ASTM D792 standards. The composite samples were prepared with dimensions of $100 \times 100 \times 40 \text{ mm}^3$. By knowing the mass m and volume V of the composite samples, the density ρ was calculated using Eq. (1):

$$\rho = \frac{m}{V}.\tag{1}$$

The water absorption percentage of the fabricated composite specimens was measured in accordance with the ASTM D2842-01 standard, using samples with dimensions of $100 \times 100 \times 40 \text{ mm}^3$. The water absorption value was calculated using Eq. (2):

Water absorption (%) =
$$\frac{(W_1 - W_0)}{W_0} \times 100$$
, (2)

where W_0 is the initial weight of specimen and W_1 is the weight of specimen after absorption of water.

Mechanical properties of gypsum composites

The compressive and flexural properties of untreated and treated HFRG composites were evaluated in accordance with TS EN 13279-2 standards. Both tests were conducted using the same universal testing machine. Composite specimens with dimensions of $160 \times 40 \times 40 \text{ mm}^3$ were used for the compressive and flexural tests. The experiments were conducted at room temperature with a crosshead speed of 2 mm/min. The flexural strength σ and modulus E_{flex} of the samples were calculated using Eqs. (3) and (4):

$$\sigma = 1.5 \times \frac{PL}{bt^2} \left(\frac{N}{mm^2} \right), \tag{3}$$

$$E_{flex} = \frac{L^3 m}{4 \text{bt}^3} \left(\frac{N}{\text{mm}^2} \right), \tag{4}$$

where L is the length of the span, P is the maximum load supported by the sample, m is the slope of the tangent to linear portion of the load-deflection curve, b and t are the width and thickness of the sample respectively. The composite specimen subjected to the compressive and flexural loading is shown in Fig. 2. For each type of composite, five specimens were tested to evaluate the compressive and flexural properties, and the average values were reported.



Fig. 2. composite specimen subjected to (a) compressive loading and (b) flexural loading

Thermal conductivity of gypsum composites

The thermal conductivity of HFRG composite specimens was determined using the steady-state hot plate method, following the procedure outlined in European Standard EN 13279-2. The composite specimens prepared with dimensions of $120 \times 120 \times 20 \text{ mm}^3$. The samples were placed between a cold plate and a hot plate, and the thermal conductivity was measured based on the temperature difference and heat flux, as indicated in Eq. (5):

$$q = \frac{k(T_1 - T_2)}{L},\tag{5}$$

where k is the thermal conductivity (W/m·K), q is the heat flux (W/m²), L is the thickness of the sample (m) and T_1 - T_2 is the difference in temperature (°C or K).

Scanning electron microscopy

To examine the fiber surface before and after alkali treatment, the microstructure of the hemp fibers was analysed by using JEOL-JSM-6390 model scanning electron microscope (SEM). To perform this study, the hemp fiber specimens were gold coated to improve the electrical conductivity for attains good quality photographs.

Results and discussion

Density

The density of a composite is a key factor influencing its mechanical properties. The experimental density of the composite depends on several factors, including interfacial bonding, void content, and the relative proportions of matrix and fiber. The measured density of neat gypsum was found to be 1.162 g/cm³. Figure 3 illustrates the impact of NaOH treatment and fiber percentage on the experimental density of HFRG composites.

It can be observed that NaOH treatment slightly improved the density of untreated gypsum composites. The highest density values were recorded for composites treated with 10 wt. % NaOH, followed by those treated with 15 wt. % NaOH, 5 wt. % NaOH, and untreated fiber-reinforced gypsum composites. The figure shows that the measured density of the fabricated composite specimens increases with a higher fiber percentage, as expected, due to the higher density (1.47 g/cm³) of the hemp fiber compared to that of the gypsum matrix (1.162 g/cm³). The results indicate that as the hemp fiber percentage increases from 0 to 12 vol.%, the measured density increases by 4.22, 4.99, 5.93, and 5.16 % for composites treated with untreated, 5, 10, and 15 wt. % NaOH, respectively.

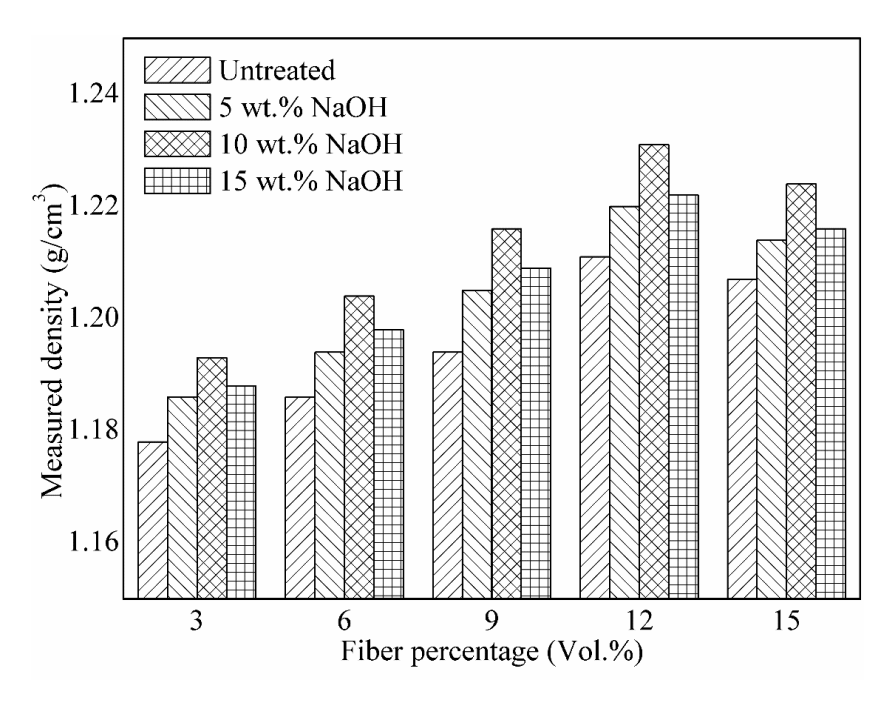


Fig. 3. Density of HFRG composites

Water absorption

Water absorption is another important physical property that depends on various factors, including humidity, void content, fiber percentage, and temperature [27]. The maximum water absorption percentage of neat gypsum is 29.02 %. Figure 4 illustrates the effects of fiber percentage and NaOH treatment on the water absorption of HFRG composites.

Water uptake rapidly increases in the early stages and slows down as immersion time increases. It was observed that untreated hemp/gypsum composite samples exhibited the highest water absorption percentage compared to alkali treated hemp/gypsum composites. The maximum water absorption value observed for the untreated composites with a 15 vol. % fiber percentage after 216 h was 44.84 %. This was followed by 41.8 % for composites treated with 5 wt. % NaOH, 41.24 % for those treated with 15 wt. % NaOH, and 40.16 % for composites treated with 10 wt. % NaOH. The reduction in water absorption percentage after alkali treatment is attributed to improved chemical bonding between the reinforcement and the matrix. These results are consistent with those reported by previous researchers [28,29].

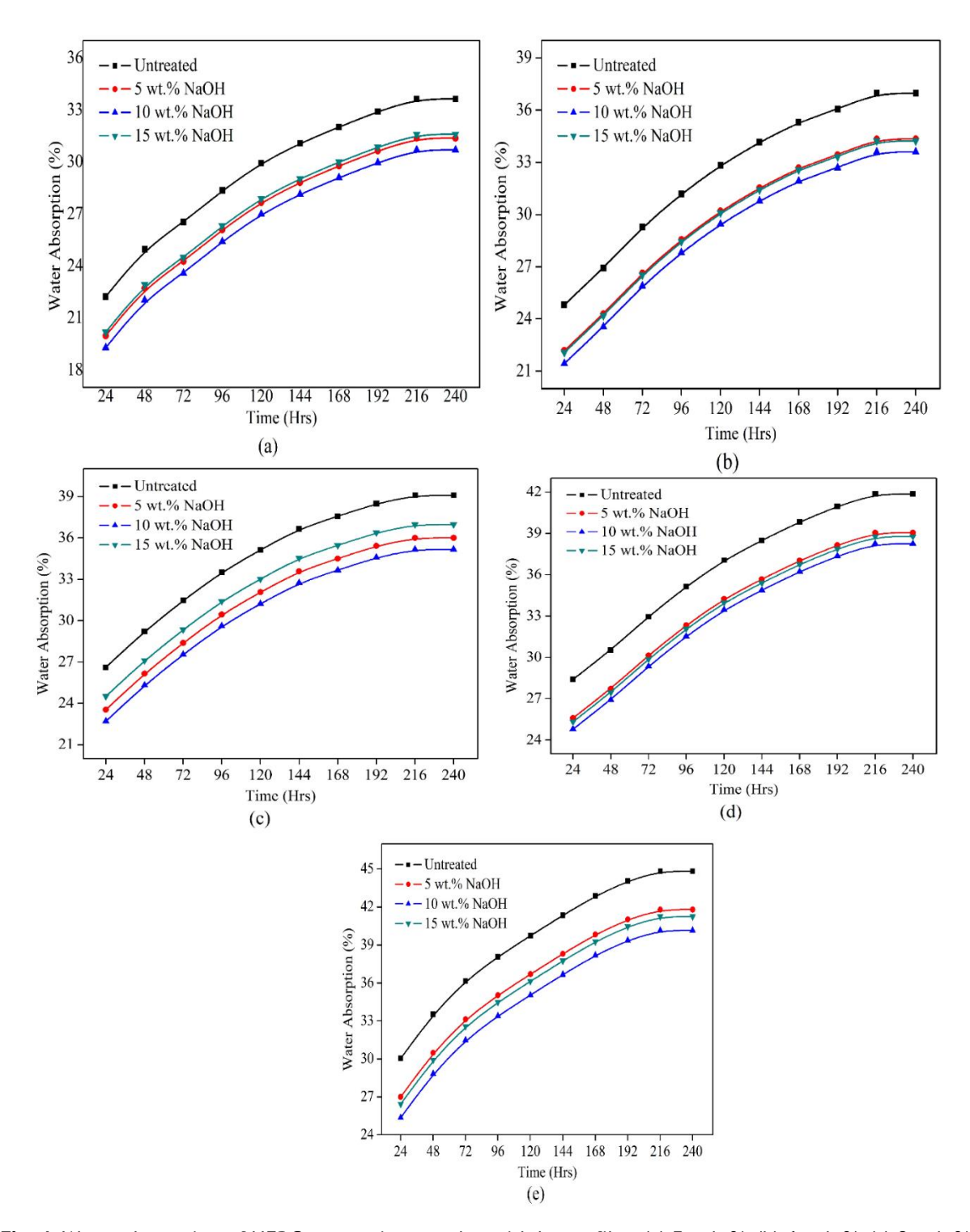


Fig. 4. Water absorption of HFRG composite samples with hemp fiber (a) 3 vol. %, (b) 6 vol. %, (c) 9 vol. %, (d) 12 vol. %, and (e) 15 vol. %

Compressive strength

Figure 5 shows the impact of fiber percentage and alkali treatment on the compressive strength of HFRG composite specimens. The compressive strength of pure gypsum was found to be 4.75 MPa. The compressive strength of the fabricated HFRG composite samples was found to increase with the fiber percentage up to 12 vol. % before decreasing at 15 vol. %. For composites with 12 vol. % fiber percentage, the compressive

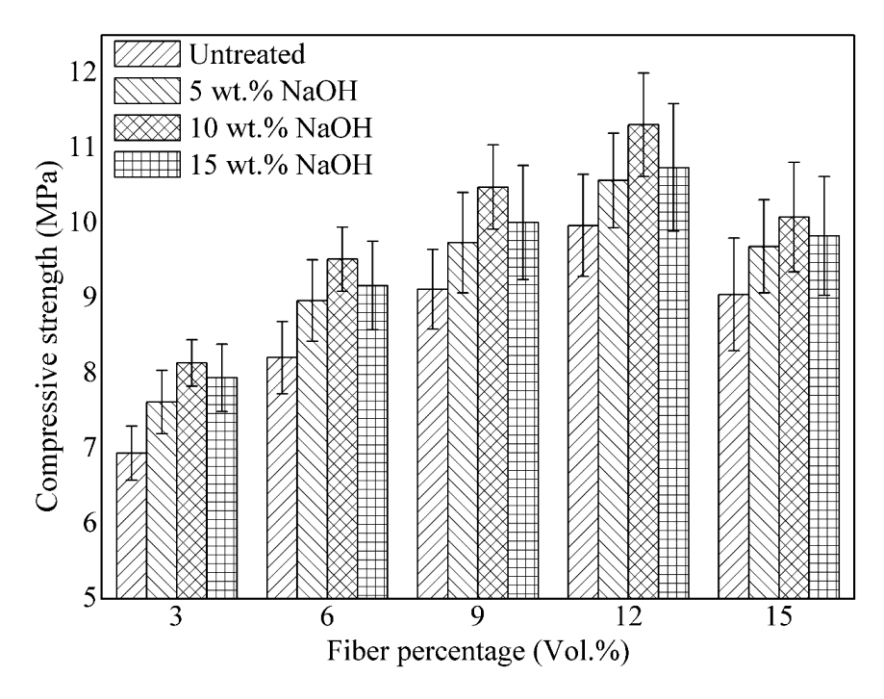


Fig. 5. Compressive strength of HFRG composites

strength increased by 85.68, 98.52, 109.8, and 94.73 % compared to neat gypsum, with NaOH concentrations of untreated, 5, 10, and 15 wt. %, respectively. Hemp fiber has a higher modulus, and NaOH treatment enhances the interfacial bonding between the hemp fiber and gypsum. Up to a 12 vol. % fiber percentage, the stress required to achieve the same deformation is relatively higher. At a 15 vol. % fiber percentage, the decrease in compressive strength is attributed to increased porosity in the gypsum from air entrainment and reduced adhesion between the hemp fibers and the gypsum [30]. Compared to untreated hemp/gypsum composites, those treated with NaOH exhibited better compressive strength. As the alkali treatment concentration increased from 5 wt. % to 10 wt. %, compressive strength improved. However, a decrease in compressive strength was observed at 15 wt. % NaOH treatment. On the other hand, the decrease in compressive strength of the 15 wt. % NaOH-treated hemp/gypsum composite is associated to the removal of binding materials from the fibers and surface damage caused by the strong NaOH concentration.

Flexural properties

Figures 6 and 7 present the average flexural strength and modulus of HFRG composites obtained from flexural tests at different fiber volume percentages (3, 6, 9, 12, and 15 %) and varying NaOH concentrations (0, 5, 10, and 15 %). The flexural strength and modulus of neat gypsum were measured at 2.48 and 462 MPa, respectively. The flexural properties of the composite specimens improved with increasing fiber content up to 12 vol. %, but a further increase to 15 vol. % resulted in a decline. At 12 vol. % fiber content, the maximum flexural strength of the HFRG composite increased to 9.15, 10.07, 10.84, and 10.36 MPa for NaOH concentrations of untreated, 5, 10, and 15 wt. %, respectively. The improvement in flexural properties up to 12 vol. % fiber content is due to proper bonding between the reinforcement and matrix phases, along with more fibers filling the voids in the composite. As the fiber content increases from neat gypsum to 12 vol. %, the flexural

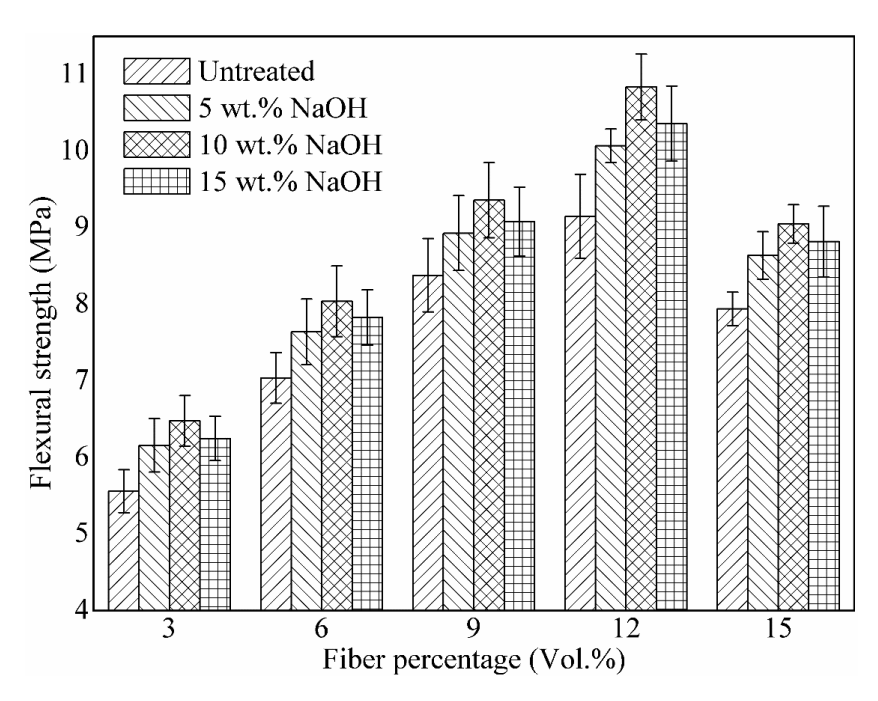


Fig. 6. Flexural strength of HFRG composites

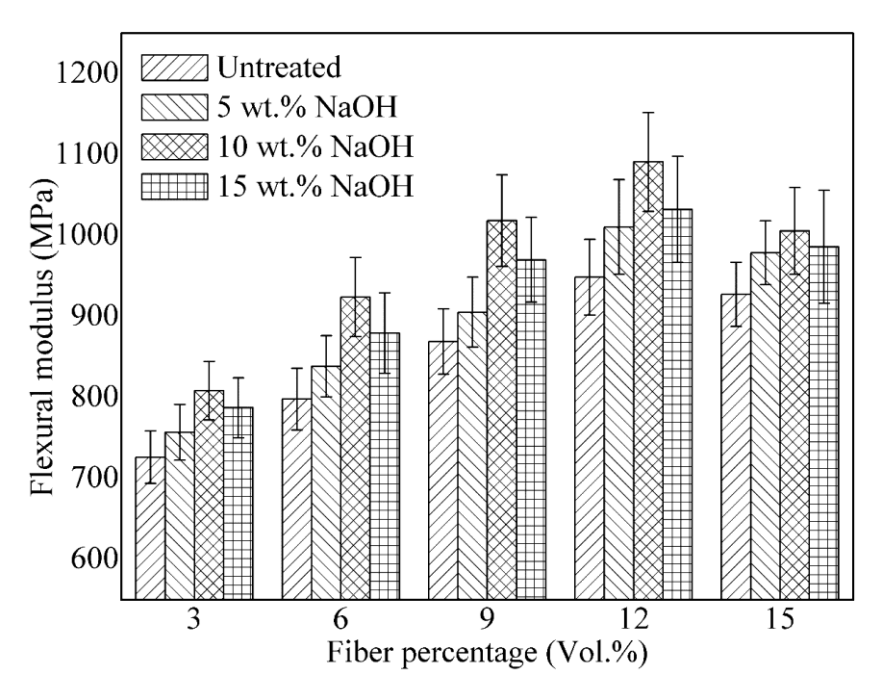


Fig. 7. Flexural modulus of HFRG composites

modulus of the composites rises by 105, 118, 136, and 123 % for NaOH concentrations of untreated, 5, 10, and 15 wt. %, respectively.

The flexural strength and modulus of alkali-treated HFRG composite specimens were found to be higher than those of untreated specimens. The primary reason for the improvement in strength and modulus with 10 wt. % NaOH treatment of hemp fibers is the removal of waxy substances and impurities from the fiber surface. This enhances mechanical interlocking and adhesive bonding between the reinforcement and the matrix, leading to better overall performance [31]. Among the tested samples, the composite with 10 wt. % alkali treatment and 12 vol. % fiber content exhibited the

highest values, with a flexural strength of 10.84 MPa and a flexural modulus of 1091 MPa. These values represent an increase of 18.4% in flexural strength and 15% in flexural modulus compared to the untreated HFRG composite. The figures also show that increasing the alkali concentration to 15 wt. % results in a decrease in flexural properties compared to 5 and 10 wt. %. This can be attributed to the excessive NaOH concentration, which removes lignin and hemicellulose from the fibers, thereby reducing the flexural properties. Similar findings have been reported by several researchers for different NaOH concentrations and fiber percentages [32–34].

Thermal conductivity

The thermal conductivity of pure gypsum was measured at 0.45 W/m·K. Figure 8 depicts the thermal conductivities of the fabricated HFRG composite specimens with varying NaOH concentrations and fiber volume percentages. The figure shows that the addition of hemp fibers into the gypsum matrix reduces the thermal conductivity of the composite material. With hemp fiber volume percentages ranging from 0 to 15 vol. %, the thermal conductivity decreased compared to neat gypsum by 13.55, 12.88, 12.22, and 11.55 % for NaOH concentrations of untreated, 5, 10, and 15 wt. %, respectively. This indicates that the addition of natural fibers to the matrix material significantly improves the thermal insulation of the composites. Furthermore, the figure suggests that the impact of NaOH treatment on thermal conductivity is less pronounced. The observed increase in thermal conductivity of composites with higher NaOH concentrations can be attributed to three key mechanisms: enhanced fiber–matrix interfacial bonding, structural modifications within the fibers, and reduced porosity. These results align well with previous literature findings [35,36].

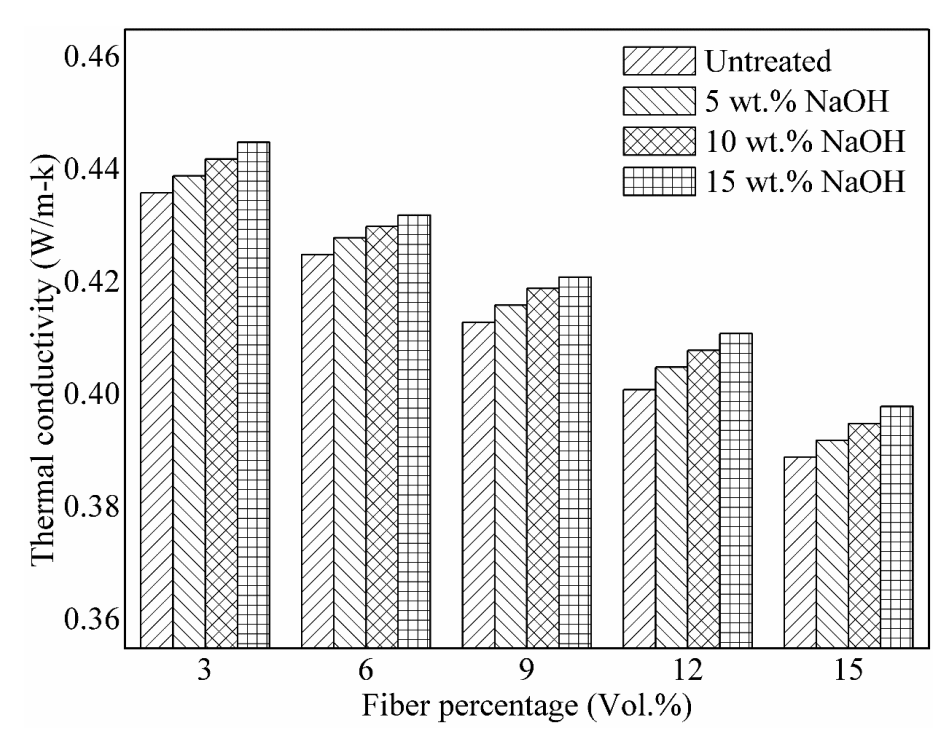


Fig. 8. Thermal conductivity of HFRG composites

Scanning electron microscopy analysis

To examine the effect of alkaline treatment on the hemp fiber surface, SEM photographs were taken of both untreated and treated hemp fibers. Figure 9 displays the SEM images of these fibers, with magnifications of $300\times$ and $1500\times$. The untreated fibers (Fig. 9(a,b)) exhibit diameters ranging from 550 to 650 µm, with their surfaces extensively covered by an organic layer primarily consisting of non-cellulosic components. Alkali treatment significantly alters fiber morphology, as evidenced by the reduction in fiber dimensions and the breakdown of fiber bundles (Fig. 9(c-f)). Furthermore, the treated fibers exhibit markedly cleaner and smoother surfaces, indicating the removal of non-cellulosic

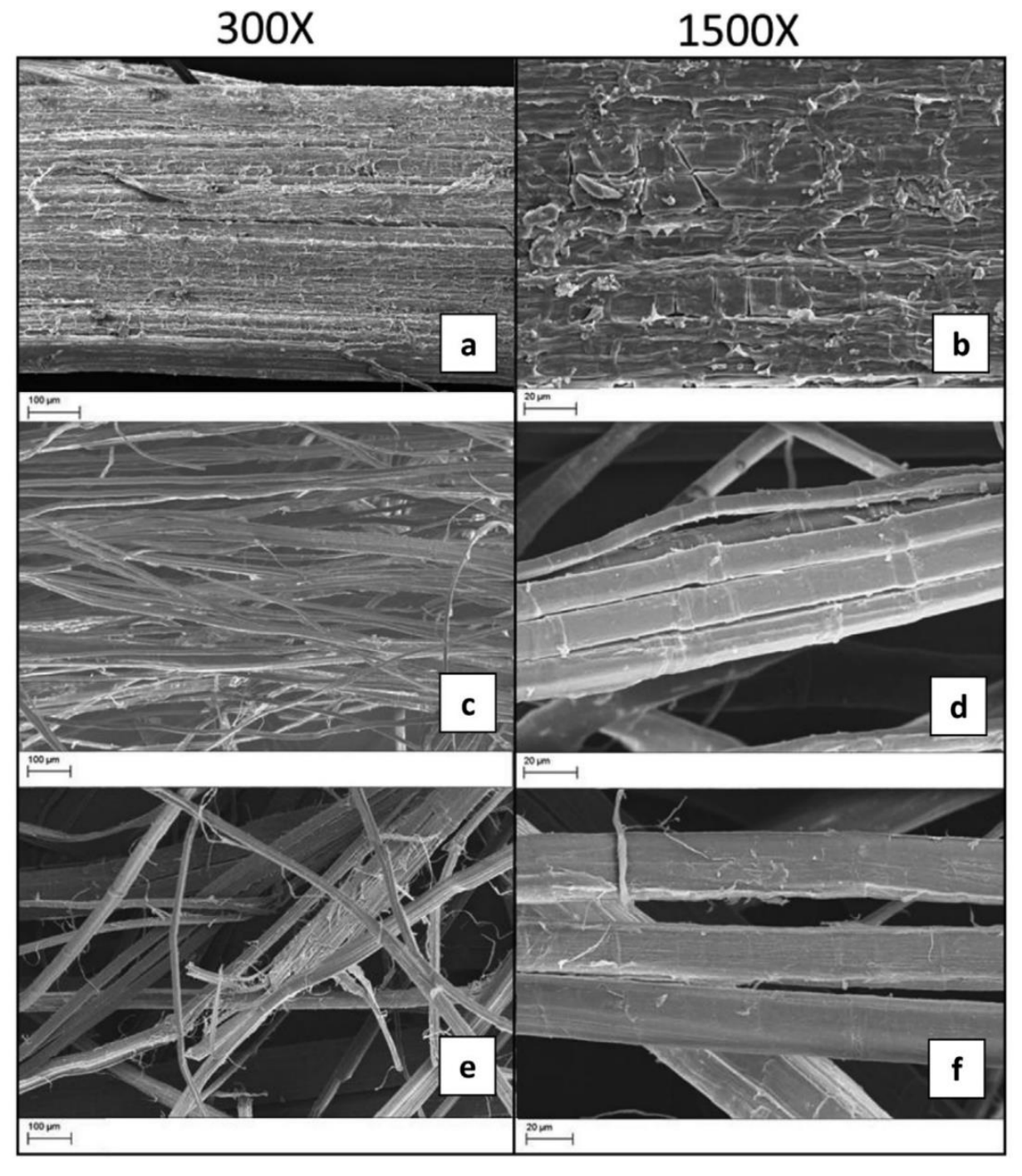


Fig. 9. SEM images of untreated and alkali treated hemp fibers

impurities. As shown in the figure, the filaments of the hemp fiber separate after alkali treatment (Fig. 9(c-f)), whereas the filaments remain combined in untreated hemp fiber (Fig. 9(a,b)). This process, where the collective bundle breaks into smaller filaments due to dissolution, is known as fibrillation [37]. Fibrillation increases the fiber's surface area, enhancing its contact with the matrix. This improved interfacial adhesion between the reinforcement and matrix can enhance the mechanical properties of the composite.

Conclusion

In this study, the effects of alkali treatment and fiber percentage on the mechanical and thermophysical properties of HFRG composites were examined in detail. The key findings of the fabricated composites are as follows:

- 1. The measured density and water absorption percentage of HFRG composites increase with a higher volume percentage of fiber. For the 10 wt. % NaOH-treated HFRG composite, the water absorption is 40.16 %, compared to 44.84 % for the untreated composite.
- 2. The compressive and flexural properties of HFRG composites improve following alkali treatment of hemp fibers. For the 10 wt.% NaOH-treated HFRG composite at 12 vol. % fiber percentage, the flexural strength and modulus increased by 337 and 136 %, respectively. Additionally, at the same fiber percentage and NaOH concentration, the compressive strength of the HFRG composite increased by 109.8 %.
- 3. The thermal insulation property of gypsum composites is significantly enhanced with the addition of hemp fiber compared to pure gypsum, offering greater energy efficiency. The impact of NaOH treatment on thermal conductivity is less pronounced compared to the effect of fiber percentage.
- 4. Therefore, these fabricated HERG composite materials are suitable for use in building applications such as wall materials and false ceilings, helping to reduce energy consumption in buildings.

CRediT authorship contribution statement

Khandavalli Sunil Ratna Kumar Sc: supervision and review of entire manuscript; Siva Bhaskara Rao Devireddy Sc: conceptualization, investigation and writing – original draft; Gopala Rao Thellaputta Sc: investigation and data curation; Battula Sudheer Kumar Sc: methodology and resources; Bala Prasad Katuru Sc: writing – review & editing.

Conflict of interest

The authors declare that they have no conflict of interest.

References

- 1. Bhale PV, Rathod MK, Sahoo L. Thermal Analysis of a Solar Concentrating System Integrated with Sensible and Latent Heat Storage. *Energy Procedia*. 2015;75: 2157–2162.
- 2. Stritih U, Tyagi VV, Stropnik R, Paksoy H, Haghighat F, Joybari MM. Integration of passive PCM technologies for net-zero energy buildings. *Sustain Cities Soc.* 2018;41: 286–295.

- 3. Mohandesi JA, Sangghaleh A, Nazari A, Pourjavad N. Analytical modeling of strength in randomly oriented PP and PPTA short fiber reinforced gypsum composites. *Comput Mater Sci.* 2011;50(5): 1619–1624.
- 4. Dalmay P, Smith A, Chotard T, Sahay-Turner P, Gloaguen V, Krausz P. Properties of cellulosic fibre reinforced plaster: Influence of hemp or flax fibres on the properties of set gypsum. *J Mater Sci.* 2010;45(3): 793–803.
- 5. Braiek A, Karkri M, Adili A, Ibos L, Ben Nasrallah S. Estimation of the thermophysical properties of date palm fibers/gypsum composite for use as insulating materials in building. *Energy Build*. 2017;140: 268–279.
- 6. Gao Z, Li G. Effect of Straw Fiber Modification on Performance of Gypsum Composite. *Adv Mat Res.* 2011;168–170: 1455–1458.
- 7. Belayachi N, Hoxha D, Slaimia M. Impact of accelerated climatic aging on the behavior of gypsum plaster-straw material for building thermal insulation. *Constr Build Mater.* 2016;125: 912–918.
- 8. Nindiyasari F, Griesshaber E, Zimmermann T, Manian AP, Randow C, Zehbe R, Fernandez-Diaz L, Ziegler A, Fleck C, Schmahl WW. Characterization and mechanical properties investigation of the cellulose/gypsum composite. *J Compos Mater*. 2015;50(5): 657–672.
- 9. Selamat ME, Hashim R, Sulaiman O, Kassim MHM, Saharudin NI, Taiwo OFA. Comparative study of oil palm trunk and rice husk as fillers in gypsum composite for building material. *Constr Build Mater.* 2019;197: 526–532. 10. Tesárek P, Novák L, Topič J, Prošek Z, Nežerka V, Lidmila M. Compression Testing of Gypsum-Based Composite Reinforced by Recycled Wires from Automobile Tires. *Applied Mechanics and Materials.* 2015;732: 393–396.
- 11. Amuthakkannan P, Manikandan V, Jappes JTW, Uthayakumar M. Effect of fibre length and fibre content on mechanical properties of short basalt fibre reinforced polymer matrix composites. *Materials Physics and Mechanics*. 2013;16(2): 107–117.
- 12. Iucolano F, Liguori B, Aprea P, Caputo D. Evaluation of bio-degummed hemp fibers as reinforcement in gypsum plaster. *Compos B Eng.* 2018;138: 149–156.
- 13. Benmansour N, Agoudjil B, Gherabli A, Kareche A, Boudenne A. Thermal and mechanical performance of natural mortar reinforced with date palm fibers for use as insulating materials in building. *Energy Build.* 2014;81: 98–104. 14. Abir N, Siddique AB, Begum HA, Gafur MA, Khan AN, Mahmud MA. Effect of fibre loading on mechanical properties of jute fibre bundle reinforced gypsum composites. *Heliyon.* 2023;9(7): e18147.
- 15. Mutuk T, Arpacioğlu K, Alişir S, Demir G. Thermal and mechanical evaluation of natural fibers reinforced gypsum plaster composite. *Journal of Metals, Materials and Minerals.* 2023;33(1): 116–123.
- 16. Gholampour A, Ozbakkaloglu T. A review of natural fiber composites: properties, modification and processing techniques, characterization, applications. *J Mater Sci.* 2020;55(3): 829–892.
- 17. Jagadeesh P, Puttegowda M, Mavinkere Rangappa S, Siengchin S. A review on extraction, chemical treatment, characterization of natural fibers and its composites for potential applications. *Polym Compos*. 2021;42(12): 6239–6264.
- 18. Shejkar SK, Agrawal B, Agrawal A, Gupta G, Pati PR. Influence of filler content and surface modification on physical and mechanical properties of epoxy/walnut shell particulate composites. *J Adhes Sci Technol*. 2023;37(7): 1215–1232.
- 19. Yadav D, Selokar GR, Agrawal A, Mishra V, Khan IA. Effect of Concentration of NaOH Treatment on Mechanical Properties of Epoxy/Sisal Fiber Composites. *IOP Conf Ser Mater Sci Eng.* 2021;1017(1): 012028.
- 20. Sair S, Oushabi A, Kammouni A, Tanane O, Abboud Y, El Bouari A. Mechanical and thermal conductivity properties of hemp fiber reinforced polyurethane composites. *Case Studies in Construction Materials*. 2018;8: 203–212.
- 21. Huber T, Müssig J. Fibre matrix adhesion of natural fibres cotton, flax and hemp in polymeric matrices analyzed with the single fibre fragmentation test. *Compos Interfaces*. 2008;15(2–3): 335–349.
- 22. Charai M, Sghiouri H, Mezrhab A, Karkri M. Thermal insulation potential of non-industrial hemp (Moroccan cannabis sativa L.) fibers for green plaster-based building materials. *J Clean Prod.* 2021;292: 126064.
- 23. Bhagat VK, Biswas S, Dehury J. Physical, mechanical, and water absorption behavior of coir/glass fiber reinforced epoxy based hybrid composites. *Polym Compos*. 2014;35(5): 925–930.
- 24. Iucolano F, Boccarusso L, Langella A. Hemp as eco-friendly substitute of glass fibres for gypsum reinforcement: Impact and flexural behaviour. *Compos B Eng.* 2019;175: 107073.
- 25. Senthamaraikannan P, Kathiresan M. Characterization of raw and alkali treated new natural cellulosic fiber from Coccinia grandis.L. *Carbohydr Polym.* 2018;186: 332–343.
- 26. Karabulut N, Aktaş M, Balcıoğlu HE. Surface Modification Effects on the Mechanical Properties of Woven Jute Fabric Reinforced Laminated Composites. *Journal of Natural Fibers*. 2019;16(5): 629–643.
- 27. Nor Arman NS, Chen RS, Ahmad S. Review of state-of-the-art studies on the water absorption capacity of agricultural fiber-reinforced polymer composites for sustainable construction. *Constr Build Mater.* 2021;302: 124174.

- 28. Jia R, Wang Q, Feng P. A comprehensive overview of fibre-reinforced gypsum-based composites (FRGCs) in the construction field. *Compos B Eng.* 2021;205: 108540.
- 29. Reddy PV, Mohana Krishnudu D, Rajendra Prasad P. A Study on Alkali Treatment Influence on Prosopis Juliflora Fiber-Reinforced Epoxy Composites. *Journal of Natural Fibers*. 2021;18(8): 1094–1106.
- 30. Suresh Babu K, Ratnam C. Mechanical and thermophysical behavior of hemp fiber reinforced gypsum composites. *Mater Today Proc.* 2021;44: 2245–2249.
- 31. Sgriccia N, Hawley MC, Misra M. Characterization of natural fiber surfaces and natural fiber composites. *Compos Part A Appl Sci Manuf.* 2008;39(10): 1632–1637.
- 32. Boccarusso L, Durante M, Iucolano F, Mocerino D, Langella A. Production of hemp-gypsum composites with enhanced flexural and impact resistance. *Constr Build Mater.* 2020;260: 120476.
- 33. Iqbal M, Azan SA, Dharmawan MR, Abhang LB. Influence of Fiber Content on the Flexural Strength and Physical Properties of Abaca Fiber-Cement-Gypsum Board. *Key Eng Mater*. 2023;951: 173–183.
- 34. Suardana NPG, Piao Y, Lim JK. Mechanical properties of hemp fibers and hemp/pp composites: effects of chemical surface treatment. *Materials Physics and Mechanics*. 2011;11(1): 1–8.
- 35. Haigh R. A Review and Thermal Conductivity Experimental Program of Mattress Waste Material as Insulation in Building and Construction Systems. *Construction Materials*. 2024;4(2): 401–424.
- 36. Touil M, Rahmoun O, Iken O, El Harti K, Saadani R, Rahmoune M. Exploring the thermal behaviour and thermo-mechanical properties of Ferula Communis reinforced plaster and mortar composites: An integrated experimental and numerical approach. *Energy Convers Manag.* 2023;289: 117119.
- 37. Sepe R, Bollino F, Boccarusso L, Caputo F. Influence of chemical treatments on mechanical properties of hemp fiber reinforced composites. *Compos B Eng.* 2018;133: 210–217.

Submitted: October 9, 2024 Revised: April 17, 2025 Accepted: June 25, 2025

Temperature-dependent phase leg and non-local thermoelastic damping and frequency shift in thermoelastic plates

R. Kumar 📵, P. Singhal 🖾 📵

Kurukshetra University, Kurukshetra, India

[™] poojaacad009@gmail.com

ABSTRACT

Thermoelastic damping and frequency shift are critical factors influencing the performance and stability of micro- and nano-scale resonators, such as those employed in MEMS and NEMS devices. Traditional thermoelastic models often overlook important scale-dependent behaviors, thermal relaxation effects, and material property variations with temperature, leading to inaccuracies at small scales. To address these limitations, the present study investigates thermoelastic damping and frequency shift in a Kirchhoff plate resonator by incorporating non-local elasticity theory, the dual-phase lag heat conduction model, and temperature-dependent material properties. In order to investigate thermoelastic damping and frequency shift of Kirchhoff plate resonator, the current work takes into account the influence of non-local, dual phase leg, and temperature dependent properties on thermoelastic theory. The governing equations, comprise equations of motion and heat conduction equation which include a temperature-dependent property, a dual-phase leg model along with non-local parameters are formulated with the assistance of Kirchhoff-Love plate theory. Under the simply supported boundary conditions, thermoelastic damping and frequency shift are analysed. The derived amounts are graphically displayed with different thickness and length values. The current work additionally deduces a specific example of interest. Results are graphically presented to illustrate key trends, and a specific numerical example is discussed to demonstrate the applicability of the model. This study enhances the accuracy of thermoelastic analysis in micro-scale resonator design by integrating advanced theoretical considerations often neglected in conventional models.

KEYWORDS

 $thermoelastic \bullet Kirchhoff-Love \ plate \ theory \bullet non-local \ dual-phase-lag \ model \bullet TDP \ model \bullet frequency \ shift \ thermoelastic \ damping$

Citation: Kumar R, Singhal P. Temperature-dependent phase leg and non-local thermoelastic damping and frequency shift in thermoelastic plates. *Materials Physics and Mechanics*. 2025;53(3): 94–115 http://dx.doi.org/10.18149/MPM.5332025_8

Introduction

It is well known that in many cases, non-uniform beams may achieve a better distribution of strength and weight than uniform beams and sometimes, it satisfies special architectural and functional requirements. Therefore, the static and dynamic analysis of beams with variable thickness has been the subject of numerous investigations because of its relevance to aeronautical, civil, and mechanical engineering. Most studies are available on variable thickness beams based on either the Euler beam or the Timoshenko beam theory.

In many advanced materials and microscale systems, the interaction between an external electric field and charge carriers is governed by the mutual competition between two dynamic processes: the electromagnetic field propagation and the carrier transport



95 R. Kumar, P. Singhal

dynamics (e.g., drift, diffusion, or thermal motion). The electric field tends to polarize the medium and accelerate charge carriers, while the carriers themselves, influenced by temperature gradients and scattering mechanisms, redistribute and modulate the local field. This interplay creates a feedback loop that can significantly influence heat conduction, damping behavior, and the dynamic response of thermoelastic systems. At micro- and nanoscales, where quantum and non-local effects become significant, the delayed response of heat carriers and non-uniform charge distribution due to size confinement can lead to non-intuitive behavior, such as enhanced damping or frequency shifts.

Thermoelastic damping (TD) is a form of structural damping that arises from the interaction between thermal and mechanical fields. In a bending thermoelastic structure, the inner side of the bend experiences compression while the outer side experiences tension. This interaction between the thermal and mechanical fields creates a thermal gradient, which results in irreversible heat generation within the structure. This heat generation subsequently leads to entropy production and ultimately causes energy dissipation.

The mechanism and magnitude of linear thermoelastic damping (TD) in a flexural vibrating thin beam have been extensively investigated. TD is commonly assessed using the inverse of the quality factor (Q) [1,2] established the theoretical basis for TD and formulated an expression to calculate the quality factor for a thin beam oscillating in its flexural mode. Thermoelastic damping in micro-beam resonators was discussed by [3].

Conventional continuum theories are often unsuitable for accurately describing the behavior of nanostructures with extremely small characteristic sizes but nonlocal continuum theories effectively describe material properties from microscopic scales up to the size of the lattice parameter, thus providing a satisfactory explanation for certain atomic-scale phenomena. In [4], it was developed non local theory of elasticity. In [5], it was introduced theory of nonlocal thermoelasticity in which stress at a point x in a continuous body is not solely determined by the strain at that point, but also by the strains at all surrounding points. In study [6], it was expected to be helpful for the theoretical modeling of thermoelasticity at the nano-scale and may be beneficial for the design of nano-sized and multi-layered devices.

Currently, most investigations into thermoelastic damping (TD) assume that material properties are temperature-independent. However, for many materials, properties such as the modulus of elasticity, thermal conductivity, and specific heat actually vary with temperature. To thoroughly examine the interaction between thermal and mechanical fields, it is essential to consider the impact of temperature-dependent material properties, even within a narrow temperature range.

The elasticity solution for the clamped- simply supported beams with variable thickness was presented in [7]. In [8], it was investigated the thermoelastic damping of vibrations in arbitrary direction in coupled thermoelastic plate. In [9], it was studied the transverse vibration in piezothermoelastic beam resonator, based on Euler-Bernoulli theory for clamped and free end conditions. In [10], it was developed a size- dependent Bernoulli-Euler beam formulation on the basis of new model of couple stress theory and prepared the mathematical formulation for clamped (C-C), simply supported (S-S) and cantilever (C-F) boundary conditions.

The influence of heat sources and relaxation time on temperature distribution in tissues was studied in [11]. In [12], it was studied the exact solution of thermoelastic

damping and frequency shift s in a nano-beam resonator. In [13], it was explored the damping characteristics in microscale modified couple stress thermoelastic circular Kirchhoff plate resonators. In [14], it was introduced effect of temperature dependent material properties on thermoelastic damping in thin beams. Some results in Moore-Gibson-Thompson thermoelasticity of dipolar bodies are examined in [15]. In [16], it was studied the thermoelastic damping in nonlocal nanobeams considering dual-phase-lagging effect. The response of nanobeams with TDP Using State-Space Method via modified couple stress theory was described in [17]. In [18], it was discussed the thermoelastic damping and frequency shift in Kirchhoff plate resonators based on modified couple stress theory with dual-phase-lag model. Study [19] focused frequency shifts and thermoelastic damping in different types of nano-/Micro-scale beams with sandiness and voids under three thermoelasticity theories. A combined model for power generation planning with reserve dispatch and weather uncertainties including penetration of renewable sources was presented in [20]. In [21], it was proposed a model for a micro-grid architecture incorporating the role of aggregators and renewable sources on the prosumer side, working together to optimize configurations and operations. The frequency shifts and thermoelastic damping in distinct micro/nano-scale piezothermoelastic fiber-reinforced composite beams under examined some three heat conduction models were presented in [22]. In [23], explored functionally graded nonlocal thermoelastic nanobeam with memory-dependent derivatives. In [24], it were discussed the effects of two temperature and laser pulse on modified couple stress thermoelastic diffusion beam. In [25], it were provided analytical modeling and numerical analysis of thermoelastic damping in ultrathin elastic films due to surface effects. In [26], it was analysed the magneto-thermoelastic vibrations of rotating Euler-Bernoulli nanobeams using the nonlocal elasticity model. A buckling analysis of thermoelastic micro/nano-beams considering the size-dependent effect and non-uniform temperature distribution was provided in [27]. In [28], it was discussed the vibration of piezo-magneto-thermoelastic nanobeam submerged in fluid with variable nonlocal parameter. In [29], it was computed phase velocities, attenuation coefficients, specific loss, penetration depth and construct the fundamental solution of the system of differential equations in the theory of an electro-microstretch viscoelastic solids in case of steady oscillations in terms of elementary functions. The propagation of Lamb waves in a homogeneous isotropic thermoelastic micropolar solid with two temperatures bordered with layers or half-spaces of inviscid liquid subjected to stress free boundary conditions was studied in [30]. In [31], it was constructed fundamental solution for the system of differential equations for steady oscillations in terms of elementary functions. A novel technique is used to study the magnetic field influence in the free surface of an elastic semiconductor medium for a one- dimensional (1D) deformation during the hyperbolic two-temperature theory to study the coupled between the plasma, thermoelastic waves was proposed in [32]. Study [33] examined the interaction between the magnetic field and the excited semiconductor medium during the microtemperature process. In [34], it was studied the effect of Hall current of elastic semiconductor medium, when the medium is exposed to very strong magnetic field. In [35], it was presented the graphical comparison by showing that the exact and numerical solutions nearly coincide with each other. The electro-magnetic-thermal-microstretch elastic mathematical-physical model of semiconductor medium was investigated in [36]. In [37], it was formulated a novel 97 R. Kumar, P. Singhal

model of a microelongated semiconductor material. Thermal and elastic interactions in isotropic microplate resonators with elastic and viscous properties, exhibiting Kelvin–Voigt behavior, under a uniform magnetic field were investigated in [38]. In [39], it was examined the modeling of the transient thermodynamic reaction of a Kirchhoff–Love thermoelastic thin circular plate that is simply supported and set on an elastic base of Winkler type. In [40], it was found that the initial stress and the fractional parameter significantly influences the varieties of field amounts. A model that is highly effective in properly depicting the unusual thermal conductivity phenomena often found in nanoscale devices was proposed in [41]. In [42], it was examined the thermoelastic behavior of functionally graded (FG) materials using a partially modified thermoelastic heat transfer model.

Basic equations

Following [6,43] the governing equation in generalized thermoelastic dual-phase-lag model without body forces and heat sources are:

Constitutive relations:

$$t_{ij} = \lambda e_{kk} \delta_{ij} + 2\mu e_{ij} - \beta T \delta_{ij}. \tag{1}$$

Equations of motion:

$$(\lambda + \mu)\nabla(\nabla \cdot \vec{u}) + \mu\nabla^2 \cdot \vec{u} - \beta\nabla T = \rho(1 - \xi_1^2 \nabla^2) \frac{\partial^2 \vec{u}}{\partial t^2}.$$
 (2)

Equation of heat conduction:

$$K\left(1+\tau_{T}\frac{\partial}{\partial t}\right)\nabla^{2}T=\left(1-\xi_{2}^{2}\nabla^{2}+\tau_{q}\frac{\partial}{\partial t}+\frac{\tau_{q}^{2}}{2}\frac{\partial^{2}}{\partial t^{2}}\right)\left(\rho C_{e}\frac{\partial T}{\partial t}+\beta T_{0}\frac{\partial e_{kk}}{\partial t}\right),$$
 where

$$e_{ij} = \frac{1}{2}(u_{i,j} + u_{j,i}). \tag{4}$$

Additionally, in Eqs. (1)–(4), the constants Lame are λ and μ . Kronecker's delta is δ_{ij} , the components of stress tensor is t_{ij} , and the components of strain tensor is e_{ij} , $\beta=(3\lambda+2\mu)~\alpha_t$, the coefficients of linear thermal expansion are α_t respectively, the temperature change is denoted by T, the displacement vector is u, the density is ρ , the Laplacian operator is Δ , and the del operator is ∇ . The coefficient of the thermal conductivity is K, the non-local parameters are represented by ξ_1,ξ_2 , the specific heat at constant strain is represented by C_e , and the reference temperature is T_0 , t as assumed to be such that $T/T_0 \ll 1$. The phase lags of the temperature gradient and the heat flux are denoted by τ_T and τ_q respectively.

To explore the impact of temperature dependent property, the following assumptions are taken as: $\lambda = \lambda_0 f(t)$; $\mu = \mu_0 f(t)$, $k = k_0 f(t)$; $\beta = \beta_0 f(t)$, $E = E_0 f(t)$, where $f(t) = 1(1 - \alpha^* T_0)$, α^* is the empirical material constant and f(t) = 1 for the temperature independent material.

Formulation of the problem

Let us examine a non-local thermoelastic Kirchhoff plate with temperature dependent properties and dual phase leg resonators that have uniform thickness h. The center of the plate is where the Cartesian coordinate system (x, y, and z) originates. When the plate is in equilibrium, it is not under any stress or strain and maintains a constant temperature of T_0 throughout. The temperature T(x, y, z, t), the displacement components u(x, y, z, t),

v(x, y, z, t), and w(x, y, z, t) are defined. The displacement components, as per Kirchhoff's-Love Plate theory, are provided by:

$$u = -z \frac{\partial w}{\partial x}, v = -z \frac{\partial w}{\partial y}, w(x, y, z, t) = w(x, y, t).$$
 (5)

Following [44], the strain and stress components are taken as:

$$\varepsilon_{xx} = -z \frac{\partial^2 w}{\partial x^2},\tag{6}$$

$$\varepsilon_{yy} = -z \frac{\partial^2 w}{\partial y^2},\tag{7}$$

$$\gamma_{xy} = -2\mu_0 f(t) z \frac{\partial^2 w}{\partial x \partial y} = -\frac{E_0 f(t) z}{(1+v)} \frac{\partial^2 w}{\partial x \partial y},\tag{8}$$

$$t_{xx} = \frac{E_0 f(t)}{(1 - v^2)} \left(\varepsilon_{xx} + v \varepsilon_{yy} - (1 + v) \alpha_T T \right), \tag{9}$$

$$t_{yy} = \frac{E_0 f(t)}{(1 - v^2)} \left(\varepsilon_{yy} + v \varepsilon_{xx} - (1 + v) \alpha_T T \right), \tag{10}$$

where E_0 and v_0 is Young's modulus and the Poisson ratio respectively, which are given by:

$$E_0 = \mu_0 (3\lambda_0 + 2\mu_0)/(\lambda_0 + \mu_0), \tag{11}$$

$$v_0 = \lambda_0 / 2(\lambda_0 + \mu_0). \tag{12}$$

Following [44,45], the bending and torsion moments are defined as follows:

$$M_x = \int_{-h/2}^{h/2} t_{xx} \, z \, dz,\tag{13}$$

$$M_{y} = \int_{-h_{/2}}^{h_{/2}} t_{yy} z \, dz,\tag{14}$$

$$M_{xy} = \int_{-h/2}^{h/2} t_{xy} \, z \, dz = M_{yx}. \tag{15}$$

Equations (13)–(15) recast with the aid of Eqs. (5)–(10), as:

$$M_{x} = -D^{*} \left(\frac{\partial^{2} w}{\partial x^{2}} + v_{0} \frac{\partial^{2} w}{\partial y^{2}} + \alpha_{T} M_{T} (1 + v) \right), \tag{16}$$

$$M_{y} = -D^{*} \left(\frac{\partial^{2} w}{\partial y^{2}} + v_{0} \frac{\partial^{2} w}{\partial x^{2}} + \alpha_{T} M_{T} (1 + v) \right), \tag{17}$$

$$M_{xy} = -\frac{\partial^2 w}{\partial x \partial y} \left(D^* (1 - v_0) \right), \tag{18}$$

where $D^* = E_0 f(t) h^3/12 \left(1-{v_0}^2\right)$ is the flexural rigidity of the plate.

The equations for shear force resultants are:

$$Q_x = \frac{\partial M_x}{\partial x} + \frac{\partial M_{xy}}{\partial y}, \quad Q_y = \frac{\partial M_y}{\partial y} + \frac{\partial M_{xy}}{\partial x}.$$
 (19)

The equation of motion (force equilibrium z in the direction) is given as:

$$\frac{\partial Q_x}{\partial x} + \frac{\partial Q_y}{\partial y} - \rho h (1 - \xi_1^2 \nabla^2) \frac{\partial^2 w}{\partial t^2} = 0.$$
 (20)

Using Eqs. (16)–(18) in Eqs. (19), (20), then the equation of motion for micro plate with symmetry about y-axes is taken as:

$$D^* \frac{\partial^4 w}{\partial x^4} + \frac{E_0 f(t) \alpha_T}{(1 - \nu_0)\beta d} \frac{\partial^2 M_T}{\partial x^2} + \rho h (1 - \xi_1^2 \nabla^2) \frac{\partial^2 w}{\partial t^2} = 0.$$
 (21)

The thermal moment is given by:

$$M_T = \beta_0 f(t) d \int_{-h/2}^{h/2} T z dz.$$
 (22)

The heat conduction equation is:

$$k_0 f(t) \left(1 + \tau_T \frac{\partial}{\partial t} \right) \nabla^2 T = \left(1 - \xi_2^2 \nabla^2 + \tau_q \frac{\partial}{\partial t} + \frac{\tau_q^2}{2} \frac{\partial^2}{\partial t^2} \right) \left(\rho c_e \frac{\partial T}{\partial t} - T_0 \beta_0 f(t) z \frac{\partial^3 w}{\partial x^2 \partial t} \right), \tag{23}$$

where

$$\nabla^2 = \frac{\partial^2}{\partial x^2} + \frac{\partial^2}{\partial z^2}.$$
 (24)

99 R. Kumar, P. Singhal

For further simplification, the following non-dimensional quantities are taken as:

$$(x', z', u', w') = (x, z, u, w)/L, (\tau'_q, \tau'_T, t') = (\tau_q, \tau_T, t)v/L, T' = T/T_0,$$

 $M_T' = M_T/d\beta T_0 h^2$, $v_0^2 = E/\rho$, $\xi_1' = \xi_1/L$, $\xi_2' = \xi_2/L$, $Q_1 = \mu_0 Q'$.

Equations (21) and (23) taking into account Eq. (24) reduce to the form:

$$\frac{\partial^4 w}{\partial x^4} + a_1 \frac{\partial^2 M_T}{\partial x^2} + a_2 \left(1 - \xi_1^2 \nabla^2\right) \frac{\partial^2 w}{\partial t^2} = 0, \tag{25}$$

$$a_{3}\left(1+\tau_{T}\frac{\partial}{\partial t}\right)\left(\frac{\partial^{2}T}{\partial x^{2}}+\frac{\partial^{2}T}{\partial z^{2}}\right)-\left(1-\xi_{2}^{2}\nabla^{2}+\tau_{q}\frac{\partial}{\partial t}+\frac{\tau_{q}^{2}}{2}\frac{\partial^{2}}{\partial t^{2}}\right)\left(a_{4}\frac{\partial T}{\partial t}-z\frac{\partial^{3}w}{\partial x^{2}\partial t}\right)=0,$$
 where $a_{1}=\frac{E\alpha_{T}T_{0}h^{2}L}{(1-v)D^{*}}$, $a_{2}=\frac{\rho hv^{2}L^{2}}{D^{*}}$, $a_{3}=\frac{k_{0}}{Lv\beta_{0}}$. (26)

Following [46], the solution of Eqs. (25) and (26) for time harmonic vibrations are taken as:

$$w(x,t) = W(x)e^{i\omega t}, T(x,z,t) = \Theta(x,z)e^{i\omega t}.$$
(27)

where ω denotes the frequency of the plate.

Substituting the values of T from Eq. (27) in Eq. (22):

$$M_{\rm T} = \beta d \int_{-h/2}^{h/2} \Theta(x, z) \ z \ dz.$$
 (28)

Making use of Eq. (28) in Eqs. (25) and (26) yield:

$$\frac{\partial^4 W}{\partial x^4} + a_1 \frac{\partial^2 M_\theta}{\partial x^2} - \omega^2 a_2 (1 - \xi_1^2 \nabla^2) W = 0, \tag{29}$$

$$a_3(1+\tau_T i\omega)\left(\frac{\partial^2 \Theta}{\partial x^2} + \frac{\partial^2 \Theta}{\partial z^2}\right) = i\omega\left(1-\xi_2^2 \nabla^2 + \tau_q i\omega - \frac{\omega^2}{2}\tau_q^2\right)\left(a_4\Theta - z\frac{\partial^2 W}{\partial x^2}\right). \tag{30}$$

Thermal field on the thickness direction

The thermal gradient of the plate is very small as compared to that along its thickness direction:

$$\left(\left|\frac{\partial\Theta}{\partial x}\right| \ll \left|\frac{\partial\Theta}{\partial z}\right|\right), \frac{\partial^2}{\partial z^2} \left[z\frac{\partial^2W}{\partial x^2}\right] \approx 0.$$
 (31)

With these considerations Eq. (30) take the form:

$$\frac{\partial^2 \theta}{\partial z^2} + R_1^2 \Theta + R_2 z \frac{\partial^2 W}{\partial x^2} = 0, \tag{32}$$

$$R_1^2 = \frac{-a_4 \tau_q^* i \omega}{a_3 + i \omega \tau_t^*}, \quad R_2 = \frac{i \omega \tau_q^*}{a_4 + i \omega \tau_t^*}, \quad \tau_t^* = a_3 \tau_T + \xi_2^2 a_4, \quad \tau_q^* = \left(1 + \tau_q i \omega - \frac{\omega^2}{2} \tau_q^2\right). \tag{33}$$

In this case, it is assumed that there is no heat across the upper and lower surfaces of the plate, then:

$$\frac{\partial \theta}{\partial z} = 0, \quad z = \pm \frac{h}{2}. \tag{34}$$

Using conditions of Eq. (34), the general solution of Eq. (30) is written as:

$$\Theta(x,z) = -\frac{R_2}{R_1^2} \left(z - \frac{\sin(R_1 z)}{R_1 \cos(R_1 h/2)} \right) \frac{\partial^2 W}{\partial x^2}.$$
 (35)

Inserting the value of Θ from Eq. (35) in Eq. (28) yield:

$$M_{\rm T} = \beta d \int_{-h/2}^{h/2} -\frac{R_2}{R_1^2} \left(z - \frac{\sin(R_1 z)}{R_1 \cos(R_1 h/2)} \right) \frac{\partial^2 W}{\partial x^2} z dz.$$
 (36)

The above equation takes the form:

$$M_{\rm T} = \frac{-\beta dR_2 h^3}{12R_1^2} [1 + f(R_1)] \frac{\partial^2 W}{\partial x^2},\tag{37}$$

where $f(R_1)$ is a complex function expressed as below:

$$f(R_1) = \frac{24}{R_1^3 h^3} \left(\frac{R_1 h}{2} - \tan \frac{R_1 h}{2} \right). \tag{38}$$

From Eq. (37):

$$\frac{\partial^2 M_\theta}{\partial x^2} = -\frac{\beta dR_2 h^3}{12R_1^2} \left(1 + f(R_1) \right) \frac{\partial^4 W}{\partial x^4}. \tag{39}$$

Equation (39) with the aid of Eq. (28) yield:

$$\frac{d^4W}{dx^4} - a_1 \frac{\beta dR_2 h^3}{12R_1^2} (1 + f(R_1)) \frac{\partial^4 W}{\partial x^4} - \omega^2 a_2 \left(1 - \xi_1^2 \left(\frac{\partial^2}{\partial x^2} + \frac{\partial^2}{\partial z^2} \right) \right) W = 0. \tag{40}$$

Simplifying Eq. (40) with the aid of Eq. (31):

$$D_{\omega}^{*} \frac{d^{4}W}{dx^{4}} + \omega^{2} a_{2} \xi_{1}^{2} \frac{d^{2}W}{dx^{2}} - \omega^{2} a_{2} W = 0, \tag{41}$$

where

$$D_{\omega}^{*} = (1 + \varepsilon(1 + f(R_{1})); \varepsilon = -\frac{a_{1}\beta dR_{2}h^{3}}{12R_{1}^{2}}.$$
 (42)

For the isothermal state of Nano beam Eq. (41) takes the following form:

$$\frac{d^4W}{dx^4} + \omega_0^2 a_2 \xi_1^2 \frac{d^4W}{dx^4} - \omega_0^2 a_2 W = 0, \tag{43}$$

where ω_0 refers to the nonlocal isothermal frequency.

Solution of Eq. (43) yields:

$$(x) = C_1 Sin\lambda_1 x + C_2 Cos\lambda_1 x + C_3 Sinh\lambda_2 x + C_4 Cosh\lambda_2 x, \tag{44}$$

where C_1 , C_2 , C_3 , C_4 are constants.

Substitution Eq. (44) in Eq. (43) yields:

$$\omega_0^2 = \frac{\lambda_1^4}{(1+\lambda_1^2 \xi_1^2)a_2} = \frac{\lambda_2^4}{(1-\lambda_2^2 \xi_1^2)a_2}.$$
 (45)

Boundary conditions

It is taken into consideration that a micro plate whose ends are either clamped-clamped (CC), simply supported (SS), clamped-clamped (CC) and clamped free (CF) in which case the following boundary conditions for the two sets [44]:

Case (i) For Clamped-Clamped (CC):
$$W = 0, \frac{\partial W}{\partial x} = 0, x = 0, L.$$
 (46)

Case (ii) For Simply Supported (SS):
$$W = 0$$
, $\frac{\partial^2 W}{\partial x^2} = 0$, $x = 0, L$. (47)

Case (iii) For Clamped Supported (CS):
$$W=0, \frac{\partial W}{\partial x}=0, \frac{\partial^2 W}{\partial x^2}=0, \ x=0,L.$$
 (48)

Case (iv) For Clamped Free (CF):
$$W=0, \frac{\partial W}{\partial x}=0$$
, at $x=0, \frac{\partial^2 W}{\partial x^2}=, \frac{\partial^3 W}{\partial x^3}=0$, $x=L$. (49)

Substituting Eq. (44) in the boundary conditions Eqs. (46)–(49), the following set of frequency equations are obtained:

CC: Case (i).
$$2 \cos \lambda_1 L \cosh \lambda_2 L + \left(\frac{\lambda_1}{\lambda_2} - \frac{\lambda_2}{\lambda_1}\right) \sin \lambda_1 L \sinh \lambda_2 L - 2 = 0.$$
 (50)

SS: Case (ii).
$$Sin(\lambda_1 L) = 0$$
. (51)

CS: Case (iii).
$$\lambda_2 Sin\lambda_1 L Cosh\lambda_2 L - \lambda_1 Sinh\lambda_2 L Cos\lambda_1 L = 0$$
. (52)

CF: Case (iv).
$$2Cos\lambda_1LCosh\lambda_2L + \left(\frac{\lambda_1}{\lambda_2} - \frac{\lambda_2}{\lambda_1}\right)Sin\lambda_1LSinh\lambda_2L + \left(\frac{\lambda_1^2}{\lambda_2^2} + \frac{\lambda_2^2}{\lambda_1^2}\right) = 0.$$
 (53)

Take note that Eq. (45) describes the relationship between λ_1 and λ_2 . These transcendental equations can be solved, and the nonlocal isothermal frequency ω_0 of each boundary condition can be found by substituting the solutions into Eq. (45).

Making use of Eq. (44) in boundary condition Eq. (47) yield:

$$Sin(\lambda_1 L) = 0. ag{54}$$

From above equation $\lambda_1 = \frac{n\pi}{L}$, $n \in I$.

101 R. Kumar, P. Singhal

Comparing Eq. (41) and Eq. (43) gives the following relation between ω and ω_0 :

$$\omega = \omega_0 \sqrt{1 + \varepsilon (1 + (f(R_1)))}. \tag{55}$$

Given that the relaxation strength value is often small ($arepsilon \ll 1$), the right-hand side of Eq. (55) can be expanded to the first order as shown below:

$$\omega = \omega_0 \left[\left(1 + \frac{\varepsilon}{2} (1 + f(\omega_0)) \right) \right], \tag{56}$$

$$\omega = \omega_0 \left[\left(1 + \frac{\varepsilon}{2} (1 + f(\omega_0)) \right],$$

$$f(\omega_0) = \frac{24}{R_1^3 h^3} \left(\frac{R_1 h}{2} - \tan \frac{R_1 h}{2} \right).$$

$$(56)$$

From Eq. (32), since the quantity R_1^2 in Eq. (33) is complex in nature, the following equations can be obtained by applying Euler's theorem:

$$R_{1} = R_{0} e^{\frac{-i\theta}{2}}, R_{0} = \sqrt{\frac{s_{0}^{*}}{L_{2}^{*}}}, \theta = \tan^{-1} \left[-\frac{\omega^{3} \rho c_{e} \tau_{q} L \nu R^{*} - K L_{1}^{*}}{K \omega^{2} \rho c_{e} \tau_{q} L \nu + \omega R^{*} L_{1}^{*}} \right], \tag{58}$$

where
$$s_0^* = \sqrt{(K^2 + \omega^2 R^{*2})(\omega^4 \rho^2 c_e^2 \tau_q^2 L^2 v^2 + {L_1}^{*2})}, \quad R^* = K \tau_T + \xi_2^2 \rho c_e L v$$

$$L_1^* = \left(\frac{\omega^3}{2}\rho c_e L v \tau_q^2 - \omega \rho c_e\right), L_2^* = K^2 + \omega^2 R^{*2}.$$

Replace ω with ω_0 in Eq. (58):

$$R_1 = \sqrt{2} p_1 \left(\cos \frac{\theta}{2} - i \sin \frac{\theta}{2} \right), \tag{59}$$

$$p_{1} = \sqrt{\frac{\sqrt{(K^{2} + \omega_{0}^{2}R^{*2})(\omega_{0}^{4}\rho^{2}c_{e}^{2}\tau_{q}^{2}L^{2}v^{2} + L_{1}^{*2})}}{2(K^{2} + \omega_{0}^{2}R^{*2})}}, 0 = \tan^{-1}\left[-\frac{\omega_{0}^{3}\rho c_{e}\tau_{q}LvR^{*} - KL_{1}^{*}}{K\omega_{0}^{2}\rho c_{e}\tau_{q}Lv + \omega_{0}R^{*}L_{1}^{*}}\right].$$
(60)

The frequency ω is complex in nature and hence:

$$\omega_n = \omega_R^m + i\omega_I^m, \omega_R^m = Re(\omega_n), \ \omega_I^m = Img(\omega_n), \tag{61}$$

$$\omega_{R}^{n} = \omega_{0} \left[1 + \frac{\varepsilon}{2} \left\{ \left(1 + \frac{6Cos\theta}{(p_{1}h)^{2}} - \frac{6\sqrt{2}Cos\frac{3\theta}{2}}{(p_{1}h)^{3}} \left(\frac{Sin\varsigma_{1} + tan\frac{3\theta}{2}Sinh(\varsigma_{1}\varsigma_{2})}{Cos\varsigma_{1} + Cosh(\varsigma_{1}\varsigma_{2})} \right) \right\} \right], \tag{62}$$

$$\omega_I^n = \frac{\varepsilon}{2} \left\{ \frac{6Sin\theta}{(p_1h)^2} - \frac{6\sqrt{2}Cos\frac{3\theta}{2}}{(p_1h)^3} \left(\frac{Sin\varsigma_1 tan\frac{3\theta}{2} - Sinh(\varsigma_1\varsigma_2)}{Cos\varsigma_1 + Cosh(\varsigma_1\varsigma_2)} \right) \right\},\tag{63}$$

where, $\varsigma_1 = \sqrt{2}p_1hCos\frac{\theta}{2}$, $\varsigma_2 = tan\frac{\theta}{2}$.

The thermoelastic damping and frequency shift in a thermoelastic circular plate are understood as follows [47]:

$$Q^{-1} = 2 \left| \frac{\operatorname{Img}(\omega_n)}{\operatorname{Re}(\omega_n)} \right|,$$

$$\omega_s = \left| \frac{\operatorname{Re}(\omega_n) - \omega_0}{\omega_0} \right|.$$
(64)

$$\omega_{\rm S} = \left| \frac{\operatorname{Re}(\omega_{\rm n}) - \omega_{\rm 0}}{\omega_{\rm s}} \right|. \tag{65}$$

Numerical results and Discussion

Equations (64) and (65) were utilized to calculate the thermoelastic damping Q^{-1} and frequency shift ω_s of the initial two vibration modes, both in the absence and presence of pair stress. MATLAB software has been utilized to perform numerical computations on magnesium material. For simply supported plates with different thickness and length values, the computed simulated results are shown graphically in Figs. 1-16 and in Tables 1–10 below.

Following [24]: $\rho = 1.74 \cdot 10^3$, $C_e = 1.0400$, $\lambda = 2.696 \cdot 10^{10}$, $\mu = 1.639 \cdot 10^{10}$, $K = 1.70 \cdot 10^2$, T = 293, $\alpha_t = 1.78 \cdot 10^{-5}$, $\tau_t = 0.04$, $\tau_a = 0.02$, $\omega = 10$.

The damping values are presented in Table 1 for different lengths and with varying values of the non-local parameter ξ_1 . The table includes lengths up to 45.2, with ξ_1 varying from 0 to 0.8, while ξ_2 is fixed at 0.04. An increase in the damping value is observed within the range of $2.32 \cdot 10^{-5}$ to $1.90 \cdot 10^{-2}$ as the length changes from 5.2 to 25.2 for $\xi_1 = 0.4$. Similarly, damping increases with the increase in ξ_1 for the same length. For instance, the damping value is $1.82 \cdot 10^{-4}$ for a length of 20.2 and $\xi_1 = 0$; this increases to $1.95 \cdot 10^{-2}$ for $\xi_1 = 0.8$ for the same length.

Table 1. Damping for different lengths keeping fixed $\xi_2 = 0.0$	Table 1.	1. Damping fo	r different	lengths I	keeping	fixed $\xi_2 = 0$.	.04
---	----------	---------------	-------------	-----------	---------	---------------------	-----

ξ_1	0.2	5.2	10.2	15.2	20.2	25.2	30.2	35.2	40.2	45.2
0	4.32	6.52	1.32	1.40	1.82	1.85	2.93	4.56	8.87	3.45
	·10 ⁻²²	·10⁻ ⁶	·10 ⁻⁷	·10⁻⁵	·10⁻⁴	·10⁻³	·10⁻³	·10⁻³	·10⁻³	·10⁻²
0.4	7.66	2.32	8.52	3.11	8.61	1.90	3.53	5.99	9.15	1.28
	·10 ⁻²¹	·10⁻⁵	·10⁻⁴	·10⁻³	·10⁻³	·10⁻²	·10⁻²	·10⁻²	·10⁻²	·10⁻¹
0.6	5.82	8.26	1.78	5.95	1.45	3.08	5.76	9.33	1.37	1.91
	·10 ⁻²⁰	·10⁻⁵	·10 ⁻³	·10⁻³	·10⁻²	·10⁻²	·10⁻²	·10 ⁻²	·10⁻¹	·10⁻¹
0.8	2.45	1.83	2.59	8.24	1.95	4.44	8.27	1.36	2.08	3.04
	·10 ⁻¹⁹	·10⁻⁴	·10⁻³	·10⁻³	·10⁻²	·10⁻²	·10⁻²	·10⁻¹	·10⁻¹	·10⁻¹

Table 2 illustrates the variation of frequency shift for different lengths with various values of ξ_1 , while maintaining ξ_2 fixed at 0.04. At a length of 5.2, the frequency shift is 1.47, which increases to $8.11 \cdot 10^3$ at a length of 40.2 for $\xi_1 = 0.4$. Similarly, the frequency shift increases from $3.21 \cdot 10^{-1}$ to $1.66 \cdot 10^2$ as ξ_1 varies from 0 to 0.8 for a length of 10.2. It is evident that the value of frequency shift increases with the increase in length and the non-local parameter ξ_1 .

Table 2. Frequency shift for different lengths keeping fixed $\xi_2 = 0.04$

- abtc 2	bte 2. Frequency shirt for different tengths keeping fixed $\zeta_2 = 0.01$										
L &1	0.2	5.2	10.2	15.2	20.2	25.2	30.2	35.2	40.2	45.2	
0	1.78 ·10⁻ ⁸	1.13	3.21 ·10 ⁻¹	5.57	34.9	1.20 ·10 ²	3.33 ⋅10 ²	6.89 ·10²	1.19 ·10 ³	1.61 ·10³	
0.4	1.86 ·10⁻ ⁸	1.47	60.2	3.30 ⋅10 ²	9.02 ·10²	1.87 ·10³	3.33 ·10³	5.38 ·10³	8.11 ·10³	1.16 ·10⁴	
0.6	4.19 ·10⁻ ⁸	3.29	1.13 ·10 ²	5.35 ·10 ²	1.41 ·10 ³	2.89 ·10³	5.07 ·10³	8.08 ·10³	1.21 ·10 ⁴	1.73 ·10⁴	
0.8	7.45 ·10⁻ ⁸	5.80	1.66 ·10²	7.32 ·10 ²	1.89 ·10³	3.77 ·10³	6.47 ·10³	1.02 ·10 ⁴	1.50 ·10 ⁴	2.12 ·10 ⁴	

Table 3. Damping for different lengths keeping fixed ξ_1 = 0.5

L ξ ₂	0.2	5.2	10.2	15.2	20.2	25.2	30.2	35.2	40.2	45.2
0	9.09·10 ⁻¹⁹	9.67·10-4	$3.64 \cdot 10^{2}$	0.153	0.367	0.327	0.321	0.0329	0.348	0.383
0.4	7.30·10 ⁻¹⁸	8.14.10-3	$6.45 \cdot 10^{2}$	0.281	0.666	0.398	0.358	0.353	0.366	0.399
0.6	1.62·10 ⁻¹⁷	1.32·10-2	7.39·10 ²	0.324	0.763	0.413	0.365	0.358	0.370	0.402
0.8	2.81·10 ⁻¹⁷	1.54·10-2	$7.78 \cdot 10^{2}$	0.341	0.8	0.419	0.368	0.359	0.371	0.403

Table 3 illustrates the variation of damping for different lengths with different values of ξ_2 , while keeping ξ_1 fixed at 0.5. At a length of 10.2, the damping value is $7.39 \cdot 10^{-2}$, which increases to $4.02 \cdot 10^{-1}$ at a length of 45.2 for ξ_2 = 0.6. Similarly, damping increases from $3.21 \cdot 10^{-1}$ to $3.68 \cdot 10^{-1}$ as ξ_2 varies from 0 to 0.8 for a length of 30.2. This analysis highlights the trend where the damping value increases with the increase in length.

Table 4 displays the variation of frequency shift for different lengths with different values of ξ_2 , while maintaining ξ_1 fixed at 0.5. At a length of 10.2, the frequency shift is $1.70 \cdot 10^2$, which increases to $1.33 \cdot 10^5$ at a length of 45.2 for ξ_2 = 0.0. Similarly, the frequency shift increases from $7.49 \cdot 10^2$ to $5.32 \cdot 10^3$ as ξ_2 varies from 0 to 0.8 for a length of 15.2. It is evident that the value of frequency shift increases with the increase in length and the non-local parameter ξ_2 .

Table 5 presents damping values for different thicknesses while fixing ξ_2 at 0.04. Four values of ξ_1 are considered: 0, 0.2, 0.6 and 0.8, with thickness ranging from 0.2 to 1. The table reveals a trend where damping decreases as thickness increases and increases with ξ_1 .

Table 4. Frequency shift for different lengths keeping fixed $\xi_1 = 0.5$

					g					
<u>L</u> ξ ₂	0.2	5.2	10.2	15.2	20.2	25.2	30.2	35.2	40.2	45.2
0	1.88 ·10 ⁻⁷	5.86	1.70 ·10 ²	7.49 ·10 ²	1.77 ⋅10³	6.98 ⋅10³	1.89 ·10⁴	4.11 ·10⁴	7.77 ·10 ⁴	1.33 ·10⁵
	.10		.10-	.10-	.10,	.10,	.10	.10	.10	.10,
0.4	4.18	3.03	3.86	1.62	3.87	2.27	6.73	1.52	2.93	5.07
0.7	·10 ⁻⁷	5.05	·10 ²	·10³	·10³	·10 ⁴	·10 ⁴	·10 ⁵	·10 ⁵	·10 ⁵
0.6	4.25	5.51	7.56	3.15	7.59	4.92	1.48	3.37	6.53	1.13
0.6	·10 ⁻⁷	5.51	·10 ²	·10 ³	·10³	·10 ⁴	·10 ⁵	·10 ⁵	·10 ⁵	·10 ⁶
0.0	4.13	7.07	1.27	5.32	1.29	8.63	2.61	5.97	1.16	2.00
0.8	·10 ⁻⁷	7.97	·10 ³	·10 ³	·10 ⁴	·10 ⁴	·10 ⁵	·10 ⁵	$\cdot 10^6$	·10 ⁶

Table 5. Damping for different thickness keeping fixed $\mathcal{E}_2 = 0.04$

	· r ɔ ·	I different t			.α <u>ς</u> 2 0.0 1				
ξ_1	0.2	0.25	0.3	0.35	0.4	0.45	0.5	0.55	0.6
0	1.12	0.714	0.32	0.273	0.111	2.76	1.31	7.35	4.51
U	1.12	0.714	0.32	0.273	0.111	·10 ⁻²	·10 ⁻²	·10 ⁻³	·10 ⁻³
0.2	0.768	0.267	0.33	2.91	4.78	5.46	4.45	3.38	2.58
0.2	0.700	0.207	0.55	·10 ⁻³	·10 ⁻³	·10 ⁻³	·10 ⁻³	·10 ⁻³	·10 ⁻³
0.6	1.81	1.13	0.719	0.477	0.333	0.255	0.212	0.176	0.138
0.8	2.93	1.93	1.28	0.876	0.631	0.495	0.422	0.366	0.302
h ξ ₁	0.65	0.7	0.75	0.8	0.85	0.9	0.95	1	
0	3.01	4.02	1.88	1.22	8.8	6.32	7.63	4.78	
0	·10 ⁻³	·10 ⁻²	·10 ⁻³	·10 ⁻³	·10 ⁻⁴	·10 ⁻⁴	·10 ⁻⁴	·10 ⁻⁴	
0.2	2.0	1.55	1.22	9.79	8.0	6.66	5.63	4.84	
0.2	·10 ⁻³	·10 ⁻³	·10 ⁻³	·10 ⁻⁴	·10 ⁻⁴	·10 ⁻⁴	·10 ⁻⁴	·10 ⁻⁴	
0.6	0.107	7.48	5.4	3.95	2.91	2.17	1.64	1.26	
0.6	0.103	·10 ⁻²	·10 ⁻²	·10 ⁻²	·10 ⁻²	·10 ⁻²	·10 ⁻²	·10 ⁻²	
0.0	0.377	0.477	0.472	9.76	7.29	5.51	4.21	3.25	
0.8	0.236	0.177	0.132	·10 ⁻²	·10 ⁻²	·10 ⁻²	·10 ⁻²	·10 ⁻²	

For instance, damping decreases from 2.93 to 1.12 as ξ_1 decreases from 0.8 to 0 for a thickness of 0.2. Conversely, damping decreases from $3.38 \cdot 10^{-3}$ to $1.12 \cdot 10^{-3}$ with the increase in thickness from 0.5 to 0.75 at $\xi_1 = 0.2$. This observation underscores the inverse relationship between damping and thickness, and the direct relationship between damping and the non-local parameter ξ_1 .

Table 6 presents various frequency shift values for different thicknesses and ξ_1 , with a fixed value of ξ_2 = 0.04. At a thickness of 0.25, the frequency shift is 1.75·10⁴, which decreases to 1.73·10⁵ at a thickness of 0.95 for ξ_1 = 0.0. Similarly, the frequency shift increases from 2.0·10⁴ to 5.42·10⁴ as ξ_1 varies from 0 to 0.8 for a thickness of 0.35. It is evident that the frequency shift decreases with an increase in thickness and increases with an increased value of the non-local parameter ξ_1 .

Table 6. Frequency Shift for different Thickness keeping fixed $\xi_2 = 0.04$

	r requericy 5in		0110 11110111	ress weep	19 117100 32	- 0.01			
ξ_1	0.2	0.25	0.3	0.35	0.4	0.45	0.5	0.55	0.6
0	2.29	3.1	1.83	2.0	6.93	6.31	5.16	4.19	3.43
0	·10 ⁵	·10 ⁴	$\cdot 10^4$	$\cdot 10^4$	$\cdot 10^{3}$	·10³	·10 ³	·10 ³	·10³
0.2	4.45	1.75	5.17	2.49	3.81	4.4	4.23	3.88	3.5
0.2	$\cdot 10^4$	·10 ⁴	$\cdot 10^{3}$	$\cdot 10^{3}$	$\cdot 10^{3}$	·10³	·10 ³	·10 ³	·10³
0.6	1.97	1.06	6.66	4.65	3.49	2.73	2.21	1.81	1.52
0.6	·10 ⁵	·10 ⁵	·10 ⁴						
0.8	2.26	1.23	7.76	5.42	4.08	3.24	2.65	2.22	1.89
0.8	·10 ⁵	·10 ⁵	·10 ⁴						
ξ_1	0.65	0.7	0.75	0.8	0.85	0.9	0.95	1	
	2.84	2.89	1.98	1.68	1.44	1.25.	1.08-	9.43	
0	·10³	·10³	·10³	·10³	·10³	·10³	·10³	·10 ²	
0.3	3.14	2.83	2.55	2.3	2.08	1.9	1.73	1.58	
0.2	·10³	·10³	·10³	·10³	·10³	·10³	·10³	·10³	
0.6	1.3	1.12	9.76	8.61	7.66	6.86	6.18	5.6	
0.6	·10 ⁴	·10 ⁴	·10³	·10³	·10³	·10³	·10³	·10³	
0.8	1.63	1.42	1.25	1.1	9.83	8.83	7.98	7.24	
0.0	·10 ⁴	·10 ⁴	·10 ⁴	·10 ⁴	·10 ³	·10³	·10³	·10³	

Table 7. Damping for different thickness keeping fixed $\xi_1 = 0.5$

ξ ₂	0.2	0.25	0.3	0.35	0.4	0.45	0.5	0.55	0.6
0	1.18	0.323	0.155	0.102	6.47 ·10 ⁻²	3.98 ·10⁻²	2.58 ·10 ⁻²	1.76 ·10⁻²	1.22 ·10⁻²
0.2	2.3	1.57	1.15	0.92	0.806	0.754	0.727	0.705	0.677
0.6	2.37	1.63	1.2	0.977	0.877	0.848	0.854	0.876	0.902
0.8	2.37	1.63	1.21	0.981	0.881	0.853	0.862	0.887	0.918
h ξ ₂	0.65	0.7	0.75	0.8	0.85	0.9	0.95	1	
0	8.61 ·10⁻³	6.23 ·10⁻³	4.59 ·10⁻³	3.44 ·10 ⁻³	2.61 ·10⁻³	2.01 ·10 ⁻³	1.57 ·10⁻³	1.24 ·10⁻³	
0.2	0.642	0.599	0.549	0.496	0.442	0.389	0.339	0.294	
0.6	0.928	0.951	0.969	0.983	0.991	0.994	0.99	0.981	
0.8	0.949	0.981	1.01	1.03	1.05	1.07	1.08	1.09	

Table 7 presents various values of damping for different thicknesses and ξ_2 , with a fixed value of ξ_1 = 0.5. The damping value increases from 9.77·10⁻¹ to 9.94·10⁻¹ with an increase in thickness from 0.35 to 0.9 for ξ_2 = 0.6. Conversely, damping decreases from 3.23·10⁻¹ to 1.63 with an increase in ξ_2 from 0 to 0.8 for a thickness of 0.25.

The Table 8 lists various frequency shift values for different thicknesses and ξ_2 , with a fixed value of ξ_1 = 0.5. At a thickness of 0.3, the frequency shift is 9878118.5, which decreases to 71532.1 at a thickness of 0.85 for ξ_2 = 0.8. Similarly, the frequency shift increases from 36698.3 to 432373 as ξ_2 varies from 0 to 0.8 for a thickness of 0.6. It is evident that the frequency shift decreases with an increase in thickness and increases with an increased value of the non-local parameter ξ_2 .

Table 8. Frequency shift for different thickness keeping fixed $\xi_1 = 0.5$

<i>h</i> ξ ₂	0.2	0.25	0.3	0.35	0.4	0.45	0.5	0.55	0.6
0	2883508	1290230	644145	348412	200973	122490	78422.1	52529.4	36698.3
0.2	1.1· ·10 ⁷	5049251	2490816	1324891	747222	442257	272814	174542	115398
0.6	2.6· ·10 ⁷	1.1· ·10 ⁷	5568845	2952666	1658042	975718	597432	378641	247411
0.8	4.5· ·10 ⁷	2· ·10 ⁷	9878118	5231594	2933246	1722637	1051994	664500	432373
h ξ ₂	0.65	0.7	0.75	0.8	0.85	0.9	0.95	1	
0	26665.5	20093.3	15650.9	12556	10335.5	8696.03	7451.61	6481.94	
0.2	78627.7	55094.4	39635.2	29236.6	22088.3	17074.3	13490.3	10881.9	
0.6	166154	114399	80591.2	57997.4	42582.1	31864	24281.4	18830.4	·
0.8	288861	197622	138150	98504.1	71532.1	52839.8	39664.4	30232.6	

Table 9. Damping and frequency shifts for different lengths keeping fixed $\xi_2 = 0.04$

			-	-		Ę	$\xi_2 = 0.0$	4				
	L	0.2	5.2	10.2	15.2	20.2	25.2	30.2	35.2	40.2	45.2	
	0	4.32 ·10 ⁻²²	6.52 ·10⁻⁶	1.32 ·10⁻⁻	1.40 ·10 ⁻⁵	1.82 ·10 ⁻⁴	1.85 ·10⁻³	2.93 ·10 ⁻³	4.56 ·10⁻³	8.87 ·10⁻³	3.45 ·10⁻²	Damping
		1.78 ·10⁻ ⁸	1.13	0.321	5.57	34.9	120	333	689	1.19 ⋅10³	1.61 ·10³	Frequency shift
	0.4	7.66 ·10 ⁻²¹	2.32 ·10 ⁻⁵	8.52 ·10⁻⁴	3.11 ·10 ⁻³	8.61 ·10 ⁻³	1.90 ·10 ⁻²	3.53 ⋅10 ⁻²	5.99 ·10 ⁻²	9.15 ·10⁻²	0.128	Damping
	0.4	1.86 ·10⁻ ⁸	1.47	60.2	330	902	1.87 ⋅10 ³	3.33 ⋅10 ³	5.38 ·10 ³	8.11 ·10 ³	1.16 ·10⁴	Frequency shift
ξ ₁	0.6	5.82 ·10 ⁻²⁰	8.26 ·10⁻⁵	1.78 ·10⁻³	5.95 ·10 ⁻³	1.45 ·10 ⁻²	3.08 ·10⁻²	5.76 ·10 ⁻²	9.33 ·10⁻²	0.137	0.191	Damping
	0.6	4.19 ·10⁻ ⁸	3.29	113	535	1.41 ·10³	2.89 ·10³	5.07 ⋅10³	8.08 ·10 ³	1.21 ·10⁴	1.73 ·10⁴	Frequency shift
	0.0	2.45 ·10 ⁻¹⁹	1.83 ·10⁻⁴	2.59 ·10⁻³	8.24 ·10 ⁻³	1.95 ·10 ⁻²	4.44 ·10 ⁻²	8.27 ·10 ⁻²	0.136	0.208	0.304	Damping
	0.8	7.45 ·10⁻ ⁸	5.8	166	732	1.89 ·10³	3.77 ⋅10³	6.47 ·10 ³	1.02 ·10 ⁴	1.5 ·10 ⁴	2.12 ·10 ⁴	Frequency shift

							$\xi_1 = 0.$	5				
	h	0.2	0.25	0.3	0.35	0.4	0.45	0.5	0.55	0.6	0.65	
		1.18	0.323	0.155	0.102	6.47 ·10 ⁻²	3.98 ·10⁻²	2.58 ·10 ⁻²	1.76 ·10 ⁻²	1.22 ·10⁻²	8.61 ·10 ⁻²	Damping
	0	2.88 ·10 ⁶	1.29 ·10 ⁶	6.44 ·10 ⁶	3.48 ·10⁵	2 ·10⁵	1.22 ·10 ⁵	7.8 ·10 ⁴	5.25 ·10⁴	3.67 ·10⁴	2.67 ·10⁴	Frequency shift
		2.30	1.57	1.15	0.92	0.806	0.754	0.727	0.705	0.677	0.642	Damping
ξ	0.2	1.1 ·10 ⁷	5.05 ·10 ⁶	2.5 ·10 ⁶	1.3 ·10 ⁶	7.47 ·10⁵	4.4 ·10 ⁵	2.73 ·10⁵	1.74 ·10⁵	1.15 ·10⁵	7.86 ·10⁴	Frequency shift
ľ		2.37	1.63	1.20	0.977	0.877	0.848	0.854	0.876	0.902	0.928	Damping
	0.6	2.6 ·10 ⁷	1.1 ·10 ⁷	5.57 ·10 ⁶	2.95 ·10 ⁶	1.66 ⋅10 ⁶	9.76 ·10⁵	5.97 ·10⁵	3.8 ·10⁵	2.47 ·10 ⁵	1.66 ·10⁵	Frequency shift
		2.37	1.63	1.21	0.981	0.881	0.853	0.862	0.887	0.918	0.949	Damping
	0.8	4.5 ·10 ⁷	2 ·10 ⁷	9.87 ·10 ⁶	5.2 ·10 ⁶	2.9 ·10 ⁶	1.72 ·10 ⁶	10.5 ·10⁵	6.64 ·10⁵	4.32 ·10 ⁵	2.9 ·10 ⁵	Frequency shift

Table 10. Damping and frequency shifts for different thickness keeping fixed $\xi_1 = 0.5$

Case (I): Figs. 1–4 demonstrate the variations of damping and frequency shift with respect to length for non-local parameters. Here we take h = 0.2, $\alpha^* = 0.025$. In Figs. 1, 2, $\xi_2 = 0.04$ and in Figs. 3, 4, $\xi_1 = 0.5$.

Figure 1 shows the variation of damping with different Lengths. In this figure, the non-local parameter ξ_1 varies for four different values i.e. 0.0, 0.4, 0.6 and 0.8. It can be observed that the value of damping increases from 0.00085 to 0.035338 for ξ_1 = 0.4 as length increases from 10.2 to 30.2. Also, it can be observed that the value of damping increases from 0.00595 to 0.00824 for 15.2 length as ξ_1 increases from 0.6 to 0.8.

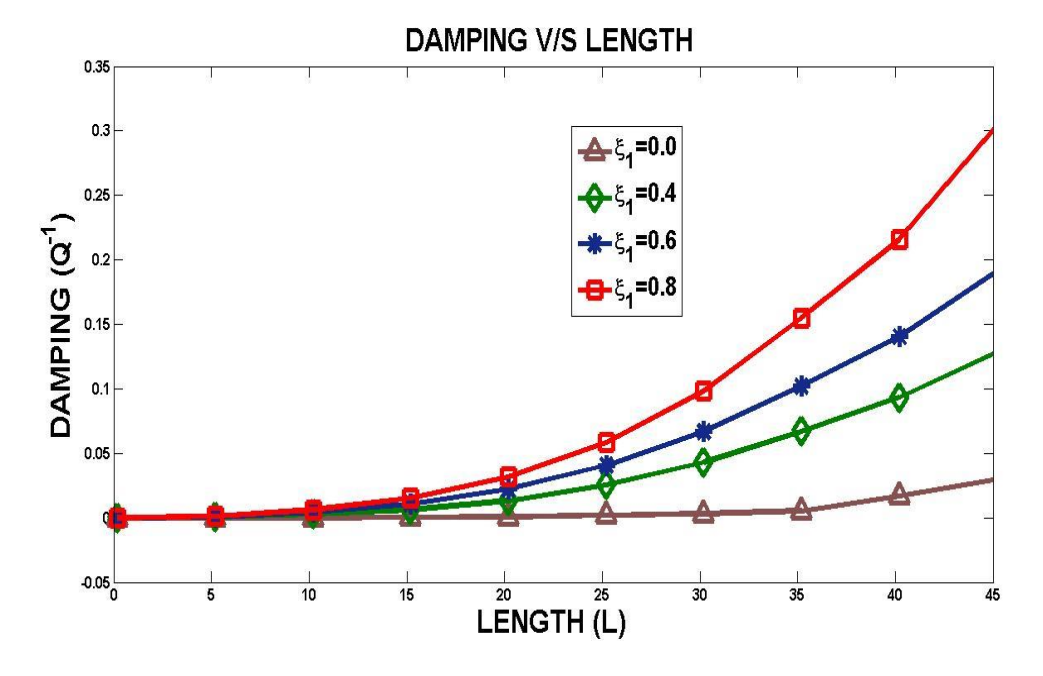


Fig. 1. Damping V/S length for $\xi_2 = 0.04$

Figure 2 depicts the graph showing the relationship between frequency shift and length, with the length varying from 0 to 45.2. The graph indicates that the damping value increases from 1.47081457 at a length of 5.2 to 1865.83847 when the length extends to 25.2 for ξ_1 = 0.4. This analysis reveals that an increase in length results in a higher damping quality factor.

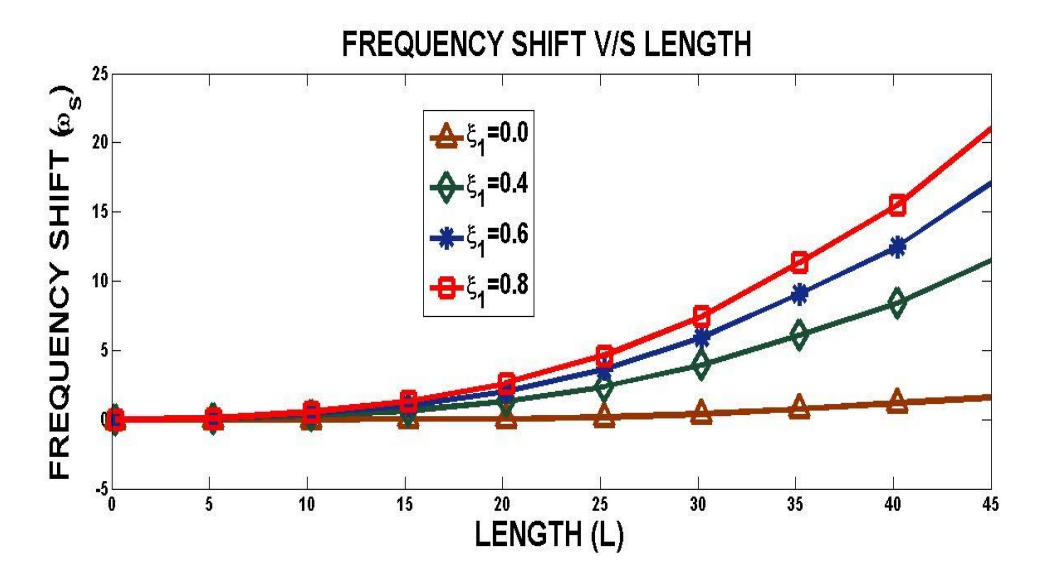


Fig. 2. Frequency shift V/S lengths for $\xi_2 = 0.04$

Figure 3 depicts the graph illustrating the relationship between damping and length, with the value of ξ_1 fixed at 0.5. In this graph, ξ_2 is set at four different values: 0, 0.4, 0.6, and 0.8. It is evident that the damping value increases with an increase in length, and damping also increases with the increase in the value of ξ_2 .

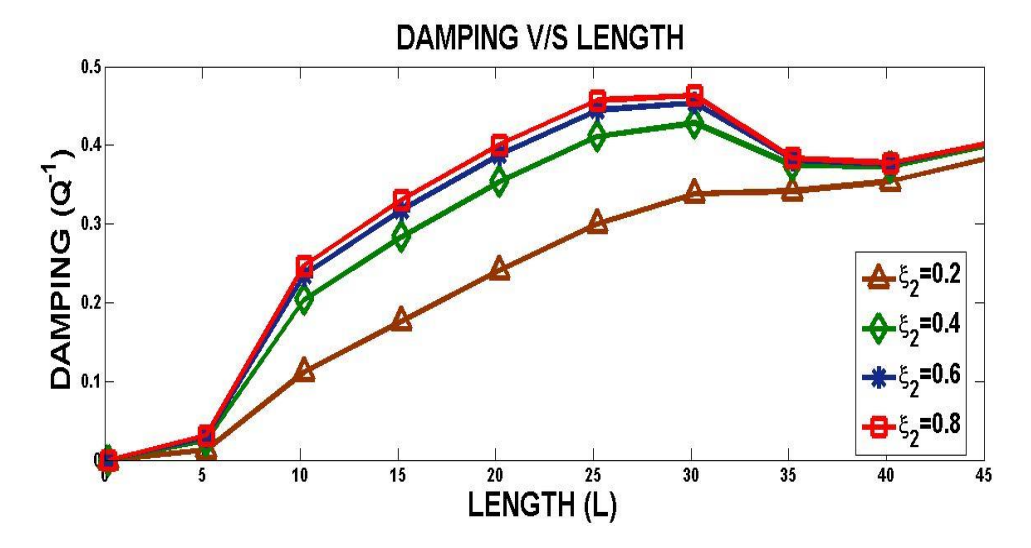


Fig. 3. Damping V/S length for $\xi_1 = 0.5$

Figure 4 presents the relationship between frequency shift and length, with the length varying from 0 to 45. The graph clearly shows that the frequency shift value increases from 1274.7908 at a length of 10.2 to 2004762.9366 when the length extends to 45.2 for ξ_1 = 0.8. This analysis indicates that an increase in length results in a higher frequency shift.

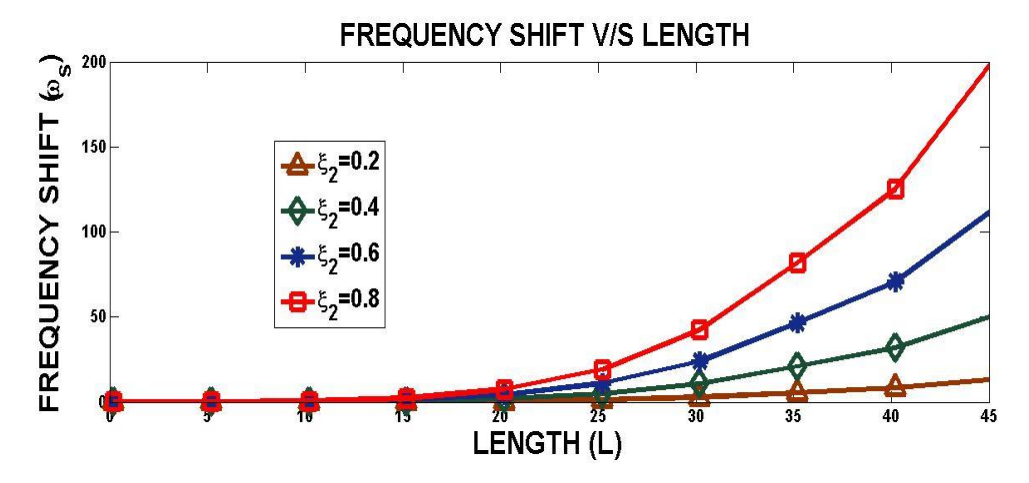


Fig. 4. Frequency shift V/S lengths for $\xi_1 = 0.5$

Case (II): Figures 5–8 demonstrate the variations of damping and frequency shift with respect to thickness for non-local parameters. Here we take L = 100, $\alpha^* = 0.025$. In Figs. 5, 6, $\xi_2 = 0.04$, and in Figs. 7, 8, $\xi_1 = 0.5$.

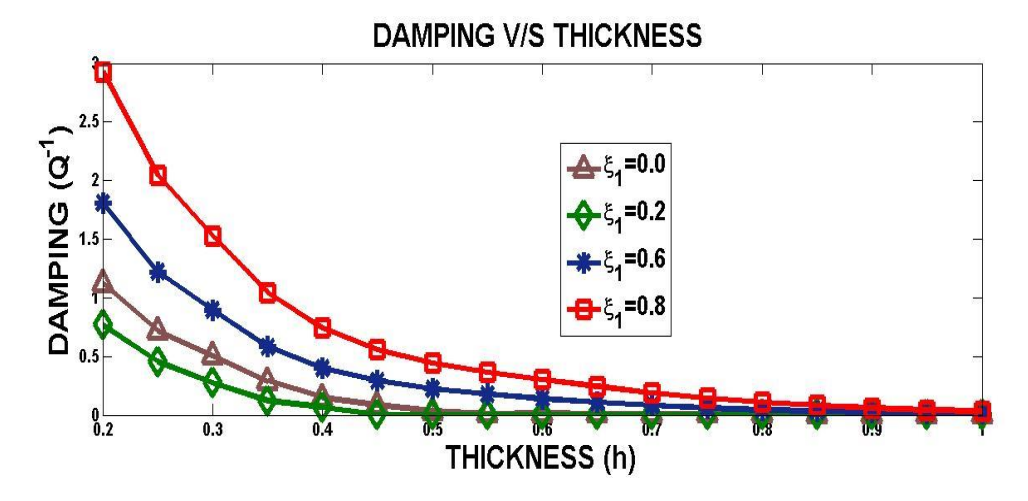


Fig. 5. Damping V/S thickness for $\xi_2 = 0.04$

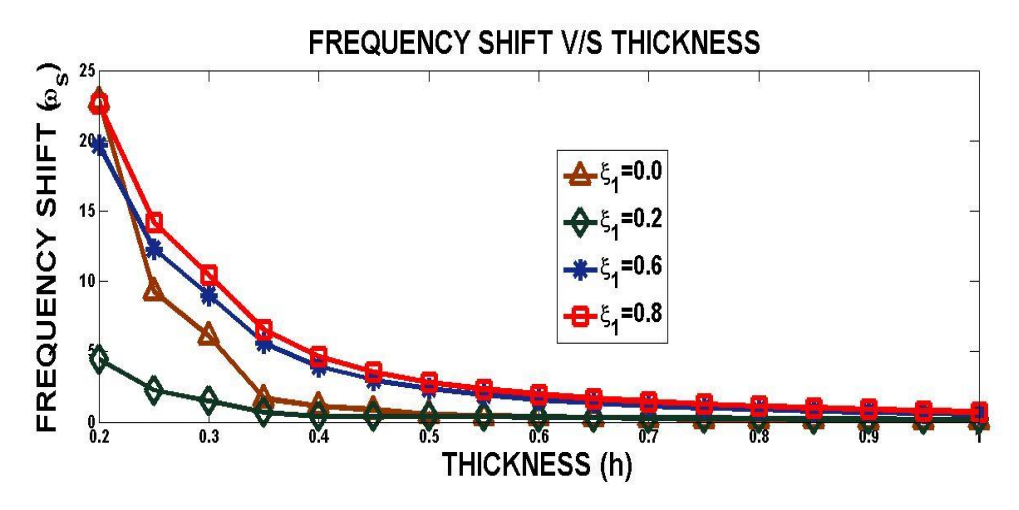


Fig. 6. Frequency shift V/S thickness for $\xi_2 = 0.04$

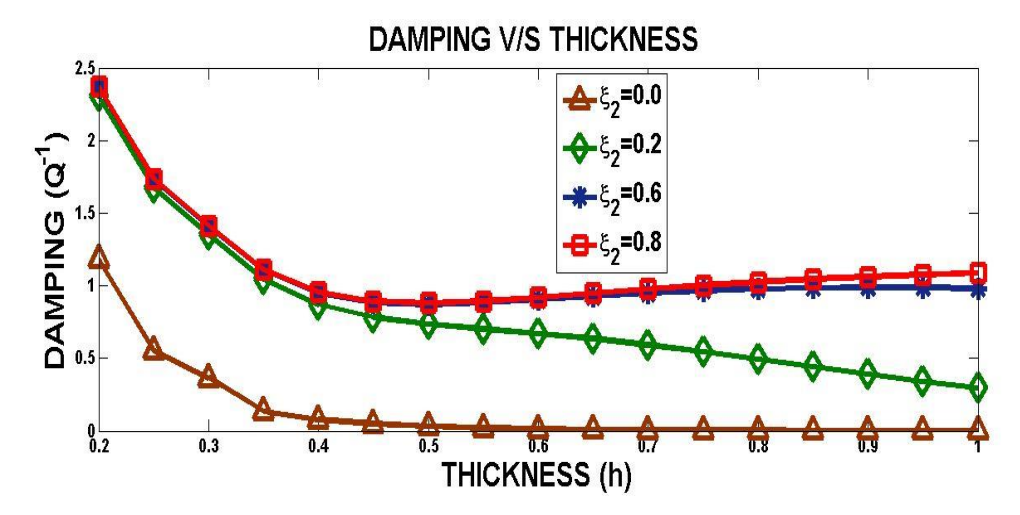


Fig. 7. Damping V/S thickness for $\xi_1 = 0.5$

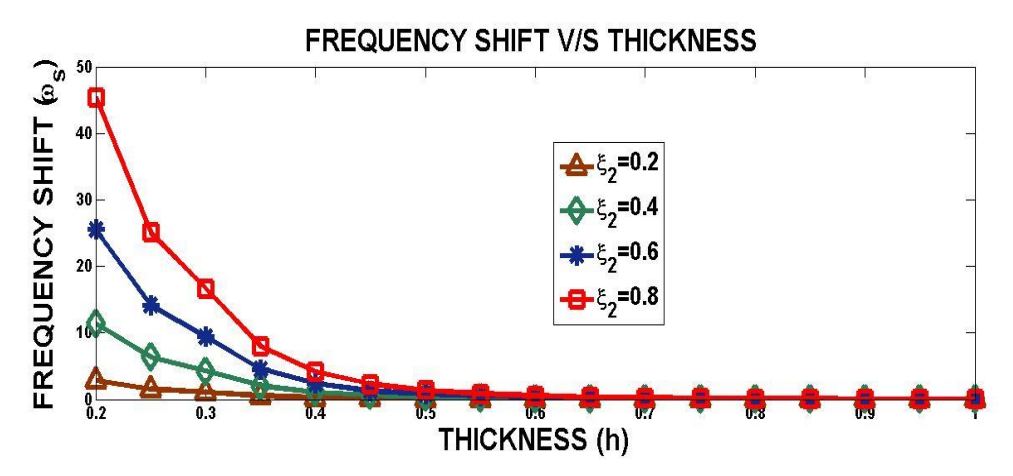


Fig. 8. Frequency shift V/S thickness for $\xi_1 = 0.5$

Figure 6 shows the graph of frequency shift versus thickness. In this graph, the thickness varies from 0.0 to 1. It can be easily observed that the value of frequency shift is 5168.949742 at a thickness of 0.3 and decreases to 2545.67 at a thickness of 0.75 for $\xi_1 = 0.2$. The frequency shift increases from 4194.238 to 22205.95 as ξ_1 varies from 0 to 0.8 for a thickness of 0.55. By analysing this graph, it is found that an increase in thickness results in a decrease in the damping quality factor, but the frequency shift increases as the non-local parameter ξ_1 increases.

Figure 7 illustrates the relationship between damping and thickness, with the value of ξ_1 fixed at 0.5. In this graph, ξ_2 is set at four different values: 0, 0.2, 0.6 and 0.8. It can be observed that the damping value increases with an increase in thickness, while the damping decreases as the non-local parameter ξ_2 increases.

Figure 8 shows the graph of frequency shift versus thickness. By analysing this graph, it is found that an increase in thickness results in a decrease in the frequency shift, but the frequency shift increases with the increased value of the non-local parameter ξ_2 .

Case (III): Figures 9–12 explain the variations of damping and frequency shift with respect to length and thickness for non-local parameters with varying empirical material constant $\alpha^* = 0.0001$, 0.004, 0.008, $\xi_1 = 0.5$, $\xi_2 = 0.04$.

In Figs. 9 and 10, h = 0.2, and in Figs. 11 and 12, L = 100. Figures 9 and 10 illustrate

the TDP effect. It can be easily analysed from these graphs that the damping quality factor and frequency shift increases with increasing length. It is also observed that with the increase in empirical material constant (α^*), the damping and frequency shift decreases.

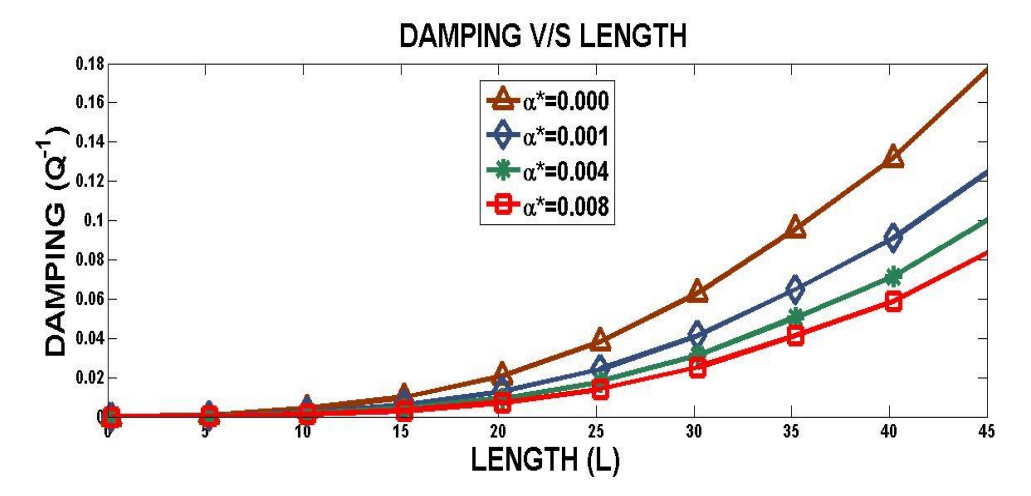


Fig. 9. Damping V/S length with TDP effect

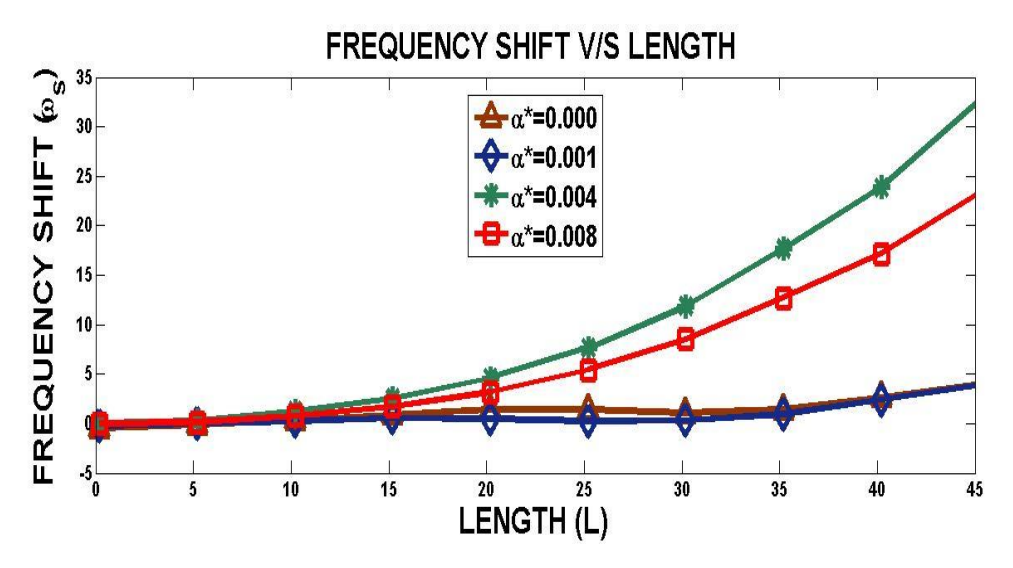


Fig. 10. Frequency shift V/S length with TDP effect

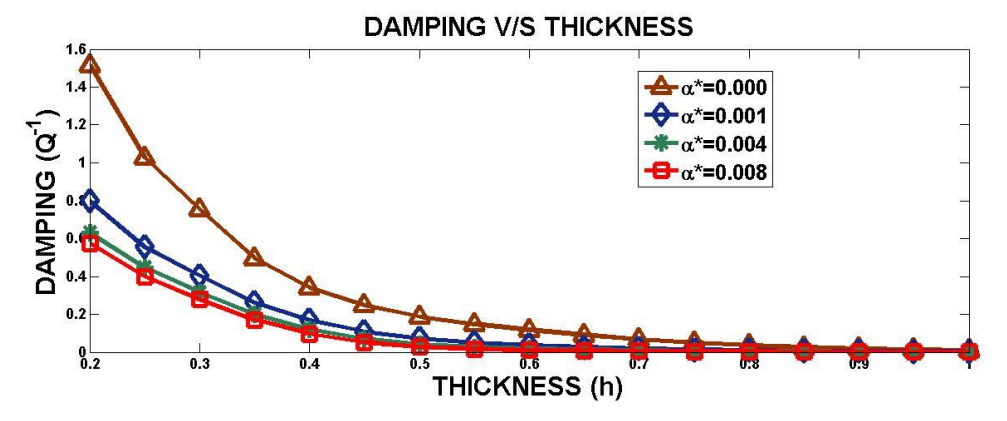


Fig. 11. Damping V/S thickness with TDP effect

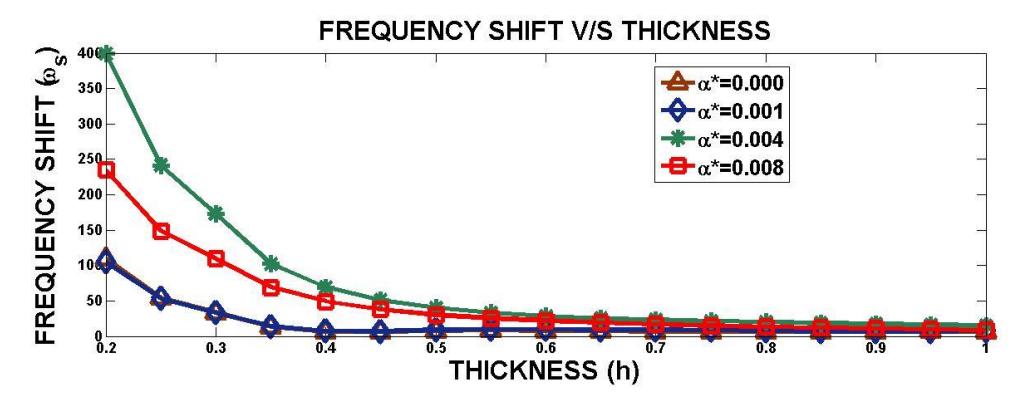


Fig. 12. Frequency shift V/S thickness with TDP effect

Figures 11 and 12 show the TDP effect. It can be analysed from these graphs that the damping and frequency shift value reduces with increasing thickness. It is also observed that with the increase in empirical material constant (α^*), the damping and frequency shift decreases.

Case (IV): Figures 13–16 demonstrate the LS and DPL models in the variations of damping and frequency shift for ξ_1 = 0.05, ξ_2 = 0.04, τ_t = 0, τ_q = 0.05, α^* = 0.025. In Figs. 13 and 14, h = 0.2, and in Figs. 15 and 16, L = 100.

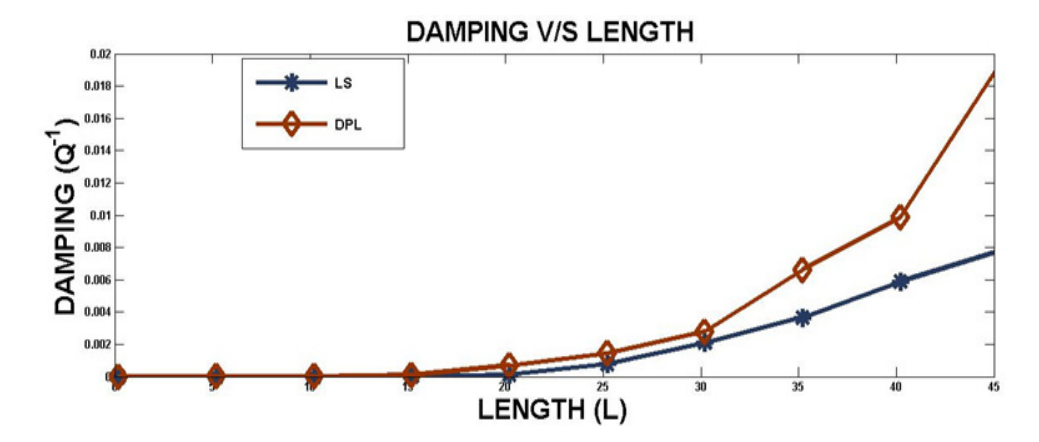


Fig. 113. Comparison of LS and DPL for damping V/S length

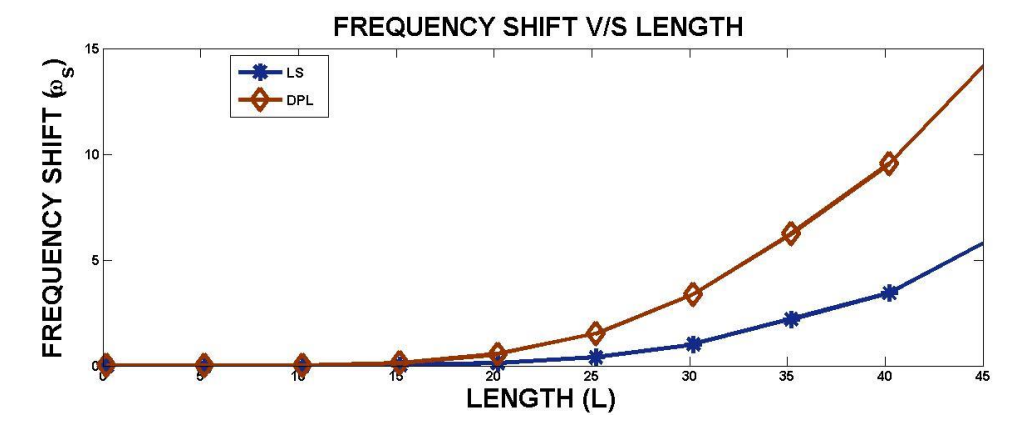


Fig. 124. Comparison of LS and DPL for frequency shift V/S length

The comparison of damping and frequency shift versus length are shown in Figs. 13 and 14. It can be seen that the damping factor and frequency shift for LS is less than for DPL. For both the LS and DPL models, the damping quality factor and frequency shift rises with increase in length.

In Figs. 15 and 16, the comparison of damping and frequency shift versus thickness are shown. In the instance of DPL theory, the damping factor and frequency shift has been observed to be higher than in LS models. The damping factor and frequency shift decreases with increase in thickness for both the LS and DPL models.

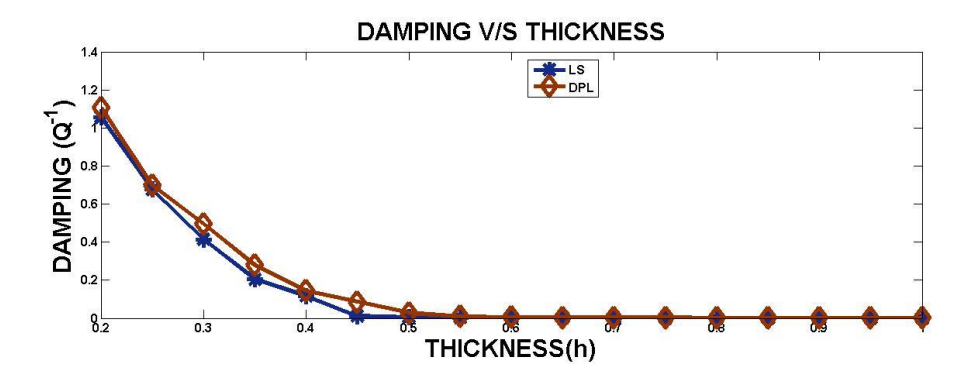


Fig. 135. Comparison of LS and DPL for damping V/S thickness

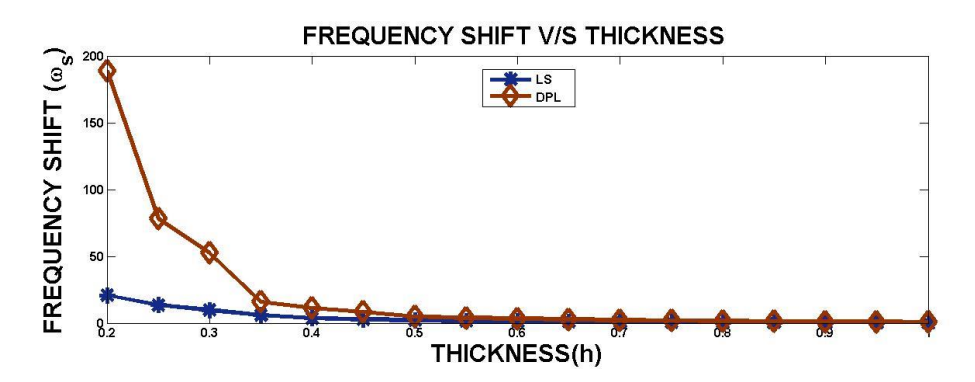


Fig. 146. Comparison of LS and DPL for frequency shift V/S thickness

Conclusions

Traditional models assume classical (local) elasticity, where stress at a point depends only on strain at that same point. The suggested model includes non-local elasticity, which accounts for size-dependent effects-essential for modelling materials at small scales, where classical theories become inaccurate. The advancement is to capture scale effects relevant to micro/nano-structures, improving the precision of stress and strain predictions. The present study investigates thermoelastic damping (TD) and frequency shift (FS) in Kirchhoff plates, considering thermoelastic theory under the influence of non-local parameters, dual-phase lag, and temperature-dependent properties. TD and FS are analysed under simply supported boundary conditions. The results are tabulated and displayed graphically with varying values of length and thickness to explore the impacts of non-local parameters, temperature dependent parameters and the comparison between LS and DPL models. It is observed that the damping quality factor and FS

increase with the increase in non-local parameters ξ_1 and ξ_2 and decreases with increasing thickness with distinct magnitude.

Damping and frequency shift are likewise detected under the TDP effect, and they increase with length. Additionally, it is noted that the damping and frequency shift diminish as the empirical material constant (α^*) increases. These graphs show also it is observed that as thickness increases, magnitude of damping and frequency shift decrease under the impact of TDP. The damping quality factor and frequency shift increase with length for both the DPL and LS versions although magnitude of these field variables for LS remains smaller than DPL.

It is concluded that the impact of non-local and temperature dependent parameters play a valuable role in processing and characterisation to improve the material property. The work presented here is useful for the researcher working in thermodynamics, engineering, material science and hyperbolic thermodynamic model.

CRediT authorship contribution statement

Rajneesh M. Kumar Scr: writing – review & editing, supervision, conceptualization; **Pooja Singhal** Scr: writing – original draft, investigation, data curation

Conflict of interest

The authors declare that they have no conflict of interest.

References

- 1. Zener C. Internal Friction in Solids. *Physical Review*. 1937;52(3): 230–235.
- 2. Zener C. Internal friction in solids II. General theory of thermoelastic internal friction. *Physical Review.* 1938;53(1): 90–99.
- 3. Sun Y, Fang D, Soh AK. Thermoelastic damping in micro-beam resonators. *International Journal of Solids and Structures*. 2006;43(10): 3213–3229.
- 4. Eringen AC, Edelen DGB. On nonlocal elasticity. *International Journal of Engineering Science*. 1972;10(3): 233–248.
- 5. Eringen AC. Theory of nonlocal thermoelasticity. *International Journal of Engineering Science*. 1974;12(12): 1063–1077.
- 6. Yu YJ, Tian XG, Xiong QL. Nonlocal thermoelasticity based on nonlocal heat conduction and nonlocal elasticity. *European Journal of Mechanics A/Solids*. 2016;60: 238–253.
- 7. Xu Y, Zhou D, Liu K. Three-dimensional thermoelastic analysis of rectangular plates with variable thickness subjected to thermomechanical loads. *Journal of Thermal Stresses*. 2010;33(12): 1136–1155.
- 8. Sun Y, Saka M. Thermoelastic damping in micro-scale circular plate resonators. *Journal of Sound and Vibration*. 2010;329(3): 328–337.
- 9. Grover D, Sharma JN. Transverse vibrations in piezothermoelastic beam resonators. *Journal of Intelligent Material Systems and Structures*. 2012;23(1): 77–84.
- 10. Alashti RA, Abolghasemi AH. A Size-dependent Bernoulli-Euler Beam Formulation based on a New Model of Couple Stress Theory. *International Journal of Engineering*. 2014;27(6): 951–960.
- 11. Sharma S, Sharma K. Influence of Heat Sources and Relaxation Time on Temperature Distribution in Tissues. *International Journal of Applied Mechanics and Engineering*. 2014;19(2): 427–433.
- 12. Abbas IA. Exact Solution of Thermoelastic Damping and Frequency Shifts in a Nano-Beam Resonator. *International Journal of Structural Stability and Dynamics*. 2015;15(6): 1–12.
- 13. Kumar R, Devi S, Sharma V. Damping in microscale modified couple stress thermoelastic circular Kirchhoff plate resonators. *Applications and Applied Mathematics*. 2017;12(2): 924–945.
- 14. Zhang H, Kim S, Choi G, Xie D, Cho HH. Effect of temperature dependent material properties on thermoelastic damping in thin beams. *International Journal of Heat and Mass Transfer*. 2019;139: 1031–1036.

- 15. Marin M, Öchsner A, Bhatti MM. Some results in Moore-Gibson-Thompson thermoelasticity of dipolar bodies. *ZAMM Zeitschrift für Angewandte Mathematik und Mechanik*. 2020;100(12): 1–13.
- 16. Borjalilou V, Asghari M, Taati E. Thermoelastic damping in nonlocal nanobeams considering dual-phase-lagging effect. *Journal of Vibration and Control.* 2020;26(11–12): 1042–1053.
- 17. Abouelregal AE, Marin M. The response of nanobeams with temperature-dependent properties using state-space method via modified couple stress theory. *Symmetry*. 2020;12(8): 1276.
- 18. Devi S. Thermoelastic Damping and Frequency Shift in Kirchhoff Plate Resonators Based on Modified Couple Stress Theory With Dual-Phase-Lag Model. *Journal of Stress Analysis*. 2020;12(3): 700–712.
- 19. Guha S, Singh AK. Frequency shifts and thermoelastic damping in different types of Nano-/Micro-scale beams with sandiness and voids under three thermoelasticity theories. *Journal of Sound and Vibration*. 2021;510: 116301.
- 20. Sharma S, Khator S. Power generation planning with reserve dispatch and weather uncertainties including penetration of renewable sources. *Smart Grid and Clean Energy*. 2021;10(4): 292–303.
- 21. Sharma S, Khator S. Micro-Grid Planning with Aggregator's Role in the Renewable Inclusive Prosumer Market. *Journal of Power and Energy Engineering*. 2022;10(4): 47–62.
- 22. Guha S, Singh AK. Frequency shifts and thermoelastic damping in distinct Micro-/Nano-scale piezothermoelastic fiber-reinforced composite beams under three heat conduction models. To be published in *Journal of Ocean Engineering and Science*. [Preprint] 2022. Available from: doi.org/10.1016/j.joes.2022.06.015.
- 23. Kaur I, Singh K. Functionally graded nonlocal thermoelastic nanobeam with memory-dependent derivatives. *SN Applied Sciences*. 2022;4(12): 312.
- 24. Kumar R, Devi S. The effects of two temperature and laser pulse on modified couple stress thermoelastic diffusion beam. *Engineering Solid Mechanics*. 2023;11(2): 217 230.
- 25. Huang D, Xiong H, Yang G. Analytical modeling and numerical analysis of thermoelastic damping in ultrathin elastic films due to surface effects. *Scientific Reports*. 2023;13(1): 46826.
- 26. Abouelregal AE, Marin M, Askar SS. Analysis of the magneto-thermoelastic vibrations of rotating Euler–Bernoulli nanobeams using the nonlocal elasticity model. *Boundary Value Problems*. 2023;2023(1): 1–23.
- 27. Ren X, Shi S. A Buckling Analysis of Thermoelastic Micro/Nano-Beams Considering the Size-Dependent Effect and Non-Uniform Temperature Distribution. *Materials*. 2023;16(19): 6390.
- 28. Selvamani R, Loganathan R, Yaylaci M, Yaylaci EU, Özdemir ME. Vibration of piezo-magneto-thermoelastic FG nanobeam submerged in fluid with variable nonlocal parameter. *Advanced Nano Research*. 2024;16(5): 489–500.
- 29. Sharma S, Sharma K, Bhargava RR. Wave motion and representation of fundamental solution in electromicrostretch viscoelastic solids. *Materials Physics and Mechanics*. 2013;17(2): 93–110.
- 30. Kumar R, Partap G. Propagation of waves in micropolar thermoelastic cubic crystals. *Applied Mathematics and Information Sciences*. 2010;4(1): 107 123.
- 31. Kumar R, Devi S, Sharma V. Plane waves and fundamental solution in a modified couple stress generalized thermoelastic with mass diffusion. *Materials Physics and Mechanics*. 2015;24(4): 72–85.
- 32. Lotfy K, Elidy ES, Tantawi RS. Photothermal Excitation Process during Hyperbolic Two-Temperature Theory for Magneto-Thermo-Elastic Semiconducting Medium. *Silicon*. 2021;13(7): 2275–2288.
- 33. Lotfy K, El-Bary AA, El-Sharif AH. Ramp-type heating microtemperature for a rotator semiconducting material during photo-excited processes with magnetic field. *Results in Physics*. 2020;19: 103338.
- 34. Lotfy K, El-Bary AA, Hassan W, Ahmed MH. Hall current influence of microtemperature magneto-elastic semiconductor material. *Superlattices and Microstructures*. 2020;139: 106428.
- 35. Alharbi AR, Almatrafi MB, Lotfy K. Constructions of solitary travelling wave solutions for Ito integro-differential equation arising in plasma physics. *Results in Physics*. 2020;19: 103533.
- 36. Lotfy K, El-Bary AA. Magneto-Photo-Thermo-Microstretch Semiconductor Elastic Medium Due to Photothermal Transport Process. *Silicon*. 2022;14(9): 4809–4821.
- 37. Ismail GM, Gepreel KA, Lotfy K, Mahdy AMS, El-Bary A, Saeed AM. Influence of variable thermal conductivity on thermal-plasma-elastic waves of excited microelongated semiconductor. *Alexandria Engineering Journal*. 2022;61(12): 12271–12282.
- 38. Abouelregal AE, Marin M, Foul A. Thermoviscoelastic Responses in Kirchhoff Circular Micro-Plate via MGT Thermoelastic Model and Modified Couple Stress Theory. *Mechanics of Solids*. 2024;59: 2269–2291.
- 39. Aldandani M, Abouelregal A. Study of Thermo-Viscoelastic Interactions in Microplates Resting on an Elastic Foundation and Subjected to External Loads Using DPL Thermoelastic Model. *Iranian Journal of Science and Technology, Transactions of Mechanical Engineering.* 2025;49: 217–233.

40. Abouelregal AE. Fibre-reinforced generalized anisotropic thick plate with initial stress under the influence of fractional thermoelasticity theory. *Advances in Applied Mathematics and Mechanics*. 2017;9(3): 722–741.

- 41. Abouelregal AE, Marin M, Foul A, Askar SS. Coupled responses of thermomechanical waves in functionally graded viscoelastic nanobeams via thermoelastic heat conduction model including Atangana Baleanu fractional derivative. *Scientific Reports*. 2024;14(1): 58866.
- 42. Abouelregal AE, Elzayady ME, Marin M. Thermoelastic modeling of functionally graded materials with cylindrical cavities utilizing higher-order fractional heat transfer models incorporating time delays. *Continuum Mechanics and Thermodynamics*. 2025;37: 31.
- 43. Tzou DY, Guo ZY. Nonlocal behavior in thermal lagging. *International Journal of Thermal Sciences*. 2010;49(7): 1133–1137.
- 44. Rao SS. Vibration of Continuous Systems. Hoboken: Wiley; 2007.
- 45. Chen W, Li X. A new modified couple stress theory for anisotropic elasticity and microscale laminated Kirchhoff plate model. *Archive of Applied Mechanics*. 2014;84(3): 323–341.
- 46. Guo FL, Song J, Wang GQ, Zhou YF. Analysis of thermoelastic dissipation in circular micro-plate resonators using the generalized thermoelasticity theory of dual-phase-lagging model. *Journal of Sound and Vibration*. 2014;333(11): 2465–2474.
- 47. Sharma JN. Thermoelastic damping and frequency shift in micro/nanoscale anisotropic beams. *Journal of Thermal Stresses*. 2011;34(7): 650–666.

Submitted: February 02, 2025 Revised: April 28, 2025 Accepted: May 29, 2025

Creep and long-term strength of high-entropy alloys

R.R. Saitova 🖾 🗓, A.R. Arutyunyan 🗓

St. Petersburg State University, St. Petersburg, Russia

[™] rigastr@yandex.ru

ABSTRACT

High-entropy alloys are a new class of metallic alloys without a principal component. These materials are attractive because of their unique structures and properties, including mechanical ones. Some high-entropy alloys based on refractory metals are considered as advanced high-temperature materials. In this regard, the study and description of the behavior of such materials under conditions of creep, fatigue and long-term strength is of great interest. In the work, to describe the creep and long-term strength of high-entropy alloys a damage conception is used. A system of interconnected kinetic equations for the creep rate and damage parameter is formulated. A compressible medium is considered, and the mass conservation law is taking into account. The damage parameter is specified in the form of the ratio of the current density of the material to the initial one. The analytical solutions of these equations are obtained. The theoretical creep and long-term strength curves are plotted and compared with the experimental results for CrMnFeCoNi and CrFeCoNi alloys. The experimental results are in good agreement with the theoretical ones.

KEYWORDS

creep • damage parameter • high-entropy alloys • long-term strength

Funding. This work has been supported by the grant of St. Petersburg State University, ID No. 119081549.

Citation: Saitova RR, Arutyunyan AR. Creep and long-term strength of high-entropy alloys. *Materials Physics and Mechanics*. 2025;53(3): 116–121.

http://dx.doi.org/10.18149/MPM.5332025_9

Introduction

As high-entropy alloys (HEAs) are being actively explored for next-generation structural materials, gaining a comprehensive understanding of their creep, fatigue, and fracture behaviors is indispensable. These three aspects of mechanical properties are particularly important because: creep resistance dictates an alloy's high-temperature applications; fatigue failure is the most frequently encountered failure mode in the service life of a material; fracture is the very last step that a material loses its load-carrying capability.

As materials with superior properties are continuously searched, HEAs, formed by the physical metallurgy of five or more metallic elements with equal or nearly equal quantities, emerge as a class of revolutionary materials. HEAs break down the traditional wisdom of alloy design in which a primary element serves as the foundation of properties, and small amounts of additional elements are inserted for fine tuning, therefore, open innumerable possibilities in developing advanced alloys [1,2].

One decade of dedicated research has revealed that many HEAs possess unparalleled properties in comparison with traditional alloys, for instance, great thermal and microstructural stability [3], high hardness [4], high strength at a wide range of temperatures [5] and excellent resistance to wear [6], corrosion [7], fatigue [8], fracture [9] and high-temperature softening [10]. Given these merits, applications of HEAs in various



117 R.R. Saitova, A.R. Arutyunyan

fields, particularly in structural engineering (e.g., used for gas-turbine engines), are being actively explored. Among many performance indices, a thorough understanding of creep, fatigue, and fracture behaviors of HEAs is crucial and indispensable to their sophisticated engineering applications.

Kinetics of damage and deformation accumulation under high temperature creep conditions

Literature survey

High-temperature creep of metals and alloys is characterized by the fact that in the body, along with the accumulation of irreversible creep deformations, the formation and development of defects (pores, micro- and macrocracks) occur, leading to fracture. In 1826, the phenomenon of creep was observed by Claude Louis Marie Henri Navier. First systematic studies on creep processes were published by Edward Neville da Costa Andrade [11].

To describe a brittle region of the long-term strength curve studies based on continuum mechanics were conducted. These studies taking into account the accumulation of damage, have led to the development of a separate direction of continuum mechanics - the Continuum Damage Mechanics. This direction was created by two outstanding Soviet scientists: L.M. Kachanov [12] and Yu.N. Rabotnov [13]. At the end of the 1950s, they considered and introduced a new parameter at creep under uniaxial tension: material continuity (Kachanov) and material damage (Rabotnov). Soon Rabotnov, based on this approach, developed the kinetic theory of creep and long-term strength.

Subsequently, significant results in this area were obtained in the Soviet Union/Russian Federation. Following Kachanov and Rabotnov, the mechanics of continuum fracture began to develop in Europe, mainly in relation to the processes of creep of metals. Since then, this area of research has been in the center of attention all over the world with regard to the development of both its foundations (not all theoretical problems have been solved) and applications [14–18].

When formulating the interrelated equations of creep and damage, the damage parameter should be given a physical meaning. To materialize the damage parameter various definitions were offered. The relative size of pores or irreversible change of volume (loosening on Novozhilov's terminology) are considered in [19]. The crack length is taken as damage parameter in [17]. Maruyama and Nosaka [20] measured damage of material based on micro-grinding using a transparent reference square grid. The ratio of the number of nodes entering the region of pores and microcracks to the total number of nodes in the grid was considered. In [21], it is analyzed dislocation density. Many authors [22–25] considered the density of the material to be the most representative characteristic of porosity and damage. Density measurement is carried out by known methods using accurate weighing in air and in liquid (hydrostatic weighing). No methods of introducing the damage parameter mentioned above allow its measurement during creep tests. To determine the damage value at a given time by these methods, it is necessary to stop the experiment, and when metallographic methods are used, in addition the specimens must be cut. In [26], a method for measuring structural changes in metal directly during high

temperature creep, without cooling and unloading of specimens is considered. It is proposed to conduct the measurement of electrical resistance of the specimens during stretching and to compare these data with the results of the length measurement of specimens at the same time values.

Kinetic equations for damage parameter and creep strain

In this paper, the parameter of continuity is determined by the ratio $\psi = \rho/\rho_0$ (ρ_0 is initial, ρ is current density) and it is considered as integral measure of the structural microdefects accumulation during long-term high-temperature creep [27,28].

Let's consider the following system of equations [29,30]:

$$\psi^{\beta} \frac{d\varepsilon}{dt} = B\sigma^{m},\tag{1}$$

$$\psi^{\alpha} \frac{d\psi}{dt} = -A\sigma^{n},\tag{2}$$

where B, A, m, n, α , β are parameters and $\varepsilon = ln(l/l_0)$ is strain.

Taking into account the mass conservation law $\rho_0 l_0 F_0 = \rho l F$ and the true stress $\sigma = \sigma_0 F_0 / F = \sigma_0 (l/l_0) (\rho/\rho_0) = \sigma_0 (\rho/\rho_0) e^{\varepsilon} = \sigma_0 \psi e^{\varepsilon}$, these equations can be written in the following form:

$$\frac{d\varepsilon}{dt} = B\sigma_0^m \psi^{m-\beta} e^{m\varepsilon},$$

$$\frac{d\psi}{dt} = -A\sigma_0^n \psi^{n-\alpha} e^{n\varepsilon}.$$
(3)

$$\frac{d\psi}{dt} = -A\sigma_0^n \psi^{n-\alpha} e^{n\varepsilon}. \tag{4}$$

The system (3)–(4) can be solved approximately, for the case of purely brittle fracture and small deformations, when the following approximations $e^{m\varepsilon} \approx 1$, $e^{n\varepsilon} \approx 1$ or $e^{m\varepsilon} \approx 1 + m\varepsilon$, $e^{n\varepsilon} \approx 1 + n\varepsilon$ can be taken into account. Let us consider each of these two cases. In the case of $e^{m\varepsilon} \approx 1$, $e^{n\varepsilon} \approx 1$, the system (3)–(4) takes the following form:

$$\frac{d\varepsilon}{dt} = B\sigma_0^m \psi^{m-\beta},
\frac{d\psi}{dt} = -A\sigma_0^n \psi^{n-\alpha}.$$
(5)

$$\frac{d\psi}{dt} = -A\sigma_0^n \psi^{n-\alpha}.$$
(6)

Under the initial conditions t=0, $\psi=1$, from Eq. (6) we get:

$$\psi = [1 - (\alpha - n + 1)A\sigma_0^n t]^{\frac{1}{\alpha - n + 1}}.$$
(7)

Under the initial conditions
$$t=0$$
, $\varepsilon=0$, from Eq. (5) we can obtain that:
$$\varepsilon=\frac{B\sigma_0^{m-n}}{A(m-\beta+\alpha-n+1)}\left\{1-\left[1-(\alpha-n+1)A\sigma_0^n t\right]^{\frac{m-\beta}{\alpha-n+1}+1}\right\} \ . \tag{8}$$

Let us consider the case of purely brittle fracture and small deformations at $e^{m\varepsilon} \approx 1 + m\varepsilon$, $e^{n\varepsilon} \approx 1 + n\varepsilon$, then the system of equations (3)–(4) can be written as:

$$\frac{d\varepsilon}{dt} = B\sigma_0^m \psi^{m-\beta} (1 + m\varepsilon); \tag{9}$$

$$\frac{d\psi}{dt} = -A\sigma_0^n \psi^{n-\alpha} (1 + n\varepsilon). \tag{10}$$

Under the conditions $m = \beta$, $n = 1 + \alpha$, the system (9)–(10) is reduced to a nonlinear differential equation of the second order [31]. Under the initial conditions t=0, $\psi = 1$, the expression for the continuity parameter has the following form:

$$\psi = e^{\left[\frac{A\sigma_0^{n-m}(m-n)}{Bm^2} \left(e^{mB\sigma_0^m t} - 1\right) - \frac{A\sigma_0^n(m-n)}{m}t\right]}.$$
(11)

Taking into account the conditions $m = \beta$, $n = 1 + \alpha$, under the initial conditions $t=0, \varepsilon=0$, from the system (9)–(10) we will have the flowing relation for creep strain

$$\varepsilon = \frac{e^{Bm\sigma_0^m t} - 1}{m}.\tag{12}$$

119 R.R. Saitova, A.R. Arutyunyan

Long-term strength criterion

Taking the fracture conditions in the form $t = t_f$, $\psi = \psi_*$, from Eq. (7) we can obtain the following long-term strength criterion:

$$t_f = \frac{1 - \psi_*^{\alpha - n + 1}}{A(\alpha - n + 1)\sigma_0^n}.$$
(13)

Comparison of the solutions obtained with experimental results

The theoretical creep curves and the experimental results on creep for CrMnFeCoNi and CrFeCoNi alloys are shown on Figs. 1 and 2, respectively [32]. The values of the coefficients used in the calculations for Eq. (8) under the condition $e^{m\varepsilon}\approx 1$, $e^{n\varepsilon}\approx 1$ and Eq. (12) under the condition $e^{m\varepsilon}\approx 1+m\varepsilon$, $e^{n\varepsilon}\approx 1+n\varepsilon$ are presented in Tables 1 and 2, respectively.

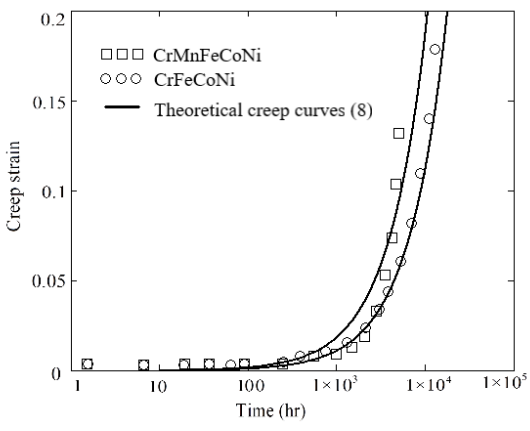


Fig. 1. Theoretical creep curves obtained by Eq. (8) and the experimental results for CrMnFeCoNi alloy at 650 °C and 50 MPa (squares) and CrFeCoNi alloy at 650 °C and 75 MPa (circles) [32]

Fig. 2. Theoretical creep curves obtained by Eq. (12) and the experimental results for CrMnFeCoNi alloy at 650 °C and 50 MPa (squares) and CrFeCoNi alloy at 650 °C and 75 MPa (circles) [32]

Table 1. The values of the coefficients used in calculations according to Eq. (8)

σ_0 , [MPa]	A , [MPa] ⁻⁶ [h] ⁻¹	B , [MPa] ⁻² [h] ⁻¹	m	n	α	β
75	3.1·10 ⁻¹⁷	2·10 ⁻⁹	2	6	6	2
50	2.8·10 ⁻¹⁶	7.5·10 ⁻⁹	2	6	6	2

Table 2. The values of the coefficients used in calculations according to Eq. (12)

σ_0 , [MPa]	B , [MPa] ⁻² [h] ⁻¹	m
75	1.9·10 ⁻⁹	2
50	5.8·10 ⁻⁹	2

Table 3. The values of the coefficients used in calculations according to Eq. (8)

	$oldsymbol{\psi}_*$	A, [MPa] ⁻⁶ [h] ⁻¹	n	α
CrFeCoNi	0.9	3.1·10 ⁻¹⁷	6	6
CrMnFeCoNi	0.9	2.8·10 ⁻¹⁶	6	6

Figure 3 shows the long-term strength curves obtained by Eq. (13) for CrMnFeCoNi and CrFeCoNi alloys at 650 $^{\circ}$ C [32]. The following values of the coefficients are presented in Table 3. It was found that a good agreement between the theoretical and experimental creep and long-term strength curves (Figs. 1–3) is observed.

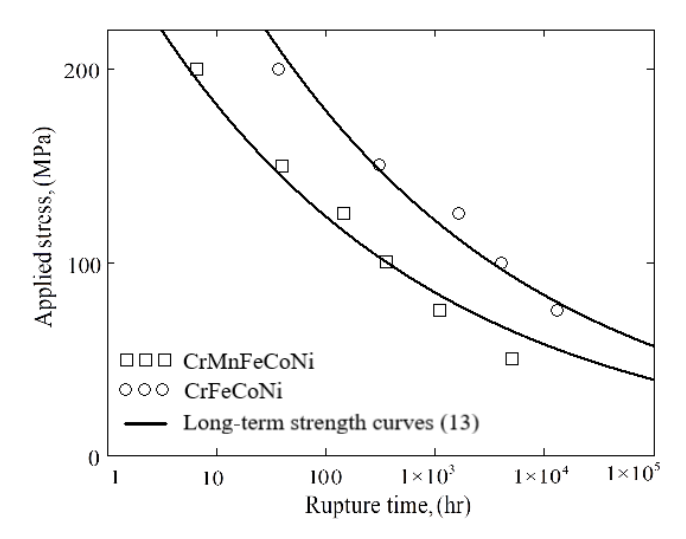


Fig. 3. Long-term strength curves obtained by Eq. (13) for CrMnFeCoNi (squares) and CrFeCoNi (circles) alloys at 650 °C [32]

Conclusions

In the paper to describe the creep and long-term strength of high-entropy alloys (HEAs) a damage conception is used. A system of interconnected kinetic equations for the creep rate and damage parameter for a compressible medium is formulated. The mass conservation law is taken into account, and the damage parameter is specified in the form of the ratio of the current density of the material to the initial one. Analytical solutions of these equations are obtained, and the long-term strength criterion is formulated. A comparison with the experimental results for CrMnFeCoNi and CrFeCoNi alloys is given. It was shown that the experimental results are in good agreement with the theoretical ones. Thus, the proposed system of interrelated kinetic equations allows us to describe the creep and long-term strength behavior of HEAs.

CRediT authorship contribution statement

Regina R. Saitova (DSCR): writing-review and editing, conceptualization, supervision, data curation; **Alexander R. Arutyunyan** (DSCR): writing-original draft, conceptualization, supervision, data curation.

Conflict of interest

The authors declare that they have no conflict of interest.

References

- 1. Zhang W, Liaw PK, Zhang Y. Science and technology in high-entropy alloys. *Science China Material*. 2018;61(1): 2–22.
- 2. Li W, Wang G, Wu S, Liaw PK. Creep, fatigue, and fracture behavior of high-entropy alloys. *Journal of Materials Research*. 2018;33(19): 1–24.
- 3. Guo S, Ng C, Lu J, Liu C, Effect of valence electron concentration on stability of fcc or bcc phase in high entropy alloys. *Journal of Applied Physics*. 2011;109(10): 103505.

121 R.R. Saitova, A.R. Arutyunyan

4. Youssef KM, Zaddach AJ, Niu C, Irving DL, Koch CC. A Novel Low-Density, High-Hardness, High-entropy Alloy with Close-packed Single-phase Nanocrystalline Structures. *Materials Research Letters*. 2014;3(2): 95–99.

- 5. Senkov ON, Senkova SV, Woodward C. Effect of aluminum on the microstructure and properties of two refractory high-entropy alloys. *Acta Materialia*. 2014;68: 214–228.
- 6. Hsu C-Y, Sheu T-S, Yeh J-W, Chen S-K. Effect of iron content on wear behavior of AlCoCrFe x Mo0.5Ni high-entropy alloys. *Wear*. 2010;268(5-6): 653–659.
- 7. Shi YZ, Yang B, Liaw PK. Corrosion-Resistant High-Entropy Alloys: A Review. Metals. 2017;7(2): 43.
- 8. Hemphill MA, Yuan T, Wang GY, Yeh J-W, Tsai C-W, Chuang A, Liaw PK. Fatigue behavior of Al0.5CoCrCuFeNi high entropy alloys. *Acta Materialia*. 2012;60: 5723–5734.
- 9. Gludovatz B, Hohenwarter A, Catoor D, Chang EH, George EP, Ritchie RO. A fracture-resistant highentropy alloy for cryogenic applications. *Science*. 2014;345(6201): 1153–1158.
- 10. Senkov ON, Wilks GB, Miracle DB, Chuang C-P, Liaw PK. Refractory high-entropy alloys. *Intermetallics*. 2010;18: 1758–1765.
- 11. Da Costa Andrade EN. On the viscous flow in metals, and allied phenomena. *Proceedings of the Royal Society.London. Series A, Containing Papers of a Mathematical and Physical Character.* 1910;84(567): 1–12.
- 12. Kachanov LM. On the time to rupture under creep conditions. *Izvestiya AN SSSR, Otdelenie Tekhnicheskikh Nauk*. 1958;8: 26–31. (In Russian)
- 13. Rabotnov YN. A mechanism of the long term fracture. In: Reshetov DN. (eds.) *Voprosy Prochnosti Materialov i Konstruktsii*. Moscow: Izdatel'stvo AN SSSR; 1959. p.5–7. (In Russian)
- 14. Leckie FA, Hayhurst DR. Constitutive equations for creep rupture. *Acta Metallurgica*. 1977;25(9): 1059–1070.
- 15. Lemaître J, Sermage JP. One damage law for different mechanisms. *Computational Mechanics*. 1997;20(1–2): 84–88.
- 16 Murakami S, Mizuno M. A constitutive equation of creep, swelling and damage under neutron irradiation applicable to multiaxial and variable states of stress. *International Journal of Solids and Structures*. 1992;29(19): 2319–2328.
- 17. Dyson BF, Taplin D. Creep damage accumulation. In: Chadwick GA, Smith DA. (eds.) *Grain Bound. Inst. Met. Spring Resident. Conf. London*. London: Academic Press; 1976. p.23–28.
- 18. Altenbach H. A nonclassical model for creep-damage processes. *Materials Physics and Mechanics*. 2001;3(1): 25–35.
- 19. Novozhilov VV. On plastic loosening. *Applied Mathematics and Mechanics*. 1965;4: 681–689. (In Russian)
- 20. Maruyama T, Nosaka T. Estimation of creep damage from observation of creep voids in centrifugal cast tube alloys. *Journal of the Society of Materials Science, Japan.* 1979;28(308): 372–378.
- 21. Estrin Y, Mecking H. A unified phenomenological description of work hardening and creep based on one-parameter models. *Acta Metallurgica*. 1984;32(1): 57–70.
- 22. Ratcliffe RT, Greenwood GW. Mechanism of cavitation in magnesium during creep. *Philosophical Magazine*. 1965;12: 59–69.
- 23. Betekhtin VI. Porosity of solids. Trans. St.-Petersburg Acad. Sci. strength problems. 1997;1: 201–210.
- 24. Arutyunyan RA. High-temperature embrittlement and long-term strength of metallic materials. *Mechanics of solids*. 2015;50(2): 191–197.
- 25. Arutyunyan AR, Arutyunyan RA. Damage and fracture of viscous-plastic compressible materials. *Materials Physics and Mechanics.* 2020;44(2): 250–255.
- 26. Lokoshchenko AM. A new method for measuring creep damage in metals. *Mechanics of Solids*. 2005;40(5): 82–92.
- 27. Brathe L. Macroscopic measurements of creep damage in metals. *Scandinavian Journal of Metallurgy*. 1978;7(5): 199–203.
- 28. Woodford DA. Density changes during creep in nickel. *Metal Science Journal*. 1969;3(11): 234–240.
- 29. Arutyunyan AR, Saitova RR. Experimental and Theoretical Investigations of High-Temperature Creep of the ENAW 5251 (AMg2) Aluminum Alloy under Step Loading. *Doklady Physics*. 2024;68(7): 203–206.
- 30. Arutyunyan AR, Saitova RR. Exact and approximate solutions of the system of interrelated equations of the theory of creep and long-term strength. *Journal of Physics: Conference Series*. 2022; 2231 (1): 012001.
- 31. Polyanin AD, Zaitsev VF. *Handbook of Exact Solutions for Ordinary Differential Equations*. 2nd ed. Chapman and Hall/CRC. 2003.
- 32. Jo M-G, Suh J-Y, Kim M-Y, Kim H-J, Jung W-S, Kim D-I, Han HN. High temperature tensile and creep properties of CrMnFeCoNi and CrFeCoNi high-entropy alloys. *Materials Science and Engineering: A.* 2022;838: 142748.

Submitted: April 10, 2025 Revised: June 23, 2025 Accepted: July 22, 2025

Evaluating the impact of functionalized graphene integration on thermal properties of CFRP composites

D.N. Choudhury 1,2 10, S.K. Panda 10

- ¹ Indian Institute of Technology (BHU) Varanasi, Varanasi, India
- ² Aircraft Research & Design Center, HAL, Bangalore, India
- [™] debendranchoudhury.rs.mec18@itbhu.ac.in

ABSTRACT

This study highlights the improvement in the thermal properties of CFRP composites modified with lower concentrations of graphene reinforcement (ADG-NH₂/epoxy/CFRP). Thermal properties such as storage modulus, loss modulus, damping factor and glass transition temperature of the composites were investigated through dynamic mechanical analysis with a temperature scan range of 30 to 200 °C and thermogravimetric analysis measurements. Five symmetrical CFRP composite laminates were prepared through a hand layup process assisted by vacuum bagging technique using various wt. % proportions (0.25, 0.5, 0.75 and 1) of ADG-NH₂/epoxy along with a neat epoxy. A slight increase of ~ 2 % in the glass transition temperature T_g was observed for the modified composites. It was observed that the ADG-NH2 composites showed ~54 % increment in storage modulus E', ~ 41 % increase in loss modulus E'' compared to neat epoxy CFRP laminate composites. Thermal stability values were determined through integral procedural decomposition temperature measurement and an enhancement from 389.1 to 411.9 °C was observed. Morphological properties of fracture surfaces were characterized by SEM micrographs and XRD analysis.

KEYWORDS

composite • CFRP • amine functionalized graphene • DMA • TGA • SEM • XRD

Citation: Choudhury DN, Panda SK. Evaluating the impact of functionalized graphene integration on thermal properties of CFRP composites. *Materials Physics and Mechanics*. 2025;53(3): 122–139. http://dx.doi.org/10.18149/MPM.5332025 10

Introduction

Many engineering and industrial applications have broadened the requirement for carbon fiber-reinforced polymer (CFRP) composites because of their superior thermal properties such as stability, high insulation, high heat resistance, low shrinkage along with enhanced mechanical properties like good dimensional stability, high tensile strength and modulus etc. [1–5]. Nano additives like 2-D Graphene sheet composed of honeycomb structure arrangement SP² carbon atoms were used in CFRP structures to enhance mechanical, electrical and thermal properties [6,7]. Covalent functionalization shows more variation in material properties and excellent bonding between the functional groups and particle surfaces. Covalent bonding between the matrix and additive enables enhanced electric charge, phonons transfer as well as mechanical load transfer across the particle / polymer interface [8–11]. In order to form a strong amide bond with epoxies, amine functionalities take part in the polymerization process [12] which is cured with amine-based hardeners and are used in the majority of structural FRPs.

Many literatures report the study of crystallization behavior of polymeric composites with the addition of very small amounts of graphene nano particles through



non-isothermal DSC experiment analysis [13]. Through thermogravimetric analysis (TGA) measurements, thermal degradation and thermal stability characteristics of polymeric composites subjected to higher thermal loading and high temperature resistance to mechanical deformations were investigated [14,15]. The viscoelastic properties of the polymeric composites subjected to continuous sinusoidal loads such as damping factor ($\tan \delta$), storage modulus (E) and loss modulus (E) were analyzed through dynamic mechanical analysis (DMA) [16,17]. Storage modulus (E) indicates the rigidity and stiffness of the polymeric structure and decreases with increase in temperature due to the movement of polymeric chain segments [18,19]. Heat-released energy with the viscous reaction of the composite was analysed by the measure of Loss modulus (E). The ratio of storage modulus (E) to loss modulus (E) was measured by damping factor ($\tan \delta$) [20,21].

Numerous studies have validated that combining synthetic fibers with plant-based fibers can enhance the viscoelastic properties of composite materials [22-24]. A high concentration of carbon-based materials has been shown to enhance the thermal conductivity of polyamide composites. In a separate study, the thermal behavior of epoxy resin-based composites was investigated by incorporating varying concentrations of graphene nanoplatelets (GNPs) - specifically 0.25, 0.5, and 0.75 wt. % - using ultrasonic dispersion. The findings revealed that the composite containing 0.75 wt. % GNPs exhibited superior thermal stability compared to the other formulations [25]. It is reported that the crystallization temperature and degree of crystallinity of polyamide graphene nanoplatelet (GNP) nanocomposites increase with higher graphene loading [26]. Rheological analysis further revealed that increasing the GNP weight percentage enhances both the storage modulus and complex viscosity of the material. At elevated graphene concentrations, a low-frequency plateau was observed, indicating a pseudo-solid-like behavior in the polymer melt. Recent studies have shown that graphene nanoplatelets (GNPs), particularly those prepared through acid treatment for improved suspension stability, significantly enhance the thermal conductivity and stability of polymer composites. When these heatexfoliated graphene layers are embedded into epoxy matrices, they yield notable improvements in thermal performance [27]. In another study, it has been shown that functionalized graphene oxide (GO)-reacted with agents such as Ceylon achieved a thermal conductivity of up to 5.8 W/m·K with 20 wt. % GO loading. Under mechanical stress, GO-based polymer composites demonstrated a higher tendency to form welldispersed nanostructures, resulting in significantly improved thermal conductivity [28].

From the existing literature, it was observed that less work has been carried out on the thermal properties of CFRP composites reinforced with low content graphene nano particles (≤ 1.0 wt. %) compared to high-content graphene-filled polymer composites. This paper reports on the preparation of amine-functionalized graphene-epoxy CFRP composites with different percentages of ADG-NH₂ loading (≤ 1 wt. %) and investigation of thermal properties and morphological properties to establish the effect of amine functionalization on the CFRP composites. This paper also describes the processing method of ADG-NH₂ into the epoxy matrix, which has enhanced the properties due to the better homogeneous dispersion of the ADG-NH₂. The main highlights of the research work are use of aerospace grade epoxy and resin with amine functionalized graphene. Significant increase in the storage modulus and loss modulus at 0.5 wt. % of ADG-NH₂ graphene content compared to the neat epoxy CFRP composites indicating better

elasticity, viscoelastic properties and energy dissipation capabilities. Minimum $\tan \delta$ for 0.5 wt. % of ADG-NH₂ graphene content compared to neat epoxy indicating better damping, energy dissipation and superior interfacial bonding between fiber and matrix interface. Fractographic analysis from scanning electron microscopy (SEM) and X-ray diffraction (XRD) clearly demonstrates the improvement of layer adhesion for increasing loading content up to compared to neat epoxy CFRP.

Materials

The amine functionalized graphene (product No.: ADG-NH₂) was received from M/s AdNano Technologies Private Limited, Shivamogga, Karnataka, India. Homogeneous dispersion (purity ~ 99 %) of the amine functionalized graphene (containing 5–10 layers of graphene) with the addition of (~ 2 to 5 %) NH₂ to graphene in order to achieve the desired exfoliation and dispersion increases the thermal conductivity and mechanical properties. The covalently functionalized graphene particles have an average thickness range of 5–10 nm and an average lateral dimension of the range 5–10 µm with bulk density and surface area of 0.1 g/cm³ and 60-200 m²/g, respectively (Fig. 1).

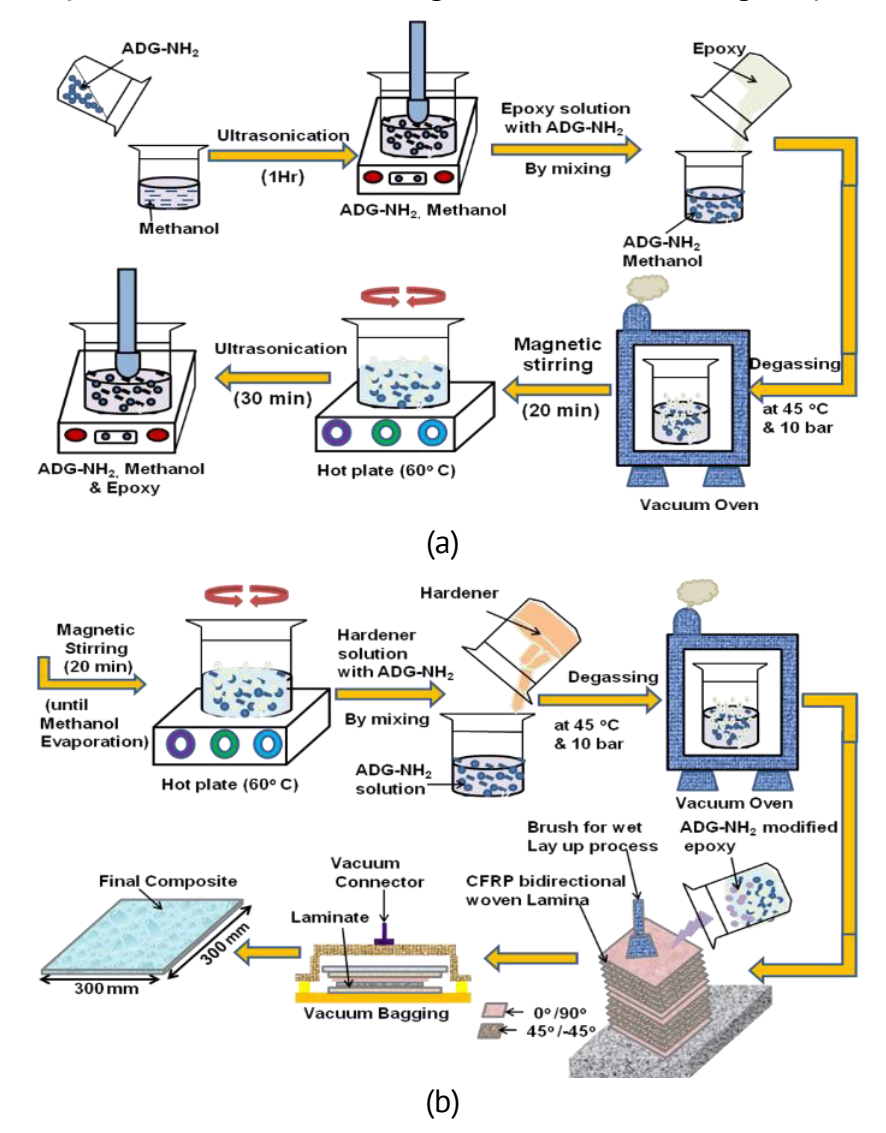


Fig. 1. Schematic diagram of processing of ADG-NH₂ (a) and (b) fabrication of laminated components

Bidirectional carbon fiber woven fabrics (T700), epoxy (LY 5052) and hardener (CH 5052) were used for this study. The high-strength non-crimp carbon fiber fabrics (Product No.: T700) were purchased from M/s Carbonext India Private Limited. Nashik, Maharashtra, India has a thickness of 0.25 mm or 250 gsm. The T700 carbon fiber fabric had an aerial weight of 634 g/m² (305 g/m² in the 90° direction, 315 g/m² in the 0° direction and was stitched together with polyester knitting thread (14 g/m²). An aerospace-grade epoxy resin (ARALDITE LY5052) and hardener (ARADUR 5052 CH) received from M/s Singhal Chemical corporation, Meerut, UP, India were used for this study. The resin was mixed with hardener with a ratio of 100:38 (wt. %). Initially a baseline T700 carbon fiber fabric CFRP composite with neat epoxy was manufactured. The mould release agent was received from Mohini Organics Pvt. Ltd., Malad (West), Mumbai, Maharastra, India and adhesive tape, release film & peel ply were purchased from Aristo Flexi pack, Daman and Diu, India. For this composite Laminate system, the densities of fiber and resin are 1.8 and 1.17 g/cm³ respectively and the nominal resin and fiber volume was of the ratio 34: 66.

Fabrication of amine functionalized graphene (ADG-NH₂)/epoxy

As shown in schematic representation (Fig. 1), during this study all the composite laminates were prepared under similar environmental conditions. The desired amine functionalized graphene (ADG-NH₂) solution loading content was added to solvent medium (methanol) and dispersed using an ultrasonic dispersion machine (Hielscher Ultrasonic homogenizer (Product No. UP400 ST) with a 22 mm probe), for 1 h to ensure the homogeneous dispersion of ADG-NH₂ by breaking the Vander walls attractive force of attraction between the nano particles. This process completely removes ADG-NH₂ aggregates, enabling effective dispersion. A large volume of methanol solvent was used for dispersion of ADG-NH₂. The base epoxy resin was then added to the ADG-NH₂/methanol dispersion and the mixture was stirred continuously with a magnetic stirrer. Methanol was evaporated from the ADG-NH₂-epoxy solution by using a rotorvap machine which was operated at 45 °C (10 bar). The resulting mixture was then allowed to settle down inside the oven at 45 °C under the vacuum at 10 bar and methanol was completely evaporated. A mixing machine with high speed of rotation (ROSS Laboratory High shear mixer (Model 100LH), NY USA) operating at 3000 rpm for 20 min was used to mix the ADG-NH₂/epoxy. The mixtures were then allowed to settle down on the beaker stand and the agglomerates were completely removed. The neat epoxy was treated similarly as the processing stage of ADG-NH₂ different wt. % filler loadings [29,30]. Hardener Aradur 5052 CH was then added to the ADG-NH₂/epoxy solution and a mixing ratio of 100:38 was incorporated, which was mixed again using the mixing machine with high speed of rotation at 3000 RPM for 20 min. Then the degassing of the suspension was carried out in a vacuum chamber (pressure ~ 10 bar) at 45 °C for approximately 20 min while manual mixing through a mechanical stirrer was carried out during the entire process. The mixture was then transferred into an open beaker at room temperature (RT), which was used for the preparation of the CFRP laminate.

Fabrication of composite laminates

Bidirectional carbon fiber was cut into 4 pieces of $300 \times 300 \text{ mm}^2$ with $0^\circ/90^\circ$ orientation and 8 pieces of $45^\circ/-45^\circ$ orientation to prepare CFRP Laminate. For fabrication of the

laminate, a 15 mm thick plane aluminum plate was considered, and its top face was cleaned thoroughly with MEK on which the laminate wet lay-up process was carried out. A release film $(300 \times 300 \text{ mm}^2)$ with 15 µm thickness was laid and on it a peel ply (30 µm) was laid. With the help of a brush, the mould release agent was applied to the peel ply and prepared adhesive resin solution (ADG-NH₂+ epoxy (LY 5052) + Hardener (5052 CH)) was applied on it. Then the first carbon fiber bidirectional woven sheet (in 0°/90° orientation) was kept on the adhesive resin solution. Then the second carbon fiber layer (at 45°/-45° orientation) was kept over the first carbon fiber layer after applying the adhesive resin solution on the first fabric uniformly with the help of a brush. To have a uniform thickness of laminates and avoid epoxy starvation between the two carbon layers, the extra amount of resins were squeezed with the help of a roller onto the carbon fiber woven sheets. The third layer was kept (at 45°/-45° orientation) on the second layer and the same procedure was followed. The 4th, 5th and 6th layers were kept at 45°/-45°, -45°/45° and 90°/0°, respectively in the same manner and the same procedure was adopted towards the preparation of twelve layers of symmetric cross-plied quasi-isotropic CFRP Laminate as shown in Fig. 1. After laying the twelfth layer, peel ply has to be kept and an aluminum plate has to be kept on the top. The carbon fiber/epoxy laminate staking sequence along with fiber orientation and thickness is shown in Fig. 1. During the manufacturing of the CFRPs, the vacuum Bagging Technique was used for curing the whole stack of laminate. In this Vacuum Bagging arrangement, first a mild steel plate was taken and cleaned thoroughly with MEK which was used to form the mould base. After treating this plate with a mould release agent, for making the mould frame Tacky tape was used, with inlet and outlet tubes. The thickness of the laminates fabricated in this entire process was between 3 to 3.5 mm, which meets standard testing requirements.

During this process in order to address air entrapment and void formation the laminate was cured at full vacuum (10 bar). The laminate was kept in this condition for 24 h curing at room temperature. Post curing, laminate was again cured for 1 h at 60 °C and then again at a higher temperature of 120 °C for 3 h. A similar procedure was adopted for the fabrication of other CFRP laminates with different ADG-NH₂/epoxy wt. % (0.25, 0.5, 0.75, and 1). The average thickness of various fabricated ADG-NH₂/epoxy/CFRP composite laminates were 3.02, 3.12, 3.23, 3.34, 3.45 mm respectively for neat, 0.25, 0.5, 0.75 and 1 wt. % ADG-NH₂/epoxy. It was observed that due to the increasing addition of ADG-NH₂ loading content, the average thickness of fabricated CFRP composite laminate increases minimally. For mechanical and morphological characterization, composites were cut into test specimens by means of a high-speed diamond cutter as per the testing standard requirements. The same fabrication technique and identical conditions were adopted for all neat epoxy resin base laminates to compare the performance of graphene content addition.

Methodology of characterization study

Morphology study of ADG-NH₂

In order to evaluate the characteristics of Amine functionalized graphene (ADG-NH₂) nano characterization methodologies such as Fourier transform infrared (FTIR) and scanning electron microscopy (SEM) were carried out. FTIR spectra of the ADG-NH₂ were carried out

using a Hoverlab FT-IR spectrophotometer (model No. HV-5500) with a 2 cm⁻¹ resolution over 64 scans. The surface was checked by using a SEM (ZEISS Microscopy, Germany, (Model EVO 15) with a 20 kV acceleration voltage of and 2.5 mm working distance.

The morphology study of the cured ADG-NH₂ enhanced CFRP composites

For this characterization, fracture surfaces were gold coated, and images were studied using a SEM. In order to enhance contrast, a thin gold layer of thickness ~ 3 nm was applied on the fracture surface of the ADG-NH₂ / CFRP composite specimen. X-ray diffraction (XRD) measurements were done with the help of a Siemens D5000 diffractometer along with a Cu-K α X-ray tube beam radiation (λ = 0.1542 nm) operated at 40 KV and 40 mA. The X-ray diffraction patterns were scanned with the help of a Nickel filter and divergences slits of 1 mm under standard braggs angle θ -2 θ conditions. The patterns were scanned over the Bragg angle (2 θ) from 1 to 30 ° at a rate of 1°/50 sec⁻¹.

Thermal gravimetric analysis

Thermal gravimetric analysis (TGA) was carried out as per the international standard ISO 11358-1 [31] at a heating rate of 10 °C/min under a nitrogen atmosphere to find the thermal stability of modified composites [32]. From the TGA thermograms, various thermal stability factors such as activation energy (E_t) for decomposition, integral procedural decomposition temperature (IPDT), initial polymer decomposition temperature (PDT) and char yield at 800 °C were determined [33]. IPDT, which indicates the thermal stability of the polymeric materials in the degraded process, was estimated from the TGA curves using the following equations:

$$IPDT = A^*K^*(\theta_f - \theta_i) + \theta_i, \tag{1}$$

$$A^* = \frac{A_1 + A_2}{A_1 + A_2 + A_3},\tag{2}$$

$$K^* = \frac{A_1 + A_2}{A},\tag{3}$$

where A^* is the ratio of the total experimental curve defined by the total TGA thermograms, K^* is the coefficient of A^* , θ_i and θ_f are the total initial and final experimental temperatures respectively and A_1 , A_2 and A_3 are the areas of the three regions into which the TGA curve is divided as shown in Fig. 2.

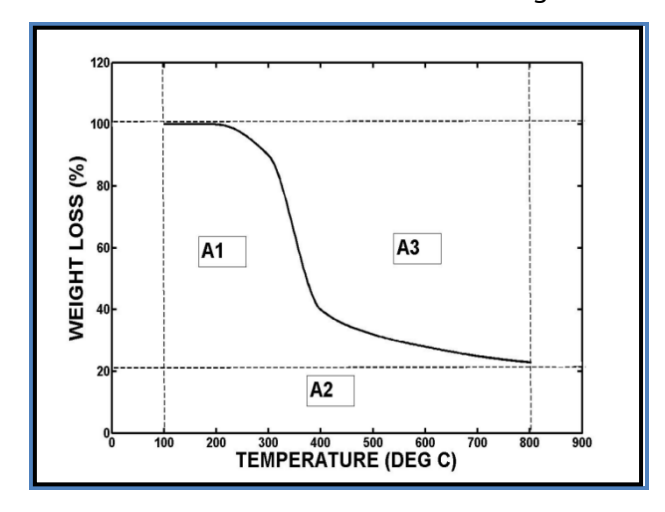


Fig. 2: Schematic representation of A1, A2 and A3

 $E_{\rm t}$ was calculated from the TGA curves using the integral method reported by Horowitz and Metzger, according to the following equations [34]:

$$\ln[\ln(1-\varphi)^{-1}] = \frac{E_t \alpha}{R\theta_{\text{max}}^2} \tag{4}$$

$$\ln\left[\ln\left(1-\varphi\right)^{-1}\right] = \frac{E_t \alpha}{R\theta_{\text{max}}^2}$$

$$\varphi = \frac{(M_i - M_a)}{(M_i - M_f)}$$
(4)

$$\alpha = \theta - \theta_{max} \tag{6}$$

where φ is the extent of decomposition, M_a , M_i and M_f are actual, initial and final masses of the sample respectively, R is the universal gas constant, θ_{max} is the absolute temperature.

Dynamic mechanical analysis

Dynamic mechanical analysis (DMA) can identify critical thermal transitions in CFRPs, such as glass transition temperature (T_q) and secondary transitions. T_q is the range of temperatures at which the polymer matrix transitions from a rigid, glassy state to a more flexible, rubbery state. Determining the composite's operational temperature limits requires an understanding of T_q . While, secondary transitions, which can affect the performance of the composite in different environmental conditions. The PerkinElmer DMA 8000(part no N5330101) machine with strain rate of 0.40 and operating at 2 Hz with a temperature range of 400 to -190 °C was used to determine $T_{\rm g}$ of the modified ADG- $NH_2/CFRP$ composites through DMA. T_q measurements were taken from the maximum values of the tan δ curve. Rectangular specimens of dimensions $3 \times 12 \times 60 \text{ mm}^3$ were used as per the ASTM D7028 standard [33]. The temperature variation from 30 to 200 °C with an increment of 2 °C/min was carried out on samples. To have repeatability of material response test was carried out on three specimens of each ADG-NH₂/ epoxy wt. % content.

By using Eq. (3), the cross-link density of the ADG-NH₂/epoxy composite with various wt. % concentrations can be found:

$$\rho = \frac{E'}{3RT},\tag{7}$$

where ρ is cross-link density in mol/cm³, E' refers to the storage modulus in MPa in the rubbery plateau region, R is the universal gas constant (8.3145 J/K mol), and T is the temperature in rubbery plateau region in Kelvin at T_q + 50.

Results and Discussion

Morphology study of ADG-NH₂

FTIR analysis of the ADG-NH₂ as received was carried out to detect functional groups and characterize covalent bonding information as shown in Fig. 3. Micrograph analysis through SEM for the as received ADG-NH₂ with the higher magnification image was carried out as shown in Fig. 4. The average lateral dimensions of the functionalized graphene particles were found to be of the order of 5 to 10 µm.

Thermal gravimetric analysis

Figure 5 represents the various zones of the TGA theromographs of ADG-NH₂/epoxy/CFRP composite (a) weight loss (%) vs temperature (°C), (b) derivative weight loss (%/min) vs temperature (°C).

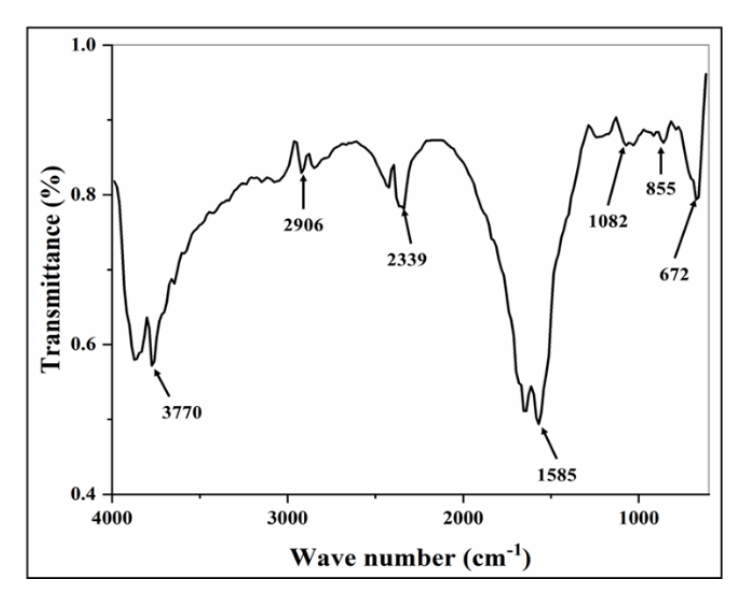


Fig. 3. FTIR spectroscopy of amine functionalized graphene (ADG-NH₂)

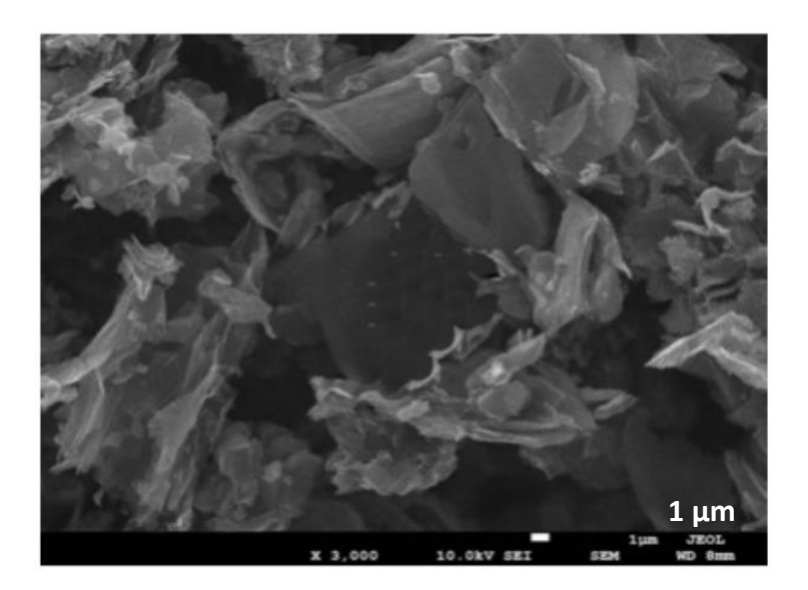


Fig. 4. SEM image of amine functionalized Graphene (ADG-NH₂)

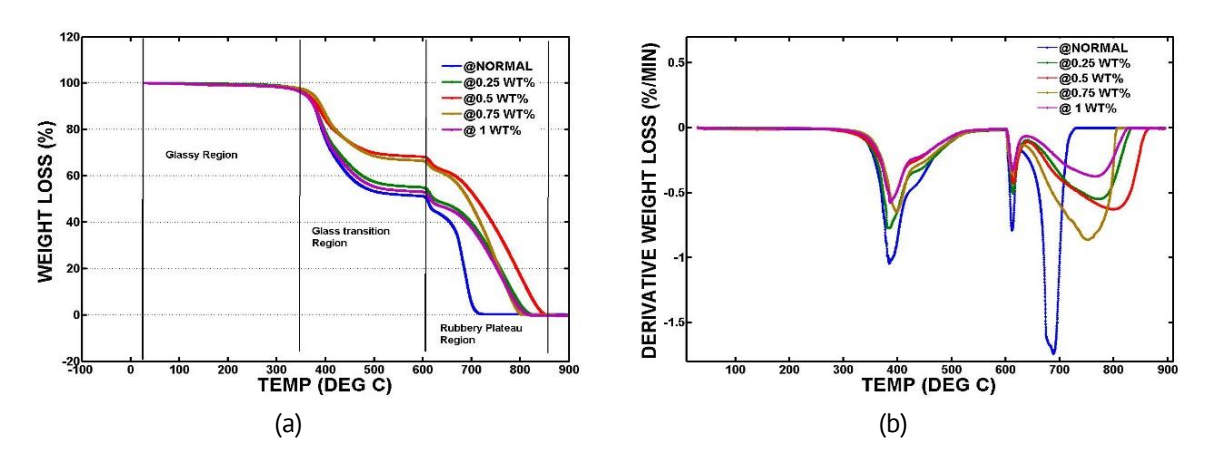


Fig. 5. TGA theromographs of of ADG-NH₂/epoxy/ CFRP composite: (a) weight loss (%) Vs temperature (°C), (b) derivative weight loss (%/min) Vs temperature (°C)

As shown in Fig. 5(a), Zone 1 is the glassy region where the first weight loss (10 %) occurs between 25 and 350 °C may be due to the less cured epoxy resin, water vaporisation and volatile impurities. As shown, Zone 2 is the glassy transition region occured between 350 and 600 °C indicating the thermal degradation of the cured epoxy. Figure 5(b) represents the derivative weight loss (%/min) vs temperature (°C) for different wt. % of graphene fillers.

The thermal stability factors, including PDT, IPDT, $E_{\rm t}$ and Char yield at 800 °C are listed in Table 1. The PDT and IPDT values of the ADG-NH₂/epoxy/CFRP composites were 362.59 and 389.1 °C, respectively. The maximum PDT and IPDT values were observed as 373.02 and 411.9 °C, respectively, occurred at 0.5 wt. % ADG-NH₂ content. An increase of ~ 14 % was observed for the activation energy ($E_{\rm t}$) values of the modified composites, which were increased from 61.63 to 69.93 KJ mol⁻¹ as listed in Table 1.

Table 1. 1 D1, 11 D1, Lt and Char	yieta at ooo k	2 141463 0036116	a moni regretimenni	
ADG-NH₂ loading, wt. %	PDT, °C	IPDT, °C	E _t , KJ/mol	Char yield at 800 °C
0	362.59	389.1	61.63	0.43
0.25	364.30	394.8	65.52	2.58
0.5	373.02	411.9	69.93	4.55
0.75	367.11	406.2	68.098	0.32
1.0	363.11	400.5	64.95	0.24

Table 1. PDT, IPDT, E_t and char yield at 800 °C values observed from TGA thermograms

Also, an increase in characteristic yields of the prepared composites at 800 °C was observed for 0.5 wt. % ADG-NH $_2$ content compared to neat epoxy and reduces subsequently beyond 0.5 wt. %. These results indicate improved thermal stability characteristics such as thermal resistance and thermal conductivity of the polymer structure due to the addition of ADG-NH $_2$ graphene fillers of up to 0.5 wt. % compared to neat epoxy. Beyond 0.5 wt. % ADG-NH $_2$ graphene fillers, there is an agglomeration formation in the epoxy network which reduces the interfacial bonding characteristics of the fiber epoxy network [33–35].

Dynamic mechanical properties

DMA uses modulus and $tan \delta$ to quantify the sample's stiffness and damping. Since the applied force is sinusoidal, the storage modulus (E') can be expressed as an in-phase component and loss modulus (E') an out-of-phase component. The elastic response of the sample is represented by the E', and the capacity to dissipate energy is represented by $tan \delta$ (i.e. E'/E'). This analysis quantifies the loss modulus (E''), storage modulus (E'), damping factor ($tan \delta$), and glass transition temperature (T_g). Figure 6 represents the viscoelastic properties of ADG-NH₂/epoxy/CFRP composites w.r.t temperature for different wt. % of ADG-NH₂ filler investigated through dynamic mechanical analysis.

Figure 6(a) represents the storage modulus (E') vs temperature of modified composites at different wt. % of ADG-NH₂. These curves depict the three significant zones

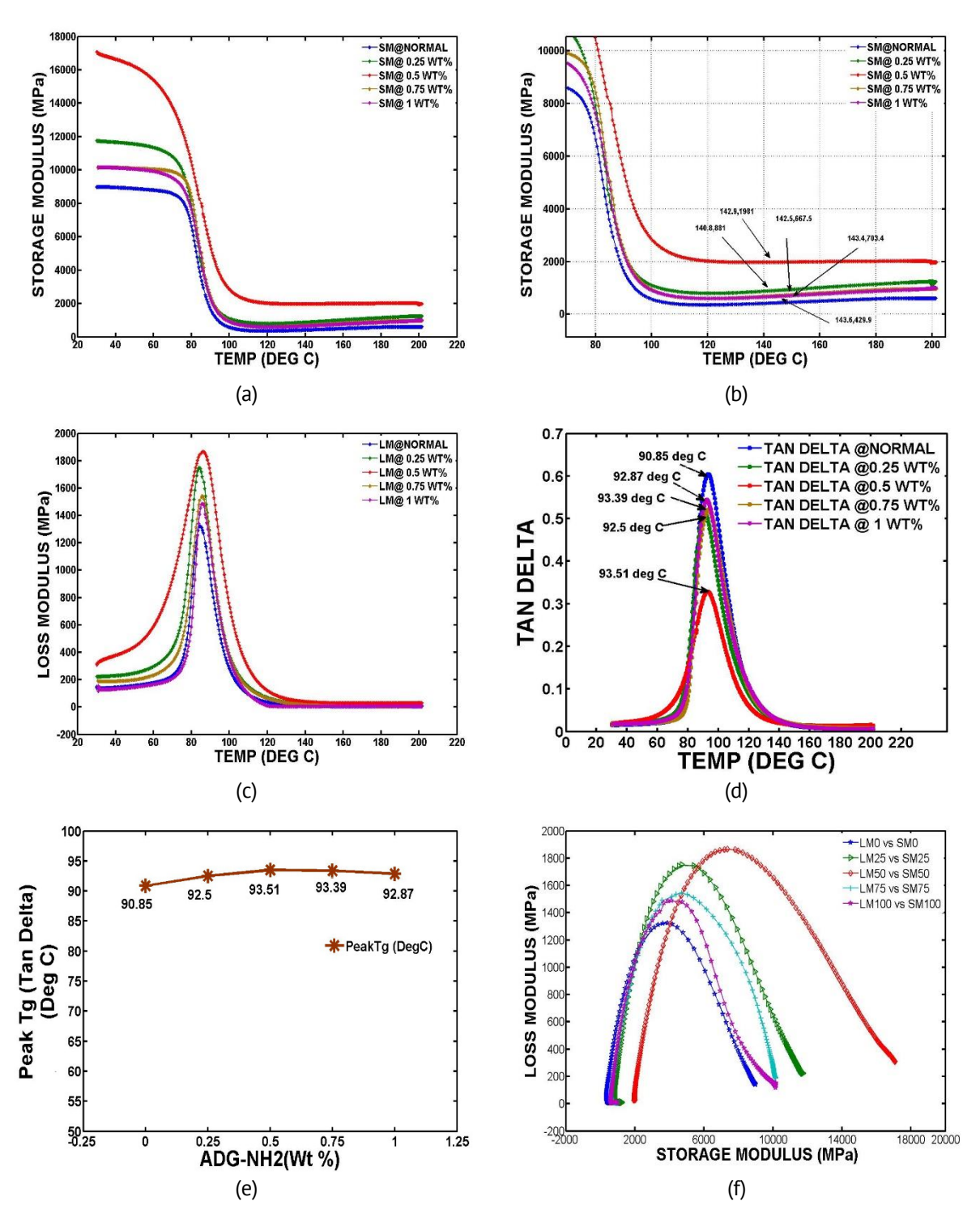


Fig. 6. Variation of (a) storage modulus vs temperature, (b) storage modulus (rescale showing T_g +50) vs temperature, (c) loss modulus vs temperature, (d) tan δ Vs temperature, (e) peak T_g w.r.t ADG-NH₂ addittion, (f) Cole-Cole plots of ADG-NH₂/epoxy/CFRP composites

of the material during the experiment, such as the glassy region (Zone 1) representing the elasticity, the rubbery transition region (Zone 2) which indicates the degradation of and decreases beyond 0.5 wt. %.

Due to the hexagonal molecular arrangement of graphene with carbon fiber atomic structure, semi compatibilty local agglomerations elasticity till it stabilizes and enters the

rubbery region (Zone 3). At 65-75 °C for all curves there is a sudden decreasing trend in all the curves indicating the end stage of the glassy region of the CFRP composite. Table 2 lists the maximum storage modulus values of the ADG-NH₂/epoxy/CFRP composite based on the experiments on the different wt. % of ADG-NH₂ in CFRP composites. As the ADG-NH₂ graphene concentration increases, E' of modified composites increased to 10325 MPa (for 0.25 wt. %), 12872 MPa (for 0.5 wt. %), 9723MPa (0.75 wt. %), 9150 MPa (1 wt. %) respectively from 8346 MPa (Neat CFRP) which corresponds to increment of 23.71, 54.22, 16.5 and 9.6 % respectively. It can be concluded from the above observations that the storage modulus increased up to 0.5 wt. % of ADG-NH₂ were formed beyond 0.5 wt. % which prevents higher elastic behavior for the rubbery transition zone across the full temperature range [36–39].

Table 2. Maximum storage modulus and loss modulus observed during the DMA of ADG-NH₂/epoxy/CFRP composite specimens

ADG-NH₂ loading,	Max storage modulus (E'),	Increase in E',	Max loss modulus E",	Increase in E",
wt. %	MPa	%	MPa	%
Neat epoxy	8346 + 41.53	0	1324 + 13.24	0
0.25	10325 + 51.63	23.71	1750 + 17.5	32.17
0.5	12872 + 64.36	54.22	1866 + 18.66	40.93
0.75	9723 + 48.62	16.5	1545 + 15.45	16.69
1	9150 + 45.75	9.6	1487 + 14.87	12.31

Figure 6(b) represents the enlarged view of storage modulus (E') values of modified composites at a temperature of T_g + 50 where the cross-link density, values are estimated for different wt. % of ADG-NH₂. Table 3 lists the cross-link density values of the modified CFRP composite using Eq. (3). The cross-link density which indicates the stiffness characteristics of the polymer structure is affected by the mobility of molecules in the polymeric chain. Its value increased up to 0.5 wt. % of ADG-NH₂ and subsequently reduced beyond 0.5 wt. %.

Table 3. Peak glass transition (T_g) and peak tg δ of ADG-NH₂ filled CFRP composites

ADG-NH ₂ loading, wt. %	Peak <i>T</i> _g , °C (loss peak)	Peak <i>T</i> g, °C (tan δ peak)	Peak tg δ	Cross link density, mol/cm ³
Neat epoxy	84.24 + 0.22	90.85 + 0.25	0.6041	0.041
0.25	84.39 + 0.25	92.5 + 0.32	0.5202	0.085
0.5	86.08 + 0.35	93.51 + 0.35	0.3284	0.191
0.75	85.72 + 0.33	93.39 + 0.33	0.5144	0.068
1	85.65 + 0.30	92.87 + 0.30	0.544	0.064

The reduction in the T_g value listed in Table 3 indicates the decrease in stiffness value of the composite material. The storage modulus values are directly related to highly cross-linked polymeric chain and vice versa [40,41].

Figure 6(c) represents the loss modulus (E'') vs temperature of modified composites at different wt. % of ADG-NH₂, which indicates the energy release by the polymer structure when subjected to cyclic loading. As illustrated in these curves the values initially increase in zone 1 i.e. glassy region and then sharply increases to the peak in Zone 2 i.e. Rubbery transition zone but sharply reduces in this region and continues up

to Zone 3 Rubbery region. It was observed that the loss modulus of approx. 41 % increased up to 0.5 wt. % of ADG-NH₂ and decreased beyond 0.5 wt. %. The inclusion of ADG-NH₂ frequently causes the loss modulus peak to broaden. This phenomenon is typically attributed to either a suppression of the relaxation process occurring inside the composite or a higher rigidity of the chain segments, hence increasing the material's heterogeneity. In the ADG-NH₂-loaded samples, the loss modulus was essentially increased for three reasons: (1) the polymer chains were unable to move freely as a result of the amino-functionalized GNP's enhancement of the crosslinking reactions between epoxy and hardener; (2) the covalent bond formed between the amino-functionalized GNP and epoxy enabled greater energy dissipation from the matrix to the aminofunctionalized GNP, and (3) demonstrating the enhanced adhesion and interfacial bonding strength between the resin matrix and carbon fiber. The addition of amino functionalized GNP raises the composites' loss modulus (E'') in comparison to the untreated composite, which in turn raises the polymer's structural mobility inside the composite. The polymer chain relaxation zones and confluence zones were observed for all the curves towards the peak loss modulus values, but relaxation zones were more for the more ADG-NH₂ graphene loading content beyond 0.5 wt. %. Peak E'' was measured at 1324, 1750, 1866, 1545 and 1487 MPa at 84.39, 84.72, 86.69, 85.33 and 85.28 °C. The increase in loss modulus values up to 0.5 wt. %, which represents the better energy dissipation and mechanical properties was may be due to the better graphene dispersion, enhancement of the cross-linking reactions between epoxy and hardener, greater energy dissipation from the matrix to the amino-functionalized GNP and enhanced fiber matrix bonding [32,42].

Figure 6(d) represents tan δ vs temperature of modified composites at different wt. % of ADG-NH₂ which indicates the damping properties as well as the material characteristics whether it is elastic or non-elastic in nature for the polymer structure. A material with a high, non-elastic strain component is indicated by a high tan δ value, whereas a low value denotes a material with high elasticity. The damping factor is governed by molecular motions and viscoelasticity, in addition to specific defects that promote damping, are dislocations, grain boundaries, phase barriers, and different interfaces. The damping factor is reduced with an increase in the bonding at the fiber/matrix interaction because of decreased mobility of the molecular chains at the fiber/matrix interface. Thus, the higher the energy losses with respect to its storage capacity, the greater will be the tan δ value in the composite system [43,44]. As depicted the curves, tan δ values obtained for different wt. % fillers 0.6041, 0.5202, 0.3284, 0.5144, 0.544 respectively for neat CFRP, 0.25, 0.5, 0.75 and 1 wt. % as listed in Table 3. The peak T_q values for all Tan δ values are shown in Fig. 6(d) and are listed in Table 3. It was observed that the peak of all the tan δ values decreased with an increase in ADG-NH2 filler content. The minimum value obtained for 0.5 wt. % represents more elasticity characteristics and better interfacial bonding compared to the maximum value obtained for neat epoxy representing better damping, energy dissipation and weak interfacial bonding between fiber and matrix interfaces [45–47].

Figure 6(e) represents the peak T_g values for different ADG/NH₂ concentrations of the CFRP matrix. The glass transition temperature T_g is defined as the temperature where (i) the middle point of E vs. temperature curve or (ii) the region where E increases with

increasing frequency at constant temperature or (iii) maximum of E' happens or (iv) maximum of tan δ arises. It was observed that a very slight increment in T_g up to 0.5 % addition of ADG/NH₂, thereafter decrement was observed.

Figure 6(f) represents the relation between the loss modulus indicating the viscoelastic material energy dissipation and storage modulus indicating the stored energy of the polymer material known as the Cole-Cole plot. These plots indicate the homogenity or hetrogenity characteristics of material w.r.t different wt. % of graphene fillers and information about the structural rigidness at high temperatures. As observed, all the curves of the composite were of a warped semicircular contour indicating their heterogeneous characteristics [48,49]. Due to localized agglomeration of the graphene particles for higher wt. % beyond 0.5, curves were displayed as imperfect semicircles indicating the viscoelastic behavior of the polymer structure [50,51].

Figure 7(a) represents the relationship between the cross-link density w.r.t ADG-NH $_2$ wt. %. Figure 7(b) represents the relationship between FWHM (full width at half maximum) of loss modulus w.r.t ADG-NH $_2$ wt. %. In both the grphs it was observed that the values are increased up to 0.5 wt. % and reduced subsequently beyond 0.5 wt. %.

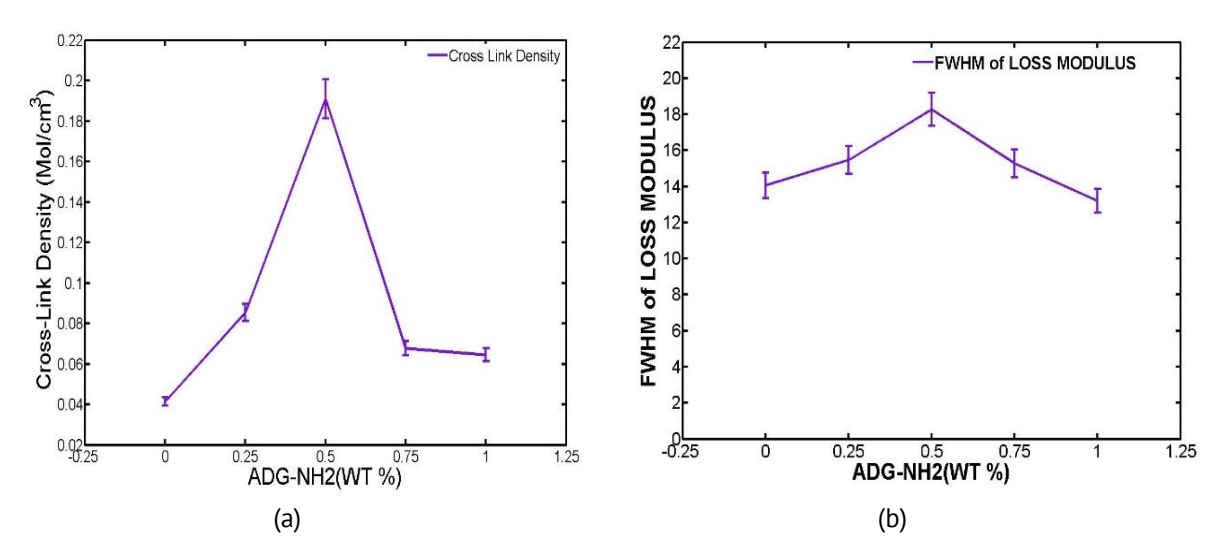


Fig. 7. Variation of (a) cross link densty Vs ADG-NH₂ filler loading corelation, (b) FWHM of loss modulus Vs ADG-NH₂ filler loading corelation

Fractographic analysis of ADG-NH₂/CFRP

SEM micrograph and XRD analysis were carried out to evaluate the physical and chemical properties along with the toughening mechanism of the ADG-NH₂ nano material for both neat epoxy and ADG-NH₂/CFRP with different wt. % filler content (0.25, 0.5, 0.75 and 1) (Fig. 8). Neat and ADG-NH₂/CFRP composites epoxy with varying filler levels (0.25, 0.5, 0.75, and 1 wt. %) were examined using SEM examination. The fracture toughness of CFRP laminate is determined by the toughness of the matrix and adherence of the carbon fibers to the matrix. Amine-functionalized graphene increases fracture toughness, because of its mechanical strength, surface area, wrinkled structure, and good interfacial adhesion with epoxy. The amine groups improve bonding with the epoxy matrix, also aiding uniform dispersion of graphene. At higher concentrations (0.75 and 1 wt. %), graphene aggregation causes stress concentration and reduced adhesion, negatively

impacting performance. SEM images confirm uniform dispersion in lower concentrations but show exposed fibers and poor bonding at 1 wt. %, explaining the decline in mechanical performance at higher filler contents.

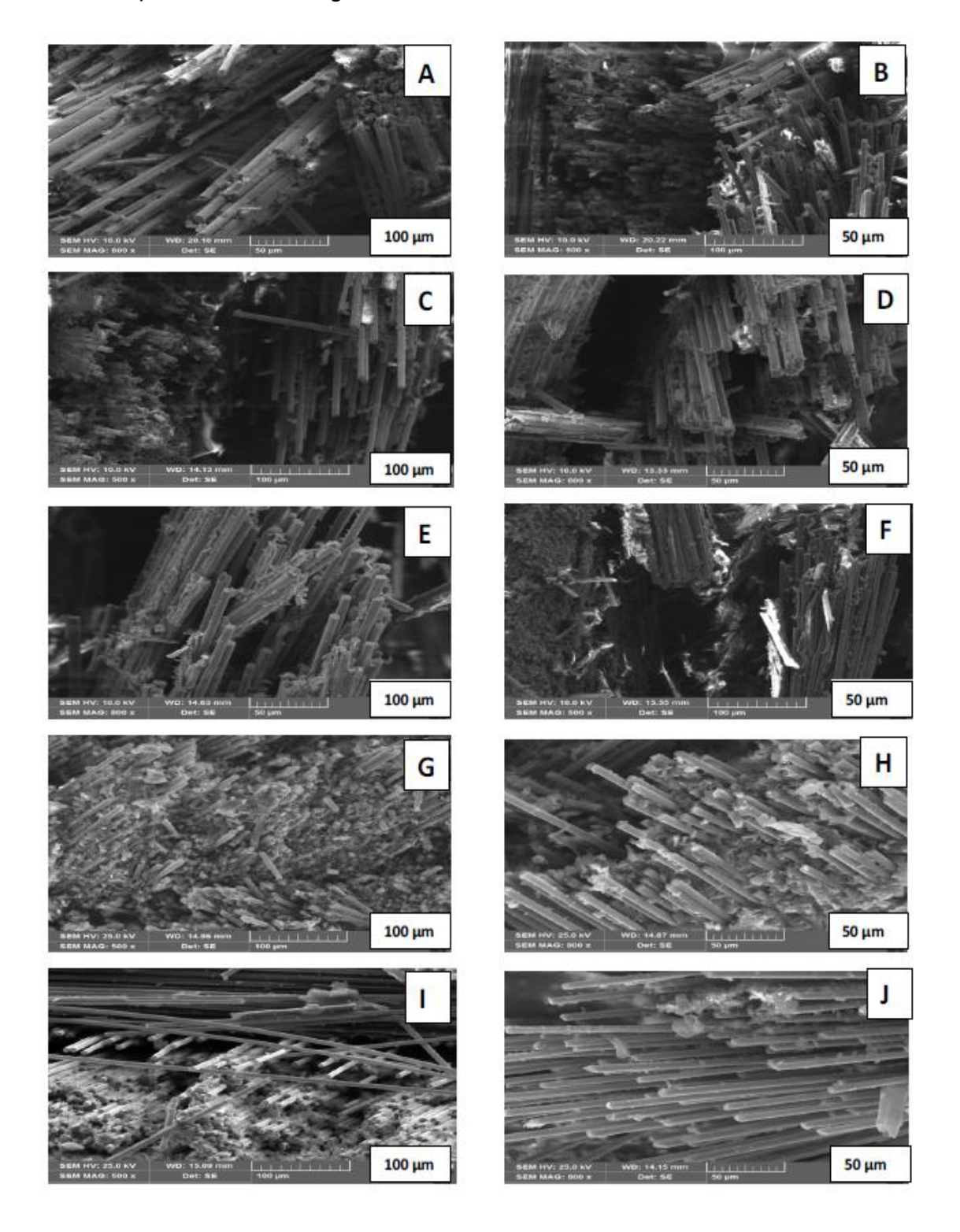


Fig. 8. SEM images of (A,B) CFRP with neat epoxy (100 μ m) & (50 μ m), (C,D) CFRP with 0.25 wt. % of graphene (100 μ m) & (50 μ m), (E,F) CFRP with 0.5 wt. % of graphene (100 μ m) & (50 μ m), (G,H) CFRP with 0.75 wt. % of graphene (100 μ m) & (50 μ m) (I,J) CFRP with 1 wt. % of graphene (100 μ m) & (50 μ m)

SEM pictures show weak mechanical properties due to brittle fracture behavior, exposed carbon fibers, and poor bonding in neat epoxy matrix. In contrast, aminefunctionalized graphene strengthens adhesion, as demonstrated by the firmly bonded carbon fibers in matrix material. As shown in Fig. 8(e,f), fractured samples with 0.5 wt. %, graphene exhibits the best interfacial strength and rough fracture surfaces, indicating plastic deformation and crack deflection. Increased surface area and energy absorption during fracture propagation are indicated by dimples, which enhance mechanical characteristics. Performance is adversely affected by graphene aggregation at higher concentrations (0.75 and 1 wt. %), which results in stress concentration and decreased adhesion in Fig. 8(g,h,l,j). The decrease in mechanical performance at increasing filler amounts can be explained by SEM images, which show exposed fibers and weak bonding at 1 wt. % but demonstrate homogeneous dispersion at lower concentrations.

X-ray diffraction (XRD) analysis was carried out on the ADG-NH₂/CFRP composite laminate to evaluate the crystallinity and interlayer distance of the nano materials. The XRD image pattern for the neat epoxy CFRP indicates that the primary peak (002) was observed at $\sim 24.89^\circ$, which represents an interlayer distance of ~ 0.357 nm, along with the (004) peak occurring at 44.60°. The XRD image pattern for ADG-NH₂/CFRP composite laminates with different wt. % filler content (0.25, 0.5, 0.75 and 1) indicates the primary

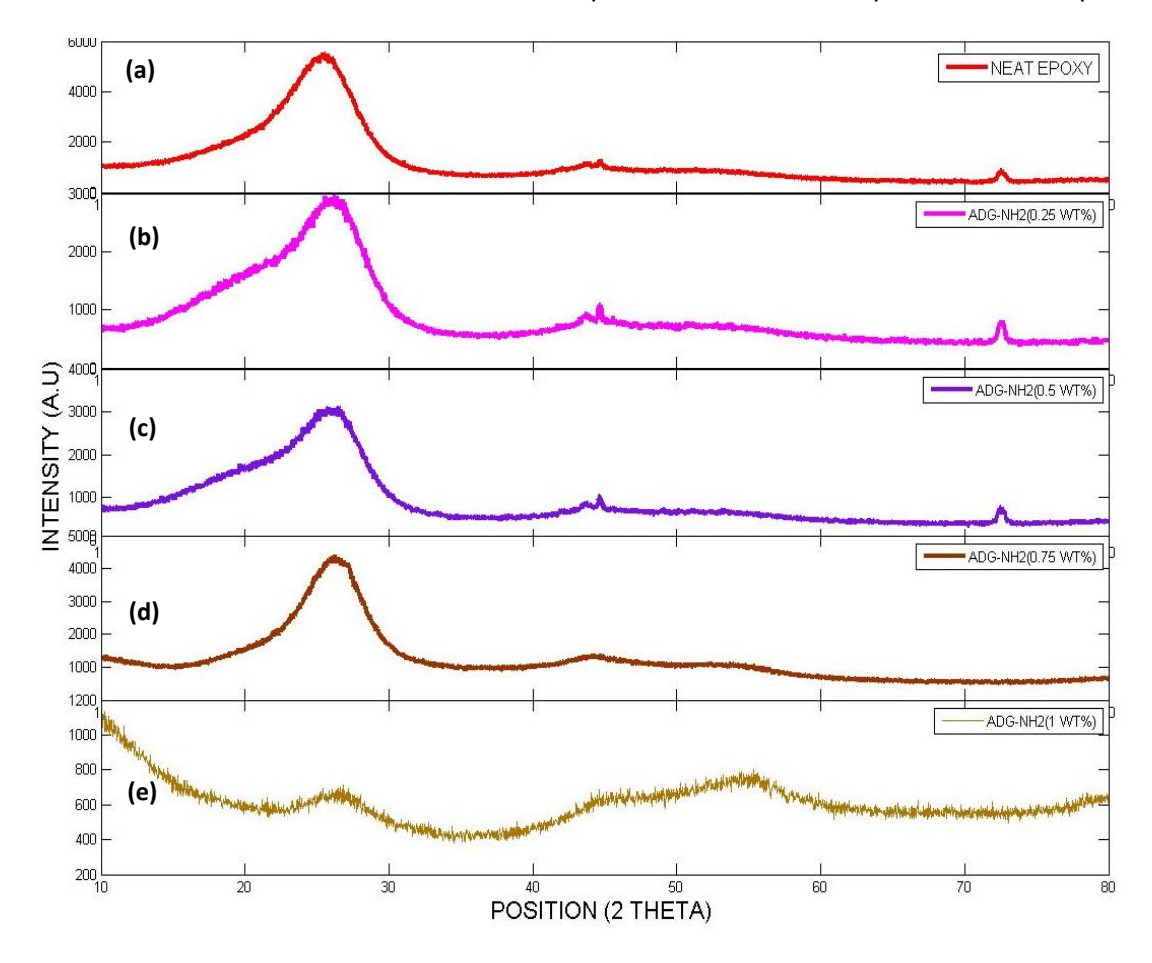


Fig. 9. XRD patterns of (a) CFRP with neat epoxy with peak 2θ =24.89°, (b) CFRP with 0.25 wt. % of graphene with peak 2θ =26.80°, (c) CFRP with 0.5 wt. % of graphene with peak 2θ =26.65°, (d) CFRP with 0.75 wt. % of graphene with peak 2θ =25.78°

(002) peak were present at ~ 26.80 , ~ 26.65 , ~ 26.90 , $\sim 25.78^\circ$ respectively which corresponds to an interlayer distance of ~ 0.332 , ~ 0.334 , ~ 0.331 , ~ 0.334 nm, respectively (Fig. 9). These XRD patterns indicate that the impurities or enormous amounts of dislocated or corrugated carbon samples are not available in the composite laminates. These diffraction patterns of the profile peaks also indicate the high degree of crystallinity in the composite laminates.

Conclusions

In order to evaluate the effect of Amine functionalized graphene (ADG-NH₂) reinforced CFRP composites on thermal properties, various specimens of different wt. % have been prepared as per ASTM requirements. The fractographic study indicates encouraging thermal properties due to an improved adhesion mechanism influenced by the homogenous dispersion of amine functionalization of graphene (ADG-NH₂).

The results of thermal characterization of modified composites evaluated through DMA reveal that an increase of ~ 55 and ~ 41 % was observed for the storage modulus and loss modulus at 0.5 wt. % of ADG-NH₂ graphene content compared to the neat epoxy, CFRP composites indicating better elasticity, viscoelastic properties and energy dissipation capabilities. The minimum tan delta values were obtained for 0.5 wt. % of ADG-NH₂ graphene content compared to neat epoxy indicating better damping , energy dissipation and superior interfacial bonding between fiber and matrix interfaces. As observed from the loss modulus curves and tan δ curves the T_g values were also observed to be improved by ~ 2 % compared to neat epoxy CFRP. Fractographic analysis from SEM and XRD clearly demonstrates the improvement of layer adhesion for increasing loading content up to compared to neat epoxy CFRP. This work demonstrates the distinct enhancements in thermal properties of laminates compared to previous results due to homogeneous dispersion of GNP in ADG-NH₂-epoxy CFRP composite and better load transfer in nanomaterial.

CRediT authorship contribution statement

Conflict of interest

The authors declare that they have no conflict of interest.

References

- 1. Chiou YC, Chou HY, Shen MY. Effects of adding graphene nano platelets and nano carbon aerogels to epoxy resins and their carbon fiber composites. *Materials & Design*. 2019;178: 107869.
- 2. Bhanuprakash L, Parasuram S, Varghese S. Experimental investigation on graphene oxides coated carbon fibre /epoxy hybrid composites: Mechanical and electrical properties. *Composites Science and Technology.* 2019;179: 134–144.

- 3. Sayam A, Rahman ANMM, Rahman MS, Smriti SA, Ahmed F, Rabbi MF, Hossain M, Faruque MO. A review on carbon fiber-reinforced hierarchical composites: Mechanical performance, manufacturing process, structural applications and allied challenges. *Carbon Letters*. 2022;32(5): 1173–1205.
- 4. Ou Y, González C, Vilatela JJ. Interlaminar toughening in structural carbon fiber / epoxy composites interleaved with carbon nanotube veils. *Composites Part A: Applied Science and Manufacturing*. 2019;124: 105477.
- 5. Li N, Wang GD, Melly SK, Peng T, Li YC, Zhao QD, Ji SD. Interlaminar properties of GFRP laminates toughened by CNTs bucky paper interlayer. *Composite Structures*, 2019;208: 13–22.
- 6. Ackermann C, Demleitner M, Guhathakurta J, Carosella S, Ruckdäschel H, Simon S, Middendorf P. Mechanical, thermal, and electrical properties of amine-and non-functionalized reduced graphene oxide/epoxy carbon fiber-reinforced polymers. *Polymer Composites*. 2023;44(8): 4937–4954.
- 7. Raj MKA, Muthusamy S, Panchal H, Ibrahim AMM, Alsoufi MS, Elsheikh AH. Investigation of mechanical properties of dual-fiber reinforcement in polymer composite. *Journal of Materials Research and Technology.* 2022;18: 3908–3915.

 8. Burger N, Laachachi A, Ferriol M, Lutz M, Toniazzo V, Ruch D. Review of thermal conductivity in composites: Mechanisms, parameters and theory. *Progress in Polymer Science.* 2016;61: 1–28.
- 9. Ma J, Q Meng, I Zaman, S Zhu, A Michelmore, N Kawashima, CH Wang, HC Kuan, Development of polymer composites using modified, high-structural integrity graphene platelets. *Composites Science and Technology*. 2014;91: 82–90.
- 10. Ahmadi-Moghadam B, Sharafimasooleh M, Shadlou S, Taheri F. Effect of functionalization of graphene nanoplatelets on the mechanical response of graphene/epoxy composites. *Materials & Design (1980-2015)*. 2015;66: 142–149.
- 11. Fang H, Bai SL, Wong CP. Microstructure engineering of graphene towards highly thermal conductive composites. *Composites Part A: Applied Science and Manufacturing*. 2018;112: 216–238.
- 12. Shen L, Zhang X, Lei Y, Liang M, Chen Y, Chen W, Zou H. Efficient reinforcement of epoxy resin with amine-rich rigid short-chain grafted graphene oxide. *Polymer Composites*. 2021;42(9): 4775–4785.
- 13. Cai Z, Meng X, Han Y, Ye H, Cui L, Zhou Q. Reinforcing polyamide 1212 with graphene oxide via a two-step melts compounding process. *Composites Part A: Applied Science and Manufacturing*. 2015;69: 115–123. 14. Li Y, Zhang H, Porwal H, Huang Z, Bilotti E, Peijs T. Mechanical, electrical and thermal properties of in-situ
- exfoliated graphene/epoxy nano composites. *Composites Part A: Applied Science and Manufacturing*. 2017;95: 229–236.

 15. Chee SS, Jawaid M, Sultan MTH, Alothman OY, Abdullah LC. Thermo mechanical and dynamic mechanical properties
- of bamboo/woven kenaf mat reinforced epoxy hybrid composites. *Composites Part B: Engineering.* 2019;163:165–174. 16. Costa C, Fonseca AC, Serra AC, Coelho JFJ. Dynamic mechanical thermal analysis of polymer composites
- 16. Costa C, Fonseca AC, Serra AC, Coelho JFJ. Dynamic mechanical thermal analysis of polymer composites reinforced with natural fibers. *Polymer Reviews*. 2016;56(2): 362–383.
- 17. Md Shah AU, Sultan MTH, Jawaid M. Sandwich-structured bamboo powder/glass fibre-reinforced epoxy hybrid composites-Mechanical performance in static and dynamic evaluations. *Journal of Sandwich Structures & Materials*. 2021;23(1): 47–64.
- 18. Saba N, Jawaid M, Alothman OY, Paridah MT. A review on dynamic mechanical properties of natural fibre reinforced polymer composites. *Construction and Building Materials*. 2016;106: 149–159.
- 19. Zeki C, Gardner DJ, Shaler SM. Dynamic mechanical thermal analysis (DMTA) of cellulose nano fibril / nano clay / pMDI nano composites. *Composites Part B. Engineering*. 2016;90: 126–132.
- 20. Saba N, Safwan A, Sanyang ML, Mohammad F, Pervaiz M, Jawaid M, Alothman OY, Sain M. Thermal and dynamic mechanical properties of cellulose nano fibers reinforced epoxy composites. *International Journal of Biological Macromolecules*. 2017;102: 822–828.
- 21. Atiqah A, Jawaid M, Sapuan SM, Ishak MR, Alothman OY. Thermal properties of sugar palm/glass fiber reinforced thermoplastic polyurethane hybrid composites. *Composite Structures*. 2018;202: 954–958.
- 22. Gupta A, Hasanov S, Fidan I. Thermal characterization of short carbon fiber reinforced high temperature polymer material produced using the fused filament fabrication process. *Journal of Manufacturing Processes*. 2022;80: 515–528. 23. Yadav A, Kumar A, Singh PK, Sharma K. Glass transition temperature of functionalized graphene epoxy composites using molecular dynamics simulation. *Integrated Ferroelectrics*. 2018;186(1): 106–114.
- 24. Kumar A, Sharma K, Dixit AR. Carbon nanotube-and graphene-reinforced multiphase polymeric composites: review on their properties and applications. *Journal of Materials Science*. 2020;55(7): 2682–2724.
- 25. Kumar A, Sharma K, Dixit AR. A review of the mechanical and thermal properties of graphene and its hybrid polymer nano composites for structural applications. *Journal of Materials Science*. 2019;54(8): 5992–6026.
- 26. Jesuarockiam N, Jawaid M, Zainudin ES, Thariq Hameed Sultan M, Yahaya R. Enhanced thermal and dynamic mechanical properties of synthetic/natural hybrid composites with graphene nanoplateletes. *Polymers*. 2019;11(7):1085.
- 27. Rashmi BJ, Prashantha K, Lacrampe MF, Krawczak P. Scalable production of multifunctional bio-based polyamide 11/graphene nano composites by melt extrusion processes via masterbatch approach. *Advances in Polymer Technology*. 2018;37(4): 1067–1075.

139 D.N. Choudhury, S.K. Panda

28. Chinnasamy S, Ramachandran M, Kurinjimalar Ramu PA. Study on fuzzy ELECTRE method with various methodologies. *REST Journal on Emerging trends in Modelling and Manufacturing*. 2022;7(4): 108–115.

- 29. Choudhury DN, Pareta AS, Rajesh AK, Panda SK. Enhanced mechanical and interfacial performances of carbon fiber reinforced composites with low percentage of amine functionalized graphene. *Polymer Composites*. 2024;45(15):13772–13790. 30. Choudhury DN, Panda SK. Effect of ADG-NH₂ functionalized graphene on fracture and impact resistance of carbon fiber reinforced composites. To be published in *Res. Eng. Struct. Mat.* [Preprint] 2025. Available from: dx.doi.org/10.17515/resm2025-588me1224rs.
- 31. International Organization for Standardization. ISO 11358-1:2022. *Plastics Thermogravimetry (TG) of polymers Part 1: General principles.* ISO; 2022.
- 32. Mushtaq, H. B. Mukhtar, A. M. Shariff. Effect of glass transition temperature in enhanced polymeric blend membranes. *Procedia Engineering*. 2016;148: 11–17.
- 33. American Society for Testing and Materials. ASTM D7028-07(2015). *Standard Test Method for Glass Transition Temperature* (DMA Tq) of Polymer Matrix Composites by Dynamic Mechanical Analysis (DMA). West Conshohocken, Pa, USA: ASTM; 2015.
- 34. Doyle CD. Estimating thermal stability of experimental polymers by empirical thermo gravimetric analysis. *Analytical Chemistry*. 1961;33(1): 77–79.
- 35. Szeluga U, Kumanek B, Trzebicka B. Synergy in hybrid polymer/nano carbon composites. A review. *Composites Part A: Applied Science and Manufacturing*. 2015;73: 204–231.
- 36. Yue L, Pircheraghi G, Monemian SA, Manas-Zloczower I. Epoxy composites with carbon nanotubes and graphene nano platelets Dispersion and synergy effects. *Carbon*. 2014;78: 268 278.
- 37. Costa C, Fonseca AC, Serra AC, Coelho JFJ. Dynamic Mechanical Thermal Analysis of Polymer Composites Reinforced with Natural Fibers. *Polymer Reviews*. 2016;56(2): 362–383.
- 38. Chen H, Ginzburg VV, Yang J, Yang Y, Liu W, Huang Y, Du L, Chen B. Thermal conductivity of polymer-based composites: Fundamentals and applications. *Progress in Polymer Science*. 2016;59: 41–85.
- 39. Hossain MK, Chowdhury MMR, Hosur M, Bolden NW. Viscoelastic Properties of Carbon/Epoxy Amino-Functionalized Graphene Nano platelet Composite. *ASME International Mechanical Engineering Congress and Exposition*. 2016;50633: V009T12A027.
- 40. Prolongo SG, Gude MR, Ureña A. Improving the flexural and thermo mechanical properties of amino-functionalized carbon nanotube/epoxy composites by using a pre-curing treatment. *Composites Science and Technology*. 2011;71(5): 765–771.
- 41. Cai Z, Meng X, Han Y, Ye H, Cui L, Zhou Q. Reinforcing polyamide 1212 with graphene oxide via a two-step melt compounding process. *Composites Part A: Applied Science and Manufacturing*. 2015;69: 115–123.
- 42. Jesuarockiam N, Jawaid M, Zainudin ES, Thariq Hameed Sultan M, Yahaya R. Enhanced thermal and dynamic mechanical properties of synthetic/natural hybrid composites with graphene nano plateletes. *Polymers*. 2019;11(7):1085.
- 43. Rasana N, Jayanarayanan K, Deeraj BDS, Joseph K. The thermal degradation and dynamic mechanical properties modeling of MWCNT/glass fiber multiscale filler reinforced polypropylene composites. *Composites Science and Technology.* 2019;169: 249–259.
- 44. Kang WS, Rhee KY, Park SJ. Thermal, impact and toughness behaviours of expanded graphite/graphite oxide-filled epoxy composites. *Composites Part B: Engineering*. 2016;94: 238–244.
- 45. Wang J, Ma F, Sun M. Graphene, hexagonal boron nitride, and their hetero structures: properties and applications. *RSC Advances*. 2017;7(27): 16801–16822.
- 46. Badgayan ND, Sahu SK, Samanta S, Sreekanth PR. Evaluation of dynamic mechanical and thermal behavior of HDPE reinforced with MWCNT/h-BNNP: an attempt to find possible substitute for a metallic knee in transfemoral prosthesis. *International Journal of Thermophysics*. 2019;40: 93.
- 47. Chee SS, Jawaid M, Sultan MTH, Alothman OY, Abdullah LC. Thermo mechanical and dynamic mechanical properties of bamboo/woven kenaf mat reinforced epoxy hybrid composites. *Composites Part B. Engineering*. 2019;163:165–174. 48. Li Y, Zhang H, Porwal H, Huang Z, Bilotti E, Peijs T. Mechanical, electrical and thermal properties of in-situ exfoliated graphene/epoxy nano composites. *Composites Part A: Applied Science and Manufacturing*. 2017;95:229–236. 49. Chandrasekhar GL, Vijayakumar Y, Nagaral M, Rajesh A, Manjunath K, Kaviti RVP, Auradi V. Synthesis and tensile behavior of Al7475-nano B4C particles reinforced composites at elevated temperatures. *Materials Physics and Mechanics*. 2024;52(3): 44–57.
- 50. Lamba NK. Quasi-static thermal response of a circular plate due to the influence of memory-dependent derivatives. *Materials Physics and Mechanics*. 2024;52(4): 163–172.
- 51. Pozdnyakov AO, Sedakova EB. Thermal analysis of wear of polymer-polymer friction pairs in vacuum and atmosphere conditions. *Materials Physics and Mechanics*. 2024;52(4): 63–80.

Submitted: February 15, 2025 Revised: February 23, 2025 Accepted: June 5, 2025

Structural and thermal changes in the polyaniline lead sulphide nanocomposite

J.B. Bhaiswar ^{1 | 2 |}, S.P. Dongre ², D. Meghe ¹

- ¹ Nagpur Institute of Technology, Nagpur, India
- ² Bhalerao Science College Saoner, India

ABSTRACT

In this study, composite films of PbS nanoparticles and PANI were used. The PbS/PANI samples were analyzed using XRD, UV-visible, FT-IR and TEM. Furthermore, the effects of PbSNPs on their optical, structural and thermal parameter were determined using DTA, UV-Visible and XRD. The UV and XRD confirmed the successful synthesis of PbS/PANI Nanocomposite. The TEM indicated homogeneous dispersion of PbS in PANI with average diameter of particle is 20nm. Besides, the broadness and reduction of PANI in XRD peaks intensity with increasing PbS is attributed to the intermolecular interactions of PANI and PbS and indicates the successful incorporation of PbS in PANI. The thermal stability was enhanced at different weight percentages of PbS nanoparticle indicated in DTA analysis. The structural changes in the Pbs nanocomposite observed in the XRD.

KEYWORDS

DTA • thermal analysis • polyaniline • Pbs • TEM • nanocomposite

Citation: Bhaiswar JB, Dongre SP, Meghe D. Structural and thermal changes in the polyaniline lead sulphide nanocomposite. *Materials Physics and Mechanics*. 2025;53(3): 140–148.

http://dx.doi.org/10.18149/MPM.5332025_11

Introduction

Polymer composites are comprehensively used in vehicle, flying, advancement, and electronic applications [1-5]. It was focused on mechanical, electrical, warm and other genuine properties. The nanocomposites are one more class of materials that exhibit superior properties compared to microcomposites [6-9]. A little development of nanoparticles essentially deals with different properties without relinquishing the light weight of polymer lattices. The nanocomposites generally suggest composites in which something like one phase has viewpoint on the solicitation for several nanometers. They can be made with the used of three particular kinds of nanoparticles. The vital sort of nanoparticles simply has one angle in the nanometer scale. They have a platelet-like development [10-14]. Soil is a certifiable delineation of the sort of nanoparticles. Another sort of nanoparticles has two parts of the nanoparticles in the nanometer scale. Nanotubes and nanofibers have a spot with this get-together [15-17]. The third sort of nanoparticles has every one of the three angles in the nanometer scale, for example, round silica particles. A collection of the sort of particles is outstandingly retentive particles. While the component of the particle may be in the solicitation for microns, the pore sizes are in the solicitation for nanometers [18,19].



[™] jitendrabhaiswar@gmail.com

The filling of nanoscopic metals into polymer lattices tends to a decision to course and change issues. For sensible purposes of nanoparticles, polymers are on a very basic level required as filling stage since they would have different qualities: they can be an electrical and warm encasing or conveyor [20]. Polymers could have a hydrophobic or hydrophilic nature and can be definitively hard plastic or flexible versatile, and so on. Ultimately, polymer filling is the least complex and most sensible way for nanostructures metal change, treatment, and application [21-23]. This has fuelled assessment concerning the preparation of metal-polymer nanocomposites. These composites most generally show up as small polymer films or powders, as this is commonly the least demanding development to design, and moreover extraordinary for exploiting the best properties. The Readiness methodologies of polymer metal nanocomposite can be named in-situ and ex-situ procedures. In the in-situ systems, the monomer is polymerized, with metal particles introduced already or after polymerization [24-26]. Then, the metal particles in the polymer structure are reduced falsely, thermally or by UV (ultraviolet) brightening, to shape nanoparticles [27]. In the ex-situ process, the metal nanoparticles are consolidated first, and their surface is normally passivized. In the current paper, Polyaniline/PbS nanocomposite arranged, and it gets examination with DTA (differential thermal analysis) for warm boundary and their solidness.

Materials and Methods

Compound combination of Polyaniline involving APS as oxidant and H_2SO_4 (Fig. 1). Unadulterated aniline broke down in 100 ml refined water with H_2SO_4 added under attractive blending for 2 h. The arrangement of ammonium per sulfate in sulphuric corrosive was then added drop-wise in the arrangement of aniline. The encourage of polyaniline acquired with dim green cloured [28]. The encourage washed with water. A PANI encourage was dried under at 50–100 °C for over 8 h. Blend of PANI/PbS nanocomposites a similar blend process was adjusted for readiness of PANI/PbS nanocomposite at various weight proportion of PbS nanoparticle. PANI nanocomposite was synthetically portrayed by infrared spectroscopy, XRD (X-ray diffraction) and TGA (thermogravimetric analysis).

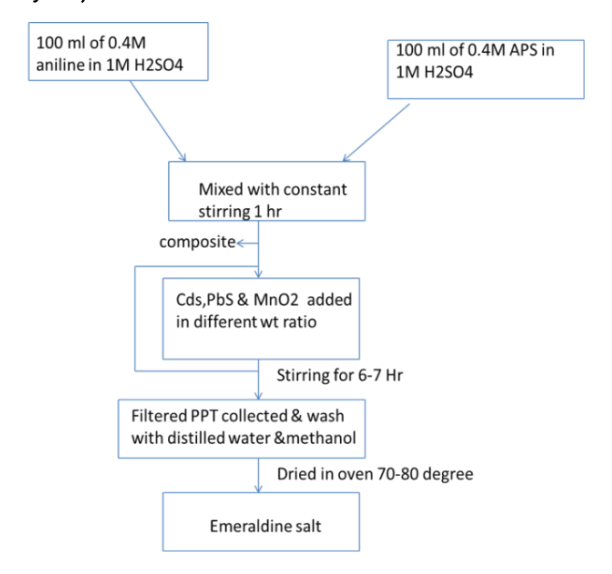


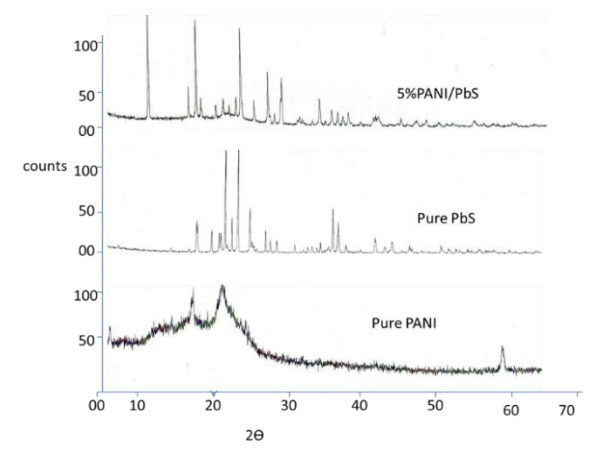
Fig.1. Scheme of synthesis of polyaniline and nanocomposite

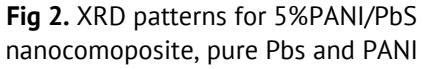
Characterization of nanocomposites

XRD with Philips PW-3071, utilizing Cu-K α radiation of frequency 1.544 Å, with examining pace of 2 °/min at 45 kV and 40 mA. Fourier transform infrared (FTIR) spectroscopy (Perkin Elmer 200) with recurrence of 400-4000 cm⁻¹. Warm examination of test recorded by Perkin-Elmer Precious stone TGA/DTA in argon air at a warming pace of 10 °/min.

XRD characterization of pure PANI and PANI/PbS Nano composite

The XRD patterns of unadulterated PANI and PbS and different wt. % of PANI/PbS nanocomposite are displayed in Figs. 2 and 3. The molecule size of translucent molecule of unadulterated PANI and the nanocomposites are determined by utilizing the Debye-Scherrer equation: $D = 0.94\lambda/\beta\cos\theta$, where D is the typical crystallite size (nm), k is the shape factor, which is much of the time relegated a worth of 0.94, λ is the frequency of Cu K α radiation (1.5418 Å), β is the full width at half limit of the diffraction top thinking about the revision because of instrumental widening (0.09°). Translucent size of glasslike molecules for unadulterated PANI, unadulterated PbS and different content (wt. %) of PANI/PbS nanocomposite are given in Table 1. From the reference diagram of XRD top plainly as 5-20 wt. % PbS nanoparticle expansions in the PANI lattice the level of crystallites of nanocomposite additionally increments. Unadulterated PANI shows glasslike reflection at explicit point in XRD and undefined at diffused foundation, accordingly it uncovers the polycrystalline construction. It is observed that degree of crystallinity increased in the nanocomposite as compared to pure PANI and PbS, indicated the structural and surface morphological changes in the nanocomposite. Nanocomposite is crystalline and has a more ordered structure compared to pure polyaniline.





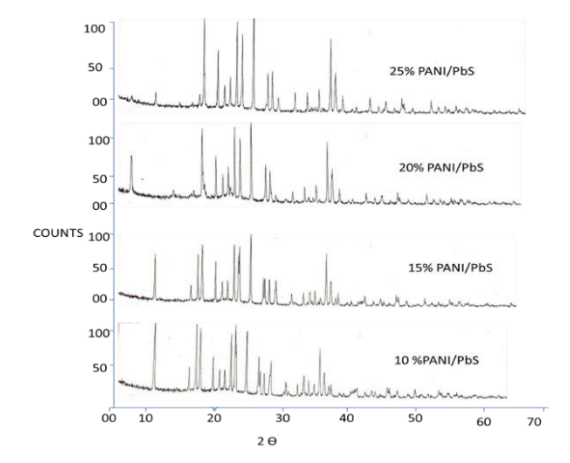


Fig. 3. XRD patterns for PANI/PbS nanocomposites with different contents of PANI

Table.1. Table indicated crystalline size of particle in nanocomposite

Sr. No	Material	Crystalline size particle, nm	D'spacing, Å	20,°
1	PURE PANI	0.710	3.520	25.270
2	PURE PbS	0.950	3.210	27.770
3	5% PANI/PbS	1.048	3.230	27.560
4	10% PANI/PbS	1.420	3.240	27.470
5	15% PANI/PbS	1.230	3.012	29.650
6	20% PANI/PbS	1.437	3.009	29.680
7	25% PANI/PbS	1.438	3.0096	29.650

Ultraviolet and visible (UV-Vis) spectroscopy of PANI/PbS nanocomposite

The most extreme assimilation frequency of unadulterated PbS and PANI/PbS nanocomposite are displayed in the (Fig. 4). In unadulterated PbS the retention frequency is getting at 263, 277 and 768 nm. It was interesting that the presence of retention groups at 400 to 500 nm in PANI/PbS nanocomposite were found. Because this band is absent from unadulterated PANI as well as unadulterated PbS. This fact demonstrated that when PbS nanoparticle collaborates with PANI some underlying change happened. The presence of this band in the nanocomposite gives the photoluminous qualities. The polaron- π^* transition band at 320 to 385 nm turns out to be more extensive and shows the red shift. This infers that the doping condition of the nanocomposites has been moved along. Such peculiarities can be credited to the presence of more noteworthy number of charges on the polymer spine by bringing nanocrystalline PbS into the polymer matrix [16].

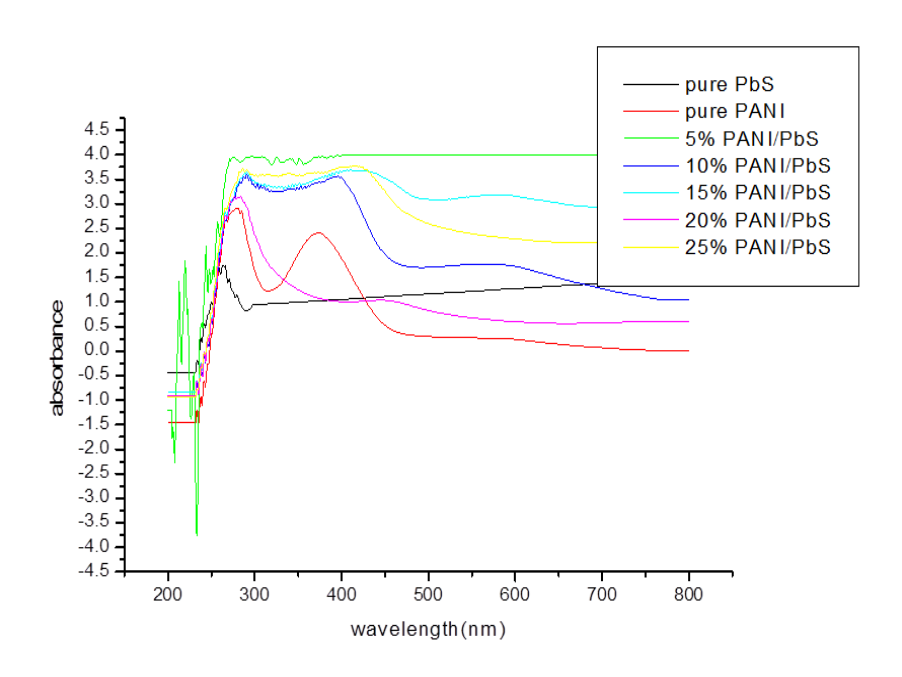


Fig. 4. UV-Vis absorption spectra of PbS/PANI nanocomposite at different wavelength

Fourier transforms infrared spectroscopy of PANI/PbS nanocomposite

Figure 5 shows FTIR spectra of pure polyaniline and PANI/PbS nanocomposites with different content (wt. %) of PbS. The incorporation of PbS nanoparticles caused the shift of some peaks of PANI and PbS. The absorption peak corresponds to polyaniline at 1566 shows red shift to 1561, 1557, 1516 and 1561 cm⁻¹ respectively at 5%PbS, 10%PbS, 15%PbS, and 20%PbS nanocomposites. The absorption peak at 1485 showed a blue shift with respect to pure PANI peak, and they were moved to 1496, 1498, 1493 and 1495 cm⁻¹ respectively at 5%PbS, 10%PbS, 15%PbS, and 20%PbS nanocomposites. Similarly, the peak at 1284, 1284, 1290 cm⁻¹, showed a blue shift with respect to pure PANI peak at 5, 10 and 20%PANI/PbS nanocomposites. But in 15%PANI/PbS nanocomposite the peak shows the blue shift as compared to pure PANI peak. The absorption peak at 1107 showed a blue shift with respect to pure PANI peak at 1179 cm⁻¹

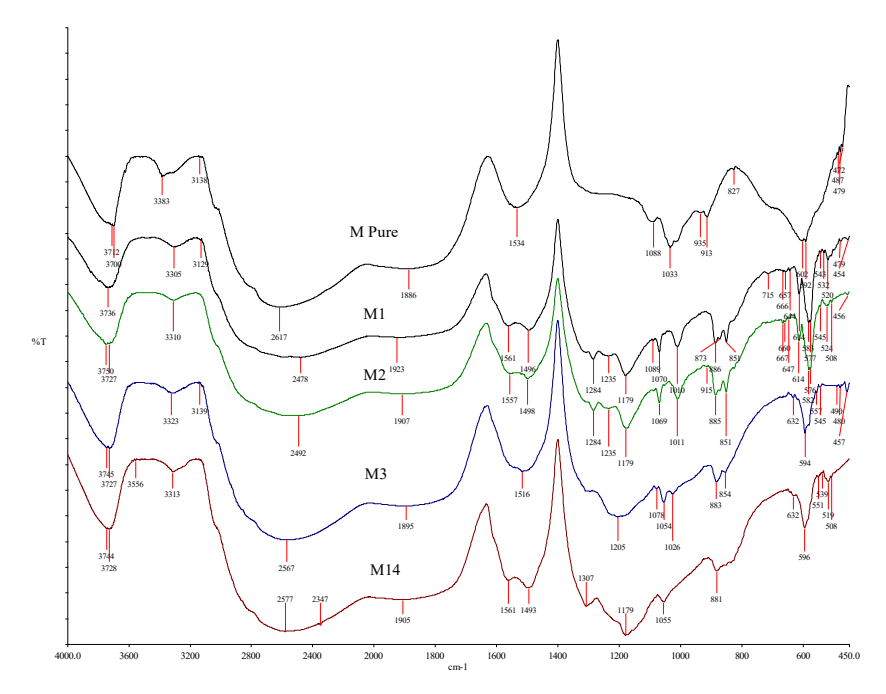


Fig. 5. FT-IR spectra of pure PANI and PANI/PbS nanocomposite

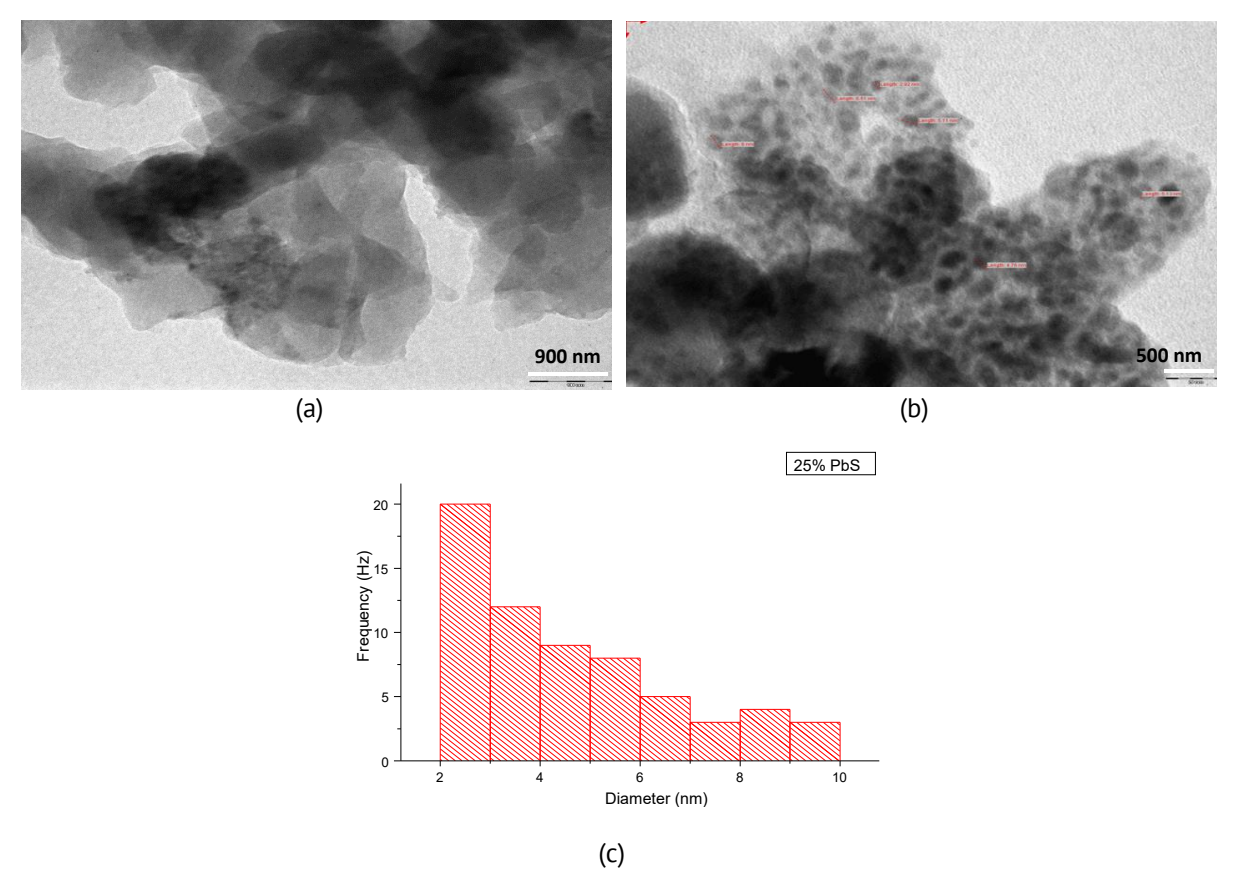


Fig. 6. TEM images of (a) pure PANI and (b) PANI/PbS nanocomposite, and average (c) diameter of particle size of nanocomposite

for 5, 10 and 20%PANI/PbS nanocomposites. PbS and PANI formed a coordination bond, and the electrons transferred from PANI to PbS which led to weakened bond strengths and the conjugated system of PANI and thus weakened vibration of PANI. The band in the

regions over 400 cm⁻¹ can be assigned to PbS stretching vibrations FTIR spectra of the PANI/PbS nanocomposite are similar to those of PANI, but the bands' characteristic of polymer backbone at 1400 and 1500 cm⁻¹ are shifted to higher values after annealing, indicating deprotonation. The peak at 1107 cm⁻¹ is suppressed after annealing to a greater extent for PANI compared to that for the nanocomposites, indicating a higher extent of deprotonation in pure PANI compared to nanocomposites. The results of FTIR spectra confirm the presence of both components in the nanocomposite.

Transmission electron microscopy of PANI/Pbs nanocomposite

Transmission electron microscopy (TEM) images (Fig. 6) show the morphology of unadulterated PbS and PANI/PbS nanocomposite doped H₂SO₄. TEM image of (10 %) PANI/PbS nanocomposite (Fig. 6(b)) shows that particles were collected into a major construction, albeit the particles were in touch with one another. Most of the particles are comparative size and have unpredictable adjusted shapes. When content (wt. %) of PbS nanoparticle expanded in the polymer, then molecule size diminished (Fig. 6(c)). The nanocomposite turns out to be more arranged structure, consequently electrical conductivity is likewise expanded [29,30]. This is additionally clear by XRD and UV spectra. The typical distance across nanoparticles is 12 nm territory.

DTA analysis of pure PANI and PANI nanocompposite

Figure 7 shows DTA thermogram of PANI/PbS (5 to 25 %) nanocomposite, which showed just endothermic tops at around 230 to 245 °C because of the vanishing of water particles caught inside the composite or bound to the polymer spine. while the change above 350 °C might be alloted because of the corruption of composite. The diminished beginning worth of temperatures from 284 °C (unadulterated PANI) to 242.59, 244.15, 233.06, 227.55 and 237.25 °C for various wt. % of (5–25 %) PANI/PbS nanocomposite demonstrated that the warm steadiness of nanocomposite is greater than that of

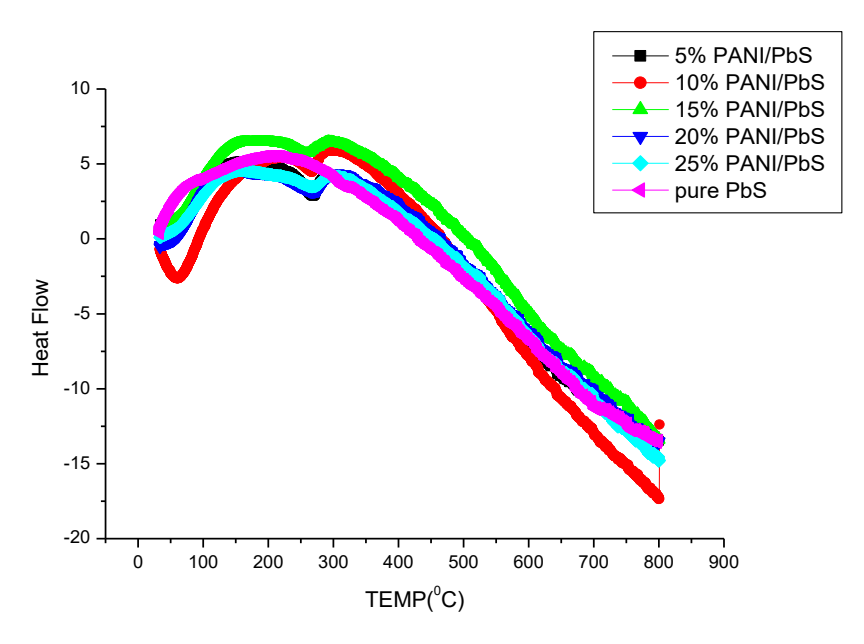


Fig. 7. The graph of differential thermal analysis of pure PbS and PANI/PbS (5-25%) nanocomposites

unadulterated PANI which could be credited to the impediment impact of nanostructures PbS as hindrances for the debasement of PANI [28–30]. In DTA of PANI the glass progress was not recognizable, in light of the fact that the glass change is covered in the top because of the evacuation of water and it doesn't display hysteresis. The exothermic progress at 99–160 °C is accepted not to be Tg. Rather it would be credited to a progression of compound responses. The diminished pinnacle temperatures of PANI/PbS nanocomposite, further show the arranged polymer structure as well as great interfacial communications between the metal oxide and the polymer grid. The DSC (differential scanning calorimetry) after-effects of composite materials are additionally found in great concurrence with TGA results which demonstrate that all the nanocomposites show least worth of beginning temperature as contrast with the unadulterated PANI.

Table 2 shows the data of warm boundary of Polyaniline nanocomposite with various content of PbS. Some changes in the softening temperature and enthalpy in PANI/PbS (5–25%) nanocomposite showed miscibility with PANI lattice.

Table 2. Th	iermal parameter o	f pure PANI ar	nd PANI/PbS	nanocomposite	5

Sr. No	Material	Melting temp, °C	Onset temp. °C	Enthalpy change, J/g	Specific heat (ΔCp), J/g×°C	Peak area
1	Pure PANI	-	284.000	-	12.270	-
2	5%PANI/PbS	268.310	246.590	47.370	9.980	264.377
3	10%PANI/Pbs	267.880	244.150	34.460	6.520	167.613
4	15%PANI/PbS	266.810	240.060	30.479	6.479	123.622
5	20%PANI/PbS	265.130	232.550	28.699	5.192	125.700
6	25%PANI/PbS	263.420	230.250	26.861	4.405	120.234

Conclusions

XRD and UV-visible spectroscopy results indicated that the structural changes take place in nanocomposite with PbS nanoparticle. Thermal analysis of PbS nanocomposite indicated that the Polyaniline powder had discernible moisture content. This phenomenon is in agreement with the XRD results. Moreover, in the first run of DTA thermal analysis, an exothermic peak at 150–310 °C was found. This peak was due to the chain cross linking, resulting from a coupling of two neighboring -N=Q=N- groups to give two -NH-B-NH groups through a link of the N with its neighboring Quindío ring. Thus, based on the thermal profile of these materials, we can say that among all composite material, the PANI/PbS composite materials, cross-linking or oxidative reaction starts at higher temperature than other composites, which indicates that the thermal stability of PANI/PbS nanocomposites is higher than oxides nanocomposites. These DTA results of composite materials are also found in good agreement with XRD results.

CRediT authorship contribution statement

Jitendra Bhaiswar, Meghe Dhiraj: writing original draft and investigation, review and editing; **Dongre Sunil** Sc: supervision of draft and conceptualization.

Conflict of interest

The authors declare that they have no conflict of interest.

References

- 1. Maziarz EP, Lorenz SA, White TP, Wood TD. Polyaniline: A conductive polymer coating for durable nanospray emitters. *J Am Soc Mass Spectrom*. 2000;11: 659–663.
- 2. Tiitu M, Talo A, Forsén O, Ikkala O. Aminic Epoxy Resin Hardeners as Reactive Solvents for Conjugated Polymers: Polyaniline Base/Epoxy Composites for Anticorrosion Coatings. *Polymer*. 2005;46(18): 6855–6861.
- 3. Ismail YA, Shin SR, Shin KM, Yoon SG, Shon K, Kim SI, Kim SJ. Electrochemical Actuation in Chitosan/Polyaniline Microfibers for Artificial Muscles Fabricated using an in Situ Polymerization. *Sensors and Actuators B: Chemical.* 2008;129(2): 834–840.
- 4. Dhand C, Das M, Sumana G, Srivastava AK, Pandey MK, Kim CG, Datta M, Malhotra BD. Preparation, Characterization and Application of PolyanilineNanospheres to Biosensing. *Nanoscale*. 2010;2: 747–754.
- 5. Saxena V, Malhotra BD. Prospects of Conducting Polymers in Molecular Electronics. *Current Applied Physics*. 2003;3(2–3): 293–305.
- 6. Pinto N, Johnson A, MacDiarmid A, Mueller C, Theofylaktos N, Robinson D, Miranda F. Electrospun Polyaniline/Polyethylene Oxide Nanofiber Field-Effect Transistor. *Applied Physics Letters*. 2003;83(20): 4244–4246. 7. Tan S, Zhai J, Xue B, Wan M, Meng Q, Li Y, Jiang L, Zhu D. Property Influence of Polyaniline on Photovoltaic Behaviors of Dye-Sensitized Solar Cells. *Langmuir*. 2004;20(7): 2934–2937.
- 8. Hosseini SH, Oskooei SHA, Entezami AA. Toxic Gas and Vapour Detection by Polyaniline Gas Sensors. *Iranian Polymer Journal.* 2005;14(4): 333–344.
- 9. Sadek AZ, W Wlodarski, Kalantar-Zadeh K, Baker C, Kaner RB. Doped and dedoped polyaniline nanofiber based conductometric hydrogen gas sensors. *Sensors and Actuators A: Physical*. 2007;139(1–2): 53–57.
- 10. Matsunaga T, Daifuku H, Nakajima T, Kawagoe T. Development of polyaniline-lithium secondary battery. *Polymers for Advanced Technologies*. 1990;1(1): 33–39.
- 11. Wang H, Hao Q, Yang X, Lu L, Wang X. Graphene oxide doped polyaniline for supercapacitors. *Electrochemistry Communications*. 2009;11(6): 1158–1161.
- 12. Kovalenko I, Bucknall DG, Yushin G. Detonation nanodiamond and onion-like-carbon-embedded polyaniline for supercapacitors. *Advanced Functional Materials*. 2010;20(22): 3979–3986.
- 13. X Huang, G Wang, M Yang, W Guo, H Gao. Synthesis of polyaniline-modified Fe3O4/SiO2/TiO2 composite microspheres and their photocatalytic application. *Materials Letters*. 2011;65(19–20): 2887–2890.
- 14. Heera TR, Cindrella L. PbS/CoS-Pani composite semiconductor films. *Materials Science in Semiconductor Processing*. 2011;14(2): 151–156.
- 15. Li Q, Zhang C, Li J. Photocatalysis and Wave-Absorbing Properties of Polyaniline/TiO2 Microbelts Composite by in Situ Polymerization Method. *Applied Surface Science*. 2010;257(3): 944–948.
- 16. Wang Y, Herron N. Semiconductor Nanocrystals in Carrier-Transporting Polymers: Charge Generation and Charge Transport. *Journal of Luminescence*. 1996;70(1–6): 48–59.
- 17. Liu XX, Zhang L, Li YB, Bian LJ, Huo YQ, Su Z. Electrosynthesis of Polyaniline/SiO2 Composite at High pH in the Absence of Extra Supporting Electrolyte. *Polymer Bulletin*. 2006;57: 825–832.
- 18. Pulin AG, Laptev MA, Alisov KA, Barskov VV, Rassokhin VA, Gong B, Kotov VS, Roshchenko GA, Balakin AM, Golubtsov M, Nurkov IR, Basati Panah M. Heat exchanger and the influence of lattice structures on its strength. *Materials Physics and Mechanics*. 2024;52(6): 61–80.
- 19. Kaminskii VV, Panov DYu, Spiridonov VA, Bauman DA, Kalganov DA, Scheglov MP, Romanov AE. Effect of high-temperature annealing on the internal friction and optical transmittance of single crystal gallium oxide. *Materials Physics and Mechanics*. 2024;52(5): 48–54.
- 20. Pozdnyakov AO, Sedakova EB. Thermal analysis of wear of polymer-polymer friction pairs in vacuum and atmosphere conditions. *Materials Physics and Mechanics*. 2024;52(4): 63–80.
- 21. Arena A, Taló M, Snyder MP, Lacarbonara W. Enhancing flutter stability in nanocomposite thin panels by harnessing CNT/polymer dissipation. *Mech. Res. Commun.* 2020;104: 103495.
- 22. Xia X, Du Z, Zhang J, Li J, Weng GJ. Modeling the impact of glass transition on the frequency-dependent complex conductivity of CNT-polymer nanocomposites. *Mech. Mater.* 2022;165: 104195.

- 23. Patnaik SS, Roy T. Viscoelastic and mechanical properties of CNT-reinforced polymer-based hybrid composite materials using hygrothermal creep. *Polym. Polym. Compos.* 2021;29(9): 1386–1402.
- 24. Ma Q, Hao B, Ma PC. In-situ characterization on the fracture behavior of three dimensional polymer nanocomposites re-inforced by CNT sponge. *Compos. Sci. Technol.* 2022;217: 109132.
- 25. Anwer AH, Ahtesham A, Shoeb M, Mashkoor F, Ansari MZ, Zhu S, Jeong C. State-of-the-art advances in nanocomposite and bio-nanocomposite polymeric materials: a comprehensive review. *Adv. Colloid Interface Sci.* 2023;318: 102955.
- 26. Jagadeesh N, Sundaram B. Adsorption of pollutants from wastewater by biochar: a review. *J. Hazard. Mater. Adv.* 2023;9: 100226.
- 27. Naz S, Gul A, Zia M, Javed R. Synthesis, biomedical applications, and toxicity of CuO nanoparticles. *Appl. Microbiol. Biotechnol.* 2023;107(4): 1039–1061.
- 28. Mei Y, Shen Z, Kundu S, Dennis E, Pang S, Tan F, Yue G, Gao Y, Dong C, Liu R, Zhang W, Saidaminov MI. Perovskite solar cells with polyaniline hole transport layers surpassing a 20% power conversion efficiency. *Chem Mater.* 2021;33(12): 4679–4687.
- 29. Deyab MA, Mele G, Bloise E, Mohsen Q. Novel nanocomposites of Ni-pc/polyaniline for the corrosion safety of the aluminum current collector in the Li-ion battery electrolyte. *Sci Rep.* 2021;11(1): 1–8.
- 30. Zhang X, Wang Y, Fu D, Wang G, Wei H, Ma N. Photo-thermal converting polyaniline/ionic liquid inks for screen printing highly-sensitive flexible uncontacted thermal sensors. *Eur Polym J.* 2021;147: 110305.

Submitted: April 16, 2025 Revised: May 3, 2025 Accepted: June 3, 2025

Effect of electromagnetic waves on the thermoelastic Hookean unbounded domains based on fractional Fourier law

N. Samir 📵, M.A. Abdou 📵, E. Awad 🗵 📵

Department of Mathematics, Faculty of Education, Alexandria University, Alexandria, Egypt

[™] e-mail: emadawad78@alexu.edu.eq

ABSTRACT

An analytical framework for time-fractional magneto-thermoelasticity in unbounded domains, focusing on heat conduction in materials exhibiting non-classical thermal behavior, are presented. Thermal transport is strongly influenced by temperature and the internal structure of the medium; in the presence of imperfections such as inclusions, voids, or microstructural defects, the heat transfer process often deviates from conventional diffusion laws. To model these complex phenomena, fractional calculus is employed, and the governing equations are reformulated using dimensionless variables. Analytical solution in the Laplace–Fourier domain was derived, with temperature distribution expressed in terms of Mittag-Leffler and Fox H-functions. The use of uncoupled thermoelastic theory allows for a simplified treatment by decoupling thermal and mechanical fields. Finally, numerical inversion techniques are used to reconstruct time-domain solutions for displacement and stress, demonstrating how fractional-order parameters influence both thermal wave propagation and material response.

KEYWORDS

Maxwell's equations • thermoelasticity • fractional derivative • uncoupled theory

Citation: Samir N, Abdou MA, Awad E. Effect of electromagnetic waves on the thermoelastic Hookean unbounded domains based on fractional Fourier law. *Materials Physics and Mechanics*. 2025;53(3): 149–164. http://dx.doi.org/10.18149/MPM.5332025_12

Introduction

In recent decades, the field of thermoelasticity has experienced considerable progress, particularly in efforts to construct a more robust and comprehensive theoretical framework that accurately describes the interplay between thermal and mechanical effects in solid materials. Despite this progress, the conventional or classical formulation of thermoelasticity - commonly referred to as the uncoupled theory - still suffers from two major deficiencies that have long been criticized for their divergence from experimentally observed behavior.

The first critical limitation of the uncoupled thermoelastic theory lies in the way it formulates the heat conduction process. In this classical approach, the governing heat equation is entirely devoid of any terms that account for mechanical or elastic influences. Essentially, the model treats thermal processes as completely independent of mechanical deformations, which is a significant oversimplification of reality. In real-world materials, especially those undergoing rapid or large deformations, temperature changes can both influence and be influenced by the mechanical stresses and strains present within the body. By excluding this coupling, the uncoupled theory fails to capture the intrinsic and complex interdependence between temperature evolution and material deformation, thereby limiting its accuracy and applicability in many practical scenarios. The second



major flaw inherent in the traditional uncoupled theory is a mathematical one, rooted in the type of partial differential equation used to describe heat conduction. Specifically, the classical heat equation is parabolic in nature. While this form is mathematically convenient and widely used, it leads to an unphysical prediction: that thermal disturbances - often referred to as "heat waves" - can propagate through a material at infinite speeds. This implication is clearly at odds with empirical evidence and experimental measurements, which have consistently shown that heat propagation in solids occurs at finite velocities. As such, the parabolic character of the classical heat equation undermines the theory's physical realism.

Building upon such foundational ideas, Biot [1] introduced what is now known as the coupled theory of thermoelasticity. This theory directly addresses the first shortcoming of the uncoupled model by introducing a mathematical coupling between the equations governing elasticity and those governing heat conduction. In doing so, Biot's formulation allows thermal fields and mechanical fields to influence each other, thereby providing a more realistic and physically consistent description of how materials behave under simultaneous thermal and mechanical loads. However, it is important to note that while Biot's theory successfully overcomes the issue of thermal-mechanical independence, it does not fully resolve the second major concern. Like the uncoupled theory, the coupled theory also employs a parabolic heat equation, and thus still predicts infinite speeds of heat propagation - a result that remains inconsistent with physical reality. Considering these enduring limitations, further theoretical developments have been pursued in the form of generalized thermoelastic theories, such as those incorporating hyperbolic heat equations or finite speed models (e.g., the Lord-Shulman and Green-Lindsay theories), which attempt to more accurately reflect the finite speed nature of heat propagation while retaining the essential coupling between thermal and mechanical fields. In an effort to overcome the first major limitation of the classical uncoupled thermoelastic theory - the complete separation between thermal and mechanical responses - Biot [1] introduced what became known as the *coupled theory of thermoelasticity*. This refined model directly links the governing equations of elasticity and heat conduction, thereby eliminating the unrealistic assumption that temperature changes and mechanical deformations occur independently. By integrating these two domains, Biot's theory offered a more realistic representation of material behavior under thermomechanical loads.

Building on the fundamental principles of fractional diffusion-wave equations, researchers have extended these ideas to the realm of thermoelasticity. In [2], for instance, a novel approach to fractional thermoelasticity was introduced, laying the groundwork for further exploration of thermomechanical interactions using fractional calculus. This line of inquiry was first explored in detail by Povstenko, who presented a quasi-static, uncoupled formulation of fractional thermoelasticity. In materials with microstructural irregularities such as voids or impurities, thermal conductivity can exhibit non-classical behavior which motivated the use of fractional-order models. One such approach employs a space-time fractional Fourier law within a quasi-static theory of fractional thermoelasticity to capture anomalous heat conduction effects [3].

At micro- and nanoscales, or under ultrafast thermal excitation, the classical heat conduction model based on Fourier's law becomes inadequate. Its assumption of local thermodynamic equilibrium breaks down under these conditions, leading to inaccurate

predictions of thermal behavior. This has driven the development of alternative models that can capture finite thermal propagation speeds and non-equilibrium phenomena. One such alternative is the ballistic-conductive (BC) model, introduced by Kovács and Ván [4] (2015), which extends the classical framework by incorporating both ballistic and diffusive thermal transport mechanisms. While the BC model improves upon the limitations of Fourier's law, analyses of its solutions have revealed a counterintuitive phenomenon: partial "immobilization" of thermal energy. This effect, considered unphysical, highlights the challenges of modeling energy transport in the transition regime between microscopic and macroscopic scales [5].

Moreover, incorporating two-temperature and nonlocal effects into thermoelastic models is essential for accurately predicting material response in ultrafast and nanoscale regimes, where classical thermoelastic theory (based on Fourier's law and instantaneous local equilibrium) fails to capture the true dynamics. To better capture thermal behavior in such regimes, especially during ultrafast processes like laser-material interaction, researchers have turned to two-temperature models. These models separate the electron and phonon subsystems, allowing for local thermal nonequilibrium. Recent extensions to these models introduce time-relaxation and spatial nonlocal effects, enabling more accurate descriptions of thermal transport in metals [6]. Analytical investigations have shown that under high-frequency excitation, key thermal parameters - such as phase velocity, penetration depth, and apparent thermal conductivity - become strongly frequency-dependent. In particular, the apparent thermal conductivity significantly decreases near the characteristic energy exchange frequency between electrons and phonons [7]. This frequency-dependent behavior leads to more complex phenomena such as thermal resonance. Within the framework of the hyperbolic two-temperature model, it has been shown that specific conditions in electron-phonon interactions can result in resonant thermal effects. These findings emphasize the importance of advanced modeling strategies—particularly those that account for microscopic energy exchange mechanisms—in accurately predicting thermal behavior in modern materials [8].

Alongside these developments, fractional-order thermoelastic models have gained attention for their ability to describe anomalous heat conduction and memory effects. For instance, in the context of a semi-infinite medium exposed to a temporally decaying laser pulse, fractional models using Laplace transform techniques have successfully derived temperature, stress, and strain distributions. These solutions, when compared to classical two-temperature models, highlight the advantages of fractional approaches in capturing the subtleties of nonlocal and time-fractional behavior in thermoelastic systems [9].

Complementary to these theoretical advancements, studies have also explored the response of double-porosity materials - complex media with two interacting pore networks - under moving loads. Using Fourier analysis and numerical inversion, researchers have examined the spatial and temporal distributions of stress and temperature, revealing how porosity significantly affects energy dissipation and wave propagation. These findings underscore the importance of microstructural design in determining thermo-mechanical performance under coupled excitations [10].

Building on this understanding of microstructural effects, further studies have investigated systems with layered structures and initial prestress, which introduce additional complexity into the thermoelastic response. In such systems, harmonic thermal

excitation leads to intricate coupling between thermal and mechanical fields. Notably, prestress conditions have been shown to alter the pole distribution of the Green function, fundamentally affecting the system's dynamic behavior. This alteration governs wave propagation, energy localization, and the emergence of resonance phenomena within layered media [11].

This paper explores the impact of electromagnetic waves on fractional thermoelastic behavior in unbounded media. In the next section, Maxwell's equations are merged with fractional heat conduction to model the interaction between thermal, elastic and electromagnetic fields. Focusing on a one-dimensional uncoupled system, the goal is to determine the displacement and temperature, linked through hydrostatic stress. The temperature equation is hyperbolic, derived from generalized heat conduction. Using Laplace and Fourier transforms, the PDEs are converted into algebraic equations, solved analytically, and then inverted to retrieve physical solutions. In the "Numerical Analysis and Discussion" sections, we present the final analytical expressions, revealing the influence of material parameters on wave propagation and thermal relaxation.

Mathematical problem

Governing equations

In this sub-section, we will delve into the fundamental equations that govern the behavior of magnetic and electric currents. These equations, collectively known as Maxwell's equations. They describe the relationship between electric and magnetic fields, as well as their interaction with matter. Now we are going to introduce Maxwell's equations as the following [12,13]:

$$\nabla \times E = -\frac{\partial B}{\partial t}, \nabla \times H = J + \frac{\partial D}{\partial t},$$

$$\nabla \cdot D = 0,$$

$$\nabla \cdot H = 0,$$
(1)

where B represents the induced magnetic field which can be expressed as $B=\mu_0H$ noting that μ_0 stands for the magnetic permeability, H describes the intensity of a magnetic field and J represents the electric current. Additionally, D represents the electric displacement field, which can be expressed as $D=\varepsilon_0E$, noting that ε_0 represents the electric permeability and E is the electric field intensity. Now we can re-write Eq. (1) as the following:

$$\nabla \times E = -\mu_0 \frac{\partial H}{\partial t}, \nabla \times H = J + \varepsilon_0 \frac{\partial E}{\partial t},$$

$$\nabla \cdot E = 0,$$

$$\nabla \cdot H = 0.$$
(2)

Furthermore, we introduce Ohm's Law that is a fundamental principle in electrical engineering that describes the relationship between voltage, current, and resistance, and we can express Ohm's law as the following [14]:

$$J = \sigma_0 \left(E + \frac{\partial u}{\partial t} \times B \right), \tag{3}$$

where u is the displacement vector, σ_0 is the electric conductivity, and by setting $\sigma_0 \to \infty$ we obtain the perfect conductivity, we also are going to introduce Lorentz force which

known as the force experienced by a charged particle moving through an electromagnetic field. The mathematical equation of Lorentz force can be described as the following:

$$F = J \times B,$$

$$F = J \times \mu_0(H_0 + h),$$
(4)

where H_0 represents the constant or background magnetic field, it can be thought of as the main steady state magnetic field present in the system. h represents the perturbation or small deviation in the magnetic field caused by external influences and $H_0 + h$ together describes the total magnetic field. Due to the linearity, we can re-write Eq. (4) as the following:

$$F = J \times B_0. \tag{5}$$

The classical theory of thermoelectricity consists of the modified Fourier law mentioned in [15]. By neglecting the electric field intensity E=0 and h=0, so the induced magnetic field becomes $B=\mu_0H_0$ providing that Eq. (3) becomes as follows:

$$J = \sigma_0 \mu_0 \left(\frac{\partial u}{\partial t} \times H_0 \right). \tag{6}$$

From the unbounded domain configuration, the displacement vector u=(u,0,0), the electric current vector J=(0,J,0) and the magnetic field vector $H_0=(0,0,H_0)$. Consequently, Eq. (6) becomes as the following [16]:

$$J = -\sigma_0 \mu_0 H_0 \frac{\partial u}{\partial t} \underline{j}. \tag{7}$$

Additionally, Eq. (5) becomes the following:

$$F = -\sigma_0 B_0^2 \frac{\partial u}{\partial t} \, \underline{i}. \tag{8}$$

The equation of motion, see [17] after inserting Eq. (8) as an expression for the external force, we obtain the following:

$$\sigma_{ij,j} = \rho \ddot{u}_i + \sigma_0 B_0^2 \frac{\partial u_i}{\partial t}. \tag{9}$$

Consequently, by recalling the constitutive relationship presented in [17], as the following:

$$\sigma_{ij} = 2\mu e_{ij} + \lambda e \delta_{ij} - \chi_0 \theta \delta_{ij} \,, \tag{10}$$

where λ and μ are correspond to the standard Lamé constants, $\theta = T - T_0$ specifically θ is the temperature of the medium, T is the absolute temperature and T_0 is the temperature of the room, $\chi_0 = (3\lambda + 2\mu)\alpha_T$, clarifying that α_T is the parameter that quantifies the linear dimensional change of a material in response to temperature changing or known as the coefficient of linear thermal expansion, σ_{ij} are representing the components of Cauchy stress tensor, δ_{ij} is the Kronecker delta function. And as mentioned above, u_i is the i-th component of displacement vector \underline{u} , $e = e_{ii} = u_{i,i} = e_{11} + e_{22} + e_{33}$ is known as the cubical dilation and e_{ij} is representing the strain tensor for linear elasticity defined that is define as: $e_{ij} = \frac{1}{2}(u_{i,j} + u_{j,i})$.

Now, the well-known stress-strain relation, see [18] can be modified by inserting Eq. (9) as the following:

$$\mu u_{i,jj} + (\lambda + \mu) u_{j,ij} - \chi_0 T_{,i} = \rho \ddot{u}_i + \sigma_0 B_0^2 \frac{\partial u_i}{\partial t}. \tag{11}$$

At this stage, we will reintroduce the thermal energy balance equation in the absence of a heat source in one dimension setting as the following [19]:

$$-q_{i.i} = \rho C_E \dot{T} + \chi_0 T_0 \, \dot{e} \,. \tag{12}$$

where $\dot{e}=\frac{\partial^2 u}{\partial x \partial t}$. Additionally, it's important to revisit the core concept of heat conduction known as Fourier's law. This principle states that the heat flux—defined as the amount of heat energy transferred per unit area per unit time—is directly proportional to the temperature gradient, which describes how temperature changes over distance. In mathematical terms, Fourier's law is written as [20,21]: $q_i=-\kappa T_{,i}$. We will adopt an alternative rule that will serve as the foundation for our proceeding analysis, offering a more understanding of heat transfer phenomena under a given conditions as follows:

$$q_i = -\kappa_{\alpha}^{RL} \mathcal{D}_t^{1-\alpha} T_{,i}. \tag{13}$$

The operator $_{a}^{RL}\mathcal{D}_{t}^{\alpha}$ denotes the left-sided Riemann-Liouville fractional derivative, which is defined for a general function, further details can be found in [22-24]. Building upon the insightful proposition by Compte and Metzler concerning the anomalous diffusion coefficient, we propose the following functional expressions for the parameter κ_{α} :

$$\kappa_{\alpha} = \kappa \tau^{1-\alpha},$$
(14)

where κ is the classical thermal conductivity, τ is a characteristic time constant. τ will be specified subsequently. Equation (14) becomes as the following:

$$q_i = -\kappa \tau^{1-\alpha} {}^{RL}_0 \mathcal{D}_t^{1-\alpha} T_{,i}. \tag{15}$$

To streamline our analysis, we will eliminate the heat flux term that appears in both the energy balance equation (12) and Eq. (15). This will be achieved by employing a suitable mathematical technique, as outlined below:

$$\rho C_E \dot{T} + \chi_0 T_0 \dot{e} = \kappa \tau^{1 - \alpha RL} \mathcal{D}_t^{1 - \alpha} T_{.ii} . \tag{16}$$

Problem setting up

In this section, we will develop a mathematical framework to describe the system outlined in Eqs. (11) and (16). This system is defined over an unbounded spatial domain $-\infty < x < \infty$, signifying that it extends infinitely in all directions. To establish a complete mathematical description, we must specify the initial conditions that govern the system's behavior. These initial conditions will serve as the starting point for our analysis and will significantly influence the subsequent evolution of the system. The initial conditions are given as follows:

$$\theta(x,0) = \theta_0 \delta(x), \quad u(x,0) = \frac{\partial u(x,0)}{\partial x} = 0, \tag{17}$$

where $\delta(x)$ is the Dirac delta function assuming that the displacement initial state is given as $u(-\infty,0)=u_{-\infty}$. By noticing the initial conditions outlined in Eq. (17), we observe that the complexity of the problem can be significantly reduced to a one-dimensional framework. This simplification arises due to the inherent nature of the initial state, which exhibits a particular symmetry that allows us to focus our analysis along a single spatial dimension. This means that all relevant physical quantities involved in the problem can be expressed as functions of the spatial variable x (one-dimensional setting) and time t. Consequently, the governing equations, represented by Eqs. (11) and (16), can be simplified to involve only derivatives with respect to these two independent variables, x and t. This reduction in dimensionality significantly simplifies the mathematical analysis and allows for more efficient numerical simulations. The simplified governing equations are as follows:

$$(\lambda + 2\mu)\frac{\partial^2 u}{\partial x^2} - \chi_0 \frac{\partial T}{\partial x} = \rho \ddot{u} + \sigma_0 B_0^2 \frac{\partial u}{\partial t},\tag{18}$$

$$\rho C_E \frac{\partial T}{\partial t} + \chi_0 T_0 \frac{\partial^2 u}{\partial x \partial t} = \kappa \tau^{1 - \alpha} {}_0^{RL} \mathcal{D}_t^{1 - \alpha} \frac{\partial^2 T}{\partial x^2}. \tag{19}$$

By employing Eq. (10) together with the previously established one-dimensional framework, the individual components of the Cauchy stress tensor can be explicitly calculated using the following procedure:

$$\sigma_{xx} = (\lambda + 2\mu) \frac{\partial u}{\partial x} - \chi_0 (T - T_0), \tag{20}$$

$$\sigma_{yy} = \sigma_{zz} = \lambda \frac{\partial u}{\partial x} - \chi_0(T - T_0). \tag{21}$$

In the context of hydrostatic stress σ_H , we focus solely on the normal components. By taking their arithmetic means, we obtain a single value that characterizes the overall pressure exerted on the material from all directions. This average pressure is what we refer to as hydrostatic stress:

$$\sigma_H = \frac{\sigma_{\chi\chi} + \sigma_{\chi\chi} + \sigma_{zz}}{3} = \left(\lambda + \frac{2}{3}\mu\right) \frac{\partial u}{\partial x} - \chi_0(T - T_0). \tag{22}$$

To facilitate a more comprehensive and insightful analysis of the problem, we will introduce a set of dimensionless variables. By systematically reducing the number of independent parameters, we can significantly streamline the mathematical model, simplifying its interpretation and analytical processing as detailed below:

$$x \to \frac{x}{c_1 \eta}, \quad u \to \frac{u}{c_1 \eta}, t \to \frac{t}{c_1^2 \eta'},$$

$$\tau \to \frac{\tau}{c_1^2 \eta'}, \quad (\sigma_{ij}, \sigma_H) \to (\lambda + 2\mu) (\sigma_{ij}, \sigma_H), \eta = \frac{\rho C_E}{\kappa},$$

$$T \to \frac{\lambda + 2\mu}{\chi_0} \theta + T_0, c_1^2 = \frac{\lambda + 2\mu}{\rho},$$
(23)

therefore, the governing equations (18) and (19) can be rewritten as the following:

$$\frac{\partial \theta}{\partial x} = \frac{\partial^2 u}{\partial x^2} - \frac{\partial^2 u}{\partial t^2} - c_0 \frac{\partial u}{\partial t},\tag{24}$$

where

$$c_{0} = \frac{\sigma_{0}B_{0}^{2}}{\eta(\lambda + 2\mu)},$$

$$\frac{\partial\theta}{\partial t} + \varepsilon \frac{\partial^{2}u}{\partial x\partial t} = \tau^{1-\alpha} {}_{0}^{RL} \mathcal{D}_{t}^{1-\alpha} \frac{\partial^{2}\theta}{\partial x^{2}},$$
(25)

where ε is the thermoelastic coupling constant and given as the following: $\varepsilon = \frac{{\chi_0}^2 T_0}{\rho c_E(\lambda + 2\mu)}$

Additionally, the constitutive relations (20)–(22) can be also rewritten in the dimensionless form as the following:

$$\sigma_{xx} = \frac{\partial u}{\partial x} - \theta,$$

$$\sigma_{yy} = \sigma_{zz} = \ell_0 \frac{\partial u}{\partial x} - \theta,$$
where $\ell_0 = \frac{\lambda}{\lambda + 2\mu}$. (26)

Additionally.

$$\sigma_H = \ell_1 \frac{\partial u}{\partial x} - \theta,$$
where $\ell_1 = \frac{(\lambda + \frac{2}{3}\mu)}{(\lambda + 2\mu)}$. (27)

Now, we are going to use the dimensionless variable on the initial condition as previously outlined in Eq. (17) as the following:

$$\theta(x,0) = \Theta_0 \delta(x),$$

$$u(x,0) = \frac{\partial u(x,0)}{\partial x} = 0 \text{ and } u(-\infty,0) = U_{-\infty},$$
(28)

where $\Theta_0 = \frac{\chi_0 \vartheta_0 c_1 \eta}{\lambda + 2\mu}$, noting that the dimensions of Dirac delta function $\delta(x)$ in our context

must be the inverse of the dimensions of x.

Solution in the transformed domain

In the subsequent analysis, we will embark on deriving an analytical solution for the temperature field within the Laplace-Fourier domain. This certain mathematical approach will enable us to delve deeper into the fundamental behavior of heat transfer within the system.

To proceed, we will apply the Laplace transform on Eq. (24), as detailed below:

$$\frac{\partial \tilde{\theta}}{\partial x} = \frac{\partial^2 \tilde{u}}{\partial x^2} - s^2 \tilde{u} - c_0 s \tilde{u},\tag{29}$$

by differentiating Eq. (29) with respect to x, we get the following:

$$\frac{\partial^2 \tilde{\theta}}{\partial x^2} = \frac{\partial^2 \tilde{e}}{\partial x^2} - s^2 \tilde{e} - c_0 s \tilde{e}. \tag{30}$$

Now, to further our analysis, we proceed by applying the Fourier transform to Eq. (30). This mathematical operation will enable us to facilitate the subsequent analysis and solution of the equation as the following:

$$-\omega^2 \hat{\theta} = -\omega^2 \hat{e} - s^2 \hat{e} - c_0 s \hat{e}. \tag{31}$$

Consequently, we apply the Laplace transform to Eq. (25), resulting in the following transformed equation:

$$s\tilde{\theta} - \Theta_0 \delta(x) + \varepsilon s\tilde{e} = \tau^{1-\alpha} s^{1-\alpha} \frac{\partial^2 \tilde{\theta}}{\partial x^2}. \tag{32}$$

To initiate our analysis, we employ the uncoupled theory of thermoelasticity by setting $\varepsilon = 0$, a simplified approach that decouples the thermal and mechanical fields. This theory assumes that mechanical deformations have a negligible influence on the temperature distribution. In other words, changes in temperature do not influence the mechanical deformation, and vice versa. Meaning that the heat conduction equation is solved independently and the effect of mechanical deformation on heat conduction is considered negligible [25].

Therefore, after applying Fourier transform on Eq. (32) which allows us to analyze the equation and get an expression for $\hat{\theta}(\omega, s)$ as the following:

$$\hat{\tilde{\theta}}(\omega, s) = \left(\frac{\Theta_0 \tau^{\alpha - 1} s^{\alpha - 1}}{\tau^{\alpha - 1} s^{\alpha} + \omega^2}\right). \tag{33}$$

We proceed by applying the rule of Fourier inverse transformation mentioned in [26]

on Eq. (33) as follows:
$$\mathcal{F}^{-1}\left\{\frac{1}{\omega^2+c^2}\right\} = \frac{1}{2c}e^{-c|x|}$$
. Therefore:
$$\tilde{\theta}(x,s) = \frac{\Theta_0\sqrt{\tau^{\alpha-1}s^{\alpha-2}}}{2}\exp\left(-\sqrt{\tau^{\alpha-1}s^{\alpha}}|x|\right). \tag{34}$$

And subsequently, by simplifying and performing the technique of partial fraction decomposition to further simplify Eq. (31), we obtain an expression for $\hat{e}(\omega,s)$ as the following:

$$\hat{\tilde{e}}(\omega,s) = \frac{\Theta_0 \tau^{\alpha-1} s^{\alpha-1}}{\tau^{\alpha-1} s^{\alpha} - s^2 - c_0 s} \left(\frac{-(s^2 + c_0 s)}{\omega^2 + s^2 + c_0 s} + \frac{\tau^{\alpha-1} s^{\alpha}}{\omega^2 + \tau^{\alpha-1} s^{\alpha}} \right). \tag{35}$$

Within the following discussion, we are going to calculate the temperature within the material. Starting by reformulating Eq. (33) to convert the temperature function from the Laplace domain, characterized by the complex variable s, back to the time domain,

characterized by the real variable
$$t$$
, we employ the inverse Laplace transform as follows [27]:
$$\tilde{\theta}(\omega,t) = \mathcal{L}^{-1}\left\{\frac{\Theta_0 s^{\alpha-1}}{s^{\alpha} + \omega^2 \tau^{1-\alpha}}\right\} = \Theta_0 E_{\alpha}(-\omega^2 \tau^{1-\alpha} t^{\alpha}), \tag{36}$$

where the symbol $E_{\alpha}(\cdot)$ denotes the Mittag-Leffler function with one parameter α , see reference [28] for more details. By applying the inverse Fourier transform to Eq. (36), referencing the relationships (A.10) and (A.20) in [18], we can derive a closed-form expression for temperature, as follows:

$$\tilde{\theta}(\omega, t) = \Theta_0 H_{1,2}^{1,1} \left[\omega^2 \tau^{1-\alpha} t^{\alpha} \, \middle| \, \begin{array}{c} (0,1) \\ (0,1), (0,\alpha) \end{array} \right]. \tag{37}$$

Upon applying the inverse Fourier transformation to Eq. (37), we arrive at the following outcome:

$$\theta(x,t) = \frac{\Theta_0}{\sqrt{4\pi}} \left(\frac{1}{\tau^{1-\alpha}t^{\alpha}}\right)^{\frac{1}{2}} \times H_{2,3}^{2,1} \left[\frac{x^2}{2^2\tau^{1-\alpha}t^{\alpha}} \middle| \frac{\left(\frac{1}{2},1\right); \left(1-\frac{\alpha}{2},\alpha\right)}{(0,1), \left(\frac{1}{2},1\right); \left(\frac{1}{2},1\right)}\right]. \tag{38}$$

The symbol $H_{p,q}^{m,n}[\cdot]$ represents the Fox H-function, a mathematical function defined in terms of the Mellin-Barnes integral, as outlined in reference [29] and. When examining the solution represented by Eq. (38), we notice that the closed-form expression of this solution can be modified or transformed. The objective of the following analysis is to determine the analytical solution for $\hat{e}(\omega,s)$, while numerical integration techniques can provide approximate solutions. To proceed with the analysis, we will apply the following inverse Fourier transform to Eq. (35) [26]:

$$\tilde{e}(x,s) = \frac{\Theta_0 \tau^{\alpha - 1} s^{\alpha - 1}}{\tau^{\alpha - 1} s^{\alpha} - s^2 - c_0 s} \times \left(\frac{-(s^2 + c_0 s)^{\frac{1}{2}}}{2} \exp\left(-(s^2 + c_0 s)^{\frac{1}{2}} |x|\right) + \frac{(\tau^{\alpha - 1} s^{\alpha})^{\frac{1}{2}}}{2} \exp\left(-(\tau^{\alpha - 1} s^{\alpha})^{\frac{1}{2}} |x|\right) \right).$$
(39)

To determine the displacement, we perform an integration of Eq. (39) with respect to the spatial variable x. This approach is based on the relationship given by $e = \frac{\partial u}{\partial x}$:

$$\tilde{u}(x,s) = \tilde{u}(-\infty,s) + \frac{\Theta_0 \tau^{\alpha-1} s^{\alpha-1}}{2\tau^{\alpha-1} s^{\alpha} - s^2 - c_0 s} (I_1 + I_2), \tag{40}$$

recalling that $\tilde{u}(-\infty,s)=\frac{u_{-\infty}}{s}$, $I_1=-(s^2+c_0s)^{\frac{1}{2}}\int_{-\infty}^x e^{-(s^2+c_0s)^{\frac{1}{2}}|\xi|}d\xi$, $I_2=(\tau^{\alpha-1}s^{\alpha})^{\frac{1}{2}}\int_{-\infty}^x e^{-(\tau^{\alpha-1}s^{\alpha})^{\frac{1}{2}}|\xi|}d\xi$ based on the sign of x. Specifically, when x>0, the absolute value simplifies to |x|=x, while for x<0, the absolute value becomes |x|=-x. To proceed systematically, we first analyze the case where x>0. Under this condition, the first and second integrals are reformulated accordingly, and their expressions are derived as follows:

$$I_{1} = -(s^{2} + c_{0}s)^{\frac{1}{2}} \left(\int_{-\infty}^{0} e^{-(s^{2} + c_{0}s)^{\frac{1}{2}}|\xi|} d\xi + \int_{0}^{x} e^{-(s^{2} + c_{0}s)^{\frac{1}{2}}|\xi|} d\xi \right), \tag{41}$$

by replacing $\xi = -X$ therefore $d\xi = -dX$ into the first part of integral (41) as:

$$I_{1} = -(s^{2} + c_{0}s)^{\frac{1}{2}} \left(\int_{0}^{\infty} e^{-(s^{2} + c_{0}s)^{\frac{1}{2}}X} dX + \int_{0}^{x} e^{-(s^{2} + c_{0}s)^{\frac{1}{2}}\xi} d\xi \right),$$

$$I_{1} = e^{-(s^{2} + c_{0}s)^{\frac{1}{2}}x} - 2.$$
(42)

And similarly for I_2 :

$$I_{2} = (\tau^{\alpha-1}s^{\alpha})^{\frac{1}{2}} \left(\int_{-\infty}^{0} e^{-(\tau^{\alpha-1}s^{\alpha})^{\frac{1}{2}}|\xi|} d\xi + \int_{0}^{x} e^{-(\tau^{\alpha-1}s^{\alpha})^{\frac{1}{2}}|\xi|} d\xi \right) =$$

$$= (\tau^{\alpha-1}s^{\alpha})^{\frac{1}{2}} \left(\int_{0}^{\infty} e^{-(\tau^{\alpha-1}s^{\alpha})^{\frac{1}{2}}X} dX + \int_{0}^{x} e^{-(\tau^{\alpha-1}s^{\alpha})^{\frac{1}{2}}\xi} d\xi \right) = 2 - e^{-(\tau^{\alpha-1}s^{\alpha})^{\frac{1}{2}}x}.$$
(43)

Therefore, in case of x > 0 the displacement $\tilde{u}(x, s)$ is given by employing Eqs. (42) and (43) into Eq. (40) as the following:

$$\tilde{u}(x,s) = \frac{u_{-\infty}}{s} + \frac{\Theta_0 \tau^{\alpha - 1} s^{\alpha - 1}}{2\tau^{\alpha - 1} s^{\alpha} - s^2 - c_0 s} \left(e^{-(s^2 + c_0 s)^{\frac{1}{2}} x} - e^{-(\tau^{\alpha - 1} s^{\alpha})^{\frac{1}{2}} x} \right), \quad x > 0.$$
(44)

Subsequently, we examine the second case, where x < 0, and incorporate this condition into the evaluation of the first and second integrals, denoted as I_1 and I_2 as the following:

$$I_{1} = -(s^{2} + c_{0}s)^{\frac{1}{2}} \left(\int_{-\infty}^{0} e^{-(s^{2} + c_{0}s)^{\frac{1}{2}|\xi|}} d\xi - \int_{x}^{0} e^{-(s^{2} + c_{0}s)^{\frac{1}{2}|\xi|}} d\xi \right), \tag{45}$$

by replacing $\xi = -X$ therefore $d\xi = -dX$ into integral Eq. (45) as: $I_1 = -(s^2 + c_0 s)^{\frac{1}{2}} \left(\int_0^\infty e^{-(s^2 + c_0 s)^{\frac{1}{2}}X} dX + \int_{-x}^0 e^{-(s^2 + c_0 s)^{\frac{1}{2}}X} dX \right) = -e^{(s^2 + c_0 s)^{\frac{1}{2}}X}.$

And similarly, for I_2 :

$$I_{2} = (\tau^{\alpha-1}s^{\alpha})^{\frac{1}{2}} \left(\int_{-\infty}^{0} e^{-(\tau^{\alpha-1}s^{\alpha})^{\frac{1}{2}}|\xi|} d\xi - \int_{x}^{0} e^{-(\tau^{\alpha-1}s^{\alpha})^{\frac{1}{2}}|\xi|} d\xi \right) =$$

$$= (\tau^{\alpha-1}s^{\alpha})^{\frac{1}{2}} \left(\int_{0}^{\infty} e^{-(\tau^{\alpha-1}s^{\alpha})^{\frac{1}{2}}X} dX + + \int_{-x}^{0} e^{-(\tau^{\alpha-1}s^{\alpha})^{\frac{1}{2}}X} dX \right) = e^{(\tau^{\alpha-1}s^{\alpha})^{\frac{1}{2}}x}.$$
(46)

Therefore, in case of x < 0 the displacement $\tilde{u}(x,s)$ is given by employing Eqs. (45) and (46) into Eq. (40) as the following:

$$\tilde{u}(x,s) = \frac{U_{-\infty}}{s} + \frac{\Theta_0 \tau^{\alpha - 1} s^{\alpha - 1}}{2\tau^{\alpha - 1} s^{\alpha} - s^2 - c_0 s} \left(e^{\left(\tau^{\alpha - 1} s^{\alpha}\right)^{\frac{1}{2}} x} - e^{\left(s^2 + c_0 s\right)^{\frac{1}{2}} x} \right), \quad x < 0.$$
(47)

By considering the contributions from all relevant components or elements, the displacement in the Laplace domain can be expressed collectively in the following form:

$$\tilde{u}(x,s) = \frac{U_{-\infty}}{s} + \frac{\Theta_0 \tau^{\alpha-1} s^{\alpha-1}}{2\tau^{\alpha-1} s^{\alpha} - s^2 - c_0 s} \begin{cases} e^{-(s^2 + c_0 s)^{\frac{1}{2}} x} - e^{-(\tau^{\alpha-1} s^{\alpha})^{\frac{1}{2}} x}, & x > 0, \\ e^{(\tau^{\alpha-1} s^{\alpha})^{\frac{1}{2}} x} - e^{(s^2 + c_0 s)^{\frac{1}{2}} x}, & x < 0. \end{cases}$$
(48)

To determine the hydrostatic stress in the Laplace domain, we formulate the expression as follows:

$$\widetilde{\sigma_H} = \ell_1 \frac{\partial \widetilde{u}}{\partial x} - \widetilde{\theta}. \tag{49}$$

At this stage, we proceed by substituting the appropriate expressions from Eqs. (34) and (48) into the previous formulation Eq. (49) as follows:

$$\widetilde{\sigma_{H}} = \ell_{1} \frac{\partial}{\partial x} \left(\frac{u_{-\infty}}{s} + \frac{\Theta_{0} \tau^{\alpha-1} s^{\alpha-1}}{2\tau^{\alpha-1} s^{\alpha} - s^{2} - c_{0} s} \begin{cases} e^{-(s^{2} + c_{0} s)^{\frac{1}{2}} x} - e^{-(\tau^{\alpha-1} s^{\alpha})^{\frac{1}{2}} x}, & x > 0 \\ e^{(\tau^{\alpha-1} s^{\alpha})^{\frac{1}{2}} x} - e^{(s^{2} + c_{0} s)^{\frac{1}{2}} x}, & x < 0 \end{cases} \right) - \left(\frac{\Theta_{0} \sqrt{\tau^{\alpha-1} s^{\alpha-2}}}{2} e^{-\sqrt{\tau^{\alpha-1} s^{\alpha}} |x|} \right).$$
(50)

Numerical analysis and Discussion

In this section, we reconstruct the solutions for displacement and hydrostatic stress in the physical domain using a suitable numerical technique. One of the most effective methods for inverting the Laplace transform is the application of the "Durbin" method or the "modified Dubner-Abate" formula [30].

$$f(x,t) = \frac{2e^{at}}{T_1} \left\{ -\frac{1}{2} \tilde{f}(x,a) + \Re \left[\sum_{k=0}^{\mathsf{NSum}} \tilde{f}\left(x,a + \frac{2\pi lk}{T_1}\right) \cos\left(\frac{2\pi kt}{T_1}\right) \right] - \Im \left[\sum_{k=0}^{\mathsf{NSum}} \tilde{f}\left(x,a + \frac{2\pi lk}{T_1}\right) \sin\left(\frac{2\pi kt}{T_1}\right) \right] \right\},$$

$$(51)$$

where the parameter T_1 satisfies the inequality $0 < t \le 2T_1$. The number of summed terms, represented as NSum, typically ranges from 10^5 for small time values to 10^7 for larger ones. values of time to yield stable results with negligible error given by the following:

$$\mathsf{ERROR}(a, t, T_1) = \sum_{k=1}^{\infty} e^{-2akT_1} \tilde{f}(x, 2kT_1 + t). \tag{52}$$

The implementation of series (51) can be carried out using an appropriate symbolic computation software. Programs such as MATHCAD or MATLAB provide powerful tools for handling symbolic calculations. On the other hand and before implementing the previous series, we have obtained an exact solution for the temperature in Eq. (38), which can be computed by the series expansion of the Fox H-function [29] as the following steps:

$$\theta(x,t) = \frac{\Theta_0}{\sqrt{4\pi}} \left(\frac{1}{\tau^{1-\alpha}t^{\alpha}}\right)^{\frac{1}{2}} \{\theta_1(x,t) + \theta_2(x,t)\},\tag{53}$$

to obtain $\theta_1(x,t)$, we are going to use $b_h=b_1=0$, $B_h=B_1=1$ and $\frac{b_1+\nu}{B_1}=\nu$, then we get the following:

$$\theta_1(x,t) = \sum_{\nu=0}^{\infty} \frac{(-1)^{\nu}}{\nu!} \left(\frac{|x|^2}{2^2 \tau^{1-\alpha} t^{\alpha}}\right)^{\nu} \frac{\Gamma\left(\frac{1}{2} - \nu\right) \Gamma\left(\frac{1}{2} + \nu\right)}{\Gamma\left(\frac{1}{2} + \nu\right) \Gamma\left(1 - \frac{\alpha}{2} - \alpha\nu\right)}.$$
(54)

Similarly, for $\theta_2(x,t)$ we use $b_h=b_2=\frac{1}{2}$, $B_h=B_2=1$ and $\frac{b_2+\nu}{B_2}=\frac{1}{2}+\nu$, then we get the following:

$$\theta_{2}(x,t) = \sum_{\nu=0}^{\infty} \frac{(-1)^{\nu}}{\nu!} \left(\frac{|x|^{2}}{2^{2}\tau^{1-\alpha}t^{\alpha}} \right)^{\frac{1}{2}+\nu} \frac{\Gamma(\frac{1}{2}-(1+\nu))\Gamma(1+\nu)}{\Gamma((1+\nu))\Gamma(1-\alpha(1+\nu))}.$$
 (55)

For our numerical computations, we have chosen copper to be our material. We will use its physical properties measured at room temperature (300 K) in our mathematical models to simulate its behavior under various conditions. Since $\tau=1/c_1^2\eta$, the dimensional characteristic constant τ is selected such that the dimensionless constant in all closed-form expressions and their series expansions equals one. Unless explicitly stated otherwise, we will adopt the following specific values for the material properties in our calculations. These values will serve as the standard parameters for the material unless alternative data is provided.

$$\alpha = 1, \tau = 0.01, \ \Theta_0 = 1, \ c_0 = 4.36d - 4.$$
 (56)

Equations (53)–(55) serve as the mathematical formulas directly applied in a numerical technique to compute the temperature. The infinite series within these formulae were approximated by summing the first seventy-one terms. Utilizing their series representation, we visually illustrate the temperature distribution in Fig. 1, that clearly demonstrates that the magnetic field has no influence on temperature, as there is no coupling between the two; $\varepsilon_0=0$. In Fig. 1, the temperature distribution is evaluated for different values of α , at $\alpha=1$ the curve leads to the normal distribution. Varying α reveals the impact of anomalous thermal conductivity. Specifically, for smaller values of α , the system exhibits low thermal conductivity, whereas larger values of α correspond

to higher thermal conductivity, leading to a wider temperature distribution within the medium.

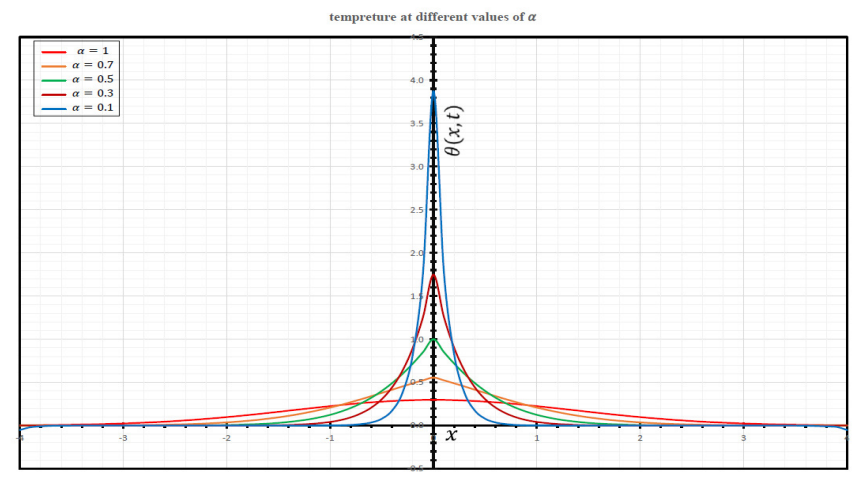


Fig. 1. The temperature distribution evaluated for different values of α

Figure 2 shows the fractional-order parameter α fixed at a representative value of 0.5, while the temperature distribution is analyzed at multiple time instances: t=0.1,0.5,1,5 and 10. Initially, the temperature exhibits a sharp peak near the origin due to the localized thermal disturbance. As time progresses, the peak diminishes and the distribution extends symmetrically, reflecting the diffusion of heat through the medium. This approach allows for the understanding of the temporal evolution of thermal propagation under anomalous heat conduction conditions. The observed behavior shows the effect of time on the diffusion of thermal energy in a medium governed by non-classical (fractional) thermal conductivity, where heat spreads more gradually and the profile undergoes significant changes in shape as time progresses.

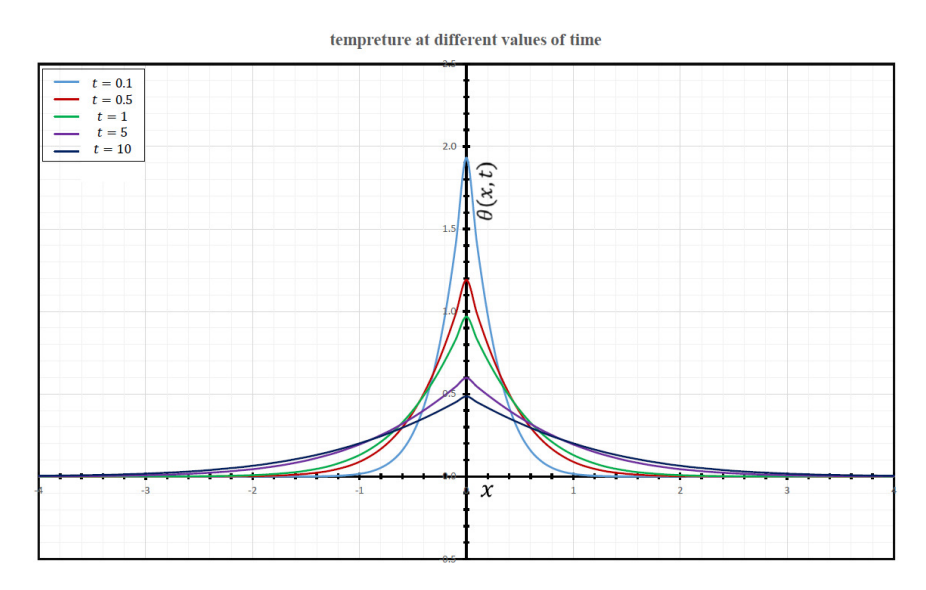


Fig. 2. The temperature distribution for various time instances t, illustrating the temporal evolution of the thermal field

In Fig. 3, the displacement field u(x,t) is presented for t=1 and various values of the fractional parameter α , showing the impact of anomalous thermal conductivity on

the mechanical response. As α decreases, the displacement profile becomes sharper and more localized, indicating stronger non-local effects and delayed thermal diffusion. This behavior indicates a significant limitation of thermal diffusion, resulting in a reduced and more constrained mechanical response. Consequently, the displacement field tends to freeze. In contrast, under normal (classical) thermal conduction, the thermal energy propagates more rapidly through the medium, leading to a broader and more extended displacement profile over space and time. This demonstrates the influence of fractional-order behavior on the deformation characteristics of the material, while Fig. 4 represents the displacement at $\alpha=0.5$ and different values of time t=0.1, 0.5, 1, 5 and 10. The results demonstrate that, as time increases, the displacement propagates and smoothens, showing the diffusive nature of the underlying thermoelastic response. The observed behavior also emphasizes the time-dependent influence of anomalous thermal conductivity on the mechanical response of the medium.

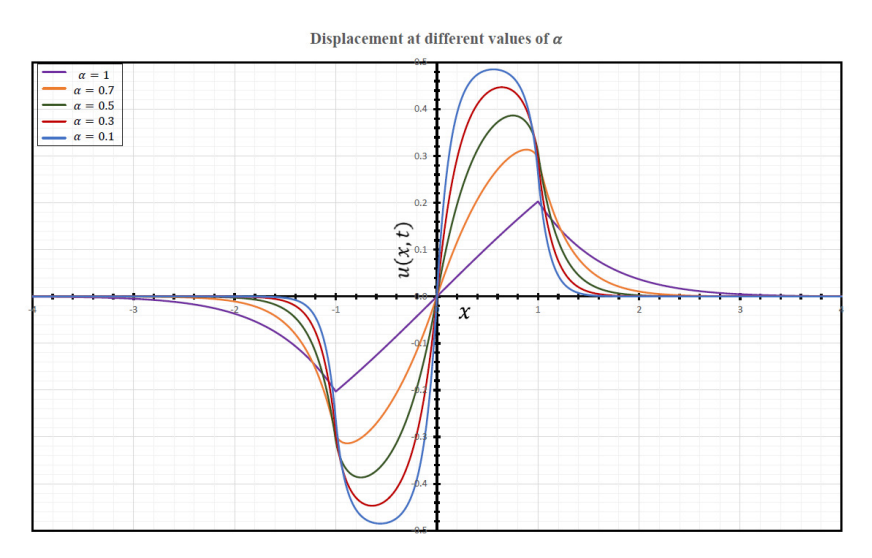


Fig. 3. As the thermal conductivity decreases—represented by lower values of the fractional parameter α is the displacement profile becomes increasingly localized and exhibits sharper curvature near the origin

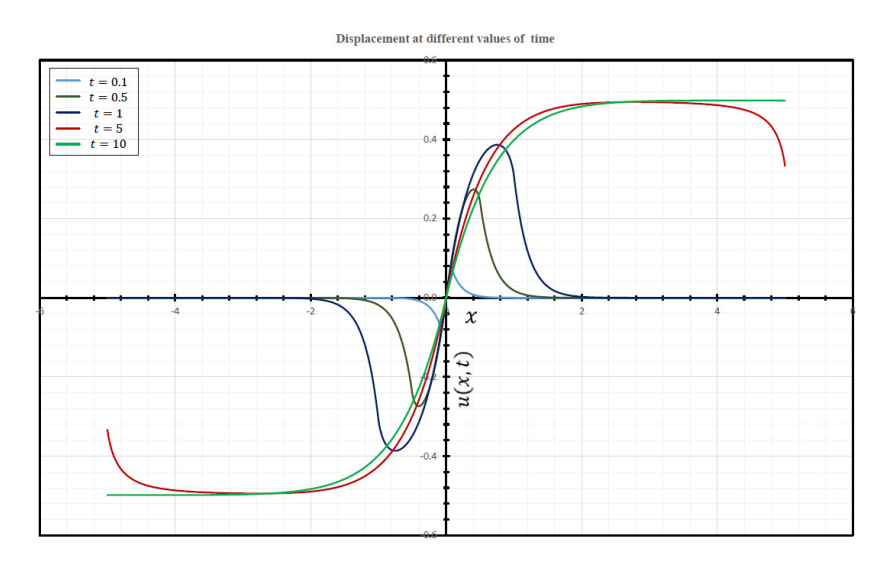


Fig. 4. The spatial profile of the displacement u(x,t) illustrated for various values of time t, highlighting the temporal evolution of the displacement field

Figure 5 represents the hydrostatic stress at t=1 and different values of α which reveal a significant role of the fractional-order parameter in governing the thermoelastic behavior of the material. As α decreases, corresponding to stronger anomalous diffusion effects, the stress profiles exhibit sharper gradients and deeper dips. This indicates an intense stress concentration. Figure 6 demonstrates the temporal evolution of the stress field, as time progresses, the stress profile becomes increasingly, well-defined and exhibits greater symmetry about the origin, with the peak values shifting spatially and magnifying in magnitude. The results show that, over time, the stress profile becomes clearer and more symmetric around the origin, with peak magnitudes shifting and deepening. This behavior reflects the dynamic coupling between thermal diffusion and mechanical deformation, further influenced by the anomalous heat conduction mechanism.

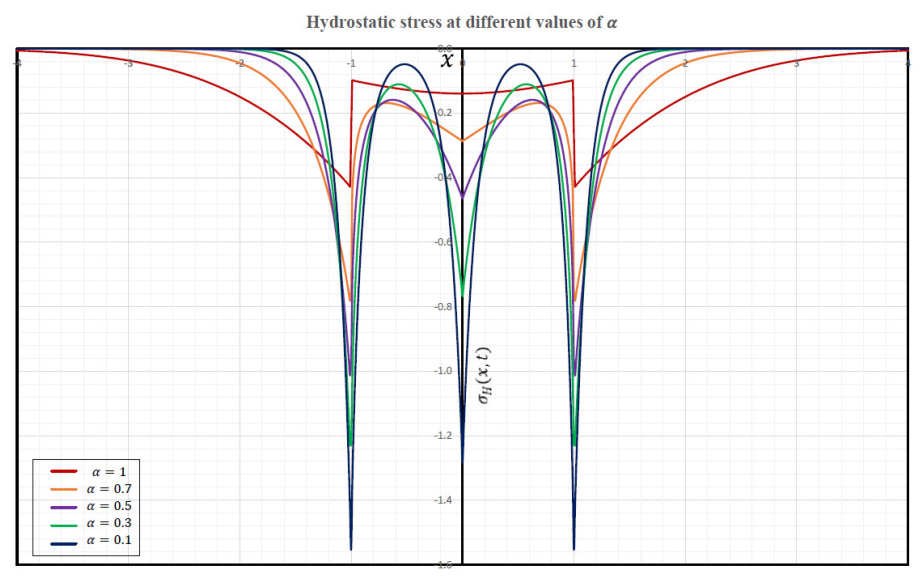


Fig. 5. The distribution of hydrostatic stress represented for various values of the fractional parameter α , illustrating the influence of anomalous thermal conductivity on the stress response

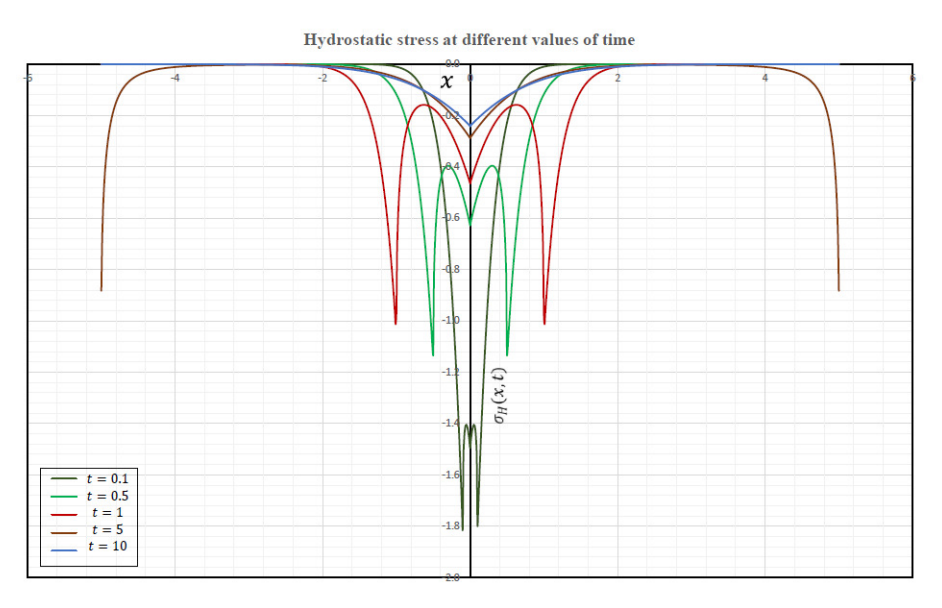


Fig. 6. The variation of hydrostatic stress presented for different time instances t, showing the temporal evolution of the stress field

Conclusions

The interaction between electromagnetic fields and fractional-order thermoelasticity in unbounded domains was studied. By incorporating Maxwell's equations into the governing system and applying Laplace and Fourier transforms, the uncoupled equations for temperature and displacement are solved analytically. The analysis reveals the finite-speed propagation of thermal and mechanical waves and highlights the effects of material parameters on the system's response. Analytical techniques are employed to solve the system, revealing that the electromagnetic effects do not significantly influence the temperature.

CRediT authorship contribution statement

Noha Samir DSC: writing – original draft, investigation, data curation; **Mohamed A. Abdou DSC**: writing – review & editing, supervision, data curation; **Emad Awad DSC**: conceptualization, supervision, writing – review & editing, investigation.

Conflict of interest

The authors declare that they have no conflict of interest.

References

- 1. Biot MA. Thermoelasticity and irreversible thermodynamics. *Journal of Applied Physics*. 1956;27(3): 240–253.
- 2. Povstenko YZ. Fractional heat conduction equation and associated thermal stress. *Journal of Thermal Stresses*. 2005;28(1): 83–102.
- 3. Samir N, Abdou MA, Awad E. On the quasi-static theory of space-time fractional thermoelasticity in the unbounded domains. *Faculty of Education Journal Alexandria University*. 2024;34(4): 313–349.
- 4. Rukolaine SA. Hyperbolicity of the ballistic-conductive model of heat conduction: the reverse side of the coin. *Zeitschrift für angewandte Mathematik und Physik.* 2024;75(2): 50.
- 5. Rukolaine S. Effects observed in the ballistic-conductive model of heat conduction. *St. Petersburg State Polytechnical University Journal. Physics and Mathematics.* 2023;16(1.2): 315–321.
- 6. Sobolev SL. Nonlocal two-temperature model: Application to heat transport in metals irradiated by ultrashort laser pulses. *International Journal of Heat and Mass Transfer.* 2016;94: 138–144.
- 7. Sobolev SL, Kudinov IV. Dispersion relation and frequency-dependent thermal conductivity of the two-temperature systems. *International Journal of Thermal Sciences*. 2025;214: 109937.
- 8. Awad E, Dai W, Sobolev S. Thermal oscillations and resonance in electron-phonon interaction process. *Zeitschrift für angewandte Mathematik und Physik.* 2024;75(4): 143.
- 9. Bassiouny E. Hyperbolic two temperature fractional order one dimensional thermoelastic model heated by a pulse of laser. *Materials Physics and Mechanics*. 2020;44(1): 66–76.
- 10. Kumar R, Vohra R. Steady state response due to moving load in thermoelastic material with double porosity. *Materials Physics and Mechanics*. 2020;44(2): 172–185.
- 11. Levi GY, Igumnov L. Some properties of the thermoelastic prestressed medium Green function. *Materials Physics and Mechanics*. 2015;23(1): 42–46.
- 12. Griffiths DJ. Introduction to electrodynamics. Cambridge University Press; 2023.
- 13. Doria R, Mendes LS. Four-Four Maxwell equations. *Modern Physics Letters A*. 2023;38(22n23): 2350106.
- 14. Jackson JD. Classical electrodynamics. John Wiley & Sons; 2021.
- 15. Ramzan M, Gul H, Mursaleen M, Nisar KS, Jamshed W, Muhammad T. Von Karman rotating nanofluid flow with modified Fourier law and variable characteristics in liquid and gas scenarios. *Scientific Reports*. 2021;11(1): 16442.
- 16. Awad E. Modeling of anomalous thermal conduction in thermoelectric magnetohydrodynamics: Couette formulation with a multiphase pressure gradient. *Physics of Fluids*. 2024;36(3): 033608.

17. Awad E, Samir N. A closed-form solution for thermally induced affine deformation in unbounded domains with a temporally accelerated anomalous thermal conductivity. *Journal of Physics A: Mathematical and Theoretical.* 2024;57(45): 455202.

- 18. Awad E, Metzler R. Crossover dynamics from superdiffusion to subdiffusion: Models and solutions. *Fractional Calculus and Applied Analysis*. 2020;23(1): 55–102.
- 19. Barrios-Piña H, Viazzo S, Rey C. Total energy balance in a natural convection flow. *International Journal of Numerical Methods for Heat & Fluid Flow.* 2017;27(8): 1735–1747.
- 20. Saichev AI, Zaslavsky GM. Fractional kinetic equations: solutions and applications. *Chaos: An Interdisciplinary Journal of Nonlinear Science*. 1997;7(4): 753–764.
- 21. Mainardi F, Luchko Y, Pagnini G. The fundamental solution of the space-time fractional diffusion equation. ArXiv [Preprint] 2007. Available from: doi.org/10.48550/arXiv.cond-mat/0702419.
- 22. Gorenflo R, Mainardi F. Fractional Calculus. In: Carpinteri A, Mainardi F. (eds.) *Fractals and Fractional Calculus in Continuum Mechanics*. Vienna: Springer; 1997. p.223–276.
- 23. Sandev T, Tomovski Z. Fractional equations and models: theory and applications. Cham, Switzerland: Springer; 2019.
- 24. Awad E, Sandev T, Metzler R, Chechkin A. Closed-form multi-dimensional solutions and asymptotic behaviors for subdiffusive processes with crossovers: I. Retarding case. *Chaos, Solitons & Fractals.* 2021;152: 111357.
- 25. Nowacki W. Thermoelasticity. Elsevier; 2013.
- 26. Fayik M, El Dhaba A, Awad E. Diffusion-induced stresses due to an impulsive mass source under non-Fickian mass transfer models. *Materials Physics and Mechanics*. 2023;51(1): 93–107.
- 27. Mainardi F, Mura A, Pagnini G. The M-Wright Function in Time-Fractional Diffusion Processes: A Tutorial Survey. *International Journal of Differential Equations*. 2010;2010(1): 104505.
- 28. Garra R, Garrappa R. The Prabhakar or three parameter Mittag-Leffler function: Theory and application. *Communications in Nonlinear Science and Numerical Simulation*. 2018;56: 314–329.
- 29. Mathai AM, Saxena RK, Haubold HJ. The H-function: theory and applications. Springer; 2009.
- 30. Awad E. Dual-Phase-Lag in the balance: Sufficiency bounds for the class of Jeffreys' equations to furnish physical solutions. *International Journal of Heat and Mass Transfer*. 2020;158: 119742.

Accepted: May 28, 2025

Submitted: January 28, 2025

Revised: May 15, 2025

Elastic deformation and elastic wave velocity in metals (Au, Cu) and interstitial alloy (CuSi) with FCC structure

Q.H. Nguyen ^{1,2} , K.V. Tran ², S.G.K. Quach ³, Q.T. Doan ⁴, N.P.A. Nguyen ⁴,

T.S.M. Nguyen ¹, D.H. Nguyen ⁵, A.T. Tran ³

- ¹ Hanoi National University of Education, Hanoi, Vietnam
- ² Dai Nam University, Hanoi, Vietnam
- ³ Vietnam National University, Hanoi, Vietnam
- ⁴ Hanoi-Amsterdam High School for the Gifted, Hanoi, Vietnam
- ⁵ Mac Dinh Chi High School, Gia Lai, Vietnam
- [™] hocng@hnue.edu.vn

ABSTRACT

A model for face centered cubic binary interstitial alloys and advance the theory of elastic deformation and wave propagation within these alloys using the statistical moment method are presented. The theory extends to include the elastic properties and wave dynamics of pure metals as a subset. The numerical simulations for metals like Au and Cu, as well as the CuSi alloy are conducted. The results obtained for Au and Cu were validated against experimental data and existing calculations. For the CuSi alloy, numerical predictions offer insights that could be confirmed by future experiments.

KEYWORDS

FCC binary interstitial alloy • elastic deformation • elastic wave propagation • statistical moment method **Citation:** Nguyen QH, Tran KV, Quach SGK, Doan QT, Nguyen NPA, Nguyen TSM, Nguyen DH, Tran AT. Elastic deformation and elastic wave velocity in metals (Au, Cu) and interstitial alloy (CuSi) with FCC structure. *Materials Physics and Mechanics.* 2025;53(3): 165–176.

http://dx.doi.org/10.18149/MPM.5332025 13

Introduction

Metals and alloys are traditional and popular materials in industry and practical life. There are substitutional alloys and interstitial alloys. In interstitial alloys, the interstitial atoms are usually non-metals such as Si, C, H, Li, etc., which are smaller in size than the main metal atom. Although the interstitial atom concentration is very small, only a few percent, it significantly affects the physical properties of the alloy. Transition metals and their interstitial alloys such as Cu, Au, CuSi, and AuSi are widely applied in superconducting wire fabrication technology [1,2].

Interstitial alloys are crucial in various aspects of human life and have long been a focus for both theoretical and experimental researchers. Investigating the deformation properties of these alloys in relation to temperature, pressure, and interstitial atom concentration is essential for predicting material strength, mechanical stability, diffusion, and other properties [3–5]. AuSi has many functional applications and unusual physical properties.

There are numerous theoretical approaches to studying the elastic deformation of metals and alloys, including the *ab initio* method, molecular dynamics method, the tight-



binding Hamiltonian method, the density functional theory, etc. In the first principles (or ab initio) method, the many-electron wavefunction is constructed from the oneelectron wavefunctions in a suitable effective potential. The calculations are based primarily on the laws of quantum mechanics and relevant physical constants such as the masses and charges of the nuclei and electrons. Ab initio has been widely used in the study of alloy deformations such as the study of the electronic and thermodynamic properties of B₂-eSi interstitial alloy by *ab initio* calculations using *ab initio* plane waves (FPPW) combined with the quasi-harmonic Debye model (QHD) [6], the study of FeH interstitial alloy by ab initio combined with DFT (the density functional theory) and GGA (generalized gradient approximation) [7], and the study of FeCrSi alloy by ab initio combined with DFT and GGA [8]. Ab initio has been used in the study of deformation of metals such as the study of the effect of pressure on the elastic properties of crystalline Au by ab initio using local density approximation (LDA) [9] and the study of the elastic modulus of the BCC (body-centered cubic)-Fe [10]. Molecular dynamics (MD) is a method of modeling atoms as a system of classical particles obeying Newtonian mechanics. Newton's second law can be used to write the equation of motion for each atom. Some works using MD to study the deformation of metals and alloys include the thermomechanical properties of CuAu alloy [11], the effect of pressure on the elastic constants of Cu, Aq and Au [12], the thermomechanical properties of some FCC (face centered cubic) transition metals [13], using Morse potential to study the temperature dependence of Young's modulus for metals Ni, Cu, Aq, Au and Al by Zahroh et al. [14]. The tight-coupled Hamiltonian (TB) method [15-17] is simpler, less computationally intensive but can be applied to larger model systems than ab initio. Recent studies have used the TB Hamiltonian method to calculate the atomic volumes, elastic constants, bulk moduli, etc. of FCC and HCP (hexagonal close-packed) crystals [17] and to study the structural properties of FCC transition metals [16]. In the density functional theory (DFT), instead of using a multi-electron wave function as in the Hartree-Fock method, the electron density plays a central role [18] and the total energy of the system is a unique function of the electron density. DFT studies of metals and alloys can be mentioned as works by Olsson et al. [19], Psiachos et al. [7] and Lau et al. [20]. In addition to the methods mentioned above, to study the properties of materials, there are other methods such as the modified embedded atom method (MEAM) [21-23], the lattice Green's function method [24], the machine learning method (MLM) [25], harmonic theory [26] and quasiharmonic theory [27], etc. From the methods presented above, we see that most of the methods for studying the deformation of metal and alloy crystals are approximate methods, not mentioning the influence of pressure on the deformation processes of the object, not considering the dependence of the deformation quantities depending on the concentration of substitutional and interstitial atoms. The results of theoretical methods for studying deformation are mostly for metals and are limited for alloys. Some results obtained from theoretical methods are not really consistent with experiments.

For example, the interaction of impurity atoms of light elements with vacancies and vacancy clusters in FCC metals was studied by MD of Poletaev et al. [28]. Among theoretical methods in studying mechanical and thermodynamic properties of metals and alloys, the statistical moment method (SMM) has significant contributions [29]. SMM is a contemporary approach in statistical physics used to examine the structure,

thermodynamic properties, elasticity, diffusion, phase transitions of metals, alloys, semiconductors, inert gases, oxides with BCC, FCC and HCP structures. SMM has been particularly applied to the thermodynamic study of cubic interstitial alloys [30–35]. Recently, the SMM has been successfully applied in the study of thermomechanical properties of multicomponent materials with complex structures such as HCP metals of Hoc et al. [36,37], ternary and binary interstitial alloys of Hoc et al. [34,38,39], perovskite-structured alloys of Hoc et al. [40–42].

There are many studies on classical wave propagation in complex materials with periodic structure [43–46]. Some work has been extended to the study of sound waves and elastic waves in other periodic media. Most of the research on this problem is based on the calculations of the plane wave method [47–51]. The planar wave method has proved to be quite effective in studying many types of periodic complex structures but is less effective for disordered chaotic systems. Multiple-scattering theory (MST) method [52,53] is based on electronic band structure calculations. The equations of motion of the particles are builded in an elastic body [54]. Some works such as the work of Grechka et al. [55] refer to the propagation of sound waves in an anisotropic medium. Mozhaev [56] showed its applicability to two- and three-partial surface acoustic waves in crystals. Additionally, Nayfeh and Chimenti [57] extend the analysis to free wave propagation in a general anisotropic plate, presenting numerical results for special cases.

In this paper, we examine the elastic deformation and wave propagation in FC binary interstitial alloys under pressure using the SMM. The next section will detail the theory and methodology and numerical results.

Theory and Methodology

Our model of FCC interstitial alloy AB assumes that the concentration of interstitial atoms B is very small compared to the concentration of main metal atoms A. In this model, atoms B are located at the body center, atoms A_1 are at the face centers, and atoms A_2 are at the vertices of the cubic unit cells [30–35].

To investigate the elastic properties of alloy AB using SMM, we first calculate the mean nearest neighbor distance between two atoms A in the alloy using the following equations [31,32,35]:

$$\frac{r_{1A}(P,T)}{y(P,T)} = \frac{r_{01A}(P,0)}{r_{01A}(P,0)} + \frac{r_{01A}(P,0)}{y(P,T)}, \quad \overline{r_{01A}(P,0)} = (1 - c_B)r_{01A}(P,0) + c_B r_{01A}(P,0),
y(P,T) = \sum_{X} c_X y_X(P,T), r_{01A}(P,0) = \sqrt{3}r_{01B}(P,0),
r_{1B}(P,T) = r_{01B}(P,0) + y_{A_1}(P,T), \quad r_{1A}(P,T) = r_{01A}(P,0) + y_{A}(P,T),
r_{1A_1}(P,T) = r_{1B}(P,T), \quad r_{1A_2}(P,T) = r_{01A_2}(P,0) + y_{B}(P,T),
y_X(P,T) = \sqrt{\frac{2\gamma_X(P,0)\theta^2}{3k_X^3(P,0)}} A_X(P,T), \quad A_X(P,T) = a_{1X}(P,T) + \sum_{i=2}^{6} \left(\frac{\gamma_X(P,0)\theta}{k_X^2(P,0)}\right)^i a_{iX}(P,T),
Z_X \equiv x_X \coth x_X, \quad x_X = \frac{\hbar}{2\theta} \sqrt{\frac{k_X}{m_X}},
a_{1X} = 1 + \frac{1}{2} Z_X, \quad a_{2X} = \frac{13}{3} + \frac{47}{6} Z_X + \frac{23}{6} Z_X^2 + \frac{1}{2} Z_X^3,
a_{3X} = -\left(\frac{25}{3} + \frac{121}{6} Z_X + \frac{50}{3} Z_X^2 + \frac{16}{3} Z_X^3 + \frac{1}{2} Z_X^4\right),
a_{4X} = \frac{43}{3} + \frac{93}{2} Z_X + \frac{169}{3} Z_X^2 + \frac{83}{3} Z_X^3 + \frac{22}{3} Z_X^4 + \frac{1}{2} Z_X^5,$$
(1)

$$\begin{split} a_{5\mathrm{X}} &= -\left(\frac{103}{3} + \frac{749}{6}Z_X + \frac{363}{2}Z_X^2 + \frac{391}{3}Z_X^3 + \frac{148}{3}Z_X^4 + \frac{53}{6}Z_X^5 + \frac{1}{2}Z_X^6\right),\\ a_{6\mathrm{X}} &= 65 + \frac{561}{2}Z_X + \frac{1489}{3}Z_X^2 + \frac{927}{2}Z_X^3 + \frac{733}{3}Z_X^4 + \frac{145}{2}Z_X^5 + \frac{31}{3}Z_X^6 + \frac{1}{2}Z_X^7. \end{split}$$

Here, $r_{1A}(P,T) \equiv a_{1A}(P,T)$ and $r_{01A}(P,0) \equiv a_{01A}(P,0)$ denote the mean nearest neighbor distances between two atoms A in the alloy under pressure P and temperature T, and under pressure P and temperature T = 0 K, respectively. The mean displacement of atom A from its equilibrium position in the alloy is indicated by $\overline{y(P,T)}$. The nearest neighbor distance between two atoms A in the pure metal is labeled $r_{01A}(P,0)$. The distance between two atoms A in the region containing the interstitial atom B is denoted by $r'_{01A}(P,0)$. The displacement of an atom X (where X can be A, A₁, A₂, B) within the alloy is represented by $y_X(P,T)$. The nearest neighbor distances between two atoms A in the pure metal or between atom X and other atoms in the alloy are represented by $r_{1X}(P,T)$ and $r_{01X}(P,0)$.

The value $r_{01X}(P,0)$ is derived either from the condition of minimum u_{0X} or from the equation of state, as detailed in [30,32,33]:

$$Pv_{0X} = -r_{01X} \left(\frac{1}{6} \frac{\partial u_{0X}}{\partial r_{01X}} + \frac{\hbar \omega_{0X}}{4k_X} \frac{\partial k_X}{\partial r_{01X}} \right), \tag{2}$$

where
$$r_{01X} \equiv r_{01X}(P,0)$$
, $v_{0X} = \frac{r_{01X}^3}{\sqrt{2}}$, $\omega_{0X} = \sqrt{\frac{k_X(P,0)}{m_X}}$, $c_X = \frac{N_X}{N}$, $N = N_A + N_{A_1} + N_{A_2} + N_B$,

 $\theta = k_B T$, k_B represents the Boltzmann constant, \hbar is the Planck constant. The symbol m_X denotes the mass of atom X. The terms u_{0X} , k_X , γ_{1X} , γ_{2X} and γ_X correspond to the cohesive energy and crystal parameters of atom X within the metal A or the alloy AB, as detailed in [30,32,33]:

$$u_{0X} = \frac{1}{2} \sum_{i=1}^{n_i} \varphi_{i0},$$

$$k_X = \frac{1}{2} \sum_{i=1}^{n_i} \left(\frac{\partial^2 \varphi_{i0}}{\partial u_{i\beta}^2} \right)_{eq} = m_X \omega_X^2, \gamma_X = 4(\gamma_{1X} + \gamma_{2X}),$$

$$\gamma_{1X} = \frac{1}{48} \sum_{i=1}^{n_i} \left(\frac{\partial^4 \varphi_{i0}}{\partial u_{i\beta}^4} \right)_{eq}, \gamma_{2X} = \frac{6}{48} \sum_{i=1}^{n_i} \left(\frac{\partial^4 \varphi_{i0}}{\partial u_{i\alpha}^2 \partial u_{i\beta}^2} \right)_{eq},$$
(3)

where $u_{i\beta}(\beta=x,y,z)$ represents the displacement of the ith particle from its equilibrium position in the direction β , φ_{i0} indicates the interaction potential between the 0th particle and the ith particle, and (...)_{eq} denotes the value of these parameters at equilibrium. The number of atoms in n_i coordination sphere is indicated by n_i , α , $\beta=x$, y, z, $\alpha\neq\beta$.

The Helmholtz free energy of the alloy AB is expressed as follows [29-33,35]:

$$\Psi_{AB} = N \psi_{AB} = N(\sum_X c_X \psi_X - TS_c^{AB}),$$

$$\Psi_{X} = N\Psi_{X} = U_{0X} + \Psi_{0X} + 3N \left\{ \frac{\theta^{2}}{k_{X}^{2}} \left[\gamma_{2X} Z_{X}^{2} - \frac{2\gamma_{1X}}{3} \left(1 + \frac{Z_{X}}{2} \right) \right] + \frac{2\theta^{3}}{k_{X}^{4}} \left[\frac{4}{3} \gamma_{2X}^{2} Z_{X} \left(1 + \frac{Z_{X}}{2} \right) - 2 \left(\gamma_{1X}^{2} + 2\gamma_{1X} \gamma_{2X} \right) \left(1 + \frac{Z_{X}}{2} \right) (1 + Z_{X}) \right] \right\},$$
(4)

 $\Psi_{0X} = 3N\theta[x_X + \ln(1 - e^{-2x_X})],$

where $c_A=1-15c_B$, $c_{A_1}=6c_B$, $c_{A_2}=8c_B$ and S_c^{AB} is the configurational entropy of the alloy AB.

Young modulus of the alloy AB is given by [31,33,34,36]:

$$E_{\text{YAB}} = E_{\text{YA}} \frac{\sum_{X} c_{X} \frac{\partial^{2} \Psi_{X}}{\partial \varepsilon^{2}}}{\frac{\partial^{2} \Psi_{A}}{\partial \varepsilon^{2}}}, E_{\text{A}} \frac{1}{\pi r_{1\text{A}} B_{1\text{A}}}, B_{1\text{A}} = \frac{1}{k_{A}} \left[1 + \frac{2 v_{A}^{2} \theta^{2}}{k_{A}^{4}} \left(1 + \frac{1}{2} Z_{A} \right) (1 + Z_{A}) \right],$$

$$\frac{1}{3\text{N}} \frac{\partial^{2} \Psi_{X}}{\partial \varepsilon^{2}} = \left\{ \frac{2}{3} \frac{\partial^{2} u_{0X}}{\partial r_{1X}^{2}} + \frac{\hbar \omega_{X}}{k_{X}} \left[\frac{\partial^{2} k_{X}}{\partial r_{1X}^{2}} - \frac{1}{2k_{X}} \frac{\partial k_{X}}{\partial r_{1X}} \right] \right\} r_{01X}^{2} + \left(\frac{\partial u_{0X}}{\partial r_{1X}} + \frac{3\hbar \omega_{X} \coth x_{X}}{2k_{X}} \frac{\partial k_{X}}{\partial r_{1X}} \right) r_{01X},$$
(5)

where $E_{\rm YA}$ is Young's modulus of the pure metal A and ε represents the strain of the alloy AB.

The bulk modulus K_{AB} , shear modulus G_{AB} , elastic constants C_{11AB} , C_{12AB} , C_{44AB} , Poisson's ratio v_{AB} , longitudinal wave velocity $V_{\ell AB}$ and transverse wave velocity V_{tAB} are calculated by Hoc et al. [30,32,33,35]:

$$K_{\rm AB} = \frac{E_{\rm YAB}}{3(1-2v_{\rm AB})},\tag{6}$$

$$G_{AB} = \frac{E_{YAB}}{2(1+y_{AB})},\tag{7}$$

$$G_{AB} = \frac{E_{YAB}}{2(1+\nu_{AB})},$$

$$C_{11AB} = \frac{E_{YAB}(1-\nu_{AB})}{(1+\nu_{AB})(1-2\nu_{AB})},$$

$$C_{12AB} = \frac{E_{YAB}\nu_{AB}}{(1+\nu_{AB})(1-2\nu_{AB})},$$

$$C_{12AB} = \frac{E_{YAB}\nu_{AB}}{(1+\nu_{AB})(1-2\nu_{AB})},$$

$$C_{12AB} = \frac{E_{YAB}\nu_{AB}}{(1+\nu_{AB})(1-2\nu_{AB})},$$

$$C_{12AB} = \frac{E_{YAB}\nu_{AB}}{(1+\nu_{AB})(1-2\nu_{AB})},$$

$$(8)$$

$$V_{AB} = c_{A}\nu_{A} + c_{B}\nu_{B} \approx \nu_{A},$$

$$(9)$$

$$\nu_{AB} = c_A \nu_A + c_B \nu_B \approx \nu_A,\tag{9}$$

$$v_{AB} = c_A v_A + c_B v_B \approx v_A,$$

$$V_{IAB} = \sqrt{\frac{2C_{44AB} + C_{12AB}}{\rho_{AB}}}, V_{tAB} = \sqrt{\frac{C_{44AB}}{\rho_{AB}}},$$
(10)

where v_A and v_B respectively are the Poisson ratios of materials A and B, $ho_{AB}=rac{m_{AB}}{v_{AB}}pprox
ho_A$, $V_{
m AB}={
m Nv_{AB}}$, $ho_{
m AB}$ and ho_A denote the densities of materials A and AB, respectively while $V_{
m AB}$ represents the volume of alloy AB.

When the concentration of interstitial atoms is zero, the characteristic quantities for elastic deformation and elastic wave propagation of the primary metal A can be ascertained. For Au, Cu, and CuSi, we utilize the Mie-Lennard-Jones (MLJ) potential as follows Magomedov [58,59]:

$$\varphi(r) = \frac{D}{n-m} \left[m \left(\frac{r_0}{r} \right)^n - n \left(\frac{r_0}{r} \right)^m \right]. \tag{11}$$

The parameters D, r_0 , n, m, the Poisson's ratio ν and the density ρ are listed in Table 1.

Table 1. Potential parameters, Poisson ratio ν and density ρ [58–60]

Interaction	т	n	<i>D/k</i> _B , K	r_0 , 10 ⁻¹⁰ m	ν	ρ , g/cm ³
Au-Au	5.5	10.5	4683	2.8751	0.39	19.283
Cu-Cu	5.5	11	3401.1	2.5487	0.37	8.932
Si-Si	6	12	32701.7	2.295	0.28	2.329

The Cu-Si interaction is also described using the MLJ n-m potential:

$$\varphi(r) = \frac{\bar{D}}{\bar{n} - \bar{m}} \left[\bar{m} \left(\frac{r_0}{r} \right)^{\bar{n}} - \bar{n} \left(\frac{r_0}{r} \right)^{\bar{m}} \right], \tag{12}$$

$$\bar{D}_{\text{Cu-Si}} = \sqrt{D_{\text{Cu-Cu}}D_{\text{Si-Si}}}, \, \bar{r}_{\text{0Cu-Si}} = \frac{1}{2}(r_{\text{0Cu-Cu}} + r_{\text{0Si-Si}}),$$
 (13)

where \bar{n} and \bar{m} are empirically determined [61]. Therefore, $\bar{D}_{\text{Cu-Si}}/k_B=10546.2$ K, $\bar{r}_{\text{0Cu-Si}} = 2.4218 \times 10^{-10} \text{ m}$, and we empirically choose $\bar{n} = 1.29$, $\bar{m} = 9.92$ by fitting the theoretical result with the experimental data of Santra et al. [2].

The numerical calculations for Au, Cu and CuSi are placed below. The calculated results for the elastic moduli E_Y and K, the volume ratio V/V_0 (where V is the volume at pressure P and V_0 is the volume at P = 0), the elastic constant C_{44} and the longitudinal wave velocity V_{ℓ} for metals Au and Cu are summarized in Table 2 and illustrated in Figs. 1–6.

Table 2. G(P,T) for Cu from SMM calculations, other calculations and experiments

P, GPa	<i>T</i> , K	<i>G</i> , GPa SMM	<i>G</i> , GPa Expt. [62]	<i>G</i> , GPa Calc. [62]	δ _{SMM-Expt. [62]} , %	$\delta_{ ext{Calc. [31]-Expt. [62]}}$, $\%$
12.1	346	5.94	6.28	5.95	5.7	5.5
12.5	348	6.00	5.90	5.99	1.7	1.5
23.2	418	7.50	7.55	7.14	0.7	5.7

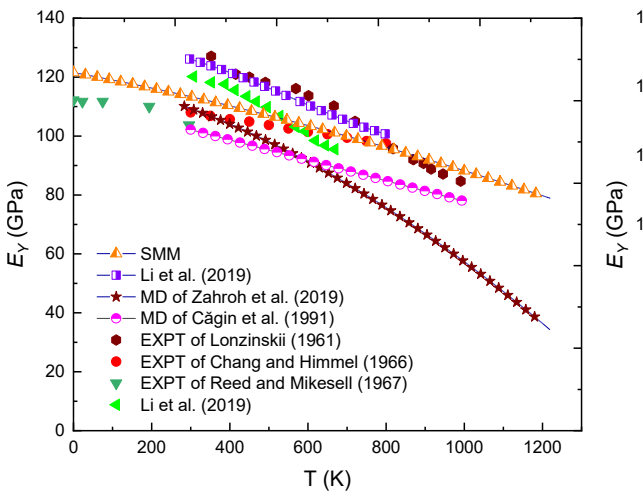


Fig. 1. The temperature dependence of Young modulus E_Y for Cu at P = 0 using SMM calculations, other calculations [13,63,64] and experiments [64–67]

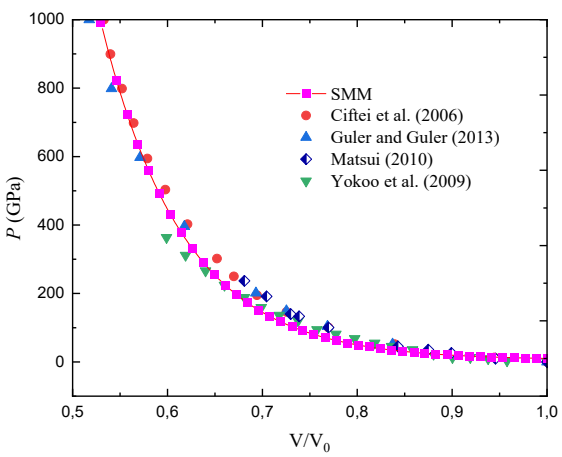


Fig. 3. The pressure dependence of volume ratio V/V_0 for Au at T = 300K using SMM calculations and other calculations [21,69–71]

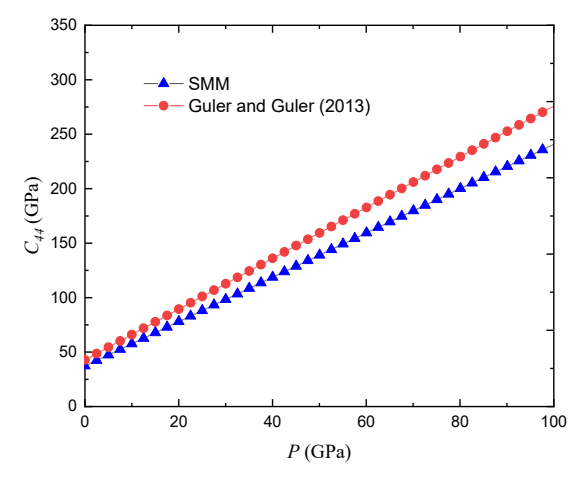


Fig. 5. The pressure dependence of elastic constant C_{44} for Au at T = 300K using SMM calculations and other calculations [21]

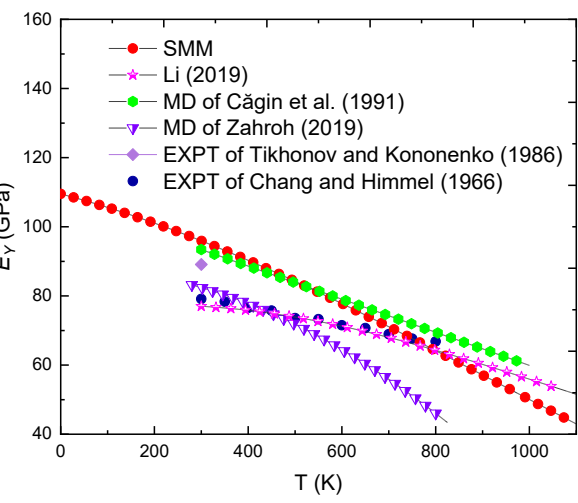


Fig. 2. The temperature dependence of Young modulus E_Y for Au at P = 0 using SMM calculations, other calculations [13,14,66] and experiments [65,68]

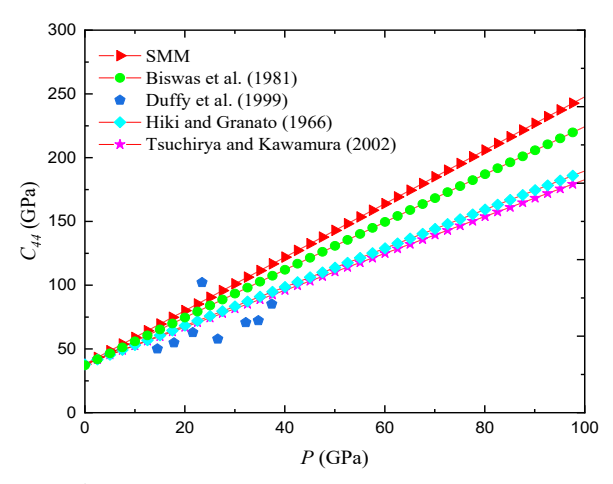


Fig. 4. The pressure dependence of elastic constant C_{44} for Au at T = 300K using SMM calculations and experiments [3,9,72,73]

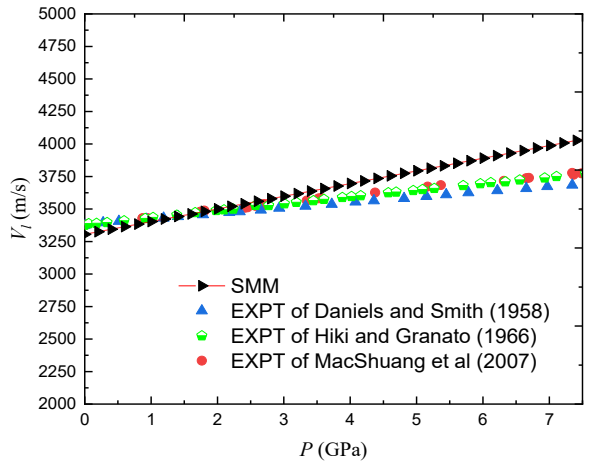


Fig. 6. The pressure dependence of longitudinal wave velocity V_{ℓ} for Au at T=300 K using SMM calculations and experiments [73–75]

In Table 2, we compare the shear modulus G of Cu calculated by the SMM with other theoretical calculations and experimental data from Peng et al. [62]. The SMM calculations are in good agreement with both the theoretical and experimental results of Peng et al. [62] with an overall error of 5.7 %. Notably, at P = 23.2 GPa, the discrepancy between the SMM calculations and experimental results is only 0.7 %, whereas the error between Peng et al. calculations [62] and experiments is 5.7 %.

Figure 1 shows the temperature dependence of Young's modulus E_Y for Cu at P=0in the range from 0 to 1200 K. The SMM calculations are in good agreement with calculations of Căgin et al. [13], Li et al. [63], Zahroh et al. [14] and experiments of Lonzinskii [64], Chang and Himmel [65], Reed and Mikesell [66], Joshi and Bhatnagar [67]. Figure 2 illustrates the temperature dependence of Young's modulus E_Y for Au at P=0 in the range from 0 to 1100 K. The SMM calculations are in good agreement with calculations of Căgin et al. [13], Li et al. [63], Zahroh et al. [14] as well as experiments of Chang and Himmel [65], Tikhonov and Kononenko [68]. Figure 3 shows the pressure dependence of volume ratio V/V_0 for Au at T=300 K in the range from 0 to 1000 GPa. The SMM calculations are in excellent agreement with other calculations of Ciftci et al. [69], Yokoo et al. [70], Matsui [71] and Guler and Guler [21]. Figure 4 illustrates the pressure dependence of elastic constant C_{44} for Au at T = 300 K in the range from 0 to 100 GPa. SMM calculations are compared with experimental data from Biswas et al. [72], Hiki and Granato [73], Duffy et al. [3], Tsuchiya and Kawamura [9]. The SMM calculations align more closely with experimental data in the range from 0 to 30 GPa than in the range from 30 to 100 GPa. Most SMM calculations are higher than the experimental values with the discrepancy increasing at higher pressures. This difference is likely due to the influence of defects such as vacancies on the metal's volume at high pressures, which is not accounted for in our model. Figure 5 presents the pressure dependence of the elastic constant C_{44} for Au at T = 300K in the range from 0 to 100 GPa calculated by SMM and other calculations of Guler and Guler [21]. The observations and comments for this figure are similar to those for Fig. 4. The pressure dependence of longitudinal wave velocity V_{ν} for Au at T = 300K in the range from 0 to 7.5 GPa is shown in Fig. 6. Here there is a good agreement between SMM calculations and experiments of Hiki and Granato [73], Daniels and Smith [74], Mao Shuang et al. [75]. The agreement between SMM calculations and experiments in the range from 0 to 2 GPa is better than in the range from 2 to 7.5 GPa.

The analysis above indicates that SMM calculations for metals Au and Cu are in very good agreement with experimental data and other calculations. In many cases, our SMM calculations are closer to the experimental values in comparison with other calculations. This provides a strong foundation for our subsequent calculations for the interstitial alloy CuSi.

The SMM calculations for elastic deformation quantities of CuSi are shown in Figs. 7 and 8. Figure 7 illustrates the silicon atom concentration dependence of Young's modulus E_Y for CuSi at T=300 K and P=0 in the range of silicon atom concentration from 0 to 5 %. These SMM calculations are compared with experimental data from Ledbetter and Naimon [76] and Santra et al. [2]. As silicon concentration increases, E_Y decreases, which is consistent with experiments of Santra et al. [2]. The closest alignment between our calculations and experimental data is at a silicon concentration of 4 %. Figure 8 shows the temperature and pressure dependence of Young's modulus E_Y for CuSi at silicon

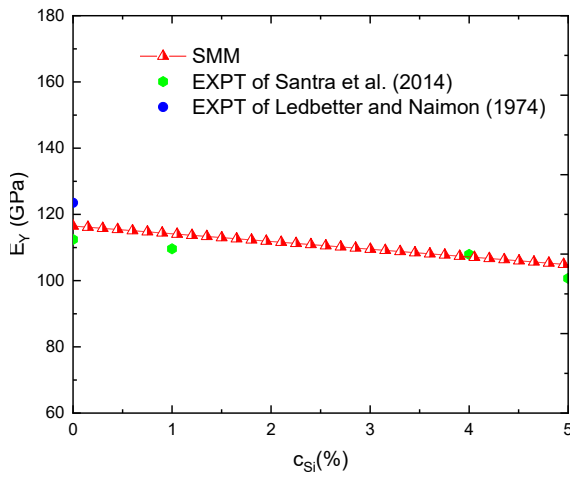


Fig. 7. The silicon atom concentration dependence of Young's modulus E_Y for CuSi at T = 300 K and P = 0 using SMM calculations and experiments [2,76]

Fig. 8. The temperature and pressure dependence of Young's modulus $E_{\rm Y}$ for CuSi at silicon concentration $c_{\rm Si}$ = 1 % using SMM calculations

concentration $c_{\rm Si}$ = 1 % in the temperature range from 0 to 1100 K and the pressure range from 30 to 70 GPa using SMM calculations. Our SMM calculations demonstrate that Young's modulus for CuSi decreases with increasing temperature and increases with increasing pressure.

Young's modulus E_Y of CuSi exhibits a decline with increasing temperature T. For CuSi with a silicon concentration of 3 % and at P=0, E_Y drops from 114.89 to 93.45 GPa as T rises from 0 to 1100 K. This is because the kinetic energy of the atoms increases with temperature, causing the lattice constants to expand, and consequently, E_Y , K, G, C_{11} , C_{12} , C_{44} , V_ℓ and V_t all decrease. Conversely, E_Y increases with pressure P. For CuSi with 1 % silicon at T=300 K, E_Y rises from 114.28 to 308.58 GPa as P increases from 0 to 70 GPa. This is due to the compressive force acting on the material, which reduces the lattice constant and results in increases in E_Y , K, G, C_{11} , C_{12} , C_{44} , V_ℓ and V_t . Additionally, E_Y decreases as the concentration of interstitial silicon atoms increases. Our SMM calculations align well with the experimental data from Santra et al. [2]. As explained by this group, when the crystal lattice of Cu is supplemented with Si, the lattice constants increase.

Increases according to a linear law. As a result, the interactions between the particles in the crystal lattice weaken and E_Y , K, G, C_{11} , C_{12} , C_{44} , V_ℓ and V_t decrease. This rule is also consistent with experiments of Smith and Burns [77], in which, when $c_{\rm Si}$ increases from 0 to 4 %, C_{44} of CuSi decreases from 75.6 to 75.5 GPa.

Conclusions

The new contribution of the paper is the development of statistical moment method (SMM) in studying the elastic deformation properties and elastic wave velocity of interstitial alloy materials with face-centered cubic (FCC) structure. By applying SMM, the paper derives the analytical expression of Helmholtz free energy, the average nearest neighbor distance between two main metal atoms, characteristic elastic deformation and elastic wave quantities such as Young's modulus, bulk compressive modulus, shear modulus, elastic constants, longitudinal wave velocity and transverse wave velocity of

binary interstitial alloys with FCC structure. The elastic deformation and elastic wave quantities of the main metal in the interstitial alloy are a special case when the interstitial atom concentration is zero. The numerical calculation results of SMM using Mie-Lennard-Jones (n-m) interaction potential, coordination sphere method, Maple and Origin softwares for Au, Cu metals are in good agreement with the experimental results and other calculation results. The numerical results for CuSi interstitial alloys are new and predictive, providing guidance for experiments. The studied temperature range is from 0 to 1200 K, the studied pressure range is from 0 to 1000 GPa and the interstitial atomic concentration range is from 0 to 5 %.

CRediT authorship contribution statement

Nguyen Quang Hoc conceptualization, methodology, validation, investigation, project management, supervisor, writing - original draft preparation, data curation, writing-review and editing; Tran Ky Vi Quach Si Gia Khoa, Doan Quang Tuan, Nguyen Ngoc Phuong Anh, Nguyen Thi Sao Mai, Nguyen Duc Hien Sc, Tran Anh Tuan investigation, data analysis, resource, software, visualization, writing—original draft preparation.

Conflict of interest

The authors declare that they have no conflict of interest.

References

- 1. Nyilas RD, Frank S, Spolenak R. Revealing plastic deformation mechanisms in polycrystalline thin films with synchrotron XRD. *JOM*: The *Journal of Minerals, Metals and Materials Society.* 2010;62: 44–51.
- 2. Santra S, Dong H, Laurila T, Paul A. Role of different factors affecting interdiffusion in Cu(Ga) and Cu(Si) solid solutions. *Proceedings of Royal Society A.* 2014;470(2161): 20130464.
- 3. Duffy TS, Shen G, Heinz DL, Shu J, Ma Y, Mao HK, Hemley RJ, Singh AK. Lattice strains in gold and rhenium under nonhydrostatic compression to 37 GPa. *Physical Review B*. 1999;60(22): 15063–15073.
- 4. Esfahani MN, Jabbari M. Molecular dynamics simulations of deformation mechanisms in the mechanical response of nanoporous gold. *Materials*. 2020;13(9): 2071.
- 5. Singh BN, Huang X, Tähtinen S, Moilanen P, Jacquet P, Dekeyser J. *Final report on in-reactor uniaxial tensile deformation of pure iron and Fe-Cr alloy.* Roskilde: Risø National Laboratory; 2007.
- 6. Zhao KM, Jiang G, Wang L. Electronic and thermodynamic properties of B_2 -FeSi from first-principles. *Physica B Condensed Metter.* 2011;406(3): 363–367.
- 7. Psiachos D, Hammerschmidt T, Drautz R. Ab initio study of the modification of elastic properties of α -iron by hydrostatic strain and by hydrogen interstitials. *Acta Materialia*. 2011;59(11): 4255–4263.
- 8. Zhang J, Su C, Liu Y. First-principles study of bcc FeCrSi binary and ternary random alloys from special quasi-random structure. *Physica B: Condensed Matter.* 2020;586: 412085.
- 9. Tsuchiya T, Kawamura K. Ab initio study of pressure effect on elastic properties of crystalline Au. *Journal of Chemical Physics*. 2002;116(5): 2121–2124.
- 10. Zhang H, Punkkinen MPJ, Johansson BS, Vitos L. Theoretical elastic moduli of ferromagnetic bcc Fe alloys. *Journal of Physics: Condensed Matter.* 2010;22(27): 275402.
- 11. Kart HH, Tomak M, Çağin T. Thermal and mechanical properties of Cu–Au intermetallic alloys. *Modelling and Simulation in Materials Science and Engineering*. 2005;13(5): 657.
- 12. Ciftci YO, Colakoglu K, Kazanc S, Ozgen S. The effect of pressure on the elastic constants of Cu, Ag and Au: a molecular dynamics study. *Open Physics*. 2006;4(4): 472–480.

- 13. Cağın T, Dereli, Uludoğan, Tomak M. Thermal and mechanical properties of some fcc transition metals. *Physical Review B*. 1985;59(5): 3468–3473.
- 14. Zahroh FF, Sugihartono I, Safitri ED. Young's modulus calculation of some metals using molecular dynamics method based on the Morse potential. *Computational and Experimental Research in Materials and Renewable Energy (CERIMRE)*. 2019;2(1): 19–34.
- 15 Mehl MJ, Papaconstantopoulos DA, Kiossis N, Herbranson M. Tight-binding study of stacking fault energies and the Rice criterion of ductility in the fcc metals. *Physical Review B*. 2000;61(7): 4894–4897.
- 16. Rosato V, Guillope M, Legrand B. Thermodynamical and structural properties of fcc transition metals using a simple tight-binding model. *Philosophical Magazine A*. 1989;59(2): 321–336.
- 17. Vocadlo L, Price GD, Wood IG. Crystal structure, compressibility and possible phase transitions in FeSi studied by first-principles pseudopotential calculations. *Acta Crystallographica Section B: Structural Science, Crystal Engineering and Materials.* 1999;55: 484–493.
- 18. Kohn W. Electronic structure of matter-wave functions and density functionals. *Review Modern Physics*. 1999;71(5): 1253–1266.
- 19. Olsson P, Abrikosov IA, Vitos L, Wallenius J. Ab initio formation energies of Fe-Cr alloys. *Journal of Nuclear Materials*. 2003;321: 84–90.
- 20. Lau TT, Först CJ, Lin X, Gale JD, Yip S, Vliet VKJ. Many-body potential for point defect clusters in Fe-C alloys. *Physical Review Letters*. 2007;98(21): 215501.
- 21. Güler E, Güler M. Geometry optimization calculations for the elasticity of gold at high pressure. *Advances in Materials Science and Engineering*. 2013;2013: 525673.
- 22. Lee B-J, Jang J-W. A modified embedded-atom method interatomic potential for the Fe-H system. *Acta Materialia*. 2007;55: 6779–6788.
- 23. Liyanage LSI, Kim SG, Houze J, Kim S, Tschopp MA, Baskes MI, Horstemeyer MF. Structural, elastic and thermal properties of cementite (Fe₃C) calculated using a modified embedded atom method. *Physical Review B*. 2014;89: 094102.
- 24. Masuda-Jindo K, Hung W. Atomistic study of fracture of crystalline materials by lattice Green's function method: Effects of anharmonicity of lattice vibration. *Journal of the Physical Society of Japan*. 2004;73(5): 1205–1215.
- 25. Mazhnik E, Oganov AR. Application of machine learning methods to predicting new superhard materials. *Journal of Applied Physics*. 2020;128(7): 075102.
- 26. Born M, Oppenheimer R. Zur quantentheorie der Molekeln. Annalen der Physik. 1927;389(20): 457 484.
- 27. Mie G. Zur kinetischen theorie der einatomigen Körper. Annalen der Physik. 2006;316(8): 657–697.
- 28. Poletaev GM, Zorya IV, Rakitin RI, Iliina MA, Starostenkov MD. Interaction of impurity atoms of light elements with vacancies and vacancy clusters in FCC metals. *Materials Physics and Mechanics*. 2020;44(1): 26–33.
- 29. Tang N, Hung VV. Investigation of the thermodynamic properties of anharmonic crystals by the momentum method, I. General results for face-centered cubic crystals. *Physica Status Solidi B-Basic Solid State Physics*. 1988;149(2): 511–519.
- 30. Nguyen HQ, Bui DT, Nguyen DH, Coman Gl. Study of nonlinear deformation of FCC-AuCuSi under pressure by the statistical moment method. *Advances in Materials Science and Engineering*. 2021;2021(5–6): 1–11.
- 31. Nguyen HQ, Nguyen HT, Coman GI, Cuong TD, Hong VL. Thermodynamic property of FCC interstitial alloy AuSi with defects. *IOP Conference Series: Materials Science and Engineering*. 2019;485(1): 012018.
- 32. Nguyen HQ, Bui DT, Nguyen DH. Stress-strain curve of FCC interstitial alloy AuSi under pressure. *Romanian Journal of Physics*. 2020;65(5–6): 608.
- 33. Nguyen HQ, Nguyen DH. Elastic deformation of alloy AuSi with FCC structure under pressure. *HNUE Journal of Science*, *Natural Science*. 2018;63(6): 74–83.
- 34. Hoc NQ, Tinh BD, Hien ND, Coman G. Nonlinear deformation of BCC metal Fe and BCC interstitial alloy FeSi: Dependence on temperature, pressure and silicon concentration. *Materials Physics and Mechanics*. 2021;47(3): 501–513.
- 35. Nguyen HQ, Bui DT, Nguyen DH, Le TD. Elastic deformation of binary and ternary interstitial alloys with FCC structure and zero pressure: Dependence on temperature, concentration of substitution atoms and concentration of interstitial atoms. *HNUE Journal of Science, Mathematical and. Physical Sciences.* 2016;61(7): 47–57.
- 36. Nguyen HQ, Phan MH, Nguyen ML, Dao NH, Pham TT, Nguyen MV, Vu CC, Nguyen SM. Study on elastic deformation and thermodynamic properties of metals Mg, Zn, Dy, Er and Gd with HCP structure by statistical moment method: Dependences on temperature and pressure. *Modern Physical Lettes B.* 2023;38(4): 2350241.
- 37. Nguyen HQ, Nguyen TD, Dat HX, Lam LT. Theoretical predictions of thermodynamic properties, elastic deformation, HCP-FCC structural phase transition and melting of iron at high temperatures up to 18000 K and high pressures up to 4000 GPa. *Physics Letters A.* 2025;535: 130281.

- 38. Nguyen HQ, Nguyen DH. Study on thermodynamic and elastic properties of B_2 -FeSi under pressure by statistical moment method according to models of interstitial and substitutional alloys. *High Temperatures-High Pressures*. 2022;51(4): 295.
- 39. Nguyen HQ, Nguyen DH, Tran VK. Elastic deformation and elastic wave velocity of iron and its binary interstitial alloys: Temperature, pressure and interstitial atom concentration dependences. *Physica B Condensed Matter*. 2022;644(5): 414134.
- 40. Nguyen HQ, Than TN, Ngo NT, Bui LN, Nguyen TN, Le LT. Toward better understanding of anharmonic structural, thermodynamic and elastic properties of CaSiO₃ perovskite under extreme condition investigated via statistical moment method. *Materialia*. 2024;34: 102105.
- 41. Nguyen HQ, Nguyen DT, Thang NN, Nguyen VH, Le LT. Melting curves of MgSiO₃ and CaSiO₃ perovskites with cubic structure at extreme condition. *Journal of Applied Physics*. 2024;136: 045103.
- 42. Nguyen HQ, Nguyen QN, Dao MT, Tran VC, Lai TT, Le TT, Nguyen AT. Thermodynamic properties of perovskite MgSiO3 with cubic structure under extreme conditions. *The European Physical Journal B.* 2024;97: 167.
- 43. Ho KM, Chan CT, Soukoulis CM. Existence of a photonic gap in periodic dielectric structures. *Physical Review Letters*. 1990;65(25): 3152.
- 44. Yablonovitch E. Inhibited spontaneous emission in solid-state physics and electronics. *Physical Review Letters*. 1987;58(20): 2059.
- 45. Yablonovitch E, Gmitter TJ. Photonic band structure: The face-centered-cubic case. *Physical Review Letters*. 1989;63(18):1950.
- 46. Wang X, Zhang XG, Yu Q, Harmon BN. Multiple-scattering theory for electromagnetic waves. *Physical Review B*. 1993;47(8): 4161.
- 47. Economou EN, Sigalas M. Stop bands for elastic waves in periodic composite materials. *Journal of Acoustical Society of American*. 1994;95: 1734–1740.
- 48. Klironomos AD, Economou EN. Elastic wave band gaps and single scattering. *Solid State Communications*. 1998;105(5): 327 332.
- 49. Kushwaha MS, Halevi P, Martinez G, Dobrzynski L. Djafari-Rouhani B. Theory of acoustic band structure of periodic elastic composites. *Physical Review B*. 1994;49(4): 2313.
- 50. Montero de Espinosa FR, Jimenez E, Torres M. Ultrasonic band gap in a periodic two-dimensional composite. *Physical Review Letters*. 1998;80(6): 1208.
- 51. Sanchez-Perez JV, Caballero D, Martinez-Sala R, Rubio C, Sanchez-Dehesa J, Meseguer F, Llinares J, Galvez F. Sound attenuation by a two-dimensional array of rigid cylinders. *Physical Review Letters*. 1998;80(24): 5325.
- 52. Butler WH, Gonis A, Zhang X-G. Multiple-scattering theory for space-filling cell potentials. *Physical Review B*. 1992;45(20): 11527.
- 53. Zhang X-G, Butler WH. Multiple-scattering theory with a truncated basis set. *Physical Review B.* 1992;46(12): 7433. 54. Bich DH. *Elastic theory*. Hanoi: VNU Publishing House; 2001.
- 55. Grechka V, Zhang L, Rector JW. Shear waves in acoustic anisotropic media. *Geophysics*. 2004;69(2): 576-582.
- 56. Mozhaev VG. Some New Ideas in the Theory of Surface Acoustic Waves in Anisotropic Media. In: Parker DF, England AH. (eds.) *IUTAM Symposium on Anisotropy, Inhomogeneity and Nonlinearity in Solid Mechanics. Solid Mechanics and Its Applications.* Dordrecht: Springer; 1995. p.455–462.
- 57. Nayfeh AH, Chimenti DE. Propagation of guided waves in fluid-coupled plates of fiber-reinforced composite. *Journal of Acoustical Society of American*. 1988;83: 1736–1743.
- 58. Magomedov MN. On calculating the Debye temperature and the Gruneisen parameter. *Journal of Chemical Physics*. 1987;61(4): 1003–1009. (In Russian)
- 59. Magomedov MN. The calculation of the parameters of the Mie-Lennard-Jones potential. *High Temperature*. 2006;44(4): 513–529.
- 60. Lide DR. CRC Handbook of Chemistry and Physics. 86th ed. Boca Raton: CRC Press; 2005.
- 61. Good RJ, Hope CJ. New combining rule for intermolecular distances in intermolecular potential functions. *Journal of Chemical Physics*. 1970;53(2): 540–543.
- 62. Peng J, Jing F, Li D, Wang L. Pressure and temperature dependence of shear modulus and yield strength for aluminum, copper, and tungsten under shock compression. *Journal of Applied Physics*. 2005;98: 013508.
- 63. Li W, Kou H, Zhang X, Ma J, Li J, Geng P, Wu X, Chen L, Fang D. Temperature-dependent elastic modulus model for metallic bulk materials. *Mechanics of Materials*. 2019;139: 103194.
- 64. Lozinskii MG. High Temperature Metallography. New York: Pergamon; 1961.

- 65. Chang YA, Himmel L. Temperature dependence of the elastic constants of Cu, Ag, and Au above room temperature. *Journal of Applied Physics*. 1966;37(9): 3567–3572.
- 66. Reed RP, Mikesell RP. Low temperature (295 to 4K) mechanical properties of selected copper alloys. *Journal of Materials*. 1967;2: 370–392.
- 67. Joshi D, Bhatnagar ML. Temperature dependence of Young's modulus of copper, silver and gold. *Indian Journal of Pure and Applied Physics*. 1970;8: 428–431.
- 68. Tikhonov LV, Kononenko GI. Mechanical properties of metals and alloys. Kiev; 1986. (In Russian)
- 69. Ciftci YO, Colakoglu K, Kazanc S, Ozgen S. The effect of pressure on the elastic constants of Cu, Ag and Au: a molecular dynamics study. *Central European Journal of Physics*. 2006;4(4): 472–480.
- 70. Yokoo M, Kawai N, Nakamura KG, Kondo K, Tange Y, Tsuchiya T. Ultrahigh-pressure scales for gold and platinum at pressures up to 550 GPa. *Physical Review B*. 2009;80(10): 104114.
- 71. Matsui M. High temperature and high pressure equation of state of gold. *Journal of Physics: Conference Series.* 2010;215(1): 012197.
- 72. Biswas SN, Van't Klooster P, Trappeniers NJ. Effect of pressure on the elastic constants of noble metals from -196 to +25°C and up to 2500 bar: II. Silver and gold. *Physica B+C*. 1981;103(2-3): 235-246.
- 73. Hiki Y, Granato AV. Anharmonicity in noble metals; Higher order elastic constants. *Physical Review*. 1966;144(2): 411–419.
- 74. Daniels WB, Smith CS. Pressure derivatives of the elastic constants of copper, silver, and gold to 10 000 bars. *Physical Review*. 1958;111(3): 713–721.
- 75. Song M, Yoneda A, Ito E. Ultrasonic measurements of single-crystal gold under hydrostatic pressures up to 8 GPa in a Kawai-type multi-anvil apparatus. *Chinese Scientific Bulletin*. 2007;52(12): 1600–1606.
- 76. Ledbetter HM, Naimon ER. Relationship between single-crystal and polycrystal elastic constants. *Journal of Applied Physics*. 1974;45(1): 66–69.
- 77. Smith CS, Burns JW. The elastic constants of Cu-4 percent Si. *Journal of Applied Physics*. 1953;24(1): 15–18.

Submitted: November 25, 2023

Revised: December 14, 2023

Accepted: February 22, 2024

Комплексное исследование вязкоупругопластических свойств нанокомпозитов с повышенной износостойкостью на основе Фторопласта-4. Часть 1

А.В. Хохлов $^{1-3}$, А.А. Охлопкова 2 , С.А. Слепцова 2 , Н.Н. Лазарева 2

П.Н. Тарасова ² , А.В. Бабайцев ⁴ , А.В. Шапорев ³, В.В. Гулин ¹⁻³

РИДИТОННА

Приведены описание технологии изготовления композитов с повышенной износостойкостью на основе фторопласта-4 (ПТФЭ), полученных введением в качестве наполнителей механоактивированных слоистых силикатов (каолинит, серпентин, бентонит) и шпинели магния, основные результаты по исследованию износостойкости, структуры и химического состава поверхности трения методами электронной микроскопии и ИК-спектроскопии, и данные механических испытаний: семейства кривых растяжения с разными скоростями до разрушения, кривых нагружения и разгрузки с разными скоростями и кривых ползучести и восстановления для разных уровней напряжения, полученные в испытаниях ПТФЭ и шести композитов, дисперсно-наполненных серпентином и шпинелью магния с массовой долей от 1 до 5 %. В первой части статьи описаны цели и система программ квазистатических испытаний полимеров и композитов для всестороннего изучения их вязкоупругопластических свойств (совокупности всех наблюдаемых в испытаниях эффектов), возможности их описания с помощью нескольких физически нелинейных определяющих соотношений вязкоупругопластичности (одно из которых учитывает взаимное влияние эволюции структуры и процесса деформирования) и методология анализа данных испытаний и выбора адекватных определяющих соотношений для их моделирования. В частности, рассмотрены признаки физической нелинейности поведения материалов, т.е. индикаторы неприменимости линейного интегрального соотношения вязкоупругости Больцмана-Вольтерры, которые можно обнаружить в испытаниях по разным программам нагружения, способы очертить диапазон линейности поведения вязкоупругого материала. Описаны испытания для предварительной диагностики типа поведения материала, если характеризовать его категориями упругий, вязкоупругий, вязкопластичный, упруговязкопластичный, и методология выбора адекватной модели для описания поведения конкретного материала. Во второй части статьи проведен первичный анализ выраженности наследственных свойств материалов, в частности скоростной чувствительности, способности к течению при постоянном напряжении, ползучести и восстановлению после разгрузки, и влияния на них состава, состояния и доли наполнителей.

КЛЮЧЕВЫЕ СЛОВА

политетрафторэтилен • нанокомпозиты • эффекты и модели вязкоупругогластичности • квазистатические испытания диаграммы деформирования • кривые нагрузки-разгрузки • кривые ползучести и восстановления кривые релаксации • скоростная чувствительность •

Финансирование. Работа выполнена при поддержке Российского научного фонда (грант № 22-13-20056). **Citation:** Хохлов АВ, Охлопкова АА, Слепцова СА, Лазарева НН, Тарасова ПН, Бабайцев АВ, Шапорев АВ, Гулин ВВ. Комплексное исследование вязкоупругопластических свойств нанокомпозитов с повышенной износостойкостью на основе Фторопласта-4. Часть 1. *Materials Physics and Mechanics*. 2025;53(3): 177 – 218. http://dx.doi.org/10.18149/MPM.5332025_14



¹ НИИ механики МГУ имени М.В. Ломоносова, Москва, Россия

² Институт естественных наук, СВФУ им. М.К. Аммосова, Якутск, Россия

³ Московский центр фундаментальной и прикладной математики, Москва, Россия

⁴ Московский авиационный институт (НИУ), Москва, Россия

[™] andrey-khokhlov@ya.ru

Systematic all-round examination of the viscoelastoplastic properties of nanocomposites with increased wear resistance based on polytetrafluoroethylene. Part 1

A.V. Khokhlov 1-3 0, A.A. Okhlopkova 2 0, S.A. Sleptsova 2 0, N.N. Lazareva 2 0,

P.N. Tarasova ², A.V. Babaytsev ⁴, A.V. Shaporev ³, V.V. Gulin ¹⁻³

- ¹ Lomonosov Moscow State University, Moscow, Russia
- ² North-Eastern Federal University, Yakutsk, Russia
- ³ Moscow Center of Fundamental and Applied Mathematics, Moscow, Russia
- ⁴ Moscow Aviation Institute (National Research University), Moscow, Russia
- [™] andrey-khokhlov@ya.ru

ABSTRACT

A description of the technology for manufacturing composites with increased wear resistance based on polytetrafluoroethylene is given. The composites were obtained by introducing mechanically activated layered silicates (kaolinite, serpentine, bentonite) and magnesium spinel as fillers. The main results of the study on wear resistance, structure and chemical composition of friction surface using electronic microscopy and infrared spectroscopy and mechanical test data are presented, including families of tensileto-failure curves at different strain rates, loading and unloading curves at different rates, and creep and recovery curves for different stress levels obtained in tests of pure PTFE and six PTFE composites particulate-filled with serpentine and magnesium spinel with a mass fraction ranging from 1 to 5 %. The first part of the article describes the objectives and system of quasi-static testing programs for polymers and composites for a comprehensive study of their viscoelastoplastic properties (a set of all effects observed in tests), the possibilities of describing them using several physically nonlinear constitutive relations of viscoelastoplasticity (one of which takes into account the mutual influence of structure evolution and the deformation process), and the methodology for analyzing test data and selecting adequate constitutive relations for their modeling. In particular, the signs of physical nonlinearity of material behavior are considered, i.e. indicators of inapplicability of the linear integral Boltzmann-Volterra viscoelasticity relation that can be detected in tests using different loading programs, and methods for outlining the range of linearity of viscoelastic material behavior. The tests for preliminary diagnostics of the type of material behavior are described, if we characterize it by the categories elastic, viscoelastic, viscoplastic, elastic-viscoplastic, and the methodology for selecting an adequate model to describe the behavior of a particular material. In the second part of the article, a primary analysis of the expression of hereditary properties of materials is carried out, in particular, speed sensitivity, the ability to flow under constant stress, creep and recovery after unloading, and the influence of the composition, state and proportion of fillers on them.

KEYWORDS

polytetrafluoroethylene • nanocomposites • wear resistance • viscoelastoplastic properties • stress-strain curves family strain rate sensitivity • failure strains • loading and unloading curves • creep and recovery curves

Funding. The research was carried out at the expense of a grant from the Russian Science Foundation, No. Russian Science Foundation (Grant No. 22-13-20056).

Citation: Khokhlov AV, Okhlopkova AA, Sleptsova SA, Lazareva NN, Tarasova PN, Babaytsev AV, Shaporev AV, Gulin VV. Systematic all-round examination of the viscoelastoplastic properties of nanocomposites with increased wear resistance based on polytetrafluoroethylene. Part 1. *Materials Physics and Mechanics*. 2025;53(3): 177–218. (In Russian)

http://dx.doi.org/10.18149/MPM.5332025_14

Введение

Задачи всестороннего экспериментального изучения вязкоупругопластических свойств материалов (полимеров, металлов и сплавов, керамик, композитов с разными типами матриц и наполнителей) при разных температурах и режимах нагружения, создания (удобного для пользователей) банка этих свойств в виде наборов кривых испытаний по разным базовым и специальным программам нагружения и наблюдаемых эффектов, а не только нескольких простейших скалярных характеристик (модуль упругости, предел прочности при растяжении, сжатии или изгибе, деформация при разрушении), проблема выбора адекватного определяющего соотношения (ОС) и надежного моделирования процессов деформирования и разрушения, длительной прочности и долговечности вязкоупругопластичных материалов и элементов конструкций с учётом физической и геометрической нелинейностей, наследственности и скоростной чувствительности по-прежнему остаются актуальными в механике, материаловедении и практике инженерных расчётов.

Из-за быстрого роста количества новых материалов и моделей для описания их поведения и повышения требований к весу, размерам, удельной прочности, долговечности, надежности и экономичности элементов конструкций и механизмов, первостепенную роль играют вопросы построения или выбора (из сотни существующих) адекватных ОС, анализа и паспортизации их свойств, возможностей и области применимости, сфер влияния их материальных функции (МФ) и феноменологических ограничений на них. С этим вопросами тесно связаны задачи разработки информативных, но экономичных комплексных программ испытаний образцов материала (желательно не слишком длительных и многочисленных), методик определения материальных параметров и функций ОС по их результатам (идентификации) и верификации ОС. Эти темы исследуются в статьях [1–13] и др., посвященных анализу, аттестации и идентификации линейного ОС вязкоупругости Больцмана-Вольтерры:

$$\varepsilon(t) = \int_0^t \Pi(t-\tau) \, d\sigma(\tau), \, \sigma(t) = \int_0^t R(t-\tau) \, d\varepsilon(\tau), \, t \geq 0,$$
 (1) и пяти более общих нелинейных ОС вязкоупругопластичности с широкими областями применимости [1-4,9-13], одно из которых учитывает взаимное влияние эволюции структуры материала и процесса деформирования [11,12]. Линейное ОС (1) описывает одномерные изотермические процессы деформирования структурно-стабильных (нестареющих) материалов, связывая истории напряжения $\sigma(t)$ и деформации $\varepsilon(t)$ в точке тела линейными интегральными операторами; оно содержит лишь одну независимую материальную функцию (МФ), т.к. функции ползучести и релаксации

 $\Pi(t)$ и R(t) связаны условием взаимной обратности операторов (1) в виде

интегрального уравнения Вольтерры [4,9].

В силу своей фундаментальной сложности, большого количества испытаний, необходимых для исследования вязкоупругопластических (а не только упругих) свойств материалов, сложности анализа данных испытаний в виде семейств кривых и многочисленности разнообразных ОС, предложенных в научной литературе для описания тех или иных конкретных материалов (при конкретных видах нагружений), многие из упомянутых тем недостаточно разработаны, а порой просто игнорируются и подменяются слабо наполненными физикой, химией и механикой вычислительными схемами. Это нередко приводит к недостоверности результатов моделирования (и

модных ныне "цифровых двойников"), опирающихся на малое количество простейших испытаний определенного типа и не способных описать комплекс основных эффектов, и укоренению неверных представлений как в научной литературе, так и в инженерной практике.

Политетрафторэтилен (ПТФЭ, фторопласт-4) – широко используемый во всем мире полимер, он обладает большим набором полезных (и во многом уникальных) химических и физико-механических свойств [14-86]: 1) очень низкий коэффициент трения, 2) гидрофобность и отсутствие налипания других материалов, включая и адгезивы, к поверхности изделий из ПТФЭ, 3) низкие водопоглощение и газопроницаемость, высокая стойкость к агрессивным средам, к воздействию воды, света, УФ-излучения, природных загрязнений, 4) высокие деформативность и пластичность (обеспечивающие широкое применение ПТФЭ в качестве материала для уплотнений и герметиков [14-22,26,27]), 5) физиологическая нейтральность, 6) сохранение многих ценных физико-механических свойств и возможность эксплуатации при низких и криогенных температурах (от -260 до +260 °C) [20,22,24,27]. Благодаря этим свойствам ПТФЭ имеет широкий спектр приложений в разных отраслях промышленности И техники: машиностроении, транспорте углеводородов, строительстве, электротехнике, медицине, пищевой, швейной, химической промышленности, военной и аэрокосмической технике. ПТФЭ особенно эффективен в качестве уплотнительного и триботехнического материала [14-22,26,27,31-86].

Из-за низкого коэффициента трения ПТФЭ широко применяется в качестве основы композитов для изготовления деталей самых ответственных узлов трения (подшипников, опор мостов и т.п). [14,17,20,22,31–86]. Он не заменим в узлах "сухого" трения, поскольку не только имеет низкий коэффициент трения по стали, но и обладает самосмазывающими свойствами. Одно из основных преимуществ ПТФЭ и КМ на его основе перед другими полимерами – обеспечение работоспособности узла трения без применения смазки в условиях циклического образования и удаления пленки переноса [85]. Детали, изготовленные на основе таких КМ, имеют меньшую массу и снижают транспортные расходы, не боятся низких температур и агрессивных сред, работают практически бесшумно, обладают демпфирующей способностью, повышают надежность и долговечность (хорошо спроектированных) узлов машин.

Однако у ПТФЭ есть и недостатки: он обладает низкой износостойкостью, коэффициентом линейного термического расширения, деформативностью (это свойство полезно в применениях ПТФЭ в качестве уплотнений и герметиков, но вредно во многих других областях применения) и быстро накапливает пластическую деформацию как при постоянной, так и при циклической нагрузках: подвержен ползучести (хладотекучести) и рэтчетингу даже при небольших нагрузках в нормальных условиях. Для улучшения свойств и расширения области применения в ПТФЭ вводят разные наполнители [17-86]: углеродные и стеклянные волокна, оксиды металлов, силикаты, детонационные наноалмазы, порошки бронзы, дисульфида молибдена, графита, кокса, слюды, меди, нитрида бора. Большинство промышленно выпускаемых материалов на основе ПТФЭ - композиции с высокой долей наполнителей (более 15-30 %), что приводит к избыточному повышению жесткости и хрупкости материала. На рынке России широко представлены следующие марки КМ на основе ПТФЭ: Ф-4К20, Ф-4К20М5, Ф4С15, Флубон-15 и Флубон-20 [22,26,32]. Эти высоконаполненные КМ обладают повышенными износостойкостью (до 1000 раз по сравнению с исходным ПТФЭ) и модулем упругости, но значительно меньшей податливостью и ресурсом деформативности, что снижает их эффективность в уплотнениях.

В работах [34,36,65–81] показано, что заметное повышение износостойкости достигается при введении малого количества (до 5 %) наполнителей (серпентин, каолинит, вермикулит, бентонит, цеолит, оксид алюминия, оксид магния, оксид кремния, базальтовое волокно, углеродное волокно) при этом деформационно-прочностные характеристики получаемого КМ сохраняются на уровне чистого ПТФЭ или повышаются (см. ниже). В работах [65–70,73,74,76–80] показано, что введение минеральных слоистых силикатов в ПТФЭ приводит к снижению износа в 700–2000 раз.

Волокнистые наполнители придают КМ на основе ПТФЭ прочность, жесткость и износостойкость [51]. В работах [70–72,77] установлено, что введение 5 % коротких углеродных волокон повышает износостойкость КМ в 70–80 раз по сравнению с исходным ПТФЭ. Основной недостаток углеродного волокна – его высокая цена (в зависимости от типа и качества углеродного волокна, от спроса на него в разных сегментах рынка его цена может существенно различаться). А сырье для производства может быть в 5-25 раз дороже, чем у стекловолокна. Возможный более дешевый наполнитель для ПТФЭ – базальтовые волокна [50,81]: они обладают высокими механическими характеристиками и термической и химической стойкостью, но технология их производства значительно проще и менее энергоемка, сырье (природного происхождения) не ограничено и значительно дешевле, а отработавшие волокна не загрязняют окружающую среду. Первые испытания показали [81], что введении 5 % коротких базальтовых волокон (диаметром 8–10 мкм) снижает износ КМ в 55 раз по сравнению с ПТФЭ.

Необходимость освоения регионов Арктики рождает повышенный спрос на разработку и применение в технических устройствах морозостойких материалов с длительным сроком службы. ПТФЭ и разрабатываемые КМ на его основе очень перспективны для решения этих задач. Перспективным представляется и сочетание указанных наполнителей с методом радиационной модификации ПТФЭ облучением малыми дозами в расплаве (чуть выше температуры плавления кристаллитов 327 °C), которое изменяет надмолекулярную структуру ПТФЭ [42,46,82]; работа в этом направлении ведется в сотрудничестве с С.А. Хатиповым. Таким образом, создание КМ на основе ПТФЭ с улучшенным комплексом эксплуатационных свойств представляет большой научный и практический интерес. Исследования КМ на основе ПТФЭ, применение новых наполнителей для повышения физико-механических свойств и развитие технологий изготовления КМ – важные задачи, решение которых требует комплексного подхода, включающего материаловедческие, технологические, механико-математические и экономические аспекты.

Эта работа – вводная статья цикла статей, посвященных всестороннему экспериментальному исследованию вязкоупругопластических свойств и моделированию поведения фторопласта-4 и нескольких семейств КМ с повышенной износостойкостью на его основе, полученных в последние 20 лет в лабораториях "Технологии полимерных нанокомпозитов" и "Полимерные композиты для Севера" Северо-Восточного федерального университета им. М.К. Аммосова введением в

качестве наполнителей слоистых силикатов (механоактивированные каолинит и серпентин, шпинель магния) и коротких базальтовых или углеродных волокон [34,36,65-81]. В данном цикле из 8-10 статей внимание будет сосредоточено на системном исследовании всего комплекса вязкоупругопластических свойств ПТФЭ и указанных нанокомпозитов (а не их отдельных характеристик) и разработке системы программ квазистатических термомеханических испытаний, позволяющих получить максимально полную информацию о реологических свойствах исследуемых материалов (которые в дальнейшем будут использованы для паспортизации КМ и подбора определяющего соотношения и моделирования их деформирования и разрушения [1-13]). После механических испытаний проводятся исследования изменений микроструктуры ПТФЭ и КМ на сканирующем электронном микроскопе.

В статье будут описаны разработанные материалы и технологии их получения, основные результаты по исследованию структуры и химического состава поверхности трения методами электронной микроскопии и ИК-спектроскопии и по повышению износостойкости этих материалов (за счет образования пленки переноса и вторичных структур в результате трибоокислительных процессов). Будет описана система программ квазистатических испытаний полимеров и композитов (по базовым и специальным программам нагружения) для комплексного изучения ИΧ вязкоупругопластических свойств (всей совокупности наблюдаемых эффектов) и методология анализа данных испытаний и выбора подходящих ОС для их моделирования. В частности, будут рассмотрены признаки физической нелинейности поведения материалов, т.е. индикаторы неприменимости линейного интегрального ОС вязкоупругости Больцмана-Вольтерры, которые можно обнаружить в испытаниях по разным программам нагружения, способы очертить диапазон линейности поведения вязкоупругого материала [87–92].

Будет приведена часть полученных за последние два года данных испытаний образцов ПТФЭ и КМ на его основе: семейства диаграмм растяжения с разными скоростями до разрушения, кривых нагружения и разгрузки с разными скоростями, кривых ползучести и восстановления для разных уровней напряжения. Будут исследована выраженность наследственных свойств материалов (скоростная чувствительность, способность к течению при постоянном напряжении, ресурс деформативности и способность к восстановлению после разгрузки), определены мгновенный модуль, предел текучести, напряжение и деформация при разрыве в зависимости от скорости нагружения, начат анализ влияния на них состава, доли и состояния наполнителей.

В дальнейшем будет подробно представлен весь накопленный объем данных испытаний и обнаруженных эффектов, будут детально проанализированы семейства диаграммм деформирования при растяжении (до разрушения) нескольких КМ, кривые нагружения и разгрузки, их скоростная чувствительность и зависимость от температуры, кривые ползучести и восстановления при разных уровнях напряжения и температуры и проведен сравнительный анализ структурных изменений исследуемых КМ под действием разных программ нагружения. По семействам построенных диаграмм деформирования, кривых нагружения и разгрузки и кривых ползучести и восстановления будет осуществляться выбор и проверка индикаторов применимости к описанию деформирования исследуемых материалов пяти

физически нелинейных ОС вязкоупругопластичности, построенных и детально изученных ранее в цикле статей [1–13] и др. Одна из важных задач всего цикла статей – комплексная характеризация и системное описание свойств ПТФЭ и КМ, проведение и анализ испытаний одних и тех же материалов по разным информативным программам: даже по чистому ПТФЭ (да и другим материалам) в научной литературе представлены только разрозненные данные испытаний по отдельным программам образцов ПТФЭ, изготовленных из разного сырья в разных условиях по разным технологиям, которые нельзя использовать вместе для выбора, идентификации и всесторонней верификации ОС для описания всего комплекса реологических свойств ПТФЭ.

Исходные материалы и технология получения КМ на основе ПТФЭ

За основу разрабатываемых и исследуемых КМ взят порошок ПТФЭ ПН-90 производимый ОАО "Галополимер Пермь" (средний размер частиц: 46-135 мкм). В качестве сырья для наполнителей в данной работе были выбраны: 1) каолинит, глинистый минерал из группы водных силикатов с общей формулой $Al_4[Si_4O_{10}](OH)_8$ (из каолина Алтайского месторождения, средние размеры частиц до измельчения – 170 мкм); 2) серпентин ($Mg_6(OH)_8[Si_4O_{10}]$) Хамеловского месторождения Мурманской области в виде крупнодисперсного порошка со средним размером частиц 3 мм; 3) шпинель магния (сложный оксид, общая химическая формула $MgAl_2O_4$) в виде нанопорошка с размером частиц 75 нм, синтезированного в Институте химии твердого тела и механохимии CO PAH (Новосибирск).

Наполнители просушивали в печи ПЭ-0041 при 120 °С в течение 4 ч. Измельчение (механоактивацию) каолинита и серпентина проводили в планетарной мельнице "Активатор – 25" (1356 об/мин, время обработки 2 мин); в результате средний диаметр частиц каолинита и серпентина составлял 100 нм, т.е. в 1700 и 30000 раз меньше, чем до активации.

ПТФЭ просушивали в печи ПЭ-0041 при 180 °С в течение 4 ч. Высушенный и охлажденный в печи ПТФЭ помещался в эксикатор (стеклянный сосуд, в котором поддерживается определенная влажность воздуха). Высушенный полимер измельчался на мельнице и просеивался через сито (№1 К). Для совмещения компонентов КМ использовался метод сухого смешения с использованием высокоскоростного лопастного смесителя (1200 об/мин).

Далее производились формование образцов КМ и спекание. Механические испытания проводились на отпрессованных образцах в форме лопаток, соответствующей ГОСТ (испытания на растяжение по разным программам) и цилиндров (столбиков), высотой 20 мм и диаметром 10 мм (испытания на износостойкость и на сжатие). Для изготовления лопаток требуется 11 г ПТФЭ, а для изготовления столбиков – 3.5 г. Образцы изготавливались по технологии холодного формования в пресс-форме в гидравлическом прессе GT-7014-H10С под давлением 50 МПа (скорость нагружения 0.45 МПа/с, время выдержки под давлением 50 МПа – 2 мин). Спекание производили в печи SNOL при температуре 375 °С в течение 90 мин, нагревание от начальной температуры 25 ± 5 °С производили со скоростью 2 °С/мин с выдержкой 30 мин при температуре 300 °С. Переход ПТФЭ из твердого состояния в

вязкотекучее происходит скачкообразно, а не плавно как у многих других термопластичных полимеров. При температуре 327 °C все кристаллиты переходят в аморфное состояние (теряют ламеллярную структуру, но сохраняют фибриллярную), но материал еще не плавится, а размягчается, становится желеобразным. При достижении температуры 350–380 °C частицы КМ "сплавляются" и получается монолитный блок. После спекания и остывания образцы-столбики для исследования триботехнических характеристик подвергались калибровке: образцы помещали в печь ES-4610 и нагревали до 180 °C, после выдержки при 180 °C в течение 30 мин, образцы прессовали под давлением 50 МПа и оставляли остывать под давлением в пресс-форме до комнатной температуры.

Влияние наполнителей на коэффициент трения и скорость износа композитов и процессы на поверхности трения

Проведены триботехнические испытания образцов ПТФЭ и шести КМ на его основе с шестью разными содержаниями наполнителей: материалы КМс-1, КМс-2, КМс-5 содержали 1, 2 или 5 % серпентина (по массе), а в образцы материалов КМсш-1, КМсш-2, КМсш-5 была добавлена еще шпинель магния (суммарная доля наполнителей – 1, 2 и 5 %) и они имели следующий состав: КМсш-1: ПТФЭ + С 0.9% + ШМ 0.1% (ШМ – шпинель магния, С – серпентин); КМсш-2: ПТФЭ + С 1.5% + ШМ 0.5%; КМсш-3: ПТФЭ + С 3.8% + ШМ 1.2%. Степень кристалличности ПТФЭ, определенная методом рентгеноструктурного анализа (на дифрактометре ARL X'TRA, Швейцария) составила 66 %, а у КМ – немного выше: от 67 до 75 % (и росла с увеличением доли наполнителей).

Коэффициент трения ПТФЭ и КМ по стали и скорость массового изнашивания определяли на универсальном высокотемпературном трибометре CETR UMT-3 (США) по схеме трения "палец-диск" (стальное контртело), при нагрузке 160 Н и скорости

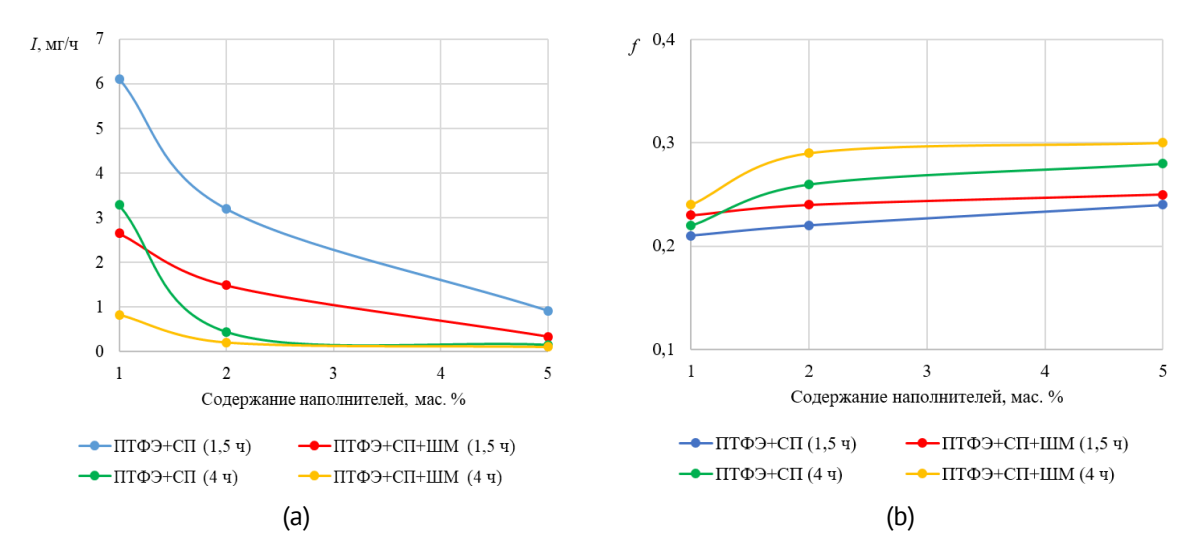


Рис. 1. Средняя скорость изнашивания I (a) и коэффициент трения f (b) композитов на основе ПТФЭ по стали в стадии приработки (длительностью 1.5 ч) и на второй стадии (4 ч) в зависимости от доли наполнителей (серпентина и шпинели магния)

[Fig. 1. Average wear rate I (a) and friction coefficient f (b) of PTFE-based composites against steel during the running-in stage (lasting for 1.5 h) and the second stage (4 h) depending on the filler content (serpentine and magnesium spinel – s or Msp)]

скольжения 0.25 м/с (частота вращения диска 96 об/мин). Испытание образцов в форме столбиков (высотой 20 мм и диаметром 10 мм) состояло из двух стадий длительностью $T_1=1.5$ ч (стадия приработки) и $T_2=4$ ч в конце каждой из которых производилось взвешивание образца и измерение потери массы Δm . Среднюю скорость изнашивания на каждой стадии оценивали по потере массы образцов Δm за время T_i : $I_i=\Delta m/T_i$ (мг/ч). Данные измерений скоростей изнашивания I и коэффициента трения f КМ по стали в зависимости от содержания наполнителей (серпентин и шпинель магния в количестве 1, 2 и 5 %) приведены на Рис. 1: синим и зеленым цветами – кривые для образцов КМс, красные и желтые – для образцов КМсш; синие и красные кривые относятся к стадии приработки ($T_1=1.5$ ч), зеленые и желтые – ко второй стадии ($T_2=4$ ч).

Одновременное введение серпентина и шпинели магния позволило повысить износостойкость материала в 1100 раз по сравнению с чистым ПТФЭ. С увеличением содержания наполнителя скорость износа заметно уменьшается, хотя коэффициент трения немного растет (кривые на Рис. 1(b) лежат в обратном порядке по сравнению с Рис. 1(a)). Рисунок 1(a) показывает, что введение шпинели магния повышает износостойкость КМ в 2 – 3 раза по сравнению с КМ, наполненным лишь серпентином. Известно, что повышение износостойкости может быть обусловлено усилением адгезионного взаимодействия компонентов в композите вследствие участия наполнителей в формировании граничного слоя на границе раздела "полимернаполнитель" [67]. Идея использования шпинели магния в качестве функциональной добавки основана на способности структурно-активного наполнителя способствовать процессу упорядоченности и ориентации при трении, участвуя в процессах трибодеструкции полимера и последующего структурирования [34].

Для более детального исследования процесса изнашивания проведены структурные исследования поверхностей трения образцов методами сканирующей электронной микроскопии (Рис. 2) и ИК-спектроскопии (Рис. 3 и 4). Их осуществляли на сканирующем электронном микроскопе Jeol JSM-7800F (JEOL, Япония) в режиме вторичных электронов, а также на ИК-спектрометре с Фурье-преобразованием 7000 FT-IR (Varian, США). ИК-спектры до и после трения получали с помощью приставки нарушенного полного внутреннего отражения в диапазоне 500-4000 см⁻¹. На Рис. 2 представлены микрофотографии (с увеличением в 500 раз) поверхностей трения ПТФЭ (а) и шести КМ на его основе (b-q): в левом столбце - КМс-1, КМс-2, КМс-5 с разной долей серпентина. А в правом – КМсш-1, КМсш-2, КМсш-3 с добавлением серпентина и шпинели магния. Поверхность трения композитов по сравнению с ПТФЭ исходным отличается большей шероховатостью фрагментированных структурных элементов в виде чешуек размером 5-40 мкм (Рис. $\frac{2}{(c-q)}$). Вторичные структуры образуются В результате протекания трибоокислительных процессов при участии матрицы, частиц наполнителей и стального контртела [73,74,76]. В процессе трения механическое и тепловое воздействия ускоряют сегментальное движение макромолекул ПТФЭ при этом разрываются межмолекулярные и даже химические связи (в точках локального перегрева), которые приводят к образованию активных центров. В дальнейшем, образованные активные центры, взаимодействуя с частицами наполнителей, образуют так называемый вторичный защитный слой [22].

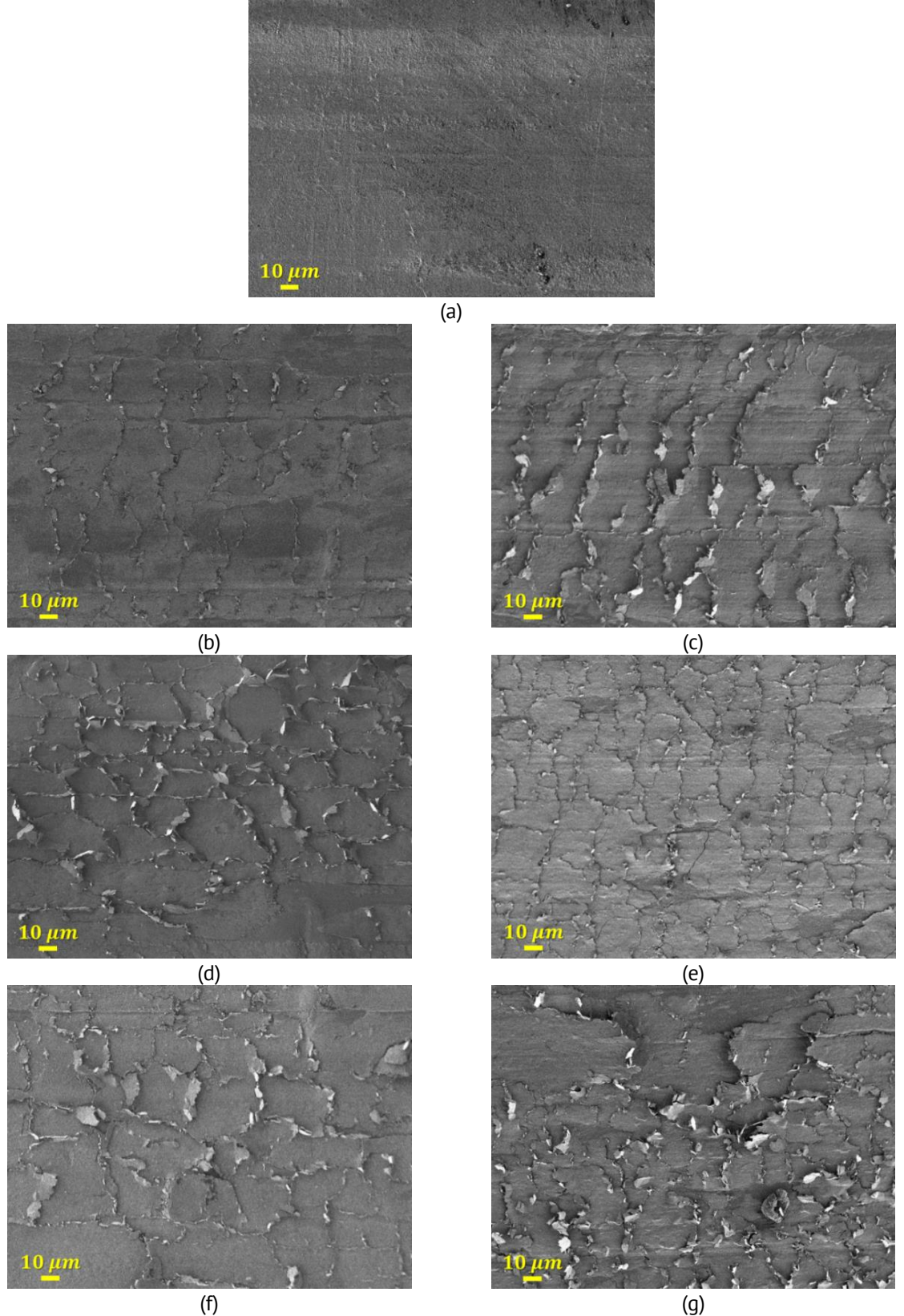


Рис. 2. Микрофотографии поверхностей трения ПТФЭ (a) и КМ на его основе: (b,d,f) КМс-1, КМс-2, КМс-5 с наполнением серпентином в 1, 2 или 5; (c,e,g) КМсш-1, КМсш-2, КМсш-5 с наполнением серпентином и шпинелью магния (составы: ПТФЭ + С 0.9% + ШМ 0.1%; ПТФЭ + С 0.5% + ШМ 0.5%; ПТФЭ + С 0.5% + ШМ 0.5%; ПТФЭ + С 0.5% + ШМ 0.5%; ПТФЭ + С 0.5% + ПТФЭ + С

На Рис. 3 представлены ИК-спектры ПТФЭ и композитов КМс-1, КМс-2, КМс-5 и КМсш-1, КМсш-2, КМсш-5 с разным содержанием наполнителей до и после трения. Во всех ИК-спектрах самые интенсивные - полосы, относящиеся к валентным колебаниям CF_2 -групп (1200 и 1146 см⁻¹). В области низких волновых чисел (в окрестности 650 см^{-1}) располагаются веерные (640 см^{-1}) и деформационные (552 см^{-1}) колебания CF₂-групп. Полосы в области 800-700 см⁻¹ относят к колебаниям молекулярных цепей в аморфной фазе ПТФЭ [39]. После 5.5 ч трения во всех ИКспектрах появляются новые полосы поглощения, соответствующие валентным колебаниям О-H связей в области 3600 – 2600 см⁻¹ и антисимметричным и симметричным колебаниям карбоксилат-анионов: 1655, 1435, 1350, 1315 и 1310 см⁻¹. Появление этих пиков подтверждает окисление концевых групп фрагментов макромолекул ПТФЭ в процессе трения (в присутствии наполнителей) [74,76]. Пики (разница в интенсивностях спектров) становятся более выраженными с ростом доли наполнителей, т.е. процессы трибоокисления ускоряются. ИК-спектры чистого ПТФЭ (черные штриховые линии) показывают, что истирание ПТФЭ (в течение 5.5 ч) не приводит к образованию кислородсодержащих групп.

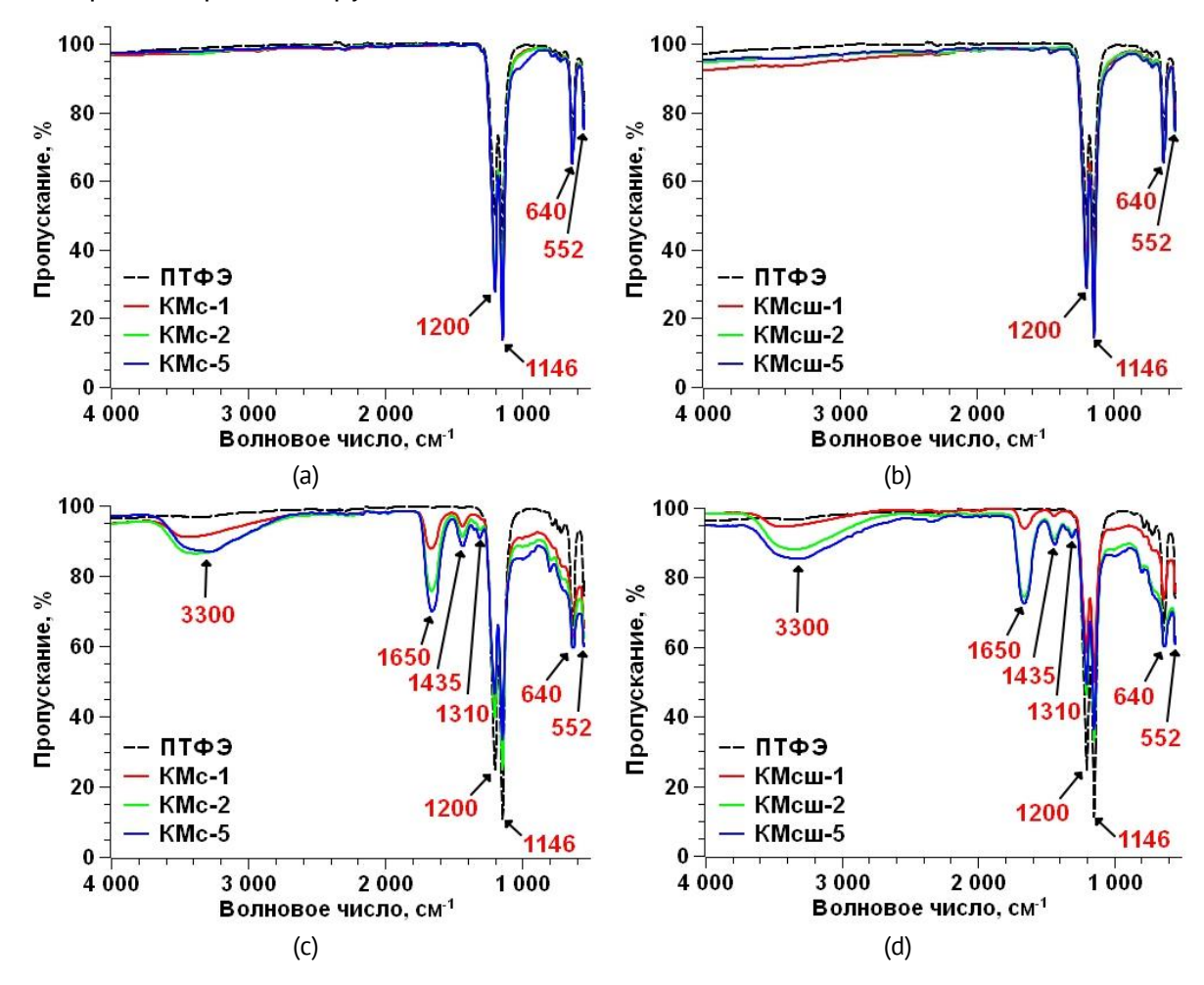


Рис. 3. ИК-спектры ПТФЭ и КМ на его основе в зависимости от содержаний наполнителей: (a,b) КМс и КМсш до трения; (c,d) КМс и КМсш после 5.5 ч трения

[**Fig. 3.** IR spectra of PTFE and its composites depending on the filler content: (a,b) Ms and CMsMsp before friction; (c,d) – CMs and CMsMsp after 5.5 h of friction]

Рисунок 4 иллюстрирует влияние добавок шпинели магния на ИК-спектры КМ с серпентином (при сохранении суммарной массовой доли наполнителя) после трения. Замена части серпентина на шпинель магния (переход от КМс к КМсш) приводит к росту интенсивностей пиков кислородсодержащих групп в дорожках трения КМсш-2 и КМсш-5, содержащих не менее 0.5 % шпинели магния, по сравнению с КМс-2 и КМс-5. Возможно, шпинель магния выступает как активный катализатор трибоокислительных процессов, что и обеспечивает значительное снижение износа композитов [73,76,79,80].

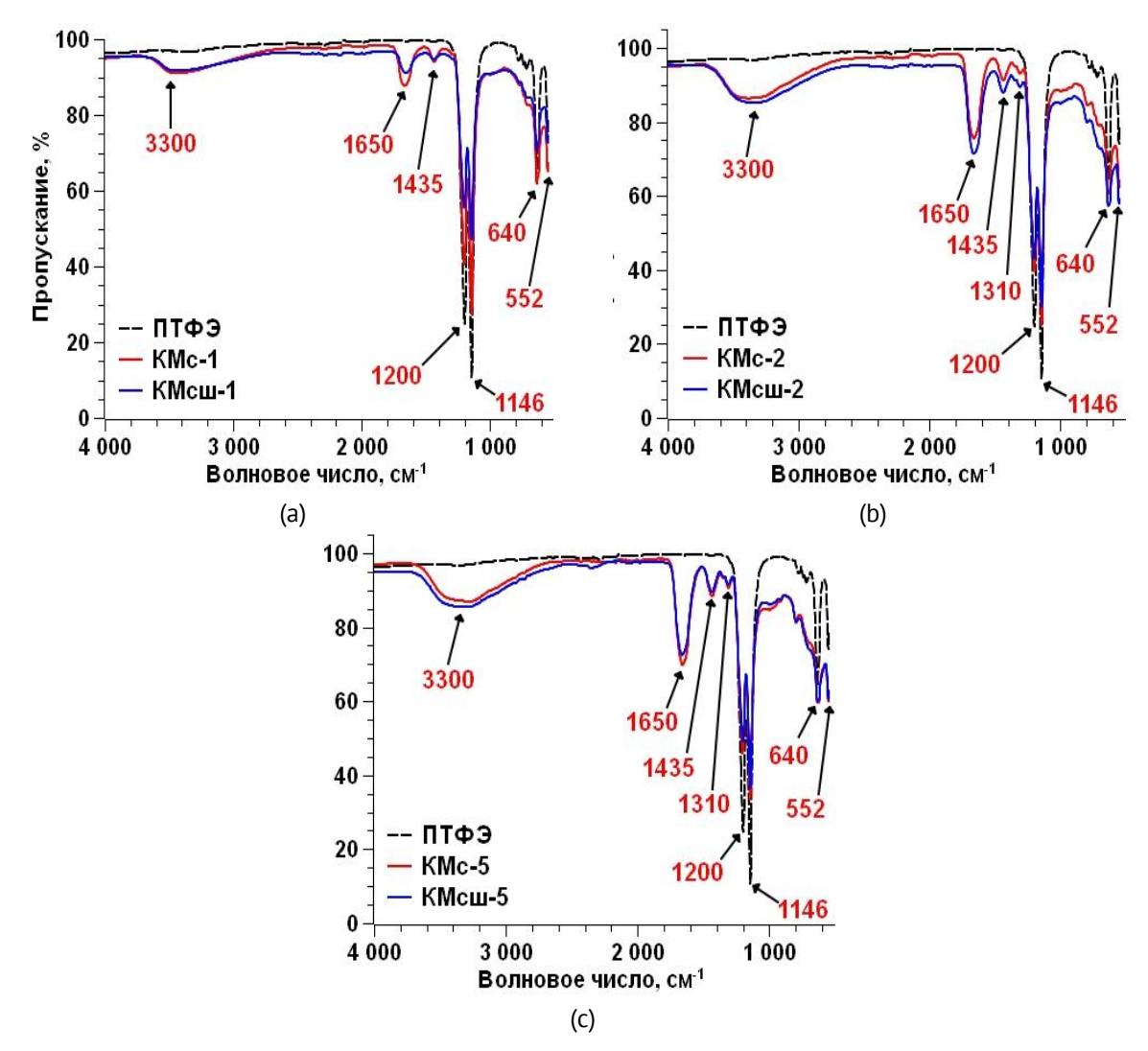


Рис. 4. Влияние добавок шпинели магния на ИК-спектры КМ с серпентином после трения: (a) сравнение КМс-1 и КМсш-1, (b) КМс-2 и КМсш-2, (c) КМс-5 и КМсш-5

[**Fig. 4.** The effect of magnesium spinel additives on the IR spectra of CMs with serpentine after friction: (a) comparison of CMs-1 and CMsMsp-1, (b) CMs-2 and CMsMsp-2, (c) CMs-5 and CMsMsp-5]

Таким образом, основной механизм повышения износостойкости КМ на основе ПТФЭ – это формирование в зоне трения защитной вторичной структуры, играющей роль твердой смазки.

Методология и система программ квазистатических испытаний полимеров и ПКМ для комплексного изучения их реономных свойств, выбора и идентификации модели

Моделирование механического поведения полимеров и ПКМ в рамках линейной (анизотропной) теории упругости (или термоупругости) допустимо лишь в области достаточно малых напряжений, деформаций и невысоких температур (ниже температуры стеклования полимера или аналогичных характерных температур для матриц иного состава). Даже в этой области механическое поведение КМ осложняется явлениями как анизотропия упругих и прочностных разносопротивляемость (при одноосных испытаниях на растяжение и сжатие она может проявляться как разномодульность или как различие кривых деформирования или ползучести при растяжении и сжатии не на начальном участке, а при более длительном деформировании). Полимеры и ПКМ нельзя считать упругими, если деформации не очень малы, скорости деформации не слишком высоки, а температура не гораздо ниже температуры стеклования полимера. Даже при невысоких температурах и нагрузках полимеры (особенно термпопласты) и композиты на их основе проявляют не только упругие свойства, но и упругопластические, вязкоупругие, вязкопластические и вязкоупругопластические, они проявляют выраженную зависимость свойств от времени, скорости нагружения, предыстории деформирования [92–113]. Для их поведения свойственны такие эффекты как ползучесть и обратная ползучесть, длительная прочность, релаксация напряжений, скоростная чувствительность кривых деформирования и нагружения, существенное отклонение ветви разгрузки от прямолинейности и наличие у нее точки перегиба, остаточная деформация после разгрузки и ее накопление при циклических нагружениях, зависимость коэффициента поперечной деформации при растяжении от времени и программы нагружения, выраженная нелинейность поведения (нелинейность зависимостей семейств кривых нагружения, ползучести и релаксации от скорости нагружения и уровней нагрузки), сильное влияние небольших изменений температуры на механическое поведение (на выраженность и скорость протекания всех упомянутых эффектов) и др. [1-13,89-114].

Поэтому, вместо характеризации основных свойств материала только тензором его упругих модулей (и прочностных характеристик: пределы прочности и предельные деформации при растяжении, сжатии, сдвиге и более сложных программах), возникает необходимость изучения всего комплекса указанных явлений, проведение испытаний образцов материала по базовым и специально разработанным программам термомеханического нагружения или деформирования при разных параметрах нагружений (уровнях температуры, нагрузки, деформации, скоростей деформации или нагружения, длительностей стадий нагружения составных программ, скачков температуры или нагрузки и т.п.) [92], и внесение в «паспорт» материала всех семейств кривых-откликов на обязательные и дополнительные программы термомеханического нагружения, отражающих зависимость этих откликов от времени и параметров нагружения (а в "паспорт" любого ОС – результатов анализа качественных свойств этих кривых-откликов): кривых ползучести и восстановления, кривых релаксации, кривых деформирования с постоянными скоростями нагружения или деформации, кривых нагружения-разгрузки, кривых

циклического нагружения при разных параметрах циклов, кривых ползучести при ступенчатом нагружении (с кусочно-постоянной нагрузкой) и др.

малых деформациях и скоростях деформирования линейное вязкоупругости (1) хорошо описывает большинство наблюдаемых при деформировании структурно-стабильных материалов основных эффектов, связанных с диссипацией наследственностью (памятью предыстории нагружения) С увеличением деформаций (напряжений) и амплитуд циклических нагрузок поведение материалов все ярче проявляет неупругость и геометрическую и физическую и нелинейности, в частности, зависимость от вида напряженносостояния, структурные деформированного изменения влияние И ИΧ термомеханические свойства материала. Изменение объема при нагружении, развитие разных видов дефектов и другие изменения структуры, объемная ползучесть и релаксация, влияние среднего напряжения (гидростатического давления) и его истории на осевые и сдвиговые деформации и связанные с ними термомеханические эффекты становятся все более существенными при описании деформирования, прочности и разрушения материалов [1-13,92-114].

Исследование выраженности вязкоупругопластических свойств и их зависимости от параметров программ нагружения и температуры требует детальной разработки и проведения обширной программы испытаний для получения семейств кривых поведения материалов при базовых программах нагружения, позволяющих получить комплексную информацию о реологических свойствах исследуемых материалов и необходимые данные для разработки, идентификации и верификации моделей их поведения (для выбора ОС для описания поведения материала в зависимости от обнаруженных в испытаниях эффектов, разработки методик идентификации и верификации построенной модели по данным испытаний) [92]. Практически важная задача при этом – анализ возможностей сокращения необходимой программы испытаний без существенной потери в информативности и в адекватности моделирования.

На первом этапе исследования материала представляется необходимым провести испытания при одноосных квазистатических нагружениях (растяжение, сжатие или сдвиг) по разным программам (см. ниже) при фиксированных температурах из рабочего диапазона (с последующим анализом структуры испытанных образцов) для исследования наличия и особенностей проявления следующих важнейших эффектов (это базовая часть необходимого списка).

Скоростная чувствительность и особенности формы диаграмм деформирования (ДД) с постоянными скоростями до разрушения образца.

При нагружении по программам $\varepsilon(t)=at$ строятся семейства откликов $\sigma=\sigma(t,a)$ и ДД $\sigma=\sigma(\varepsilon,a)$ при разных скоростях деформирования a (или скоростях движения захвата, как часто бывает на практике), изучается выраженность зависимости семейства ДД $\sigma=\sigma(\varepsilon,a)$, мгновенного и касательного модуля, предела текучести (если он есть), напряжения и деформации при разрушении от скорости a при фиксированных величинах температуры; исследование существования равновесной диаграммы (предельной при скорости деформирования, стремящейся к нулю).

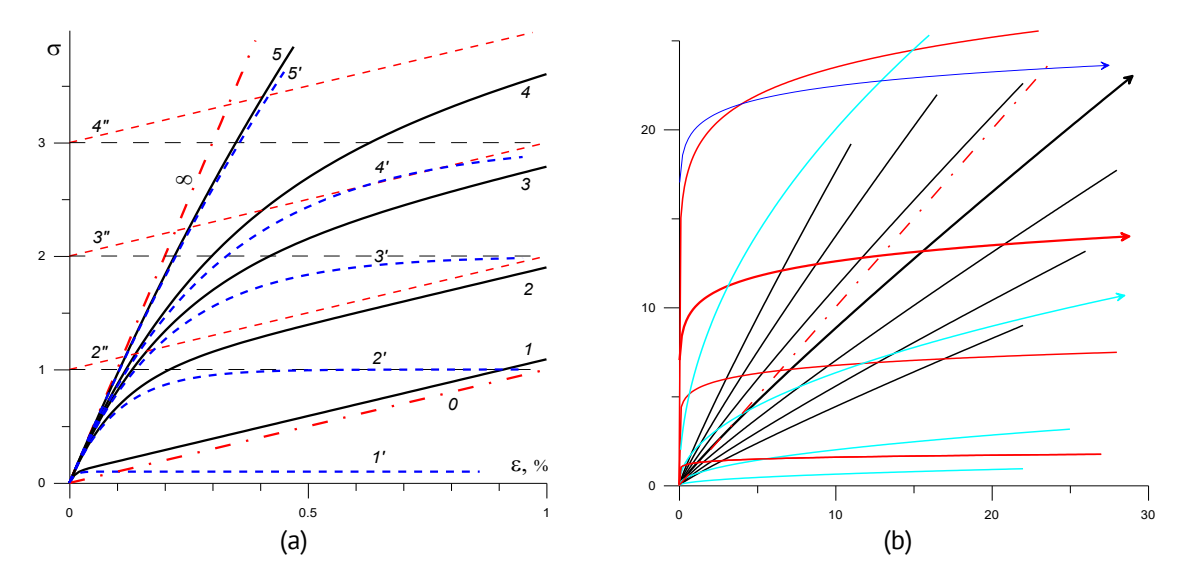


Рис. 5. Диаграммы деформирования с разными скоростями $\sigma = \sigma(\varepsilon, a)$, порождаемые линейным ОС вязкоупругости (1) с разными функциями ползучести при разных скоростях деформирования a: (а) порождаемые моделями Кельвина, Максвелла и Фойгта; (b) порождаемые степенной функцией ползучести с показателями n = 0.1 (черные ДД), n = 0.5 (голубые) и n = 0.9 (красные)

[**Fig. 5.** Stress-strain curves at different strain rates $\sigma = \sigma(\varepsilon, a)$, generated by linear viscoelastic constitutive equation (1) with different creep functions at various strain rates a: (a) generated by the Maxwell, Voigt, and standard linear solid models; (b) generated by the power-law creep function with exponents n = 0.1 (black curves), n = 0.5 (blue curves), and n = 0.9 (red curves)]

У большинства структурно-стабильных материалов семейства ДД $\sigma = \sigma(\varepsilon, a)$ возрастают по a [1–3,6,7,9,13,88,92] но у материалов с изменяющейся в процессе деформирования структурой монотонность по a может нарушаться [12].

На Рис. 5 приведены семейства ДД $\sigma = \sigma(\varepsilon, a)$, порождаемые линейным ОС вязкоупругости (1) с разными функциями ползучести, при разных скоростях деформирования: порождаемые моделями Максвелла, Фойгта и Кельвина (Рис. 5(a), трехзвенная модель с двумя упругими элементами, "standard linear solid"), т.е. моделями с функцией ползучести (ФП) вида:

$$\Pi(t) = \alpha t + \beta - \gamma e^{-\lambda t}, \lambda > 0, \alpha, \beta \geq 0, \gamma \in [0, \beta],$$
 и порождаемые степенной ФП $\Pi(t) = ct^n, n \in (0; 1),$ с показателями $n = 0.1$ (черные ДД), $n = 0.5$ (голубые) и $n = 0.9$ (красные) [88,92].

На Рис. 6 приведены семейства ДД $\sigma = \sigma(\varepsilon, a)$, порождаемые физически нелинейными ОС вязкоупругости Ю.Н. Работнова [93,98]:

$$\varphi(\varepsilon(t)) = \int_0^t \Pi(t-\tau) \, d\sigma(\tau), \, \sigma(t) = \int_0^t R(t-\tau) \, \varphi'(\varepsilon(\tau)) d\varepsilon(\tau), \, t \geq 0,$$
 обобщающим линейное ОС введением второй МФ ф (функции нелинейности) [7,9] (Рис. 6(a)), нелинейным ОС вязкоупругопластичности типа Максвелла [3,6] (Рис. 6(b) и черные ДД на Рис. 6(c)):

 $\varepsilon(t) = E^{-1}F(\sigma(t)) + \eta^{-1}\int_0^t V(\sigma(\tau))d\tau$, или $\dot{\varepsilon} = E^{-1}[F'(\sigma)\dot{\sigma} + \tau_r^{-1}V(\sigma)],\ t>0$, (4) где F(x) и V(x) – возрастающие МФ, управляющие зависимостью упругой и вязкопластической компонент деформации от напряжения) и моделью течения тиксотропных вязкоупругопластичных сред, учитывающей взаимное влияние эволюции структуры и процесса деформирования [11,12] (Рис. 6(c,d)). Разные цвета ДД на Рис. 6(a) соответствуют разным парам МФ ОС Работнова: красные ДД для функции нелинейности [7,9]:

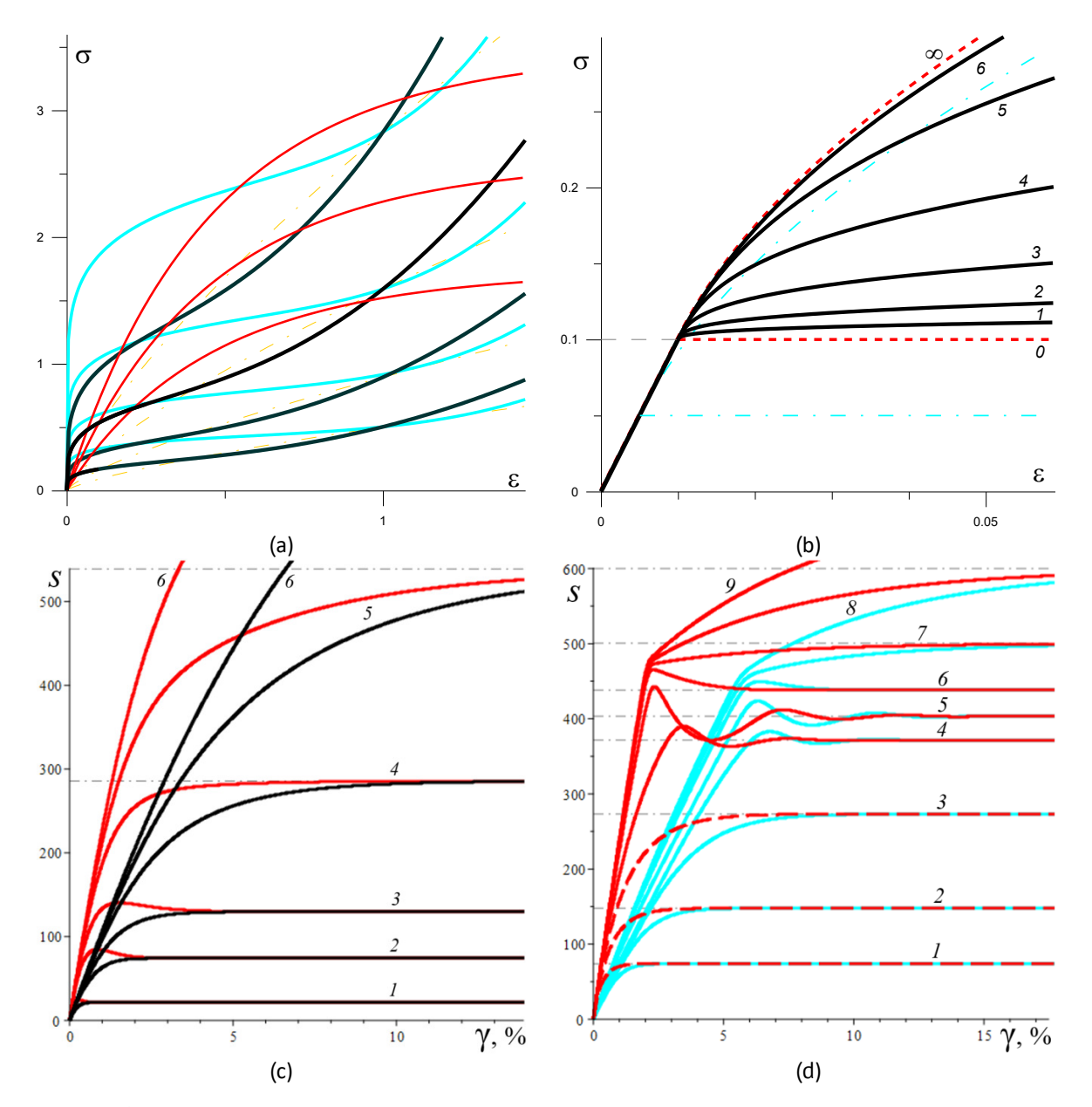


Рис. 6. Диаграммы деформирования с разными скоростями, порождаемые тремя физически нелинейными ОС для вязкоупругопластичных материалов при разных скоростях деформирования: ОС Работнова (3) с разными МФ (a), ОС типа Максвелла (4) ((b) и черные ДД на (c)) и ОС, учитывающим эволюцию структуры (c,d) [1–3,6,7,9,12]

[Fig. 6. Stress-strain curves at different strain rates $\sigma = \sigma(\epsilon, a)$, generated by physically nonlinear Rabotnov constitutive equation (3) (a), Maxwell-type constitutive equation (4) ((b) and black stress-strain curves in (c)), and the model of thixotropic viscoelastic-plastic media flow accounting for structure evolution (c,d)]

$$\varphi(u) = \sigma_*(1 - e^{-u/B}), u \ge 0, \Phi(x) = \varphi^{-1} = B \ln[\sigma_*/(\sigma_* - x)], x \in [0; \sigma_*),$$
 (5) имеют горизонтальные асимптоты, черные и голубые ДД соответствуют МФ:
$$\Phi(x) = 0.5C(x^m + x^{1/m}).$$
 (6)

Красные и голубые ДД на Рис. 6(d) соответствуют одинаковому набору скоростей сдвига, но отличаются начальным значением структурированности материала (одним из материальных параметров модели), от которой зависят модуль сдвига и вязкость (и время релаксации). Аналогичные по форме ДД наблюдаются в испытаниях разных материалов (см. семейства ДД ПТФЭ и КМ на его основе во второй части статьи).

По семейству откликов $\sigma = \sigma(t,a)$ (по его зависимости от a) можно оценить линейности поведения (применимости линейного материала вязкоупругости (1)), т.е. диапазон скоростей, в котором отклик $\sigma = \sigma(t,a)$ пропорционален скорости a ($\sigma(t,a)/a$ не зависит от a). Подчеркнем, что это лишь необходимое условие линейности, и лучше использовать его нарушение как достаточное условие неприменимости линейной теории [87-90,92]: если зависимость отношения $\sigma(t,a)/a$ от a становится заметной (превышает заданный допуск в рабочем диапазоне времен), то использовать линейное ОС (1) нельзя. Отметим, что важно использовать именно отклик $\sigma = \sigma(t, a)$ как функцию времени, а не деформации, ибо OC (1) порождает ДД вида $\sigma(\varepsilon, a) = P(\varepsilon/a)\varepsilon$, где P(t) – осреднение функции релаксации [87,88,92], и эта функция не линейна по a ($\sigma(\varepsilon,a)/a$ зависит от a). Нельзя использовать линейное ОС (1) и в том случае, когда экспериментальные ДД имеют точки перегиба (Рис. 6(а)) и участки выпуклости вниз (линейное ОС при любых а порождает возрастающие выпуклые вверх ДД $\sigma(\varepsilon)$ [88,92] – см. Рис. 5).

По семейству откликов $\sigma=\sigma(t,a)$ (по его зависимости от a) можно оценить диапазон линейности поведения материала (применимости линейного ОС вязкоупругости (1)), т.е. диапазон скоростей, в котором отклик $\sigma=\sigma(t,a)$ пропорционален скорости a ($\sigma(t,a)/a$ не зависит от a). Подчеркнем, что это лишь необходимое условие линейности, и лучше использовать его нарушение как достаточное условие неприменимости линейной теории [87–90,92]: если зависимость отношения $\sigma(t,a)/a$ от a становится заметной (превышает заданный допуск в рабочем диапазоне времен), то использовать линейное ОС (1) нельзя. Отметим, что важно использовать именно отклик $\sigma=\sigma(t,a)$ как функцию времени, а не деформации, ибо ОС (1) порождает ДД вида $\sigma(\varepsilon,a)=P(\varepsilon/a)\varepsilon$, где P(t) — осреднение функции релаксации [87,88,92], и эта функция не линейна по a ($\sigma(\varepsilon,a)/a$ зависит от $\sigma(\varepsilon,a)$). Нельзя использовать линейное ОС (1) и в том случае, когда экспериментальные ДД имеют точки перегиба (Рис. 6(a)) и участки выпуклости вниз (линейное ОС при любых $\sigma(\varepsilon,a)$) порождает возрастающие выпуклые вверх ДД $\sigma(\varepsilon)$ [88,92] — см. Рис. 5).

Целесообразно начать с испытаний на деформирование с постоянными скоростями до разрушения образца, поскольку (минимальные и максимальные) напряжения и деформации при разрушении σ_* и ε_* (как и пределы упругости и текучести) послужат важными ориентирами при планировании испытаний без разрушения образца, при выборе параметров более сложных программ нагружений (на нагрузку-разгрузку, ползучесть и восстановление, ступенчатое и циклическое нагружение и др. – см. ниже и вторую часть статьи).

Аналогично при нагружении $\sigma(t) = bt$ с постоянной скоростью b>0 строятся и изучаются семейства откликов $\varepsilon(t,b)$ и ДД $\varepsilon(\sigma,b)$ (или $\sigma=\sigma(\varepsilon,b)$) при разных скоростях нагружения [6,9,90]. Линейное ОС (1) при любом b порождает возрастающие выпуклые вверх кривые нагружения $\sigma=\sigma(\varepsilon,b)$ [90], качественно близкие по форме к ДД на Рис. 5. Нельзя использовать линейное ОС (1) в том случае, когда экспериментальные кривые нагружения имеют точки перегиба и участки выпуклости вниз (Рис. 6). Все нелинейные ОС, рассмотренные выше [1–13], способны описывать самые разные формы кривых нагружения и для проверки их применимости нужны более тонкие количественные индикаторы [1–13,92,114,115].

Зависимость диаграмм деформирования от температуры

Построение ДД при фиксированных скоростях деформирования, но при разных температурах из рабочего диапазона, определение минимальной температуры, при которой на диаграмме появляется выраженная площадка текучести (горизонтальный участок), исследование зависимости мгновенного модуля, пределов пропорциональности и текучести, напряжения и деформации при разрушении и показателя скоростной чувствительности материала от температуры и т.п.

В квазистатических испытаниях большинства стабильных материалов (в которых не происходят химические, фазовые и структурные превращения) с ростом температуры наблюдается смещение вниз кривых релаксации и смещение вверх кривых ползучести, увеличение скоростей ползучести и релаксации, смещение вниз всех ДД $\sigma = \sigma(\varepsilon, a)$ и $\sigma = \sigma(\varepsilon, b)$ с постоянными скоростями деформирования или нагружения, уменьшение мгновенного модуля и предела текучести (если есть площадка текучести на ДД). В статье [3] этот вопрос изучен для нелинейного ОС типа Максвелла (4) с произвольными МФ и зависимостями модуля упругости и вязкости E = E(T) и $\eta = \eta(T)$ от температуры и доказан критерий: чтобы теоретические кривые деформирования, релаксации и ползучести ОС (4) вели себя при изменении температуры так же, как и кривые изотермических испытаний большинства стабильных вязкоупругопластичных материалов, необходимо и достаточно, чтобы E и η , E E0 можно и достаточно, чтобы E1 и E3 можно и достаточно, чтобы E4 и E4 и E5 можно, например, задать их в виде E6 можно, например, задать их в виде E7 можно, например, задать их в виде E6 можно.

Особенности кривых нагружения-разгрузки-восстановления материала

Эти кривые (КНР) строятся по результатам испытаний по трехстадийным программам нагружения:

 $\sigma(t)=bt$ при $t\in[0;t_1],\,\sigma(t)=-bt+2bt_1$ при $t\in(t_1;2t_1),\,\sigma(t)\equiv0$ при $t>2t_1,$ (7) где $t_1=T/2>0$ – длительность полуцикла нагружения с постоянной скоростью b>0 (Рис. 7(a)). Исследуются криволинейность или прямолинейность ветви разгрузки на кривой нагружения-разгрузки, зависимость максимальной и остаточной деформации от температуры и скорости нагружения и разгрузки, скорость и полнота восстановления после снятия нагрузки [6,114]. Нагружения проводятся с разными скоростями b_i до величин максимального напряжения $\hat{\sigma}_i=b_it_1$ (например, $\hat{\sigma}=i\sigma_*/10$, где σ_* – минимальное напряжение при разрушении, найденное в серии 1). На Рис. 7(a) третья стадия с $\sigma(t)\equiv0$ обрезана: она намного длительнее.

По результатам испытания (7) строятся отклики – зависимость деформации от времени $\varepsilon(t;t_1,b_i)$ при разных $\hat{\sigma}_i=b_it_1$ (Рис. 8(a,c)), по которым (после исключения параметра времени) строятся КНР $\sigma(\varepsilon;t_1,b_i)$ при разных скоростях b_i (Рис. 8(b,d)). Необходимо построить и КНР при разных длительностях нагружения t_1 (см. ниже и [6,114]). На Рис. 8(a,b) приведены отклики $\varepsilon(t;t_1,b_i)$ и КНР $\sigma(\varepsilon;t_1,b_i)$ образцов композита на основе ПТФЭ с 5 % мелкодисперсного серпентина при растяжении по программам (7) (Рис. $\pi(t_1,t_2)$) с $\pi(t_1,t_2)$ 0 с $\pi(t_2,t_3)$ 1 с $\pi(t_1,t_2)$ 3 показана только четверть стадии восстановления). На Рис. $\pi(t_1,t_2)$ 4 отклики $\pi(t_2,t_3)$ 6 и $\pi(t_3,t_4)$ 6 нелинейного ОС типа

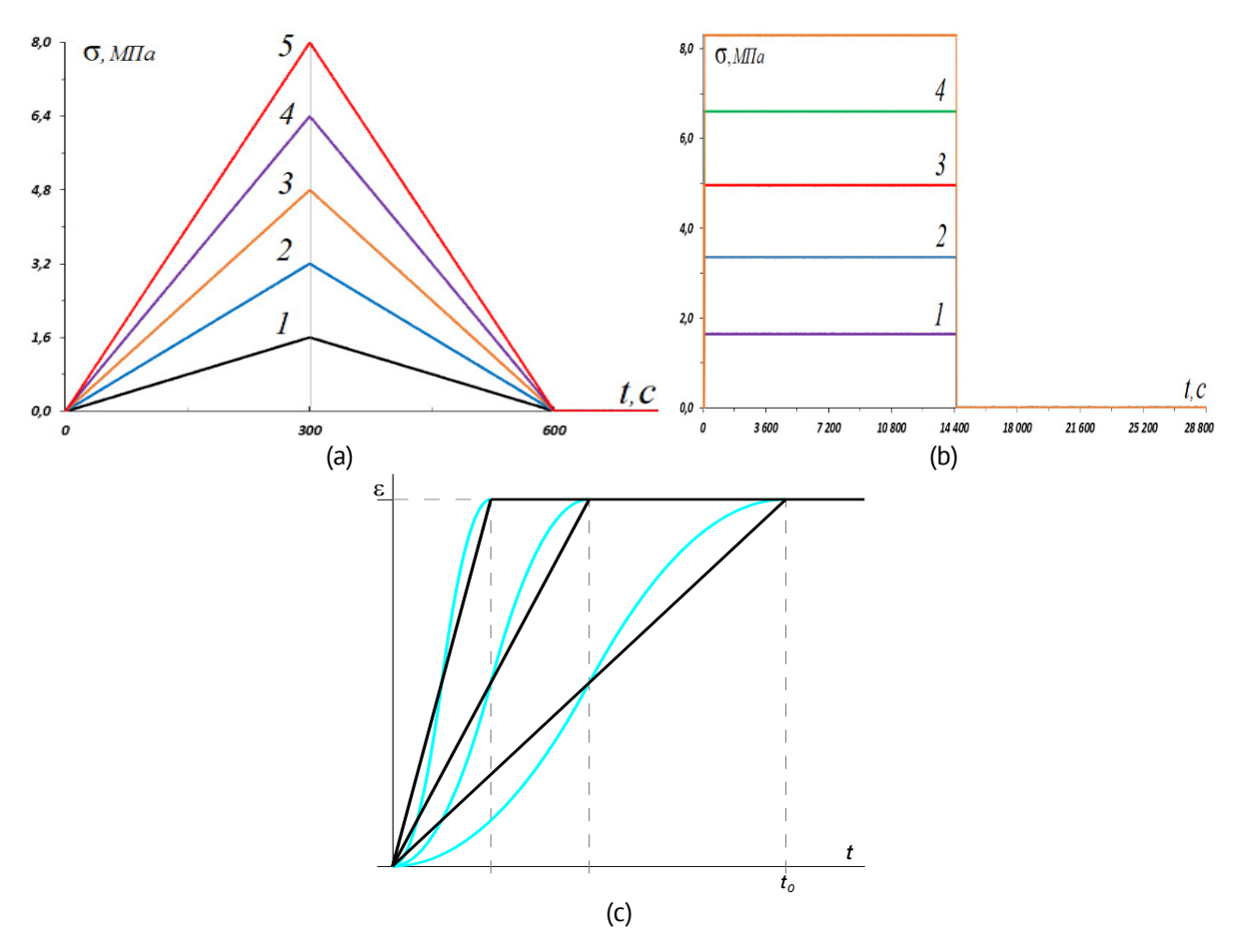


Рис. 7. Программы нагружения (7), (8), (9) в испытаниях на нагрузку-разгрузку- восстановление, на ползучесть и восстановление и на релаксацию напряжений с учетом начальной стадии с разными параметрами нагружения

Fig. 7. Loading programs (7), (8), (9) for loading-unloading-recovery tests, creep and recovery tests, and stress relaxation tests taking into account the initial stage with different loading parameters

Максвелла (4) (с временем релаксации $\tau_r = 1$) на нагружение (7) с фиксированным $t_1 = 5$ и разными скоростями b = 0.01i, i = 1, ..., 8 [6].

Отклики образцов ПТФЭ на треугольный импульс нагрузки (7) (Рис. 8(a,b)) с деформацией, продолжающей расти и в начале разгрузки, и с большими остаточными деформациями качественно весьма сходны с наблюдаемыми в испытаниях асфальтобетонов, твёрдых топлив и других материалов. В испытаниях комплексных полиэфирных нитей [114] он не проявлялся. Этот эффект не связан с нелинейностью поведения материала: его описывает даже линейное ОС (1), даже простейшая линейная модель Максвелла [6]. КНР, порождаемые нелинейным ОС типа Максвелла (4) (Рис. 8(c,d)) и нелинейным ОС для тиксотропных сред, учитывающим эволюцию структуры [11,12], качественно схожи по форме с КНР ПТФЭ и композитов на его основе на Рис. 7(a,b), поэтому (после проверки системы индикаторов по КНР и по кривым ползучести) эти ОС можно примерить к описанию поведения ПТФЭ [6,114].

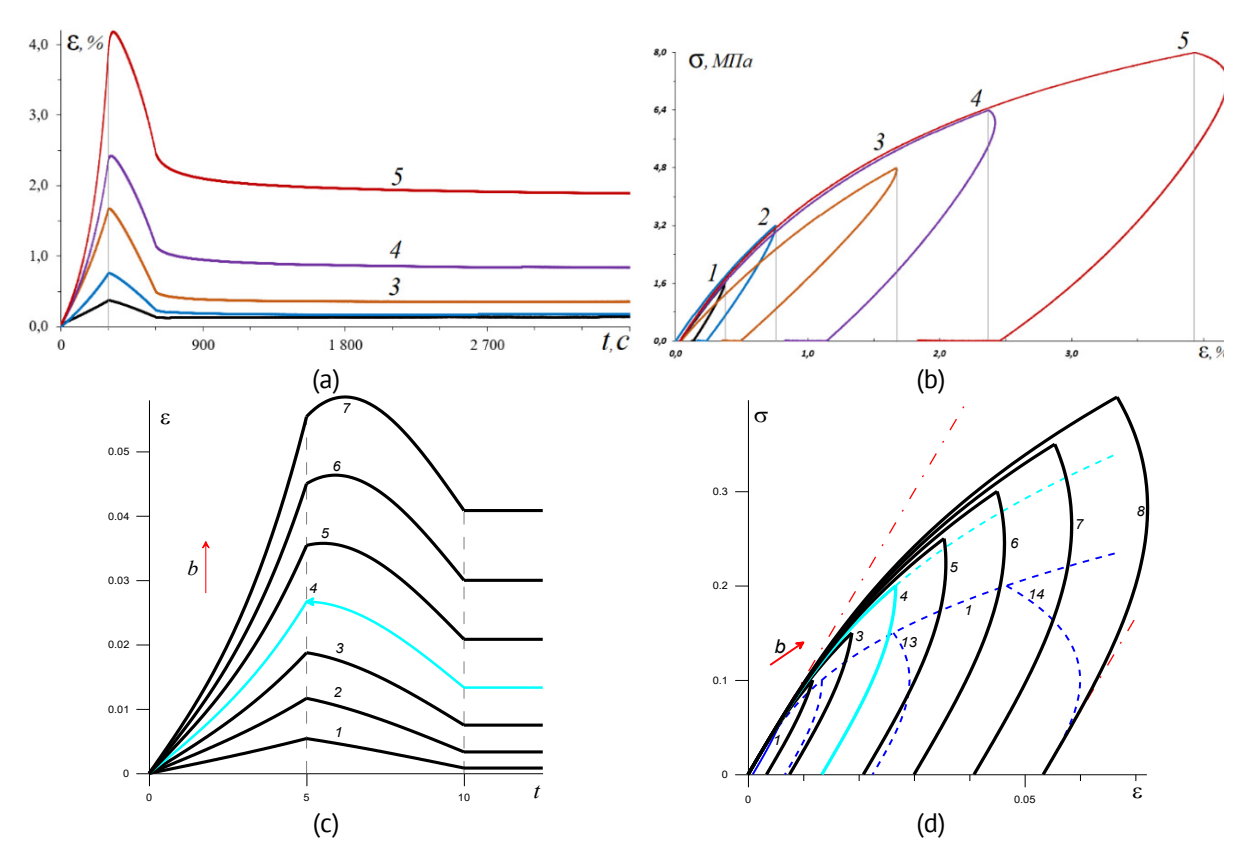


Рис. 8. Отклики на программу нагружения-разгрузки-восстановления (7): (a,b) экспериментальные отклики $\varepsilon(t,b)$ и $\sigma(\varepsilon,b)$ образца КМ на основе ПТФЭ при $t_1=300$ с, $\hat{\sigma}=i\sigma_*/10,\,i=1,...,5$; (c,d) отклики $\varepsilon(t;t_1,b_i)$ и $\sigma(\varepsilon;t_1,b_i)$ нелинейного ОС типа Максвелла (4) (с временем релаксации τ_r =1 для фиксированного $t_1=5$ и разных скоростей $b=0.1i,\,l=1,...,8$

Fig. 8. Responses to the load-unload-recovery program (7): (a,b) experimental responses $\varepsilon(t,b)$ and $\sigma(\varepsilon,b)$ of the PTFE-based composite samples at t_1 = 300 s, $\hat{\sigma} = i\sigma_*/10$, i = 1, ..., 5; (c,d) – responses $\varepsilon(t;t_1,b_i)$ and $\sigma(\varepsilon;t_1,b_i)$ of the nonlinear Maxwell-type constitutive equation (4) (with a relaxation time $\tau_r = 1$) for a fixed t_1 = 5 and different strain rates b = 0.01i, i = 1,...,8]

Ползучесть при постоянной нагрузке

Быстрое нагружение на начальной стадии до заданного уровня напряжения, можно считать мгновенным при математической обработке для ее упрощения: $\sigma(t) = \bar{\sigma} h(t)$, t > 0, где h(t) – функция Хевисайда (Рис. 7(b), первая стадия). Измеряется развитие деформации во времени и строится семейство кривых ползучести (КП) $\varepsilon(t;\bar{\sigma})$ при разных уровнях напряжения $\bar{\sigma}$ (Рис. 9), изучается зависимость средней и минимальной скорости ползучести от уровня напряжения $\bar{\sigma}$ и от температуры, склонность материала к ограниченной ползучести (наличие горизонтальных асимптот у кривых ползучести) или к установившейся ползучести и течению при достаточно высоких температурах (ищется нижняя граница температур, при которых ползучесть не замедляется с времени вплоть до разрушения) [1-4,8,89,115]. Первый случай моделируется, например, линейным ОС вязкоупругости ОС (1) или нелинейным ОС Работнова (3) с ограниченной функцией ползучести [4,89,90], а второй – этими же ОС с функцией ползучести, имеющей наклонную асимптоту, или нелинейным ОС вязкоупругопластичности типа Максвелла [5,8] и его обобщениями [10,13]. По зависимости экспериментальных кривых ползучести от напряжения $ar{\sigma}$ определяется диапазон линейности поведения материала (диапазон напряжений, в котором

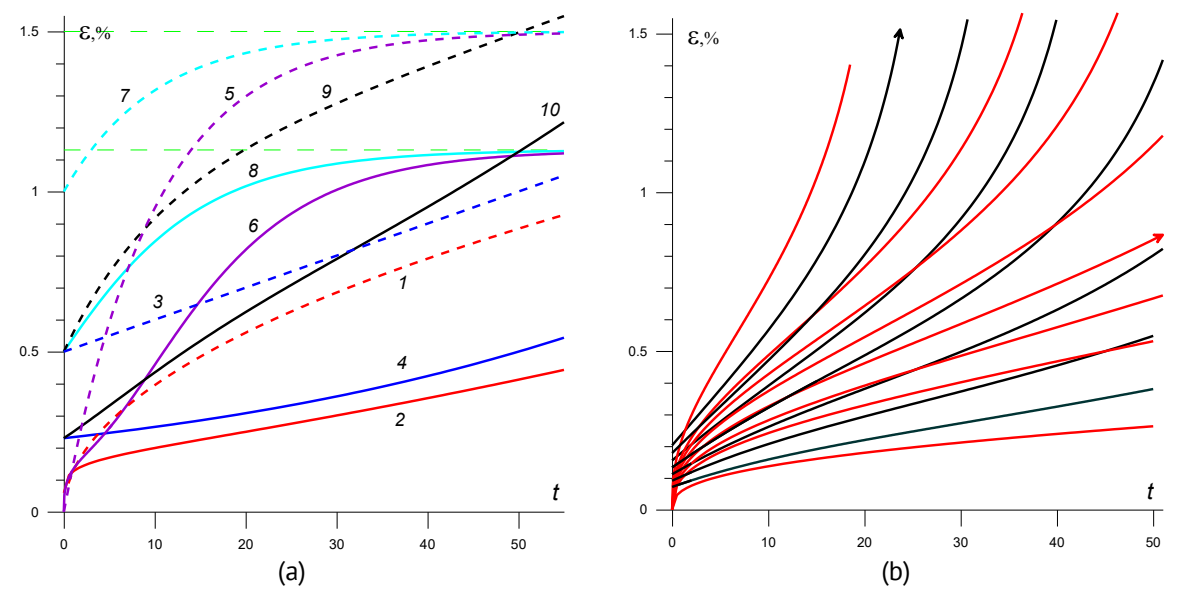


Рис. 9. Кривые ползучести, порожденные ОС Работнова (3) и линейным ОС (1) с разными МФ: (а) КП пяти линейных моделей с разными ФП (степенной ФП – КП 1 или ФП вида (2) – штриховые КП 3,5,7,9) и пяти нелинейных моделей с МФ (6) и теми же пятью ФП (КП 2,4,6,8,10) для $\bar{\sigma}=1$; (b) КП для разных напряжений $\bar{\sigma}$, порожденные двумя вариантами ОС Работнова (3) с МФ (5) с $B=\sigma_*=0.1$, и разными ФП: степенной ФП с показателем n=1/3 (красные КП) или ФП (2) с $\lambda=0.1$, $\alpha=0.02$, $\beta=1$, $\gamma=0.5$

[**Fig. 9.**Creep curves generated by the nonlinear Rabotnov constitutive equation (3) and the linear constitutive equation (1) with different creep functions: (a) creep curves of five linear models with different creep functions (power-law function – creep curve 1 or function of the form (2) – dashed creep curves 3,5,7,9) and five nonlinear models with a material function (6) and the same five creep functions (creep curves 2,4,6,8,10) for $\bar{\sigma}$ = 1; (b) creep curves for different stresses $\bar{\sigma}$ generated by two variants of the Rabotnov constitutive equation (3) with material function (5) with B = 0.005, σ_* = 1.5, and different creep functions: power-law function with exponent n = 1/3 (red curves) or function (2) with λ = 0.1, α = 0.02, β = 1, γ = 0.5]

податливость $\varepsilon(t;\bar{\sigma})/\bar{\sigma}$ не зависит от уровня напряжения), точнее, диапазон (не)применимости линейной вязкоупругости). Подчеркнем, что это лишь необходимое условие линейности и лучше использовать его нарушение как достаточное условие нелинейности: если зависимость податливости $\varepsilon(t;\bar{\sigma})/\bar{\sigma}$ от $\bar{\sigma}$ становится заметной (превышает допуск), то использовать линейное ОС вязкоупругости нельзя.

На Рис. 9 приведены КП, порожденные линейным ОС (1) и ОС Работнова (3) с разными МФ. На Рис. 9(а) приведены КП $\varepsilon(t,\bar{\sigma})=\bar{\sigma}\Pi(t)$ (с $\bar{\sigma}=1$) пяти линейных моделей: с ФП $\Pi=t^{0.5}/800$ (кривая 1) и с четырьмя ФП вида(2): с $\gamma=0$, $\alpha=0.0001$, $\beta=0.01$ (модель Максвелла), с $\alpha=0$, $\beta=\gamma=0.015$, $\lambda=0.1$ (Фойгта), с $\alpha=0$, $\beta=0.01$, $\gamma=0.005$, $\lambda=0.1$ (модель Кельвина с тем же временем ретардации $\tau=1/\lambda=10$), модель Бюргерса (последовательное соединение моделей Максвелла и Фойгта) с $\lambda=0.1$, $\alpha=0.0001$, $\beta=0.01$, $\gamma=0.005$ (штриховые кривые 3,5,7,9), а также – КП 2,4,6,8,10 пяти вариантов ОС Работнова (3) с теми же пятью ФП и МФ (6) с C=0.5, m=3. У КП 2,4,6,10 есть участки выпуклости вниз, КП 2 (модели со степенной ФП) содержит все три типичные стадии ползучести (замедленной, установившейся и ускоренной ползучести), КП 6,8 обладают горизонтальными асимптотами (как и 5,7). Примечательно, что КП 6 модели Фойгта с МФ (6) имеет две точки перегиба. У степенной ФП $\Pi(0)=0$, как и у модели Фойгта, но ещё и $\dot{\Pi}(0)=\infty$, и у КП нет горизонтальной асимптоты (т.к. $\Pi(\infty)=\infty$). КП 3 линейной модели Максвелла прямолинейна, а КП 2 и 10

нелинейных моделей (для степенной ФП и для модели Бюргерса) имеют выраженный участок установившейся ползучести (близки к прямолинейным). На Рис. 9(b) приведены $\mathsf{K}\Pi\,\varepsilon(t,\bar{\sigma}) = \Phi(\bar{\sigma}\Pi(t))$ с разными уровнями напряжения $\bar{\sigma}$ двух вариантов ОС Работнова с МФ (5) с B=0.005, $\sigma_*=1.5$ и двумя ФП: ФП (2) с $\lambda=0.1$, $\alpha=0.02$, $\beta=1$, $\gamma=0.5$ или степенной ФП $\Pi=t^{1/3}/3$. Для степенной ФП $-\bar{\sigma}=0.5;0.8;0.9;1.0;1.1;1.2;1.3;1.7$ (красные КП), для ФП модели Бюргерса – $\bar{\sigma} = 0.4; 0.5; 0.6; 0.7; 0.8; 0.9; 1$ (чёрные КП); стрелками помечены КП с $\bar{\sigma} = 1$. Все эти КП имеют точку перегиба и все три типичные стадии ползучести. Т.к. МФ $\Phi(x)$ из (5) обладает асимптотой $x = \sigma_*$, то КП $\varepsilon(t) = A \ln[\sigma_*/(\sigma_* - \bar{\sigma}\Pi(t))]$ неограниченно растут при $\Pi(t) \to \sigma_*/\bar{\sigma}$, если только $\bar{\sigma} >$ ФΠ $\sigma_*/\Pi(\infty)$ (для указанных ЭТО выполнено при т.к. $\Pi(\infty) = \infty$), т.е. КП имеют вертикальную асимптоту $t = t_*(\bar{\sigma})$, где $\Pi(t_*) = \sigma_*/\bar{\sigma}$ (можно трактовать t_* как время до разрушения, а $t_*(\bar{\sigma})$ как кривую длительной прочности [1,4,91]).

Если исследуется длительная прочность при ползучести [1-3,91], то надо проводить испытание до разрушения, чтобы определить зависимость времени разрушения при ползучести от напряжения, т.е. построить кривую длительной прочности при данной температуре или несколько кривых при разных температурах, чтобы исследовать зависимость длительной прочности от температуры. По данным испытаний образцов на ползучесть при фиксированном уровне напряжения и при разных постоянных температурах можно построить семейство кривых ползучести и для каждого напряжения и построить (спрогнозировать) единую кривую ползучести на существенно большем интервале времени, чем время испытаний (на основе температурновременной аналогии, если она справедлива для исследуемого материала).

Восстановление (обратная ползучесть) при полной разгрузке после ползучести

Восстановление изучается в испытаниях из двух длительных стадий: стадии ползучести при достаточно низких нагрузках $\bar{\sigma}$, как правило, не превышающих 0.5...0.7 предела прочности σ_* , и не слишком большом времени их приложения T (чтобы исключить разрушение) и стадии восстановления после полной разгрузки (оно может продолжаться долго и потому надежно оценить необратимую часть деформации можно только в длительных испытаниях) [4,8,13,89,115]. Если нагрузка и разгрузка проводятся быстро, можно считать их мгновенными и считать, что программа нагружения состоит из двух стадий (а не четырех) и описывается формулой:

$$\sigma(t) = \bar{\sigma}[h(t) - h(t - T)], \, \bar{\sigma} > 0, \, T > 0, \tag{8}$$

(прямоугольный импульс нагрузки длительности T). По данным испытания строится семейство кривых ползучести и восстановления (КПВ) $\varepsilon(t;\bar{\sigma},T)$ при разных напряжениях $\bar{\sigma}$ (Рис. 10) и разных длительностях стадий ползучести и восстановления после снятия нагрузки. Изучается скорость и глубина восстановления, стабилизация и величина остаточной деформации (к концу испытания) в зависимости от уровня нагрузки и длительности нагружения (и температуры).

На Рис. 10(а) приведены экспериментальные КПВ образцов композитов на основе ПТФЭ с 5 % серпентина, модифицированных дозой облучения 80 кГр в расплаве по технологии [41,42,46,82], измеренные в испытаниях по программе Рис. 7(а): длительности стадий ползучести и восстановления – по 4 ч, $\bar{\sigma} = i\sigma_*/10$,

 $i=1,\ldots,5,\;\sigma_*=16$ МПа, т.е. $\bar{\sigma}=1.6;\;3.2;\;4.8;\;6.4;\;8.0$ МПа. На Рис. 10(b) приведены КПВ, порожденные тремя ОС [13]: 1) линейным ОС вязкоупругости (1) с функцией ползучести $\Pi=At^u,\;u=1/3,\;A=0.03,\;$ – красные штриховые кривые без скачка в момент $t=T;\;$ 2) нелинейным ОС типа Максвелла (4) [8] – голубые штриховые кривые; 3) нелинейным ОС, полученным их скрещиванием [13] – черные КПВ.

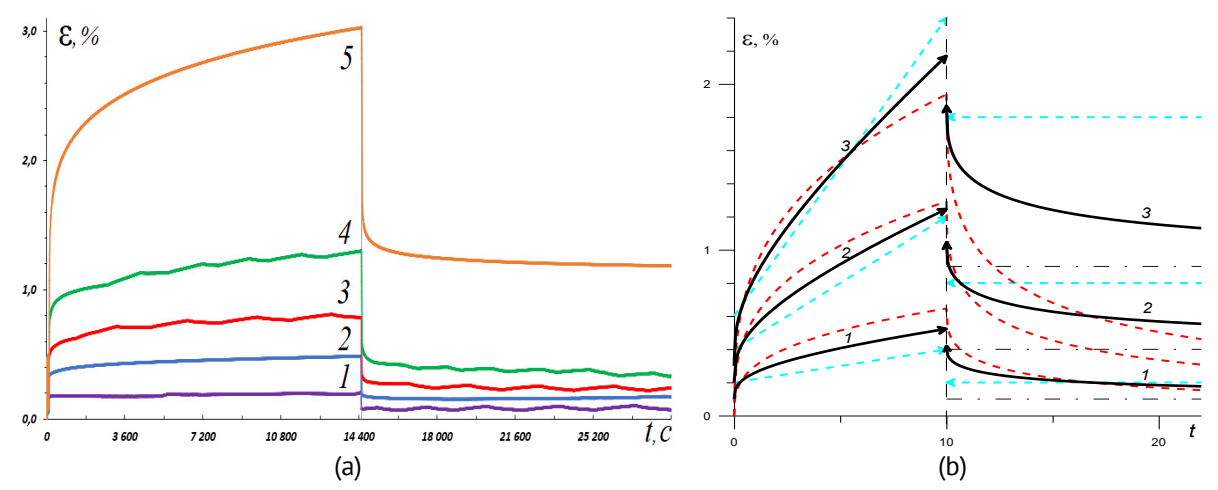


Рис. 10. Кривые ползучести и восстановления $\varepsilon(t; \bar{\sigma}, T)$ в испытаниях по программе (8): (а) КПВ образцов композитов на основе ПТФЭ с 5 % серпентина, модифицированных дозой облучения 80 кГр в расплаве по технологии [41,42]; (b) КПВ, порожденные тремя ОС [13]: линейным ОС (1) с функцией ползучести $\Pi = At^u$, u = 1/3, A = 0.03 (красные штриховые кривые), нелинейным ОС типа Максвелла (4) (голубые штриховые кривые) и нелинейным ОС, полученным их скрещиванием [13] (черные КПВ) **Fig. 10.** Creep and recovery curves $\varepsilon(t; \bar{\sigma}, T)$ in tests according to the program (8): (a) experimental creep and recovery curves of PTFE-based composite samples with 5 % serpentine, modified by irradiation (the dose of 80 kGy) in melt according to technology [41,42]; (b) creep and recovery curves generated by three constitutive equations [13]: a linear viscoelasticity model (1) with creep function $\Pi = At^u$, u = 1/3, A = 0.03 (red dashed curves), the nonlinear Maxwell-type model (4) (blue dashed curves), and the nonlinear model obtained by their hybridization [13] (black creep and recovery curves)

Релаксация напряжений при постоянной деформации

Деформирование с высокой скоростью на начальной стадии до заданного уровня деформации, можно считать мгновенным при математической обработке для ее упрощения: $\varepsilon(t) = \bar{\varepsilon}h(t), \ \bar{\varepsilon} > 0$. Отклики материала или ОС на такие процессы – семейство кривых релаксации (КР) $\sigma(t;\bar{\varepsilon})$. Изучаются зависимость КР от времени (выпуклость вниз, горизонтальная асимптота, спектр времен релаксации и т.п.) и от заданного уровня деформации $\bar{\epsilon}$, определяется диапазон (не)применимости линейной вязкоупругости ПО независимости экспериментального модуля релаксации $\rho = \sigma(t; \bar{\varepsilon})/\bar{\varepsilon}$ от $\bar{\varepsilon}$ (в линейной вязкоупругости $\rho(t; \bar{\varepsilon})$ не зависит от $\bar{\varepsilon}$ и совпадает с функцией релаксации) [4,7]. Подчеркнем, что независимость $\rho(t;\bar{\varepsilon})$ от $\bar{\varepsilon}$ – лишь необходимое условие линейности и лучше использовать его нарушение как достаточное условие нелинейности. Следует заметить также, что *подобие КР* $\sigma(t;\bar{\varepsilon})$ (т.е. свойство $\sigma(t; C\bar{\varepsilon}) = C\sigma(t; \bar{\varepsilon})$) совсем не гарантирует линейность поведения материала: например, физически нелинейное ОС Работнова порождает подобные кривые релаксации $\sigma(t,\bar{\varepsilon})=\varphi(\bar{\varepsilon})R(t)$ при мгновенном нагружении и способно моделировать любой тип зависимости модуля релаксации $ho(t;ar{arepsilon})$ от уровня

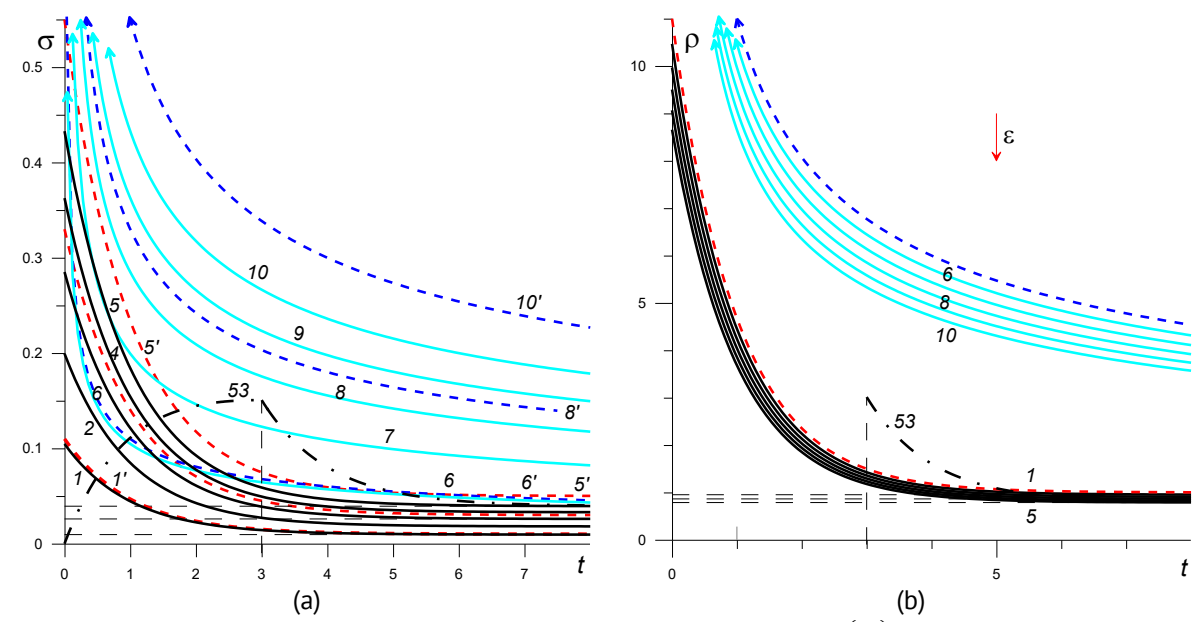


Рис. 11. (а) Кривые релаксации и (b) модули релаксации $\rho(t;\bar{\varepsilon})=\frac{\sigma(t;\bar{\varepsilon})}{\bar{\varepsilon}}$ для $\bar{\varepsilon}=0.01i,\ i=1,...,5,$ порождаемые двумя нелинейными ОС Работнова (3) с МФ (5) с $B=\sigma_*=0.1$ и разными ФР: с регулярной ФР $R=A\left(e^{-\frac{t}{\tau}}+r\right), A=10, \tau=1, r=0.1$ (кривые 1-5) и неограниченной ФР $R=A(t^{-\alpha}+r), A=10, \alpha=0.5, r=0.1$ (кривые 6-10). Штриховые линии 1',3',5' (красные) и 6',8',10' (синие) – КР линейных моделей с теми же ФР для $\bar{\varepsilon}=0.01;0.03;0.05$

Fig. 11. Relaxation curves (a) and relaxation moduli $\rho(t;\bar{\varepsilon})=\sigma(t;\bar{\varepsilon})/\bar{\varepsilon}$ (b) for $\bar{\varepsilon}=0.01i, i=1,...,5$, generated by two versions of nonlinear Rabotnov constitutive equations (3) with the material function (5) with $B=\sigma_*=0.1$ and different relaxation functions: the regular relaxation function $R=A(e^{-t/\tau}+r),$ A=10, $\tau=1,$ r=0.1 (curves 1-5) and the unbounded relaxation function $R=A(t^{-\alpha}+r),$ A=10, $\alpha=0.5,$ r=0.1 (curves 6-10). The dashed lines 1', 3', 5' (red) and 6', 8', 10' (blue) represent the relaxation curves of the linear models with the same relaxation functions for $\bar{\varepsilon}=0.01; 0.03; 0.05$

деформации (убывание, возрастание, немонотонность) при надлежащем выборе МФ (Рис. 11(b)) [7]. Другие примеры соблюдения подобия КР, порожденных нелинейным ОС, дают нелинейное ОС, предложенное в статье [1] и ОС течения тиксотропных вязкоупругопластичных сред [11,12]. По испытаниям при разных температурах исследуется зависимость семейства КР (скорости и полноты релаксации) от температуры [3].

На Рис. 11(а) приведены КР для $\bar{\varepsilon}=0.01i,\ i=1,\ldots,5$, порождаемые двумя нелинейными моделями Работнова (3) с МФ (5) с $B=\sigma_*=0.1$, и разными функциями релаксации (ФР): с ФР (модели Кельвина) $R=A(e^{-t/\tau}+r),\ A=10,$ $\tau=1,\ r=0.1$ (черные КР 1-5) и с неограниченной ФР $R=A(t^{-\alpha}+r),\ A=10,$ $r=0.1,\ \alpha=0.5$ (голубые КР 6-10). У обеих моделей $R(\infty)=0.1$ (одинаковый длительный модуль) и потому их КР с одинаковым $\bar{\varepsilon}$ имеют общую асимптоту $\sigma=0.1\bar{\varepsilon}$. Штриховые линии 1',3',5' (красные) и 6',8',10' (синие) – КР линейных моделей (1) с теми же ФР для $\bar{\varepsilon}=0.01;0.03;0.05$. Кривая 53 – КР ОС Работнова с ФР модели Кельвина при гатр-деформировании с $\bar{\varepsilon}=0.05$ и $t_*=1$ (см. ниже).

На Рис. 11(b) приведены графики модулей релаксации $\rho(t;\bar{\varepsilon})=\sigma(t;\bar{\varepsilon})/\bar{\varepsilon}$ тех же двух моделей для $\bar{\varepsilon}=0.01i,\;i=1,\ldots,5$ (кривые 1–5 и 6–10); $\rho(\bar{\varepsilon})$ убывает по $\bar{\varepsilon}$. Штриховые линии – графики модулей релаксации двух линейных моделей: для ОС (1) $\rho(t)=R(t)$ (не зависит от $\bar{\varepsilon}$).

При любых МФ семейство КР ОС Работнова $\sigma(t,\bar{\varepsilon}) = \varphi(\bar{\varepsilon})R(t)$ (и линейного OC(1)) возрастает по параметру $\bar{\varepsilon}$ (КР сдвигаются вверх с ростом уровня деформации), а каждая КР убывает по времени (это необходимые индикаторы их применимости). Для ОС, учитывающего взаимное влияние эволюции структуры и процесса деформирования [11,12], второе свойство сохраняется, а первое нарушается из-за изменения структурированности в процессе релаксации.

Влияние длительности начальной стадии нагружения или деформирования на кривые ползучести или релаксации

Нагружение на испытательных машинах не может быть мгновенным в отличие от идеализации и следует изучить погрешность и пределы допустимости такой идеализации), исследование наличия (и скорости) затухания памяти в зависимости от скорости и уровня нагружения [5,7,87] и температуры [3]. Например, испытания с произвольными монотонными начальными стадиями деформирования (Рис. 7(с)) или по программам с постоянной скоростью деформирования на начальной стадии (ramp tests) с несколькими разными длительностями начальной стадии t_0 (rise time), т.е. с разными скоростями деформирования $a = \bar{\varepsilon}/t_0$ при фиксированном целевом уровне деформации $\bar{\varepsilon}$ [7,87]: $\varepsilon(t) = at$ при $t \in [0;t_0]$, $\varepsilon(t) = \bar{\varepsilon} = \mathrm{const}$ при $t \geq t_0$.

Такие испытания включены в европейские и американские стандарты. Начальную стадию деформирования и влияние ее длительности t_0 на экспериментальные и теоретические КР $\sigma(t;\bar{\varepsilon},t_0)$, на их отклонение от КР при мгновенном нагружении $\sigma(t;\bar{\varepsilon})$ и на "окно наблюдения" релаксации $t>kt_0$, k>1,

мгновенном нагружении $\sigma(t;\bar{\varepsilon})$ и на "окно наблюдения" релаксации $t>kt_0,\,k>1,$ следует учитывать при обработке КР, получаемых в испытаниях материалов, при идентификации ОС и при определении области линейности поведения материала (ибо идентификации ОС и при определении области линейности поведения материала

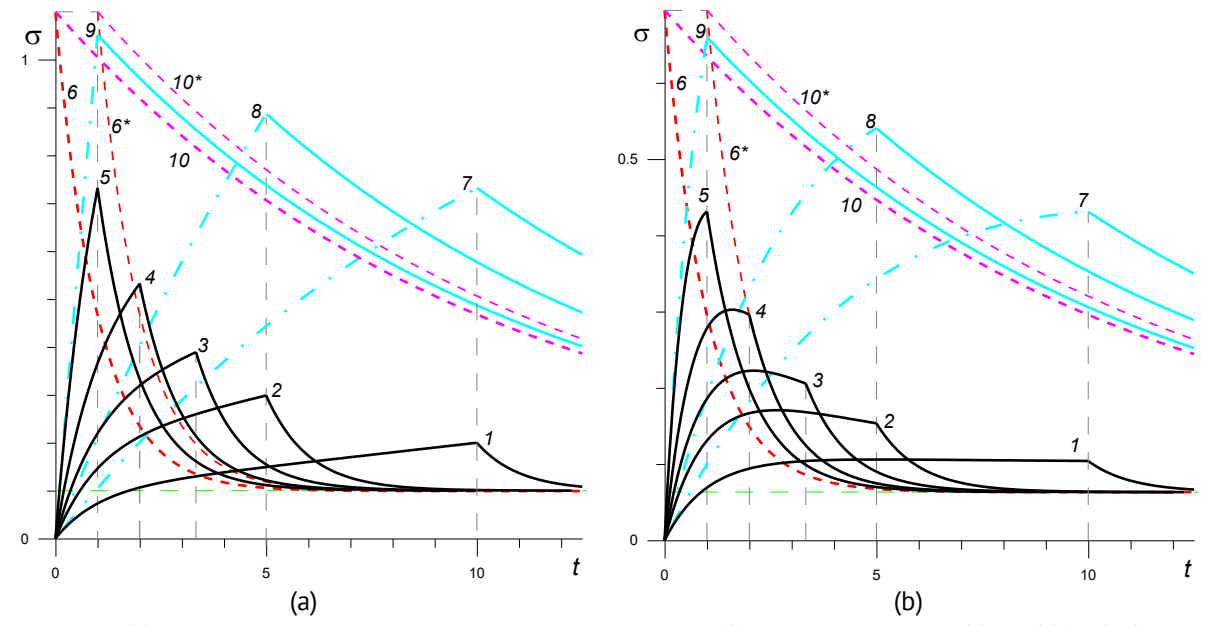


Рис. 12. Кривые релаксации $\sigma(t;\bar{\epsilon},t_0)$ при нагружении (9) с $\bar{\epsilon}=0.1$ и $t_0/\tau=10;5;10/3;2;1$, порождаемые линейным ОС (1) (a) и нелинейным ОС Работнова (3) с функцией нелинейности (5) (b) [7,87] **[Fig. 12.** Relaxation curves $\sigma(t;\bar{\epsilon},t_0)$ generated by the linear constitutive equation (1) (namely, the Standard linear solid model) (a) and the nonlinear Rabotnov constitutive equation (3) with the nonlinearity function (5) (b) under the ramp loading (9) with $\bar{\epsilon}=0.1$ and $t_0/\tau=10;5;10/3;2;1$

(ибо t_0 влияет на модуль релаксации $\rho(t; \bar{\varepsilon}, t_0) = \sigma(t; \bar{\varepsilon}, t_0)/\bar{\varepsilon}$) [7,87]. Типичные КР $\sigma(t; \bar{\varepsilon}, t_0)$, т.е. отклики на процессы (9), показаны на Рис. 12.

На Рис. 12(а) приведены КР 1–5, порожденные линейной моделью Кельвина с временем релаксации $\tau=1$ при деформировании по программе (9) с $\bar{\varepsilon}=0.1$ и $t_0/\tau=10$; 5; 10/3; 2; 1, т.е. со скоростями a=0.01; 0.02; 0.03; 0.05; 0.05; 0.05; 0.05; красная КР 6 идеальная КР $\sigma(t;\bar{\varepsilon})$ при мгновенном нагружении $\varepsilon(t)=\bar{\varepsilon}h(t)$ (предельная кривая семейства КР при $t_0\to 0$) [87]. Общая асимптота всех КР при $t\to \infty$ – прямая $\sigma=\bar{\varepsilon}Ar=0.1$. Для сравнения шрих-пунктиром намечены КР $\sigma(t;\bar{\varepsilon},t_0)$ модели Кельвина с увеличенным в 10 раз временем релаксации для $t_0=10$; 5; 1 (кривые 7–9) и идеальная КР 10. На Рис. 12(b) приведены КР, порожденные нелинейным ОС Работнова (3) с функцией нелинейности (5) с B=0.1, для тех же программ деформирования (9) [7].

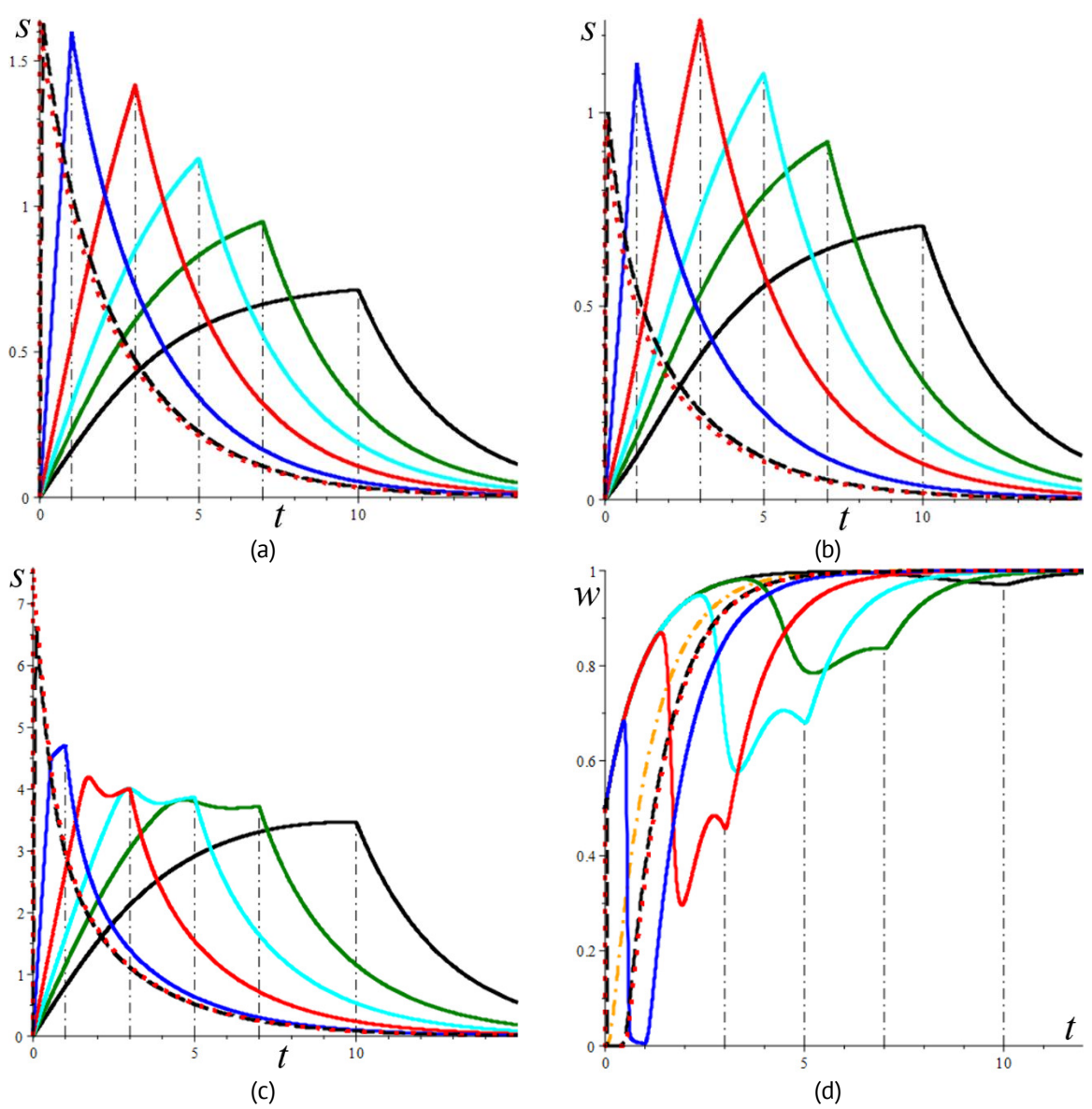


Рис. 13. Зависимость КР $\sigma(t; \bar{\varepsilon}, t_0; w_0)$, порождаемых ОС, учитывающим эволюцию структуры, при гатр-нагружении (9) с $\bar{\varepsilon}=1$ % (для $w_0=0.5$ (a) и $w_0=0$ (b)) и $\bar{\varepsilon}=5$ % (с,d) от длительности начальной стадии $t_0/\tau=0.1; 1; 3; 5; 7; 10$ **Fig. 13.** Dependence of the relaxation curves $\sigma(t; \bar{\varepsilon}, t_0; w_0)$ generated by the constitutive equation that accounts for structural evolution under ramp loading (9) with $\bar{\varepsilon}=1$ % (a) for $w_0=0.5$, (b) for $w_0=0$) and $\bar{\varepsilon}=5$ % (c,d) on the duration of the initial stage $t_0/\tau=0.1; 1; 3; 5; 7; 10$

На Рис. 13(a,b) приведены КР $\sigma(t; \bar{\varepsilon}, t_0; w_0)$, порождаемые ОС, учитывающим взаимное влияние эволюции структуры и процесса деформирования [11,12], с временем релаксации $\tau = 1$ и МФ $g = e^{7s}$, при деформировании по программе (9) для $\bar{\varepsilon} = 1 \%$, и длительностей начальной стадии $t_0/\tau = 0.1; 1; 3; 5; 7; 10$. Рисунок 13(a,b) отличаются только начальным занчением структурированности материала: $w_0 = 0.5$ (Рис. 13(a)) или $w_0=0$ (Рис. 13(b)). Красная пунктирная КР – для $t_0=0$; на всех рисунках КР с $t_0/\tau=0.1$ (черная штриховая КР) близка к ней. При $w_0=0.5$ КР $\sigma(t; \bar{\varepsilon}, t_0; w_0)$ имеют примерно такой же вид как и KP, порожденные линейным ОС (1) (Рис. 12(а)), поскольку структурированность быстро выходит на стационарное значение $(w_* = 0.98 \approx 1$ для рассматриваемой модели) и меняется не сильно (увеличивается в 2 раза к моменту t=5). Но при $w_0=0$ (Рис. 13(b)) значение напряжения в конце начальной стадии $\hat{\sigma}(t_0; \bar{\epsilon}; w_0) = \sigma(t_0; \bar{\epsilon}, t_0; w_0)$ уже не убывает монотонно с ростом длит HC, а достигает максимальной величины при $t_0/\tau = 3$ (красная кривая) и только потом убывает по t_0 . Это происходит из-за того, что структурированность (см. желтую штрих-пунктирную кривую на Рис. 13(d), с ней сливаются графики $w(t; 1, t_0; 0)$ при всех t_0 , когда $\bar{\varepsilon}=1$ %) очень быстро растет к стационарному значению и быстро меняется от 0 до 1: более низкая скорость в значительно более структурированном и жестком материале вызывает большие напряжения. На Рис. 13(c,d) приведены КР $\sigma(t;ar{arepsilon},t_0;w_0)$ и графики структурированности $w(t;ar{arepsilon},t_0;w_0)$ для $ar{arepsilon}~=~5~\%$ и $w_0=0.5.$ На этих KP напряжение $\hat{\sigma}$ уже не является наибольшим, ибо из-за высокой скорости деформирования на начальной стадии с $t_0/\tau = 0.1; 1; 3; 5; 7$ (в 5 раз выше, чем на Рис. 13(a,b)) структурированность успевает значительно упасть (Рис. 13(d)).

При фиксированной длительности начальной стадии семейство КР $\sigma(t;\bar{\varepsilon},t_0;w_0)$ может немонотонно зависеть от уровня деформации $\bar{\varepsilon}$ (что невозможно для линейного ОС (1)) и кривые с большим $\bar{\varepsilon}$ могут нырять ниже из-за заметного падения структурированности на начальной стадии и вызванного им увеличения скорости релаксации.

Диаграммы деформирования со скачками скорости деформации или нагружения

Исследуется влияние скачка скорости деформирования в некоторый момент времени на ДД $\sigma = \sigma(\varepsilon, a)$ в испытаниях из двух стадий с разными скоростями:

$$\varepsilon(t) = a_1 t \text{ при } t \in [0; t_1], \ \varepsilon(t) = a_2 (t - t_1) + a_1 t_1 \text{ при } t > t_1.$$
 (10)

По ним строятся семейства откликов $\sigma=\sigma(t;a_1,t_1,a_2)$ и ДД $\sigma=\sigma(\varepsilon,a_1,a_2)$ при разных скоростях деформирования и сопоставляются с ДД $\sigma=\sigma(t,a_1)$ и $\sigma=\sigma(t,a_2)$ (см. Рис. 14(а) для титанового сплава ВТ-6 при температуре 900 °C из [116]). Такие испытания используются при исследовании металлов и сплавов в состоянии сверхпластичности [88,116–118], но они вполне информативны и для деформативных полимеров с высокой скоростной чувствительностью и КМ на их основе (и для гелей и расплавов полимеров в испытаниях на сдвиг): в них по зависимости величины скачка напряжения в момент t_1 от скачка скорости a_2-a_1 и от скорости затухания памяти о первой стадии нагружения можно определить величину показателя скоростной чувствительности материала [88], особенности зависимости напряжения течения от скорости и другие характеристики материала. На Рис. 14(b) приведены ДД $\sigma=\sigma(t;a_1,t_1,a_2)$, порождаемые четырехзвенной линейной моделью вязкоупругости с

функцией релаксации $R(t) = A_1 e^{-t/\tau_1} + A_2 e^{-t/\tau_2}$, т.е параллельным соединением двух моделей Максвелла с временами релаксации $\tau_1 = 1$, $\tau_2 = 10$, при нагружении (10) с $t_1 = 5$; 10; 15, $a_1 = 1$ (кривая 1 - ДД $\sigma = \sigma(t, a_1)$) и $a_2 = 0.5$; 0.1; 0.01 (ДД $\sigma = \sigma(t, a_2)$ — штриховые черные кривые 2-4, все они обладают горизонтальными асимптотами $\sigma = a_2(A_1\tau_1 + A_2\tau_2)$); ДД $\sigma = \sigma(\varepsilon, a_1, a_2)$ может иметь точку экстремума в интервале $\varepsilon > \varepsilon_1$, если $\tau_1 \ln 2 < t_1 < \tau_2 \ln 2$ (это иллюстрируют голубые ДД, соответствующие $t_1 = 1$; 3; 5; 6.5). Но нырок под ДД $\sigma = \sigma(\varepsilon, a_2)$ (как на Рис. 14(a)) линейное ОС (1) не моделирует. Однако его способно моделировать ОС, учитывающее эволюцию структуры при деформировании [11,12].

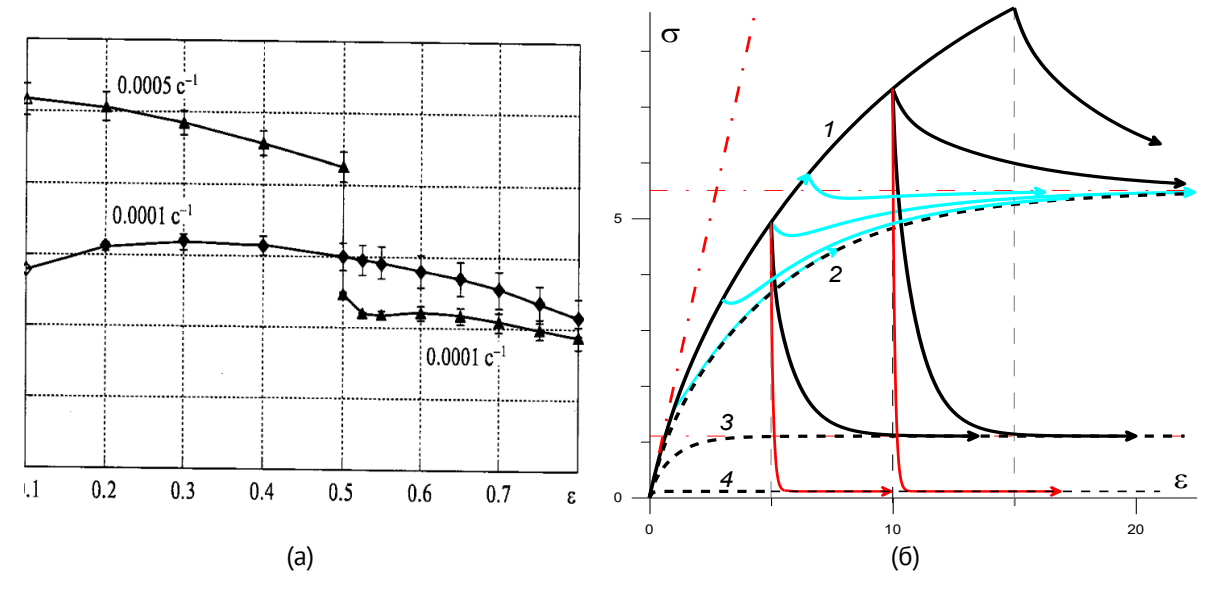


Рис. 14. ДД $\sigma = \sigma(t; a_1, t_1, a_2)$ со скачком скорости деформирования: (а) ДД титанового сплава ВТ-6 при температуре 900 °C [116]; (b) ДД порождаемые параллельным соединением двух линейных моделей Максвелла с временами релаксации $\tau_1 = 1, \tau_2 = 10$

Fig. 14. Stress-strain curves $\sigma = \sigma(t; a_1, t_1, a_2)$ with a jump in strain rate: (a) stress-strain curves of the VT-6 titanium alloy at temperature of 900 °C; (b) stress-strain curves generated by a parallel connection of two linear Maxwell models with relaxation times $\tau_1 = 1$, $\tau_2 = 10$

Ползучесть при ступенчатых нагружениях

Исследуются отклики материала или ОС на процессы нагружения с произвольным количеством ступеней при одноосным и неодносном нагружениях, эффекты при неполной разгрузке, при перестановке ступеней нагружения, скачки деформации при догрузке и разгрузке, наличие экстремумов деформации на отдельных ступенях, асимптотика, затухание памяти [1–4,8,89,91,92,115,119,120]. Испытания на ползучесть (при растяжении-сжатии, сдвиге, сложном НДС) при ступенчатых нагружениях позволяют уловить и обследовать разные аспекты поведения материала и детали реализации многих эффектов собрать более богатую информацию для выбора, идентификации и верификации определяющих соотношений по сравнению с КП при постоянном напряжении (такие КП все модели описывают адекватно при правильной настройке). В частности, они позволяют обнаружить признаки нелинейности в поведении материала, исследовать зависимость кривых ползучести от уровня напряжения и предыстории нагружения [1–4,8,89,91,92,115,119,120], восстановление и остаточную деформацию при полной и частичной разгрузке [4,8], влияние перестановки ступеней

нагружения [119] скорость затухания памяти, эффекты, сопровождающие скачок напряжения вниз или его быстрое убывание за малый промежуток времени (dip tests, non-monotonic creep behavior) [4,89,115], влияние скачков напряжения на длительную прочность и отклонение от правила линейного суммирования повреждённости (Miner's rule, linear damage rule, cumulative damage theory) [120].

Эффекты при циклических нагружениях с разной формой, амплитудой и коэффициентом асимметрии цикла

При мягких периодических нагружениях (когда задается программа по напряжению) исследуются накопление остаточной деформации, возрастание или убывание (возможно, стремление к нулю) скорости ее накопления с увеличением числа циклов, склонность к рэтчетингу или приспособлению материала (в зависимости от температуры); строятся кривые малоциклового нагружения при разных параметрах циклов [4,6,89,92,115].

На Рис. 15(а) приведены КП для мягкого *отнулевого* ступенчатого циклического нагружения с полуциклом T=5 и размахом $\bar{\sigma}=1$, порождаемые четырьмя линейными моделями (1) с разными ФП: 1) модели со степенной ФП с показателем n=0.5 (чёрная КП); 2) модели Бюргерса (2) с $\lambda=0.1$ (время ретардации $\tau=1/\lambda=10$), $\alpha=0.001$, $\beta=0.015$, $\gamma=0.01$ (голубая КП); 3) модели Фойгта (2) с $\lambda=0.1$, $\alpha=0$, $\beta=\gamma=0.01$ (красная КП); 4) модели Максвелла (синяя КП) с $\Pi=\alpha t+\beta$, $\alpha=0.001$,

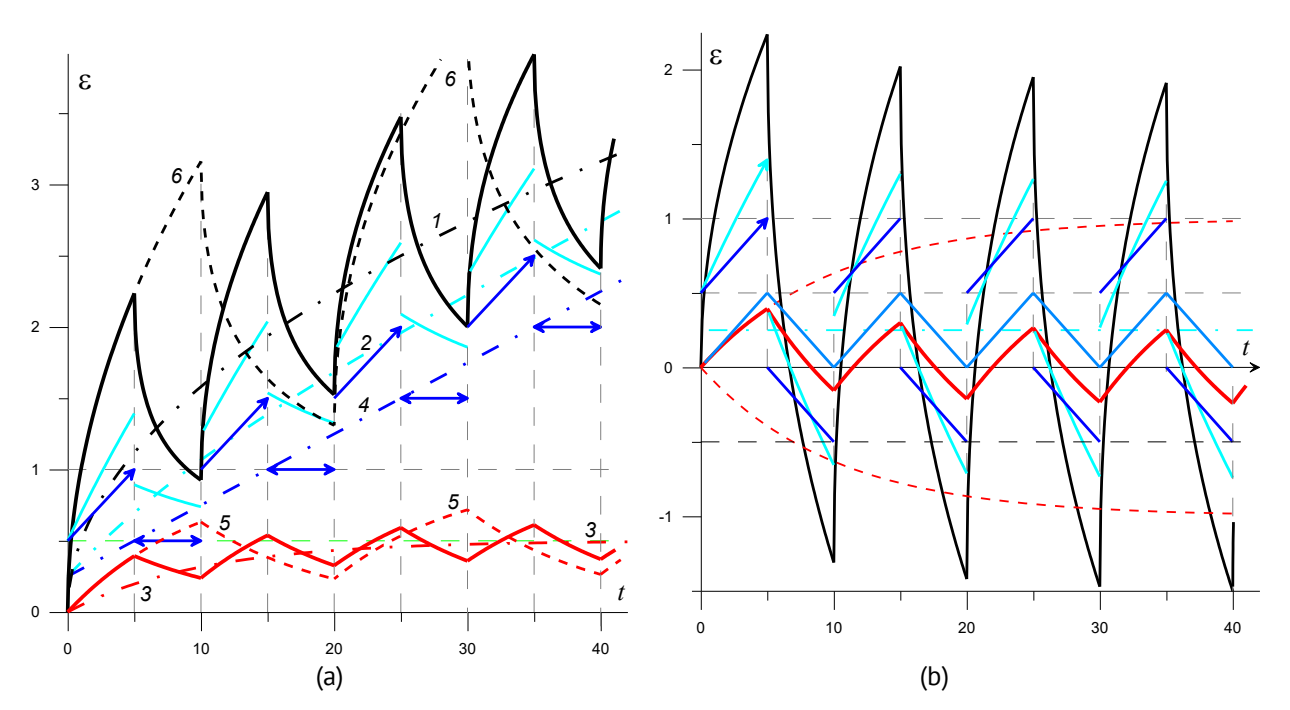


Рис. 15. Кривые циклического нагружения, порожденные пятью линейными моделями (1) со степенной ФП (чёрные КП) и ФП вида (2) (красные кривые – модели Фойгта , синие – модели Максвелла, голубые – модели Бюргерса): (а) для отнулевого ступенчатого цикла с отдыхом ($t_i=iT,\,T=5,\,\sigma_{2k-1}=\bar{\sigma},\,\sigma_{2k}=0$), (b) для симметричного ступенчатого цикла ($\sigma_{2k-1}=\bar{\sigma},\,\sigma_{2k}=-\bar{\sigma}$)

Fig. 15. Cyclic loading curves generated by five linear models (1) with the power-law creep function (black curves) and the creep functions of the form (2) (red curves – the Voigt model, blue curves – the Maxwell models, cyan curves – the Burgers models): (a) for a zero-to-tension step cycle with a relaxation period ($t_i = iT$, T = 5, $\sigma_{2k-1} = \bar{\sigma}$, $\sigma_{2k} = 0$); (b) for a symmetric step cycle ($\sigma_{2k-1} = \bar{\sigma}$, $\sigma_{2k} = -\bar{\sigma}$)

 $\beta=0.005$ (время релаксации $\tau=\beta/\alpha=5$) [89]. Модели Бюргерса и Максвелла регулярны ($\Pi(0)\neq 0$), и потому их КП имеют в точках t=kT разрывы со скачками $\pm \bar{\sigma}\Pi(0)$; свойство v>0 вызывает накопление пластической деформации [4,89]. У модели Фойгта и степенной модели v=0 и $\Pi(0)=0$, и потому КП непрерывны при всех t>0. Штрих-пунктирные кривые 1-4 – обычные КП этих моделей при постоянном напряжении $\sigma=0.5\bar{\sigma}$ (среднем за цикл), при достаточно больших t КП моделей Максвелла и Бюргерса, имеющие наклонную асимптоту $\varepsilon=\alpha t+\beta$ лежат не ниже, а выше степенной КП $t=0.5\bar{\sigma}$ 0. Для модели Фойгта и степенной модели дополнительно приведены КП с удвоенной длительностью цикла, т.е. $t=0.5\bar{\sigma}$ 0 (штриховые кривые $t=0.5\bar{\sigma}$ 0).

На Рис. 15(b) приведены КП тех же пяти линейных моделей (1), что и на Рис. 15(a), но для *симметричного* циклического ступенчатого нагружения, состоящего из одинаковых прямоугольных полуциклов растяжения и сжатия длительности T и амплитуды $\bar{\sigma}$. Все КП ограничены на луче $t \geq 0$, у всех КП участки возрастания и убывания чередуются, а последовательности максимальных и минимальных деформаций циклов $\{M_i\}$ и $\{m_i\}$ убывают, ограничены и имеют пределы, средняя деформация $\varepsilon_i = 0.5(M_i + m_i)$ убывает и $\varepsilon_i \to 0.5\bar{\sigma}v$ при $i \to \infty$ [91]. Штрихпунктирные красные кривые – обычные КП модели Фойгта при $\bar{\sigma} = \pm 1$ (при достаточно больших временах максимальные деформации M_i и $|m_i|$ при циклическом нагружении в 4 раза меньше, чем предельные деформации ползучести при $\bar{\sigma} = \pm 1$).

Проявления физической нелинейности в поведении материала

С увеличением деформаций (напряжений) и амплитуд циклических нагрузок поведение материалов все ярче проявляет неупругость и геометрическую и физическую и нелинейности, в частности зависимость от вида напряженно-деформированного состояния, структурные изменения и их влияние на термомеханические свойства материала. Изменение объема при нагружении, развитие разных видов дефектов и другие изменения структуры, объемная ползучесть и релаксация, влияние среднего напряжения (гидростатического давления) и его истории на осевые и сдвиговые деформации и связанные с ними термомеханические эффекты становятся все более существенными при описании деформирования, прочности и разрушения материалов [92]. Основные эффекты и признаки нелинейности обсуждались выше, а подробнее – в статьях [1–13,87–92,114,115,119,120].

Прежде всего следует изучать характер нелинейности зависимостей семейств кривых ползучести и релаксации от уровней нагрузки и деформации, а семейств диаграмм деформирования $\eta \geq 0$ и $\sigma = \sigma(\varepsilon, b)$ от скорости деформирования или нагружения [1-13,87-90,92,114]. Нередко случается, что нелинейности поведения материла приписывают эффекты, адекватно описываемые в рамках линейной теории, вытекающие лишь из наличия наследственности и присущие всем (почти всем) линейно вязкоупругим материалам (при достаточно малых деформациях и скоростях) [92]. Точное знание арсенала возможностей и границ области применимости линейного OC вязкоупругости (1) и имманентных порождаемых ею базовых теоретических кривых, вытекающих из постулатов наследственности, линейности и инвариантности относительно сдвигов по времени интегральных операторов (1), связывающих истории напряжений и деформаций,

необходимо для грамотного моделирования, для выбора или построения более сложных и точных моделей поведения реономных материалов, использующих линейную теорию вязкоупругости и обобщающих ее в определённых аспектах, для их идентификации, аттестации и сопоставления, и, в целом, – для совершенствования расчётных схем и методов расчёта конструкций.

Например, криволинейность диаграмм деформирования C постоянными скоростями $\sigma(\varepsilon,a)$ и $\sigma(\varepsilon,b)$ свидетельствует лишь о том, что материал не ведет себя линейно упруго, и еще не говорит о физической нелинейности: линейно вязкоупругие материалы имеют непрямолинейные диаграммы деформирования (Рис. 5), зависящие от скорости. Нельзя использовать линейное ОС вязкоупругости (1) в том случае, когда экспериментальные ДД $\sigma(\varepsilon,a)$ и $\sigma(\varepsilon,b)$ или кривые ползучести имеют точки перегиба и участки выпуклости вниз (Рис. 6 и 9), поскольку линейное ОС (1) при любой скорости нагружения порождает возрастающие выпуклые вверх и ДД $\sigma(\varepsilon,a)$ и $\sigma(\varepsilon,b)$ [88,90] (Рис. 5) и при любом уровне деформации – выпуклые вверх кривые ползучести [4,89]. Еще один пример индикатора нелинейности: немонотонность зависимости семейства экспериментальных КР материала $\sigma(t; \bar{\epsilon}, t_0)$ при гатр-нагружении (9) от параметров t_0 и $\bar{\varepsilon}$ (при фиксированном t): ведь семейство КР $\sigma(t;\bar{\varepsilon},t_0)$, порождаемое линейным ОС (1) монотонно по t_0 и $\bar{\varepsilon}$ [87]. Нелинейное ОС Работнова (3) [7] или ОС, учитывающее эволюцию структуры [12], способны моделировать как монотонную, так и немонотонную зависимость семейства КР $\sigma(t; \bar{\varepsilon}, t_0)$ от t_0 и $\bar{\varepsilon}$. Другие индикаторы (не)применимости линейного ОС (1) разобраны выше и в статьях [1-13,87-92,114,115,119,120].

Мониторинг и анализ изменения поперечной и объемной деформации образцов

В процессе всех указанных выше изотермических испытаний на растяжение-сжатие изучаются наличие объемной ползучести, пластического разрыхления, поврежденности и структурных изменений, зависимость их морфологии и количественных мер от уровня температуры, эволюция коэффициента поперечной деформации со временем и в зависимости от программы нагружения, его (не)монотонность и возможность смены знака [90,121]. Наличие объемной деформации в испытаниях на сдвиг свидетельствует о том, что объемные деформации и деформации формоизменения не независимы и нельзя использовать ОС, в которых шаровые части и девиаторы тензоров напряжений и деформаций разделяются и связаны независимыми уравнениями.

Экспериментальное и теоретическое исследование особенностей поведения материалов при неодноосных нагружениях

В частности, исследование возможностей по моделированию влияния объемной ползучести и гидростатического давления и его скачков на механическое поведение (на кривые испытаний и эффективные свойства) КМ и способности разных версий ОС описывать влияние вида напряженно-деформированного состояния, в частности дилатацию и разносопротивляемость растяжению-сжатию при ползучести и других видах нагружения. Анализ пределов применимости постулатов о независимости объемной деформации от касательных напряжений (от девиатора тензора напряжений), а сдвиговых деформаций – от среднего напряжения (давления), об упругой связи между объемной деформацией и средним напряжением в точке (т.е.

пренебрежения объемной ползучестью), постулата о постоянстве коэффициента Пуассона и постулата о несжимаемости материала в зависимости от диапазонов температур и нагрузок. Конечно, исследования анизотропии и поведения полимеров и КМ при неодноосных нагружениях требуют гораздо более обширного списка программ испытаний, чем одноосные программы предыдущих пунктов, с которых следует начинать исследование, но это темы последующих работ.

Самые информативные испытания на начальном этапе исследований и диагностика типа поведения материала

На начальном этапе исследований по проектированию и отработке программ испытаний, методик регистрации данных испытаний и их обработки можно ограничиться только сериями испытаний 3.1-3.5 по программам $\varepsilon(t)=at$ и (7), (8) (Рис. 7). Каждая из них требует проведения, как минимум, 5-7 испытаний при разных параметрах программ нагружения (их количество надо умножить на $3\div 5$ повторных испытаний для осреднения и оценки разброса). Если нужны свойства при разных температурах, то потребуется 15-30 испытаний при разных параметрах программ нагружения. Например, испытания на ползучесть следует проводить при 3-4 значениях температуры (на первом этапе –лишь при комнатной температуре) и при 4-5 уровнях напряжения (не выше 0.5...0.7 предела прочности при максимальной температуре). При этом длительность испытания T (еще один важный параметр) должна быть достаточно большой, чтобы все особенности развития ползучести проявились на кривых ползучести. В испытаниях на восстановление при нулевой нагрузке (8) появляется еще один параметр нагружения — длительность стадии восстановления (или ее отношение к длительность стадии ползучести под нагрузкой T).

Одна из самых информативных программ испытаний (серия 3.3) – нагружение с последующей полной разгрузкой и наблюдением восстановления при нулевой нагрузке (7) для и построения кривой нагружения-разгрузки-восстановления (отклика образца на нагружение (7)) – см. Рис. 8 и детально – в [6,114].

На Рис. 16 приведены отклики ОС, учитывающего взаимное влияние эволюции структуры и процесса деформирования [11,12,115], с временем релаксации $\tau = \eta_0/G_0 = 1$ и МФ $g = e^{7s}$ на программу нагружения-разгрузки-восстановления (7) с фиксированным $t_1 = 2$, разными максимальными напряжениями $s_i = 3; 4; 5; 6$ и скоростями нагружения $b_i = s_i/t_1$ (кривые 3,4,5,6) для начальных значений структурированности $w_0 = 0$; 0.5; 1 (голубые, синие и красные кривые 3′,4′,5′,6′). На Рис. 16(a,b) – графики деформации $\gamma(t;t_1,b_i)$ и структурированности $w(t;t_1,b_i)$, на Рис. 16(c) – кривые нагружения-разгрузки-восстановления (КНР) $\sigma(\gamma; t_1, b_i)$. Очевидно, формы КНР, порожденных ОС учитывающего взаимное влияние эволюцииструктуры и нелинейного ОС типа Маквелла (Рис. 7(c,d)), сходны (и качественно похожи на КНР ПТФЭ, приведенные на (Рис. 7(a,b)), но с ростом напряжения может произойти обвал структурированности (кривые 5,6 и 5',6' на Рис. 16(b)), вызывающий "изломы" на кривых нагружения (кривые 5,6 и 5',6' на Рис. 16(с) похожи на двухзвенные ломаные, привычные в моделях упругопластичности с упрочнением) и усиливающий эффект возрастания деформации на стадии разгрузки. На кривых 3,4 и 3',4' (для малых напряжений) на Рис. 16(a,c) этих эффектов еще нет, хотя немонотонность w(t) появляется уже при $s_i = 4$ (Рис. 16(b)). На Рис. 16(d) приведены КНР для s = 3, но для начальных значений структурированности $w_0 = 0; 0.1; 0.3; 0.5; 0.7; 1$, показывающие, как с ростом w_0 выпуклость вниз кривой нагружения меняется на выпуклость вверх, как убывает деформация (для малого напряжения w(t) монотонно возрастает при всех w_0 – см. кривые s_0 и s_0 на Рис. 16(b)) и как уменьшается площадь "петли" под КНР, равная удельной диссипации энергии в точке, и остаточная деформация после полной разгрузки.

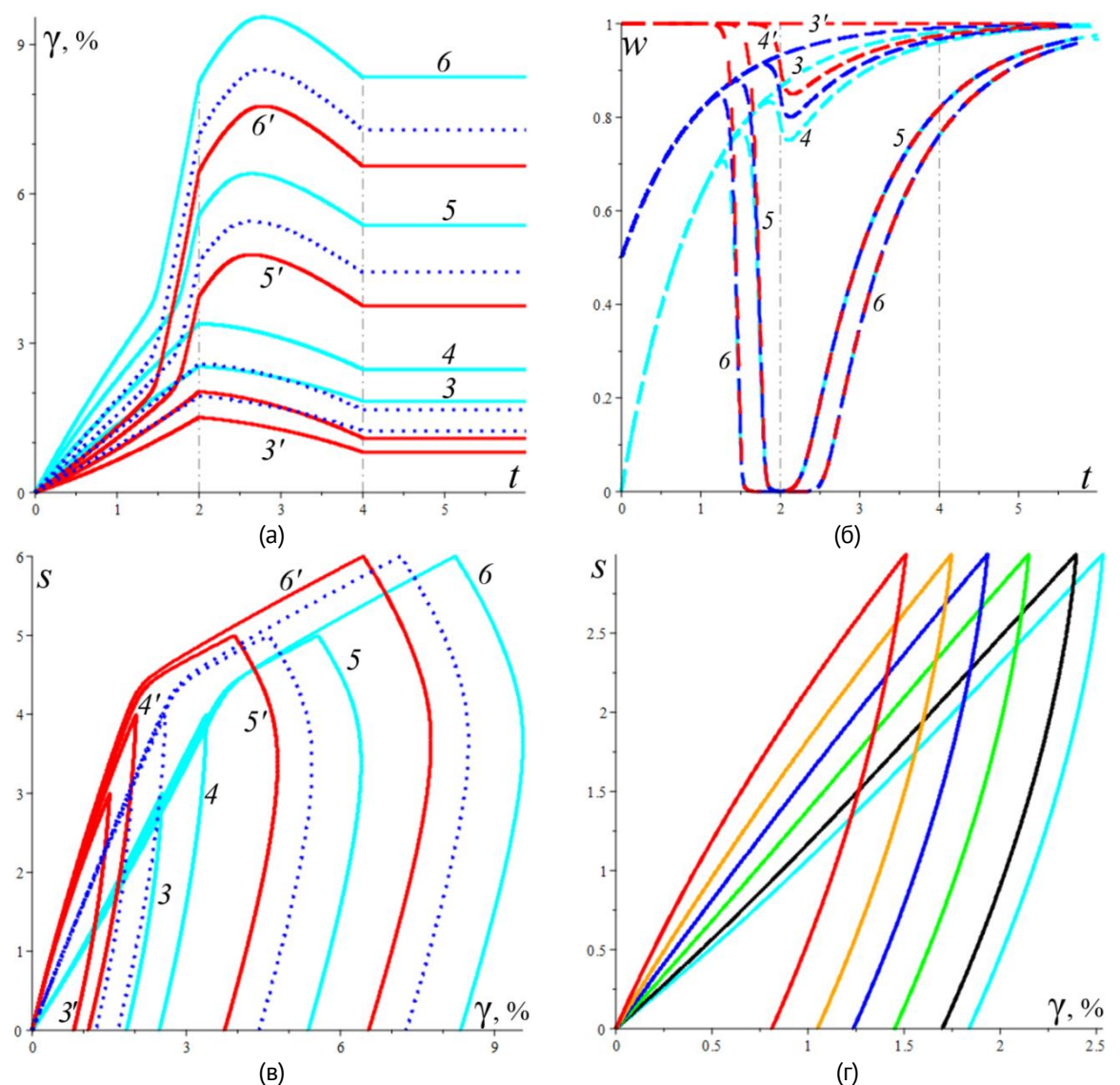


Рис. 16. Отклики ОС, учитывающего взаимное влияние эволюции структуры и процесса деформирования, с временем релаксации $\tau=1$ на программу нагружения-разгрузки-восстановления (7) с $t_1=2$ и разными максимальными напряжениями $s_i=3;4;5;6$ (кривые 3,4,5,6) для разных начальных значений структурированности w_0 : (a-c) графики деформации $\gamma(t;t_1,b_i)$, структурированности $w(t;t_1,b_i)$ и кривые нагружения-разгрузки-восстановления $\sigma(\gamma;t_1,b_i)$ для $w_0=0;0.5;1$ (голубые, синие и красные кривые 3,4,5,6); (d) КНР $\gamma(t;t_1,b_i)$, для $w_0=0;0.1;0.3;0.5;0.7;1$ при максимальном напряжении s=3

Fig. 16. Responses of the constitutive equation that accounts for the mutual influence of deformation and structural evolution (with the relaxation time $\tau = 1$) to the loading-unloading-recovery program (7) with $t_1 = 2$ and different maximum stresses $s_i = 3; 4; 5; 6$ (curves 3, 4, 5, 6) for different initial structuredness values w_0 : (a-c) deformation graphs $\gamma(t; t_1, b_i)$, structuredness graphs $w(t; t_1, b_i)$ and loading-unloading-recovery curves $\sigma(\gamma; t_1, b_i)$ for $w_0 = 0; 0.5; 1$ (cyan, blue, and red curves 3', 4', 5', 6'); (d) loading-unloading-recovery curves $\sigma(\gamma; t_1, b_i)$ for $w_0 = 0; 0.1; 0.3; 0.5; 0.7; 1$ and maximum stress s = 3

С помощью испытаний вида (7) (лучше серии испытаний с разными максимальными напряжениями и скоростями нагружения и, возможно, при разных уровнях температуры, если требуется исследовать зависимость свойств от температуры) удобно провести предварительную диагностику типа поведения материала (в первом приближении), если характеризовать его категориями упругий, вязкоупругий, вязкопластичный, упруговязкопластичный:

- (1) если кривая разгрузки ложится на кривую нагрузки при достаточно низких скоростях деформирования (нет петли гистерезиса), то материал можно считать упругим (в исследованном диапазоне напряжений, деформаций, скоростей нагружения и температур);
- (2) если петля гистерезиса есть, но нет остаточной деформации (она достаточно быстро полностью исчезает после разгрузки, становится меньше допуска), то материал можно считать вязкоупругим;
- (3) если петля гистерезиса есть и сохраняется остаточная деформация (после полной разгрузки и длительной выдержки деформация стремится к ненулевой горизонтальной "асимптоте", восстановление "выдыхается"), то нельзя пренебрегать способностью материала накапливать необратимую деформацию и материал следует рассматривать как упруговязкопластичный (см. например, Рис. 8 и 16);
- (4) если выполняются условия п. 3, но кривая нагружения (и разгрузки) не зависит от скорости нагружения (в исследованном диапазоне скоростей и температур), а остаточная деформация практически не релаксирует (восстановление заканчивается за малое время, например, равное длительности стадии нагружения-разгрузки, и далее деформация не меняется с течением времени), то материал можно считать упругопластичным.

Усложнение программы испытаний (7) введением дополнительной стадии выдержки при постоянной ненулевой нагрузке (после первой стадии нагрузки, перед стадией разгрузки) весьма полезно для уточнения "диагноза": если на этой стадии наблюдается рост деформации (ползучесть), то материал можно квалифицировать как упруговязкопластичный или вязкоупругий, а если деформация постоянна, то – как упругий или упругопластичный (различие между ними будет заметно на стадии разгрузки, как было описано выше).

В принципе для такого экспресс-анализа типа поведения материала можно провести серию испытаний на обратную ползучесть, т.е. нагружение прямоугольным ипмпульсом напряжения, быструю ("мгновенную") разгрузку и последующую выдержку при нулевой (или почти нулевой) нагрузке. Но по сути испытания будут проводиться по той же программе нагружения, имеющей очертание трапеции, но нагрузка и разгрузка будут считаться "мгновенными" (это упрощение, схематизация программы нагружения при обработке результатов испытаний).

В сущности, перечисленные качественные свойства можно рассматривать как первичные индикаторы для *предварительного выбора класса ОС*, которые стоит использовать для описания поведения материала [92]. Этих грубых свойств не достаточно для выбора конкретного ОС и необходимы привлечение данных дополнительных испытаний и учет более тонких эффектов поведения материала, проявляющихся как при нагружениях (7), так и при других программах испытаний (при циклических нагружениях, при ступенчатой ползучести и т.п.).

Лучше не только провести испытания по программе (7) на сжатие, растяжение и сдвиг (многие материалы обладают разносопротивляемостью, выражающейся не только в разномодульности, но и разном виде кривых ползучести и деформирования при растяжении и сжатии), но и провести испытания еще и по программе, дополненной таким же циклом с изменением знака нагрузки, причем в двух версиях: сначала растяжение – потом сжатие и наоборот. Это естественные подход к программам циклического нагружения (серия испытаний 11 из списка п. 3) с симметричным циклом и с отнулевым циклом (Рис. 15); последние в ряде случаев удобно или целесообразно проводить по схеме трехточечного изгиба [122–127].

Заключение

Статья посвящена комплексному экспериментальному изучению вязкоупругопластических свойств политетрафторэтилена и нескольких семейств композитов (КМ) с повышенной (в 2000 раз) износостойкостью на его основе, полученных в последние годы в лабораториях Института естественных наук СВФУ им. M.K. Аммосова введением В качестве наполнителей слоистых силикатов (механоактивированные вермикулит, каолинит, серпентин, бентонит), шпинели магния и коротких базальтовых или углеродных волокон. Приведены описание технологии изготовления композитов и основные результаты работ по исследованию структуры и химического состава поверхности трения методами электронной микроскопии и ИКспектроскопии и повышению износостойкости этих материалов за счет образования пленки переноса и вторичных структур в результате трибоокислительных процессов. Описаны цели и система программ квазистатических испытаний полимеров и композитов для всестороннего изучения их вязкоупругопластических свойств (совокупности всех наблюдаемых в испытаниях эффектов), возможности нескольких физически нелинейных определяющих соотношений вязкоупругопластичности (одно из которых учитывает взаимное влияние эволюции структуры и процесса деформирования) по их описанию и методология анализа данных испытаний и выбора адекватных определяющих соотношений для их моделирования. В частности, рассмотрены признаки физической нелинейности поведения материалов, т.е. индикаторы неприменимости линейного интегрального соотношения вязкоупругости Больцмана-Вольтерры, которые можно обнаружить в испытаниях по разным программам нагружения, способы очертить диапазон линейности поведения вязкоупругого материала. Описаны испытания для предварительной диагностики типа поведения материала (в первом приближении), если вязкоупругий, характеризовать его категориями упругий, вязкопластичный, упруговязкопластичный, и методология выбора адекватной модели для описания поведения конкретного материала.

Во второй части статьи будут приведен и проанализирован большой объем данных испытаний на растяжение по разным программам образцов-лопаток из чистого ПТФЭ и шести КМ на его основе с наполнением серпентином или серпентином и шпинелью магния (до 5 % по массе): полученные семейства диаграмм растяжения $\sigma(\varepsilon,a)$ с разными скоростями до разрушения, кривых нагружения-разгрузки-восстановления $\varepsilon(t;t_1,b_i)$ и $\sigma(\varepsilon;t_1,b_i)$ с разными скоростями и длительностями стадии нагружения и кривых ползучести и восстановления $\varepsilon(t;\bar{\sigma},T)$ для разных уровней постоянной нагрузки и

длительностей ее приложения. Будет проведен первичный анализ выраженности наследственных свойств материалов, в частности скоростной чувствительности, способности к течению при постоянном напряжении, ресурса деформативности и способности к восстановлению после разгрузки, и влияние на них состава и доли наполнителей. Будут определены базовые скалярные характеристики материалов: мгновенный модуль, предел текучести, напряжение и деформация при разрыве в зависимости от скорости нагружения и др. Будут приведены результаты исследования на сканирующем электронном микроскопе изменений микроструктуры испытанных образцов ПТФЭ и композитов с разным содержанием наполнителей в зонах разрушения образцов (по сравнению с исходной структурой). Будет исследовано влияние малых долей наполнителей на структуру и многие вязкоупругопластические свойства материалов.

Авторский вклад

Владимирович Хохлов ОSC **S**: разработка концепции, Андрей проведение исследования, курирование данных, написание рукописи и редактирование, научное руководство; Айталина Алексеевна Охлопкова (разработка концепции, Афанасьевна Слепцова ^{© SC®}: Сардана руководство; разработка научное концепции; Надежда Николаевна Лазарева (с проведение исследования, Прасковья Николаевна Тарасова **^{®SC}**: курирование данных; исследования; Арсений Владимирович Бабайцев (проведение исследования; Шапорев 😎 : проведение Валерьевич исследования;

CRediT authorship contribution statement

Andrew V. Khokhlov conceptualization, investigation, data curation, writing – original draft & editing, supervision; Aitalina A. Okhlopkova conceptualization, supervision; Sardana A. Sleptsova conceptualization; Nadezhda N. Lazareva conceptualization; investigation; Arseny V. Babaytsev conceptualization; Artemii V. Shaporev conceptualization; Nadezhda N. Lazareva conceptualization; investigation; Arseny V. Babaytsev conceptualization; Artemii V. Shaporev conceptualization; investigation; Arseny V. Babaytsev conceptualization; Investigation; Artemii V. Shaporev conceptualization; Investigation; Arseny V. Gulin conceptualization; Investigation; Investigatio

Конфликт интересов

Авторы заявляют об отсутствии конфликта интересов.

Conflict of interest

The authors declare that they have no conflict of interest.

Литература / References

- 1. Khokhlov AV. Constitutive relation for rheological processes: Properties of theoretic creep curves and simulation of memory decay. *Mechanics of Solids*. 2007;42(2): 291–306.
- 2. Khokhlov AV. Fracture criteria under creep with strain history taken into account, and long-term strength modeling. *Mechanics of Solids*. 2009;44(4): 596–607.

- 3. Хохлов АВ. Нелинейная модель вязкоупругопластичности типа Максвелла: моделирование влияния температуры на кривые деформирования, релаксации и ползучести. Вестик Самарского гос. техн. унта. Сер. физ.-мат. науки. 2017;21(1): 160–179. (Khokhlov AV. The nonlinear Maxwell-type model for viscoelastoplastic materials: Simulation of temperature influence on creep, relaxation and strain-stress curves. J. Samara State Tech. Univ., Ser. Phys. Math. Sci. 2017;21(1): 160–179. (In Russian))
- 4. Khokhlov AV. Comparative analysis of properties of stress relaxation curves and creep curves under multi-step loadings generated by the Rabotnov quasi-linear relation and the Boltzmann-Volterra linear viscoelasticity relation. *Composites and Nanostructures*. 2024;16(1): 20–55. (In Russian)
- 5. Хохлов АВ. Идентификация нелинейной модели упруговязкопластичности типа Максвелла по кривым ползучести с начальной стадией нагружения. Часть 2. Методики. *Деформация и разрушение материалов*. 2017;10:
- 2–9. (Khokhlov AV. Identification methods of Maxwell-type nonlinear viscoelastoplastic model, based on creep curves with initial ramp loading. Part II. Methods. *Deformatsiya I razrushenie materialov*. 2017;(10): 2–9. (In Russian))
- 6. Khokhlov AV. Applicability indicators and identification techniques for a nonlinear Maxwell-type elastoviscoplastic model using loading-unloading curves. *Mechanics of Composite Materials*. 2019;55(2): 195–210.
- 7. Khokhlov AV. Analysis of Properties of Ramp Stress Relaxation Curves Produced by the Rabotnov Nonlinear Hereditary Theory. *Mechanics of Composite Materials*. 2018;54(4): 473–486.
- 8. Хохлов АВ. Индикаторы применимости и методики идентификации нелинейной модели типа Максвелла для реономных материалов по кривым ползучести при ступенчатых нагружениях. *Вестник МГТУ им. Н.Э. Баумана. Сер. Естественные науки.* 2018;6: 92–112. (Khokhlov AV. Applicability Indicators and Identification Techniques for a Nonlinear Maxwell-Type Elasto-Viscoplastic Model using Multi-Step Creep Curves. *Herald of the Bauman Moscow State Technical University. Natural Sciences.* 2018;(6): 92–112. (In Russian))
- 9. Khokhlov AV. Properties of the Set of Strain Diagrams Produced by Rabotnov Nonlinear Equation for Rheonomous Materials. *Mechanics of Solids*. 2019;54(3): 384–399.
- 10. Khokhlov AV. Generalization of a nonlinear Maxwell-type viscoelastoplastic model and the simulation of creep recovery curves. *Mechanics of Composite Materials*. 2023;59(3): 441–454.
- 11. Khokhlov AV, Gulin VV. Analysis of the Properties of a Nonlinear Model for Shear Flow of Thixotropic Media Taking into Account the Mutual Influence of Structural Evolution and Deformation. *Phys Mesomech.* 2023;26: 621–642.
- 12. Khokhlov AV, Gulin VV. Families of stress-strain, relaxation, and creep curves generated by a nonlinear model for thixotropic viscoelastic-plastic media accounting for structure evolution. Part 2. Relaxation and stress-strain curves. *Mechanics of Composite Materials*. 2024;60(2): 259–278.
- 13. Khokhlov AV. Hybrid of a nonlinear Maxwell-type viscoelastoplastic model with the linear viscoelasticity constitutive equation and properties of crossbred creep and stress-strain curves. *Materials Physics and Mechanics*. 2024;52(4): 114–140.
- 14. Черский ИН. *Полимерные материалы в современной уплотнительной технике*. Якутск: Якутское книжное изд-во, 1975. (Cherskiy IN. Polymer materials in modern sealing technology. Yakutsk: Yakutskoeknizhnoeizdatel'stvo; 1975. (In Russian))
- 15. Уолл Л. Фторполимеры. Москва: Мир; 1975. (Wall LA. Fluoropolymers. Moscow: Mir; 1975. (In Russian)
- 16. Паншин ЮА, Малкевич СГ, Дунаевская ЦС. *Фторопласты*. Ленинград: Химия; 1978. (Panshin YuA, Malkevich SG, Dunaevskaya CS. *Fluoroplastics*. Leningrad: Himiya; 1978. (In Russian))
- 17. Истомин НП, Семенов АП. Антифрикционные свойства композиционных материалов на основе фторполимеров. Москва: Наука; 1981. (Istomin NP, Semenov AP. Antifriction properties of composite materials based on fluoropolymers. Moscow: Nauka; 1981. (In Russian))
- 18. Пугачев АК, Росляков ОА. *Переработка фторопластов в изделия*. Ленинград: Химия; 1987. (Pugachev AK, Roslyakov OA. *Processing of fluoroplastic into products*. Leningrad: Himiya; 1987. (In Russian)) 19. Булманис ВН. *Рекомендации по применению фторопластовых композитов для уплотнительных устройств*. Якутск: ЯФ СО АН СССР; 1988. (Bulmanis VN. *Recommendations for the use of fluoroplastic*
- 20. Машков ЮК, Полещенко КН, Поворознюк СН, Орлов ПВ. *Трение и модифицирование материалов трибосистем*. Москва: Наука; 2000. (Mashkov YuK, Poleschenko KN, Povoroznyuk SN, Orlov PV. *Friction and modification of tribosystem materials*. Moscow: Nauka; 2000. (In Russian))

composites for sealing devices. Yakutsk: YaF SO AN SSSR; 1988. (In Russian))

- 21. Хрулев ВМ. Полимерсиликатные композиции в строительстве. УФА: ТАУ; 2002. (Hrulev VM. Polymer silicate compositions in construction. Ufa: TAU; 2002. (In Russian))
- 22. Машков ЮК, Овчар ЗН, Суриков ВИ, Калистратова ЛФ. *Композиционные материалы на основе политетрафторэтилена*. Москва: Машиностроение; 2005. (Mashkov YuK, Ovchar ZN, Surikov VI, Kalistratova LF. *Composite materials based on polytetrafluoroethylene*. Moscow: Mashinostroeniye; 2005. (In Russian))
- 23. Бузник ВМ, Фомин ВМ, Алхимов АП, Игнатьева ЛН. Металлополимерные нанокомпозиты.

Новосибирск: Изд-во СО РАН; 2005. (Buznik VM, Fomin VM, Alhimov AP, Ignat'eva LN. *Metal-polymer nanocomposites*. Novosibirsk: Izdatel'stvo SO RAN; 2005. (In Russian))

- 24. Михайлин ЮА. *Термоустойчивые полимеры и полимерные материалы*. СПб: Профессия; 2006. (MihajlinYuA. *Heat-resistant polymers and polymer materials*. Saint Petersburg: Professiya; 2006. (In Russian)) 25. Козлов ГВ, Заиков ГЕ, Стоянов ОВ, Кочнев АМ. *Дисперсно-наполненные полимерные нанокомпозиты*. Казань: КНИТУ; 2012. (Kozlov GV, Zaikov GE, Stoyanov OV, Kochnev AM. *Dispersion-filled polymer nanocomposites*. Kazan: KNITU; 2012. (In Russian)) 26. Авдейчик СВ. *Машиностроительные фторокомпозиты: структура, технология, применение*. Гродно; 2012. (Avdeychik SV. *Mechanical fluorocomposites: structure, technology, application*. Grodno: Grodnenskiy gosudarstvennyy universityet imeni Yanki Kupaly; 2012. (In Russian))
- 27. Логинов БА, Виллемсон АЛ, Бузник ВМ. *Российский фторполимеры: история, технологии, перспективы.* Москва: Гиицветмет; 2013. (Loginov BA, Villemson AL, Buznik VM. *Russian fluoropolymers: history, technology, prospects.* Moscow: Giicvetmet; 2013. (In Russian))
- 28. Stan F, Fetecau C. Study of stress relaxation in polyteyrafluoroethylene composites by cylindrical macroindentation. *Composites*. 2013;(47): 298–307.
- 29. Полуэктов ВЛ, Баронин ГС, Бузник ВМ, Худяков ВВ, Полуэктова СЛ. Упрочняющая твердофазная технология получения профилированных изделий из нанокомпозитов на основе Ф-4 с использованием интенсивной пластической деформации. Вестник Тамбовского университета. Серия: Естественные и технические науки. 2016;21(3): 1250–1254. (Poluektov VL, Baronin GS, Buznik VM, Hudyakov VV, Poluektova SL. Strengthening solid-phase technology for producing profiled products from nanocomposites based on F-4 using severe plastic deformation. Bulletin of Tambov University. Series: Natural and technical sciences. 2016;21(3): 1250–1254. (In Russian)) 30. Николаева ИП, Огородов ЛИ, Яковлева ЕЛ. Ползучесть модификаций политетрафторэтилена при различных режимах нагружения. Строительство уникальных зданий и сооружений. 2017;3(54): 7–17. (Nikolaeva IP, Ogorodov LI, Yakovleva EL. Creep of polytetrafluoroethylene modifications under various loading conditions. Construction of unique buildings and structures. 2017;54(3): 7–17. (In Russian))
- 31. Tanaka K, Kawakami S. Effect of various fillers on the friction and wear of polytetrafluoroethylene-based composites. *Wear.* 1982;79(2): 221–234.
- 32. Сиренко ГА. *Антифрикционные карбопластики*. Киев: Техника; 1985. (Sirenko GA. Anti-friction carboplastics. Kazan: Tekhnika; 1985. (In Russian))
- 33. Biswas SK, Vijayan K. Friction and wear of PTFE. *Wear.* 1992;158(1–2): 193–211.
- 34. Охлопкова АА. Физико-химические принципы создания триботехнических материалов на основе политетрафторэтилена и ультрадисперных керамик. Дисс. д-ра техн. наук. Гомель; 2000. (Okhlopkova AA. Physico-chemical principles of creating tribological materials based on polytetrafluoroethylene and ultradisperse ceramics. Gomel; 2000. (In Russian))
- 35. Суриков ВИ. Повышение эксплуатационных свойств композитов на основе политетрафторэтилена путем структурной многоуровневой модификации: дис. д-ра техн. наук. Омск; 2001. (Surikov VI. Improving the performance properties of polytetrafluoroethylene-based composites through multi-level structural modification. Omsk; 2001. (In Russian)) 36. Охлопкова АА, Адрианова ОА, Попов СН. Модификация полимеров ультрадисперсными соединениями. Якутск: Якутский филиал АН СО РАН; 2003. (Okhlopkova AA, Adrianova OA, Popov SN. Modification of polymers with ultrafine compounds. Yakutsk: Yakutskiy filial AN SO RAN; 2003. (In Russian)) 37. Friedrich K, Zhang Z, Schlarb A. Effects of various fillers on the sliding wear of polymer composites. Compos. Sci. Technol. 2005;65(15-16):2329–2343.
- 38. Shi Y, Feng X, Wang H, Lu X. Tribological properties of PTFE composites filled with surface-treated carbon fiber. *J. Mater. Sci.* 2007;42: 8465–8469.
- 39. Ignat'eva LN, Buznik VM. IR-spectroscopic examination of polytetrafluoroethylene and its modified forms. *Russ J Gen Chem.* 2009;79: 677–685.
- 40. Shi Y, Feng X, Wang H, Lu X. The effect of surface modification on the friction and wear behavior of carbon nanofiber-filled PTFE composites. *Wear.* 2008;264(11-12):934–939.
- 41. Ginzburg BM, Pozdnyakov AO, Tochil'nikov DG, Tuichiev S, Shepelevskii AA. Tribological characteristics of composites based on poly(tetrafluoroethylene) and fullerene carbon. *Polym. Sci. Ser. A.* 2008;50: 865–873.
- 42. Hatipov SA, Artamonov NA. A new antifriction and sealing material based on radiation-modified polytetrafluoroethylene. Russ *J Gen Chem.* 2009;79: 616–625.
- 43. Vail JR, Burris DL, Sawyer WG. Multifunctionality of single-walled carbon nanotube-polytetrafluoroethylene nanocomposites. *Wear.* 2009;267: 619–624.

- 44. Zhu J, Shi Y, Feng X, Wang H, Lu X. Prediction on tribological properties of carbon fiber and TiO2 synergistic reinforced polytetrafluoroethylene composites with artificial neural networks. *Materials & Design*. 2009;30(4): 1042–1049.
- 45. Машков ЮК, Кропотин ОВ. *Трибофизика и структурная модификация материалов трибосистем.* Омск, 2009. (MashkovYuK, Kropotin OV. *Tribophysics and structural modification of materials of tribosystems.* Omsk: Izdatel'stvo OmGTU; 2009. (In Russian))
- 46. Сытый ЮВ, Чурсова ЛВ, Хатипов СА, Сагамонова ВА. Свойства и применение радиационно-модифицированного фторопласта-4рм. *Авиационные материалы и технологии*. 2012;25(4): 48–55. (SytyjYuV, Chursova LV, Hatipov SA, Sagomonova VA. Properties and application of radiation-modified fluoroplastic F-4RM. *Aviation Materials and Technologies*. 2012;25(4): 48–55. (In Russian))
- 47. Chen B, Wang J, Yan F. Boston ivy-like clinging of dendritic polytetrafluoroethylene nano-ribbons to the surface of carbon fiber. *Composites Part A: Applied Science and Manufacturing*. 2012;43(7): 1028–1031.
- 48. Chen B, Wang J, Yan F. Synergism of carbon fiber and polyimide in polytetrafluoroethylene-based composites: Friction and wear behavior under sea water lubrication. *Materials & Design*. 2012;36: 366–371. 49. Ye J, Khare HS, Burris DL. Transfer film evolution and its role in promoting ultra-low wear of a PTFE nanocomposite. *Wear*. 2013;297(1-2): 1095–1102.
- 50. Wang J, Chen B, Liu N, Han G, Yan F. Combined effects of fiber/matrix interface and water absorption on the tribological behaviors of water-lubricated polytetrafluoroethylene-based composites reinforced with carbon and basalt fibers. *Composites Part A: Applied Science and Manufacturing.* 2014;59: 85–92.
- 51. Кропотин ОВ, Машков ЮК, Егорова ВА, Кургузова ОА. Влияние углеродных модификаторов на структуру и износостойкость полимерных нанокомпозитов на основе политетрафторэтилена. *Журнал Технической Физики*. 2014;84(5): 66–70. (Kropotin OV, MashkovYuK, Egorova VA, Kurguzova OA. The influence of carbon modifiers on the structure and wear resistance of polymer nanocomposites based on polytetrafluoroethylene. *Journal of Technical Physics*. 2014;84(5): 66–70. (In Russian))
- 52. Higaki Y, Ishige R, Takahara A. Fluoropolymer Surfaces/Interfaces. In: *Handbook of Fluoropolymer Science and Technology*. 2014. p.433–450.
- 53. Harris KL, Pitenis AA, Sawyer WG, Krick BA, Blackman GS, Kasprzak DJ, Junk CP. PTFE tribology and the role of mechanochemistry in the development of protective surface films. *Macromolecules*. 2015;48(11): 3739–3745. 54. Kropotin OV, Mashkov YK, Egorova VA, Kurguzova OA. Effect of carbon modifiers on the structure and wear resistance of polytetrafluoroethylene-based polymer nanocomposites. *Technical Physics*. 2014;59: 696–700.
- 55. Ebnesajjad S. Fluoroplastics, volume 2: Melt processible fluoropolymers-the definitive user's guide and data book. Oxford; 2015. 56. Будник ОА. Структурные изменения матрицы ПТФЭ-композитов. Вестник БГТУ им. В.Г. Шухова. 2015;(4): 104–112. (Budnik OA, Berladir KV, Budnik AF, Rudenko PV. Structural changes in the matrix of
- PTFE composites. *Bulletin of BSTU named after. V.G. Shukhova.* 2015;(4): 104–112. (In Russian))
- 57. Harris KL, Pitenis AA, Sawyer WG, Krick BA, Blackman GS, Kasprzak DJ, Junk CP. PTFE tribology and the role of mechanochemistry in the development of protective surface films. *Macromolecules*. 2015;48(11): 3739–3745.
- 58. Кропотин О.В. Износостойкие ПТФЭ-композиты для повышения надежности металлополимерных герметизирующих устройств изделий машиностроения. Диссертация, к.т.н. Омск; 2016. (Kropotin OV. Wear-resistant PTFE composites to improve the reliability of metal-polymer sealing devices for mechanical engineering products. Omsk; 2016. (In Russian))
- 59. Son F, Wan Q, Wang T. Effects of glass fiber and molybdenum disulfide on tribological behaviors and PV limit of chopped carbon fiber reinforced polytetrafluoroethylene composites. *Tribology International*. 2016;104: 392–401.
- 60. Wang L, Wang S, Wen D, Wang G, Yang L. The study of the composite material Go/CF/PTFE tribological property. *MATEC Web of Conferences*. 2017;130: 09005.
- 61. Негров ДА, Еремин ЕН, Корусенко ПМ, Несов СН. Влияние ультразвуковой активации на структурообразование политетрафторэтилена, модифицированного нитридом бора. *Омский научн. вестник. Сер. Авиац.-ракет. и энергетич. машиностроение.* 2017;1(2): 57–63. (Negrov DA, Eremin EN, Korusenko PM, Nesov SN. Effect of ultrasonic activation on the structure formation of polytetrafluoroethylene modified with boron nitride. *Omsk Scientific Bulletin. Aviation, missile and power engineering series.* 2017;1(2):57–63. (In Russian)) 62. Машков ЮК, Рубан АС, Рогачев ЕА, Чемисенко ОВ. Изменение структуры и износостойкости ПТФЭ-нанокомпозитов при различных методах структурной модификации. *Динамика систем, механизмов и машин.* 2017;5(2): 188–193. (MashkovYuK, Ruban AS, Rogachev EA, Chemisenko OV. Changes in the structure and wear resistance of PTFE nanocomposites with various methods of structural modification. *Dynamics of systems, mechanisms and machines.* 2017;5(2):188–193. (In Russian))

- 63. Машков ЮК, Кургузова ОА, Рубан АС. Разработка и исследование износостойких полимерных материалов. *Вестник СибАДИ*. 2018;15(1): 36–45. (MashkovYuK, Kurguzova OA, Ruban AS. Development and research of wear-resistant polymer materials. *SibADI Bulletin*. 2018;15(1):36–45. (In Russian))
- 64. Чемисенко OB. Структура и свойства нанокомпозита на основе политетрафторэтилена, модифицированного диоксидом кремния и скрытокристаллическим графитом. Диссертация, к.т.н. Омск; 2018. (Chemisenko OV. Structure and properties of a nanocomposite based on polytetrafluoroethylene modified with silicon dioxide and cryptocrystalline graphite. Omsk; 2018. (In Russian))
- 65. Okhlopkova AA, Sleptsova SA. Influence of Nanoceramics on the Properties of Polytetrafluoroethylene. *Mechanics of Composite Materials*. 2003;39: 123–128.
- 66. Okhlopkova AA, Sleptsova SA, Parnikova AG, Ul'yanova TM, Kalmychkova OY. Triboengineering and physicomechanical properties of nanocomposites based on PTFE and aluminum oxide. *Journal of Friction and Wear*. 2008;29:466–469.
- 67. Sleptsova SA, Afanas'eva ES, Grigor'eva VP. Structure and tribological behavior of polytetrafluoroethylene modified with layered silicates. *J. Frict. Wear.* 2009;30: 431–437.
- 68. Gogoleva OV, Okhlopkova AA, Petrova PN. Development of self-lubricating antifriction materials based on polytetrafluoroethylene and modified zeolites. *Journal of Friction and Wear.* 2014;35: 383–388.
- 69. Kirillina YV, Lazareva NN, Sleptsova SA, Okhlopkova AA. Effect of organomodified layered silicates on the properties and structure of polytetrafluoroethylene. *Polym. Sci. Ser. A.* 2016;58: 95–101.
- 70. Охлопкова АА, Стручкова ТС, Алексеев АГ, Васильев АП. Разработка и исследование полимерных композиционных материалов на основе активации политетрафторэтилена и углеродных наполнителей. Вестник СВФУ. 2015;4(48): 51–63. (Okhlopkova AA, Struchkova TS, Alekseev AG, Vasil'ev AP. Development and research of polymer composite materials based on the activation of polytetrafluoroethylene and carbon fillers. NEFU Bulletin. 2015;4(48): 51–63. (In Russian))
- 71. Okhlopkova AA, Struchkova TS, Vasilev AP, Alexeev AG. Studying the properties and structure of polytetrafluoroethylene filled with Belum modified carbon fibers. *Journal of Friction and Wear*. 2016;37: 529–534.
- 72. Васильев АП, Охлопкова АА, Стручкова ТС, Алексеев АГ, Иванова ЗС. Разработка антифрикционных материалов на основе политетрафторэтилена с углеродными волокнами. Вестник СВФУ. 2017;59(3): 39–
- 47. (Vasil'ev AP, Okhlopkova AA, Struchkova TS, Alekseev AG, Ivanova ZS. Development of antifriction materials based on polytetrafluoroethylene with carbon fibers. *NEFU Bulletin*. 2017;59(3): 39–47. (In Russian))
- 73. Sleptsova SA, Kapitonova YV, Lazareva NN, Makarov MM. Wear-resistant polymer composites based on polytetrafluoroethylene and layered silicates. *KnE Materials Science*. 2016;2016: 149–154.
- 74. Sleptsova SA, Okhlopkova AA, Kapitonova IV, Lazareva NN, Makarov MM, Nikiforov LA. Spectroscopic study of tribooxidation processes in modified PTFE. *Journal of Friction and Wear*. 2016;37: 129–135.
- 75. Sleptsova SA, Lazareva NN, Fedoseeva VI, Kapitonova YV, Okhlopkova AA. The Influence of Metal Cations of Mechanoactivated Bentonite on Tribochemical Processes in PTFE. *Journal of Friction and Wear.* 2018;39(6): 469–475.
- 76. Лазарева НН. *Разработка триботехнических материалов на основе политетрафторэтилена и механоактивированных слоистых силикатов Дис. канд. техн. наук.* Якутск, 2019. (Lazareva NN. *Development of tribological*
- materials based on polytetrafluoroethylene and mechanically activated layered silicates. Yakutsk; 2019. (In Russian)) 77. Vasilev AP, Struchkova TS, Nikiforov LA, Okhlopkova AA, Grakovich PN, Shim EL, Cho JH. Mechanical and tribological properties of polytetrafluoroethylene composites with carbon fiber and layered silicate fillers. *Molecules*. 2019;24(2): 224.
- 78. Gladkina NP, Sleptsova SA, Fedoseeva VI, D'yakonov AA. Effect of Silica Modified with Aluminum Ions on the Structure
- and Properties of Composite Materials Based on Polytetrafluoroethylene. *Polymer Science, Series A.* 2022;64(3):187–193. 79. Kapitonova IV, Lazareva NN, Tarasova PN, Okhlopkova AA, Laukkanen S, Mukhin VV. Morphology
- analysis of friction surfaces of composites based on PTFE and layered silicates. *Polymers*. 2022;14(21): 4658. 80. Kapitonova IV, Tarasova PN, Okhlopkova AA, Lazareva NN, Khokhlov AV. Frictional Properties and Wear of Composites Based on PTFE/Layered Silicates. *Tribology Online*. 2023;18(2): 10–17.
- 81. Ushkanov AA, Sleptsova SA, Okhlopkova AA, Lazareva NN, Khokhlov AV, Gorohova SV, Ammosova AP. The influence of basalt fiber on the properties and structure of composites based on polytetrafluoroethylene. *Composites and Nanostructures*. 2022;14(2): 117–129.
- 82. Obvintsev AYu, Serov SA, Sadovskaya NV, Khatipov SA, Bouznik VM. Mechanism of the Effect of Gamma Irradiation on the Surface Properties of Polytetrafluoroethylene. *J. Surf. Investig.* 2018;12: 988–993.
- 83. Campbell KL, Sidebottom MA, Atkinson CC, Babuska TF, Kolanovic CA, Boulden BJ, Junk CP, Krick BA. Ultralow Wear PTFE-Based Polymer Composites—The Role of Water. *Macromolecules*. 2019;52(14): 5268–5277.
- 84. Sedakova EB, Kozyrev YP. Estimation of the Tribotechnical Efficiency of Polytetrafluoroethylene Filling (review). *Journal of Machinery Manufacture and Reliability*. 2021;50(3): 236–242.

Behavior of Graphite Composites of Polytetrafluoroethylene (PTFE) Irradiated by the Electron Beam. Polymers. 2020;12(8): 1676. 86. Luo C, Pei J, Zhuo W, Niu Y, Li G. Phase transition behavior and deformation mechanism of polytetrafluoroethylene under stretching. RSC Advances. 2021;11(63): 39813 – 39820. 87. Khokhlov AV. Two-sided estimates for the relaxation function of the linear theory of heredity via the relaxation curves during the ramp-deformation and the methodology of identification. *Mechanics of Solids*. 2018;53(3): 307 – 328. 88. Хохлов АВ. Общие свойства показателя скоростной чувствительности диаграмм деформирования, порождаемых линейной теорией вязкоупругости, и существование максимума у его зависимости от скорости. Вестник Самарского гос. техн. ун-та. Сер. Физ.-мат. науки. 2020;24(3): 469–505. (Khokhlov AV. Properties of the strain rate sensitivity function produced by the linear viscoelasticity theory and existence of its maximum with respect to strain and strain rate. J. Samara State Tech. Univ., Ser. Phys. Math. Sci. 2020;24(3): 469–505. (In Russian)) 89. Хохлов АВ. Анализ общих свойств кривых ползучести при циклических ступенчатых нагружениях, порождаемых линейной теорией наследственности. Вестник Самарского гос. техн. ун-та. Сер. Физ.-мат. науки. 2017;21(2): 326–361. (Khokhlov AV. Analysis of creep curves produced by the linear viscoelasticity theory under cyclic stepwise loadings. J. Samara State Tech. Univ., Ser. Phys. Math. Sci. 2017; 21(2):326 – 361. (In Russian)) 90. Хохлов АВ. Анализ влияния объемной ползучести на кривые нагружения с постоянной скоростью и эволюцию коэффициента Пуассона в рамках линейной теории вязкоупругости. Вестник Самарского гос. техн. ун-та. Сер. Физ.-мат. науки. 2019;23(4): 671–704. (Khokhlov AV. Analysis of the bulk creep influence on stress-strain curves under tensile loadings at constant rates and on Poisson's ratio evolution based on the linear viscoelasticity theory. J. Samara State Tech. Univ., Ser. Phys. Math. Sci. 2019; 23(4): 671-704. (In Russian)) 91. Khokhlov AV. Creep and long-term strength of a laminated thick-walled tube of nonlinear viscoelastic materials loaded by external and internal pressures. *Mechanics of Composite Materials*. 2021;57(6):731–748. 92. Хохлов АВ. Особенности поведения вязкоупругопластических материалов, модели и система программ квазистатических испытаний полимеров и композитов для комплексного изучения их свойств и выбора и идентификации определяющих соотношений. Высокомолекулярные соединения. 2024;66(3): 157-211.

85. Barylski A, Swinarew AS, Aniołek K, Kaptacz S, Gabor J, Stanula A, Waśkiewicz Z, Knechtle B. Tribological and Mechanical

94. Москвитин BB. Сопротивление вязкоупругих материалов (применительно к зарядам ракетных двигателей на твердом топливе). Москва: Hayka; 1972. (Moskvitin VV. Resistance of Viscoelastic Materials (with Applications to Solid Propellant Rocket Engine Charges). Moscow: Nauka; 1972. (In Russian))

(Khokhlov AV. The Main Features of Viscoelastoplastic Materials Behavior, Models, and the System of Quasistatic Tests for Polymers and Composites aimed at All-round Study of Their Properties and Selection and Identification of Constitutive Relation. *Vysokomolekulârnye soedineniâ*. *Seriâ* C. 2024;66(3): 157–211. (In Russian)) 93. Работнов ЮН. Ползучесть элементов конструкций. Москва: Наука; 1966. (Rabotnov YN. *Creep of*

- 95. Бугаков ИИ. *Ползучесть полимерных материалов*. Москва: Hayka; 1973. (Bugakov II. *Creep of Polymer Materials*. Moscow: Nauka; 1973. (In Russian))
- 96. Findley WN, Lai JS, Onaran K. Creep and Relaxation of Nonlinear Viscoelastic Materials. Amsterdam: North Holland; 1976.
- 97. Виноградов ГВ, Малкин АЯ. *Реология полимеров*. Москва: Химия; 1977. (Vinogradov GV, Malkin AY. *Rheology of Polymers*. Moscow: Khimiya; 1977. (In Russian))
- 98. Работнов ЮН. Элементы наследственной механики твердых тел. Москва: Наука; 1977. (Rabotnov YN. Elements of Hereditary Mechanics of Solids. Moscow: Nauka; 1977. (In Russian))
- 99. Гольдман АЯ. Объемная деформация пластмасс. Ленинград: Машиностроение; 1984. (Goldman AY. Bulk Deformation of Plastics. Leningrad: Mashinostroenie; 1984. (In Russian))
- 100. Гольдман АЯ. Прогнозирование деформационно-прочностных свойств полимерных и композиционных материалов. Ленинград: Химия; 1988. (Goldman AY. Prediction of Deformation and Strength Properties of Polymer and Composite Materials. Leningrad: Khimiya; 1988. (In Russian))
- 101. Tschoegl NW. The Phenomenological Theory of Linear Viscoelastic Behavior. Heidelberg: Springer; 1989.
- 102. Drozdov AD. Mechanics of Viscoelastic Solids. New York: Wiley & Sons; 1998.
- 103. Strobl GR. *The Physics of Polymers: Concepts for Understanding Their Structures and Behavior.* Berlin: Springer; 2007.
- 104. Han CD. *Rheology and Processing of Polymeric Material, Vols. 1–2.* Oxford: Oxford University Press; 2007.
- 105. Betten J. Creep Mechanics. Berlin: Springer; 2008.

Structural Elements. Moscow: Nauka; 1966. (In Russian))

- 106. Brinson HF, Brinson LC. *Polymer engineering science and viscoelasticity*. New York: Springer; 2008.
- 107. Lakes RS. Viscoelastic Materials. Cambridge: Cambridge University Press; 2009.
- 108. Leblanc JL. Filled Polymers. Boca Raton: CRC Press; 2010.
- 109. Malkin AY, Isayev AI. Rheology: Concepts, Methods, Applications. 2nd ed. Toronto: ChemTec Publishing; 2012.

- 110. Argon AS. The Physics of Deformation and Fracture of Polymers. Cambridge: Cambridge University Press; 2013.
- 111. Bergstrom JS. Mechanics of Solid Polymers. Theory and Computational Modeling. Elsevier; 2015.
- 112. Люкшин БА, Шилько СВ, Панин СВ. Дисперсно-наполненные полимерные композиты технического и медицинского назначения. Новосибирск: Изд. СО РАН; 2017. (Lukshin BA, Shilko SV, Panin SV. Dispersed-Filled Polymer Composites for Technical and Medical Applications. Novosibirsk: SB RAS; 2017. (In Russian))
- 113. Grellmann W, Seidler S, editors. Polymer Testing. 3rd ed. Munich: Hanser; 2022.
- 114. Khokhlov AV, Shaporev AV, Stolyarov ON. Loading-unloading-recovery curves for polyester yarns and identification of the nonlinear Maxwell-type viscoelastoplastic model. *Mechanics of Composite Materials*. 2023;59(1): 129–146.
- 115. Khokhlov AV, Gulin VV. Influence of Structural Evolution and Load Level on the Properties of Creep and Recovery Curves Generated by a Nonlinear Model for Thixotropic Viscoelastoplastic Media. *Phys Mesomech.* 2025;28: 66–90.
- 116. Bkhattacharya SS, Bylya OI, Vasin RA, Padmanabhan KA. Mechanical behavior of titanium alloy Ti-6Al-4V with unprepared microstructure under jumpwise variations of the strain rate in the superplastic state. *Mechanics of Solids*. 2009;44(6): 951–958.
- 117. Кайбышев ОА. *Сверхпластичность промышленных сплавов*. Москва: Металлургия; 1984. (Kaibyshev OA. *Superplasticity of Industrial Alloys*. Moscow: Metallurgiya; 1984. (In Russian))
- 118. Padmanabhan KA, Vasin RA, Enikeev FU. *Superplastic Flow: Phenomenology and Mechanics*. Berlin: Springer; 2001.
- 119. Khokhlov AV. Fading memory effect and asymptotic commutativity under multi-step loadings in the linear viscoelasticity theory. *Composites and Nanostructures*. 2022;15(4): 208–232.
- 120. Хохлов А.В. Кривые длительной прочности нелинейной модели вязкоупругопластичности типа Максвелла и правило суммирования повреждѐнности при ступенчатых нагружениях. Вестник Самарского гос. техн. ун-та. Сер. физ.-мат. науки. 2016;20(3): 524–543. (Khokhlov AV. Long-term strength curves generated by the nonlinear Maxwell-type model for viscoelastoplastic materials and the linear damage rule under step loading. J. Samara State Tech. Univ., Ser. Phys. Math. Sci. 2016;20(3): 524–543. (In Russian))
- 121. Khokhlov AV. Hybridization of a Linear Viscoelastic Constitutive Equation and a Nonlinear Maxwell-Type Viscoelastoplastic Model, and Analysis of Poisson's Ratio Evolution Scenarios under Creep. *Physical Mesomechanics*. 2024;27(3): 229–255.
- 122. Алексеенко ВО. Износостойкие композиты на основе сверхвысокомолекулярного полиэтилена с армирующими волокнами для полимер-металлических трибосопряжений в машиностроении. Диссертация на соискание ученой степени кандидата технических наук. Томск: ТПУ; 2019. (Alekseenko VO. Wear-resistant composites based on ultra-high molecular weight polyethylene with reinforcing fibers for polymer-metal tribological interfaces in mechanical engineering. Tomsk; 2019. (In Russian))
- 123. Межгосударственный совет по стандартизации, метрологии и сертификации. ГОСТ 4648-2014 (ISO 178:2010). Пластмассы. Метод испытания на статический изгиб. Москва: Стандандартинформ; 2014. (Interstate council for standardization, metrology and certification. GOST 4648-2014 (ISO 178:2010). Plastics. Method for determining the flexural properties. Moscow: Standartinform; 2014. (In Russian))
- 124. Федеральное агентство по техническому регулированию и метрологии. ГОСТ Р 57866-2017 Композиты полимерные. Метод определения характеристик при изгибе. Москва: Стандандартинформ; 2017. (Federal agency for technical regulation and metrology. GOST R 57866-2017. Polymer composites. Method for determining flexural characteristics. Moscow: Standartinform; 2017. (In Russian))
- 125. International Organization for Standardization. ISO 14125:1998. *Fibre-reinforced plastic composites*. *Determination of flexural properties*. 1998.
- 126. American Society for Testing and Materials. ASTM D7264/D7264M-2021. Standard test method for flexural properties of polymer matrix composite materials. 2021.
- 127. Khokhlov AV, Galyshev SN, Atanov BI, Orlov VI. Effect of Delamination of Low Shear Strength Materials on Fracture and Test Results under Three-Point Bending. *Physical Mesomechanics*. 2025;28(4): 439–467.

MATERIALS PHYSICS AND MECHANICS

53 (3) 2025

УЧРЕДИТЕЛИ

Санкт-Петербургский политехнический университет Петра Великого **Адрес:** 195251, Санкт-Петербург, Политехническая ул., д. 29 Институт проблем Машиноведения Российской академии наук **Адрес:** 199178, Санкт-Петербург, Большой пр-кт В.О., д. 61

ИЗДАТЕЛЬ

Санкт-Петербургский политехнический университет Петра Великого **Адрес:** 195251, Санкт-Петербург, Политехническая ул., д. 29

Журнал зарегистрирован в Федеральной службе по надзору в сфере связи, информационных технологий и массовых коммуникаций (РОСКОМНАДЗОР), свидетельство ПИ №ФС77-69287 от 6 апреля 2017 года.

РЕДАКЦИЯ ЖУРНАЛА

Профессор, д.т.н., академик РАН, **А.И. Рудской** – главный редактор
Профессор, д.ф.-м.н., член-корр. РАН, **А.К. Беляев** – главный научный редактор
Профессор, д.ф.-м.н. **И.А. Овидько** (1961 - 2017) – основатель и почетный редактор
Профессор, д.ф.-м.н. **А.Л. Колесникова** – ответственный редактор
Профессор, д.ф.-м.н. **А.С. Семенов** – ответственный редактор
К.ф.-м.н. **Л.И. Гузилова** – выпускающий редактор
К.ф.-м.н. **Д.А. Китаева** – редактор, корректор

АДРЕС И ТЕЛЕФОН РЕДАКЦИИ

199178, Санкт-Петербург, Большой пр-кт В.О., д. 61

Тел. редакции: +7(812)552 77 78, доб. 224

E-mail редакции: mpmjournal@spbstu.ru Компьютерная верстка Л.И. Гузилова

Подписано в печать 17.10.2025 г. Выход в издания в свет: 31.10.2025 г. Формат 60х84/8. Печать цифровая Усл. печ. л. 10.0. Тираж 100. Заказ____. Цена: Бесплатно

Отпечатано в Издательско-полиграфическом центре Политехнического университета Петра Великого

Адрес: 195251, Санкт-Петербург, Политехническая ул., 29 Тел.: +7(812)552 77 17

Contact problems with a stamp in the form of an acute-angled wedge acting on an anisotropic composite layer	1-8
V.A. Babeshko, O.V. Evdokimova, O.M. Babeshko, V.S. Evdokimova	
Static and dynamic analysis of trapezoidal cantilever plates E. Kumari, B. Choudhary	9-23
Enhancing EDM performance of Monel-400 super alloy through process parameter optimization: RSM-based experimental and microstructural analysis M.R. Panda, S.K. Mishra, P.K. Sahoo	24-36
Effect of traverse speed on three-point bending behavior and surface quality of AA5083-H111 friction stir welds M.A.A. Hanifi, M. Zemri, M. Merzoug	37-47
Polymer weld characterization and defect detection through advanced image processing technique G.C. Ganesha, C. Mukti, S. Arungalai Vendan, R. Sharanabasavaraj	s 48-68
General model of the carbonate acidizing process with different injection rate R.M. Ganopolskij, K.M. Fedorov, A.E. Folomeev	69-78
Influence of alkali treatment and fiber percentage on the mechanical and thermophysical properties of gypsum composites filled with hemp fiber K. Sunil Ratna Kumar, S.B.R. Devireddy, T. Gopala Rao, B. Sudheer Kumar, K. Bala Prasad	79-93
Temperature-dependent phase leg and non-local thermoelastic damping and frequency shift in thermoelastic plates R. Kumar, P. Singhal	94-115
Creep and long-term strength of high-entropy alloys R.R. Saitova, A.R. Arutyunyan	116-121
Evaluating the impact of functionalized graphene integration on thermal properties of CFRP composites D.N. Choudhury, S.K. Panda	122-139
Structural and thermal changes in the polyaniline lead sulphide nanocomposite J.B. Bhaiswar, S.P. Dongre, D. Meghe	140-148
Effect of electromagnetic waves on the thermoelastic Hookean unbounded domains based on fractional Fourier law N. Samir, M.A. Abdou, E. Awad	149-164
Elastic deformation and elastic wave velocity in metals (Au, Cu) and interstitial alloy (CuSi) with FCC structure Q.H. Nguyen, K.V. Tran, S.G.K. Quach, Q.T. Doan, N.P.A. Nguyen, T.S.M. Nguyen, D.H. Nguyen, A.T. Tr	165–176
Комплексное исследование вязкоупругопластических свойств нанокомпозитов с повышенной износостойкостью на основе Фторопласта-4. Часть 1 А.В. Хохлов, А.А. Охлопкова, С.А. Слепцова, Н.Н. Лазарева, П.Н. Тарасова, А.В. Бабайцев, А.В. Шапорев, В.В. Гулин	177-218

